Du photon unique aux applications

R. Barbier

Habilitation à Diriger des Recherches

Délivrée par

L'UNIVERSITE CLAUDE BERNARD LYON 1

Soutenance le 7 Mai 2012

Par

Rémi BARBIER

DU PHOTON UNIQUE AUX APPLICATIONS

A soutenir devant la commission d'examen :

Président du Jury   **Monsieur Stavros Katsanevas**

Rapporteurs   **Monsieur Pierre Antilogus**
Monsieur Thierry Gys
Monsieur Pierre Magnan

Examinateurs   **Monsieur Christophe Dujardin**
Monsieur Christian Morel

Lyon 1

IN2P3
Les deux infinis

Du photon unique aux applications

Rémi BARBIER

Université Claude Bernard - Lyon I

29 mai 2012

Liminaires

Dix neuf années dont quinze en tant que Maître de conférences constituent mon expérience de recherche. Je compte trois mobilités thématiques.

La première a été mon passage de la physique nucléaire théorique à l'analyse de données en physique des particules sur l'expérience DELPHI au CERN.

La deuxième correspond à mon implication dans la R&D sur les détecteurs. Ce changement a été effectué en deux temps. Tout d'abord je me suis consacré au développement d'une chaine de détection de deux modules de μTEP. Puis j'ai initié une activité de R&D sur les CMOS électro-bombardés.

Mon activité de responsabilités a démarré relativement tôt puisque j'ai été sollicité pour prendre la coordination vacante d'une Action Concertée Incitative (ACI) technologies pour la santé en 2002 qui portait entre autres sur des MaPMT, des HPD et des APD pour l'imagerie du petit animal via la tomographie par émission de positons.

Ce projet comportait une action de transfert de technologie en lien avec un financement régional. Cela a été l'occasion de me confronter assez tôt à la problématique du transfert de propriété intellectuelle du secteur académique au secteur privé.

Mon activité de R&D sur les ebCMOS n'était pas reconnue comme une recherche "officielle" au départ, en 2003, et ce n'est que grâce aux soutiens entre autre de Stavros Katsanevas et des directeurs successifs Jean-Eudes Augustin et Yves Déclais que j'ai pu monter progressivement ce groupe au sein de l'IPNL. Le poids induit par ma collaboration sur les capteurs CMOS avec l'équipe de Marc Winter a très certainement dû jouer un rôle important vis à vis de la direction de l'IN2P3.

Il y a quand même eu des passages difficiles, sans financement et sans vision claire sur les technologies disponibles. C'est avec le groupement d'intérêt scientifique, GIS PHOTONIS IN2P3 et notre collaboration sur le prototype ebMIMOSA5 avec l'IPHC de Strasbourg que l'activité a réellement décollé.

Lorsque j'observe des images de milliers de spots suivis en parallèle à 500 Hz par le logiciel temps réel avec une précision intra-pixel sur leur position calculée alors que ceux-ci reçoivent en moyenne moins de un photon par millième de seconde, j'apprécie le chemin parcouru.

Je retiendrai de mon expérience, que la R&D est avant tout une aventure humaine et un fil conducteur qui se révèle au fur et à mesure. Le travail en équipe est très enrichissant et c'est toujours avec une grande joie que je vois un membre de l'équipe donner par son travail du corps à notre projet et nous fait avancer dans nos objectifs.

La construction de la "petite" histoire, sous la forme d'un mémoire est irrémédiablement faussée en rapport aux investissements de chacun...

... reste le fil conducteur : la "vision" aux photons uniques.

Il deviendra surement une réalité dans les années à venir.

Résumé

Ce mémoire, rédigé dans le but d'obtenir le diplôme d'habilitation à diriger des recherches, reprend sous deux formes différentes mes dix neuf années de recherche.

Les deux premiers chapitres traitent de mon activité la plus récente de R&D sur les capteurs CMOS électro-bombardés (ebCMOS) et a nécessité un travail de synthèse et de rédaction sur ce domaine de recherche. Il existe en effet peu d'ouvrages ou d'articles de référence sur les ebCMOS et leur applications, autres que ceux portant sur la vision nocturne.

Ainsi, le premier chapitre concerne, d'une part, l'état de l'art en 2012 sur les photo-détecteurs de photons uniques et d'autre part une revue détaillée qui couvre tous les aspects du capteur ebCMOS. J'aborde tout d'abord les performances intrinsèques de l'ebCMOS puis traite les applications envisagées. Les perspectives d'évolution de ce capteur sont abordées en détail par composant technologique.

Le deuxième chapitre traite des différents aspects de l'activité de R&D de l'équipe et des services techniques associés : les bancs de caractérisations, les prototypes produits, les systèmes d'acquisition Gbits Ethernet, les logiciels de traitement en ligne et hors ligne et enfin les applications envisagées et testées. Ce chapitre se termine par les publications de référence des deux prototypes produits, ebMIMOSA5 et LUSIPHER, afin de fournir au lecteur les résultats chiffrés des performances atteintes.

Le troisième chapitre contient les travaux de recherche antérieurs à la création du groupe ebCMOS. Il s'agit de mon activité de R&D sur des systèmes de détection pour la micro Tomographie par Emission de Positons, μTEP, et surtout de mon travail d'analyse de données dans l'expérience DELPHI pour la recherche de la supersymétrie suivant les modes violant la R-parité par des termes de couplages trilinéaires UDD. Les partenaires supersymétriques recherchés ont été les neutralinos et les charginos dans un premier temps puis les squarks et les sleptons dans un deuxième temps. Les diagrammes d'exclusion dans le cadre de modèle de supersymétrie en sont les principaux résultats.

Pour chacune des activités menées, une introduction présente ce qu'a été mon investissement vis à vis du domaine de recherche, les objectifs de départ et les résultats obtenus dans le contexte de l'époque. Les principales publications liées à ces recherches suivent la présentation qui en a été faite. L'article collectif publié dans *Physics Report* sur la supersymétrie violant la R-parité n'est pas inclus en totalité, car trop volumineux. J'ai simplement introduit le chapitre 7 où réside ma principale contribution à l'effort collectif.

Liste des tableaux

Table des figures

Table des matières

Introduction

L'œil humain pèse environ 7 grammes, a une longueur d'environ 2,5 cm et contient de l'ordre de 10^8 photo-récepteurs composés de cônes pour la vision de jour et de bâtonnets pour la vision de nuit. Le nerf optique est formé de 10^6 axones ganglionnaires connectés aux nombreuses cellules bipolaires qui récoltent les signaux électriques générés par les photo-récepteurs. La compression des données analogiques est déjà à ce niveau d'un facteur cent ! Les cônes et les bâtonnets sont adaptés à des conditions d'éclairement et des scènes différentes.

Les bâtonnets sont achromatiques, sensibles à quelques photons, ont une résolution spatiale faible, sont plus bruyants, ne sont pas présents dans la fovéa, ont des temps de réponse lents et sont dédiés à la détection de mouvements.

Les cônes sont optimisés sur trois couleurs (B,V,R, trois pigments), sont dix fois moins sensibles que les bâtonnets, ont une bonne résolution spatiale, sont rapides et peu bruyants, sont concentrés dans la fovéa et perçoivent des variations rapides de stimuli. L'œil et le cerveau humain est un système de photodétection polyvalent d'une impressionnante complexité, susceptible d'une grande qualité de traitement de l'information bas niveau lui facilitant l'interprétation et l'anticipation.

A la lecture de ces quelques lignes descriptives de l'œil humain, on ne peut s'empêcher de penser au concept du capteur d'images équivalent basé sur les technologies de l'électronique 3D, association de substrats hétérogènes par via au travers du silicium.

Nous sommes capables de concevoir et de fabriquer des capteurs d'images qui dépassent les performances de l'œil dans des domaines précis de la photodétection : sensibilité, vitesse, longueur d'onde. Mais nous ne sommes pas encore parvenus au niveau de sa complexité, éternel dialogue entre le digital binaire et l'analogique.

Pourquoi la sensibilité aux photons uniques ?

Si l'on oublie momentanément la dualité onde-corpuscule on peut penser que le détecteur parfait est celui qui est capable de détecter, c'est-à-dire de localiser parfaitement et de temporaliser tous les photons qui le pénètrent sans ajouter de bruit. L'avancée des connaissances dans le domaine de la photodétection, comme celle des domaines scientifiques qui utilisent les photons du domaine IR-NIR-VIS-UV, tendent irrémédiablement, de par l'augmentation de la résolution temporelle souhaitée, vers ce quantum d'information : le photon.

Le comptage très rapide et résolue de photons uniques offre de nouvelles fonctionnalités d'imagerie comme par exemple :

– de descendre à une résolution temporelle inférieure à l'échelle temporelle du phénomène physique ou biologique étudié.
– de pouvoir multiplier le nombre d'échantillons pour un temps donné à un coût donné (bio-puce haut-débit).
– de traiter l'information photonique à une résolution temporelle inférieure à celle nécessitée par l'humain pour lui rendre une image digitale (traitée) à son échelle temporelle (bruit, quantification, position intermédiaire, dynamique).
– d'utiliser plusieurs bandes passantes de longueur d'ondes ou plusieurs distances focales pour rendre une image à l'échelle temporelle humaine plus précise et contenant plus d'information.
– de pratiquer l'imagerie quantique sub-shot noise [1].

Cette quête du photon unique reste cependant un peu contre-intuitive car l'information sur un émetteur, sa position par exemple, est d'autant plus précise que le nombre de photons détectés est grand $(1/\sqrt{n_\gamma})$. C'est bien avec ce dilemme que la R&D que je mène depuis une dizaine d'années doit vivre. Mais ce n'est pas une raison suffisante pour éviter d'étudier l'imagerie sous l'angle de ces conditions extrêmes, c'est-à-dire, quand ce n'est plus une succession d'images mais de points. Nous sommes en quelques sortes les ancêtres du concept futuriste présenté par E. Fossum sur le "Quantum Imaging System" et notamment de ses "jots"[1].

La notion de suivi spatiotemporel d'émetteurs de photons en mouvement puise dans cette problématique. Quelle est l'information souhaitée ? Nous recherchons la meilleure mesure de la position possible de l'émetteur pour une vitesse donnée sachant que si celle-ci augmente, le nombre de photons reçus moyen par temps d'intégration diminue et et se rapproche de l'unité.

Par exemple, le mouvement Brownien avec un coefficient de diffusion de 1 $\mu m^2 s^{-1}$ nécessite des temps d'intégration inférieurs à 5 ms en microscopie de fluorescence super-résolue si l'on veut éviter la perte de résolution due au déplacement de la source.

Pourquoi le CMOS électro-bombardé (ebCMOS) est un excellent candidat pour localiser et compter les photons uniques ?

Le capteur ebCMOS n'est pas un concept de détecteur nouveau et a déjà existé sous la forme de l'ebCCD et surtout des HPD (Hybrid Photon Detector) développées dans les années 2000 sous l'impulsion du CERN. Le principe de la sensibilité aux photons uniques allié à la résolution temporelle était présent dans ce concept d'imagerie Cerenkov. Seule la résolution spatiale manquait pour de l'imagerie haute résolution. Il est évident que cette R&D sur les ebCMOS n'aurait jamais eu lieu sans ces travaux pionniers sur les HPD.

---

1. Iota : la plus petite

Grâce aux évolutions technologiques récentes, l'ebCMOS devient particulièrement intéressant pour de l'imagerie aux photons uniques.

Il en possède dans tous les cas les bonnes propriétés :
– La rapidité du capteur CMOS,
– La linéarité du gain due au champ électrique,
– Le traitement en ligne hautement parallélisable,
– Le faible bruit de comptage d'obscurité,
– La fonction d'étalement du capteur permettant une résolution intra-pixel.

Nous avions à l'esprit à cette époque qu'avec la résolution spatiale en plus, l'ebCMOS pouvait être un excellent candidat à l'imagerie de photons uniques pour la biologie. Restait encore a en faire la démonstration en fabriquant un prototype. Il nous manquait "simplement" le fabriquant de tube et de cathode ainsi que le concepteur de la puce et le partenaire capable de fournir l'amincissement souhaité !

C'est l'avènement des CMOS amincis et passivés par la face arrière dédiés à la détection de particules chargées, qui a donc joué le second rôle moteur. L'équipe de Marc Winter est aussi à l'origine de la réussite de ce projet. Une dernière raison extra-scientifique qui a joué un rôle évident est la présence de l'ebCMOS dans la programmation FELIN de la DGA.

Le détecteur ebCMOS : un projet de R&D ?

Le projet ebCMOS n'est pas devenu subitement un projet englobant l'ensemble des activités actuelles de l'équipe représentées schématiquement dans la Figure 1. J'ai en effet débuté en 2001 cette activité en essayant, avec mes propres moyens, de lire le MIMOSA1 qui m'avait été fourni sans trop de documentation par l'IPHC.

Puis des moyens de caractérisation par bombardement électronique ont été mis au point avec au départ peu de succès. En effet, en plus de n'avoir aucun système d'acquisition fiable, les différentes couches métalliques et d'oxyde en face avant étaient bien trop épaisses pour permettre une détection électronique par la face avant. Cela, je ne l'ai su que bien plus tard. C'est avec le MIMOSA5 aminci que tout à réellement décollé, tant du point de vue de l'efficacité des collaborations que des moyens techniques et humains.

La suite n'est qu'une succession de "projets", de réponses à des appels d'offre avec plus ou moins de succès (plutôt moins que plus d'ailleurs) et de collaboration permettant d'aboutir aux objectifs initiaux. Cette démarche de R&D a donc abouti au projet LUSIPHER, acronyme de "Large-scale Ultra-fast SIngle-PHotoelectron recordER qui est illustré au travers de ses performances dans le synoptique de la Figure 2.

Comme cela est visible dans la Figure 1, la suite logique de la réussite dans la réalisation du prototype était et reste de démontrer son intérêt dans les différentes applications qui a priori nécessitent vitesse et sensibilité. C'est la phase que nous sommes en train de terminer cette année 2012 avec un retour scientifique en termes de collaborations et de publications dans des domaines très variés. Je souhaite que l'équipe ebCMOS arrive à publier de manière significative dans les domaines de l'optique adaptative, de la vidéo-microscopie, de la bio-physique avec l'idée de super-résolution sur le mouvement Brownien et de l'imagerie temps réel et haut-débit.

En ce qui concerne les collaborations avec des champs disciplinaires différents de
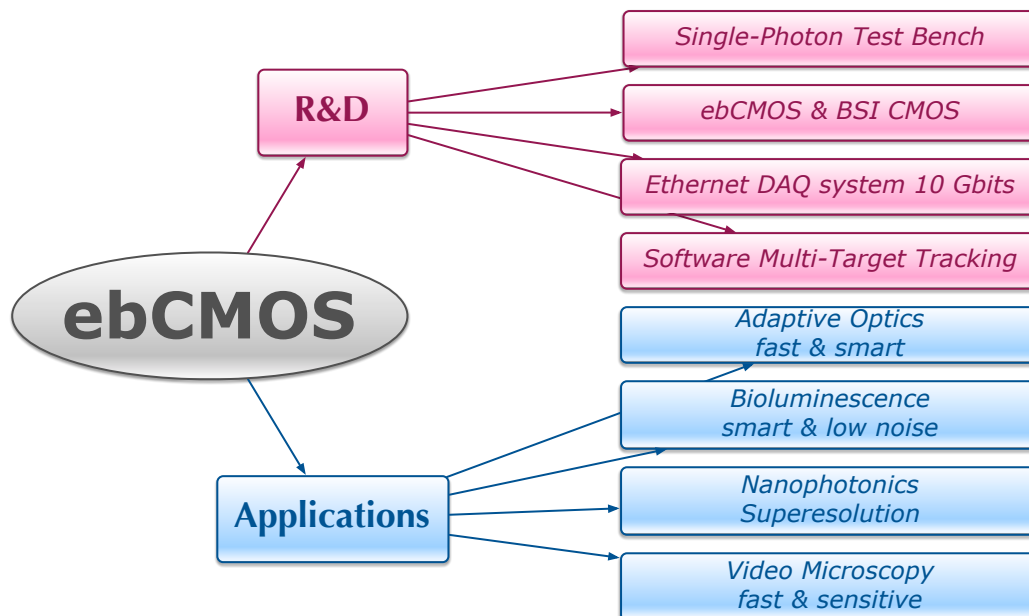
FIGURE 1 – Activités du groupe ebCMOS
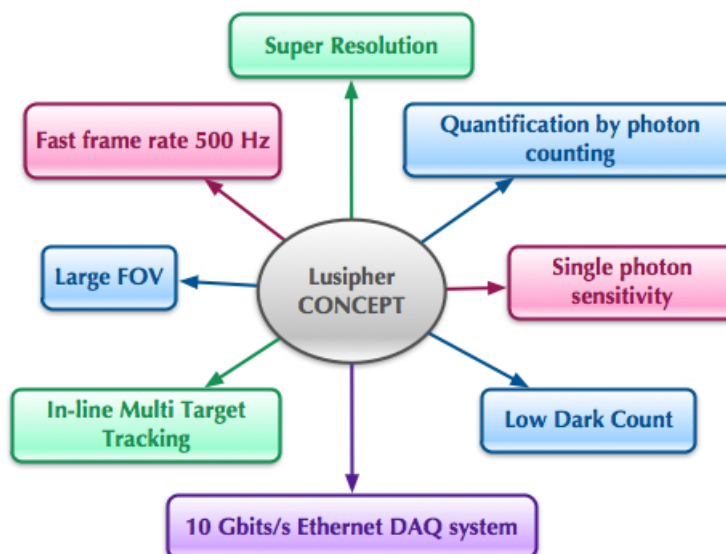
FIGURE 2 – Synoptique du concept LUSIPHER.

celui de la R&D , il est important que nos publications sur le prototype soient suffisamment abouties au niveau des méthodes avant la collaboration scientifique. Il est toujours délicat de faire valoir huit ans de R&D dans l'esprit de physiciens ou de biologistes concentrés sur leur problématique scientifique.

Contenu du mémoire

La difficulté rencontrée dans la rédaction de ce mémoire est qu'il doit relater mon activité de recherche depuis mon travail de doctorat. Celle-ci, du fait de ma mobilité thématique a subi de sérieux virages et j'ai donc opté pour une présentation plus détaillée de mes 9 dernières années de R&D sur l'ebCMOS. Cette thématique constitue la majeure partie rédigée de mon mémoire et correspond aux deux premiers chapitres.

Le premier introduit la notion de capteur de photons uniques et d'imagerie aux photons uniques avec une discussion détaillée de l'ebCMOS. Le deuxième chapitre est une présentation des activités du groupe ebCMOS d'un point de vue thématique et chronologique.

J'ai dans un troisième chapitre présenté mes activités antérieures dont j'ai joint les principales publications. J'aurai pris soin auparavant de décrire brièvement le contexte et le travail personnel fourni.

Chapitre I

Détection de photons uniques

A   Etat de l'art

A.1   Détecter le photon

A.1.1   Position du problème

L ES photons du spectre visible ont des énergies de l'ordre de l'électron-volt. Ainsi tout détecteur sensible aux photons uniques, assujetti à un effet photoélectrique dans le matériau, disposera d'une énergie du même ordre de grandeur pour produire un signal de détection identifiable. Il s'en suit une lecture du porteur de charge (électron ou trou) particulièrement difficile sans un système de multiplication des porteurs primaires à moins de bénéficier d'un système de lecture dont le bruit associé est très inférieur en moyenne à l'électron. Cet exercice devient d'autant plus difficile qu'il est nécessaire de le répéter pour des millions de pixels.

Les technologies standards dont nous disposons et les conditions d'utilisation visées (vitesse de lecture, température et nombre important de pixels) nous poussent à privilégier pour notre R&D la voie de la multiplication avant lecture. Cela ne signifie pas que la voie du très bas bruit est à abandonner.

Avec l'avènement des CMOS scientifiques (sCMOS), qui proposent des bruits en moyenne inférieurs à 1 e- RMS, le domaine du bas bruit est en pleine effervescence et devient un milieu ou la compétition est rude. Cependant les performances de bruit nécessaires à l'imagerie par photons uniques ne sont pas encore atteintes.

La conversion du photon en électron peut se produire de manière interne ou externe au volume de photo-conversion selon que le porteur de charge créé par effet photo-électrique est émis dans le vide ou reste dans le matériau de conversion. On peut classer arbitrairement les détecteurs de photons uniques en deux catégories : les détecteurs de type tube à photo-cathode et les détecteurs à état solide. Le processus de multiplication (gain) avant lecture sera différent suivant la catégorie du détecteur.

Le détecteur à l'état solide est reconnu comme supérieur dans son efficacité de photo-conversion, mais il a en contrepartie des faiblesses intrinsèque à son processus de

multiplication, qui se concrétisent par des facteurs de bruit en excès (Excess Noise Factor, ENF) plus importants ou par des inefficacités de collection de porteurs ou d'ionisations secondaires (ionisations par impacts).

C'est bien dans le processus de détection dans son ensemble, de la photo-conversion au comptage proprement dit, qu'il est nécessaire d'évaluer les performances de chacun des détecteurs de photons uniques. Malheureusement, trop souvent les acteurs de ces développements oublient cet impératif d'exhaustivité en se focalisant sur la partie du processus qui les avantage en termes de performances. J'espère éviter cet écueil dans ce mémoire.

Notons également que les inconvénients de chacune des catégories de détecteurs ont des implications plus ou moins dommageables en fonction de l'application photonique envisagée. La difficulté réside finalement dans la compréhension de l'impact de chacune des étapes de la photodétection sur la mesure souhaitée.

Le panorama devient plus complexe si l'on considère les détecteurs hybrides qui associent la photo-conversion par une photo-cathode à la détection électronique par un capteur solide (silicium). Cette catégorie de détecteurs hybrides est généralement classée dans la catégorie tube à vide bien qu'elle emprunte de nombreuses spécificités de l'autre catégorie. Elle tente en effet d'allier les avantages de chacun sans trop prendre de leurs défauts. Le détecteur ebCMOS en est une bonne synthèse.

A.1.2   Les tubes à photo-cathode et les capteurs à état solide

Il n'existe pas de classification universelle des photodétecteurs (par processus, par application, par gamme d'énergie ...). Notre choix suit, dans un soucis de synthèse, la présentation du paragraphe précédent. En découpant le processus global de la détection du photon, de la photo-conversion à l'identification numérique du photon, nous pouvons identifier quatre étapes, quelque soit le photodétecteur :

1. la photo-conversion
2. la collection des porteurs de charges primaires par l'étage de multiplication
3. la multiplication de la charge primaire en charges secondaires (gain de multiplication)
4. la conversion des porteurs de charges secondaires en signal électrique mesurable avec amplification (lecture analogique puis numérique)

Pour chaque étape, il est nécessaire de considérer l'efficacité du processus suivant deux critères : la perte du signal physique et l'association de bruits au signal physique. La figure I.1 illustre notre propos par quelques exemples donnés pour chaque critère et pour chaque étape.

A.2   La détection du photon pas à pas

Revenons sur quelques notions essentielles des photodétecteurs introduites dans la Figure I.1 afin d'en faire ressortir les critères importants auxquels doivent être soumis les détecteurs de photons uniques.
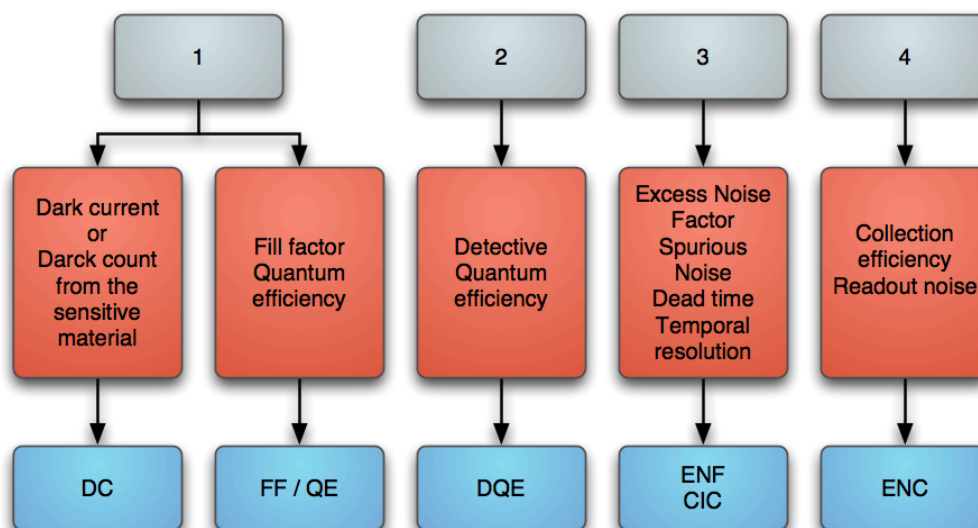
FIGURE I.1 – La détection du photon découpée en quatre étapes (photo-conversion, collection, multiplication, lecture). Exemple de bruits et de pertes de signal associées.

A.2.1   L'efficacité Quantique (QE)

Elle est le premier paramètre contraignant les performances d'un photodétecteur. Elle n'a malheureusement pas toujours la même définition selon les détecteurs. La définition choisie dans ce document est le rapport entre le nombre de porteurs de charge générés par effet photoélectrique et le nombre de photons incidents. L'efficacité quantique dépend essentiellement du matériau sensible utilisé et de sa section efficace photo-électrique. Les trois chiffres clés concernant les efficacités quantiques sont grossièrement 20%, 40% et 80%, correspondant respectivement aux photo-cathodes de seconde génération (cathodes à métaux alcalins), de troisième génération (semi-conducteur de type AsGa) et aux détecteurs solides en général à base de silicium.
Ainsi, c'est avec un facteur deux ou quatre en leur défaveur que les détecteurs à photo-cathode entament le processus de photodétection. Nous pensons que les pertes et les bruits induits par les étapes successives du processus compensent ce déséquilibre en faveur du silicium dans la mesure ou le régime de fonctionnement reste de l'ordre d'une trentaine de photons.

A.2.2   Le facteur de remplissage (FF)

Il intervient juste en amont de la probabilité de photo-conversion puisqu'il concerne le rapport entre la surface sensible et la surface totale de la cellule de détection (pixel en général). Il est parfois multiplié directement par la probabilité de photo-conversion pour donner une QE effective. Ce paramètre est évidemment relié à la taille de gravure de la technologie utilisée pour la conception des pixels. On remarque que le plus souvent le

gain en taille est compensé par une augmentation de la complexité et donc du nombre de transistors dans le pixel (3T à 8T). Le facteur de remplissage entre particulièrement en compte dans les structures à pixels où l'électronique de lecture est intégrée. C'est le cas par exemple pour les matrices de SPAD (Single Photon Avalanche Diode) ou les capteurs CMOS illuminés par la face avant avec des FF de l'ordre de 20% et 50%, respectivement.

A.2.3   L'efficacité de collection de charges (CCE)

Il existe pour les détecteurs silicium une perte d'efficacité après la photo-conversion, au niveau de la collection des charges primaires qui contribuent au processus de multiplication ou de génération du signal électrique mesurable. C'est pourquoi l'efficacité quantique des CCD est parfois donnée en prenant en compte les pertes d'efficacité dues à la collection de charge et au facteur de remplissage. Remarquons que cela ne simplifie pas toujours une comparaison honnête entre les photodétecteurs.

A.2.4   L'efficacité de détection du photon (PDE)

Nous pensons qu'il est préférable d'utiliser dans le régime du photon unique la notion d'efficacité de détection du photon plutôt que la QE effective. La PDE est définie généralement (cela peux varier suivant les articles) comme le rapport entre le nombre de photons ayant conduit à un signal identifiable à un photon, i.e, bien au dessus de la valeur du bruit de lecture (valeur à préciser en fonction de la pureté et de l'efficacité souhaitée), et le nombre de photons incidents sur la surface de détection. La PDE prend ainsi en compte tous les facteurs potentiels de perte de signal tout au long du processus de détection :

- efficacité quantique

- facteur de remplissage

- efficacité de collection des charges primaires

- efficacité de multiplication des charges primaires en charges secondaires

- efficacité de conversion des charges secondaires en un signal électrique mesurable supérieur au bruit de lecture ($> 3 - 5\sigma$).

C'est ainsi que nous pouvons aisément vérifier qu'en mode comptage de photons un emCCD BSI (Back Side Illuminated) bien que possédant une efficacité quantique de 95% montre une PDE de l'ordre de 40%.

A.2.5   Le processus de multiplication (G et ENF)

Un aspect important de la détection au photon unique est l'impact du processus de multiplication (G ou M) sur la quantification du signal reçu. Ce processus de multiplication est par nature stochastique. Le facteur de bruit en excès (ENF) associé au processus de multiplication peut jouer un rôle important si la charge récoltée en signal de sortie (unité de convertisseur analogique numérique, ADCU) sert de variable soit pour quantifier directement un processus physique soit pour entrer indirectement comme un facteur de

pondération dans une mesure physique. Le bon exemple est la mesure de la position d'un émetteur par le calcul du centre de gravité des charges déposées. Nous reviendrons sur ce point très important dans la suite de ce mémoire.

A.2.6 Le bruit de comptage d'obscurité (DC)

La dernière notion importante, que nous mentionnons dans cette brève introduction sur les paramètres essentiels du processus de détection du photon unique, est celle du bruit de comptage d'obscurité. Il est principalement lié au choix du processus de multiplication. En effet, introduire un processus de multiplication dont l'ordre de grandeur est la centaine, introduit nécessairement une génération "spontanée" de charges secondaires similaires à celles obtenues pour un véritable photon. Nous le nommerons comptage d'obscurité ou DC par la suite puisqu'il est obtenu par une chaine de comptage sans aucune source de lumière.

Le taux de comptage d'obscurité de certains détecteurs peut s'avérer prohibitif pour certaines applications nécessitant la mesure de signaux aux photons uniques. Nous pouvons légitimement nous poser la question de la pertinence d'un détecteur sensible aux photons uniques qui présente des taux de comptage d'obscurité de l'ordre du MHz, produits par quelques centaines de pixels si la source de photons émet dans un régime Poissonien (μ de l'ordre de quelques unités). Je pense aux matrices de SPAD, les SiPM.

A.2.7 L'association de la sensibilité et de la vitesse

Les exigences sur les performances peuvent être durcies en imposant aux photodétecteurs d'être :

- rapides : fréquence de trames supérieure à 250 Hz,

- précis : résolution micrométrique,

- à large champ de vue : $\sim$1cm^2 pour 1Kx1K pixels,

- sans temps mort : cycle utile de 100%.

Dans ce cas il est nécessaire de passer les différentes étapes de la photodétection au crible de ces critères de performances qui peuvent être incompatibles suivant les processus de détection, de multiplication et de lecture envisagés.

Les diagrammes I.2 et I.3 proposent une vue d'ensemble des photodétecteurs au travers des quatres étapes de la photodétection présentées dans ce chapitre. Ces deux synoptiques permettront d'éclaircir la discussion sur l'état de l'art à venir.

A.3 Les diodes à avalanches pour photons uniques : matrices de SPAD

La voie de la R&D sur les processus d'avalanche dans une jonction pn par l'application d'un champ électrique élevé n'est pas nouvelle puisque déjà explorée dans les années 60-70 par des pionniers tels McIntyre et Haitz [2]-[3]-[4]. Pour une valeur de champ électrique
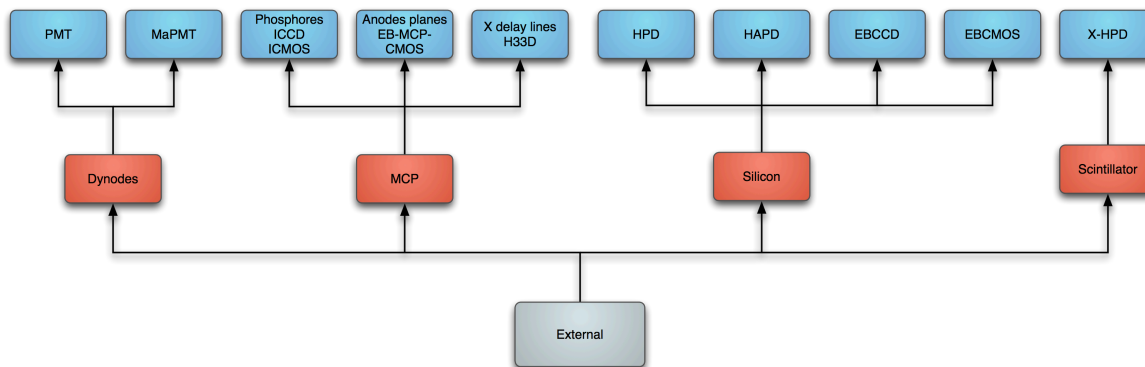
FIGURE I.2 – Classification des photodétecteurs de type tube à photo-cathode par les différentes étapes du processus de détection : niveau gris pour la photo-conversion externe, niveau rouge pour le processus de multiplication et le niveau bleu pour les différents types de lecture des charges secondaires.
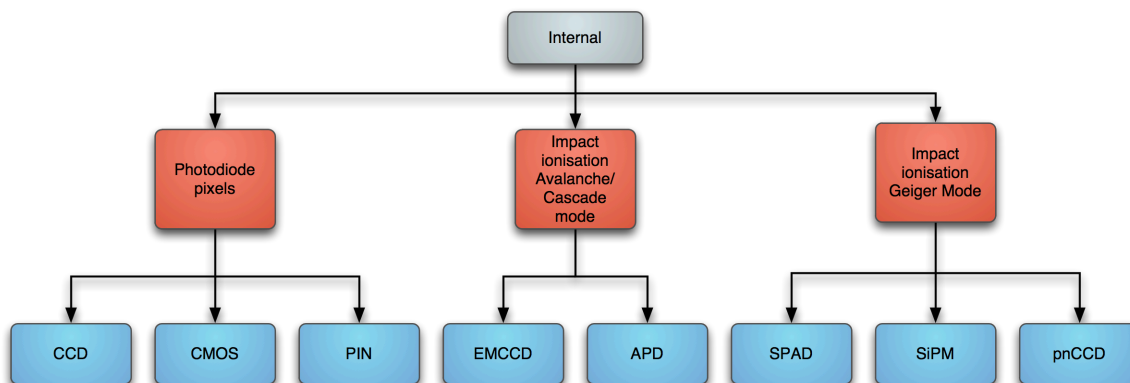
FIGURE I.3 – Classification des photodétecteurs de type état solide par les différentes étapes du processus de détection : niveau gris pour la photo-conversion interne, niveau rouge pour le processus de multiplication et le niveau bleu pour les différents types de lecture des charges secondaires. Principe de photodétection pour les détecteurs à l'état solide.

légèrement supérieure à la valeur de claquage (survoltage de quelques volts), la jonction fonctionne en mode Geiger en présence d'un porteur de charge photo-converti.

C'est sous l'impulsion de groupes de recherche russes que les performances de matrices de SPAD ont fortement progressé pour devenir des photodétecteurs qu'ils ont nommés SiPM pour "Silicon PhotoMultiplier". On trouve dans la littérature autant d'acronymes que de groupes travaillant sur le sujet. Une des difficultés du mode Geiger est la mise en œuvre du quenching qui était passif (résistance en série) au commencement de cette R&D .

Parmi les évolutions sur le quenching passif nous remarquons le travail intéressant de l'équipe MPI Munich qui développe avec succès un processus de fabrication où la résistance de quenching est intégrée au bulk (dopé à 10^{12}) grâce à une région déplétée entre les zones de fort champ [5]. Les points forts de cette technologie sont la dureté aux radiations, la bonne PDE et le coût. C'est un développement à suivre de prêt (voir la publication également d'un groupe de Pékin [6]).

Depuis quelques années de nombreux efforts se sont portés sur le quenching actif avec l'utilisation des technologies CMOS pour développer une véritable électronique de quenching. Je pense ici aux travaux de E. Charbon [7] ou des équipes italiennes travaillant avec STM [8].

Nous voyons apparaître dans ce que l'on nomme "Digital SiPM", i.e. une nouvelle génération de photodétecteurs qui utilisent la technologie CMOS standard afin d'élaborer un système d'acquisition embarqué sur puce dont la sensibilité est le photon unique. Il y a notamment des travaux intéressants d'une équipe de Milan (imagerie active) et surtout de la Start-Up Digital-SiPM de Philips [9]. Des applications à l'imagerie TEP sont envisagées. Le quenching actif offre une amélioration importante des performances notamment grâce à la possibilité de masquer les pixels bruyants.

Pour fixer les ordres de grandeur on retiendra que le DC est de l'ordre de la centaine de kHz/mm² voir le MHz/mm² à 300 K. La taille des pixels reste encore importante comparée à celle des capteurs d'images CMOS standards. Les facteurs de remplissage obtenus sont très variables et les PDE qui en découlent sont de l'ordre de 20%. C'est le prix à payer de l'intégration !

De toute évidence, la réduction des pas de gravures proposée par les technologies CMOS et la possibilité d'utiliser des tensions "hautes" (5-6V en technologie 0.18 μm), n'a pas fini d'offrir de nouvelles possibilités aux concepteurs pour améliorer ces performances de résolution spatiale. Cela s'effectuera certainement au détriment du bruit DC car celui-ci augmente avec le nombre de cellules SPAD.

Le courant noir peut être diminué (suppression par état logique des SPADs bruyants de la matrice) mais reste néanmoins prohibitifs pour des applications optiques aux photons uniques. Un refroidissement du capteur peut être envisagé pour réduire ce DC mais rend plus complexe l'intégration du capteur. Le problème de la diaphonie optique (photon UV) nécessiterait un cloisonnement des pixels pour éviter les doubles comptages.

Il est également important de considérer le flux de photons incidents des applications visées, car la dynamique de ce type de capteur est liée aux nombre de SPAD dans la matrice, qui n'ont du fait du mode Geiger utilisé, aucune possibilité de différencier l'arrivée

de un ou plusieurs photons dans le pixel pendant le temps de quenching. La seule solution dans ce cas est l'augmentation de la fréquence de lecture des SPAD qui évidemment ne favorise pas une augmentaîon de la surface sensible conditionnée par une augmentation du nombre de pixels.

En conclusion, ce domaine très actif est à notre avis prometteur pour l'éclosion de nouveaux concepts de détection aux photons uniques. Cette remarque est d'autant plus justifiée que ces technologies CMOS SPAD seront très certainement associées d'ici quelques années aux technologies d'intégration 3D. Dans ce cas, de nombreuses difficultés liées à l'intégration et à la miniaturisation seront surmontées. Nous essayerons, tant que possible, de prendre en considération ces éléments d'avenir prometteurs dans le choix de nos programmes de R&D futurs.

A.4   Les capteurs d'images bas bruit en CMOS : sCMOS

Les capteurs d'images CMOS étaient considérés comme beaucoup plus bruyants que les capteurs CCD (FPN du fait des SF). Ils étaient "restreints" principalement à des marchés de gros volume de type "mobile phone" ou de vision industrielle. L'évolution récente des technologiques CMOS et des conceptions d'architecture pixels tend à réduire cet écart voir inverser la tendance.

Nous voyons apparaître sous l'impulsion des travaux de B. Fowler (Fairchild Imaging) des CMOS bas bruits dits "scientifiques" ou sCMOS [10]. Il semble maintenant que les objectifs de développement résident dans la combinaison d'architecture à la fois bas bruit et de grande gamme dynamique. Cette évolution semble néanmoins provenir au départ de R&D pour la vision nocturne.

Les sCMOS ont des pixels au minimum à quatre transistors avec une architecture pixel de type "pinned photodiode" présentant un bruit temporel moyen de lecture de l'ordre de l'électron. Ce niveau de bruit ne donne pas complètement la sensibilité aux photons uniques mais l'ordre de grandeur qui vient d'être gagné offre déjà de nombreuses possibilités d'applications tout en conservant les points forts des CMOS que sont la parallélisation par colonne des sorties, la vitesse de lecture, la faible consommation et la possibilité de développer des systèmes sur puce.

Nous pensons qu'avec ces niveaux de bruits le sCMOS se place en concurrence directe des intensificateurs d'images et des CCD refroidis. Ce n'est pas surprenant de voir PHOTONIS sortir en 2012, via une filiale aux USA, une caméra sCMOS bas bruit nommée Xscell pour le marché scientifique (avec un argumentaire on ne peut plus ressemblant à celui que nous avions développé dans le cadre de notre collaboration de R&D GIS IN2P3/PHOTONIS).

D'un point de vue technique, nous remarquons que la réduction du bruit de lecture associée à l'amincissement et le "post-processing" de la face arrière (BSI CMOS) permettra d'améliorer significativement le rapport signal à bruit à taille de pixel donnée par l'augmentation du facteur de remplissage. Cependant il faut garder en mémoire que la distribution des bruits moyens des millions de pixels ressemble plus à une distribution de Landau qu'à une distribution Gaussienne. Cela signifie qu'une imagerie aux photons

uniques acceptable en terme de bruit sur image nécessiterait un bruit moyen de l'ordre du cinquantième d'électron au minimum. Cela laisse encore une marge de progression à parcourir pour cette technologie bas bruit pour atteindre l'imagerie aux photons uniques étant supposé que ce soit son objectif (ce n'est à mon avis pas le cas pour l'instant). Nous pensons que le CMOS bas bruit, le sCMOS, a donc de beaux jours devant lui mais qu'il ira difficilement sur des domaines d'applications aux photons uniques voir à très bas niveau de lumière (μLux) surtout si les volumes restent faibles en rapport des investissements nécessaires pour gagner deux ordres de grandeur.

A.5   Les CCD à multiplication électronique : emCCD

La solution à l'augmentation du rapport signal à bruit, inverse à celle de la diminution du bruit de lecture, est l'augmentation du signal primaire par un processus de multiplication stochastique des porteurs de charges.

L'emCCD (electron multiplying CCD) est le capteur qui utilise pour l'instant le mieux cette possibilité de multiplication des capteurs CCD [11]. Il est clair que l'utilisation de l'ionisation électronique par impact (de probabilité α de l'ordre de 1.5 %) dans des registres de gain (tension de l'ordre de 30 V appliquée sur une des trois phases du transfert de charge), c'est-à-dire répétée plusieurs centaines de fois (512), permet de multiplier la charge primaire par un facteur 1000, $(1 + \alpha)^{512}$.

Les emCCD sont des photodétecteurs arrivés à maturité du point de vue technologique. Ils ont prouvé leur intérêt notamment dans la biologie en proposant des sensibilités jamais atteintes en technologie CCD refroidi auparavant. C'est un capteur qui conserve une bonne gamme dynamique (réduite bien sur quand le gain est requis) une taille de pixel entre 16 et 8 microns et des cadences de lecture standard en pleine trame. La rapidité ($>$ 30 Hz et $<$ 500 Hz) est obtenue au prix de la réduction de la fenêtre de pixels ou du binning (2x2) ou (4x4) qui induit une perte soit du champ de vue soit de la résolution spatiale. Une chance pour les R&D sur les ebCMOS réside dans le fait que l'emCCD nécessite un refroidissement important et bien contrôlé (-80°C) qui le rend difficilement adaptable à de l'embarqué.

Dans les cinq années à venir l'emCCD verra apparaitre des technologies CMOS concurrentes ou la multiplication électronique pourra être incluse non plus en bas de colonne, comme c'est le cas pour les emCCD, mais dans l'architecture même des pixels (brevet Teledyne et E2V récemment). Cette option ouvre de véritables portes pour la recherche et l'innovation tant du point de vu capteur que du point de vue des applications.

Le second point important à considérer sur l'emCCD est son facteur d'excès de bruit qui est de l'ordre de 2 pour des valeurs de gain de multiplication électronique supérieures à 300. Pour une dérivation mathématiquement correcte et plus générale de l'ENF, nous conseillons la lecture de l'article de Hollenhorst [12] plutôt que celle généralement référencée de Robbins [11].

Le "point faible" de l'emCCD rencontré dans certaines applications apparait clairement lorsque l'on trace la densité de probabilité du nombre d'électrons secondaires pour différentes valeurs de photons. Nous voyons que l'utilisation de la charge comme informa-
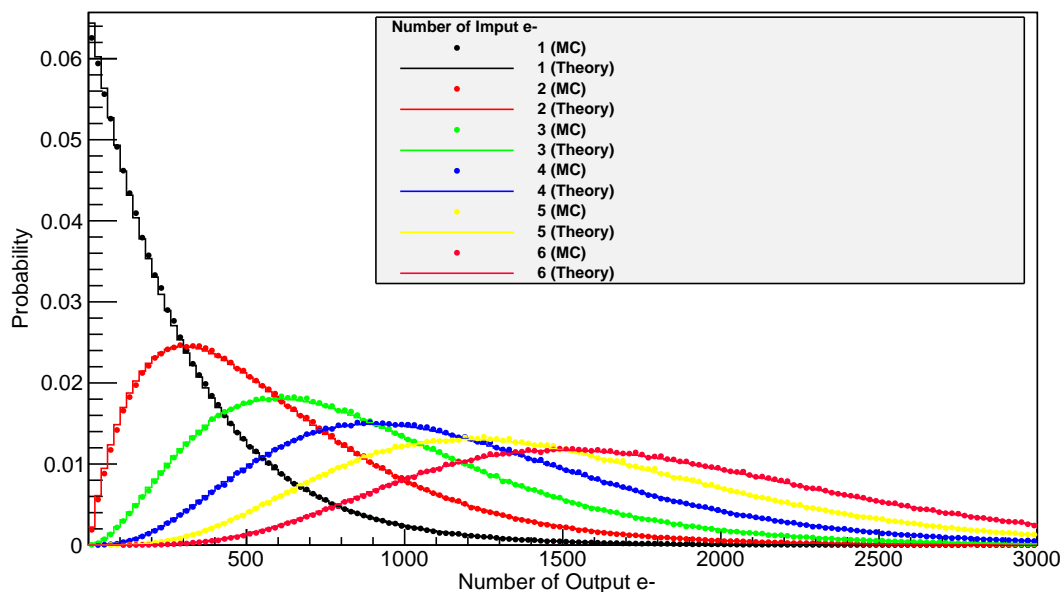
FIGURE I.4 – Distribution du nombre d'électrons après multiplication en fonction du nombre de photons incident.

tion peut conduire par exemple à un taux de comptage ou à une position du centre de gravité des charges détériorée par l'ENF lorsque l'emCCD est en régime de comptage de photons (G=300). Sa capacité de comptage est d'autant plus réduite que le recouvrement des densités de probabilité pour quelques photons est évidente (voir la Figure I.4).

Nous pensons et nous avons montré par simulation Monte Carlo du processus de gain et par le calcul de la limite de Cramèr-Rao sur la précision de localisation, que dans ce cas de figure un photodétecteur de type électron bombardé aura de meilleurs performances.

Je rappelle également que les charges induites par l'horloge de transfert de charge génèrent de faux porteurs primaires dans le registre de multiplication. Ce phénomène dit de "Clock Induced Charge" (CIC) à un effet de type comptage sombre non négligeable lorsque le gain est supérieur à 300 et que l'application nécessite du comptage de photons. C'est une des raisons principales du refroidissement à -80°C des puces E2V dans le système de caméras emCCD. Le CIC par pixel, étant généré par le signal d'horloge, sera bien évidemment linéairement proportionnel à la fréquence trame. Ainsi, l'augmentation du nombre de trames par seconde (vidéo-microscopie rapide par exemple) conduit à une augmentation proportionnelle du bruit CIC.

Pour fixer les idées, nous pouvons calculer le DC induit par le CIC pour les caméras les plus sensibles d'ANDOR Technology. Le DC équivalent est de l'ordre de 600 Hz/mm^2 à 30 images par seconde. Ce DC est multiplié au moins par 10 pour les versions de puces emCCD rapides.

Pour comparaison, l'ebCMOS à cathode S25 (la plus bruyante) est de l'ordre de

100 Hz/mm² à 10°C. C'est pourquoi je pense que pour un régime de haute fréquence de trames (1-10 kHz) les capteurs CMOS électro-bombardés sont préférables. Je mentionne pour information, qu'il existe une version de capteur CCD en mode Geiger par colonne, développée par l'équipe Allemande du MPI à Munich, dans les années 90, pour la mission XMM-Newton. Ce capteur a été conçu pour la détection des X [13].

A.6   Les photodétecteurs à base de MCP

Les capteurs à intensificateur d'images, les iCCD ou plus récemment les iCMOS, sont des détecteurs matures et largement utilisés. Ils possèdent, d'après moi, peu de possibilités d'évolutions majeures. Les galettes de micro-canaux sont déjà très optimisées (pores de 2-3 microns) et la perte de résolution et de rapport signal à bruit sont principalement dus à la génération d'une image intensifiée sur l'écran de phosphore d'où le terme d'ailleurs d'intensificateurs d'images. Des tentatives timides portent sur l'utilisation de CMOS rapide pour l'imagerie de molécules uniques [14].

Plus prometteurs, sont les photodétecteurs utilisant les galettes à micro-canaux avec une lecture directe des électrons secondaires, i.e. sans passer par un écran de phosphore. Le choix du système de lecture des charges est varié.

Il peut s'agir de lignes à retard dans les deux directions pour localiser l'amas de charge comme cela est le cas pour le prototype X33D [15] mais aussi de pads métalliques connectés à un ASIC de lecture très rapide comme c'est le cas avec le développement collaboratif entre une équipe anglaise, le CERN et la société Photek [16]. On note également un travail du FNAL [17] sur ce sujet. Les résolutions temporelles obtenues sont remarquables, 10 ps, et pourront être utilisées pour de la mesure de temps de vol. Ces développements sont en cours et nous attendons la publication finale de l'ensemble des performances des prototypes.

Finalement, nous constatons que les photodétecteurs à tube comportant des galettes à micro-canaux sont essentiellement prévus pour des applications ultra rapides de type temps de vol ou de la spectroscopie de corrélation de fluorescence. C'est pourquoi mis à part le développement de l'intégration (passages vide,connecteurs, processus cathode) la majeure partie des efforts fournis dans ce domaine se porte sur les ASICs afin d'améliorer la résolution sur l'étiquetage temporel. Remarquons que dans ce cas limite de résolution temporelle, le nombre de photons est de quelques centaines et non pas dans le régime Poissonien [17].

Il existe également une voie intéressante pour les MCP en vision nocturne. En effet, l'intégration d'un capteur CMOS à pads sensibles aux charges électriques introduit directement dans le tube à vide, l'ebMCP-CMOS, est une évolution technologiquement envisageable par les fabricants de tubes. Cela nécessite la mise au point d'un capteur CMOS avec des pads (pixels) pouvant échantillonner les charges secondaires issues des pores de la galette. La résolution spatiale qui est liée au premier ordre à la distance galette-CMOS et au pas des pixels peut très certainement être améliorée.

Il s'agit dans ce domaine d'investir sur de la conception de CMOS à faible bruit spatial fixe, FPN, et à faible dispersion de la réponse des pixels, PRNU. Mécaniquement, des

distances cathode-galette de quelques dizaines de micron doivent pouvoir être atteintes en fonction des tensions appliquées. Cette voie peut être choisie par les industriels qui voudront conserver leur chaine de production de galettes qui ont nécessitées des investissements importants et le développement de savoir faire.

A.7   Les capteurs silicium electro-bombardés

Bien que le principe de photodétection soit le même, les ebCCD et les ebCMOS ne sont pas utilisés dans les mêmes domaines d'applications. Les ebCCD, plus consommateurs en énergie et peu favorables à de l'embarqué, ont surtout été développés par la société Hamamatsu pour des applications scientifiques et industrielles où le comptage de photons est primordial. Les ebCCD peuvent en effet être utilisés soit dans le cadre de l'imagerie de fluorescence ou de la vidéo-microscopie, soit pour de l'imagerie Cherenkov en proposant une augmentation de la surface sensible (réduction par profil de champ de type fontaine ou croisée généré par des électrodes circulaires) [18].

Je peux simplement mentionner dans ce paragraphe sur l'état de l'art que l'ebCMOS a été, jusqu'à présent, majoritairement développé pour de la vision nocturne par la société INTEVAC. Les points forts de ce capteur sont pour de l'embarqué ou du portatif (lunette), sa sensibilité, sa faible consommation et ses possibilités fonctionnelles : fenêtrage, numérisation par ADC en colonnes parallèles, système sur puce). Il souffre cependant du problème de halo issu d'électrons rétro-diffusés par le silicium (diamètre égal à quatre fois le gap cathode-CMOS).

C'est en étudiant ce phénomène que nous avons été conduits à déposer un brevet sur les méthodes de traitement des ebCMOS aux photons uniques. Le capteur ebCMOS associé à ce type de méthodes et de traitement, étendu au domaine des UV (Solar Blind) peut être particulièrement adapté pour des domaines de surveillance de type départ de feu ou suivi d'objets propulsés.

Nous pensons néanmoins que l'avenir des ebCMOS ne réside pas uniquement dans les domaines de la vision nocturne pour la sécurité et la défense. Nous tenterons de montrer dans la deuxième partie de ce chapitre que l'ebCMOS peut avoir d'autres avantages pour un tout autre domaine d'applications : *l'imagerie scientifique.*

D'un point de vue historique, le développement des ebCMOS scientifiques a largement bénéficié des travaux pionniers sur les Photo Diodes Hybrides (HPD) notamment mené au CERN [19, 20, 21].

B   Le détecteur CMOS électro-bombardé (ebCMOS)

B.1   Principe de fonctionnement

L'ebCMOS fonctionne sur le même principe que l'ebCCD, c'est-à-dire celui du bombardement, par des photo-électrons accélérés par un champ électrique intense (∼kV/mm) de la face arrière amincie de la puce. Le schéma de principe ainsi qu'une photographie du

prototype ebCMOS, LUSIPHER, sont présentés dans la Figure I.5. Le gain du capteur est donné en première approximation pour une tension d'accélération, V_0, et une énergie perdue dans la couche d'entrée dite "morte", E_0, par :

$$G = \frac{qV_0 - E_0}{3.6}$$

D'après cette expression des gains de 3000 peuvent être atteints pour des tensions couramment employées en focalisation de proximité (gap < quelques mm) conduisant à des champs électriques maximum de l'ordre de 10 V/μm. Cependant cette approximation brutale doit être modifiée afin de prendre en compte les différents phénomènes physiques induisant des pertes de charges secondaires crées dans le silicium.
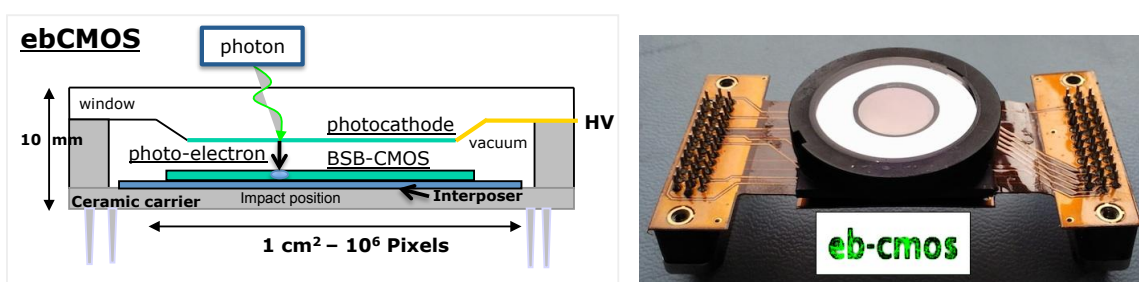
FIGURE I.5 – Schéma de principe d'un ebCMOS (gauche). Photographie du capteur ebC-MOS LUSIPHER de diamètre utile 12 mm (droite).

Parmi les paramètres qui influencent les performances de l'ebCMOS, il faut distinguer deux catégories : celle des technologies tubes à photo-cathodes et celle des capteurs CMOS. Nous illustrons le propos en montrant dans la figure I.6 les deux étapes majeures du processus de photodétection d'une source ponctuelle émettrice. D'après ces schémas de principe nous observons que les photo-électrons n'ont pas tous la même trajectoire du fait de leur vitesse initiale non nulle suivant le plan perpendiculaire au champ électrique. On nommera, par la suite, cette perte de résolution la *PSF* du tube (Point Spread Function). Le deuxième phénomène spatial, appelé *PSF* du CMOS est lié à la diffusion des porteurs de charge secondaires dans la couche de diffusion dite "couche épitaxiale" comme cela est représenté dans la Figure I.6. Cette *PSF* a essentiellement deux effets, l'un sur la résolution spatiale et l'autre sur le rapport signal à bruit.

Considérer cependant ces catégories (tube et silicium) indépendamment ne donne pas une bonne vision des progrès potentiels de ce genre de photodétecteur. Tout l'intérêt de cette R&D réside dans ce "dialogue" entre deux domaines technologiques à priori distincts et qui d'après nous, pourraient fusionner dans les années à venir grâce à des ruptures technologiques, si les volumes des marchés le nécessite. Nous reviendrons sur ce point dans la section prospectives de ce chapitre.
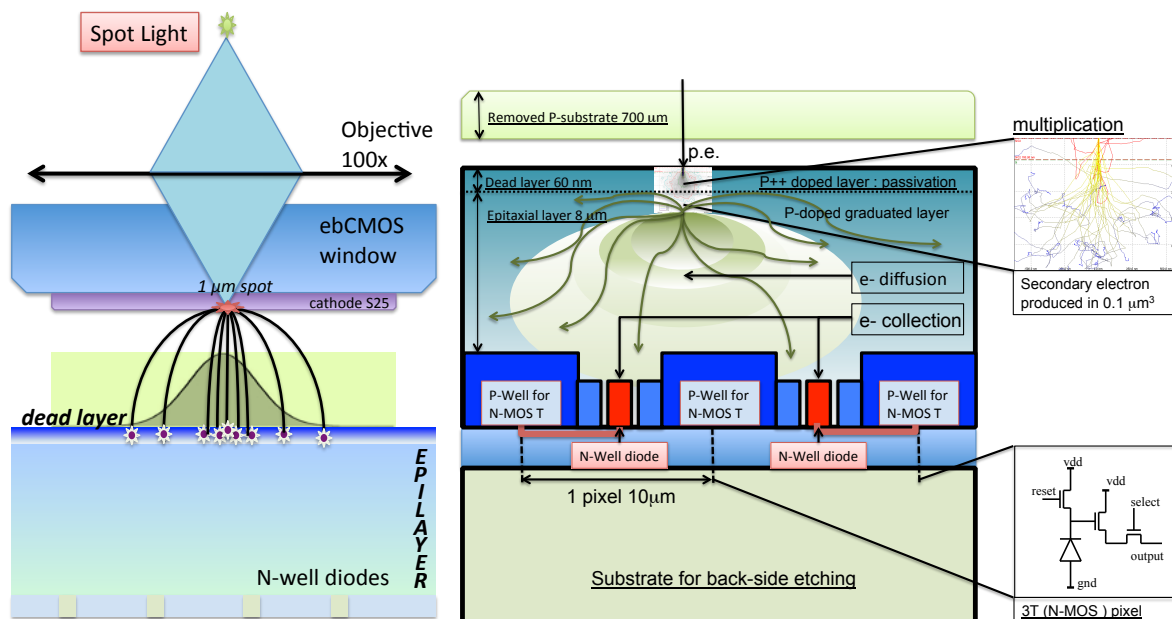
FIGURE I.6 – Schéma de principe de l'émission des photo-électrons suite à une illumination ponctuelle de l'ebCMOS (gauche). Schéma de principe de la multiplication des charges dans la face arrière du CMOS aminci (droite).

B.2 Performances intrinsèques de l'ebCMOS

Afin de fournir une vision complète sur ce détecteur, nous proposons le tableau I.1 qui en répertorie les paramètres ajustables et leur impact sur les performances intrinsèques :

B.2.1 L'efficacité quantique

L'efficacité quantique est reconnue comme le point faible des photodétecteurs à photo-cathode. Elle est la résultante de deux facteurs en compétition : l'absorption du photon par le matériau et l'émission du photo-électron dans le vide par le même matériau. L'augmentation de l'épaisseur favorise le premier mais diminue le deuxième. On comprend mieux dorénavant que l'optimisation du rendement des photo-cathodes procède en premier lieu de l'empirisme. On donne généralement l'expression de la QE sous la forme [22] :

$$QE \sim (1 - R)\frac{P_\nu}{\mu}\frac{P_e}{1 + 1/(\mu L)} \tag{I.1}$$

où R est le coefficient de réflexion, P_ν, la probabilité d'être au-dessus du niveau du vide, μ le coefficient d'absorption (section efficace photoélectrique), L la longueur moyenne d'échappement du photo-électron et P_e la probabilité d'échappement de l'électron dans le vide (effet tunnel). les paramètres R, P_ν et μ dépendent du matériau alors que L et P_e dépendent de la qualité du cristal et de l'affinité électronique obtenue par activation pour abaisser la barrière de potentiel. D'importants progrès ont été obtenus récemment par Hamamatsu sur les Gen II qui proposent des ultra- et super-bialkali (K-Sb-Cs) avec

Evolution des performances de l'ebCMOS		
- paramètre	↗ ↘	- commentaire
Sensibilité, SNR		
- couche morte	↘	- ep. < 70 nm pour HV ∼ 2 kV
- épaisseur de la couche epitaxiée	↘	- CCE / pixel ↗
- dopage de la couche épitaxiée	↘	- gradient ou hte résistivité
- activation p++ face arrière	↗	- recombinaison ↘
- isolation pixel	↗	- DTI - diode
- QE de la photo-cathode	↗	- Gen II (UBA) ou Gen III
Bruit		
- E = V / d	↘	- réduire l'effet de champ (DC)
- bruit pixel	↘	- pinned photodiode
- qualité du vide	↗	- retour ionique
- activation p++	↗	- qualité du recuit laser
Dynamique		
- bits/pixel	↗	- ADC 10 bits après CDS
- capacité du puits	↗	- 30 000 électrons
Résolution spatiale		
- distance cathode-cmos	↘	- psf du tube $\sigma < 10\ \mu$m
- psf cmos	↘	- meilleure FTM
- pas du pixel	↘	- meilleure FTM
- isolation pixel	↘	- diaphonie pixel
- dopage de la couche épitaxiée	↗	- gradient - hte résistivité
Résolution temporelle		
- horloge pixel	↘	25 ns - 40 MHz ou plus
- frame rate	↗	nombre de sorties col. //
- nombre de pixels / ligne	↘	mais faible champ de vue
- gating de la photo-cathode	↘	alimentation rapide
- transistors / pixel	↗	global/rolling Shutter
Débit de données		
- nombre de colonnes //	↗	nombre de sortie (200 !)
- fréquence de numérisation	↗	horloge ADC 25 ns - 40 MHz
- débit de sorties / voie	↗	1 Gbits/s

TABLE I.1 – Liste des paramètres ajustables de l'ebCMOS en fonction de leur impact sur les performances associées.

42% de QE à 350 *nm*. Les marges de progrès ont semble-t-il été obtenues sur la qualité de la structure cristalline [23].

L'activation permet en partie d'optimiser la QE pour une gamme plus ou moins large de longueurs d'onde mais néanmoins reste inférieure à 25% (plutot 15-20 %) pour les cathodes standard à base de métaux alcalins (Gen II) et à 40% pour les cathodes à une affinité électrique négative (Gen III). Ces dernières sont en contrepartie plus bruyantes et se rapprochent en termes de courant d'obscurité à une cathode S25 (S20 étendue vers le rouge).
Il faut remarquer d'une part que la fabrication de cathodes Gen III nécessite des processus liés à l'industrie du "silicium" (substrat AsGa, manipulation de wafer) complètement différent de ceux utilisés pour la Gen II. Le passage de la Gen II à la Gen III demande aux industriels des investissements lourds et subventionnés. On note l'apparition de nouveaux procédés de fabrication des tubes Gen III (Hamamatsu) qui ne nécessitent plus l'emploi d'un film protecteur de la cathode AsGa. Cela leur donne ainsi un avantage certain vis à vis de la GEN II. La Gen III est une brique technologique sensible car elle est la clé pour la vision nocturne. C'est pourquoi elle est difficile d'accès pour des développements de prototypages d'ebCMOS à visée scientifique. Ainsi, l'efficacité quantique de l'ebCMOS scientifique que nous avons produit est pour l'instant celle de la Gen II. Cependant, je ne désespère pas de convaincre un partenaire industriel du bien fondé de l'AsGa pour les applications en biologie qui utilisent de plus en plus de marqueurs fluorescents dans le rouge et le proche infra-rouge. Nous ne développerons pas plus cet aspect qui reste relativement confidentiel à ce jour. Un statut récent sur le sujet se trouve dans le chapitre 5 de la référence [24].

B.2.2   La sensibilité ou rapport signal à bruit

La contre partie de l'efficacité quantique est l'excellent rapport signal à bruit des capteurs à technologie hybride. Le gain de multiplication lié à la haute tension est tout d'abord linéaire en fonction de la haute tension appliquée et le bruit est additif, ce qui limite le facteur de bruit en excès par rapport au technologie emCCD (bruit "multiplicatif"). Une illustration de notre propos se trouve dans la Figure I.7 qui montre les distributions simulées par MonteCarlo du nombre d'électrons secondaires disponibles dans la couche épitaxiale de l'ebCMOS. La simulation de la rétro-diffusion a été ajoutée. La perte d'énergie dans la couche morte a été simulée avec une distribution Normale d'énergie déposée dans la couche morte. Il est assez instructif de comparer cette Figure avec celle de l'emCCD (Figure I.4).

En ce qui concerne le rapport signal à bruit, la probabilité de détecter un faux photon par pixel issu du bruit du CMOS est de l'ordre de 10^{-5} grâce à la méthode du clustering autour du pixel touché à plus de trois fois son bruit. L'effet de la sélection est illustré par la Figure I.8.
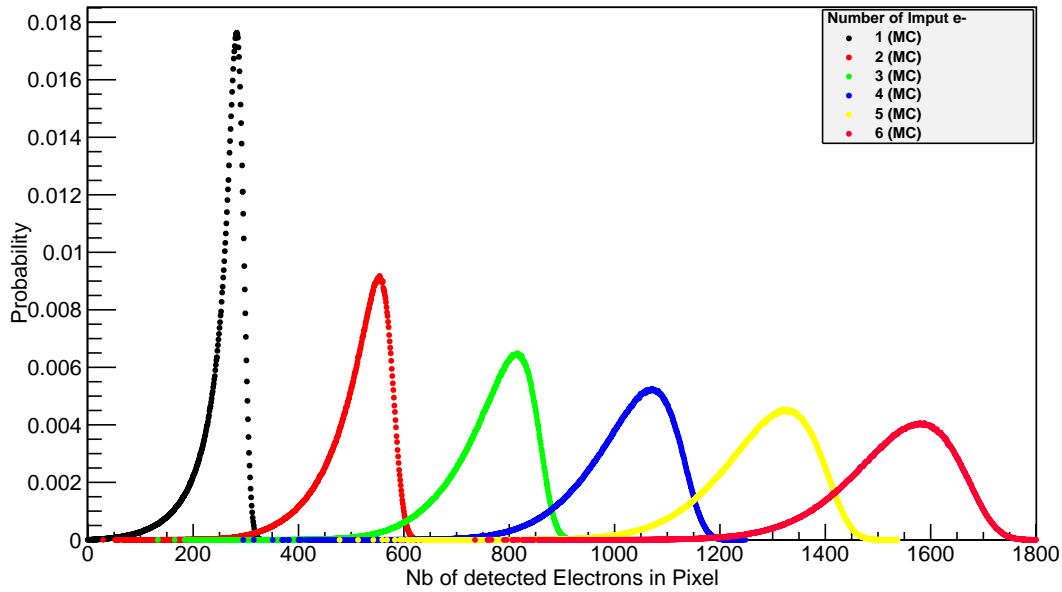
FIGURE I.7 – Distributions du nombre d'électrons secondaires disponibles après le processus de multiplication pour un ebCMOS pour différents nombre de photons en entrée. La rétro-diffusion est incluse dans la simulation.
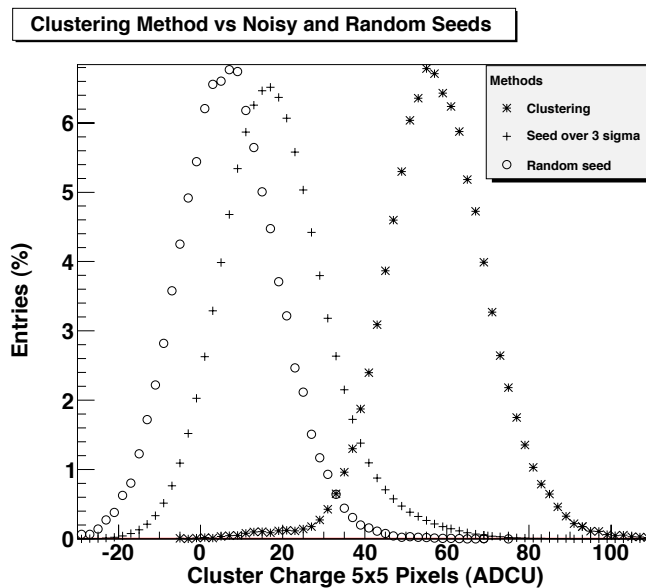
FIGURE I.8 – Distributions du signal après "clustering" du photo-électron. Un "clustering" aléatoire ou sur les pixels chauds sans haute tension appliquée montre la séparation du signal et du bruit du CMOS.

B.2.3   La résolution spatiale

B.2.3.i   La PSF du tube

La résolution spatiale de l'ebCMOS est liée à deux densités de probabilité spatiale, appelées *PSF* (Point Spread Function) tube et CMOS, décrites par le schéma de principe de la Figure I.6.

La *PSF* du tube est liée à l'angle d'émission du photo-électron émis par la photo-cathode. La distribution angulaire peut être ramenée à une distribution radiale des vitesses. En considérant une distribution de Maxwell des vitesses radiales et un champ accélérateur constant, obtenu par focalisation de proximité (champ électrique perpendiculaire à la surface cathode et CMOS), la densité de probabilité obtenue est une gaussienne [1] [25, 26].

Dans la référence [26] l'auteur propose une étude de la résolution du tube avec MCP à partir de cette modélisation de la PSF tube en fonction de la distance d entre la cathode et la galette, de l'énergie radiale initiale moyenne, $\overline{V}_{0r}$, et de la tension accélératrice, V. L'écart type σ_T de la *PSF* du tube s'écrit :

$$\sigma_T \quad \propto \quad d \sqrt{\frac{\overline{V}_{0r}}{V}} \tag{I.2}$$

D'après cette relation, on voit clairement que le facteur dominant de la résolution spatiale est la distance d de transit du photo-électron. La figure I.9 montre les courbes d'iso-résolution (σ_T=cte) en fonction de d et V. Nous tirons de ces courbes les enseignements suivants :

1. Le champ électrique responsable du comptage d'obscurité est limité à des valeurs allant de 10 kV/mm à 4 kV/mm. L'intersection de cette droite avec la courbe d'iso-résolution souhaitée indique la limite supérieure sur d et V applicable à l'ebCMOS.

2. La haute tension, V_{min}, indique la tension minimale nécessaire à l'obtention d'un signal détectable sur les diodes du fait de la présence de la couche morte. Par exemple, c'est-à-dire une valeur d'énergie perdue de 1,2 keV correspond à une couche morte de l'ordre de 70 nm. Cette constante contraint la borne inférieure dans l'encadrement des iso-résolutions atteignables.

3. Une résolution comprise entre 10 et 15 microns nécessite des distances de transit de l'ordre du millimètre et des tensions inférieures à 4 kV. C'est exactement ce que nous avons réalisé avec nos prototypes ebMIMOSA5 et LUSIPHER.

4. Dans la perspective de développements futurs, il est intéressant de remarquer qu'une résolution inférieure à 5 microns (environ 200 pl/mm) nécessite une distance d cathode-cmos inférieure à 300 microns et une tension d'accélération inférieure à

---

1. Une distribution empirique obtenue à partir d'ajustement de résultats expérimentaux est parfois utilisée à la place de la Gaussienne. Cette distribution complique la formule analytique de la résolution. Elle peut être employée dans le cadre de calculs numériques de résolution, voir l'équation (5.10) de la référence [25].
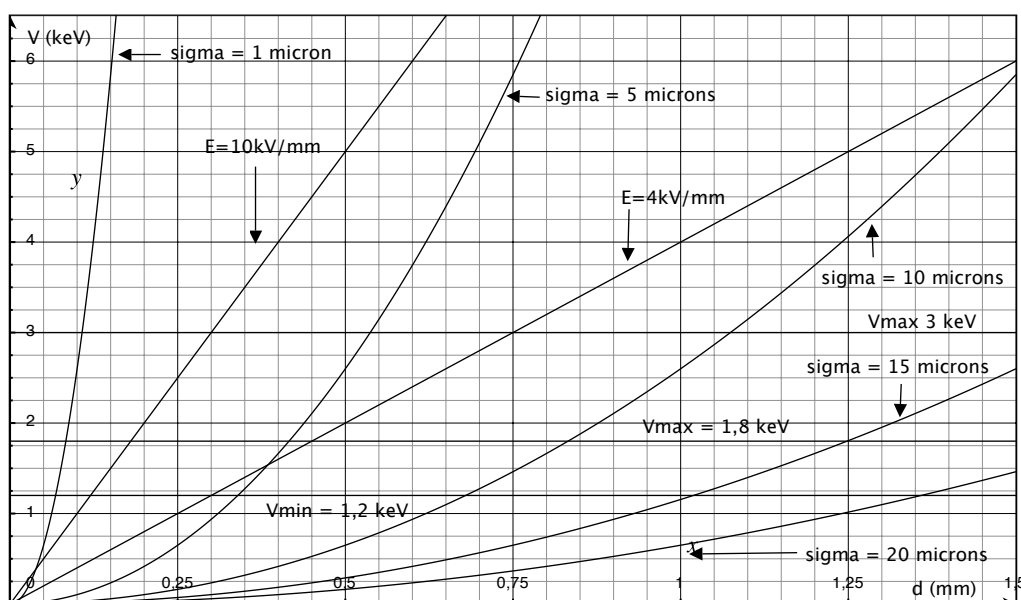
FIGURE I.9 – Courbes de résolution (σ_t) en fonction des paramètres de l'ebCMOS, la distance cathode-CMOS et la tension accélératrice, obtenue avec l'équation I.2 pour une valeur de $\overline{V}_{0r} = 0.26$ eV.

1.8 kV ! Cette valeur de tension est d'autant plus importante qu'elle permet d'éviter le vieillissement des tubes.

En effet, il est nécessaire de fonctionner à des énergies de photo-électrons inférieures au seuil de production des X dans le silicium (1.8 keV) pour éviter l'accumulation des électrons dans les couches d'oxyde qui provoque une augmentation du bruit des pixels. Dans cette hypothèse la couche morte ne doit pas excéder 10 à 15 nanomètres ! Cette dernière exigence nécessite un post-traitement très performant de la face arrière par implantation de Bore suivi d'un recuit laser homogène.

5. On se rappellera que la résolution à un micron est la résolution limite de cette technologie ebCMOS.

B.2.3.ii   La passivation et la couche épitaxiale

Elle est le paramètre clé de la résolution spatiale. La *PSF* de diffusion CMOS en est le second. En résumé du paragraphe précédent nous pouvons affirmer que l'épaisseur de la couche de passivation (couche morte) impacte au premier ordre la résolution spatiale au travers de la contrainte sur la valeur de la tension accélératrice et par conséquent sur la distance cathode-CMOS. C'est pourquoi il est naïf de juger les performances d'un ebCMOS sur la taille de ses pixels.

Il y a cependant d'autres facteurs non négligeables à prendre en compte. La résolution spatiale dépend également de la *PSF* du CMOS aminci, c'est-à-dire de la forme de la

distribution des électrons secondaires qui est échantillonnée par les diodes de collection. Deux paramètres sont à prendre en compte pour la diminution de cette *PSF*.

Le premier est la distance parcourue par les électrons secondaires avant d'être collectés par les diodes. Cette distance est liée à l'épaisseur de la couche épitaxiale qui peut varier entre quelques microns et une dizaine de microns.

Le deuxième est la composition de la couche épitaxiée. La résistivité et/ou le profil de dopage de cette couche jouent en effet un rôle important sur la *PSF* CMOS. Plus précisément, une diminution de la diffusion est obtenue soit par l'utilisation d'une couche épitaxiale de haute résistivité (1000 Ω.cm) afin de favoriser une zone de charge d'espace étendue avec une polarisation standard de la technologie considérée (3,3 V), soit par l'implantation d'un gradient de dopage de Bore pour favoriser la diffusion des charges en direction des diodes de collection.

B.2.3.iii   la conception des pixels

La conception de l'architecture des pixels d'un ebCMOS, bien que majoritairement orientée vers la minimisation du bruit temporel reste cependant concernée par la résolution spatiale via la diffusion.

Il est ainsi possible de réduire la *PSF CMOS* grâce aux possibilités offertes par certaines technologies CMOS, comme par exemple du dopage P profond et la protection à ces dopages afin de provoquer une "canalisation" des charges vers les puits N. L'utilisation de tranchés profondes d'isolation (DTI) permettent aussi de concevoir des pixels isolés. Il faut cependant toujours conserver la priorité sur la minimisation du bruit du pixel et à la maximisation de la collection de charge (deux paramètres antinomiques).

Les architectures pixels standards comportent au moins 5 transistors avec des technologies CMOS dites "pinned photodiodes". Le transistor de transfert permet d'isoler la diode de collection du suiveur, ("source follower"). Les technologies CMOS auxquelles nous avons eu accès dans nos projet n'offraient pas cette possibilité d'architecture.

Dans ce type d'architecture et de technologie, la présence de diodes de collections de type N interdit la présence de caissons N pour les transistors P-MOS. Cela explique en partie pourquoi nous avons systématiquement travaillé avec des pixels 3T (Reset, SF, Sélection). La conséquence directe est la nécessité de faire un double échantillonnage corrélé (CDS) soit sous forme de clamping en bas de colonne soit à l'extérieure de la puce (par soustraction de 2 frames consécutifs après Reset).

C'est cette dernière solution qui a été privilégiée pour des raisons de simplicité et de prise de risques minimum. Néanmoins ce choix a pour conséquence de reporter la complexité sur le système d'acquisition.

B.2.3.iv   la résolution en mode d'imagerie

La résolution sur image, qui peut être mesurée par exemple avec une mire USAF, est généralement donnée par sa fonction de transfert de modulation (FTM) qui mesure le contraste sur capteur en fonction d'un objet de type réseau périodique de lignes claires et sombres (en transmission ou en émission) étalonné en nombre de paires de lignes par millimètre. La déviation standard de la *PSF* résultante obtenue par la somme quadratique
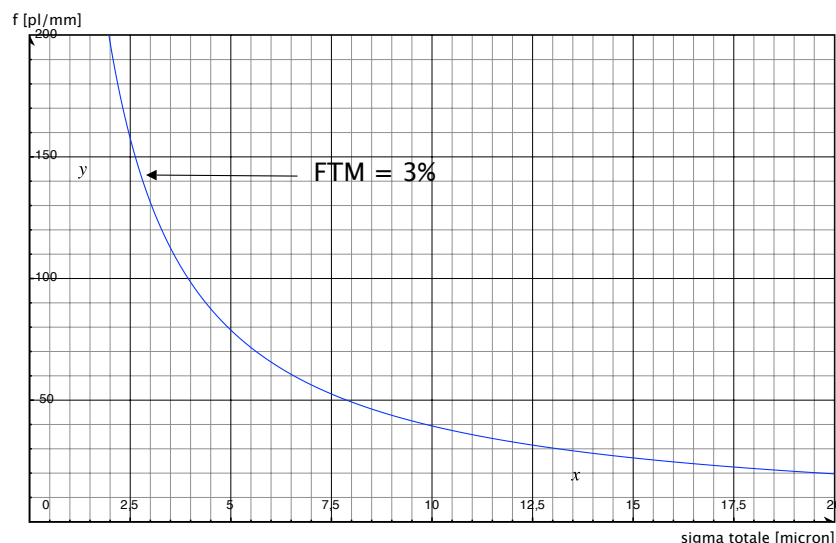
FIGURE I.10 – Courbe de résolution (MTF) à 3% de contraste en fonction de la résolution totale σ de l'ebCMOS dans l'hypothèse, "pas trop fausse", d'une *PSF* Gaussienne.

des *PSFs* du tube et du CMOS ($\sigma^2 = \sigma_t^2 + \sigma_d^2$) peut être utilisée afin de calculer FTM dans l'hypothèse de *PSF* Gaussiennes [25]. La relation entre FTM et σ de la *PSF*, pour de la focalisation de proximité, s'écrit :

$$FTM \quad = \quad e^{-8\pi^2 f^2 \sigma^2} \tag{I.3}$$

A titre d'exemple, une valeur de 3 % de contraste correspond à une relation entre la fréquence limite f_3 en paires de lignes par millimètre et σ en millimètre de la forme :

$$f_3 \quad \simeq \quad \frac{0.395}{\sigma} \tag{I.4}$$

Une *PSF* totale, avec un σ égale à 15 μm, conduit à une fréquence limite à 3% de 26 pl/mm comme cela peut être vérifié sur la Figure I.10.

Remarquons que cette modélisation qui semble à priori brutale donne des résultats très proches de nos mesures sur nos prototypes. Ainsi nous pouvons calculer qu'une augmentation de la résolution à 75 pl/mm nécessite une *PSF* totale de l'ordre de 5 μm, i.e. un gap cathode-CMOS de l'ordre de 400 μm. Cela donne une idée des marges de progression de ce capteur pour les applications dans le domaine de la vision nocturne.

B.2.4   De l'amincissement et du choix entre substrats de "SOI" ou "bulk" ?

Deux voies sont possibles : les substrats "SOI" ou "bulk". L'avantage du premier réside dans un meilleur contrôle de l'épaisseur de la couche épitaxiale après décapage de la face arrière par la présence d'une couche pouvant stopper la gravure. Des épaisseurs de 2-3 microns sont envisageables. Nous pouvons légitimement nous poser la question de la possibilité

d'obtenir avec un substrat SOI une face arrière avec une couche morte inférieure à 50 nm sans post-traitement ?

La solution "bulk" à l'avantage de la simplicité mais ne permet pas d'obtenir un décapage reproductible inférieur à 8-10 microns et un écart type de quelques microns. Nous pouvons légitimement imaginer que l'utilisation de substrats de haute résistivité permettra de réduire, par l'augmentation de la zone de charge d'espace, la zone de diffusion libre de 10 à quelques microns. Le "post-processing" est également nécessaire car il n'est pas évident qu'après amincissement la passivation initiale puisse conduire à une couche morte inférieure à 50 nm. Nous n'avons pas, à notre connaissance, au moment ou ce chapitre est écrit, une réponse définitive quand au meilleur choix technologique. D'autres facteurs (coût, fondeur) doivent entrer certainement en compte.

B.2.5 Les bruits de l'ebCMOS

B.2.5.i Le bruit du pixel

Le gain de multiplication peut être poussé à des valeurs relativement élevés (> 3000) mais au détriment de la résolution spatiale (augmentation de la distance de transit) si l'on se place à champ électrique constant. Ainsi, pour des capteur d'image ebCMOS, le gain ne peut être aussi élevé que voulu et le développement de pixels bas bruit devient un facteur aussi important que celui de l'amincissement.

Pour des applications autour de 2 kV, un bruit temporel de pixel inférieur à 5-8 électrons est nécessaire. Il faut en effet prendre en compte non seulement la perte de charge secondaires due à la couche morte mais aussi la diffusion des porteurs de charge sur plusieurs pixels qui réduit le rapport signal à bruit par pixel. Des gains de l'ordre de 200 sont plus réalistes dans les conditions de meilleure résolution spatiale ce qui signifie qu'avec 10 électrons de bruit une sélection des pixels sièges pour la reconstruction d'un amas de pixels de type événement "photo-électron" seuillée à 50 électrons (5σ) présuppose 25% de collection de charges sur le pixel principal. Cela implique une architecture pixel et une couche épitaxiée bien optimisée.

B.2.5.ii Le comptage d'obscurité

Quel que soit le type d'amplification permettant d'atteindre la sensibilité aux photons uniques il y a toujours une contrepartie à payer dans l'apparition du comptage d'obscurité. Ce bruit correspond à la détection d'électrons par le silicium issus non pas d'une photo-conversion mais d'une émission spontanée par la photo-cathode soit par effet thermique soit par effet de champ. Dans la gamme de champs électriques utilisés par les ebCMOS nous pouvons affirmer que l'effet de champ domine si la photo-cathode reste à température ambiante. Les effets de la température sur le comptage d'obscurité sont bien mesurés et un effet de plateau est clairement visible lorsque l'on diminue celle-ci pour atteindre la seule contribution restante, le comptage par effet de champ (autour de 10°C pour une cathode de type S20 (Na_2KSb - 70 nm d'épaisseur). La cathode S25 nécessite un refroidissement plus important pour atteindre ce seuil.

Le deuxième paramètre bien connu favorisant le comptage d'obscurité est le champ

électrique responsable de l'abaissement de la barrière de potentiel par effet Schottky. Cela augmente d'une part la QE mais aussi malheureusement le DC. Cela explique la présence de la limite supérieure décrite par une droite dans la figure I.9.

Le comptage d'obscurité dépend également du type de photo-cathode. Nous avons mesuré par exemple un facteur 10 sur le DC entre les cathode S20 (maximum dans le vert) et à cathode S25 (maximum dans le rouge). Ce bruit de comptage d'obscurité qui paraît important et qui varie entre le Hertz et quelques centaines de Hz par mm² de silicium est cependant le DC le plus bas parmi les capteurs à photons uniques. En effet, un rapide calcul à partir des spécifications données pour l'emCCD le plus sensible donne une valeur qui dépasse largement celle de l'ebCMOS pour des fréquences trames comparables (DU897 - 600 Hz/mm², 30 fps).

Nous traiterons plus en détail ce point dans la section concernant les applications puisque la minimisation du comptage d'obscurité peut être un point crucial pour l'observation d'événements rares ou de très faible luminance comme cela est le cas pour l'observation de la bioluminescence marine.

B.2.5.iii   Les retours d'ions

Le retour d'ions sur la photo-cathode est responsable de spots intenses sur image. C'est une particularité des capteurs hybrides. L'ionisation d'atomes résiduels provoque le bombardement de la cathode par les ions positifs générés. Ce bombardement a pour effet la génération d'un nombre important d'électrons accélérés suivant la *PSF* du tube sur le capteur CMOS. Cela affecte non seulement l'image courante mais aussi le vieillissement de la photo-cathode et plus particulièrement les cathodes de troisième génération. La qualité du vide est donc primordiale pour la limitation de ce bruit. Cela implique des contraintes fortes sur les bâtis de pompage. Dans la cadre de l'imagerie aux photons uniques, le retour d'ions n'est pas un véritable problème car il est aisément filtré par l'application de quelques critères sur la forme et la charge de l'amas de charges.

B.2.5.iv   La rétro-diffusion

La rétro-diffusion (BS) des photo-électrons par le silicium est bien plus un inconvénient pour l'ebCMOS que les retours d'ions. Dans les énergies considérées (autour de 2 keV), le pourcentage d'électrons rétro-diffusés est loin d'être négligeable, puisqu'il est de l'ordre de 18%. Ces électrons rétro-diffusés ont deux conséquences sur le processus de détection. D'une part la rétro-diffusion induit une perte d'efficacité de détection puisque une majeur partie de ces électrons ne déposent pas suffisamment d'énergie pour générer un signal détectable par les diodes des pixels. Pour du fonctionnement en mode comptage de photons c'est cet effet qui détériore grandement la précision du comptage au-delà de deux photons.

D'autre part les rétro-diffusés génèrent un halo lorsqu'un point très lumineux est dans le champ de vue (lampadaire, phare, ...). Ce halo recouvre la véritable image jusqu'à un diamètre égal à $4d$ (d est la distance cathode-cmos) et devient très handicapant pour les conditions opérationnelles de la vision nocturne.

Ce problème connu des ebCMOS a été corrigé par la société INTEVAC qui a breveté le procédé. Cette solution, qui montre des résultats satisfaisants, propose l'ajout
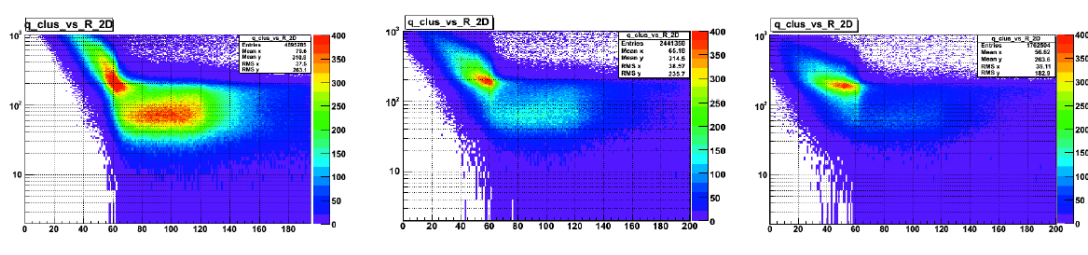
FIGURE I.11 – Distribution des charges des amas (échelle Log suivant Y) en fonction de leur distance au spot (axe X) pour 3 intensités différentes (du plus au moins intense de gauche à droite). On observe clairement la zone des rétro-diffusés dont la densité diminue avec l'intensité du spot.

d'une grille sur la surface du CMOS pour supprimer les trajectoires électroniques à grand angle de rétro-diffusion au détriment de l'efficacité de détection (masquage de la surface sensible).

Au cours de nos tests sur les ebCMOS nous avons été amenés a traiter ce problème d'une façon logicielle pour des flux relativement faible mais néanmoins provoquant un halo (voir les Figures I.11 et I.12). Cela nous à conduit à déposer un brevet de méthodes sur le traitement aux photons uniques qui corrige en partie le problème du halo [27]. La Figure I.12 montre un halo mesuré et corrigé sur notre premier prototype ebMIMOSA5.

B.2.6   La dynamique

Comme tous les capteurs de photons uniques, l'ebCMOS souffre d'une dynamique peu étendue dans le cadre d'un fonctionnement avec gain. La dynamique peut être "artificiellement" augmentée par la réduction du gain de multiplication, c'est-à-dire la haute tension. Dans ce cas, la sensibilité aux photons uniques est perdue. La capacité de puits des diodes utilisées couramment sont de l'ordre 30 ke-. Pour un gain de 200 en considérant 50% de la charge sur un pixel, la dynamique obtenue est de l'ordre de 300 photons.

Nous ne connaissons pas à ce jour d'utilisation de CMOS spécifiquement conçus pour posséder une grande gamme dynamique en configuration ebCMOS. Cela semble envisageable sous conditions de compatibilité des technologies CMOS à l'amincissement et à la passivation mais aussi de la compatibilité des architectures pixels à grande gamme dynamique et la détection d'électrons face arrière.

B.2.7   La résolution temporelle et le flux de données

La résolution temporelle de l'ebCMOS peut être regardée suivant deux critères. Le premier est donné par la vitesse de lecture d'un pixel qui est indépendante du nombre de pixels à lire. La limite basse est contrainte par le temps de diffusion des charges secondaires qui est de l'ordre de 100 ns pour une couche épitaxiée à dopage standard (50 Ωcm) et de 10 microns d'épaisseur. Cela correspond au temps nécessaire pour que 90% des charges
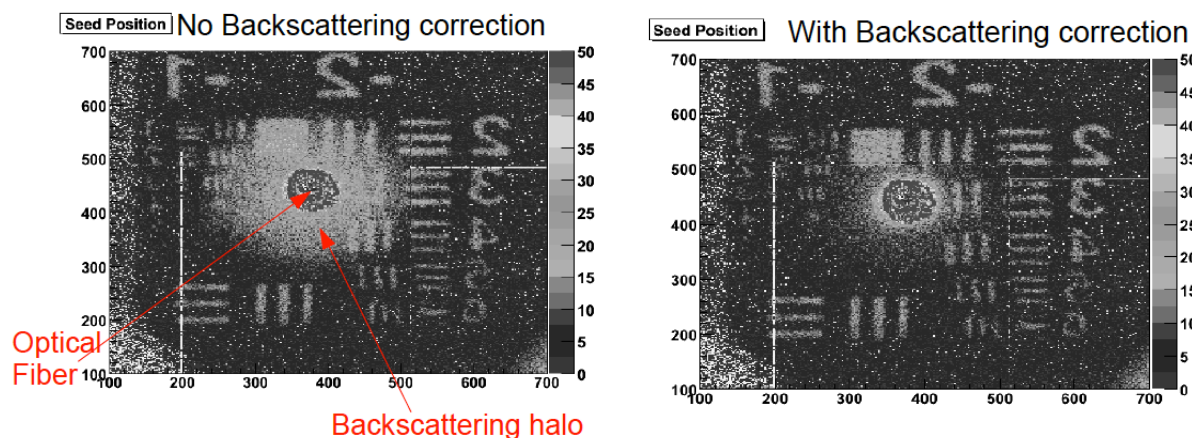
Figure I.12 – Image d'un halo généré sur notre premier prototype ebMIMOSA5 par une source intense localisée fabriquée sur banc optique (fibre optique introduite dans la mire). C'est avec ce type d'images que nous avons étudié les caractéristiques des amas reconstruits pour le traitement des rétro-diffusés.

secondaires disponibles arrivent aux diodes de collection par diffusion thermique.

Le deuxième critère est le temps d'intégration du capteur qui est donné par la durée du "séquençage" nécessaire à la lecture de la matrice de pixels. Des fréquences d'horloge couramment employées variant entre 10 et 100 MHz. L'ordre de grandeur est donc la vingtaine de nano-secondes par pixel. Il est bien entendu qu'il est pour l'instant impossible de lire parallèlement l'ensemble de ces pixels (un million pour un capteur d'images de taille acceptable). Par conséquent, la résolution temporelle est réellement contrainte par le nombre de sorties parallèles implantées dans le système de lecture de la puce. C'est pourquoi la limitation apparait dans le nombre de sorties physiques de la puce ou dans la possibilité de multiplexer des colonnes voisines.

A titre d'exemple, une lecture parallèle de 1024 colonnes utilisant une horloge pixel de 25 ns aboutit à une durée de lecture d'un capteur Mega-pixels de 26 μs et à une fréquence trame de 39 kHz. Cette fréquence conduit à des débits de sorties multiplexées bien trop grands pour les technologies actuelles. Sans multiplexage, ce débit nécessiterait un nombre de sorties bien trop grand.

Dans les deux cas, le débit de sortie est particulièrement difficile à gérer. En effet, une colonne de pixels (8 bits) lue à 40 MHz conduit à un débit par colonne de 320 Mbits/s. Pour les 1024 colonnes cela correspond à un débit de l'ordre de 320 Gbits/s ! Il apparait néanmoins qu'une architecture proposant une fréquence trame de 1 kHz c'est-à-dire de l'ordre de 8 Gbits/s est envisageable si 25 sorties à 320 Mbits/s sont utilisées en parallèle. Ainsi, nous voyons que pour un capteur d'image 1Kx1K de 1 cm^2 peut atteindre des fréquences trames supérieures au kHz en conservant des débits acceptables pour des systèmes d'acquisition robustes utilisant un lien Ethernet 10 Gbits/s ou 40 Gbits/s.

Passer à des fréquences trames supérieures à 10 kHz nécessitera soit des sorties de

puces dépassant le Gbits/s soit une réduction de données sur puces. Dans ce dernier cas, il faut s'assurer que le domaine d'application ne procure pas des taux d'occupation de pixels supérieurs à 10%. En effet, au delà de 10%, la suppression de pixels est inutile, voir dangereuse, du fait de la transmission de l'adresse des pixels. A titre d'exemple, une luminance de 100 mLux correspondant à un niveau de nuit très claire produit de l'ordre de 0.13 photon/10μm²/0.1 ms. Nous ne sommes pas très loin d'une imagerie aux photons uniques applicable à la vision nocturne !

Le flux de données accepté par le système d'acquisition reste au bout du compte le principal problème lié à l'augmentation de la fréquence trame dans une optique d'imagerie en continue, sans temps mort. Bien sur, l'utilisation de mémoires locales permet de contourner le problème. En réalité, elle ne fait que le reporter puisqu'il est nécessaire par la suite de consacrer du temps pour relire la mémoire (cas de la vision industrielle).

A notre connaissance, un débit de 40 Gbits/s semble être la limite actuelle avec un nombre de sorties raisonnable. La solution du stockage temporaire sur mémoire puis lecture différée reste privilégiée quand l'application le permet.

B.2.8   Le vieillissement

Les processus physiques liés au vieillissement de l'ebCMOS sont de différentes natures. Les premiers sont liées à la durée de vie du tube et l'autre à celle du capteur CMOS. Dans le premier cas, il s'agit de conserver la qualité de la cathode qui subie le bombardement des ions résiduels. La détérioration de la qualité du vide remet aussi en cause son fonctionnement et doit donc être pris en compte dans l'étude du vieillissement.

En ce qui concerne le capteur CMOS, il s'agit plus d'un problème lié à l'irradiation électronique dans les énergies du keV. Au-delà de 1.8 keV, il y a en effet génération de rayons X par le silicium et par conséquent une irradiation qui provoque l'accumulation de charges électriques dans les couches d'oxyde. Une augmentation du bruit des pixels en est la conséquence visible. La maîtrise du bruit pixel, comme cela a été déjà mentionné, impose une valeur de fonctionnement maximum de la haute tension dans la problématique (industrielle) du vieillissement des ebCMOS. Cet aspect a largement été observé sur les ebCCD utilisés à des énergies supérieures à 3 kV du fait de la présence d'une couche morte en face arrière relativement épaisse.

B.2.9   Le comptage de photons

Il nous semble nécessaire d'être précis dans l'utilisation du terme comptage de photons pour un détecteur sensible aux photons uniques. Si le flux de photons est tel que la probabilité pour qu'un pixel reçoive plus d'un photon pendant la durée de l'intégration de la charge est négligeable (inférieure à quelques pour cents), alors quelque soit son mode d'amplification (avalanche, ionisation par impact ou champ électrique de tube) un mode binaire permettra d'effectuer un vrai comptage de photons par sommation.

Dans le cas contraire (moyenne inférieure à 10 photons), à mon avis majoritaire en imagerie, le mode de multiplication et donc le facteur de bruit en excès joue un rôle primordial dans la capacité du capteur à procéder à un véritable comptage.
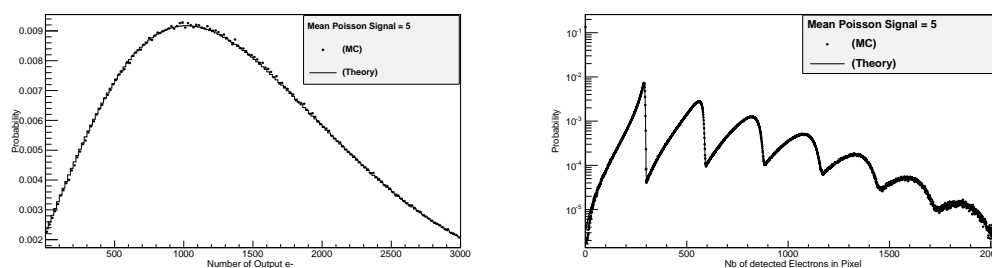
FIGURE I.13 – Simulation Monte Carlo des densités de probabilité des électrons secondaires pour un emCCD (gauche) et un ebCMOS (droite) simulées pour un nombre nombre moyen de photons incidents égale à 5.

Pour pouvoir effectuer un comptage réel il est nécessaire que les densités de probabilité du nombre d'électrons en sortie soient nettement séparées en fonction du nombre de photons reçus. Comme nous pouvons le constater avec les simulations Monte Carlo assez réalistes que nous effectuons des capteurs ebCMOS et emCCD que ce n'est réellement pas le cas pour ce dernier. La Figure I.13 illustre notre propos.

B.2.10 La résolution sur le pouvoir de localisation des ebCMOS

Il existe une différence importante entre la mesure de localisation d'une source ponctuelle et la mesure d'une résolution de *FTM* notamment pour le capteur de type ebCMOS. En effet, les différentes *PSF* jouent un rôle bénéfique dans le premier cas alors qu'elles le pénalisent dans le second. Ainsi, lorsque l'on cherche à localiser une source ponctuelle isolée, il est possible d'obtenir une information sur la valeur de sa position avec une précision bien meilleure que celle obtenue en fréquence spatiale. L'accumulation de plusieurs dizaines ou centaines de photons permet de reconstruire par le calcul du barycentre des charges ou photo-électrons la position moyenne de la source ponctuelle émettrice.

Pour mémoire, le nombre de photons par spot utilisés en optique adaptative est de l'ordre de 200. La résolution dans l'approximation du détecteur parfait (sans bruit et sans perte de résolution), varie en $\sigma_{tot}/\sqrt{n_\gamma}$ où n_γ est le nombre moyen de photon détectés par image de la source et σ_{tot} la déviation standard de la *PSF* totale du système (optique $\oplus$ capteur). C'est exactement la méthode utilisée pour la super-résolution de nano-balises (marqueurs) en microscopie de fluorescence lorsque les sources ponctuelles sont suffisamment isolées (méthode de type STORM). Dans le cas de l'ebCMOS, ce n'est plus simplement la *PSF* optique du microscope mais sa convolution avec les *PSF* du capteur qui est à considérer. C'est finalement grâce à la *PSF* totale et à la linéarité du gain que la reconstruction de la position moyenne de l'émetteur est particulièrement optimale (précise) en comparaison de celle obtenue avec un emCCD.

En effet, je pense que **dans le régime de l'imagerie aux photons uniques** (en réalité de 1 à 20 photons détectés par image et par balise suivie), le capteur ebCMOS est le mieux adapté à la localisation de "balises photoniques". A titre d'exemple d'ordre

paramètres externes	paramètres internes
- intensité (A) et λ de la source	- durée d'intégration (τ)
- position de la cible (x_s, y_s)	- bruit de lecture du pixel (e- RMS)
- forme/taille de la cible (point)	- taille du pixel (pitch)
- bruit de photons (Poisson)	- efficacité quantique (η)
- grandissement optique (M)	- courant d'obscurité - DC (Poisson)
- PSF optique (σ_o)	- PSF de diffusion CMOS (σ_d)
- ouverture numérique (NA)	- PSF tube (σ_t)
- efficacité optique (%)	- gain de multiplication (G)

TABLE I.2 – Listes des paramètres internes et externes à l'ebCMOS entrant dans le calcul de la précision de localisation d'un émetteur fixe.

de grandeur, un CMOS de pitch de 10 μm et une *PSF* ebCMOS de 13 μm donne une déviation standard sur la position de la source sur le capteur inférieure à 2 μm pour un nombre de photons détectés supérieur à 200. Ce résultat a été vérifie et simuler par nos soins.

Nous espérons que cette approche nouvelle conduira à des résultats particulièrement intéressant pour des mesures de phénomènes nécessitant un pouvoir de localisation rapide et précis. Nous estimons que cela sera le cas très rapidement dans les domaines de la bio-photonique avec la super-résolution rapide de nano-émetteurs et de l'optique adaptative avec l'utilisation de filtres de Shack-Hartmann (matrices de spots pour l'analyse de front d'ondes). Cette idée sera discutée en détails dans la section sur les applications et fait l'objet du travail de Doctorat de T. Cajgfinger.

La précision de localisation est un facteur qui dépend de nombreux paramètres expérimentaux. Je dresse dans le Tableau I.2 la liste des ces paramètres. Certains sont liés au photodétecteur et à son processus d'amplification, avant et pendant la lecture des charges secondaires, alors que d'autres sont liés aux conditions particulières de l'imagerie (bruit de photons, grossissement ...).

Les études de précision de localisation sont basées soit sur des simulation Monte Carlo des différentes *PSF* soit sur le calcul de la valeur limite inférieure de l'erreur sur l'estimateur de la position dite **limite de Cramèr-Rao**. Cette dernière permet de calculer la valeur limite d'un estimateur non biaisé par l'intermédiaire de l'information de Fisher. Il suffit donc d'écrire la densité de probabilité par pixel de mesurer un certain nombre d'électrons en fonction de l'ensemble des paramètres de la détection et des densités de probabilité. La valeur de l'estimateur, $\widehat{\theta}$, qui maximise cette fonction de vraisemblance est tout simplement le centre de gravité des charges des pixels.

B.2.11 L'estimateur non biaisé de localisation

L'estimateur de localisation, $\widehat{\theta}$, est une statistique d'une variable aléatoire X dont la densité de probabilité paramétrée $f(X;\theta)$ est connue et régulière (dérivable et dont les bornes d'intégration ne dépendent pas du paramètre θ). On définit l'information de Fisher à partir du logarithme de la fonction de vraisemblance θ, $L(\theta) = lnf(X;\theta)$:

$$I(\theta) = E\left(\left[\frac{\partial}{\partial\theta}lnf(X;\theta)\right]^2\right) \tag{I.5}$$

I est l'information sur le paramètre θ contenue dans la variable aléatoire X. Pour un échantillon $X = \{x_1, x_2, ...x_n\}$ l'information de Fisher est nI La limite de Cramèr-Rao (notée CRB) est la borne inférieure de la variance de l'estimateur non-biaisé : $\sigma_\theta^2 \geqslant \frac{1}{nI}$. Nous soulignons ici qu'il s'agit d'une valeur limite c'est-à-dire qu'elle n'est pas obligatoirement atteinte.

Remarquons également qu'il est possible de définir la CRB d'un estimateur biaisé par la relation : $\sigma_\theta^2 \geqslant \frac{[\tau'(\theta)]^2}{nI}$ où τ est la fonction de biais définie par $E(\widehat{\theta}) = \tau(\theta)$.

Dans l'étude que nous menons sur la précision de localisation nous estimons la CRB pour $n = 1$ (une image) correspondant à une mesure pour un flux de photon en général donné par une distribution de Poisson. Nous pourrions également étendre notre étude à des sources sub-Poisson (sub-shot noise) comme cela a été proposé dans la référence [28]-[29]. Dans la pratique, il "suffit" de déterminer la fonction de vraisemblance qui dépend des paramètres cités dans le Tableau I.2. Dans le cas d'un détecteur dont les informations par pixel sont indépendantes, l'information globale est la somme des informations par pixel obtenue par la densité de probabilité d'électrons secondaires après lecture. Dans le cas d'un détecteur parfait ou dans celui de l'ebCMOS à comptage et localisation de photons, l'information de Fisher est calculée sur toute la surface du détecteur englobant la *PSF* optique avec une variable aléatoire spatiale de la position mesurée du photon, x, est une densité de probabilité $p(\mathbf{x};\theta)$. Cette dernière est choisie Gaussienne et représente la convolution des trois Gaussiennes, optiques, tube et diffusion CMOS. C'est d'après les premiers résultats obtenus par Th. Cajgfinger, le cas le plus proche de celui du détecteur parfait (à faible flux). Dans ce dernier cas, la matrice d'information de Fisher s'écrit :

$$I(\theta) = \begin{pmatrix} \int_{\Re^2} \frac{1}{p(\mathbf{x};\theta)}\left(\frac{\partial p(\mathbf{x};\theta)}{\partial\theta_1}\right)^2 dx_1 dx_2 & \int_{\Re^2} \frac{1}{p(\mathbf{x};\theta)}\frac{\partial p(\mathbf{x};\theta)}{\partial\theta_1}\frac{\partial p(\mathbf{x};\theta)}{\partial\theta_2} dx_1 dx_2 \\ \int_{\Re^2} \frac{1}{p(\mathbf{x};\theta)}\frac{\partial p(\mathbf{x};\theta)}{\partial\theta_1}\frac{\partial p(\mathbf{x};\theta)}{\partial\theta_2} dx_1 dx_2 & \int_{\Re^2} \frac{1}{p(\mathbf{x};\theta)}\left(\frac{\partial p(\mathbf{x};\theta)}{\partial\theta_2}\right)^2 dx_1 dx_2 \end{pmatrix} \tag{I.6}$$

avec (θ_i, $i = 1, 2$) l'estimateur des position en x et y dans le plan du capteur.

Les résultats publiés jusqu'à présent tiennent compte de l'ensemble des effets expérimentaux en introduisant une fonction de vraisemblance dépendante de ces paramètres à travers des densités de probabilités Gaussienne et de Poisson suivant les cas (voir [30] pour la nanophotonique).

Il est remarquable que l'ensemble des articles consacrés à ce sujet ont depuis systématiquement utilisés la modélisation des CCD faite à l'origine par Snyder [31] pour l'imagerie en astrophysique alors que pratiquement tous les systèmes d'imagerie de microscopie de

fluorescence sont équipés de capteur emCCD. Aucun modèle de diffusion, notamment nécessaire pour décrire correctement les CCD ou les CMOS amincis par la face arrière et aucun modèle de gain de type emCCD n'ont été introduits jusqu'à présent dans les calculs de la CRB.

Le travail de doctorat de T. Cajgfinger porte en partie sur l'introduction des modèles de gain et de diffusion dans les calculs de Cramèr-Rao et les simulations Monte Carlo associées. Des comparaisons aux mesures expérimentales font aussi partie de ces objectifs. Je ne souhaite pas dans ce mémoire entrer plus en détail sur les fonctions de vraisemblance que nous avons introduites afin de laisser la primeur à une publication ainsi qu'au mémoire de T. Cajgfinger. Les premiers résultats ont été présentés à IS&T/SPIE 2011 "Electron Imaging" San Francisco 23-27 Janvier 2011 et publiés [32]. Cet aspect nous semble primordial avec l'augmentation prévisible de la vitesse d'acquisition des images et donc la réduction du nombre de photons par image et par émetteurs. L'idée reste évidemment l'étude de dynamiques biologiques avec la reconstruction rapide d'un grand nombre d'émetteurs ou l'analyse de front d'onde par la mesure des positions de spots avec une précision prédite et vérifiée pour un flux de photons donnés.

B.2.12   Pourquoi l'ebCMOS est particulièrement bien adapté à de la localisation ?

La simulation Monte Carlo et la limite de Cramèr-Rao permettent une comparaison de la précision de localisation de l'ebCMOS et de l'emCCD dans différentes configuration d'imageries notamment dans le régime de photons uniques. Intuitivement, on pourrait penser que la faible efficacité quantique condamne l'ebCMOS face à l'emCCD. Toutefois le facteur d'excès de bruit de l'emCCD joue un rôle non négligeable dans le calcul du centre de gravité à peu de photons. Ainsi, pour des efficacités quantiques supérieures à 20%, la performance de précision de localisation de l'ebCMOS dépasse celle de l'emCCD, comme cela est visible dans la Figure I.14.

Le résultat précédent est obtenu pour des émetteurs fixes par rapport au temps d'intégration du capteur. Or toutes les applications envisagées nécessitent la localisation d'émetteurs en mouvement. Ces mouvements peuvent être contraints, confinés ou browniens. Dans le cas des émetteurs en mouvement, il y a un compromis entre la vitesse de l'émetteur (la cadence image) et le nombre de photons émis par celui-ci (la résolution).

C'est ce problème qu'adressent de manières différentes les articles de 2010 de Michalet [33] et de Berglund [34] afin d'optimiser la durée d'intégration et le nombre d'images à considérer pour calculer le déplacement quadratique moyen afin de remonter au coefficient de diffusion du mouvement brownien. Le travail de Th. Cajgfinger a pour objectif final d'aboutir à l'estimation de ces paramètres dans le cadre de l'acquisition aux photons uniques par une modélisation réaliste des photodétecteurs à gain et à diffusion. C'est à ce niveau que nous essayons d'introduire le concept de suivi des émetteurs par l'accumulation des positions des photons successifs ainsi que des méthodes de type Kalman spatio-temporel.
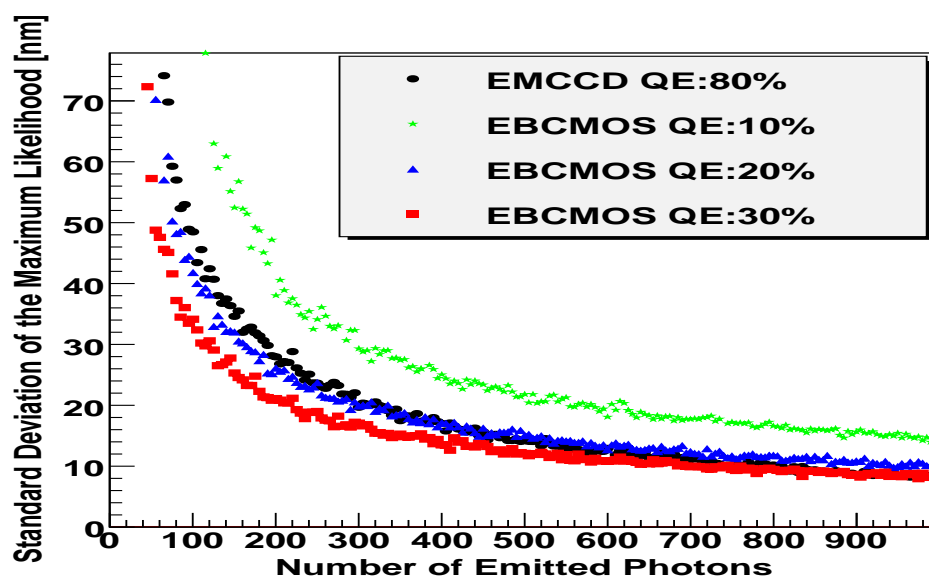
FIGURE I.14 – Simulation Monte Carlo de la précision de localisation pour les capteurs ebCMOS et emCCD en fonction du nombre de photon émis par la source pour différentes QE de l'ebCMOS.

B.2.12.i   Le pouvoir de suivi spatio-temporel de l'ebCMOS

Suivre un émetteur pose essentiellement deux problèmes relativement distincts : identifier et propager (suivre) la cible. La problématique de l'identification, lorsque l'on se situe dans l'imagerie aux photons uniques, est moins une question de reconnaissance de forme qu'une recherche de densité surfacique d'impacts plus élevés que le shot-noise ! C'est véritablement ce qui complique l'exercice. C'est en raisonnant en termes de compromis entre efficacité et pureté de cibles identifiées que nous pouvons développer un algorithme d'identification. La grande différence avec les algorithmes habituels de suivi de "cibles" multiples est que l'ingrédient de départ n'est pas une position estimée de l'émetteur sur le capteur au travers d'une reconnaissance de forme mais une liste d'impacts de photons, i.e une liste d'amas de charges de la matrice de pixels. Les étapes permettant l'identification et la confirmation de la présence d'un émetteur sont les suivantes :

1. Lister les amas de charge répertoriés sur la matrice courante

2. Rechercher tous les amas qui sont susceptibles de correspondre à l'impact d'un ou de plusieurs photo-électrons dans un rayon de pixels donné. Cela correspond à la supression du bruit de lecture pixel et des retours ioniques.

3. Calculer la position des impacts avec une précision de 2/10 de pixel. Cette résolution intra-pixel est obtenue grâce au calcul du centre de gravité des charges, corrigé par une fonction η, elle-même obtenue à partir de l'inversion de la fonction cumulative d'une distribution spatiale plate de bruit DC.

4. Rechercher est identifier une zone circulaire de l'ordre de grandeur de la *PSF* tube,

disque signal, pour laquelle la densité d'impacts est supérieure à la densité autour du disque signal, couronne de bruit de fond. Cela permet de sélectionner les candidats avec un rapport signal à bruit local.

5. Lister les candidats "émetteurs".

6. Comparer la liste courante avec une liste de candidats existants afin de valider les émetteurs ou de créer de nouveaux émetteurs.

7. Mettre en pose les candidats émetteurs non retenus

8. Supprimer de la liste les émetteurs "véritablement" éteints.

Remarquons que cet algorithme d'identification peut être séparé de la fonctionnalité d'affichage des cibles qui doit avoir ces propres règles de rapport signal à bruit sur cible et de persistance. Une fois l'émetteur pré-identifié et en cours de validation il est nécessaire de le propager si celui-ci possède un déplacement. Nous employons dans ce cas un suivi spatio-temporel (2D+t) soit par plus proche voisin, soit par filtre de Kalman. Il s'agit dans ce dernier de faire passer une trace dans une succession (t) de plans d'impacts (2D). Plusieurs options existent pour la mise en œuvre du filtre de Kalman (2D+t), notamment dans la définition du vecteur d'état (position et/ou vitesse) et du vecteur de mesure (photo-électron ou COG). Nous avons déjà observé que pour certains mouvements à changement de direction brutal (en rapport aux quelques ms de durée d'intégration capteur) des filtres de Kalman étendus (EKF) sont nécessaires. Les premières études seront publiées dans la thèse de Th. Cajgfinger. Cependant nous utilisons déjà ce type de suivi pour les nano-cristaux fluorescents. Je ne souhaite pas entrer plus dans les détails sur ce point dans le cadre de ce mémoire. Mais il y a ici un lien évident entre super-résolution statique, mouvement brownien et floutage dû à la vitesse de la particule pour le calcul des déplacements quadratiques moyens (à moyenne temporelle ou non). A titre d'illustration la Figure I.15 montre les résultats d'une simulation Monte Carlo du suivi d'une particule ponctuelle animée d'un mouvement brownien 2D grâce à un filtre de Kalman 2D+t.

B.3   Prospectives sur l'ebCMOS

B.3.1   Les CMOS amincis : architecture et technologie CMOS

Nous avons vu dans la section précédente que l'amincissement du capteur CMOS et surtout le post-processing, composé d'un amincissement contrôlé de la face arrière et d'une ré-implantation de Bore en surface sont les points clés des performances de l'ebCMOS. Nous discutons dans cette section les possibilités d'évolution dans ce domaine qui pourraient fortement modifier les performances. La technique de l'amincissement évolue rapidement car elle touche des marchés de capteurs d'images à grand volume où la tendance est à la réduction de la taille des pixels qui induit une diminution du nombre de photons reçus par pixel. La réduction du bruit de lecture ne peut pas compenser complètement cette diminution de signal qui pose par conséquent des contraintes fortes sur le facteur de remplissage et nécessite l'emploi de capteurs amincis par la face arrière (BSI). Des couches de passivation introduite dans le processus de la technologie SOI de l'ordre de
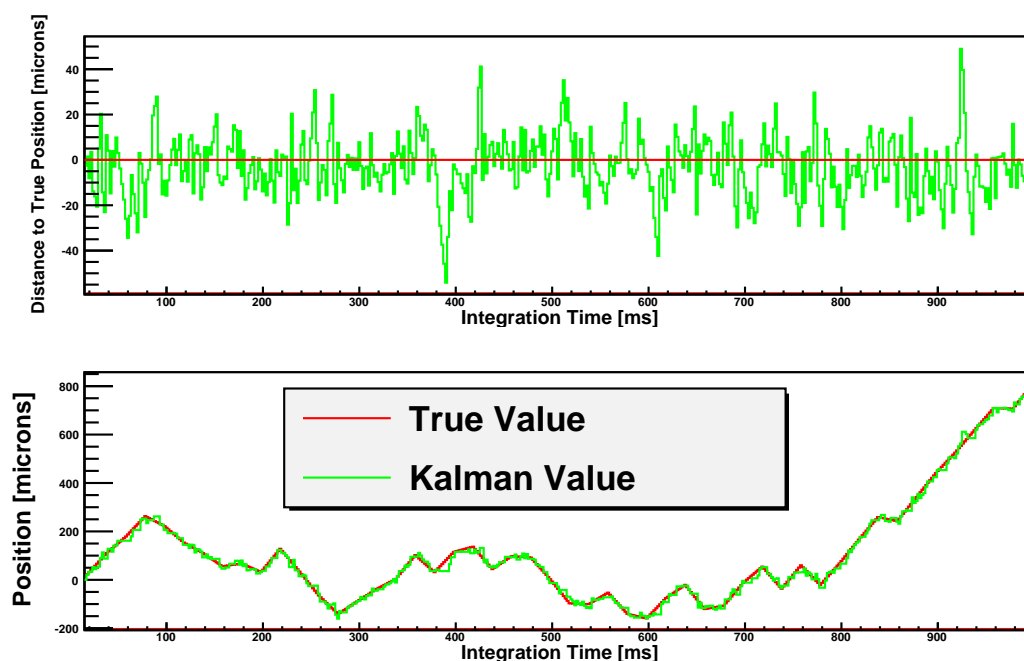
FIGURE I.15 – Résultats sur le suivi et la résolution sur le suivi du filtre de Kalman (2D+t) pour une simulation Monte Carlo d'une trajectoire d'une particule ponctuelle animée d'un mouvement brownien 2D.

170 nm sont désormais disponibles avec des couches épitaxiales amincies contrôlées par etch-stop. L'ebCMOS bénéficie de ces développements. Mais ceux-ci restent insuffisant pour obtenir des couches de passivations inférieures à 30 nm (nécéssité d'une passivation après décapage) et des efforts particuliers doivent être menés suivant trois directions :

1. contrôler l'amincissement de la couche épitaxiale avec une tolérance inférieure au micromètre afin de travailler avec des couches épitaxiales inférieures à 2 μm pour réduire la *PSF* CMOS et augmenter le SNR par pixel. L'alternative à ce développement, pas obligatoirement incompatible, et l'utilisation d'une couche de haute résistivité pour augmenter la zone de charge d'espace et donc de diminuer la zone de diffusion afin également de diminuer la contrainte sur l'épaisseur de la couche épitaxiale décapée.

2. contrôler la profondeur l'implantation et le profil de dopage du Bore afin de diminuer l'épaisseur de la couche morte.

3. contrôler les paramètres employés pour le recuit laser. Ils sont essentiels et demandent un ajustement délicat entre durée et intensité et de bonnes reproductibilité et homogénéités.

Pour la partie CMOS (structure pixel et architecture de lecture) nous voyons trois voies d'amélioration :

1. La structure des pixels peut être modifiée afin de réduire la *PSF* du CMOS. L'utilisation de tranchés profondes (DTI) déjà en vigueur dans les capteurs d'images

standards est une solution privilégiée si la technologie le permet. Une maîtrise de la quantité de charge partagée entre les pixels pourrait être un moyen de réduire la contribution du bruit pixel au taux de déclenchement du photon unique par la sélection d'un amas plutôt que celle d'un pixel unique (utile en mode comptage). L'utilisation de pixels de pitch inférieur à 5 μm bénéficierait avantageusement de DTI.

2. Le bruit temporel du pixel peut être réduit à 1 électron. Cela améliorera grandement le SNR du photo-électron unique et permettra la diminution du gain et du GAP cathode capteur CMOS, et par conséquent, augmentera la résolution spatiale du capteur et sa dynamique.

3. A plus long terme, les technologies d'intégration 3D (E3D) par l'utilisation de via verticaux (TSV pour Through Silicon Via) permettra une "révolution" dans les capteurs d'images. Même si la principale utilisation du TSV apparaît dans la fabrication de mémoire (principalement grâce au volume du marché), les avantages qu'elle apporte pour les capteurs d'images sont nombreux. Nous donnons ici une liste des apports escomptés de l'électronique 3D à l'imagerie :

   (a) Les connections TSV étant plus courte apporteront une diminution de la consommation, qui sera surement compensé par l'augmentation de la complexité des circuits ! Cela est très important lorsque le nombre de voies de lecture (ou pixels) à augmentation quadratique.

   (b) Les TSV offrent un accès en parallèle et simultanément à l'ensemble de la matrice de pixels. Les fréquences de lecture du capteur d'images n'as plus pour limite le temps de lecture d'une colonne de pixels mais celui d'une lecture d'un pixel. Ainsi le temps de collection de la charge du volume sensible deviendra le facteur limitant.

   (c) D'après le point précédent, le nombre de voies de sorties lues en parallèle est dangereusement augmenté pour des débits de données acceptables par les technologies de communication les plus rapides (Ethernet 40 ou 100 Gbits/s par exemple). Irrémédiablement, nous verrons apparaître des architectures 3D plus complexes afin de réduire le taux de données à transférer (données correspondant à un signal physique).

   Nous pouvons imaginer qu'augmenter par un facteur 1000 la fréquence trame d'un capteur d'image réduira d'autant le taux d'occupation des pixels. Cette hypothèse simplificatrice est à notre avis légèrement optimiste car elle présuppose un taux d'émission des sources constant. Le niveau de concentration des données ainsi que la logique appliquée devra par conséquent être soigneusement évalué. Nous pouvons cependant remarquer qu'une lecture d'un capteur d'images à la fréquence trame de 1 MHz permet l'acquisition aux photons uniques par des pixels de 4 microns de pitch d'une luminance de 1 lux (1 photon/μs/pixel). Ainsi l'E3D nous permettra d'observer aux photons uniques des scènes d'une luminance de 1 Lux c'est-à-dire d'un niveau de nuit 1 correspondant à un crépuscule sombre !

(d) Il faut remarquer que les outils de simulations de la propagation des charges mais aussi des effets thermiques permettront une véritable conception des architectures en 3D. La contrainte de refroidissement ou tout au moins d'un certain contrôle de la température et de ces effets sur les signaux électriques doivent être pris en compte à la conception pour gagner en fiabilité. Cette contrainte est d'autant plus présente que le nombre de voies lues en parallèle est important.

(e) L'accès parallèle aux pixels permettra un gain dans la gamme dynamique intra-scène quasiment "infinie" si un processus de gain intra-pixel ajustable peut être implémenter par pixel.

(f) Pour des fréquences trame standards (inférieure au kHz) la mise en parallèle des voies de sortie peut permettre une réduction de la fréquence d'horloge de lecture des pixels c'est-à-dire de passer du MHz au kHz. Dans ce cas une étude des bruits de lecture doit être revue à ces nouvelles fréquences.

(g) La connexion par l'arrière proposée offerte par les TSV permet d'imaginer la fabrication de plus grande surface de détection par l'aboutement de capteurs d'images sans perte liées aux zones de connexion face avant et aux architectures de lecture situées autour de la matrice de pixels.

(h) Les techniques de l'E3D nécessitent de nombreux progrès technologiques dans la manipulation de wafers amincis. Il est évident que l'une des difficultés de production des ebCMOS se situe dans cette manipulation et dans la possibilité de connecter la face arrière amincie sans l'utilisation de wedge bonding qui perturbe les lignes de champ de la focalisation par proximité et qui limite en partie la diminution de la distance cathode-capteur CMOS à quelque centaines de microns.

L'enjeu réside donc dans la possibilité de rassembler dans un même processus industriel des techniques de collages de wafers, d'amincissement et les techniques de pompages ultra-vide et de processus cathodes troisième génération. Dans ce cas, des lunettes de nuit (et non plus de soleil) seraient envisageables.

Il y a certes des problèmes techniques non résolus qui limitent encore l'application des TSV à un large domaine de la photodétection mais il s'agit vraisemblablement d'une question de modèle économique qui peut justifier de nombreux investissements pour des marchés escomptés de gros volumes. De nombreuses applications de niche mais également de la physique des hautes énergies pourraient bénéficier très avantageusement de ce type d'évolutions mais malheureusement ne trouvent aucun modèle économique viable pouvant justifier de tels investissements.

B.3.2   Tubes et Photo-cathodes

Il est difficile d'anticiper l'évolution des technologies tubes car les technologies utilisées (relativement empiriques) sont connues des seuls fabricants au nombre limité. On peut

imaginer cependant que la diminution du gap entre cathode et capteur CMOS reste l'enjeu principale pour les années à venir (MTF). Le gain viendra peut être de méthodes de fabrication plus simple ou à meilleur rendement ce qui permettra de diminuer les couts de production de ce type de capteur qui sur le papier est celui qui à le moins de composants et qui est le plus simple. La solution "rêvée" pour la fabrication des tubes restent pour nous une solution wafer (AsGa) sur wafer (CMOS) avec l'E3D et un FPGA sur céramique en flip-chip. En ce qui concerne le futur de la photo-conversion, il faut mentionner les progrès effectués dans les nanotechnologies. Les travaux de l'équipe canadienne Sargent [35]-[36] montrent que ce domaine apportera certainement des solutions nouvelles tant du point de vue de l'amplification de la lumière en amont que dans la possibilité de changer de processus cathode pour en faciliter la production. Il faudra néanmoins atteindre des efficacités quantiques comparable au Gen III ce qui ne semble pas le cas pour l'instant. La diminution de la haute tension utilisée de quelques kV à quelques centaines de volt sera également un gain de simplicité de fabrication et d'intégration pour les différentes applications de l'ebCMOS.

B.4   Domaines d'applications de l'ebCMOS

B.4.1   La nano-photonique

Dans ce mémoire, nous entendons par nano-photonique, l'observation (identification, quantification, suivi) de nano-émetteurs de photons dans le domaine du visible. Ces sources ponctuelles ont des dimensions allant de quelques nanomètres à quelques dizaines de nanomètres. Elles ont toute pour propriété de posséder un spectre d'absorption décalé par rapport au spectre d'émission. L'association judicieuse de filtres en émission et en transmission permet de les détecter par un microscopie optique, champ large ou par ondes évanescentes (TIRF).

La nature de ses balises fluorescentes peut être très variable. On compte parmi elles les protéines fluorescentes (GFP,YFP,...), les molécules uniques, les nano-cristaux semi-conducteurs (CdSe), les nano-diamants (fNanoD). De nombreux développement existent dans ce domaine qui évoluent et progressent très rapidement. C'est un domaine à la frontière entre la chimie et la biologie car la difficulté réside dans l'association des traceurs fluorescents aux processus, aux entités, aux fonctions biologiques ciblés tout en respectant les conditions du vivant (la photo-toxicité, le photo-blanchiment). L'amélioration du rapport signal à bruit en termes de photons émis tant du point de vue des sources de photons que de la méthode de microscopie sont pour moi les facteurs essentiels des progrès à venir.

Néanmoins, de nouveaux capteurs d'images rapides et sensibles restent nécessaires afin d'aborder des problématiques biologiques, qui jusque là, restaient cachées du fait de temps d'intégration trop longs ou de sensibilité trop faible des capteurs d'images utilisés (on pense ici à l'hypothèse d'ergodicité [37] et à la problématique des diffusions anormales). Un domaine de la microscopie de fluorescence ou nous pensons qu'il existe des marges de progrès liés à ces facteurs est celui de la super-résolution, i.e. une résolution inférieure au critère de Rayleigh [38]. Dans la mesure où le nombre de sondes fluorescentes est suffi-

samment faible pour avoir une densité de sources permettant leur observation de manière univoque spatialement (ou séparable) il est possible de calculer leur position moyenne avec une précision dépassant celle du critère de Rayleigh, s_0=1.22 $\lambda/(2$ NA$)$ $\sim$ 250 nm. Cette précision de localisation peut atteindre le nanomètre si la statistique en photons est suffisamment grande (2000) et si les conditions de rapport signal à bruit sont favorables. Les techniques dites de microscopie de reconstruction stochastique, STORM [39], comme le PALM (Photo-Activated Localization Microscopy), permettent d'atteindre cette résolution avec l'emploi de capteur d'images de type emCCD.

Deux problématiques peuvent être abordées par l'ebCMOS avec des apports intéressants. D'un point de vue statique c'est le grand nombre de balises photoactivables que l'ebCMOS peut aller reconstruire en parallèle. Ainsi l'obtention rapide et quasiment en temps réel d'un grand nombre de positions de marqueurs permet d'imager des structures (typiquement des membranes) à l'échelle nano-métrique. L'apport de la rapidité et du haut-débit de l'ebCMOS est incontestable dans ce domaine.

D'un point de vue de la dynamique, le tracking de particules uniques rapides et super-résolues est un enjeu important à l'échelle nano-métrique pour remonter au type de mouvements des nano-objets (browniens, confinés, forcés...) [33] dans les différents milieux. Habituellement la mesure du déplacement quadratique moyen (MSD) pour différents intervalles de temps permet d'obtenir une estimation du coefficient de diffusion seulement si le nombre d'échantillons tend vers l'infini, ce qui n'est expérimentalement pas le cas. Des travaux proposent de nouveaux estimateurs à base de moyenne temporelle (SRMS) de processus Gaussien [40]-[41].

Ce travail théorique n'intègre pour l'instant pas les erreurs expérimentales de mesure sur la position en fonction des capteurs utilisés et du temps d'intégration. En effet il y a un véritable compromis à trouver entre la durée d'exposition, qui doit être diminuée pour éviter le floutage du au déplacement, et la précision de localisation qui nécessite un nombre suffisant de photons [33]. Nous allons porter nos efforts sur ce point avec la thèse de T. Cajgfinger.

Je ne souhaites pas aborder dans ce document tous les sujets d'intérêt de l'ebCMOS pour la nanophotonique mais il y a très certainement à regarder du coté du suivi en 3D avec la méthode de la PSF à double hélice (DH-PSF) utilisée dans [42] et développée par Pavani et Piestun [43].

Pour les aspects biotechnologies, il me semble que les capacités de quantification à haut-débit de l'ebCMOS seraient un atout pour le développement de méthode de séquençage de l'ADN à la molécule unique par l'imagerie de matrice de "nanopores" [44].

B.4.2   La vidéo-microscopie

Dans le domaine de la vidéo-microscopie, l'ebCMOS tire plus son avantage de la rapidité que de sa sensibilité aux photons uniques. Néanmoins des capteurs CMOS très rapides existent (la caméra Photron par exemple) mais ils ont le désavantage de ne pas fonctionner en continu et surtout de ne pas présenter la sensibilité requise pour des temps d'intégration aussi courts en rapport au nombre "supportable" de photons émis par la biologie.

L'ebCMOS, propose grâce à son gain, le meilleur compromis entre rapidité et sensibilité. L'observation en microscopie de champ sombre de la nage des bactéries *E. Coli* en est un bon example. La fréquence de rotation des flagelles servant à la propulsion est supérieure à la centaine de Hertz est l'étude de la cinématique de la ré-orientation du corps des bactéries nécessite des fréquences d'images supérieures à 250 Hz. Cette fréquence d'image est nécessaire pour avoir une bonne précision sur leur orientation et leur trajectoire "instantanée". De bons rapports signal à bruit sont obtenus à des fréquences d'images de 500 Hz avec des flux de photons par bactérie autour de la dizaine en microscopie de champ sombre. De plus, la possibilité de capturer en continu les données brutes étend notoirement l'efficacité de l'analyse par l'augmentation du temps utile et donc du nombre de bactéries suivies. Cela facilite l'étude statistique sur une plus grande population car obtenue sur une plus grande durée.

Le chapitre suivant aborde ce sujet traité dans le cadre d'une collaboration avec l'équipe de L. Lemelle et de C. Place de l'Institut Joliot-Curie à l'ENS de Lyon. Une publication sur le sujet est en cours de rédaction et se confronte au travaux de Berg qui est la référence dans ce domaine [45, 46, 47, 48, 49].

B.4.3   L'optique adaptative

La mesure du front d'onde par des matrices, dites filtre de Shack-Hartmann, est principalement utilisée en astrophysique sur les télescopes [50]. Il s'agit de mesurer précisément le front d'onde à la pupille du télescope en l'échantillonnant par une matrice de micro-lentilles. Les positions des centres des spots permettent de remonter, après comparaison à une position de référence, le gradient des vecteurs d'onde. Les performances requises pour les futurs télescopes géant (20-40 m), type ELT, sont d'après les spécialistes de ce domaine, pour ce qui est de l'échelle de temps : la milliseconde. Avec un diamètre de Fried, $r_0 = 10$ cm à λ égale à 500 nm, on a un temps de cohérance de 3 ms qui contraint la fréquence de trames. De plus, le nombre de spots à suivre en boucle fermée sera de plusieurs milliers.

Du point de vu de sa sensibilité et de son pouvoir de pointé et surtout de sa capacité à traiter en parallèle et indépendamment des spots pour atteindre la résolution voulue en fonction du nombre de photon signal reçus, le capteur ebCMOS mérite d'être soumis aux contraintes de l'optique adaptative sur télescope de manière plus détaillée (simulation de la correction de la PSF en fonction des paramètres de l'atmosphère, du télescope et de l'ebCMOS).

Ce programme est prévu pour les mois à venir et devrait aboutir à une publication prouvant l'intérêt de ce capteur pour ce domaine. Reste à savoir si l'on arrivera à toucher la communauté de l'instrumentation sur télescope. Pour l'instant la précision de localisation sur capteur atteint actuellement sur nos bancs de tests atteint 2-4 micron en moins de 100 photons avec quelques photons par milliseconde et par spot.

Enfin, un développement d'une fenêtre de photo-cathode dédiée à l'optique adaptative, c'est-à-dire intégrant une matrice de 400000 micro-lentilles, sont envisageables ! L'usage de GPU (Graphical Processor Unit) permettrait de soutenir le flux dans le calcul

des barycentres.

B.4.4   La bioluminescence marine

La biodiversité des grands fonds marins (60% de la surface terrestre à une altitude inférieure à -2400 m, voir la Figure I.16) reste encore mal connue et l'une des voies d'observation est la bioluminescence. La bioluminescence marine peut être utile à de nombreux domaines d'études portant sur des problématiques très diverses de biologie, d'écologie et d'environnement telles que la biodiversité et la contribution des océans au cycle du carbone. La bioluminescence est l'émission de lumière visible par un organisme vivant du fait
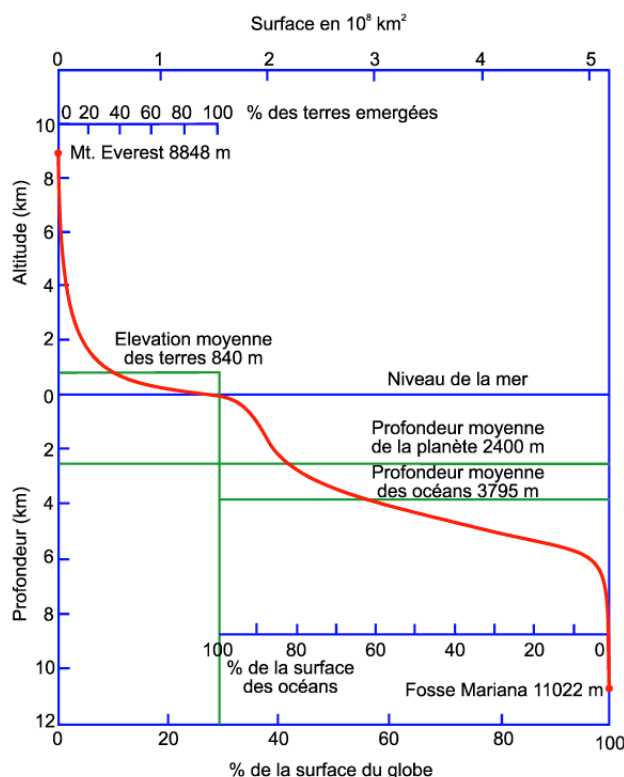
fig. 2.4 répartition des terres et des mers

FIGURE I.16 – Répartition de la surface terrestre en fonction de l'altitude. La profondeur moyenne de la planète est de -2400 m. (source : http ://lecalve.univ-tln.fr/oceano/plan.htm.

de l'association (dans la plupart des cas) de la luciférine et de la luciférase. Les phénomènes de bioluminescence sont très présents dans le milieu marin et notamment dans les grands fonds [51]. Ils peuvent être stimulés ou spontanés et peuvent correspondre à des nécessités de types attaque, défense ou communication pour les espèces animales.

Dans le domaine de la bioluminescence marine, la première des exigences est l'obtention de la meilleur sensibilité possible sans une augmentation du bruit de fond du capteur.

Applications	rapidité	pouvoir de pointé	comptage de photon	bas bruit	smart	faible conso
Bioluminescence	+	+++	•	+++	++	•
Nano-photonique	+++	+	+++	•	•	•
Vidéo-microscopie	+++	+	•	•	•	•
Vision nocturne	•	•	•	•	+++	+++
Bio-puce	+++	+	+++	•	+	•
Opt. adaptative	+++	+++	+	•	•	•

TABLE I.3 – Tableau des avantages de l'ebCMOS en fonction des applications mentionnées dans le texte.

En effet, certains phénomènes de bioluminescences émettent peu de photons (10^6/s dans 4π) sur une très courte période (1 ms $\sim$ 10 s). Le phénomène est observable uniquement dans des conditions de noir parfaites comme cela est le cas dans les grands fonds marins. La bioluminescence n'étant pas stimulée par un laser (cas de la fluorescence) une contrainte supplémentaire réside dans la nécessité d'observer en permanence et d'être capable de déclencher l'enregistrement de la séquence d'images susceptibles de comporter de l'information par rapport à une image de bruit du capteur.

La priorité pour les détecteurs de bioluminescence est par conséquent la minimisation du bruit et la sensibilité aux photons uniques et la capacité à auto-déclencher la conservation des données sur disque. La rapidité n'est nécessaire que pour des phénomènes de type flash ou de mouvements avec changements de trajectoire ou lorsque les courants sont très forts (20-40 cm/s).

Face à ces contraintes d'observation on comprend aisément que l'ebCMOS est bien adapté. En plus de sa sensibilité aux photons uniques et de son taux de comptage d'obscurité faible, il peut effectuer un véritable comptage de photons par image permettant une prise de décision de suivi ou de stockage des données. Nous en avons fait la preuve avec notre prototype LuSEApher/Biocam installé sur le site ANTARES à -2500 m.

De manière plus générale, je pense que le détecteur ebCMOS est particulièrement bien adapté aux applications de vison de nuit pour lesquelles la principale exigence est la détection d'un très faible flux de photons parmi un bruit restreint de photons. Des applications de type suivi ou surveillance dans des longueurs d'onde autre que le visible, nous pensons essentiellement aux applications UV Solar Blind, rentrent dans cette catégorie.

B.4.5   Positionnement et prospectives sur les applications

Nous venons de proposer différentes applications de vision aux photons uniques pour lesquelles l'ebCMOS peut être intéressant. Le tableau I.3 donne une synthèse de l'adéquation entre les performances de l'ebCMOS et les applications mentionnées dans ce chapitre.

J'ai volontairement peu discuté la gamme dynamique dans ce chapitre puisque le sujet concerne l'imagerie aux photons uniques. Il existe cependant un sujet d'étude intéressant qui correspond en termes d'imagerie aux flux de photons intermédiaires entre imagerie aux photons uniques et imagerie à haut flux. J'entends par là, un algorithme capable de traiter des flux de photons entre 10 et 30 par objet et par image. Dans ce cas, il y a trop de photons pour élaborer un traitement par photon unique, du fait des recouvrements de charges, mais encore pas suffisamment de photons pour travailler avec une image de pixels bien contrastée et suffisamment continue dans ces niveaux de gris.

Le deuxième point concerne le suivi de cibles, notamment rencontré dans la nano-photonique. Les progrès futurs dans l'ingénierie des sondes fluorescentes et des marquages fonctionnels ou anatomiques ainsi que celle de la microscopie (notamment le 3D) devront tirer parti des nouvelles possibilités de vitesse et de sensibilité offertes par les capteurs à bas niveau de lumière. Lors de nos tests sur site, nous avons constaté le plus souvent que les limitations sur le tracking provenaient plus d'un rapport signal à bruit de photons très défavorable pour du suivi à la milliseconde que du capteur lui-même.

Un point caractéristique de l'ebCMOS non suffisamment exploité pour l'instant est sa capacité à compter très précisément le nombre de photons moyen (Poisson voir "sub-Poisson" [29]) sur une échelle de temps adaptée à la dynamique observée. La capacité de quantification du taux d'émission d'un émetteur unique permettrait par exemple de faire de la quantification des bio-puces à la molécule unique sans amplification préalable. Je conseil la lecture de [44] sous l'angle de vue de l'ebCMOS. Par exemple, nous avons montré dans le cadre de notre campagne de tests à Nanoptec (Eq. Dujardin-Ledoux), que le clignotement des nano-cristaux de CdSe pouvait être suivis et quantifié à la milliseconde sur plusieurs dizaines de nano-particules en parallèle.

Chapitre II

Le projet ebCMOS

A   Imagerie de photons uniques

A.1   Contexte du projet

L'ebCMOS, utilisé jusqu'à présent en vision nocturne, n'avait jamais fait l'objet d'une étude approfondie en imagerie aux photons uniques. Le projet de R&D ebCMOS, démarré à l'IPNL en 2002, s'est déroulé en deux étapes : une **preuve de faisabilité** et une **preuve de concept**. Le concept répond à une problématique de l'imagerie rapide basée sur la distribution spatio-temporelle des photons uniques enregistrés.

En se plaçant dans le cas extrême du bas flux de photons, l'ebCMOS doit détecter (identifier), quantifier (comptage) et suivre (propager) de nombreuses sources de lumière dans un grand champ de vue. On comprend mieux ainsi l'acronyme LUSIPHER de **L**arge-scale **U**ltra-fast **SI**ngle-**PH**oton record**ER**.

Les sources de photons considérées dans cette R&D sont ponctuelles ou peu étendues (sur quelques dizaines de pixels), émettent un nombre de photons par durée d'intégration du pixel dans un régime Poissonien (1 à 30 photons), ont des mouvements qui correspondent à des déplacements maximum sur capteur du micron par milliseconde.

Les trois questions clés auxquelles nous avons du répondre sont :

1. Comment identifier à la milliseconde les sources parmi un bruit de fond de photons ?

2. Comment quantifier au dixième de photon et localiser au micron la source de photons à la milliseconde ?

3. Comment suivre l'ensemble des cibles identifiées et caractériser leur type de mouvement (confiné, contraint, brownien, ...) ?

La première question porte sur des problématiques de type :

- génération, apparition et validation des cibles,

- survie et disparition des cibles,

- efficacité et pureté des cibles en fonction des bruits, de la sensibilité, et de la moyenne temporelle souhaitée.

La deuxième question concerne, d'une part, la résolution spatiale en fonction des *PSF*s du détecteur pour la localisation et d'autre part, le processus de gain nécessaire à la quantification. La troisième question découle des deux précédentes et aborde la notion de suivi, de lissage de trajectoires et de mesure de déplacements moyens permettant de remonter au mouvement des objets ciblés. Par exemple, il peut s'agir de l'étude de mouvements Browniens dans des milieux biologiques ou de reconstruction de fronts d'ondes déformés par leur passage dans l'atmosphère.

A.2 Solution et mise en œuvre

La réponse donnée par le concept d'ebCMOS à la problématique de l'imagerie aux photons uniques se décline en trois objets et techniques d'acquisition et de traitement des données :

1. un capteur ebCMOS aux performances de sensibilité et de rapidité supérieure à l'ebCMOS de vision nocturne,

2. un système d'acquisition puissant à très haut-débit,

3. des algorithmes de traitement temps réel pour l'extraction de l'information (position, intensité, vitesse des sources...).

Chaque point a nécessité une R&D longue et difficile tant du point de vue technologique que scientifique. C'est un travail de longue haleine qui se devait de progresser en parallèle sur des domaines assez différents :

1. l'amincissement et la passivation des CMOS,

2. la diminution de la distance cathode-CMOS avec des tolérances faibles pour éviter les claquages,

3. la conception et le développement des bancs et des méthodes de tests pour les caractérisations des CMOS (face avant et face arrière) et des ebCMOS,

4. la conception et le développement des sources de photons uniques dont le spot est localisé et déplacé au micron pour une caractérisation intra-pixel aux photons uniques,

5. la conception et la fabrication de systèmes d'acquisition versatiles et ouverts d'abord avec une électronique de lecture possédant un taux de transfert de 1 Gbits/s puis de 10 Gbits/s,

6. la conception et le développement des algorithmes rapides et "légers" de reconnaissance d'amas de charges,

7. la conception et le développement des algorithmes d'identification et de suivi de sources ponctuelles établis à partir des photo-électrons identifiés par image,

8. la conception et le développement d'un logiciel d'acquisition capable de recevoir et de traiter jusqu'a 10 Gbits/s de données proposant une interface utilisateur qui permet de visualiser en temps réel le résultat des pré-traitements ou de sauvegarder les données brutes sans perte,

9. le développement d'une simulation réaliste prenant en compte tous les bruits majeurs des capteurs de type emCCD, sCMOS et ebCMOS,

10. le calcul de la limite de de Cramèr-Rao sur la précision de localisation par l'introduction du gain de multiplication et des bruits associés.

Pour situer le niveau d'investissement en matière de ressources humaines, j'ai compté plus de 20 chercheurs, ingénieurs et techniciens qui ont travaillé de manière significative sur ce projet depuis 2004.

Les étapes suivies permettant la démonstration de faisabilité, **prototype ebMI-MOSA5**, ont été les suivantes :

– caractériser le gain et la sensibilité de CMOS amincis de grande taille et de fréquence d'image 25 Hz (fourni par l'IPHC) par des études en bombardement électronique sous irradiation X et sous lumière violette focalisée.
– collaborer avec la société PHOTONIS afin d'intégrer le CMOS aminci dans un tube conçu à cet effet.
– caractériser les prototypes ebCMOS fabriqués.
– développer un système d'acquisition dédié ainsi que son logiciel.
– tester les ebCMOS sur site dans des conditions d'utilisation standard (système de caméra).

Ces étapes réalisées sur trois années (2004-2007) nous ont permis de montrer que l'on pouvait fabriquer ce type de détecteur et évaluer ses performances. Malheureusement la fréquence trame étant standard, il n'était pas possible de tester le concept d'imagerie aux photons uniques à la milliseconde.

En effet il est important de mentionner à ce niveau que le fonctionnement de MI-MOSA5 à 25 images par seconde nécessitait des luminances relativement faible en rapport à celles utilisées dans l'imagerie de marqueurs fluorescents dans la mesure où l'exigence du photon unique en était l'enjeu. Ce point crucial nous a conduit à travailler sur une évolution du projet avec pour objectif une fréquence trame de 1000 images par seconde afin de descendre aux photons uniques avec des luminances "standards".

Il a donc été nécessaire de relancer une fabrication d'un capteur CMOS rapide et de l'amincir (collaboration avec l'industriel SAGEM DS) puis de l'intégrer dans un tube à photo-cathode produit par PHOTONIS. Ce deuxième prototypage nous a permis de travailler en amont sur différentes versions d'amincissements, de passivation et de substrats. Nous avons ainsi pu progresser sur de nombreux points liées à la *PSF* du capteur CMOS. Finalement, la caractérisation complète des différentes versions de puces, nous a permis de choisir la mieux adaptée à nos besoins de détection de photons uniques (meilleure CCE et gain). La production d'un nouveau système d'acquisition dédié ainsi que de son logiciel d'acquisition a été rendue nécessaire par les taux de transferts requis. La partie tests sur site a démarré en 2010 et ce prolonge avec une phase de développement logiciel en fonction des applications envisagées tant du point de vue VHDL sur le FPGA que logiciel sur les CPUs de la station d'acquisition. Il est clair que les méthodes d'identification et de suivi continuent de faire l'objet de nos développements principaux afin de s'adapter aux conditions, notamment de bruit de photons, différentes que nous rencontrons sur site ou en laboratoire. Nous sommes à présent, en 2012, dans la phase de retour scientifique de notre investissement dans cette R&D .

B   Caractérisations des CMOS amincis et des ebCMOS

B.1   Types de caractérisation

Lorsque l'on considère la complexité et le coût de la fabrication d'un ebCMOS on prend vite conscience qu'il est nécessaire d'approfondir en amont sa connaissance du capteur CMOS **avant et après** son amincissement et sa passivation. Dans une première étape, les CMOS sont caractérisés sur circuit imprimé en face avant pour la mesure du bruit temporel des pixels, de la dispersion des piédestaux après double échantillonnage corrélé et d'une calibration X par une source de Fer 55 émettrice de deux raies à 5,899 keV (24,4%) et à 6,49 keV (2,9 %). Dans le cas peu probable où la conversion des X est complètement contenue dans la diode N, l'événement enregistré est utilisé pour une calibration du facteur de conversion en e-/ADCU, avec l'hypothèse d'une énergie moyenne par électron/trou générés de 3.6 eV. Cela nécessite une source de Fer 55 de forte activité afin de réduire la durée de l'acquisition.

Les efficacités de collection de charges sur le pixel central (le pixel ayant le plus de charge collectée) ainsi que celle de l'amas de pixels autour du pixel central peuvent être aussi obtenues à partir de ce type de données. D'après les mesures que nous avons effectuées sur plusieurs générations de puces CMOS nous avons pu constater que les mesures en X donnaient en général des valeurs d'efficacité de collection de charges assez proches de celles obtenues par le bombardement électronique (CCE(X)∼CCE(e-)).

J'ai longuement insisté sur le fait que l'un des paramètres essentiels de l'ebCMOS est la qualité de la couche de passivation de la face arrière. C'est pourquoi deux types de caractérisation ont été menées afin d'aboutir à une meilleure compréhension des effets liés à cette couche. La première est celle du bombardement électronique par une source d'électrons uniques. Elle permet principalement d'évaluer la perte d'énergie dans la couche morte (et donc son épaisseur), l'homogénéité du processus de passivation, l'efficacité de collection de charge moyenne obtenue sur le pixel central, la collection maximum de la charge par la considération d'un amas de pixels. La deuxième est consacrée à un aspect conditionnant la résolution spatiale : la mesure de la *PSF* du CMOS. La méthode est optique et nécessite le balayage par pas micrométriques de la surface du pixel avec un spot focalisé dont la longueur d'onde est appropriée à l'épaisseur estimée de la couche morte (en général vers le proche UV pour des couches inférieure à 100 nm).

La caractérisation de l'ebCMOS nécessite également un banc optique pour une étude précise de la PSF du tube à vide. La méthode est basée sur la localisation des photons uniques et permet d'éviter une déconvolution numérique de la *PSF* du CMOS. Ces bancs de tests ont été décrits dans les articles cités dans ce rapport. Seule une revue synthétique des bancs est présentée dans les sections suivantes. Ces bancs développés au cours de cette R&D ont été transférés à des industriels qui avaient des problématiques de caractérisation similaires. On peut notamment lire dans le mémoire de doctorat de Romain Cluzel une bonne partie des caractérisations que nous effectuons dans notre salle de bancs de tests.

La problématique de l'amincissement est au centre de son travail [52].

Le Tableau II.1 récapitule les mesures possibles ainsi que les paramètres étudiés sur les différents bancs de tests conçus au Laboratoire dans le cadre de notre R&D .

Bancs	Mesures / histogramme	Paramètres
X Fe^{55}	Q pixel siège	calibration e-/ADCU
X Fe^{55}	Q de l'amas	CCE en X - Gain total
X Fe^{55}	Q du pixel siège vs Q amas	CCE sur pixel siège
X Fe^{55}	Q pixel $\pm$ 1 du pixel siège	diaphonie pixel
BE	Q pixel siège	Gain sur pixel siège
BE	Q de l'amas	Gain totale
BE	Q pixel siège / Q de l'amas	CCE à Gain fixé
BE	Q amas vs HV	couche morte et CCE
BE	Densité des impacts	Homogénéité de la passivation
BE	Q amas vs HV	Seuil de détection
BE	Q amas vs HV + diff. CMOS	Efficacité passivation
Opt. CMOS	Q amas	Calibration du spot sur Qphe
Opt. CMOS	Champ plat	PTC, PRNU, FPN, ...
Opt. CMOS	Q pixels vs position spot	*PSF* CMOS
Opt. CMOS	Q pixels vs position spot	*PSF* CMOS
Opt. ebCMOS	Image 2D des phe uniques	*PSF* Tube
Opt. ebCMOS	FWHM(*PSF* Tube) vs λ	Energie initiale radiale phe
Opt. ebCMOS	Nombre Phe / Nbre trigger	Efficacité vs SNR photon
Opt. ebCMOS	FWHM(*PSF* Tube) vs HV	Effet Schottky

TABLE II.1 – Tableau des mesures possibles sur les différents bancs de tests conçus au laboratoire pour notre R&D et des paramètres étudiés.

B.2   Bancs de tests de CMOS

B.2.1   Banc de tests à rayons X

Une photographie du banc de tests "source X" et le principe de la mesure ainsi que les histogrammes caractéristiques reconstruit s à partir de la conversion totale dans la diode sont présentés dans les Figures II.1 et II.2. Un système de refroidissement par effet Peltier ainsi qu'une distribution d'azote ont été ajoutés au boitier contenant la source de Fer 55 afin de contrôler la température de la puce. Pour les tests effectués en dessous du point de rosée, l'azote est utilisé pour remplacer l'air et éviter les problèmes de condensation.
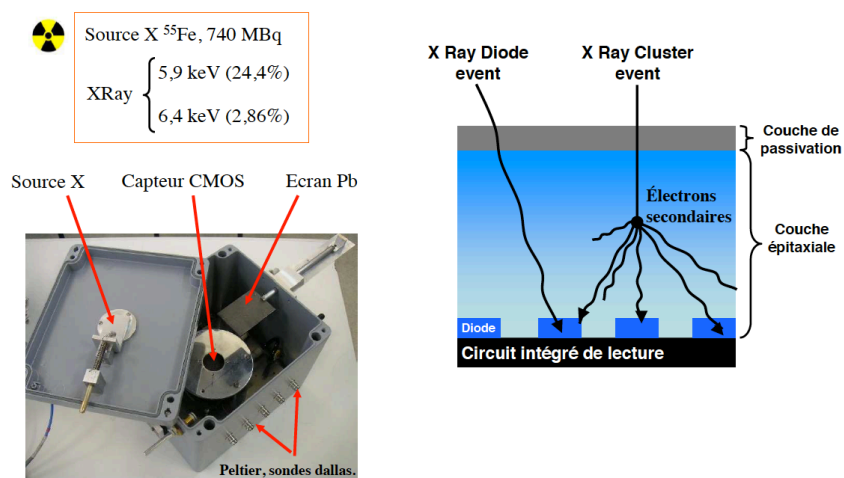
FIGURE II.1 – Principe de mesure et photographie du banc à rayonnements X d'une source de Fer 55.

B.2.2   Banc de tests optique

Le principe de la mesure sur le banc optique est illustré par la Figure II.3. Les photographies du banc optique conçu pour la caractérisation des CMOS amincis sont présentées dans la Figure II.4. Ce banc de tests, composé d'un support de tube de microscope est déplacé par pas de 1 micron dans les trois directions. Le plan du CMOS aminci est ajustable suivant les trois degrés de liberté angulaires par rapport à l'axe optique. Un exemple de *PSF* CMOS mesurées pour différents types de substrats utilisés est présenté dans la Figure II.5. Avec l'utilisation de longueur d'onde proche de l'UV les résultats d'un balayage intra-pixel par le spot focalisé a permis une comparaison particulièrement intéressante des données avec les simulations TCAD (IPHC), comme nous pouvons le voir dans le graphe de la Figure II.6 obtenu pour le CMOS aminci MIMOSA5 conçu en technologie AMS 0.6 μm.

B.2.3   Banc de tests par bombardement électronique

Le principe de la méthode du bombardement électronique s'est fortement inspiré de la R&D faite au CERN sur les HPD à cette période pour l'expérience LHCb. Le schéma de principe ainsi que la photographie du banc de tests sont présentés dans la Figure II.7. La Figure II.8 montre des histogrammes de charge pour différentes valeurs de haute tension. L'ajustement de la charge moyenne reconstruite en fonction de la haute tension nous renseigne sur le gain de multiplication du CMOS aminci.

Une modélisation simple (linéaire) du gain de multiplication présentée dans la Figure II.9 permet de remonter aux paramètres principaux des CMOS amincis. Je n'entrerai pas dans la discussion de la partie non-linéaire à basse énergie qui reste un problème intéressant de physique et de modélisation de la recombinaison et de la diffusion des charges

> Diode Conversion Factor
>
> C = 4,6 e⁻ / ADC
>
> Charge Collection Efficiency
>
> $$CCE_{XRay} = \frac{Q \text{ (cluster 5x5 pixels)}}{Q \text{ (diode 100\%)}}$$

Epilayer resistivity	Standard	Resistive	Profiled
CCE_XRay	32 %	25 %	60 %

CCE_XRay increased by a factor 2 for profiled epilayer resistivity
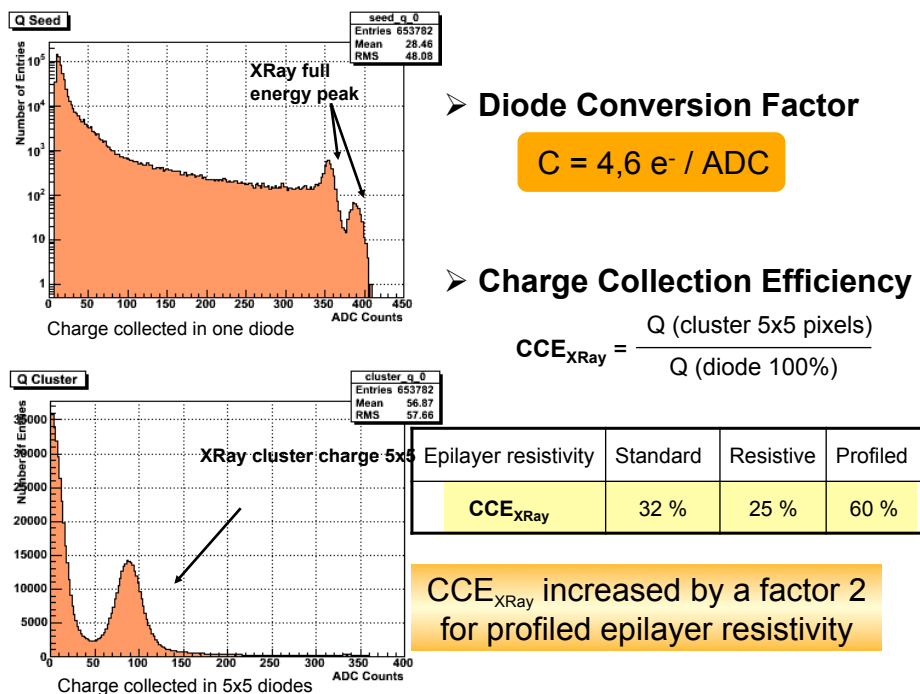
FIGURE II.2 – Méthode de calibration sur le banc X pour le calcul de l'efficacité de collection de charges.

proches de la couche de passivation.

B.3   Banc de tests pour les ebCMOS

Le banc de tests pour les ebCMOS est identique au banc optique pour les CMOS amincis (figure II.4).

Cependant, la procédure de focalisation du spot sur le plan de la photo-cathode diffère de celle d'une focalisation simple sur un CCD ou un CMOS avec un spot intense. Le réglage est effectué en deux temps. Une première focalisation est effectuée à haut flux avec une haute tension relativement basse puis une deuxième focalisation plus fine permet de descendre aux photons uniques par l'ajout de filtres à densité neutre. Ensuite, on reconstruit la *PSF* du tube par accumulation d'images. La reconstruction de l'impact du photo-électron est précise grâce à l'utilisation du barycentre des charges déposées dans l'amas de pixels touchés.

L'utilisation d'une fonction dite η a pour objet de corriger le biais introduit par l'échantillonnage par les pixels. La fonction η s'obtient à partir de l'inversion de la fonction cumulative des positions reconstruites d'une distribution uniforme des impacts. Elle permet d'obtenir une résolution sur la position du photo-électron indépendante de la position du spot par rapport au centre du pixel. Remarquons que cela n'est pas vrai pour les détecteurs pixels sans diffusion comme les emCCDs (erreur de l'ordre de 5 à 10% avec un gain 300). Cette méthode permet un balayage de la photo-cathode mais également
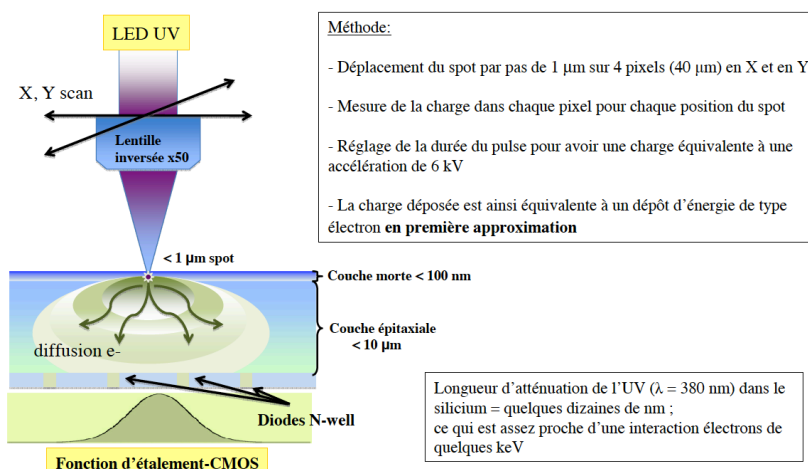
FIGURE II.3 – Schéma de principe de la mesure de *PSF* des CMOS amincis.
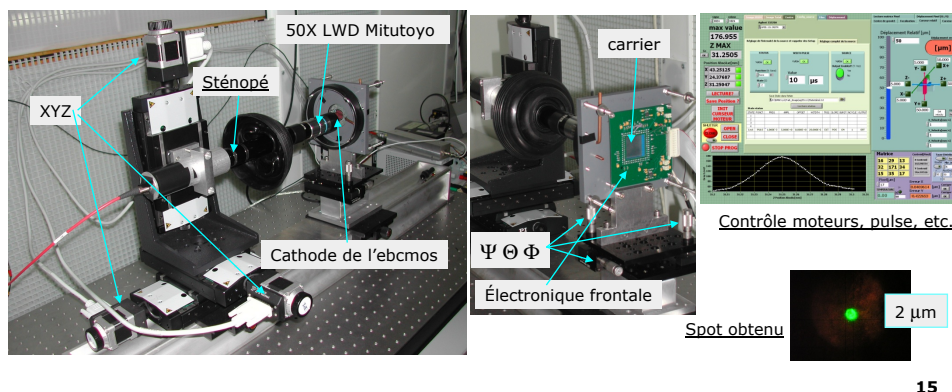
FIGURE II.4 – Photographie du banc optique pour la caractérisation des CMOS amincis.

une mesure précise de la *PSF* du tube. C'est une méthode qui n'utilise pas la déconvolution de la *PSF* expérimentale par celle du CMOS aminci. La précision, l'écart type, sur la largeur à mi-hauteur de la *PSF* tube mesurée avec la méthode du photon unique est inférieure à deux microns. Elle nous a permis de mettre en évidence les variations de la *PSF* du tube en fonction de la longueur d'onde initiale. Ces résultats ont été publiés dans la référence [58]. La Figure II.10 montre un exemple d'image intégrée de la distribution reconstruite des photons uniques par image lorsque le spot a été positionné à l'aplomb du centre d'un pixel.
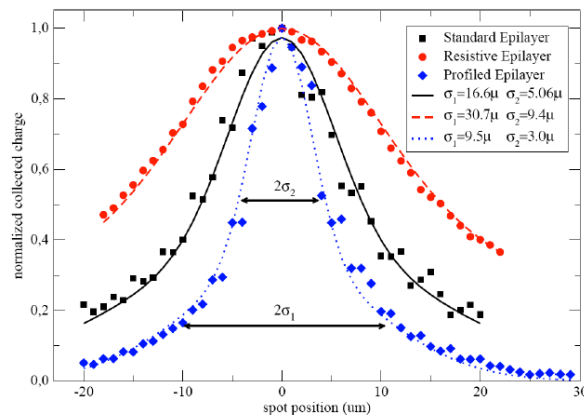
Résistivité couche épitaxiale	Standard	Résistive	Graduée
FWHM$_2$ = 2,35 σ_2	12 µm	22 µm	7 µm

FIGURE II.5 – Exemple de *PSF* mesurées de CMOS amincis ayant des substrats qui comportent des couches épitaxiales à dopages différents.

B.4   Développement programmé des méthodes de caractérisation

Cette R&D nous a conduit jusqu'à présent à mettre au point 3 types de bancs de tests (en X, en électrons et en photons UV-VIS) et à développer les méthodes de caractérisation des puces amincies et des ebCMOS. Certaines de ces méthodes, qui sont fondées sur la détection de l'électron unique, sont nouvelles en rapport aux méthodes usuelles de test des CMOS ou des CCD (Photon Transfert Curve, MTF, PRNU). Elles peuvent être employées pour tester tous les détecteurs à gain de multiplication sensibles aux photons uniques.

C'est à cela que nous allons nous employer dans les années à venir en participant à un projet de R&D avec un industriel pour la caractérisation de pixels à gain. Nous aurons essentiellement deux objectifs en ce qui concerne la caractérisation. Le premier consiste à reprendre l'existant "classique" (PTC avec gain de multiplication) avec la possibilité d'inter-calibration des détecteurs bas niveau de lumière, comme l'emCCD, le sCMOS et l'ebCMOS. Cela nécessite l'achat d'un équipement de métrologie en photométrie (sphère intégrante ...). Le deuxième objectif est l'élaboration d'un banc de mesure de gain et de PDE absolus basés sur l'émission de deux photons corrélés par un cristal non-linéaire (de type BBO par exemple). Sur le plan de la physique cela touche au domaine des sources photoniques dites "sub-Poisson". Ce programme ambitieux est prévu pour 2012-2013.
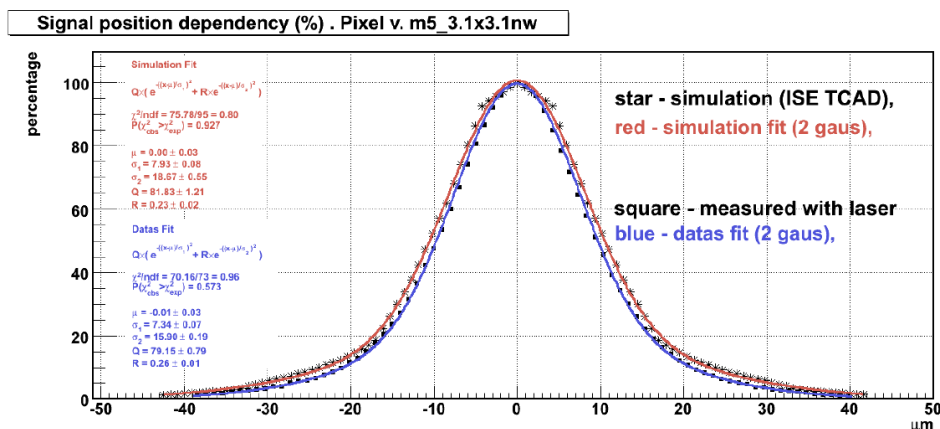
FIGURE II.6 – Comparaison de la *PSF* CMOS mesurée et de la simulation TCAD du MIMOSA5 aminci (technologie AMS 0.6 μm).

C   Preuve de faisabilité, 2004-2007 : le prototype eb-MIMOSA5

La première étape de cette R&D consistait à montrer la faisabilité d'une HPD à base de CMOS, via le fabricant de tubes PHOTONIS, avec une focalisation de proximité inférieure au millimètre et une tension de fonctionnement inférieure à 8 kV. Je rappelle que la société INTEVAC proposait déjà depuis quelques années un ebCMOS sous ITAR dédié à la vision nocturne (EBAPS Technology). En 2003, PHOTONIS n'avait probablement aucune puce amincie à sa disposition pour effectuer les tests de faisabilité notamment de pompage et d'intégration dans la céramique. C'est essentiellement pour cela que PHOTONIS s'est intéressé à notre projet de R&D basé sur les puces amincies de l'équipe de Marc Winter de l'IPHC. La puce en question est le capteur MIMOSA5 qui est une réplique de grande taille, 1Kx1K, du capteur MIMOSA1 (pixel 3T en technologie AMS 0.6μm) [54]. L'amincissement a été effectué par ATMEL (Grenoble) dans le cadre du projet européen SUCIMA [55]. Les premiers tests ont été conduits par W. Dulinski et G. Deptuch de l'IPHC sur les bancs de tests des HPD du CERN [56]. Le projet d'intégration du MIMOSA5 aminci dans un tube à vide a duré plus de 4 ans, de 2003 à 2007. La preuve de faisabilité a abouti de manière positive malgré les difficultés techniques rencontrées.

Nous avons pu d'une part mesurer les performances de l'ebCMOS et d'autre part le tester pour l'imagerie de fluorescence en mode comptage de photons. Ce travail a largement été présenté et publié [53]. Il nous a surtout permis de nous convaincre de l'intérêt d'augmenter la cadence de lecture afin de faire la preuve du concept de l'imagerie rapide aux photons uniques.

Je ne traiterai pas dans ce document les aspects liés à la partie concernant l'étude de faisabilité du tube par PHOTONIS. Nous pouvons simplement affirmer que le rendement sur les premiers prototypes a été normalement faible. Comme on peut s'en douter, le
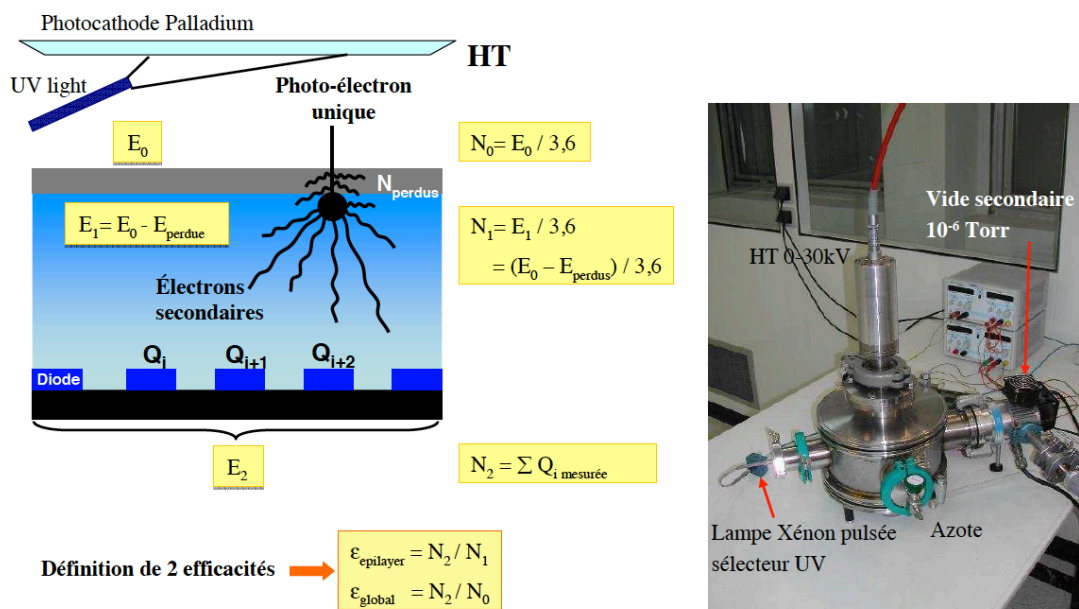
FIGURE II.7 – Méthode du banc par bombardement électronique et photographie du banc de tests fermé. On voit clairement l'entrée de la fibre optique dans l'enceinte à vide.

passage à un rendement industriellement compatible au coût de production et de vente de ce type de capteurs est une toute autre problématique que celle de la recherche et développement en laboratoire. Il existe cependant des actions de "bon sens" qui permettent des gains importants dans ce domaine.

C.1   La puce MIMOSA5 amincie

Ce document ne décrira pas le fonctionnement et la caractérisation du MIMOSA5 qui ont déjà été publiés à plusieurs reprises [57]. Je mentionnerai simplement que l'étape cruciale qui nous a posé le plus de difficultés était le taux de réussite de la connexion par bonding sur les plages d'accueil de la face arrière et leur tenue à l'étuvage. Aucune conception spécifique n'avait été prévue pour de la connexion face arrière. La couche métallique accueillant le bonding était donc la métal-3 ! De plus les plages d'accueil n'étaient atteignables qu'au travers d'un puits assez profond (10-15 μm) et étroit (70 μm) particulièrement défavorable à du "wedge bonding". La Figure II.11 illustre mes propos. Des tentatives de connexion par "ball bonding" ont échoué. Finalement, après une étude poussée des paramètres "optimum" du bonding (puissance, durée ...) l'experte de l'IPHC a réussi à produire des puces connectées avec des tenues de quelques "petits" grammes. Cette étape difficile nous a permis par la suite d'anticiper le problème par la conception de plages d'accueil dédiées à la connexion face arrière pour la gravure de celle-ci. Des connections de type "ball" sont maintenant envisageables sur des plages d'accueil plus larges. Elles permettent la conception de nouvelles structures de connexion de la puce dans le tube. L'objectif final reste la
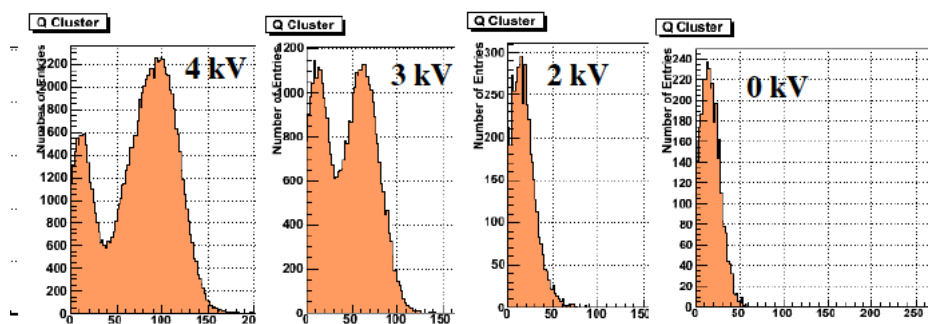
FigurE II.8 – Exemple de distribution de la charge des amas de pixels reconstruits après détection du pixel siège de l'interaction de l'électron accéléré.

connexion par l'arrière avec un passage vide-air grâce à l'E3D. Il suffit d'être patient.

C.2   Le système d'acquisition Ethernet 1 Gb/s

La durée d'une lecture complète du capteur CMOS MIMOSA 5, séquencé à 10 MHz et lu par 4 sorties en parallèle est de 26 ms. Le débit numérique correspondant pour un codage des pixels sur 12 bits est de 484 Mbits/s. Nous avons utilisé jusqu'en 2008 le système d'acquisition fourni par Gilles Claus de l'IPHC pour mener nos études sur l' ebMIMOSA 5. Il était prévu dès le début du projet que l'IPNL s'engagerait sur un nouveau système d'acquisition dédié à l'imagerie par capteur CMOS. Le lien Ethernet en UDP a été choisi pour s'engager dans la voie du temps réel. Une carte de développement ALTERA possédant 40 entrées/sorties pour accueillir des cartes mezzanines a permis de tester les options d'acquisition sans passer par la conception et la production d'une carte dédiée complète embarquant un FPGA, de la mémoire et des ADCs. Seule une carte d'interface permettant de contrôler (séquencer) le MIMOSA et d'échantillonner les signaux des pixels à 10 MHz a été conçue au laboratoire par C. Guérin du service électronique de l'IPNL. Ce fut une étape d'apprentissage sur la lecture des capteurs CMOS. Le système d'acquisition 1 Gbits/s Ethernet conçu à l'IPNL est présenté dans la Figure II.12.

C.2.1   Résultats et Performances

L'ebMIMOSA5 a été étudié et caractérisé avec précision par N. Estre (Post-Doc dans l'équipe de 2006 à 2009). Les premiers résultats ont été présentés à la conférence ICATPP, en octobre 2007, à Côme. Les premières images obtenues sur site (à l'IGBMC et à l'ENS Paris) en microscopie de fluorescence ont été présentées en juillet 2008 à la conférence "New Developpement in Photon Detection" à Aix les Bains. Le comptage de photons a été obtenu avec une haute tension de 8 kV comme cela est visible dans la Figure II.13. Lorsque le nombre moyen de photons devient suffisamment important pour que la probabilité d'avoir des recouvrements d'amas de photo-électrons ne soit plus négligeable, le comptage de
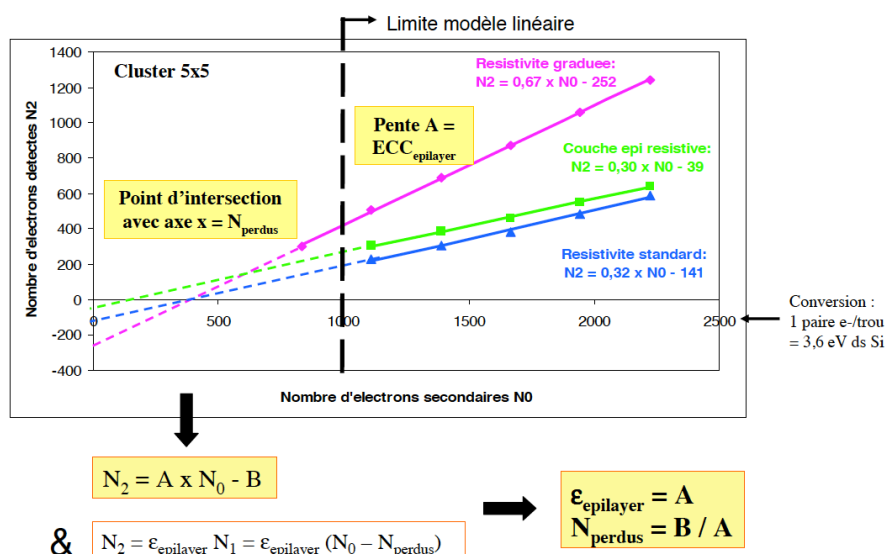
FIGURE II.9 – Exemple de courbe de gain reconstruite par variation de la haute tension sur le banc BE et mesure des paramètres associés.

photons devient plus difficile à réaliser. Nous avons montré qu'un algorithme de type recuit déterministe améliore le comptage de photons par le partage de charge des pixels. La partie droite de la Figure II.13 montre l'effet d'un algorithme utilisant le recuit déterministe sur la capacité de comptage de l'ebCMOS. Cette méthode itérative est cependant difficilement utilisable en ligne.

D   Preuve de concept, 2008-2011 : LUSIPHER

D.1   Objectifs et contraintes du développement

Il s'agit d'apporter, par la fabrication d'un ebCMOS rapide, la preuve du concept de suivi de sources ponctuelles par la détection et l'association de photons uniques. La mise en œuvre de ce concept d'imagerie comporte trois composants :

1. Un ebCMOS rapide constitué de sa puce amincie et de sa photo-cathode,

2. Un système d'acquisition haut débit Ethernet fonctionnant en continu et sans temps mort,

3. Un logiciel de traitement temps réel qui reconstruit, grâce à des tâches parallélisées, les positions centres d'accumulation de photons pour identifier et suivre de nombreux émetteurs en parallèle.

Nous pouvons regarder plus en détail les objectifs liés à ces trois composants du système. L'ebCMOS doit contenir une puce CMOS amincie offrant une cadence d'images 10 a 20 fois supérieure à celle utilisée de manière standard en imagerie de fluorescence sans
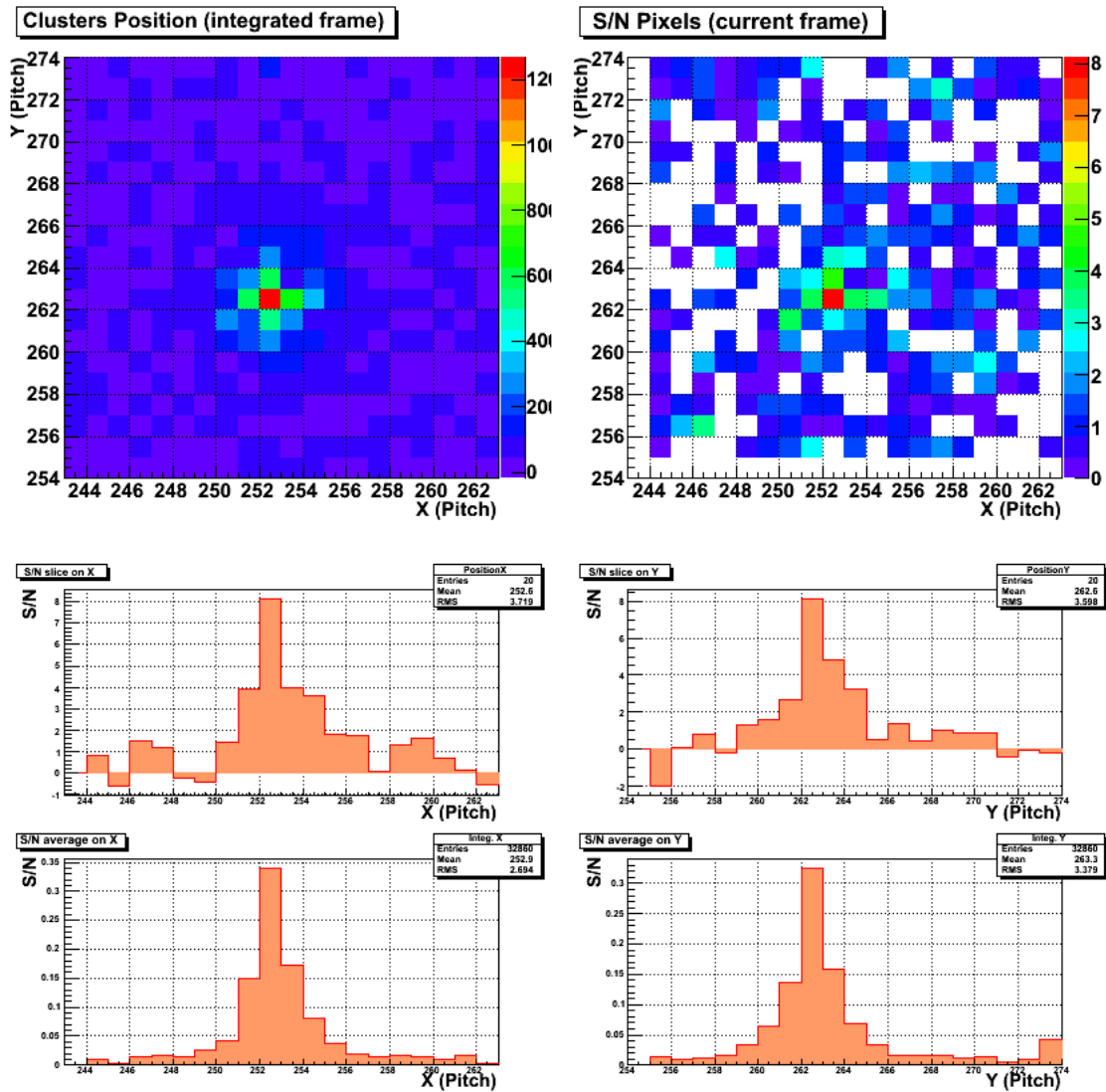
FIGURE II.10 – Image intégrée et image courante de la distribution des charges des pixels dans la zone de focalisation du spot sur la cathode en 2D et en projection X et Y.
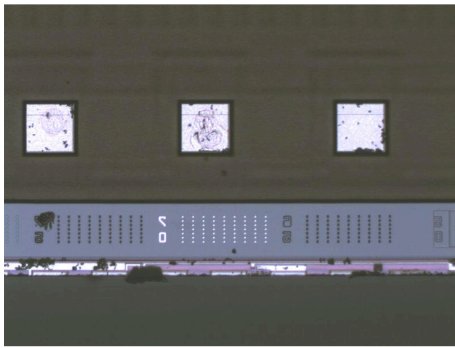
Figure 15 : puce 4 : vues optique des pads
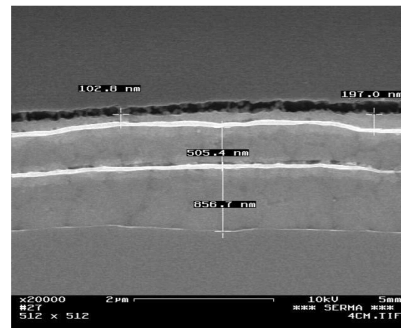
Figure 18 : puce 4, MEB : mesures de l'Aluminium en bord et au centre du pad

FIGURE II.11 – Photographie et coupe TEM des plages de bonding du MIMOSA 5 aminci qui nous ont posées de sérieux problèmes. On observe clairement les trois couches métalliques de la technologie AMS 0.6 μm.
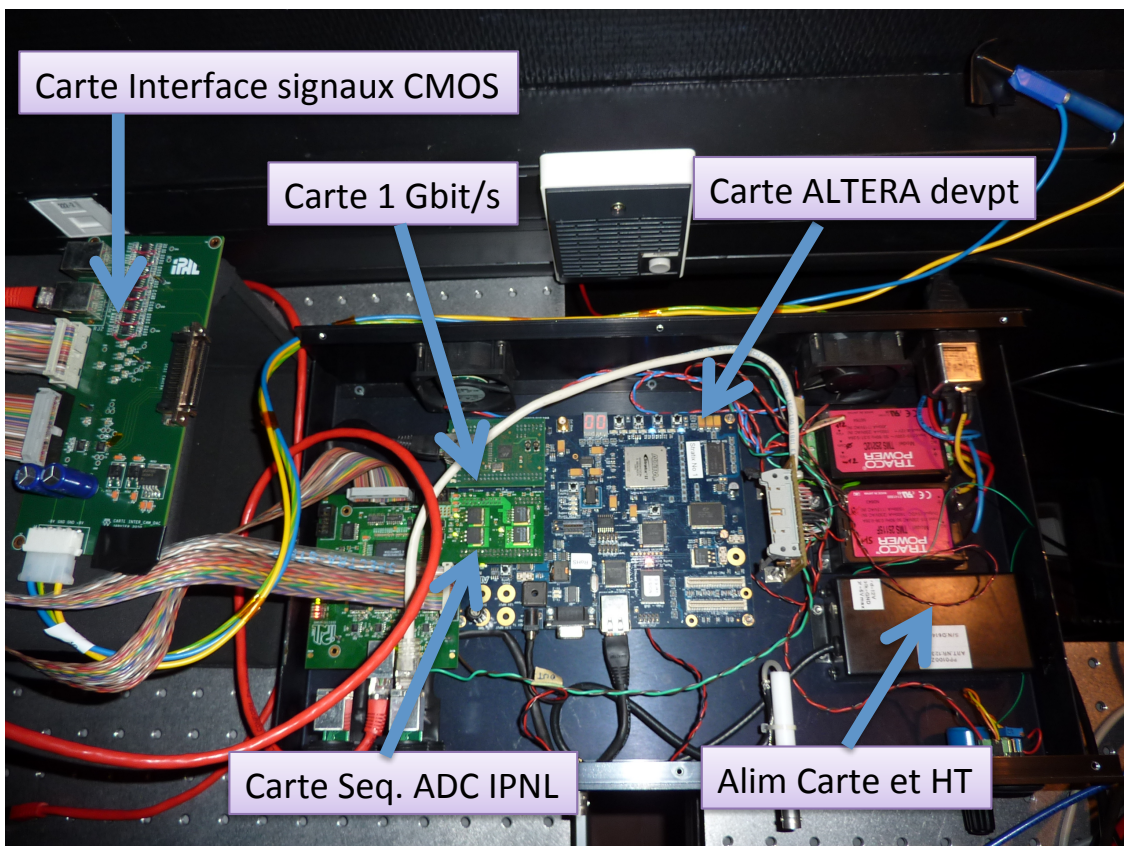
FIGURE II.12 – Photographie du système d'acquisition prototype 1 Gbits/s. La carte verte en L correspond à la carte produite par l'IPNL pour séquencer et relire la puce MIMOSA 5. La carte de développement ALTERA est la carte bleue. La petite carte verte mezzanine rectangulaire est la sortie 1 Gbits/s.
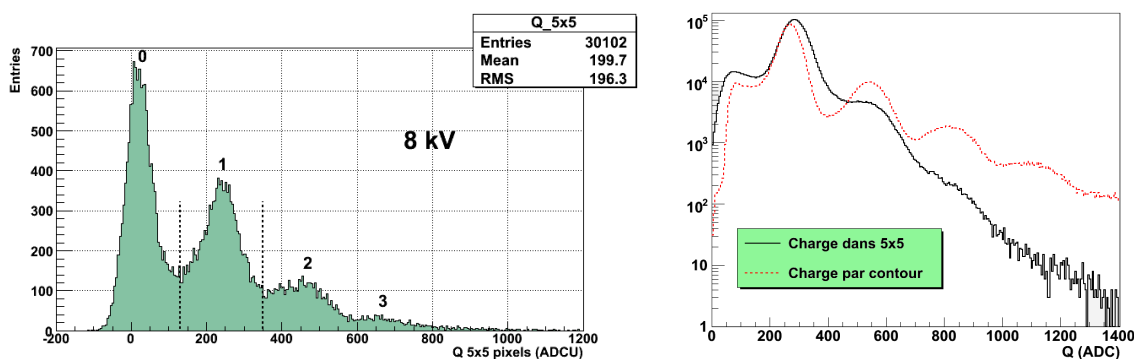
Figure II.13 – Comptage de photons avec l'ebCMOS, ebMIMOSA5, pour une moyenne Poisson à 0.8 et une charge par amas 5x5 classique (gauche). Comptage de photons avec et sans recuit déterministe obtenu par l'ebCMOS ebMIMOSA 5 (droite).

fenêtrage ou ré-échantillonnage. Il doit bien évidemment offrir une sensibilité aux photons uniques (une passivation après amincissement inférieure à 100 nm) et une résolution spatiale de quelques microns pour rester dans les résolutions de l'emCCD. Le comptage sombre (DC) doit être bien inférieur au bruit de photons du plan objet (auto-fluorescence, off-focus...). Il doit également offrir un flux de données brutes en sortie suffisamment large pour pouvoir fonctionner en continu et sans perte. La surface sensible, i.e. le champ de vue image, doit être suffisamment importante pour suivre plusieurs centaines de particules en parallèle.

Nous avons tout d'abord élaboré le cahier des charges de la puce "lucy" avec les membres de l'équipe de M. Winter de l'IPHC : J. Baudot, M. Trimpl, W. Dulinski, et A. Dorokhov. Un run multi-projet exploratoire de la technologie BICMOS-7RF de STMicroelectronics comportant des puces tests a permis d'étudier différentes variantes de diodes (16 conceptions de diodes testées). Le temps ingénieur alloué à ce projet était fortement contraint par les autres projets majeurs de l'équipe de l'IPHC. Nous avons donc convergé rapidement sur une conception privilégiant la robustesse (pixel 3T, 10 microns de pitch) et qui limitait les risques sur l'efficacité de collection de charges (nous avions le droit à un seul run d'ingénierie).

La production des puces a été prise en charge et pilotée par notre partenaire SAGEM DS dans le cadre d'un projet collaboratif. L'amincissement et la passivation sont restés la propriété de notre partenaire.

Le tube et la cathode ont été pris en charge par PHOTONIS dans le cadre du GIS. Nous avons eu accès uniquement à des cathodes de deuxième génération S20 et S25. PHOTONIS a essentiellement investi pour ce projet, d'une part du temps ingénieur pour la mise au point du processus de pompage et du suivi de production des tubes et d'autre part sur les composants (essentiellement la céramique "interposer" lien entre la puce et le support de tube).

Des contraintes d'origine diverses ne nous ont pas permis de remplir tous nos objectifs. La puce produite est lue à une fréquence pixel maximale de 40 MHz avec 8 sorties parallèles pour 2 matrices de 400 x 400 pixels. Cette architecture conduit à une durée de trame de 1 ms donc à une cadence image de 1000 Hz. Cependant, le double échantillonnage corrélé doit être effectué à l'extérieur de la puce par une soustraction de deux trames consécutives après un Reset des pixel. Cela réduit la fréquence des images utiles à 500 Hz. J'aurai appris au moins à être plus vigilant dans l'énonciation du cahier des charges !

La gamme dynamique de la puce CMOS a malheureusement été réduite par l'utilisation d'un gain trop important dans le buffer de sortie de la puce et conduit assez vite à la saturation des pixels malgré une capacité de puits tout à fait correcte (20 ke-). L'épaisseur de la couche épitaxiée après amincissement devait être de l'ordre de 8 μm alors qu'elle est sur les puces amincies de l'ordre de 10 μm. La passivation aurait pu être bien meilleure que 80-100 nm. Nous avons bénéficié de plusieurs substrats possédant des couches épitaxiées de trois types de résistivité : 50 Ω.cm, 200 Ω.cm et graduée.

Les contraintes de résolution spatiales nécessitaient un espacement cathode-puce de l'ordre de 0.8 mm. Nous avons obtenus des ebCMOS fonctionnels avec des espacement plutôt de l'ordre du millimètre. C'est essentiellement la distance entre le haut de la boucle du fil de bonding sur le pourtour de la puce qui est le facteur limitant. D'autres solutions que le wedge-bonding existaient mais elles étaient non accessibles. La multiplicité des partenaires n'a pas favorisé une intégration de la puce dans le tube particulièrement "propre". Ce facteur est prépondérant pour aboutir à une qualité de tube et un rendement acceptable.

Nous avons mis à peu près deux ans pour sortir les premiers ebCMOS LUSIPHER, si l'on considère le départ du projet à la conception de la puce et le stop au moment des premiers tests sur les ebCMOS fonctionnels. L'analyse à posteriori des retards pris sur le projet laissent a penser qu'il faut réduire le nombre de partenaires et surtout le nombre d'étapes suivies par la puce. Les plus gros retards ont cependant été induits d'un côté par des causes extérieures liées au partenariat (absolument incontrôlables et qui n'ont rien à voir avec la technologie) et d'un autre côté essentiellement par des défauts dans la documentation.

Concernant le système d'acquisition, la voie privilégiée a été la communication par Ethernet car elle possède une marge d'évolution importante grâce à l'accroissement des débits de transfert liés à l'évolution des réseaux Ethernet (40 Gbits/s et 100 Gbits/s) sur fibre optique. Nous sommes déjà bien loin des débits classiques des systèmes d'acquisition classiques en continu des caméras (Caméra Link, USB2 et 3, GigaE). A ce choix du mode de transfert des données du système d'acquisition vers le serveur s'est ajouté celui du pré-traitement des images après numérisation des données brutes. Cet objectif induit nécessairement une capacité de calcul en continu ("FIFO full") mise en œuvre par des FPGA (Field Programmable Gate Array) puissants mais couteux. La mémoire du FPGA reste relativement limitée pour du pré-traitement d'image de méga-pixels codés sur 12 bits. Il a donc été nécessaire de concevoir dans l'architecture du DAQ une forte bande passante vers de la mémoire de type DDR2 (Double Data Rate). Plusieurs contrôleurs d'écriture/lecture de mémoires DDR ont été implémentés en parallèle. La liste suivante

résume les objectifs et les contraintes imposées au DAQ :

1. Contrôler les séquences de lecture de la puce (générateur).

2. Réceptionner et numériser jusqu'à 16 voies analogiques à une fréquence maximum de 65 MHz sur 12 bits.

3. Etre ouvert à des CMOS méga-pixels à sorties numériques.

4. Posséder une capacité de stockage temporaire des données et effectuer du traitement de données bas niveaux (reconstruction de l'image, calcul de CDS, soustraction de piédestaux, recherche d'amas de pixels touchés),

5. Encapsuler les données et les envoyer sur le réseau Ethernet à un débit continu nominal de 10 Gbits/s.

Les objectifs du système d'acquisition ont été atteints notamment grâce au financement obtenu dans le cadre de la valorisation du brevet Barbier-Estre sur une méthode de traitements aux photons uniques (Appel à Projet de Maturation Technologique du PRES de Lyon).

Le logiciel d'acquisition a été développé tout au long du projet. Le premier objectif était la récupération sans perte de données via le lien 10 Gbits/s Ethernet. Les développements se sont poursuivis par l'implémentation d'algorithmes en ligne et la programmation d'une interface utilisateur. Il n'a pas été nécessaire jusqu'à présent de développer du code utilisant les processeurs sur carte graphique (''GPU computing'') pour la version exploitation de LUSIPHER 800x800. Cependant des tests sur les traitements d'images bas niveaux été menés par un membre de l'équipe logiciel dans un objectif de prospectives (carte TESLA). Les prochaines versions d'ebCMOS 2Kx2K nécessiteront certainement l'utilisation du calcul sur GPU.

Il est cependant envisageable que nous arrivions à implémenter certaines fonctions de haut niveau dans le FPGA. Cela me semble encore une hypothèse probable mais elle n'a pas ma faveur dans la mesure ou le corpus des algorithmes de suivi utilisés n'est pas fixé définitivement. La réactivité logicielle face à l'évolution des contraintes me semble naturellement meilleure et il est plus facile de reporter des contraintes sur la puissance de calcul des CPUs en utilisation des librairies d'optimisation de type SSE ou des GPU avec CUDA ou OpenCL. Il est intéressant de noter que Nvidia et Mellanox ont travaillé sur du logiciel permettant d'éviter une recopie via le CPU entre la carte Ethernet Mellanox et la carte GPU Nvidia.

D.2   Les prototypes LUSIPHER

Parmi une quinzaine d'ebCMOS LUSIPHER produits entre 2009 et 2010, huit ebC-MOS ont été utilisables pour des tests. Les meilleurs ont été intégrés à un système de caméra complet 2x(400x800) pixels. Ainsi, quatre caméras ont été produites par le service instrumentation. Deux d'entre elles utilisent des cathodes S20 optimisées pour le vert et deux autres ont des cathodes S25, c'est-à-dire étendues vers le rouge. Trois systèmes d'acquisition 10 Gbits/s ont été produits et trois stations de travail HP Z800 (16 cœurs) sont utilisables avec le logiciel d'acquisition de traitement et de suivi de particules uniques.
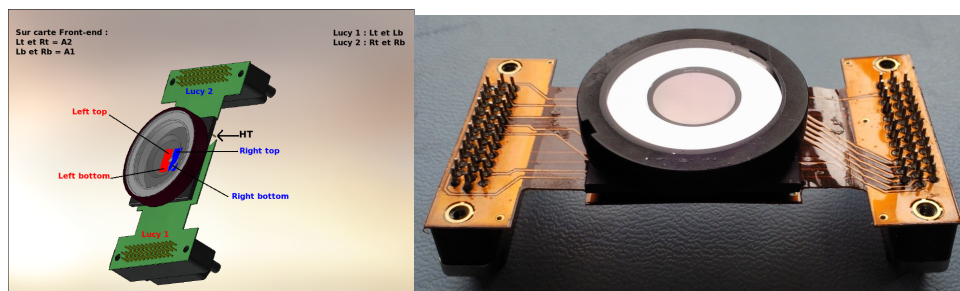
FIGURE II.14 – Schéma du montage de 2 puces dans l'ebCMOS connecté par le kapton souple sortant sur les électroniques frontales. Photographie de l'ebCMOS connecté au kapton.

Un ebCMOS avec une cathode de type S20 a été intégré dans un système embarqué pour l'observation de la bioluminescence marine sur le site ANTARES. Ce développement sera discuté dans la section concernant la bioluminescence. La Figure II.14 montre le schéma de montage d'un ebCMOS LUSIPHER avant son intégration dans la caméra et une photographie du tube monté sur son kapton.

D.3 Le système d'acquisition Ethernet 10 Gb/s

Ce document n'as pas pour objet de traiter dans les détails tous les aspects techniques notamment ceux du système d'acquisition. Deux articles ont été soumis aux conférences *NDIP 2011 Lyon* et *IEEE NSS 2011 Valence (Esp.)*. Mis à part les délais, qui ont été multipliés par deux, je considère que sur le plan technique ce projet d'acquisition est une réussite. Nous avons acquis un savoir faire stratégique sur l'acquisition de données par lien Ethernet. Une version avec fibre otique a été validée et ouvre la voie vers le 40 ou 100 Gbits/s et de l'acquisition déportée sur plusieurs centaines de mètre. L'extension des fonctionnalités de la carte aux puces, 2Kx2K à sorties numériques a également été validée par la lecture du CMV4000 de CMOSIS.

D.4 Le logiciel de traitement temps réel et son évolution

Le logiciel de traitement a été développé progressivement suivant les objectifs ordonnés de la manière suivante :

1. Panneau de configuration des 4 puces lucy de l'ebCMOS, configuration des puces via Ethernet.

2. Reception et stockage sans pertes via le protocole UDP Ethernet et une carte réseau 10 Gbits/s Mellanox.

3. Effectuer les algorithmes de bases de traitement d'une image (reconstruire l'image avec soustraction des piédestaux).

4. Afficher une image à 25 Hz (images sommées ou moyenne glissante).
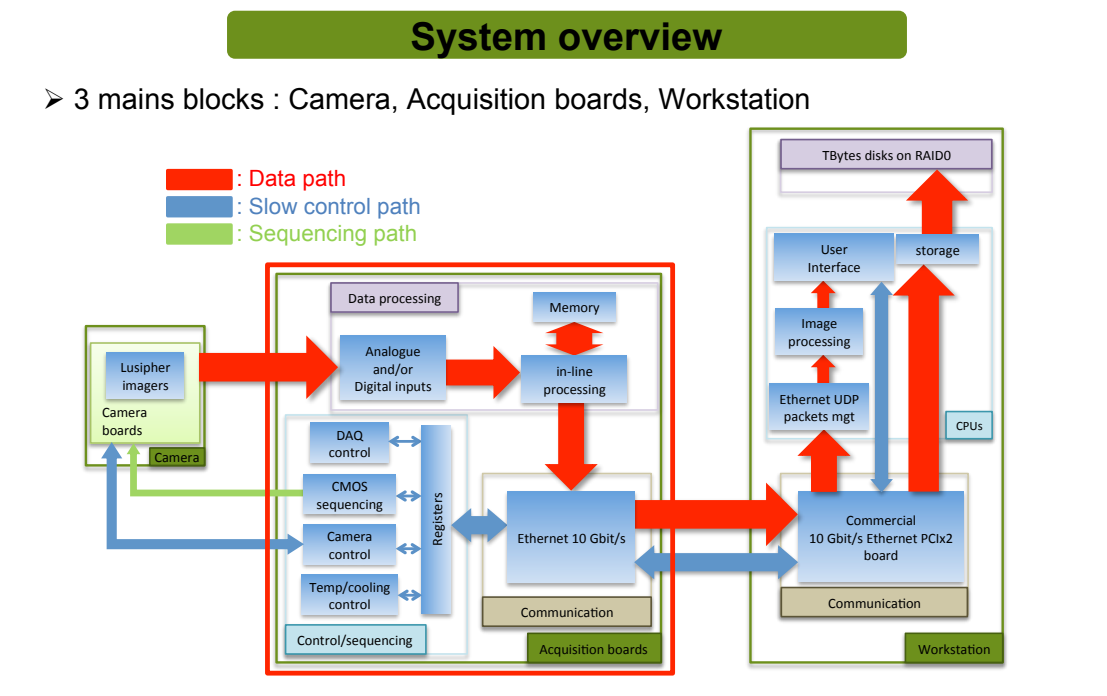
FIGURE II.15 – Schéma de principe du flux de données de l'acquisition 10 Gbits/s.

5. Affichage au ralenti pendant plusieurs secondes (emploi d'un "buffer" circulaire) .

6. Filtrage du bruit pixel par l'utilisation d'un Kalman temporel par pixel.

7. Filtrage des retours ioniques.

8. Recherche de photo-électrons dans l'image courante (2 ms).

9. Génération, pause, mise à jour et extinction des cibles reconstruites

10. Filtrage spatio-temporel des cibles par Kalman

11. Affichage des cibles reconstruites

12. Extraction de l'information des cibles validées : moyenne Poisson par frame, position intrapixel (1 micron) ...

Le logiciel de traitement développé par des physiciens et des informaticiens a beaucoup évolué depuis ses débuts avec l'acquisition à 1 Gbits/s. Une station de travail à 16 processeurs est suffisante pour faire tourner en parallèle des tâches (thread) et suivre environ 2500 cibles à une fréquence trame de 250 Hz.

A une fréquence de 500 Hz certaines tâches sont dans un état critique en termes de charge des cœurs et l'emploi de GPU pourrait devenir nécessaire si l'optimisation du code ne suffit plus. De plus une multiplication des processeurs sur la carte mère de la station de travail au-delà de 16 n'est économiquement pas raisonnable. Il faut noter que des optimisations ont été nécessaires (via NUMA) notamment au niveau de l'utilisation intelligente et hiérarchisée du "Northbridge" et du "Southbridge" par les différentes taches. L'implémentation des algorithmes de calcul sur nombre flottants a été optimisée grâce aux librairies Intel SSE.
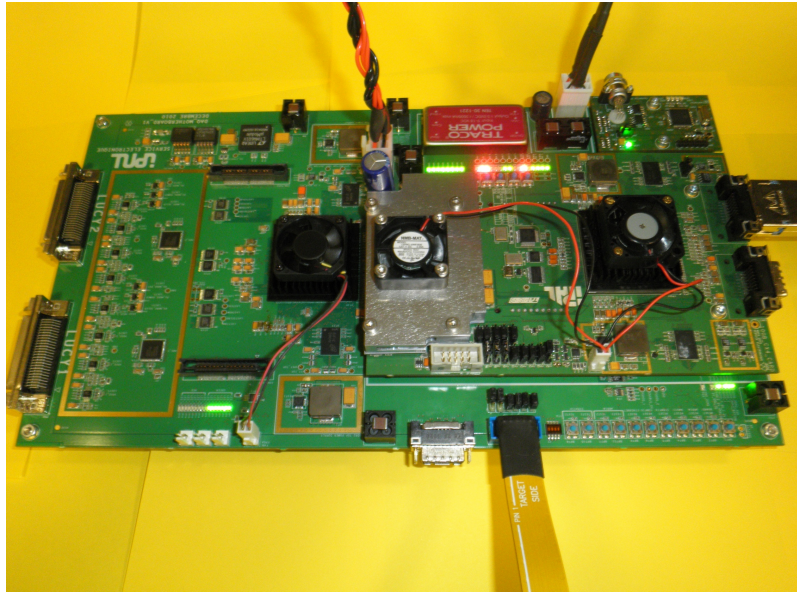
FIGURE II.16 – Photographie de la carte mère surmontée de la carte fille 10 Gbits/s Ethernet.

D.5   Les chiffres clés du prototype LUSIPHER

Les performances de la caméra LUSIPHER ont largement été étudiées sur les bancs de tests et en conditions réelles d'imagerie sur plusieurs expériences de microscopie de fluorescence. Le Tableau II.2 reprend les principales caractéristiques du prototype LUSIPHER. Les chiffres de référence de la caméra LUSIPHER se trouve dans la référence [58].

BSB CMOS	Frame Rate	PSF CMOS	PSF Tube	Dark Count	Sensibilité
2x(400x800) pixels	-125 fps	$\sigma_{\mathrm{cmos}}^{G}$	σ_{tube}	cathode S20 :	QE (530 nm)
10μm pitch	-250 fps	2.7μm	10.5μm	15 Hz/mm^2	
Epitaxial layer	-500 fps			cathode S25 :	
< 10μm		Gauss $\oplus$	Gaussian	400 Hz/mm^2	threshold
Passivation	Rolling-	Lambert	UCD	cathode gap	2,5 kV
< 80 nm	Shutter	FWHM 30μm	12 mm	1 mm	gain 300 e-

TABLE II.2 – Résumer des caractéristiques et des performances de l'ebCMOS Lusipher.

E Les applications

E.1 Etude du pouvoir de localisation de l'ebCMOS

Nous avons eu l'occasion de tester le pouvoir de pointé de l'ebCMOS dans des conditions de microscopie différentes : ENS Ulm équipe M. Dahan, IGBMC JL Voenesch plateforme d'imagerie et surtout Nanoptec équipe C. Dujardin du LPCML. L'étude la plus précise a cependant été obtenue sur notre banc optique avec la focalisation d'un spot de diamètre inférieur au micron (figure II.17) et un taux moyen de photons par image et par spot dans le régime Poissonien.
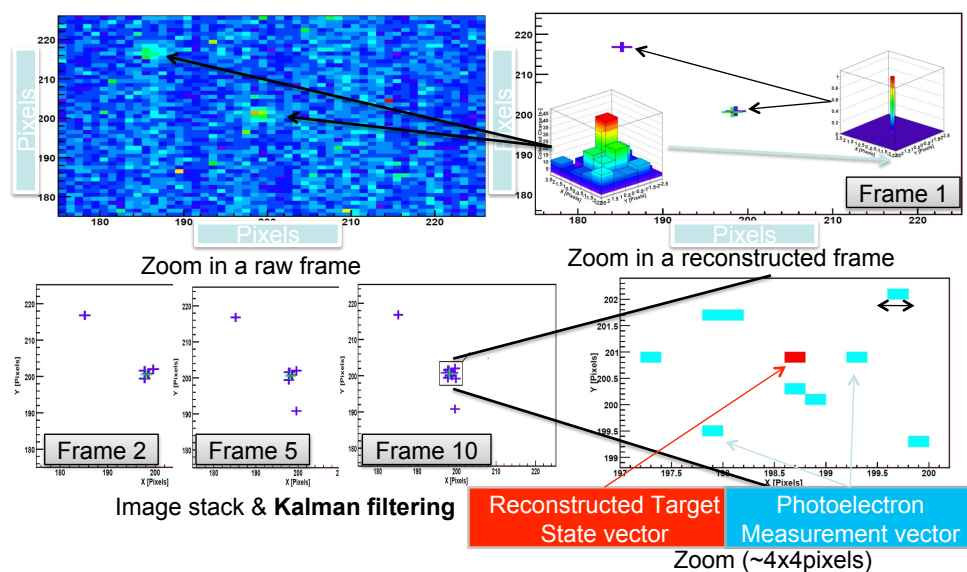
FIGURE II.17 – Schéma explicatif de la méthode de reconstruction d'un émetteur unique à partir de l'enregistrement des photons image par image. La résolution obtenue est intra-pixel.

Une résolution de 1 μm est obtenue en 60 photons détectés. Le taux de faux et l'efficacité dépend fortement du bruit de fond comme on pouvait s'y attendre (voir Figures II.18).

E.2 La localisation et le suivi de nanoparticules

Je passe ici la description des aspects de microscopie et de fluorescence et tente de reprendre les conclusions principales qui découlent de mes expériences de tests de suivi de nanoparticules.

● Lors d'une identification de particule unique il est souhaitable de définir un rapport signal à bruit local. Cela permet de suivre des particules dans tout le champ de vue bien que l'illumination de l'excitation ne soit pas homogène (figure II.20).
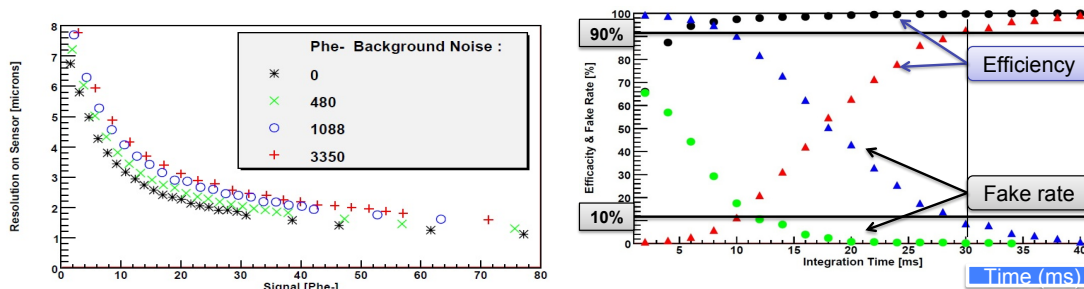
FIGURE II.18 – Précision de localisation dans différente condition de bruit de photons en fonction du nombre de photons détectés par l'ebCMOS sur le banc optique avec un spot unique (gauche). Efficacité et pureté mesurées de l'algorithme d'identification du spot pour deux valeurs de bruit de fond (droit). Le nombre moyen de photons par image et par spot est inférieur à 2.
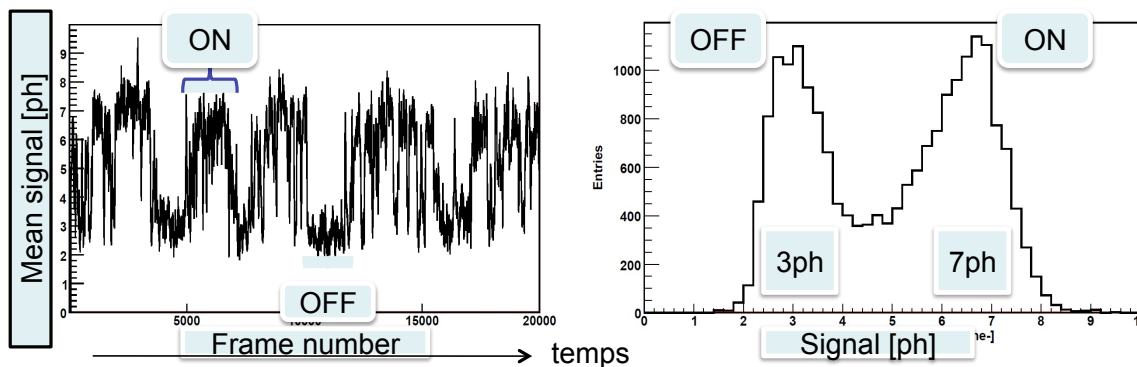
FIGURE II.19 – Observation du clignotement ("blinking") de nanoparticules fluorescentes de CdSe de 20 nm fixées.

- Le filtre de Kalman spatial n'est pas toujours bien adaptés à du suivi de mouvement brownien car il nécessite l'introduction d'un bruit important de processus dans l'équation de mise à jour du vecteur d'état nuisible à un bon pouvoir de pointé. Cette étude est en cours.

- Le suivi temporel associé à la quantification par photons (Poisson) est un atout important de ce capteur. Le "blinking" de nano-cristaux a été observé avec des taux de photons par image et par nanoparticule de CdSe inférieure à 7 (figure II.19).

- Le mouvement Brownien a été observé et les coefficients de diffusion mesurés par l'intermédiaire du calcul du déplacement quadratique moyen (figure II.21). Des résultats préliminaires sur les coefficients de diffusion ont été obtenus. Des coefficients de l'ordre de $1\mu m^2 s^{-1}$ ont été obtenus pour des CdSe de 10-20 nm dans l'eau. Je rappelle que pour l'observation de particules uniques en biologie des valeurs inférieures à $10^{-2}\mu m^2 s^{-1}$ correspondent à un mouvement brownien peu diffusant alors que 1

QDs identifiées après 20 images · Somme sur 20 000 frames
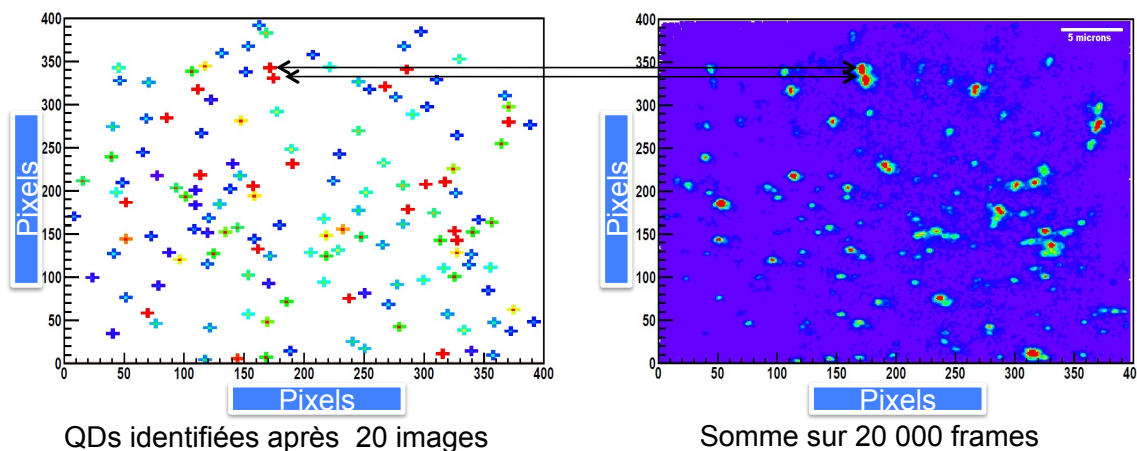
FIGURE II.20 – Exemple d'une image intégrée (somme sur 1000 images) et d'une image courante obtenu par tracking des positions reconstruites des nanoparticules fluorescentes.

$\mu m^2 s^{-1}$ correspond à un cas limite nécessitant des temps d'intégration de quelques millisecondes. L'influence du bruit sur la précision de la mesure reste à faire. L'ebcMOS est donc véritablement dans la bonne gamme de fréquence trame.

- Les conditions de bruits de fond photons sont primordiales pour une bonne identification des particules uniques. Les techniques de microscopie par ondes évanescentes (TIRF) sont préférables à celles du champ large où le bruit de photons ("off-focus") rendent difficile le suivi par accumulation de photons.
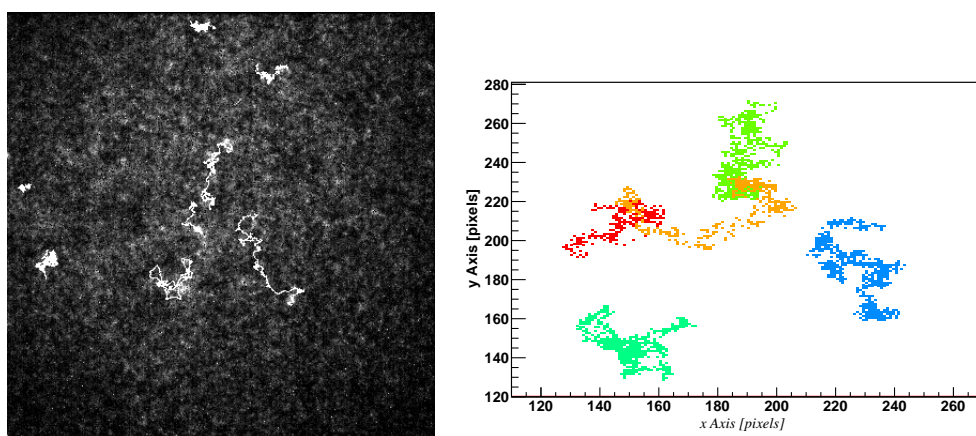
FIGURE II.21 – Traces reconstruites de nanoparticules fluorescentes dans des conditions difficiles de bruit de photons parasites (@ NanOptec 2011).

E.3   La vidéo-microscopie rapide et sensible en champ sombre

Cette application porte sur l'étude de la nage de la bactérie *E. Coli* en surface. Nous avons effectué en 2011 pendant deux semaines des tests de la caméra ebCMOS sur de la microscopie en champ sombre avec l'équipe de L. Lemelle et C. Place à l'Institut Joliot Curie, ENS Lyon. L'objectif principal était d'étudier un corpus de trajectoires de bactéries afin de caractériser précisément la réorientation du corps lors du phénomène de "tumbling" en surface (proche d'une interface). Le point de départ de cette étude réside dans la possibilité offerte par la rapidité et la sensibilité de la caméra ebCMOS pour établir une paramétrisation assez fine de la cinématique de la bactérie. Les trajectoires observées s'avèrent assez complexes du fait de la propulsion induite par les flagelles qui jouent le rôle d'hélices et qui se solidarisent puis se désolidarisent à intervalle régulier. Ce phénomène produit un effet d'oscillation du corps qui s'ajoute à la trajectoire "régulière". Le "tumbling" survient pendant cette trajectoire oscillante régulière et il est encore difficile de le quantifier de manière systématique (ralentissement, rotation...). De nombreuses séquences ont été
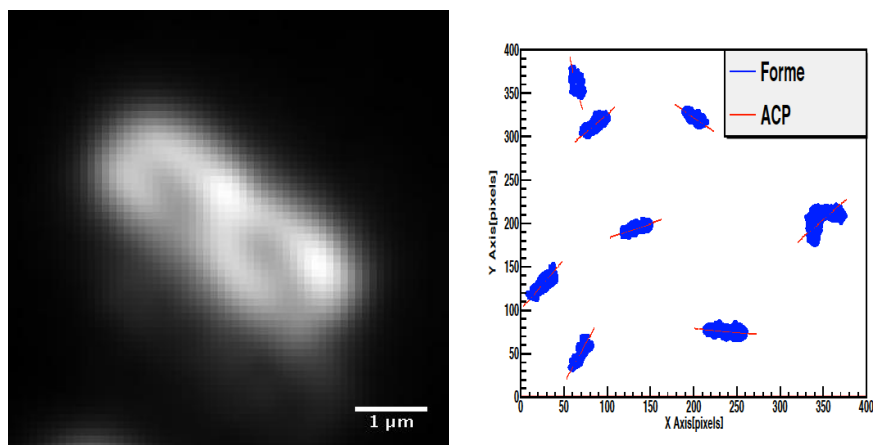
FIGURE II.22 – Image reconstruite d'une bactérie *E. Coli* à partir de 2500 images prisent à 500 Hz au x100 (gauche). La figure de droite montre les axes principaux des bactéries obtenus par la méthode de la composante principale (matrice de covariance de la forme ou de la charge)

enregistrées à trois types de grossissement x20, x60, et x100 ainsi que pour trois fréquences d'images 125, 250 et 500 Hz. Après filtrage du bruit de photons les bactéries sont clairement identifiables comme cela est montré dans la Figure II.22. Une analyse en composante principale permet d'obtenir une mesure de l'orientation de la bactérie dans le plan (ce n'est que sa projection) à 500 Hz (Figure II.22). Une vitesse moyenne glissante est également calculée à partir de la position soit du centre de gravité des charges soit du centre de la forme reconstruite.

Les oscillations du corps sont clairement mises en évidence ainsi que le changement brusque de direction lors du "tumbling" (Figure II.23).

Une analyse différente utilisant la transformation en ondelettes est en cours à l'ENS.
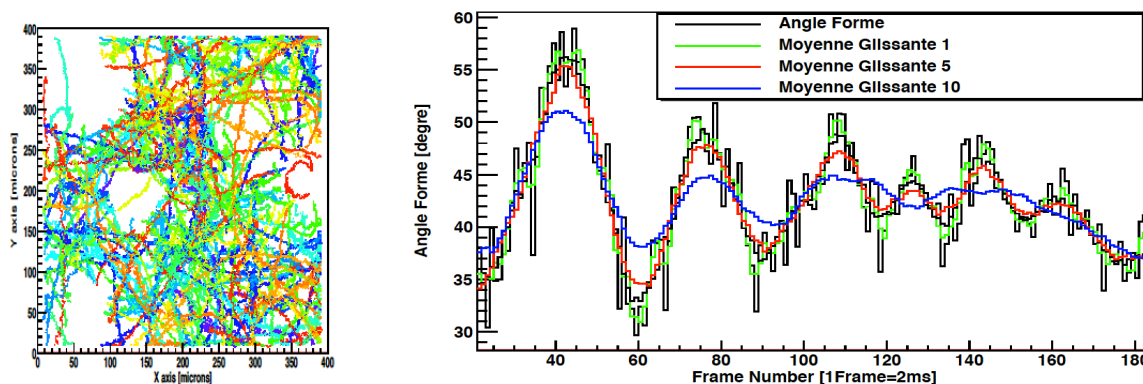
FIGURE II.23 – Ensemble des trajectoires reconstruites des bactéries obtenues à 500 Hz au x100. Observation de la direction du corps de la bactérie pendant la nage (droite). On observe aisément l'oscillation du corps à 500 Hz.

Nous devrions aboutir dans les prochains mois à une modélisation de la nage et du "tumbling". Nous pensons qu'il devrait être possible d'observer précisément le phénomène de décélération de la bactérie avant l'événement de "tumbling" afin de lever l'incertitude sur ce qui n'est pour l'instant dans ce domaine qu'une hypothèse de travail acceptée par la communauté. Cette mise en évidence systématique sur un grand nombre d'échantillons permettra par sa systématisation d'initier une étude complète des effets de la chimio-taxie sur la réorientation des bactéries et donc sur la manière dont elles explorent l'espace. Si nous voyons que ces études portent leur fruit il est fort probable qu'un système complet reste au laboratoire Joliot-Curie pour des études biologiques. Cependant un effort supplémentaire sur le logiciel sera nécessaire afin de passer à une version production exploitable par des biologistes.

En conclusion de ces premiers tests et de ces premières analyses nous pouvons affirmer que l'association de la sensibilité et de la vitesses du système de caméra ebCMOS a apporté à ce domaine d'imagerie de nouvelles possibilités tant du point de vue de la statistique des échantillons observés que de la qualité du tracking obtenu.

E.4 Analyse de front d'onde par filtre de Shack-Hartmann pour l'optique adaptative

Les tests pour cette application ont eu lieu jusqu'à présent au laboratoire sur nos bancs de tests optiques. Le montage est simple puisque constitué d'une source ponctuelle (fibre mono-mode) située à une distance de 1 m d'une matrice de micro-lentilles. La photo-cathode du capteur ebCMOS est placée dans le plan focal image (9 mm) des micro-lentilles en tenant compte des interfaces air-verre.

La micro-lentille SUSS MicroOptics, 150 μm de pas, focalise plus de 2600 spots sur le tube LUSIPHER complet 800x800 pixels. Chaque position de spot est reconstruite pour
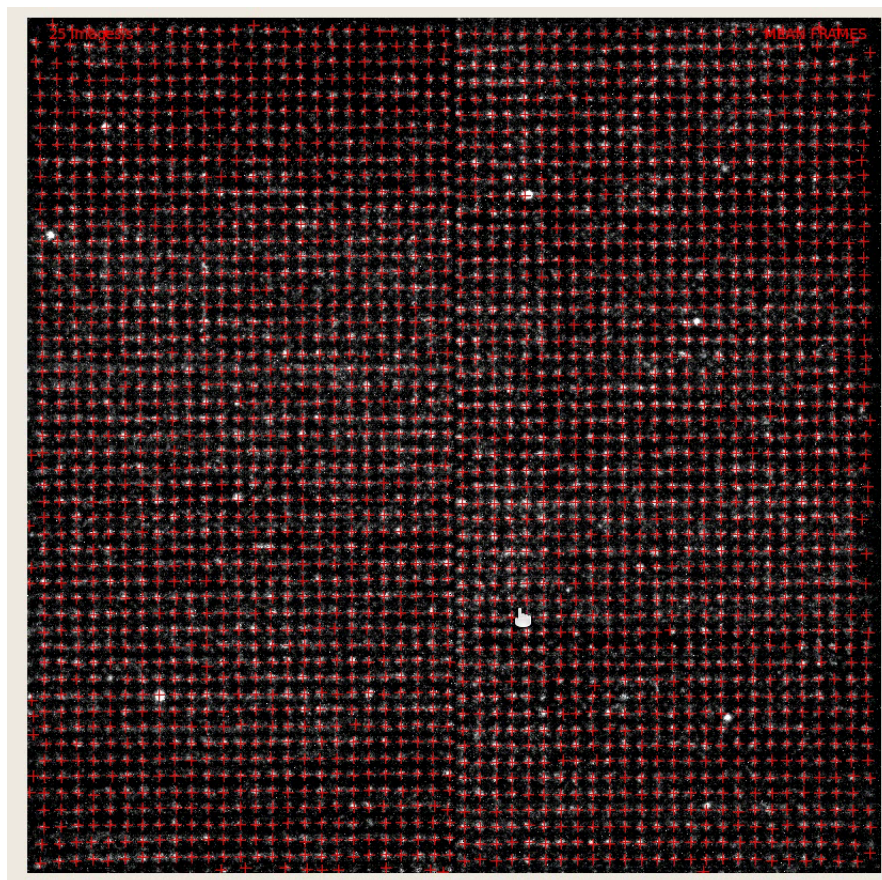
FIGURE II.24 – Capture d'écran de la matrice de 2500 spots suivis à 500 Hz par le logiciel en ligne (Z800, HP, 16 cores). Le taux de photons par spot et par image est de l'ordre de deux. Les spots blancs sont donnés par l'image en charge à 25 Hz. Les croix rouges sont les positions calculées des spots toutes les 2 ms avec une mise à jour de visualisation à 50 Hz.

un nombre de photons donnés ou un nombre d'acquisitions données. Une analyse hors-ligne de résolution sur les positions des spots est menée en parallèle au développement du code en ligne. Elle est en cours de finalisation pour la rédaction d'un article sur l'optique adaptative. Le traitement temps réel de spots pour son utilisation en boucle fermée pour la correction du front d'onde sur télescope devrait faire l'objet d'une seconde publication. La résolution en fonction du nombre de photons détectés (RMS sur la position vraie estimée sur un très grand nombre d'images) tend rapidement vers 2 μm.

Les résultats obtenus en ligne montrent une résolution du même ordre de grandeur que le résultat hors-ligne. Ce résultat sera présenté à SPIE Photonics Europe 2012 à Bruxelles. Lorsque j'observe sur l'écran de la station de travail une matrice de croix représentant les positions des spots calculées à 500 Hz et moins de deux photons en moyenne par spot j'ai la sensation que notre R&D est enfin sur le point d'aboutir (figure II.24).

E.5 L'observation de la bioluminescence marine : LuSEApher

E.5.1 Mesure de séquences de bioluminescence sur le Module Instrumentale Interdisciplinaire d'ANTARES à -2500 m.

C'est un projet décidé en Mars 2010 avec objectif d'immersion de la caméra sur le site d'ANTARES en octobre 2010. Quatre mois ont suffi aux ingénieurs de l'IPNL
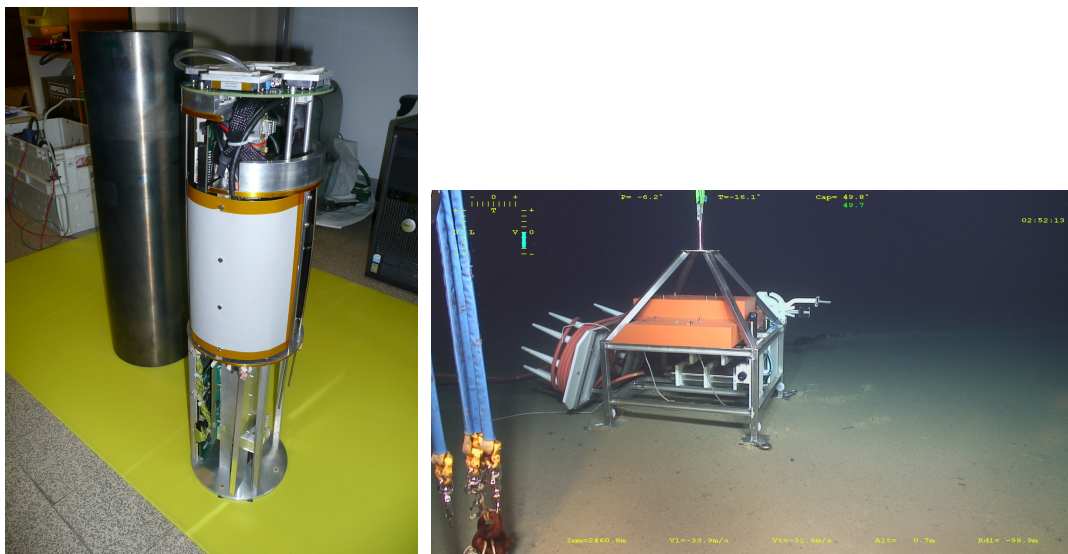
FIGURE II.25 – Photographie de la caméra LuSEApher avant son montage définitif (gauche). Photographie prise par le ROV de la MII placée à -2500 m (ANTARES) sur laquelle est embarquée la caméra LuSEApher (droite).

pour fabriquer le système embarqué complet à partir des éléments existants de la caméra développée pour la microscopie. Les parties logiciels et DAQ ont été allégées pour faciliter le contrôle déporté de la caméra. Le pilotage lent a été réécrit par M. Ageron du CPPM afin de ne pas perdre la main sur le système en cas de coupure brusque de l'alimentation. Des modes de redémarrage automatique ont aussi été installés. Nous avons eu deux jours (un week-end) pour effectuer les tests optiques liés à l'intégration de l'objectif devant la caméra. Nous avions opté pour une profondeur de champ large avec des objets entre 30 cm et 2 m. Il semblerait que la majorité des séquences enregistrées sont "off-focus", c'est-à-dire trop près du hublot car dans la plupart des cas la bioluminescence est activée mécaniquement (turbulence, choc avec la caméra). Les photographies de la Figure II.25 montrent la MII prise par le ROV et la caméra avant son insertion dans le tube de titane. Les photographies de la Figure II.26 montrent la face avant et arrière de la caméra montée.

La mise au point de la caméra, notamment de son seuil de déclenchement de la remontée des données à terre a été poursuivie après l'immersion. Le seuil de décision d'enregistrement de la séquence a été fixé à 14 photons détectés par image afin d'éviter un

FIGURE II.26 – Photographies de l'avant et de l'arrière de la caméra montée dans son tube en titane de 50 cm de long. On voit le hublot qui permet l'observation avec un objectif classique de caméra. On voit également le seul câble sortant de la caméra qui délivre le courant et le câble Ethernet 100 Mbits/s.

déclenchement trop fréquent sur les retours ioniques du tube à vide. Cependant le bruit moyen, qui a été mesuré précisément dans les conditions normales de mesure (15 °C au niveau du capteur, 35 °C au niveau du PC) est inférieur à 1 photon par image. Cela offre une sensibilité au phénomène de bioluminescence très importante.

Le tri des événements remontés est alors effectué suivant des critères de distributions spatiale et temporelle des photons mesurés. Les événements les plus fréquents ont en moyenne 20 photons par image.

Les images les plus lumineuses peuvent atteindre plusieurs centaines de photons par image. La durée moyenne des séquences est de l'ordre de la seconde. Les séquences les plus longues sont de l'ordre de 10 secondes (Figure II.27). L'identification des espèces responsables de la bioluminescences est difficile à effectuer car les événements sont souvent mal focalisés et comportent assez peu de photons. Il faut bien garder à l'esprit qu'il s'agissait plus initialement d'une campagne de tests et de preuve de faisabilité que d'une réelle campagne de mesures biologiques.

La version 2 de LuSEApher tentera de répondre aux problématiques de l'auto-focus ou de l'imagerie 3D (mesure de la distance à l'objet). Cela reste particulièrement difficile et peu conventionnel vu le nombre de photons disponibles en quelques millisecondes. Mais ce challenge me semble particulièrement intéressant pour développer de nouvelles méthodes d'acquisition mettant à profit la sensibilité et la vitesse pour obtenir les distances des émetteurs. Nous avons deux concept à tester à ce sujet : un utilise la dynamisue de lentille liquide, l'autre utilise les techniques dite "4D Field". L'immersion de LuSEApher 2 est programmée pour fin 2012 avec la disponibilité d'un ROV d'IFREMER.
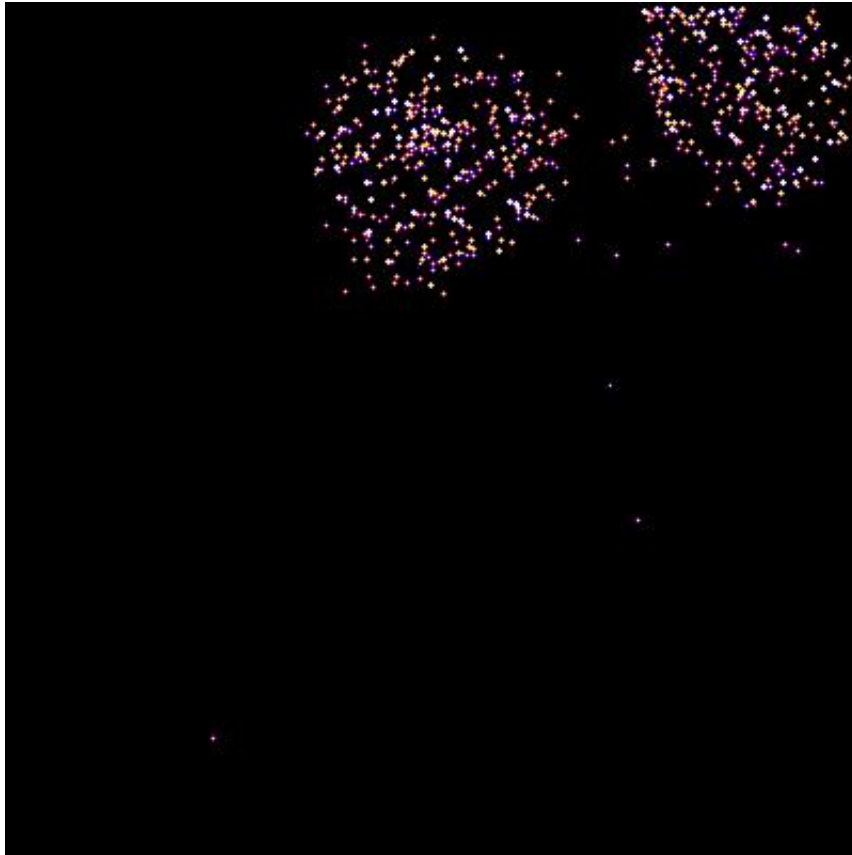
FIGURE II.27 – Image des photons reconstruits (16 ms, 400x400 pixels) sur la séquence du 22 février 2011 où apparait alternativement puis simultanément deux sources de bioluminescence.

F   Publications sur les prototypes ebCMOS

F.1   Publications sur le prototype LUSIPHER

A single-photon sensitive ebCMOS camera: The LUSIPHER prototype

R. Barbier [a,b,*], T. Cajgfinger [a,b], P. Calabria [a,b], E. Chabanat [a,b], D. Chaize [a,b], P. Depasse [a,b], Q.T. Doan [a,b], A. Dominjon [a,b], C. Guérin [a,b], J. Houles [a,b], L. Vagneron [a,b], J. Baudot [c,d], A. Dorokhov [c,d], W. Dulinski [c,d], M. Winter [c,d], C.T. Kaiser [e]

[a] Université de Lyon, Université Lyon 1, Lyon F-69003, France
[b] CNRS/IN2P3, Institut de Physique Nucléaire de Lyon, Villeurbanne F-69622, France
[c] Université Louis Pasteur Strasbourg, Strasbourg, France
[d] CNRS/IN2P3, Institut Pluridisciplinaire Hubert Curien, Strasbourg F-67037, France
[e] PHOTONIS Netherlands BV, Roden B.O. Box 60, 9300 AB Roden, The Netherlands

ARTICLE INFO

ABSTRACT

Processing high-definition images with single-photon sensitivity acquired above 500 frames per second (fps) will certainly find ground-breaking applications in scientific and industrial domains such as nano-photonics. However, current technologies for low light imaging suffer limitations above the standard 30 fps to keep providing both excellent spatial resolution and signal-over-noise. This paper presents the state of the art on a promising way to answer this challenge, the electron bombarded CMOS (ebCMOS) detector. A large-scale ultra fast single-photon tracker camera prototype produced with an industrial partner is described. The full characterization of the back-thinned CMOS sensor is presented and a method for Point Spread Function measurements is elaborated. Then the study of the ebCMOS performance is presented for two different multi-alkali cathodes, S20 and S25. Point Spread Function measurements carried out on an optical test bench are analysed to extract the PSF of the tube by deconvolution. The resolution of the tube is studied as a function of temperature, high voltage and incident wavelength. Results are discussed for both multi-alkali cathodes as well as a Maxwellian modelization of the radial initial energy of the photo-electrons.

© 2011 Elsevier B.V. All rights reserved.

1. Introduction

The main goal of low light level imaging is to improve sensitivity up to single photon on a large array of pixels with micrometer resolution and a limited dark count. Many devices such as EMCCD [1], pnCCD [2], electron bombarded CCD or APS [3,4], HPD [5], ICCD [6], H33D [7] and ICMOS [8] can achieve this limit of sensitivity and tend to push the state of the art to a faster frame rate on a larger field of view while keeping good spatial resolution. This will require the next generation of low light detectors to increase the data throughput and the signal conditioning on the very Front End of the detection process. At a certain luminance level (µLux) and a certain frame rate (kHz) the number of pixels per frame collecting photons is low. Then single-photon counting imaging with data reduction processes is more appropriate to sustain the data rate.

This article aims to describe the latest developments of a promising way to answer this challenge, the electron bombarded CMOS (ebCMOS) detector. This Hybrid Photon Detector [5] concept is not new. Nevertheless, the emerging technology of back-side passivation allows such HPD to benefit from the potentially high frame rate of CMOS pixel sensors. We proved in Ref. [9] the principle of single-photon detection with electro-bombarded CMOS sensors using MIMOSA 5, a chip developed for charge particle tracking in the framework of high energy physics experiments.

We are convinced that continuous single-photon detection and processing with a dedicated back-thinned CMOS sensor could open a new field of kHz frame rate applications.

This is the main goal of our Large-scale Ultra-fast SIngle-PHoton trackER (LUSIPHER) project by integrating a CMOS sensor specifically designed for low energy electron localization. A diagram of the ebCMOS photodetector as well as a picture of the LUSIPHER prototype are shown in Fig. 1.

The targeted applications in Fluorescence Microscopy are mainly STORM (Stochastic Optical Reconstruction Microscopy) techniques such as Photo-activated Localization Microscopy (PALM [10] and sptPALM [11]), single nanoscale emitters tracking

* Corresponding author at: Institut de Physique Nucléaire de Lyon, 4 rue E. Fermi, Villeurbanne F 69622, France. Tel.: +33 472 431 222; fax: +33 472 431 452.
E-mail address: rbarbier@ipnl.in2p3.fr (R. Barbier).
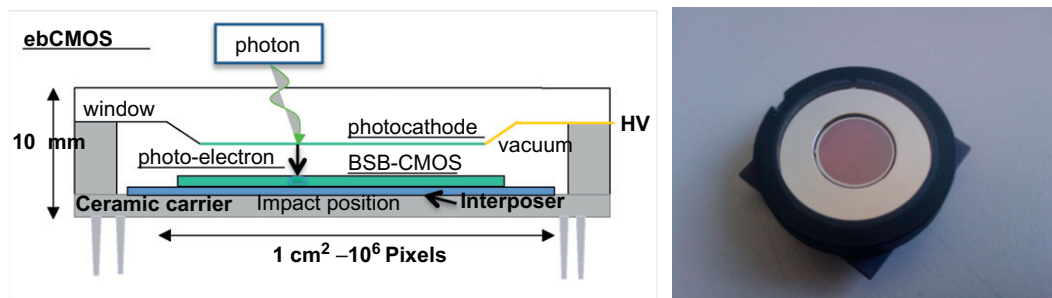
Fig. 1. Diagram of the ebCMOS (left). Picture of the ebCMOS prototype called LUSIPHER (right). The high voltage is provided to the cathode by a pin out of the carrier. The cathode tube active diameter is 12 mm.

(single molecule or quantum dots in cells) over a large field of view [12]. Our camera could also improve significantly imaging techniques which are limited by the frame rate and/or the sensitivity of the cameras such as Spinning Disk Confocal Microscopy. For a review of single molecule detection and photon detectors in Fluorescence Microscopy see Ref. [13].

The aim of this paper is to present the characterization and the performance of a fast-readout LUSIPHER camera system based on a back-side bombarded CMOS pixel array (BSB-CMOS). Section 2 describes the camera prototype, i.e. the CMOS chip architecture and the camera design with its readout architecture. A method for the characterization of back-thinned CMOS is developed and results obtained on two different epitaxial layer doping profiles are reported.

In Section 3, the detailed performances obtained with the two ebCMOS tubes are discussed. Dark count rate has been measured versus temperature and high voltage (gain) for two different multi-alkali photo-cathodes (SbNaKCs) called S20 and S25 (this latter is also called red-extended S20R). A dedicated study of the vacuum tube spatial resolution has been developed using a focused light spot with a controlled photon flux down to single photon per image. The Point Spread Function (PSF) of the tube, PSF-tube, is fitted from the deconvolution of the experimental PSF and the PSF of the CMOS, PSF-CMOS. Parameters and experimental conditions (temperature, high voltage, wavelength, photocathode type) driving the PSF-tube are explored. Finally, the PSF measurement is used to compute the Modulation Transfer Function (MTF) of the device. These results are compared with MTF measurement obtained with an USAF 1951 test chart.

2. LUSIPHER prototype description

2.1. Detection principle

In the proximity-focusing configuration, an electron emitted by the photo-cathode is accelerated to a given energy thanks to the high voltage and then detected by the CMOS pixel array. The pixelization localizes the impact and provides an estimation of the primary photo-conversion position. In order to reach a good spatial resolution (FWHM $< 30\ \mu m$) and to limit the cathode dark current (10^{-5} electron/pixel/ms), an electron energy lower than 3 keV and a cathode-CMOS gap length smaller than 1 mm are mandatory.

However, the stopping range of 2 keV electrons in silicon amounts to about 50 nm [14,15]. Therefore, the thickness of the entrance dead layer of the back-side passivated CMOS shall not exceed 60 nm (typical) to ensure single photo-electron sensitivity at 2.5 kV. This has been verified independently with the Casino software [16], that is a Monte Carlo software developed for low

energy beta interaction in solids using the modified Bethe–Bloch formula of Ref. [17].

Fig. 2 depicts the various processes involved in the photo-electron detection by the BSB-CMOS as well as a schematic view of the sensor layers. The secondary electron multiplication, diffusion and collection occur in the epitaxial layer which covers the overall chip surface. The detection fill factor is therefore 100%. Nevertheless the secondary electrons are produced at the top of the P-doped epitaxial layer and have to drift towards the N-well diodes before being collected. Therefore, the epilayer thickness has to be the thinnest to improve the collection probability and reduce the spreading over several pixels. The state of the art in chemical and mechanical etching of the bulk wafer can produce a $(8 \pm 2)\ \mu m$ epitaxial layer thickness. In order to optimize further our device, an epitaxial layer featuring a graduated doping (see next section for details) was produced. The doping gradient aims at producing a local electric field to improve the charge collection. The Silicon On Insulator (SOI) wafer technology could offer an even better alternative in the future.

2.2. Back-thinned CMOS sensor description

2.2.1. Chip design

The chip integrated into the LUSIPHER camera is a CMOS pixel array designed in $0.25\ \mu m$ technology by the IPHC Strasbourg group [18]. This chip consists of two adjacent matrices of 400×400 pixels with $10\ \mu m$ pixel pitch. Hence, the sensitive area amounts to $4 \times 8\ mm^2$ surrounded by a pad ring as displayed in Fig. 2.

The chip sequencing and readout is electrically separated in two 400×400 pixel matrices. For each matrix, the analogue readout is performed by four parallel output buffers which address four consecutive pixels in a row at each readout clock. Therefore, the two 400×400 pixel arrays are read out in 1 ms with a maximum pixel clock of 40 MHz, since two readout sequences are necessary to evaluate the useful pixel signal from the difference between the pixel integrated signal and the pixel reset value.

Indeed, the small pixel pitch does not allow the implementation of the micro-circuits to perform the Correlated Double Sampling (CDS) inside the pixel. Two readout modes have been implemented in the chip for proceeding with the CDS. One mode minimizes integration time to 1 ms but with 50% dead time and the other mode, referred to as the Rolling Shutter mode, maximizes the duty cycle (100%) with a 2 ms integration time due to double readout of the same row. In any case the image rate is 500 Hz with an initial 1 kHz readout rate of the pixel array.

A dedicated large pad ring to accommodate wedge bonding from the chip back-side has been designed with a total of 38 I/O pads. The architecture of the pixel has been optimized by simulation, exploiting the specific features of the $0.25\ \mu m$
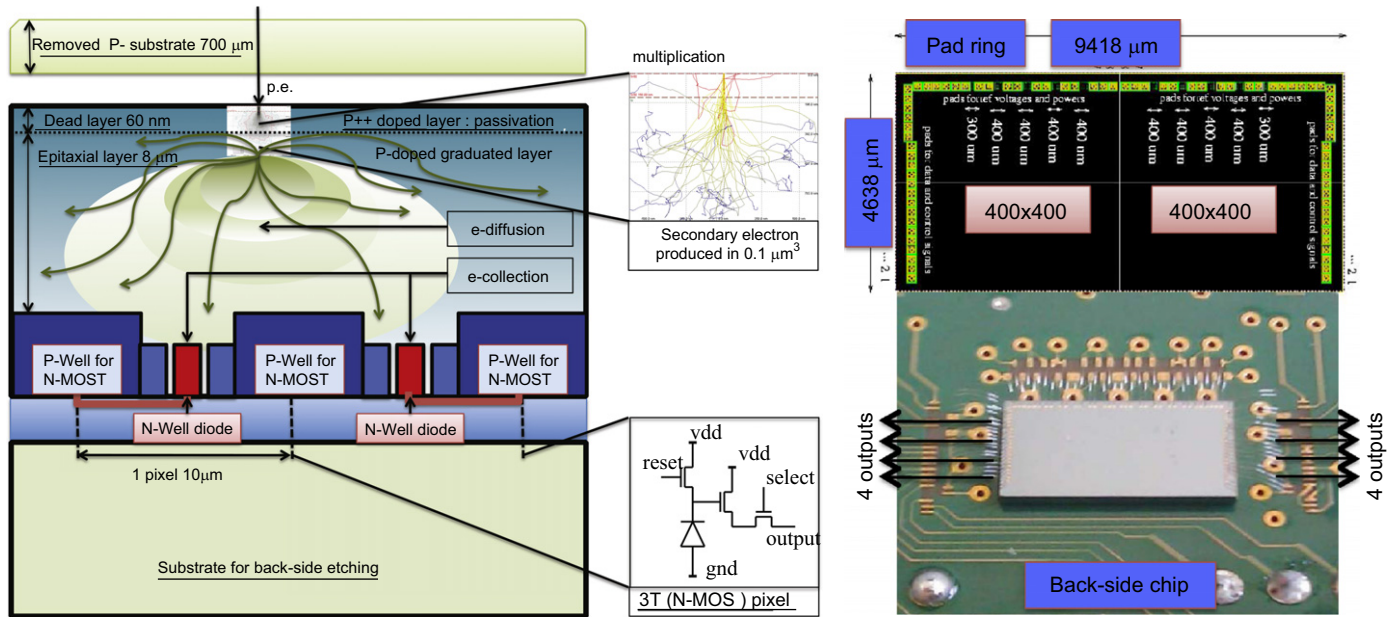
Fig. 2. Schematic view of the ebCMOS camera with the various layers depicted and their corresponding processes. Note that the vertical scale is increased by a large factor with respect to the horizontal scale (left). On the right (top), a drawing of the pad ring with dimensions. On the right (bottom), a picture of the sensor mounted on its servicing board for X-ray measurement.
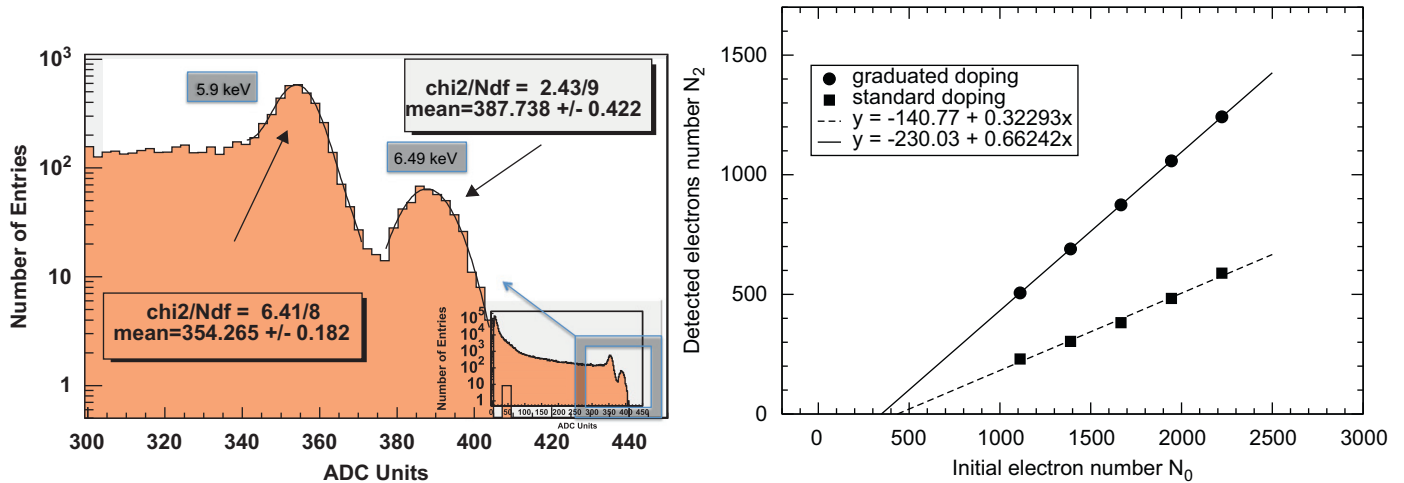
Fig. 3. Charge distribution of the seed pixel obtained with an X-ray ^{55}Fe source (left). The two peaks correspond to the full energy peak calibration (5.9 and 6.49 keV) of the N-well diodes. Gain curve obtained from single-electron bombardment into an HPD set-up (right). Linear part of the curve (above 4 keV initial energy) gives the information on the Charge Collection Efficiency (slope) and on the energy lost in the dead layer. The initial electron number is obtained by dividing the initial energy by the mean energy necessary for electron–hole pair creation in silicon (3.6 eV).

technology. The pixel micro-circuitry includes a simple three transistors (3T) with an N-well diode for charge collection. Wafer etching and post-processing steps have been performed by an industrial partner. Two different P-doped profiles of the epitaxial layer have been tested. The standard layer exhibits a uniform doping corresponding to $50\,\Omega$ cm resistivity. The second profile aims to increase the Charge Collection Efficiency. It features a boron doping graduated from 10^{19} down to 10^{15} atoms/cm^3 over a few micrometers depth. Thereafter, this epitaxial layer will be referred to as "graduated".

2.2.2. Collecting diode calibration with an X-ray source

Illumination with an X-ray ^{55}Fe source allows to calibrate the N-well diodes of the pixels. Full energy peak corresponding to a total conversion in a single-pixel (N-well diode) of 5.9 and 6.5 keV

X-rays are fitted to compute the conversion factor C (e-/ADCU). Using the hypothesis of a mean energy of 3.6 eV to create an electron–hole pair in silicon, a conversion factor C equals to (4.8 ± 0.2)e-/ADCU has been measured. The pixel equivalent noise charge distribution gives a most probable value of 7.8e^- and a mean value of 9.2e^- for a 10 MHz readout clock. Fig. 3 shows the seed pixel charge distribution.

The two full energy peaks, emerging from the tail of the distribution are also used to compute the Charge Collection Efficiency (CCE). The CCE is given by the ratio between the 5×5 pixel cluster charge corresponding to an X-ray conversion into the epitaxial layer and the N-well diode contained X-ray conversion peak of Fig. 3.

The results are reported in the first column of Table 1. The graduated epitaxial layer exhibits a CCE better than a factor of two in comparison to the standard profile. This improvement is

Table 1
Charge Collection Efficiency and gain measurements (cluster of 5×5 pixels) in X-ray calibration and in electron bombardment experiment. The mean number of electrons lost in the dead layer are also reported.

Doping profile	X-ray	Electron bombardment			
	CCE (%)	ε (%)	$\Delta E_0/3.6$ (electrons)	Gain at 4 kV (electrons)	ε_g at 4 kV (%)
Standard (50 Ω cm)	32	32	441	230	22
Graduated	60	66	376	506	46

attributed to the benefit of the local electric field generated by the doping gradient which helps focusing secondary electrons drift towards the N-well collecting diodes.

2.2.3. Low energy electron sensitivity and Charge Collection Efficiency

The most important building blocks of an ebCMOS is the back-thinned CMOS pixel array for back-side bombardment. For the purpose of estimating the sensitivity to low energy electrons, we used a HPD test bench consisting of a vacuum chamber (10^{-5} mbar) with a palladium cathode illuminated by a Xenon arc lamp source through an optical fibre. UV light generates, by photo-conversion, electrons which are then accelerated by an adjustable electric field to the desired energy in the range 0–20 keV. An electron flux of a few thousands per cm^2 is produced per UV flash. The UV light flash trigger is synchronized with the beginning of the chip readout sequence.

Therefore, each frame contains isolated single-electron events. One event being made of a group of adjacent hot pixels. The sum of pixel charges in such a cluster accounts for the number of secondary electrons collected by the CMOS sensor. The plot in Fig. 3 (right part) represents the average number of secondary electrons collected in a 5×5 pixel cluster with respect to their initial number. We learn from the linear behaviour of the curve, that the gain, i.e. the ratio between the secondary electron numbers collected and generated, does not depend on E_0 in the considered energy range. Interestingly, the extrapolation of the line down to zero collected electrons cuts the generated charge axis at a non-zero value. This non-zero number reveals the existence of a so-called dead layer in which the secondary electrons generated will never be collected as signal.

The gain curve is linearly fitted with the expression: $G = aE_0 - b = \varepsilon(E_0 - \Delta E_0)/3.6$. It gives access to ΔE_0, the energy lost in the dead layer and to ε, the CCE of the secondary electrons generated beyond the dead layer. The ε factor takes into account recombinations which occur during the secondary electron drift towards the diodes.

In this simple model, it is assumed that ΔE_0 is a constant for an initial energy E_0 greater than 5 keV. It has been checked by simulation that this first order approximation is justified for a dead layer thickness smaller than 60 nm [19]. The net results obtained for CCE from the passivation process and from the epitaxial layer thickness are taken into account by the computation of the global efficiency, defined by $\varepsilon_g = 3.6\ G/E_0$. In this case, one takes into account the amount of electrons lost in dead layer and drift volume.

Table 1 summarizes the results obtained for the two epitaxial layer profiles. We conclude from this table that the graduated epitaxial layer shows the best CCE. This result is compatible with the factor of two found using the X-ray measurements. The 6% difference observed between CCE X-ray and epsilon for the graduated epitaxial layer is probably due to the difference of

interaction depth between electrons and X-rays. This difference is not observed for the standard epitaxial layer probably because its uniform doping profile cannot generate a depth-dependent electric field. The discrepancy could also stem from an overestimation of the charge recombination in the dead layer. A future work based on a larger number of sensors and variety of doping processes will investigate these hypotheses in more details.

2.2.4. Diffusion measurement in the epitaxial layer: PSF-CMOS

It is well-known that the electron diffusion through the silicon epitaxial layer drives the spatial resolution of the CMOS sensor. Furthermore the diffusion process inside the epitaxial layer is an interesting physical variable to increase our understanding of the passivation process. The charge carriers generated in a very small volume at the back side are spread over about 25 N-well diodes (accounts for 90% of all the charges). The geometrical extension of the signal from a single primary electron is quantified by the PSF-CMOS. Because of the local electric field generated by the non-uniform doping profile, the PSF obtained with the graduated epitaxial layer is expected to be narrower (i.e. better for the image definition) than the PSF obtained with the standard uniform layer.

Experimentally, the PSF-CMOS is measured with an optical test bench [9] on different samples for each epitaxial layer. A focused light spot, narrower than the pixel pitch, illuminates the CMOS back-side at a controlled distance from the pixel centre. The amount of electrons collected in the pixel and its neighbours is stored, while the spot scans the pixel area with 2 μm steps. Fig. 4 shows the distribution of the individual pixel signal with respect to the spot distance to the collecting diode of this pixel. Different wavelengths in the visible spectrum have been tested. The shortest available wavelength (380 nm) has been chosen since the attenuation length of the order of 100 nm corresponds to the mean stopping range in silicon of an electron of a few keV energy [14].

The PSF-CMOS measurements have been normalized into a probability density function (p.d.f.). Fig. 4 shows clearly the improvement between the two epilayers. The shape of the p.d.f. is not strictly Gaussian and there is no physical reason for this. The best function that fits the distribution obtained for the standard epitaxial layer is a geometrical function. This geometrical function is obtained by computing the solid angle of each pixel versus the position of the starting point of the isotropic diffusion of the electrons. The normalized solid angle p.d.f. (called geometrical in what follows) is numerically derived from the formula given by for a pixel position X_0 and Y_0 by

$$F(X_0, Y_0) = \frac{\Delta\Omega}{4\pi} = \frac{1}{4\pi} \int_{X_0 - \Delta/2}^{X_0 + \Delta/2} \int_{Y_0 - \Delta/2}^{Y_0 + \Delta/2} \frac{H dX dY}{(X^2 + Y^2 + H^2)^{3/2}}$$

where Δ is the pixel pitch (10 μm) and H is the distance between the back side and the diode plane (epitaxial layer thickness).

The p.d.f. of the graduated epitaxial layer shows a sharper distribution with a FWHM = 9.2 μm instead of 18.4 μm for the standard epitaxial layer. The p.d.f cannot be fitted with a single geometrical p.d.f. The fit converges with an additional broader Gaussian. This Gaussian takes into account the electric field effect on the carriers during the diffusion process. This characterization shows already that it is possible to gain an understanding of the CMOS post-processing complementary to the MTF computation based on analytical models of charge carrier diffusion [20].

2.3. Camera system design

2.3.1. Tube design

The BSB-CMOS with graduated epitaxial layer has shown the best performance for CCE and for the PSF. Two chips of this type
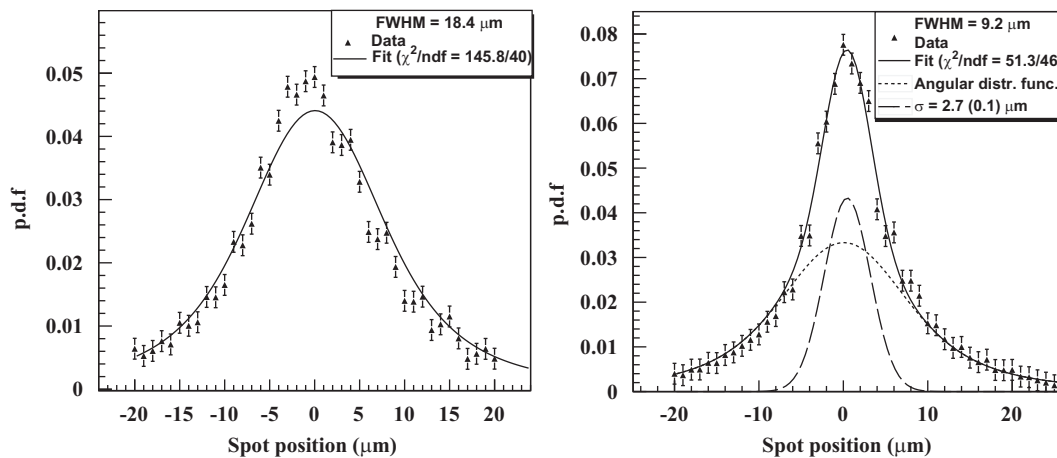
Fig. 4. PSF-CMOS measurement for standard epitaxial layer (left) and for graduated epitaxial layer (right). The PSFs have been normalized to produce probability density function (p.d.f.) for a better comparison between different epitaxial layer processes. The angular distribution function is the geometrical contribution (Lambert law) to PSF-CMOS. It is called geometrical in the text.
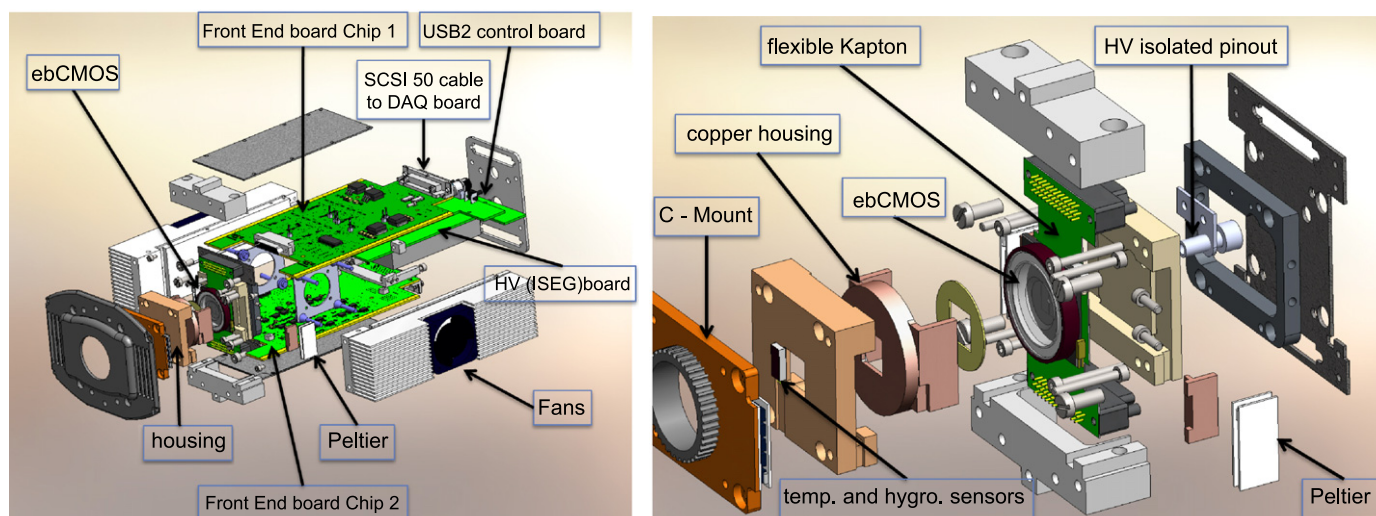
Fig. 5. Drawing of the four boards integrated in the camera (left). Drawing of the camera head module with the different components surrounding the ebCMOS (right).

have been mounted into the cavity of a ceramic carrier and sealed by a cathode window realized by Photonis SA[1] (see Fig. 1). The cathode-sensor gap is about 1 mm in order to accommodate a high voltage working point around 3 kV. The useful cathode diameter of 12 mm encloses the BSB-CMOS. Two multi-alkali cathodes, S20 and S25, have been produced to provide the best quantum efficiency either in the green part of the spectrum for S20 or in the red wavelength for S25. The typical quantum efficiency of the S20 (S25) cathode produced for our prototypes is 23% (15%) for a 480 nm (605 nm) wavelength.

2.3.2. Camera design

The ebCMOS has been integrated into a camera designed by the instrumentation group at IPNL. The camera is composed of the following blocks (see drawings of Fig. 5):

(i) the head module integrating the ebCMOS,
(ii) the USB2 slow control board controlled by a microchip [21],
(iii) the high voltage board equipped with an ISEG module (HVmax = −4 kV and Imax = 10 μA) [22],

(iv) the two Front End boards connected to the head module with a flexible Kapton.

A detailed view of the head module is shown in the drawings of Fig. 5 (right). It has been carefully shielded to avoid electromagnetic noise. The copper part of the camera head housing the ebCMOS is cooled with two Peltiers to maintain the cathode temperature below 15 °C in order to limit the dark current (see Section 3.2). The head module integrates also temperature and hygrometry sensors. There is no specific cooling needed for the CMOS sensor that operates at room temperature. The CMOS chip is maintained at a stable temperature, thanks to the thermal conductivity of the ceramic carrier. A stable cathode temperature within ± 0.1 °C is obtained for a reference value set between 0 and 25 °C. Two controlled fans are installed on each side of the camera to maintain the temperature inside the camera below 35 °C. The camera weights 2.5 kg and the overall dimensions reach $20 \times 6 \times 5$ cm^3. A picture of the camera is shown in Fig. 6 (right).

The microchip [21] of the control board implements the following functionalities:

• communicate with the acquisition server with usb2 or Ethernet protocol,

- set the Front End board voltage references,
- set and get the voltage reference (6 V max) of the high voltage module,
- set the Peltier voltage references,
- set the fans ON/OFF,
- set and get the temperature and hygrometry of the sensors.

The CMOS signals acquired by the Front End boards are directly sent to the acquisition board with the two SCSI 50 cables as shown in Fig. 5.

2.4. Gigabit Ethernet acquisition system

The Rolling Shutter mode implemented in the chips requires the acquisition board to proceed firstly with a digitization of the analogue outputs and secondly with a memorization of the reset value of each pixel in order to subtract it from the signal value of the pixel. A Field Programmable Gate Array (FPGA) connected to DDR memories is used. At the output level of the 4 ADCs (12 bits) the data throughput handled by the FPGA is 3.84 Gbits/s.

The online computation time for each event is limited to 2 ms in order to support continuous readout of the pixel array. The camera does not operate with the standard strategy of storing multiple images for a few seconds followed by a delayed data processing. The main idea is to provide a Real Time camera offering a 100% duty cycle allowing a continuous observation.

After CDS computation the data throughput for the 400×400 pixel array coded at 8 bits/pixel corresponds to 640 Mbits/s at 500 fps. We developed an acquisition prototype board based on an ALTERA development board [23] with an FPGA Stratix 2 to implement the CDS function and to test cluster finding algorithms. The control sequences and the analogue part of the acquisition are implemented on a homemade mezzanine board. A second mezzanine card is used for the 1 Gb/s Ethernet transfer to the acquisition work station using UDP protocol. The right picture of Fig. 6 shows the main components of the Data Acquisition module connected to the chip and to the acquisition server.

The acquisition work station receives the frames through its Ethernet Board, writes them on hard disk as raw data and, at the same time, performs calculations to finally display them to the user. The continuous high-rate frame flow requires a powerful computer. The software is multi-threaded and runs on a computer (Intel E5430) embedding two quad cores.

The acquisition process is in a master/slave configuration, triggered by the incoming packets. One thread is used to receive the UDP packets (20% of a core), one thread writes the packets directly to the mass storage (20% of a core), one thread builds the frames from the UDP packets and calculates the SNR (50% of a core), three threads are dedicated to seed selection and cluster finding (180% of a core), one thread applies a temporal filtering (100% of a core) and one thread performs deconvolution and manages the display (80% of a core). For 400×400 pixels at 500 fps, the global CPU load is about 4.5 cores. By a simple extrapolation, for $1K \times 1K$ pixel array at a rate of 1000 fps, we see that the number of cores required is not acceptable. The necessary breakthrough will come from massively parallel computing on GPU and from a Real Time OS to improve the thread management.

3. LUSIPHER performances

3.1. Single photo-electron measurement

Single photo-electron cluster reconstruction is the basic element of a good high frame rate tracking algorithm of a single-photon emitter such as Quantum Dots or single fluorescent molecules. The single-photon event filter selects a pixel cluster composed of a 5×5 pixel array centred on the pixel which has the highest signal-over-noise ratio (SNR), called the seed pixel.

The seed pixel selected with a SNR ≥ 5 is the trigger of the clustering procedure. This selection reduces the pixel noise effect on the fake photon rate to 10^{-6}/pixel/frame. With a mean noise of 8 electrons one can say that 40 electrons is the lower limit of charge collected by a pixel to start the clustering procedure. A typical single photo-electron event obtained for HV=2.8 kV is shown in Fig. 7 and the accumulation of such events gives the single photo-electron spectrum presented in the same figure.

3.2. Dark count measurement

The electron emissions by the cathode (thermionic, field effect) are the principal contribution to the dark count (DC) rate. The mean DC is measured as a function of temperature between 6 and 20 °C and high voltage between 2 and 3 kV. Measurements with S20 photo-cathode gives a very low DC rate, 15 Hz/mm² (typical) for the whole range of temperature and high voltage.

ALTERA Development board
FPGA STRATIX 2

ADC/FPGA (CMOS SEQ.)

Eth 1Gb/s

Ethernet Data Acquisition System
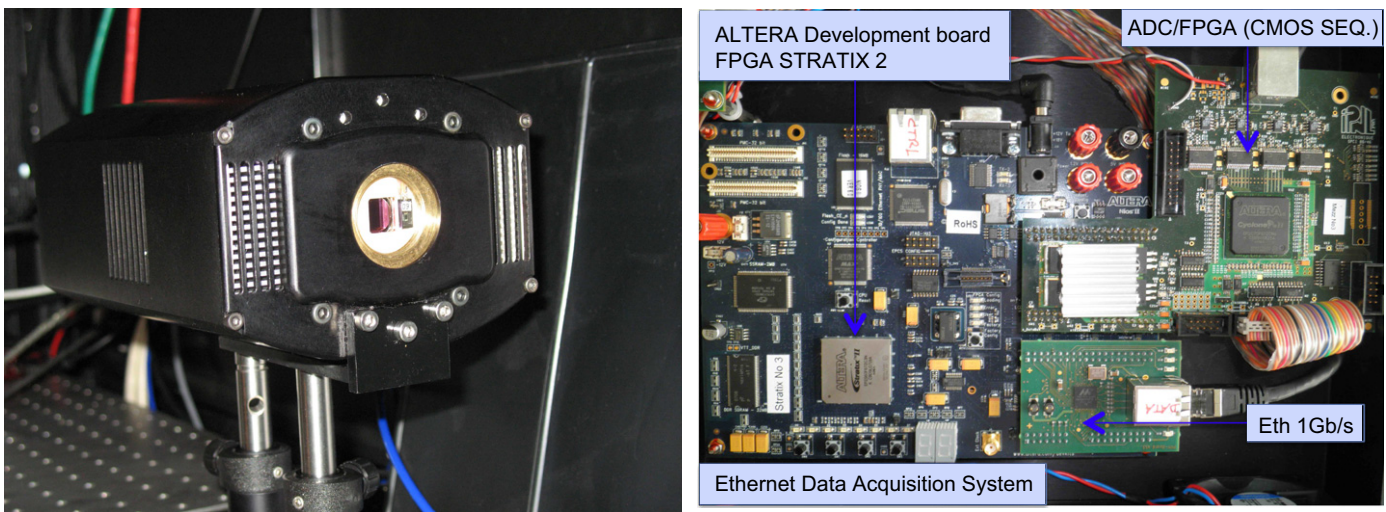
Fig. 6. Picture of the camera designed by the instrumentation group at IPNL (left). Picture of the data acquisition system with ALTERA development board and mezzanines (right).
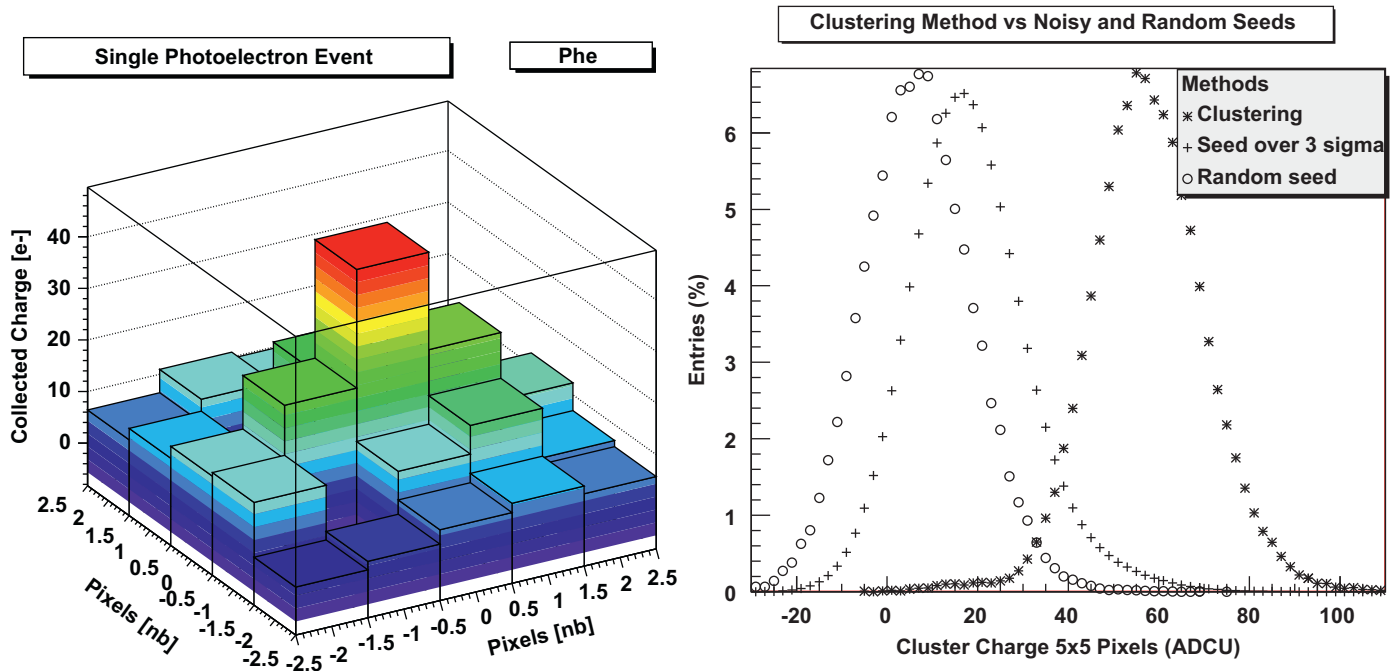
Fig. 7. Single photo-electron event recorded for HV=2.8 kV (left). The single photo-electron spectrum corresponds to the sum of 5×5 pixels centred around the seed pixel (right). To illustrate the power of the selection, the same 5×5 cluster is shown with random selection (circle) or on selected seed pixel with SNR greater than 3 (cross). The single photo-electron spectrum is clearly above the pixel noise.
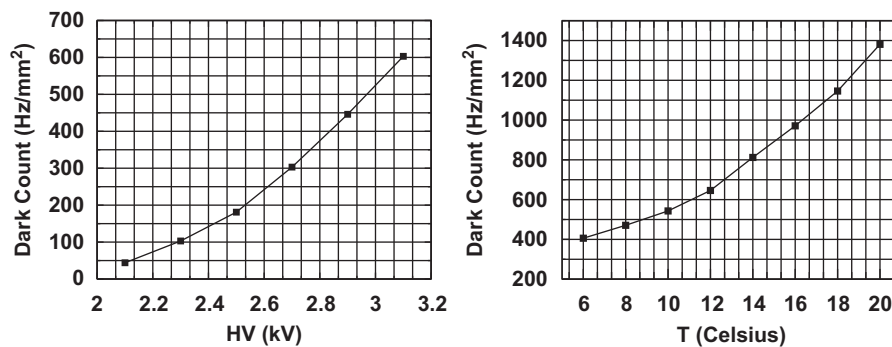
Fig. 8. Mean dark count rate measurement versus high voltage with $T=6\,°C$ (left) and versus temperature with HV=2.8 kV (right) for the multi-alkali S25 cathode.

The field effect is not dominant with an electric field of 3 kV/mm. This has to be compared with our previous result of Ref. [9] on an ebCMOS with an electric field of 6 kV/mm and a DC rate of 100 Hz/mm² at 10 °C. Results with the S25 cathode are summarized in Fig. 8. As expected the S25, which is red-extended, is more noisy (lower potential barrier) with a DC rate of around 400 Hz/mm² at 6 °C (HV=2.8 kV). A lower cooling temperature should decrease this DC rate. Nevertheless this DC rate is still lower than those of the most sensitive EMCCD (DU-897 Andor Technology) which suffers from Clock Induced Charge (called spurious noise).

The ion feed back is also a well-known source of HPD noise. These events are due to ionization of residual atoms or molecules that subsequently bombard the cathode. Their rate depends on the quality of the vacuum. Ion cathode bombardment produces a burst of electrons emitted by the cathode into a localized cluster charge of 10×10 pixels. This event is very different from single photo-electron event and can be removed by simple online processing. The rate of ion feed back background measured in dark conditions are 19 Hz/mm² for the S25 cathode and less than 1 Hz/mm² for the S20 cathode. This noise is suppressed by software using temporal filter and appropriate cluster charge cut.

3.3. Point Spread Function measurement of the ebCMOS: PSF-tube computation

The PSF of the tube, PSF-tube, originates from the radial initial energy (transverse to the accelerating electric field) of the photo-electron. This energy depends on many parameters such as the cathode type, the wavelength of the incident photon and the electric field at the cathode surface. A PSF model of a proximity-focusing tube has been developed in Ref. [24].

By introducing a Maxwellian distribution for the radial initial emission energy of the electron, the author obtains a Gaussian distribution for the PSF-tube characterized by the standard deviation σ_{tube}:

$$P(r) = P(0)e^{-r^2 V/(4d^2 V_r)}, \quad \sigma_{tube} = d\sqrt{\frac{2V_r}{V}} \tag{1}$$

where $P(0)$ is the peak value of the PSF, r is the radial distance from the maximum, V is the voltage across the gap, d is the cathode-CMOS gap length and V_r is the mean radial emission energy of the photo-electrons in eV.

The measurement of the PSF-tube has been obtained by focusing a light spot on the cathode. The number of photons per
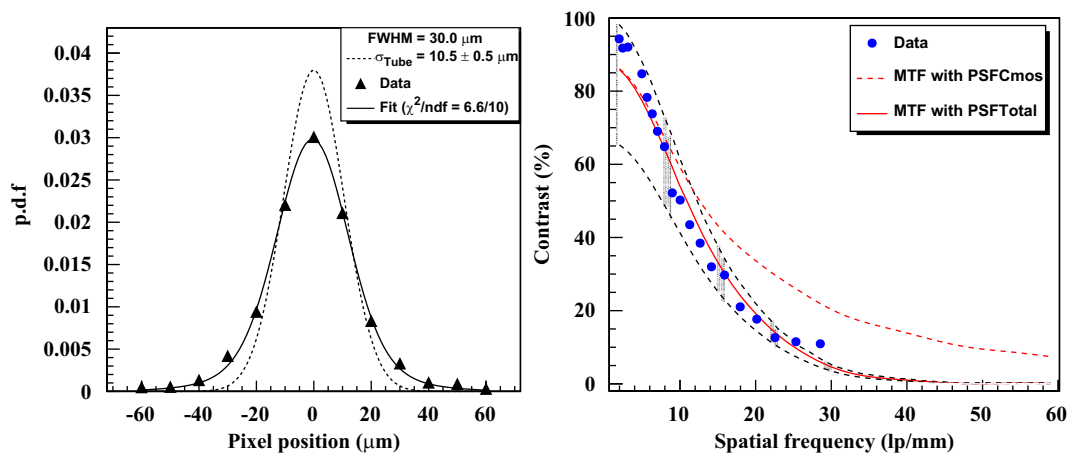
Fig. 9. Experimental overall PSF of the ebCMOS used for deconvolution by PSF-CMOS to compute the PSF-tube (left). Modulation transfer function computed with the experimental PSFs versus the spatial frequency (right). The full line corresponds to the MTF with the PSF-ebCMOS. The dashed line corresponds to the MTF of the CMOS only (PSF-CMOS). The hatched area corresponds to the range of MTF computed with a noise added to the input image in the range (0%–25%) of the maximum input intensity.

Table 2
Results on sigma tube (Gaussian) of the fit by deconvolution with PSF-CMOS versus λ_0, HV and T for the two multi-alkali cathode types S20 and S25. Typical error on σ_{tube} is $\pm$ 0.5 μm.

HV (kV)	σ_{tube} (μm)		T (°C)	σ_{tube} (μm)		λ_0 (nm)	σ_{tube} (μm)		V_r (eV)	
$\lambda_0 = 640$ nm	S20	S25	$\lambda_0 = 640$ nm	S20	S25	HV = 2.8 kV	S20	S25	S20	S25
2	11.1	11.3	10	10.2	9.1	380	14.5	9.0	0.26	0.10
2.2	10.7	10.6	12	10.4	9.2	395	17.8	9.9	0.39	0.09
2.4	10.5	9.9	14	10.6	9.5	White	14.2	8.2	0.25	0.11
2.6	10.5	9.7	16	10.6	9.6	518	13.2	9.2	0.22	0.08
2.8	10.5	9.3	18	10.7	9.7	590	12.6	8.5	0.20	0.12
3	10.0	9.4	20	10.7	9.6	640	11.0	10.0	0.15	0.10

frame has been tuned to be Poisson distributed in the region of interest (single-photon measurement regime). The spot can be considered as a point source. It corresponds to the diffraction limit of a microscope objective ($\times 10$ or $\times 50$) demagnifying the light output from a monomode fibre of 8 μm core connected to a LED. The spot has been positioned by micrometric displacement stages at the centre of a pixel. An integrated image with a symmetric distribution of the charge around the central pixel in both directions gives a cross-check of the central position of the spot. The experimental PSF, PSF-ebCMOS, is obtained by integrating 2000 images in the region of interest defined by 13×13 pixels centred on the spot position. The result is shown in Fig. 9 where the PSF has been normalized.

The PSF-ebCMOS convolutes both the PSF-CMOS and the PSF-tube. But the non-Gaussian behaviour of the PSF-CMOS prevents a simple quadratic computation of σ_{tube} using σ_{ebCMOS} and σ_{CMOS}. Therefore, we extract σ_{tube} from a fit to the measured PSF-ebCMOS distribution with a convolution between the PSF-CMOS and expression (1).

Fig. 9 displays such a fit where the excellent agreement of our model with the data can be observed. This deconvolution procedure has been applied on both S20 and S25 cathodes. It yields a precision of 0.5 μm on σ_{tube}, good enough to explore the variations with temperature, high voltage and wavelength of incident photons. The results are summarized in Table 2.

The S20 and S25 PSF-tubes seem to be independent of the high voltage between 2.2 and 3 kV. The σ_{tube} is 10.5 μm for S20 and 9.5 μm for S25. To interpret the high voltage dependency of PSF-tube (1 μm over 800 V variation) it is necessary to remember that the increase of high voltage reduces the transit time and therefore reduces PSF-tube. But it should also increase the radial

initial energy by the Schottky effect at the cathode surface (the potential barrier is reduced by the local electric field as $\sqrt{V}$) and therefore compensate for the previous effect. This experimental result on high voltage dependency shows that it is not necessary to increase too much the high voltage to improve the resolution since at the same time the cathode DC rate also increases. The temperature dependency of σ_{tube} is not significant between 10 and 20 °C. However, in the same temperature range, the reduction of the DC at low temperature is significant for the red-extended cathode S25.

Our observations (see Table 2) indicate that the PSF-tube is mostly impacted by the incoming photon wavelength. For the S20 cathode, σ_{tube} strongly decreases with the photon energy (the wavelength increases). This effect is less pronounced for the S25 cathode. This is probably due to the cathode optimization for the red part of the spectrum and therefore the increase of the semiconductor layer thickness.

The cathode-CMOS gap length has been measured optically. The measurements give (1000 ± 50) μm for S20 and (930 ± 50) μm for S25 cathodes.

These values were input to the PSF-tube model described above, and from which we derive the radial emission energy versus input wavelength. The values of V_r deduced from Eq. (1) are in agreement with measurements of Ref. [24]. Note the unexpected point measurement for S20 at 380 nm that gives a shorter PSF-tube than for 395 nm. This behaviour seems not to be a statistical fluctuation of the measurement since we already saw this behaviour for the EBMI5 prototype with a S20 cathode. Similar effects have been discussed in Ref. [25] but without a clear conclusion on its origin. More measurements with different wavelengths should be performed to give a conclusion on this effect.

Various MTFs can be derived from our PSFs measurements. The right part of Fig. 9 displays the MTFs computed for the CMOS sensor only (from PSF-CMOS) and for the ebCMOS camera (from PSF-ebCMOS). The large deviation observed confirms that the gap length between the cathode and the CMOS is the most important parameter for the image resolution. The charge diffusion inside the BSB-CMOS epitaxial layer plays only a second order role.

The LUSIPHER camera features a 25 lp/mm spatial resolution at 10% contrast. However, we shall underline that in a photon counting mode, more sophisticated algorithms based on the measured PSF can be used. This will be the subject of a future work.

Nevertheless the result obtained on MTF measurements reinforces the idea that the back-side passivation of the CMOS is the corner stone for good spatial resolution. It is the limiting parameter for the reduction of the gap length between the cathode and the CMOS.

4. Conclusion

This work aims to be the reference paper for the LUSIPHER ebCMOS device. This paper has established the nominal characteristics and the performances for our scientific-grade LUSIPHER camera which is intended to be used in Fluorescence Microscopy experiments.

The LUSIPHER prototype is the result of a partnership between IN2P3 (IPNL-IPHC) and Photonis SA. The chip (0.25 μm technology) has been designed by the *CMOS and ILC* team of IPHC and founded within an industrial partner. The device has been fully characterized at IPNL with an optical bench and an electron bombardment bench.

The DC rate has been studied carefully for both cathode types and measured for different high voltages and temperatures. Typical numbers of 15 Hz/mm^2 for S20 and 400 Hz/mm^2 for S25 are measured. This is well below the spurious charge rate (clock induced charge effect) of the most sensitive EMCCD camera systems.

Furthermore we have shown that the measurement methods developed in this paper give access to key parameters such as Charge Collection Efficiency, PSF of the BSB-CMOS with different P-doped epitaxial layer and PSF of the tube with its wavelength dependency. A typical PSF-tube of 10 μm has been measured. PSF-tube shows a good stability ($\Delta\sigma < 1$ μm) with temperature and high voltage in the test range. The largest variation is observed for the S20 cathode versus the photon wavelength with a variation > 3 μm (30%).

The MTF computation based on the PSF measurement has been compared with MTF measured with an USAF test chart. A 25 lp/mm is obtained at 10% of contrast. The most limiting parameter on spatial resolution is the gap length between the cathode and the CMOS.

It is natural to think that 1 mm is not the minimum gap width that can be achieved during integration inside the vacuum tube. Smaller gaps will be obtained with new CMOS integration processes which will certainly make a breakthrough in the next few years with 3D Integration Technology avoiding rear face wire bonding. We are convinced that 10 nm dead layer, 400 μm gap and 1000 V are achievable and will certainly push the performance of the ebCMOS in the near future.

Moreover a working point at 1 kV prevents from the ageing effects (observed on the EBCCDs that works at 10 kV) thanks to the X-ray production threshold for silicon (around 2.7 keV). The silicon X-rays are the main sources of ageing effects by producing

the ionization charges which accumulate towards silicon oxide and generate a noise increase. Ageing effects related to vacuum degradation has not been measured in this study. This parameter is strongly correlated to the vacuum quality obtained during the bake-out process.

During the project 10 prototypes have been produced by Photonis SA. With a special care in the transfer process (cathode production) and in the back-side wire bonding process an industrial production of a fully reliable product is realistic.

The final proof of concept of many single emitters tracking at single-photon sensitivity such as fluorescent beads were not in the scope of this paper. A paper dedicated to tracking methods and their effects on the localization accuracy of single emitters is in preparation. Today, more recent CMOS technologies, than the one employed here, would allow the design and production of a 4 MegaPixel ebCMOS sensor with 1 kHz frame rate and a PSF-tube well below 10 μm. Such a device would establish a top grade benchmark for the temporal and spatial tracking of a few thousand single emitters needed in many scientific and biotechnology low light applications.

References

[1] C.D. Mackay, et al., SPIE 4306 (2001) 289.
[2] R. Hartmann, et al., Nucl. Instr. and Meth. A 568 (2006) 118.
[3] L. Benussi, et al., Nucl. Instr. and Meth. A 442 (2000) 154.
[4] White paper intevac: EBAPS(TM) next generation, low power, digital night vision, in: OPTRO 2005 International Symposium, Paris, France, May 10, 2005.
[5] R. Desalvo, et al., Nucl. Instr. and Meth. A 315 (1992) 375;
C. D'Ambrosio, H. Leutz, Nucl. Instr. and Meth. A 501 (2003) 463.
[6] I.P. Czorba, Image tubes, in: J.L. Davis (ed.), The Howard W. Sams Engineering-Reference Book Series, 1985.
[7] X. Michalet, et al., Nucl. Instr. and Meth. A 567 (2006) 133.
[8] T. Ohnuki, et al., Proc. SPIE 6092 (2006) 1.
[9] W. Dulinski, Nucl. Instr. and Meth. A 546 (2005) 274;
R. Barbier, et al., Nucl. Instr. and Meth. A 610 (2009) 54.
[10] E. Betzig, et al., Science 313 (2006) 1642.
[11] S. Manley, et al., Nature Methods 5 (2) (2008) 155.
[12] M. Thompson, M. Lew, M. Badieirostami, W.E. Moerner, Nano Lett. 10 (2010) 211.
[13] X. Michalet, et al., J. Mod. Opt. 54 (3–4) (2007) 239.
[14] M.K. Ravel, A.L. Reinheimer, Backside-thinned CCDs for keV electron detection, Charge-coupled devices and solid state optical sensors II, in: Proceedings of the SPIE, vol. 1447, 1991, p. 709.
[15] D.C. Joy, et al., Scanning Microsc. 10 (3) (1996) 653.
[16] D. Drouin, et al., Scanning 29 (2007) 90.
[17] D.C. Joy, S. Luo, Scanning 11 (1989) 176.
[18] R. Turchetta, et al., Nucl. Instr. and Meth. A 458 (2001) 677;
M. Caccia, et al., Nucl. Phys. B (Proc. Suppl.) 125 (2003) 133;
G. Deptuch, Nucl. Instr. and Meth. A 543 (2005) 537;
G. Deptuch, Nucl. Instr. and Meth. A 570 (2007) 165.
[19] R. Cluzel, Etude de la passivation du silicium dans des conditions d'irradiation électronique de faible énergie, Ph.D. Thesis, Claude Bernard Lyon-I University, 2010.
[20] I. Djité, et al., Modeling and measurement of MTF and quantum efficiency in CCD and CMOS image sensors, in: E. Bodegom, V. Nguyen (Eds.), Sensors, Cameras, and Systems for Industrial/Scientific Applications XI, Proceedings of SPIE Electronic Imaging, vol. 7536, 2010, p. 75360H-1.
[21] Microchip, Ref. PIC 18F4550.
[22] ISEG (Iseg-hc.de) High Voltage Module, Ref. MHn 50 103 5 2.5.
[23] Altera's Nios II Development Kit, Stratix II Edition, Ref. DK-NIOS2-S60N.
[24] E. Eberhardt, Appl. Opt. 16 (8) (1977) 2127.
[25] R. Brooks, et al., Wavelength-dependent resolution and electron energy distribution measurements of image intensifiers, in: R.E. Longshore, A. Sood (Eds.), Infrared and Photo-electronic Imagers and Detector Devices II, Proceedings of the SPIE, vol. 6294, 2006, p. 62940W.

Single-photon sensitive fast ebCMOS camera system for multiple-target tracking of single fluorophores: application to nano-biophotonics.

Thomas Cajgfinger[a] Eric Chabanat[a] Agnes Dominjon[a] Quang T. Doan[a]
Cyrille Guerin[a] Julien Houles[a] Remi Barbier[a]

[a] IPNL, Université de Lyon, Université Lyon 1, CNRS/IN2P3,
4 rue E. Fermi - 69622 Villeurbanne cedex, France

ABSTRACT

Nano-biophotonics applications will benefit from new fluorescent microscopy methods based essentially on super-resolution techniques (beyond the diffraction limit) on large biological structures (membranes) with fast frame rate (1000 Hz). This trend tends to push the photon detectors to the single-photon counting regime and the camera acquisition system to real time dynamic multiple-target tracing. The LUSIPHER prototype presented in this paper aims to give a different approach than those of Electron Multiplied CCD (EMCCD) technology and try to answer to the stringent demands of the new nano-biophotonics imaging techniques. The electron bombarded CMOS (ebCMOS) device has the potential to respond to this challenge, thanks to the linear gain of the accelerating high voltage of the photo-cathode, to the possible ultra fast frame rate of CMOS sensors and to the single-photon sensitivity. We produced a camera system based on a 640 kPixels ebCMOS with its acquisition system. The proof of concept for single-photon based tracking for multiple single-emitters is the main result of this paper.

Keywords: ebCMOS, EMCCD, single-photon counting, multiple-target tracking, Cramer-Rao Bound, localisation accuracy, Kalman filter, Quantum Dots

1. INTRODUCTION

Nano-scale localisation and tracking of fluorescent beacons with a wide-field fluorescence microscope and super-resolution imaging techniques expand the spectrum of applications in biophotonics. The progress of these last years are relied on mainly three domains : the development of fluorescent emitters, the design of new optical imaging systems and the development of new fast and sensitive photon detectors. Fluorescent beacons tend to offer a better signal over noise ratio and a better stability for longer time lapse recording of physical or biological processes. Such fluorescent emitters are either single molecule or nano-particles which are nano-crystals like Quantum Dots (QDs) or photo-luminescent nano-diamonds (PNDs) with size ranging from a few nanometres to a few tenth of nanometres. Localisation of these beacons is obtained with different super-resolution techniques such as photo-activated localisation microscopy (PALM)[1] or stochastic optical reconstruction microscopy (STORM).[2,3] In these methods the main objective is to go beyond the diffraction limit by accumulating photon statistics from single emitters distributed according to point spread function (PSF) of the optical and camera systems. The single-emitter position is obtained by fitting the integrated intensity distribution recorded by the pixels of the photon detector.

The accuracy obtained with super-resolution methods can achieve a few nanometres in 2D. The 3D tracking uses more sophisticated optical techniques[4,5] but is not very different from the point of view of the photon detection. In any case improvements on stability and quantum yield of single-emitters will require faster photon-detectors.[6] Thus progress in photon detection will bring its contribution to the challenging dynamic multiple-target tracing with single-photon sensitivity, super-resolution, high-data throughput and high frame rate on a large population of moving nano-emitters.[7] Translating this trend in terms of photon detection performances gives to the camera system an interesting wish list and trade-off :

Corresponding author: R. Barbier, E-mail: r.barbier@ipnl.in2p3.fr.

- An increase of the frame rate to achieve the millisecond time scale will reduce the number of photons received from a single-beacon to a few per frame and increase dangerously the data throughput.

- A better quantification requires at this frame rate a single-photon sensitivity and a true counting ability with gain linearity.

- Tracking multiple-targets with Brownian motion and a coefficient diffusion D of the order of 20 μm^2/s requires an update of the position every few milliseconds.[8,9] Therefore this forbids long integration time followed by off-line fitting procedure of the intensity profile.

- Real time multiple-target tracking on a large field of view of nanometres emitters requires fast tracking and deconvolution algorithms based on photon counting.

One possible answer to this challenge is to develop a new generation of photo-detectors that implements the concept of large-scale ultra-fast single-photon tracking. There are few existing devices[10,11] that use a different detection principle than the Electron Multiplying CCD technology.[12] Indeed, it is difficult for a photon detector to fulfill all requirements of the wish list given above. Electron Multiplying CCD is a mature technology that offers a good sensitivity, thanks to the register gain, but has some draw backs (low frame rate, clock induced charge noise, EM noise) that have not yet been studied properly for these super-resolution imaging techniques. On the contrary, cathode devices are potentially more rapid and sensitive to one photon but with the drawback of weak quantum efficiency. A discussion on the pros and the cons of EMCCD and photon counting imaging detector can be found in Ref.[13] Nevertheless ebCMOS device has never been study yet in the scope of super-resolution techniques.

This paper is organized as follows. We present first in section 2 the principle of detection of an ebCMOS and the performances of the LUSIPHER prototype. The results of the characterization concern : single-photon sensitivity, dark count rate and spatial resolution. The full camera system composed of dedicated board with Gigabit Ethernet link is also described since it is an important part of the system to attend the continuous readout and avoid memory buffering and post readout that limit the continuous tracing to a few seconds. In section 3 we discuss the localisation accuracy on a single-emitter in terms of Cramer-Rao bound (CRB) and MonteCarlo simulation for three different photon detection devices: the scientific CMOS (sCMOS),[14] the Electron Multiplying CCD and the electron bombarded CMOS (ebCMOS).[11,15] The CRBs are computed by taking into account the different amplification and noise processes of each device. The localisation accuracy is also derived with typical super-resolution imaging conditions from Monte-Carlo simulations. The contribution of the quantum efficiency of the ebCMOS to the resolution is studied. Then measurements obtained with different optical set ups are described in section 4. A new method for spatio-temporal reconstruction of the centre of the spot is presented in section 4.1. This method is based on single photo-electrons (Phe) measurement of the ebCMOS. The efficiency of this method is proved in section 4.2 with different measurements under controlled photon background and signal (less than one photon per frame). In the same idea, the multiple-target tracking ability of the ebCMOS is shown by photon counting imaging of a light pattern produced by a microlens array with 150 microns pitch (Shack Hartmann). In section 5, dynamical target tracking is addressed. Monte-Carlo simulations of two different 2D motions of a single-emitter are presented as examples. Then as a proof of concept the target identification and tracking method is applied on single-quantum dots raw images taken by LUSIPHER prototype with a wide field microscope designed for fluorescent nano-particles imaging. The temporal imaging is obtained by photon-number quantification at millisecond time scale. Blinking of QDots is observed and quantified. These results show that a high data-throughput identification and tracking of several hundreds of single emitters is achievable by our LUSIPHER camera system.

2. EBCMOS CAMERA SYSTEM : PRINCIPLE AND PERFORMANCES

2.1 ebCMOS principle

An ebCMOS is an Hybrid Photon Detector combining a photo-cathode and a Back Side Bombarded (BSB) CMOS, both placed in a vacuum tube. A schematic of the detection principle is shown in Fig. 1. Amplification process is performed by an accelerating electric field applied between the cathode and the detector. The gain is given by the number of secondary electrons collected by the diodes of the CMOS after diffusion inside the epitaxial layer. It is given roughly by $CCE \times \frac{E_0 - E_{\text{dead}}}{3.6}$ where CCE is the charge collection efficiency of the epitaxial layer, E_0, the initial energy of the Phe and E_{dead}, the energy lost in the entrance dead layer (passivation). This detector concept uses the diffusion process of the secondary charges and then the charge sharing between pixels to give access by centre of gravity computation to an intra-pixel precision on the impact position of the Phe. Typical cathode-CMOS gap dimension and maximum gain (High Voltage) are fixed by the necessary limitation of electron cathode emission. Thus to maintain a low dark count rate ($10^{-5} e^-$/pixel/ms) and a good spatial resolution it is necessary to work with E_0 lower than 3 keV and a cathode-CMOS gap width lower than 1 mm. Photo-electrons detection is performed by the epitaxial layer of the CMOS which gives a 100% fill factor.
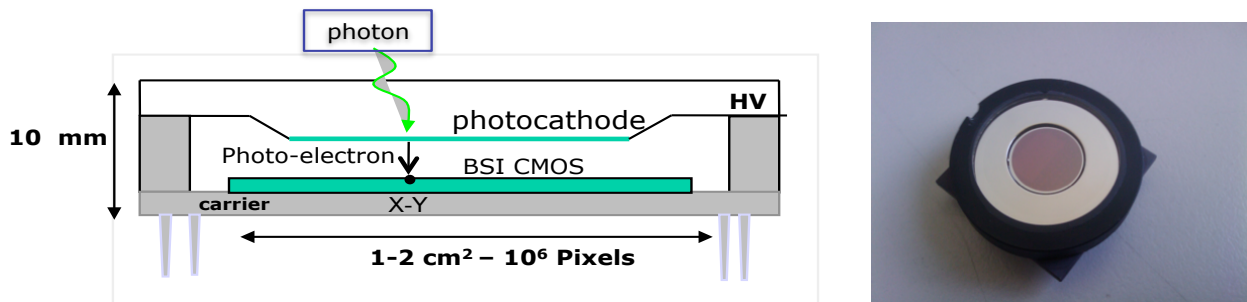
Figure 1. Schematic principle of an ebCMOS (left). The high voltage is provided to the cathode by a pin out of the carrier. Picture of the ebCMOS prototype LUSIPHER (right).

Nevertheless to be sensitive to single Phe, a back side bombardment of the sensor is required because of the electronic layers that prevent any low energy particle detection from the front side. Furthermore, the thickness of the entrance layer of the CMOS i.e. the passivated layer must be lower than 100 nm to minimize the number of recombined electrons, E_{dead}. The P-doped epitaxial layer has to be also thin since it is a drift volume for the secondary electrons created at the top of the epitaxial layer and collected by the N-well diodes at the bottom of this one. The epitaxial layer of LUSIPHER has a thickness of about 10 μm. Gain curves and the diffusion process measurement of LUSIPHER can be found in Refs.[15, 16] A picture of the vacuum tube closed by the cathode window is shown in Fig. 1 (right). The useful cathode diameter (UCD) of 12 mm encloses two face to face BSB CMOS chips. Two types of multi-alkali cathodes, S20 or S25, have been deposited by Photonis SA for the production of 10 prototypes. The typical maximum quantum efficiency for S20 (S25) is 23% at 480 nm (15% at 605 nm).

2.2 ebCMOS camera system

The ebCMOS has been integrated into a camera designed by IPNL instrumentation group (see picture of Fig.2). One BSB CMOS chip is composed of two matrices of 400x400 pixels with a 10 μm pitch that gives a 32 mm^2 sensitive area. Two BSB CMOS chips are enclosed in one LUSIPHER ebCMOS which potentially offers 800x800 pixels detection area with a separation line of 100 μm width. The Data Acquisition System has been fully developed by IPNL electronic group. A slow control board has been designed to produce, drive and control the voltage reference of the chip, the applied high voltage of the ebCMOS and the power supply of the Pelltier cooling of the cathode. The two 160 kPixels matrices of one chip are read out in parallel with 8 outputs which corresponds to 4 consecutive pixels per matrix with the idea to treat a 4x4 block at the same time in the clustering process performed by FPGA of the DAQ board. Designers implemented two readout modes: either Rolling Shutter (500 fps - 2 ms integration time) or Test Mode (500 fps - 1 ms integration time - 50% duty cycle).
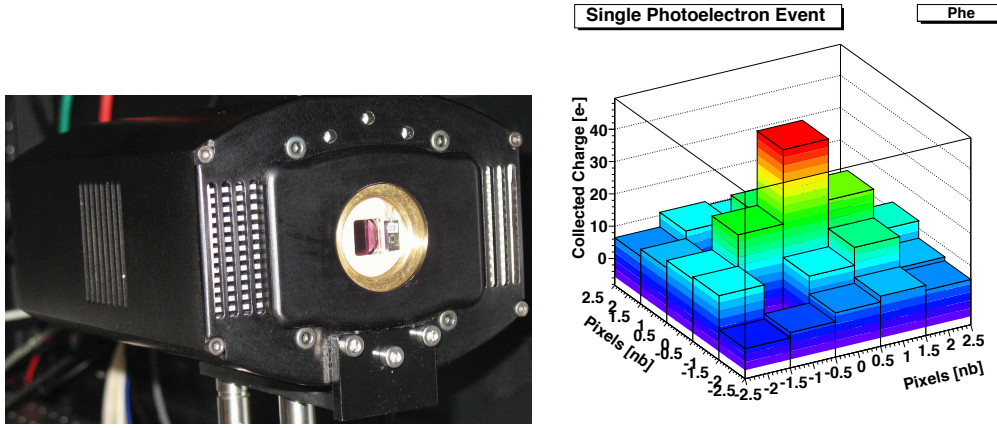
Figure 2. Picture of the ebCMOS camera system (left). Visualisation of a single Phe event on the Back Side Bombarded CMOS (right). The pixel response is calibrated in e- unit and the mean pixel noise is 8 e- RMS.

In any case the maximum frame rate obtained with a 40 MHz readout pixel clock is 500 fps due to the necessary Correlated Double Sampling (CDS) even if the chip is readout at 1 kHz frame rate. Four analogue outputs of 4 consecutive pixels of the same matrix are sampled by four on board ADCs (12 bits). The data throughput from one chip in front of the FPGA is 1.92 Gb/s. All data are continuously read out after CDS computation and sent (8 bits) to the acquisition workstation through 1 Gb/s Ethernet link with UDP protocol.

2.3 Performances

The main characteristics and performances of the LUSIPHER ebCMOS are summarized in Table 1.

Single Photon Sensitivity: a single Phe event is reconstructed from the deposited charge into a cluster of pixels (5x5 typically). The cluster selection presented in Sec. 4.1 has a sensitivity to the CMOS pixel noise of the order of 10^{-6}/pixel/frame. This means that single-photon sensitivity of ebCMOS is free of CMOS noise. A typical single Phe event obtained for HV=2.8 kV is shown in Figure 2.

Dark Count: the dominant noise of the ebCMOS device is the dark count (DC) spontaneously generated by the photo-cathode due to thermionic or field effects. The S20 cathode shows a very low DC rate of 15 Hz/mm^2 on a temperature range from 6°C and 20°C and a high voltage < 3 kV. The S25 cathode is more noisy as expected since it is more sensitive in the red part of the visible spectrum. The DC rate measured is of the order of 400 Hz/mm^2. This DC rate is still lower than those of the most sensitive EMCCDs which suffer from Clock Induced Charge (called spurious noise). The second source of cathode noise is the Ion Feed Back. This event is very different from single-Phe events and can be removed by simple on-line processing. The rate of ion feed back background measured in dark conditions is 19 Hz/mm^2 for the S25 cathode and much below than 1 Hz/mm^2 for the S20 cathode.

Point Spread Function of the ebCMOS: the PSF of the ebCMOS is a convolution of two PSFs: the first one, called PSF$_{tube}$ is governed by the amplification stage (proximity focusing electric field) and the second one, called PSF$_{cmos}$, is due to the charge sharing in the epitaxial layer. The PSF$_{tube}$ is the result of non zero radial initial energy of the Phe emitted by the photo-cathode. This energy depends mainly on the electric field and on the wavelength of the converted photon. The PSF$_{tube}$ cannot be measured directly. It is deduced from the deconvolution of the total PSF of the ebCMOS by the PSF$_{cmos}$.[15, 16]

Table 1. Summary of the characteristics and performances of the ebMOS LUSIPHER camera system.

BSB CMOS	Frame Rate	PSF CMOS	PSF Tube	Dark Count	Sensitivity	Acquisition Software
2x(400x800) pixels	-125 fps	σ_{cmos}^{G}	σ_{tube}	cathode S20:	QE (530 nm)	FPGA
10μm pitch	-250 fps	2.7μm	10.5μm	15 Hz/mm^2	25 % max	Eth 1 Gb/s
Epitaxial layer	-500 fps			cathode S25:		
$< 10\mu$m	Readout	Gauss $\oplus$	Gaussian	400 Hz/mm^2	threshold	CPU
Passivation	Rolling-	Lambert	UCD	cathode gap	2,5 kV	multithreading
< 80 nm	Shutter	FWHM 30μm	12 mm	1 mm	gain 300 e-	on-line filtering

3. COMPUTATION OF LOCALIZATION ACCURACY : STATIC CASE

Localisation accuracy of a single-emitter position is driven in a first approximation by the square root of the number of detected photons during an integration time corresponding to a given number of frame taken by a photon detection device. But in a low photon flux regime it is necessary to take into account the parameters of the detection system such as the noise of the detector and its amplification process. In some sense it is more correct to consider the detective quantum efficiency (detection efficiency after the amplification process) than the quantum efficiency (the ratio between the number of photo-converted electrons and the incoming photons) as the dominant parameter of the localisation accuracy. We did not found in the literature the computation of the Cramer-Rao bound for EMCCD and ebCMOS devices and their comparison versus the background and signal conditions of the super-resolution techniques. On the contrary the CRB has been derived for CCD cameras for astrophysics imaging[17] first and for fluorescence imaging and super-resolution[18] later. In this section localisation accuracy are compared for three photon detectors using two different approaches. The first one is the CRB through the Fisher information Matrix. The second approach is a Monte-Carlo simulation of the full set-up and detectors such as different point spread functions, detector noises and amplification processes as in Ref.[18]

3.1 Cramer-Rao Bound and Monte-Carlo simulation of the localisation accuracy for ebCMOS, EMCCD and sCMOS

The Fisher information matrix measures the amount of information that an observable random variable X carries about an unknown parameter θ using the likelihood function of θ, $L(\theta) = f(X;\theta)$. The Fisher information is defined by:

$$I(\theta) = E\left(\left[\frac{\partial}{\partial\theta}lnf(X;\theta)\right]^2|\theta\right) \tag{1}$$

which implies $0 \leq I(\theta) < \infty$. The CRB states that the variance of any unbiased estimator is at least as high as the inverse of the Fisher information.[19] The Fisher information matrix of a 2D position measurement by a pixel array with readout noise is of the form:[18]

$$I(\theta) = \gamma E[N(t)]\begin{pmatrix} \int_{\Re^2} \frac{1}{q(x,y)}\left(\frac{\partial q(x,y)}{\partial x}\right)^2 dxdy & \int_{\Re^2} \frac{1}{q(x,y)}\frac{\partial q(x,y)}{\partial x}\frac{\partial q(x,y)}{\partial y}dxdy \\ \int_{\Re^2} \frac{1}{q(x,y)}\frac{\partial q(x,y)}{\partial x}\frac{\partial q(x,y)}{\partial y}dxdy & \int_{\Re^2} \left(\frac{1}{q(x,y)}\frac{\partial q(x,y)}{\partial y}\right)^2 dxdy \end{pmatrix} \tag{2}$$

where $q(x,y)$ is the likelihood function, $N(t)$ is a Poisson random process with mean At, $E[N(t)] = At$. Then γAt is the total number of photons arriving on the detector during integration time t by taking into account the optical efficiency γ. The first step to obtain CRB is to derive the likelihood function for each device. We consider in this paper that the sCMOS has no photo-charge sharing between pixels (this would not be the case if we consider Back Side Illuminated CMOS). Then the likelihood function of the sCMOS is the same than for CCD but with a lower readout noise (typical 1.4 e-). The computation of the likelihood takes into account pixel pitch with K pixels noted $C_1...C_K$. Each pixel receives a Poisson distributed photon background with mean b_kt and has a readout gaussian noise with mean η_k and variance σ_k^2. Then the total number of photons collected by each pixel k is defined by $\nu_\theta(k) = \mu_\theta(k) + b_kt$ where $\mu_\theta(k) = \gamma At \int_{C_k} f_\theta$. In this last equation f_θ represents the total PSF coming from the optical apparatus but also from the detection process. EMCCD and sCMOS devices

have no spatial spread process since the photon sampling is performed by pixel without cross talk. Then the total PSF is optical. In case of ebCMOS device the total PSF is a convolution of the optical PSF with the PSF of the detector (See Ref[15] for more details on the different PSF measurements). The functions $f^{\text{sCMOS,EMCCD}}$ and f^{ebCMOS} are then defined by:

$$f_\theta^{\text{sCMOS,EMCCD}} = \frac{J_1^2(\alpha\sqrt{x^2+y^2})}{\pi(x^2+y^2)} \quad \text{with} \quad \alpha = \frac{2\pi\text{NA}}{\lambda} \qquad f_\theta^{\text{ebCMOS}} = \frac{1}{2\pi\sigma_g^2}e^{-\frac{x^2+y^2}{2\sigma_g^2}} \qquad (3)$$

where NA is the numerical aperture, λ is the wavelength, J_1 is the Bessel function of the first kind and σ_g is the standard deviation of the overall resolution of the ebCMOS.

Likelihood functions for sCMOS and ebCMOS detectors are simple since there is no gain process after the charge collection by the pixels and is given by:[18]

$$q_{\theta,k}(z) = \frac{1}{\sqrt{2\pi}\sigma_k}\sum_{l=0}^{\infty}\frac{[\nu_\theta(k)]^l e^{-\nu_\theta(k)}}{l!}e^{-\frac{1}{2}\left(\frac{z-l-\eta_k}{\sigma_k}\right)^2}, z \in \Re \qquad (4)$$

On the contrary the Electron Multiplied (EM) process of an EMCCD occurs in the gain register after charge collection by the pixel array. Taking into account the gain process the likelihood function of the EMCCD detector becomes:

$$q_{\theta,k}(z) = \frac{1}{\sqrt{2\pi}\sigma_k}\sum_{l=0}^{\infty}\sum_{i=0}^{\infty}\frac{i^l}{l!}e^{-i}e^{-\frac{1}{2}\left(\frac{z-l-\eta_k}{\sigma_k}\right)^2}P(n,\nu_\theta(k),g), z \in \Re \qquad (5)$$

In equation (5) the gain process, $P(n,m,g)$, gives the probability to obtain n output electrons from m input electrons with an EM gain $g = (1+\epsilon)^N$ (N is the number of shift registers and ϵ the impact ionisation probability per shift). One can find in Ref.[20] the expression of the EM gain:

$$P(n,m,g) = \frac{(n-m+1)^{m-1}}{(m-1)!(g-1+\frac{1}{m})^m}\exp\left(-\frac{n-m+1}{g-1+\frac{1}{m}}\right), n \geq m \qquad (6)$$

In order to perform numerical simulation we used the typical values for the experimental parameters reported in Tab. 2 and 3.

Table 2. Common optical parameters used for CRB computation and Monte-Carlo simulation.

σ_{opt}	Scattering Noise	Optical Efficiency	λ(nm)	NA	Magnification
$8\mu m$	660 photons/pixel/s	0.033	520	1.4	100×

The chosen parameters table of table 2 are those of Ref.[18] This has the advantage to allow a cross-check on the CRB computation for CCD detector that we implemented for this purpose. The results are in agreement within 1%.

Table 3. Specific parameters for Monte-Carlo simulation and CRB computations of the three devices.

Parameters	sCMOS	ebCMOS	EMCCD
Pixel Array Size	11x11	11x11	7x7
Pixel Dimensions (μm)	6.5	10	16
Readout Noise (e-/pixel)	1.4	10	30
Acquisition time (ms)	10	2	30
Quantum efficiency	0.57	0.15	0.80
Gain	-	300	300

Figure 3 shows the percentage of variation of the localisation accuracy versus the position of the emitting target relative to the center of the pixel for the three detectors. An interesting result is that pixel sampling of

the EMCCD and sCMOS detectors introduces a target position dependency of the localisation accuracy. This result has been also observed in Ref[18] and is well-know in High Energy Physics pixel detector. First we can see that the accuracy variation is less pronounced for EMCCD (7% max) than for sCMOS (30% max). Second, the ebCMOS detector shows an interesting stable resolution accuracy versus the target position compared with the centre of the pixel, thanks to the detector PSF.
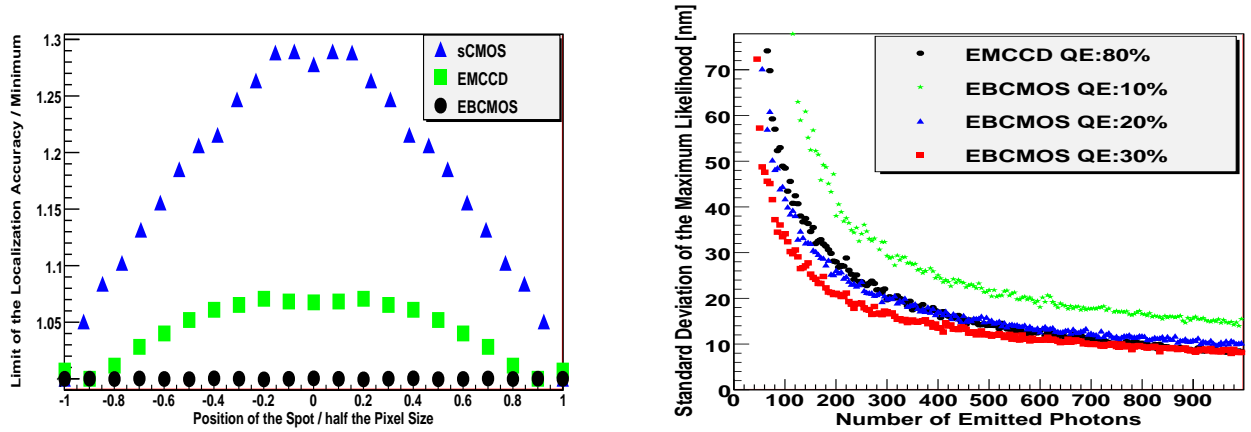
Figure 3. Computed percentage of variation of CRB versus the position of the emitting target relative to the center of the pixel for the three detectors : EMCCD, sCMOS and ebCMOS detectors (left). Monte Carlo Simulation of localisation accuracy for ebCMOS, EMCCD and sCMOS for different signal (right).

A Monte-Carlo simulation has been implemented to compare these three detectors adding specific detector noises such as cathode dark current and ion feedback for the ebCMOS detector, clock induced charge and stochastic multiplication process (responsible to the excess noise factor) for the EMCCD. The localisation accuracy in this simulation is obtained by computing the variance of the position given by a likelihood fit for 300 simulated events. Figure 3 shows the localisation accuracy for different mean numbers of emitted photons for the EMCCD and ebCMOS detectors. Different ebCMOS quantum efficiencies have been simulated to show its effect on the resolution. A major result of this simulation is that for a low photon signal emitted by the target (<300 photons/frame), the ebCMOS detector has a better precision than EMCCD if its quantum efficiency is greater than 20%. A systematic study of EMCCD and ebCMOS is out of the scope of this contribution and will be published soon.

4. MEASUREMENT OF SINGLE EMITTER LOCALIZATION ACCURACY OF LUSIPHER PROTOTYPE

4.1 Method based on the single-photon imaging ability of ebCMOS

A clustering method has been implemented to select the pixels corresponding to a Phe interaction into the silicon (see Fig 2 for a typical Phe event). The main idea is to obtain a selection criteria which is insensitive to the readout noise of the CMOS sensor. A cluster of pixels is therefore considered instead of only one pixel with the highest value, thanks to the diffusion process into the epitaxial layer. The charge distribution of the selected array of pixels is used to compute the centre of gravity of the Phe impact which is considered as the Phe impact position. An intra-pixel localisation accuracy is obtained that is five times smaller than the pixel pitch (10 μm).

The three main selection criteria for the cluster selection are listed below:

- **A seed pixel:** a pixel with signal to noise ratio (snr) greater than 3. To avoid overlapping the seed pixel has to be the highest among the 24 pixels around (5×5 pixel array).

- **A number of secondary pixels:** the number of pixels in the cluster that are greater than a cut. To take into account the different possibilities of charge sharing due to the impact localisation relative to the centre of the seed pixel, the cut depends on the snr value of the seed.

- **A cluster charge:** the sum of the charge of the pixels of the cluster. A number of Phes is associated to the cluster with calibration abacus based on the gain linearity. For example the counting experiment of Sec. 5.3 has more than 94% single-photon tagged clusters .

Phe reconstruction with intra-pixel resolution is the building block of the target identification algorithm. A target should been seen as a spatio-temporal volume with a high density of Phes. Therefore the Phe list of one frame is compared to the lists of consecutive frames. In more details an algorithm analyses the list of Phe and maps Phes to existing targets. The more difficult task in tracking is the identification process, the genesis of a target. In our case, creation of a new target is linked to a high spatio-temporal density of Phes in a region of interest of the order of the overall PSF in space dimension and 10 frames in temporal dimension. Moreover the generated targets are validated or deleted after a period of 10 frames and then becomes true targets. Figure 4 describes an example of identification in noisy conditions (high photon background) by showing the three steps of the same frame (4 ms).
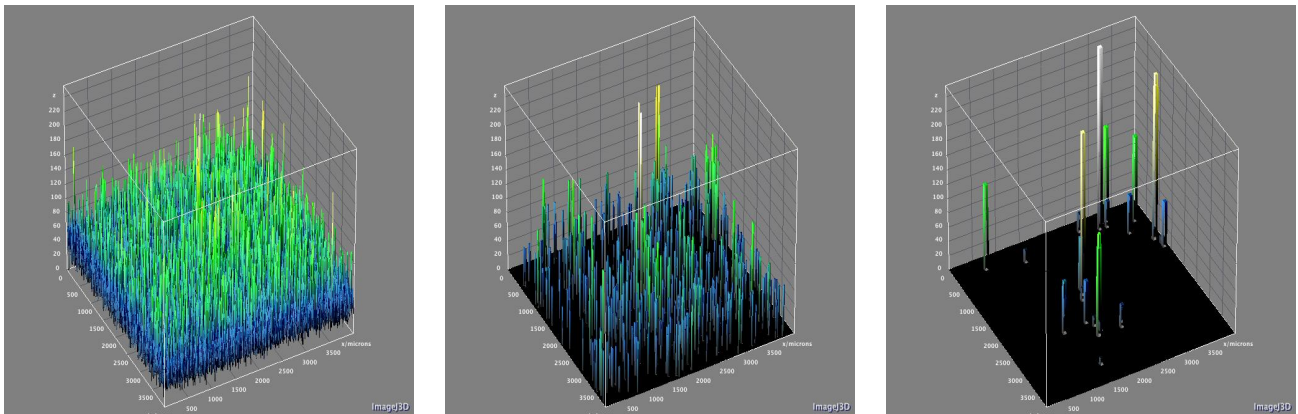
Figure 4. Picture of the same event during QDot tracking: raw image (left), image of Phes (centre), image of identified targets (right)

4.2 Results

4.2.1 Single spot measurement

An optical fibre (8 μm core) connected to a triggered LED (640 nm) through neutral density filters is demagnified by a microscope objective* on the sensor cathode plane. This creates a spot with a diameter lower than 1 μm and a tunable number of photons per frame (2 ms). To create different photon background conditions an integrating sphere illuminates continuously the detector plane. Three light intensities were chosen and gave 480, 1088 and 3350 Phes per frame. Translating these numbers in pixel occupancy rate give 3%, 6.8% and 20% respectively (remind that for one Phe at least 9 pixels are concerned). This has to be compared with an average number of signal photon of 1.56 per frame for the spot (<15.6% occupancy rate).

First, this set up gives a measurement of the localisation accuracy of the ebCMOS device in the photon counting regime. Second, it shows the efficiency of the algorithm to identify the spot versus the purity of the signal (fake rate). Of course the selection criteria could be tuned to be more efficient if less purity (higher error rate) is accepted. This depends obviously on the background conditions. Figure 5 shows the distribution in the noise free case of the difference between the calculated position after 50 frames (100 ms integration time) tracking duration and the position obtains with the whole statistics (20000 frames - 40 s). The variance of the

---

*MITUTOYO M Plan APO 50X, WD=13mm, f=4mm, NA=0.55

distribution is used to estimate the localisation accuracy. A standard deviation of 1.2 microns (0.12 pixels) on the sensor (image) plane is measured. Extrapolating this result to 100X magnification gives 12 nm resolution on the single-emitter after 100 ms integration time with single-photon counting per frame.

The loss of resolution due to photon background is shown on Figure 5. The photon background has a minor effect on the localisation accuracy but, as expected, it has an important effect on the target identification efficiency and fake rate as shown in the left part of Fig. 6. Without photon background only five frames (10 ms) are necessary to isolate the spot (1.56 Phe /2 ms) instead of three to four times more for noisy conditions. This has to be taken into account for future experiments in biological conditions and in the choice of the intensity of the laser excitation of the fluorophores.
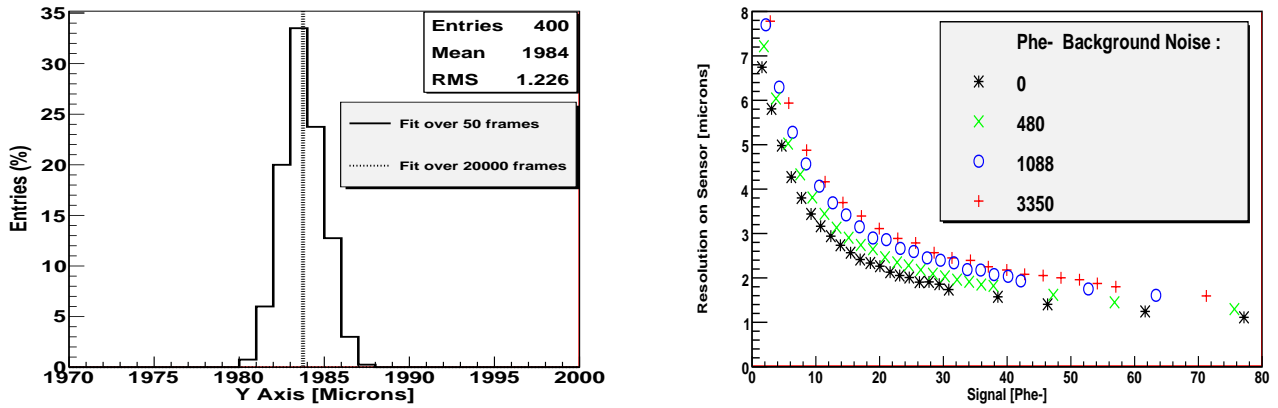
Figure 5. Distribution of the difference between the calculated position after 50 frames (100 ms integration time) tracking duration and the position obtained with the whole statistics (20000 frames - 40 s) (left). On **sensor** resolution versus the mean number of detected photons for different background noise settings (right).
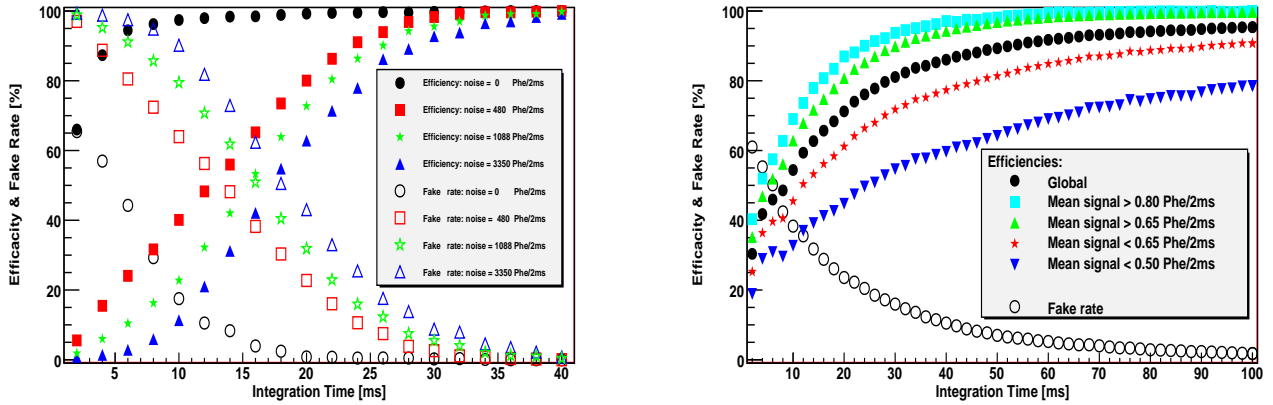
Figure 6. Spot tracking efficiency and fake rate in % versus the number of frames translated into integration time: 2 ms/frame (left). Microlenses spots tracking efficiency and fake rate versus the number of frames translated into integration time: 2 ms/frame (right).

4.2.2 Multiple-spot measurement

To increase the number of spots with controlled experimental conditions we designed an optical set up based on a microlenses array usually used for adaptive optics (Shack Hartmann)[†]. The microlenses are illuminated by a collimated optical fibre to create a square array of several hundreds of spots separated by a $(150\pm0.25)\mu$m pitch. Figure 7 shows the integrated Phe image (50 frames, 100 ms) obtained with the tracking algorithm. The algorithm find a total of 684 spots in total after 100 ms (50 frames) with a mean Phe per spot per frame (2 ms) equal to 0.6 (see Fig. 7). The tail of the distribution is due to a non uniform intensity of the illumination of the microlenses by the collimated fibre. The efficiency and the error rate versus the integration time (number of frames x 2 ms) is shown in Fig. 6. This plot describes the dependency of the efficiency and error rate to the signal photon rate. One can observe that the spot with the lowest mean Phe are those with the lowest efficiency as can be expected. When Phe rate tends to 1 (> 0.8 Phe/2ms in Fig. 6) the integration time necessary to identify all the spots is of the order of 30 ms. Figure 8 presents the distribution of the difference between fitted positions of
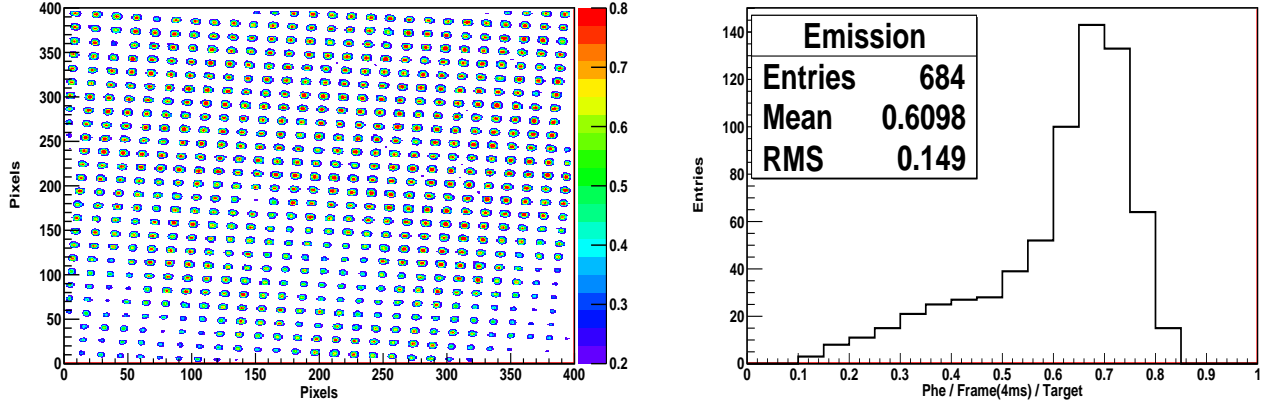
Figure 7. Integrated Phe image after target identification (50 frames, 100 ms) obtained with the microlenses. 684 spots are identified (left). The illumination intensity from collimated fibre is not homogeneous. The distribution of the mean number of detected Phe/frame(2ms)/spot is plotted (right). The typical number of Phe signal per spot and per frame (2 ms) is 0.6.

the 684 spots using the whole statistics (3450 frames) and the position reconstructed after 100 ms of tracking. To increase the statistical significance the procedure has been repeated on the whole statistics every 50 frames (69 trials). The RMS of the distribution on the difference is equal to 3.88 μm. Using the pitch precision of the microlenses $(150\pm0.25)\mu$m one can compute the reconstructed pitch from the spot positions of two consecutive pixels in both directions X and Y. Figure 8 (right) shows the results obtained for the 684 spots after 50 frames of tracking. The mean value of the measured pitch is 151.2 μm. One can see that the RMS of the measured microlens pitch is compatible with the RMS of distribution of the position measurement (5.95 μm to be compared with $\sqrt{2}$x $3.88 = 5.48\mu$m).

5. MULTIPLE-TARGET SINGLE-PHOTON BASED TRACKING OF QUANTUM DOTS WITH A WIDE FIELD MICROSCOPE

5.1 Single-photon-based tracking method

LUSIPHER prototype is dedicated to the tracking of single emitters over a large field of view. Section 3 describes a method to identify and to localise static fluorescent beacons. Imaging in nano-biophotonics requires tracking of moving fluorescent emitters. The method presented in this section is based on the same identification process than in the static case but to take into account motion a Kalman tracking algorithm[21] is added. The

---

[†]SUSS MicroOptics, numb. 11-1190-106-000 pitch 150 μm, pitch accuracy $\pm0.25\mu$m, radius of curvature ROC=5.212 mm, NA=0.005, dimensions=15mm x 15mm x 0.9mm
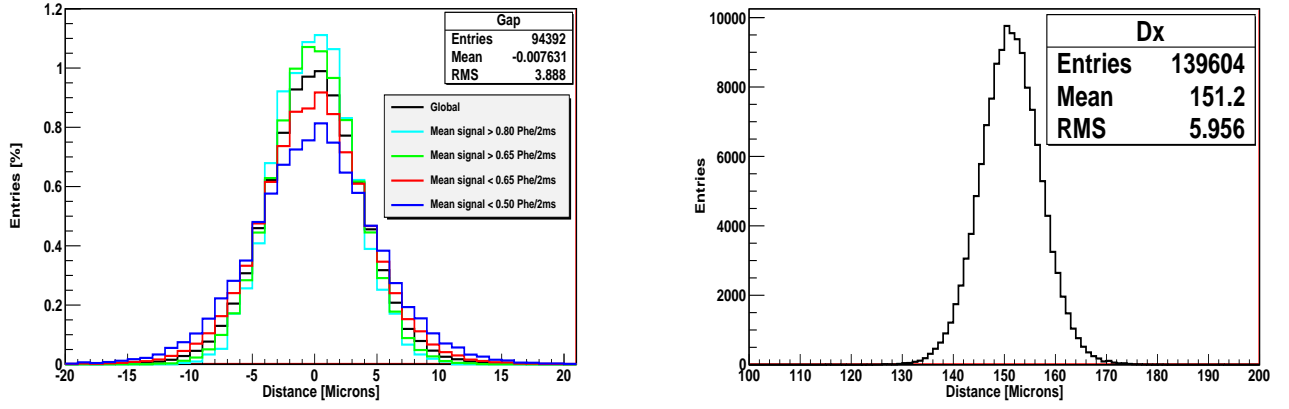
Figure 8. Distribution of the difference between fitted positions of the spots using the whole statistics (3450 frames) and the position reconstructed after 50 frames (100 ms) of tracking for the 684 identified spots (left). Distribution of the reconstructed pitch from the difference between the spot positions of two consecutive pixels in both directions X and Y and after 50 frames (100 ms) of tracking (right).

Kalman filter is well-known in many computer vision applications and has already been used and optimized in biological video-microscopy.[22] Nevertheless we introduce for the first time a new concept of Kalman tracking of single emitters based on the intra-pixel localisation of each detected photon, thanks to the single-photon sensitivity and the gain linearity of the ebCMOS that provide a true photon counting. The Kalman filter method implements a deconvolution on the fly of the overall PSF ($PSF_{Optics} \otimes PSF_{ebCMOS}$) and could give access to Real-Time super-resolution imaging. Computational complexity and noise robustness are the two factors that are carefully optimized in the choice of the algorithm since our main objective is to implement an on-line and Real-Time multiple-target tracking of single emitters in parallel. This concept is strongly dependent from the ebCMOS clustering ability of the camera system for data handling reduction (CMOS noise) and Phe identification and localisation at the millisecond time scale. In this section, Monte-Carlo simulations of reconstructed trajectories for different motions are given as example. Preliminary results obtained with a wide field microscope on QDots are given as a proof of concept.

The global steps of this method are summarized as follow:

- Step 1: Phe reconstruction and creation of a list of their position (intra-pixel precision).

- Step 2: Phe association to existing targets. More than one Phe can be associated to one target delimited by a max radius of 5 pixels : Phe_{target} list. Non tagged Phes create new targets.

- Step 3: Propagation and update of the target status (new, validated, in pause or eliminated) on the basis of the Phes density compared to Phe background around.

- Step 4: Propagation and update of the target position, state position-vector $(X,Y)_{target}$, with a Kalman algorithm using the successive measurement vector, $(X,Y)_{Phe}$ from the Phe list Phe_{target}.

- Step 5: Propagation and update of the velocity-vector $(VX,VY)_{target}$, with a Kalman algorithm using the measurement vector, $(\Delta X, \Delta Y)_{target}$. The expected future position, $(X,Y)_{target}$, and velocity, $(VX,VY)_{target}$, are computed for the next frame.

5.2 Trajectory Monte-Carlo simulations

A Monte-Carlo simulation is an important tool for tracking algorithm development since the true trajectory is known. Two motions of a point-like object with typical readout and dark count noises have been simulated

with the Monte-Carlo presented in Sec.3.1. The magnification of the microscope has been set to $100\times$ and a mean of 5 signal Phes per frame is obtained on the sensor. The velocity of the uniform linear motion is set to 34 nm/2 ms (3.4 μm/2 ms) in the object plane (in image plane). The velocity of 2D random motion is set to 100 nm/2 ms (10 μm/2 ms) in the object plane (in image plane) with a random direction updated every 10 frames. Figure 9 shows the reconstructed trajectory and the true position (dimension Y) for the two simulated motions. The differences between the two positions (true-reconstructed) are also reported. The results presented in this
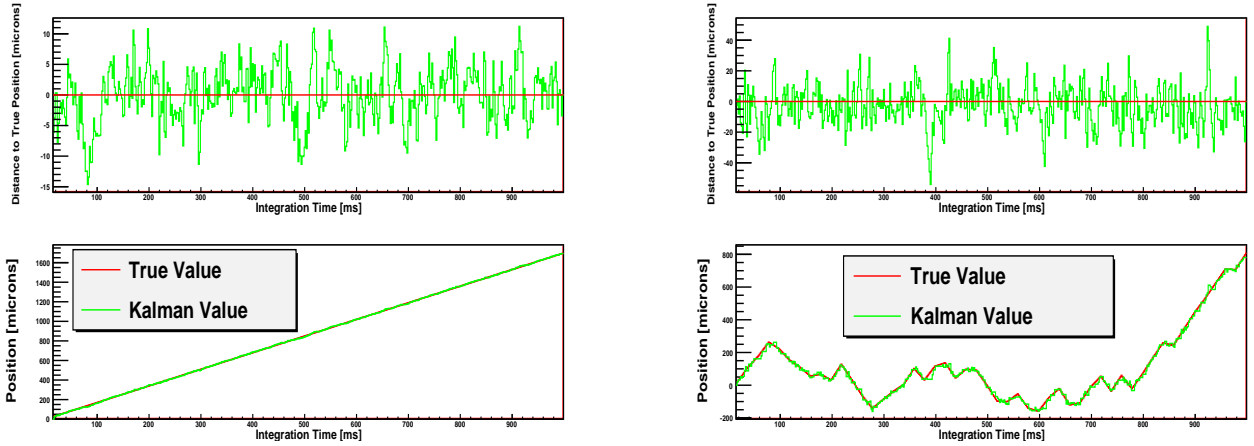
Figure 9. 2D uniform linear motion simulated (3.4 μm/2 ms on sensor) and reconstructed trajectories (left). 2D random motion simulated (10 μm/2 ms on sensor) and reconstructed trajectories (right). Difference between true and computed position is also reported on the top.

paper are encouraging but a dedicated study on the determination of the choice of the process and measurement noises introduced in the Kalman filter has to be performed.

5.3 Quantum Dots imaging

The Kalman tracking algorithm developed with the previous Monte-Carlo simulation has been tested with QDots imaging[‡]. The true total number of QDots has been derived from the whole statistics corresponding to 20 000 frames (40 s). The emission wavelength of QDots is 605 nm (Invitrogen). The excitation wavelength is 473 nm and the power has been tuned with optical densities (10 mW). A pass-band filter filter centred at 610nm (width 10nm) has been used in front of the camera. Figure 10 presents the tracking result of the algorithm by comparing the left image which represents the Phe integrated image and the centred image which represents each identified spot by a cross with a color code proportional to the mean. This gives an idea of what could we expect for a Real-Time simultaneous localisation and quantification of QDots. The tracking efficiency is shown in the right part of Fig. 10. The algorithm detects 75 % of the targets within the first 200 ms (100 frames).

QDots imaging is performed in more standard signal over noise ratio condition than the previous one (spot set up). The photon-counting ability of the ebCMOS sensor allows a temporal tracking of the photon-emission. Therefore blinking properties of single-quantum dots can be observed. A sliding window of 60 ms has been defined for temporal analysis of the mean Phe per QDot and observation of the ON/OFF states. The temporal distribution of the sliding mean is shown in Fig. 11. One can clearly observe the blinking. Histogram of the mean signal is also represented and shows a clear separation of the ON and OFF states. The OFF state shows a mean background noise of 3 Phes per frame per target.

[‡]Dujardin Team, NanOptec Centre of Lyon, D. Amans, G Ledoux, F. Kulzer
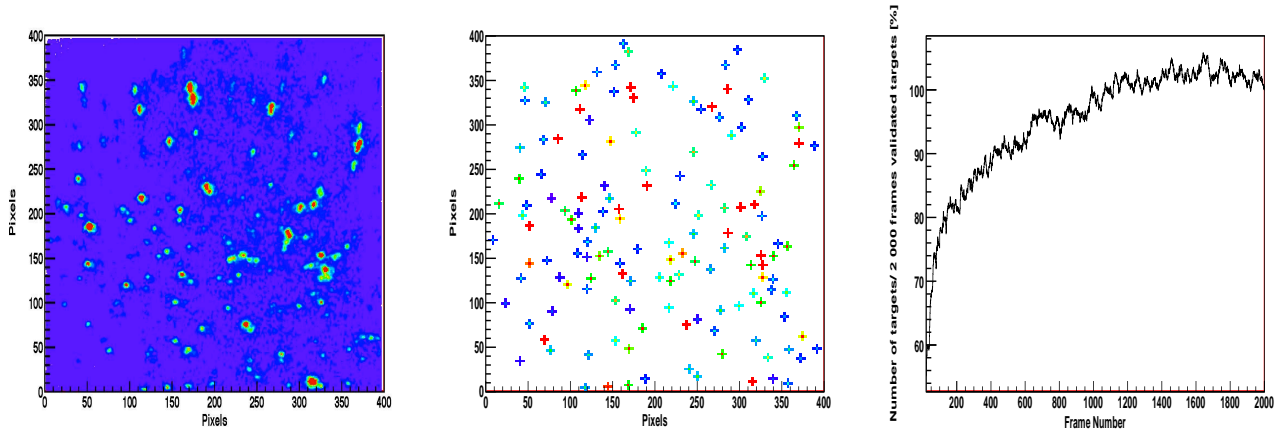
Figure 10. Integrated image over 20000 frames of Phes (left). Image of the corresponding validated targets after 40 s of tracking (centre). Target detection efficiency (number of targets validated at frame n divided by the number of targets validated after 2 000 frames versus the frame number (right). One frame integration time is 2 ms.
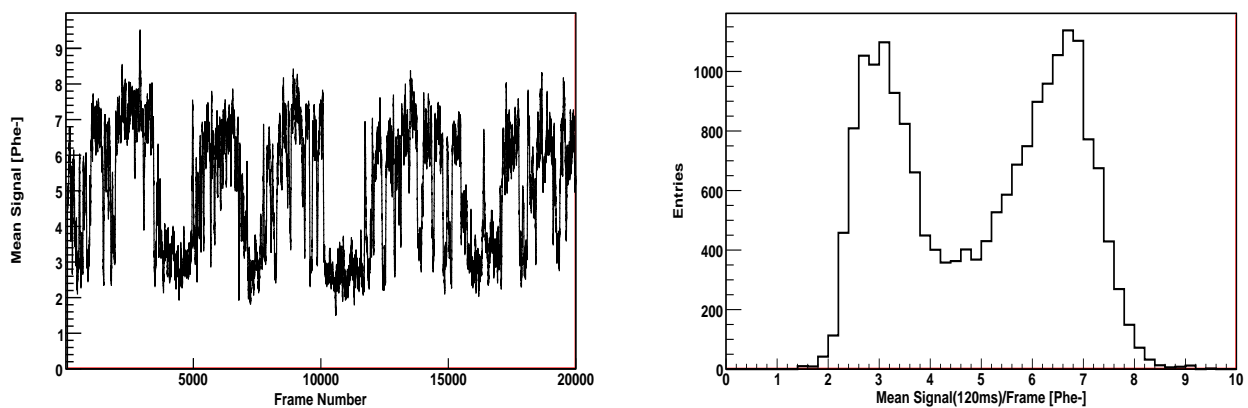
Figure 11. Temporal distribution of the mean Phe/frame of a single-QD over 20 000 frames, 40 s (left) . The blinking is clearly visible. Histogram of the mean shows ON/OFF peaks separated by a factor two.

6. CONCLUSION AND PROSPECTS

We have shown in this paper that an ebCMOS camera system is an interesting candidate for high data throughput super-resolution imaging of fluorescent multiple-target tracking. First the localisation accuracy has been addressed with the CRB and Monte-Carlo computation for three devices: sCMOS, EMCCD and ebCMOS. The role of pixelated detection and the quantum efficiency of the ebCMOS on the localisation accuracy has been studied. Experimental set up with single spot or multiple spots (microlenses) has been designed and produced for resolution measurement on single-emitters versus the signal and background photon conditions. A resolution on the sensor of 1.2μm with a pitch of 10μm is achieved after 70 detected Phe. The multiple-spot identification has been described and shows promising results for the design of new applications in high-data throughput screening at single molecule level high data throughput[23] or in low light Adaptive Optics. By imaging Quantum Dots with a wide field microscope set up we proved that LUSIPHER was able to track a few hundred of single-quantum dots in parallel. The quantification aspect is also addressed by observation of blinking and ON OFF states in terms of sliding mean of photon number/frame. Monte-Carlo simulation of single-emitter motions has been shown by introducing a new concept of tracking method based on single-photon impact list and Kalman filtering. It has been shown recently that Mean Squared Displacement (MSD) measurements on Brownian motion of nano-scale

emitters has to take into account the errors of localisation in the computation of the diffusion coefficient.[8,9] This paper shows that the LUSIPHER camera system with the new single-photon based tracking method presented in this paper could address the MSD measurements of nano-particles with high coefficient diffusion. We evaluated that the possible breakthrough of this concept relies on a Real-Time Tracking with GPU computing. Such a development is under way with a new acquisition system based on FPGAs with a true 20 Gb/s data throughput Ethernet link to the workstation and a GPU Tesla board.

REFERENCES

[1] Betzig, E., Patterson, G., Sougrat, R., Lindwasser, O., Olenych, S., Bonifacino, J., Davidson, M., Lippincott-Schwartz, J., and Hess, H., "Imaging intracellular fluorescent proteins at nanometer resolution," *Science* **313**(5793), 1642–1645 (2006).

[2] Bates, M., Huang, B., Dempsey, G., and Zhuang, X., "Multicolor super-resolution imaging with photo-switchable fluorescent probes," *Science* **317**(5845), 1749–1753 (2007).

[3] Hell, S., "Far-field optical nanoscopy," *Science* **316**(5828), 1153–1158 (2007).

[4] Thompson, M., Lew, M., Badieirostami, M., and Moerner, W., "Localizing and tracking single nanoscale emitters in three dimensions with high spatiotemporal resolution using a Double-Helix point spread function," *Nano Letters* **10**(1), 211–218 (2010).

[5] McMahon, M., Berglund, A., Carmichael, P., McClelland, J., and Liddle, J., "3D particle trajectories observed by orthogonal tracking microscopy," *ACS Nano* **3**(3), 609–614 (2009).

[6] Michalet, X., Colyer, R., Scalia, G., Kim, T., Levi, M., Aharoni, D., Cheng, A., Guerrieri, F., Arisaka, K., Millaud, J., Rech, I., Resnati, D., Marangoni, S., Gulinatti, A., Ghioni, M., Tisa, S., Zappa, F., Cova, S., and Weiss, S., "High-throughput single-molecule fluorescence spectroscopy using parallel detection," *Proc. SPIE Quantum Sensing and Nanophotonic Devices VII,* **7608** (2010).

[7] Serge, A., Bertaux, N., Rigneault, H., and Marguet, D., "Dynamic multiple-target tracing to probe spatiotemporal cartography of cell membranes," *Nature Methods* **5**(8), 687–694 (2008).

[8] Michalet, X., "Mean square displacement analysis of single-particle trajectories with localization error: Brownian motion in an isotropic medium," *Physical Review E* **82**(4) (2010).

[9] Berglund, A., "Statistics of camera-based single-particle tracking," *Physical Review E* **82**(1) (2010).

[10] Michalet, X., Siegmund, O., Vallerga, J., Jelinsky, P., Millaud, J., and Weiss, S., "Photon-counting H33D detector for biological fluorescence imaging," *Nuclear Instruments & Methods in Physics Research Section A* **567**(1), 133–136 (2006).

[11] Barbier, R., Baudot, J., Chabanat, E., Depasse, P., Dulinski, W., Estre, N., Kaiser, C., Laurent, N., and Winter, M., "Performance study of a MegaPixel single photon position sensitive photodetector EBCMOS," *Nuclear Instruments & Methods in Physics Research Section A* **610**(1), 54–56 (2009).

[12] Mackay, C., Tubbs, R., Bell, R., Burt, D., Jerram, P., and Moody, J., "Sub-electron read noise at MHz pixel rates," *Proc. SPIE Sensors and Camera Systems for Scientific, Industrial, and Digital Photography applications II* **4306**, 289–298 (2001).

[13] Michalet, X., Colyer, R., Antelman, J., Siegmund, O., Tremsin, A., Vallerga, J., and Weiss, S., "Single-Quantum dot imaging with a photon counting camera," *Current Pharmaceutical Biotechnology* **10**(5), 543–558 (2009).

[14] Fowler, B., Liu, C., Mims, S., Balicki, J., Li, W., Do, H., Appelbaum, J., and Vu, P., "A 5.5Mpixel 100 frames/sec wide dynamic range low noise CMOS image sensor for scientific applications," *Proc. SPIE Sensors, Cameras, and Systems for Industrial/Scientific Applications XI* **7536** (2010).

[15] Dominjon, A., Chabanat, E., Depasse, P., Barbier, R., Baudot, J., Dulinski, W., Dorokhov, A., and Winter, M., "LUSIPHER large-scale ultra-fast SIngle PHoto-Electron trackeR," *Proc. 2009 IEEE Nuclear Science Symposium Conference Record, VOLS 1-5* , 1527–1531 (2009).

[16] Barbier, R., Cajgfinger, T., Calabria, P., Chabanat, E., Chaize, D., Depasse, P., Doan, Q. Q., Dominjon, A., Guerin, C., Houles, J., Vagneron, L., Baudot, J., Dorokhov, A., Dulinski, W., Winter, M., and Kaiser, C., "A single-photon sensitive ebcmos camera with 500 hz frame rate : the lusipher prototype, submitted to," *Nuclear Instruments & Methods in Physics Research Section A* **xx**(xx), xx (2010).

[17] Snyder, D., hammoud, A., and White, R., "Image recovery from data acquired with a Charge-Coupled-Device camera," *Journal of the optical society of America A-optics image science and vision* **10**(5), 1014–1023 (1993).

[18] Ober, R., Ram, S., and Ward, E., "Localization accuracy in single-molecule microscopy," *Biophysical Journal* **87**(2), 1399–1399 (2004).

[19] Rao, C. R., [*Linear Statistical Inference and its Applications*], John Wiley & Sons, New York (1965).

[20] Tubbs, R., *Lucky Exposures: Diffraction Limited Astronomical Imaging Through the Atmosphere*, ph. d, University of Cambridge (2003).

[21] Kalman, R. E., "A new approach to linear filtering and prediction problems," *J. Basic Eng.* **82**, 35–45 (1960).

[22] Wu, P., Agarwal, A., Hess, H., Khargonekar, P., and Tseng, Y., "Analysis of Video-Based microscopic particle trajectories using kalman filtering," *Biophysical Journal* **98**(12), 2822–2830 (2010).

[23] McNally, B., Singer, A., Yu, Z., Sun, Y., Weng, Z., and Meller, A., "Optical recognition of converted DNA nucleotides for Single-Molecule DNA sequencing using nanopore arrays," *Nano Letters* **10**(6), 2237–2244 (2010).

F.2   Publication de référence sur la caméra de bioluminescence LuSEApher

An ebCMOS camera system for marine bioluminescence observation: The LuSEApher prototype

A. Dominjon [a,*], M. Ageron [c], R. Barbier [a,b], M. Billault [c], J. Brunner [c], T. Cajgfinger [a,b], P. Calabria [a], E. Chabanat [a,b], D. Chaize [a], Q.T. Doan [a], C. Guérin [a], J. Houlès [a], L. Vagneron [a]

[a] CNRS/IN2P3, Institut de Physique Nucléaire de Lyon, Villeurbanne F-69622, France
[b] Université de Lyon, Université Lyon 1, Lyon F-69003, France
[c] CNRS/IN2P3, Centre de Physique des Particules de Marseille, Marseille, F-13288, France

ABSTRACT

The ebCMOS camera, called LuSEApher, is a marine bioluminescence recorder device adapted to extreme low light level. This prototype is based on the skeleton of the LUSIPHER camera system originally developed for fluorescence imaging. It has been installed at 2500 m depth off the Mediterranean shore on the site of the ANTARES neutrino telescope. The LuSEApher camera is mounted on the Instrumented Interface Module connected to the ANTARES network for environmental science purposes (European Seas Observatory Network). The LuSEApher is a self-triggered photo detection system with photon counting ability. The presentation of the device is given and its performances such as the single photon reconstruction, noise performances and trigger strategy are presented. The first recorded movies of bioluminescence are analyzed.

To our knowledge, those types of events have never been obtained with such a sensitivity and such a frame rate. We believe that this camera concept could open a new window on bioluminescence studies in the deep sea.

1. Introduction

Bioluminescence — the emission of visible light by an organism as a result of a natural chemical reaction — has been found across a broad range of organisms especially in the sea. Marine organisms from bacteria to fish use bioluminescence for vital functions [1]. To understand these interactions and the distribution of the luminous population in correlation with oceanographic measurements such as temperature, current velocity or salinity, innovative instruments and platforms have to be developed. Most of previous bioluminescence observations come from vertical profiling instruments at different locations [2]. Time series of oceanographic measurements combined with light survey offered by a smart and ultra-sensitive light sensor in a single location could open new opportunities to a better knowledge of biodiversity in the sea [1].

The ANTARES neutrino telescope [3] is one of few deep-sea cabled networks of visible light detectors. It offers the unprecedented opportunity to install, operate and read out in real time additional devices thanks to the Secondary Junction Box deployed

in 2010. Various time series of observations are currently taken. They range from geophysical measurements to bioluminescence recordings.

Measurements of bioluminescence time series performed by the ANTARES Photo Multiplier Tube (PMT) network have been already reported in [4]. Unfortunately PMTs are single channel photo-detectors and cannot provide an image of the organisms responsible for this bioluminescence.

This is why two consecutive attempts to achieve a better understanding of detected bioluminescence have been performed on the ANTARES site. As a first step, two commercial self-triggering cameras had been installed in the ANTARES framework. During their three years of operation, the feasibility of in-situ observations of bioluminescence with low level light sensors could be demonstrated [5]. The second one, described in this paper, has been launched in 2010 with the production of a custom Low Light Camera System (LuSEApher) based on the LUSIPHER concept previously introduced for fast fluorescence imaging and photon counting in biology and nano-photonics [6].

Section 2 describes the LuSEApher prototype and gives its performances. The performances of the photo-detector itself, the electro-bombarded CMOS (ebCMOS) sensor, are published in [7]. In Section 3, the bioluminescence event trigger strategy is developed. In Section 4, the first results obtained during 6 months of

* Corresponding author. Tel.: +33 472 431 074; fax: +33 472 431 452.
E-mail address: a.dominjon@ipnl.in2p3.fr (A. Dominjon).
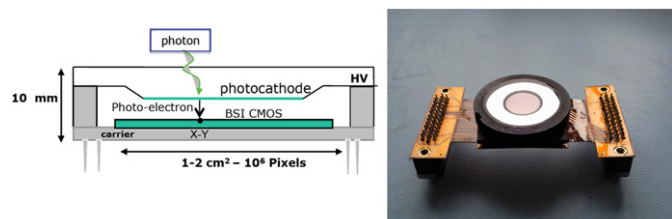
Fig. 1. Schematic view of an ebCMOS (left), picture of the ebCMOS prototype (right).

data taking period is presented to underline the relevance of such devices for deep-sea oceanographic platform. A tentative taxonomy of the interesting bioluminescence events will be proposed and foreseen prototype developments are discussed.

2. LuSEApher prototype

2.1. ebCMOS principle

The ANTARES infrastructure has been used to deploy a secondary junction box (SJB) for environmental science purposes (ESONET). One of the instruments connected to the SJB is the LuSEApher camera. The heart of the system is a back-thinned CMOS pixel array produced by an IN2P3[1] collaboration (IPNL[2]/IPHC[3]). The chip consists of two matrices of 400×400 pixels with $10\,\mu m$ pitch. Only one matrix is used in the LuSEApher camera system. To be sensitive to single photo-electron, a back side bombardment of the sensor is required because of the electronic layers that prevent any low energy particle detection from the front side. Our system combines a photo-cathode and a Back Side Bombarded (BSB) CMOS, both placed in a vacuum tube. Fig. 1 shows the detection principle of this ebCMOS (electron bombarded CMOS). Typical cathode-CMOS gap dimension and maximum gain (High Voltage) are fixed by the necessary limitation of electron cathode emission. Thus, to maintain a low dark count rate ($10^{-5}e^-$/pixel/ms) and a good spatial resolution it is necessary to work with an initial energy lower than 3 keV and a cathode-CMOS gap of the order of 1 mm.

2.2. Electronic design

The ebCMOS has been integrated into a camera designed by the IPNL instrumentation group. The Data Acquisition System has been fully developed by the IPNL electronic group. The slow control of the ebCMOS is done by a PIC 18F4550 microcontroller. Operating voltage, chip temperature control, high voltage control and power supply can be set and monitored from the shore. The DAQ board is based on an Altera Stratix 2 development board with 2 mezzanines: one contains four 12-bits ADCs to read out 4 channels of the 400×400 pixels in parallel; the second one contains a 1 Gbit/s Ethernet link. The chip readout clock can be chosen between 5 MHz and 40 MHz that means a frame rate of 62.5 to 500 Hz. Note that the final frame rate is divided by 2 because of the need of the Correlated Double Sampling (see Ref. [6]).

All systems communicate with a PCM 9562 Single Board Computer via its Ethernet port. This embedded PC is used to control both DAQ and slow control. It is based on two 1.67 GHz CPUs with 2GB RAM and used to compute the pixel signal over

noise ratios to perform single photoelectron identifications. Those tasks are performed in real-time.

2.3. Mechanical setup

In order to immerse the LuSEApher camera, all the systems (ebCMOS, slow control, DAQ, CPU boards) are integrated in a 15 cm diameter and 60 cm long titanium cylinder as shown in Fig. 2. The cylinder is divided in three compartments:

- the front side compartment (analogical part) is composed of the analog part of the camera with the glass window and the camera lens, the ebCMOS and the slow control boards
- the central compartment (numerical part) contains the DAQ board and the embedded PC, behind a copper screen and thermal foam for electromagnetic compatibility and cooling through the titanium tube
- the rear compartment is devoted to the power-supply elements and connectors (48 V, 100 Mbit/s, Ethernet).

At the ANTARES site the deep sea water has a stable temperature of 13 °C and provides permanent cooling. One single cable connects via a waterproof connection the camera LuSEApher to the Instrumentation Module (MII), which itself is connected to the Secondary Junction Box (SJB). The electric consumption of the system is less than 100 W as requested by the Instrumentation Module specifications.

2.4. Camera optics

The optical part is composed of a TAMRON CCTV Lens (Ref. 12VM412ASIR) placed in front of the ebCMOS. To realize an aperture in the flange of the tube, an adapted glass window has been chosen with a thickness of 12.7 mm and a diameter of 51 mm able to resist to the pressure at a 2500 m depth. The distance between the window and the camera lens is 20 mm. The diameter of the aperture of the flange is 35 mm (Fig.3).

The optical parameters have been chosen to obtain the best optical performances in the range [0.30 m–2 m]. The optical focal length determines the magnification and the field of view of the system. The TAMRON lens is a vari-focal lens ranging between 4 mm and 12 mm focal length. In order to obtain the largest field of view, we have to choose the shorter focal length, but the retaining ring of the window limits the field of view. A focal length of 6 mm has been chosen. It was the best compromise between the magnification, the focal depth and the field of view.

The diaphragm aperture has been opened to the maximum value to optimize the light collection instead of the depth of focus. The maximum aperture of this TAMRON lens corresponds to an "Fnumber" of 1.2.
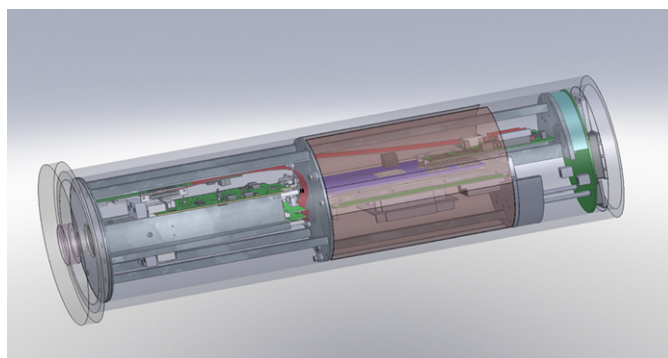
Fig. 2. The complete integrated LuSEApher camera.
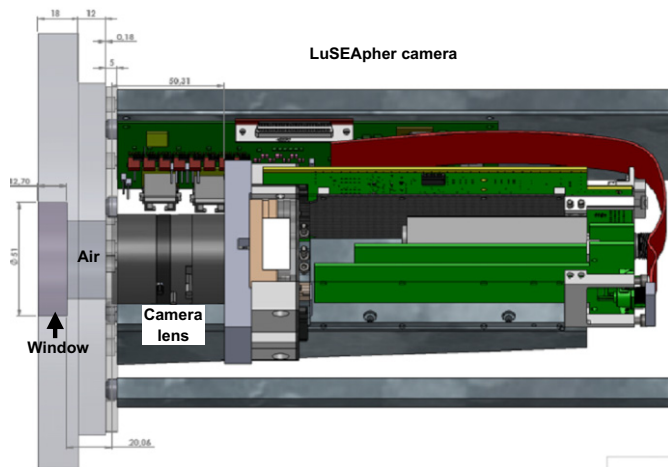
Fig. 3. Scale view of front side of the LuSEApher camera (optical part and front end electronics) closed by the flange and the glass window.
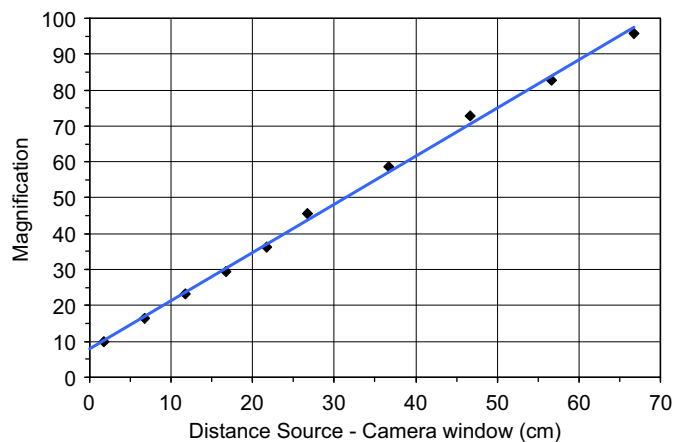
Fig. 4. Camera magnification versus source position.

We developed a test bench to characterize the assembly (window+optics+camera) identical to the LuSEApher camera. We measured a field of view of 68.5 cm $\pm$ 0.5 cm at one meter distance ($35° \pm 2°$) and a depth of field of almost 2 m.

We characterized the magnification of the system using a USAF test chart placed at different distances with respect to the camera window. Fig. 4 shows the measured magnification versus the position of the source. For example, if we consider a bioluminescent source at the window level ($z = 0$ cm on the graph), the magnification coefficient is of the order of 8.

3. Bioluminescence data acquisition

3.1. Trigger strategy

The LuSEApher camera is able to detect bioluminescence with single photon sensitivity. A single photoelectron event is triggered by one fired pixel and selected by pattern recognition on the cluster charge (5×5 pixels around the seed pixel typically). The selection criteria of a photoelectron are the following:

- A seed pixel with a charge value greater than 3 times its noise
- A cluster with 30% of the first neighboring pixels with more than 50% of the seed charge
- A cluster with 50% of the second neighboring pixels with more than 30% of the seed charge
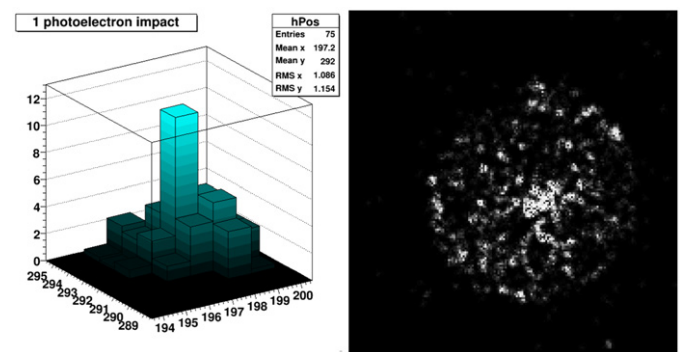
Fig. 5. A single photo-electron event (left). A typical measured event with reconstructed photo-electrons (right).

A typical cluster of a single photoelectron event obtained for HV = 2.8 kV is shown in Fig. 5 (left).

Since it is impossible to store continuously all data due to limited storage capacity, a smart survey has to be implemented. The survey is based on the number of detected photons per frame thanks to the counting ability of the ebCMOS and to its low dark count. Therefore the main point in the trigger strategy on bioluminescence is to increase the sensitivity by decreasing the threshold on the number of detected photons per frame. It is found that with a threshold of 14 reconstructed photoelectrons (phe⁻) per frame, an event is a good candidate for bioluminescence. This threshold could be lowered by a factor two with a dedicated ion feedback rejection. Ion feedback events are due to residual ions in the vacuum tube hitting the photocathode and giving strong signals in the frame. The measured rate of ion feedback background is 5×10^{-3} per frame (≈ 0.3 Hz).

Once an event is triggered, data are extracted from a circular buffer with the beginning at 50 frames (~ 1 s) before the trigger until 300 frames (~ 5 s) after the last bioluminescence frame. This will be called a *sequence* in the following. The typical sequence duration is around 1 s, thus a total of 7 s of data (70 Mbytes) are buffered on a local (SSD) disk. During the 16 ms duration of a frame the system manages to reconstruct each photoelectron on line for making a decision for the readout. The Fig. 5 (right) shows a typical measured bioluminescence sequence obtained with the accumulation of reconstructed photoelectrons during 200 frames.

3.2. Noise performances

The measurement of the contribution of the CMOS pixel noise to the photon selection has been done (HV off) and gives one fake photon per frame (10^{-6}/pixel/frame). Therefore the single-photon sensitivity of the ebCMOS is not deteriorated by CMOS noise (8 electrons RMS) [7].

The dominant noise source is the Dark Count (DC) due to thermionic electron emissions from the cathode. The photocathode of LuSEApher is a multi-alkali S20. The DC measurement at 2500 m depth gives a rate of 0.78 photons/frame for HV = 2.8 kV. This value is in agreement with camera characterizations already made in laboratory [7]. The LuSEApher DC is measured daily. The LuSEApher camera system is thus a very low noise camera able to achieve single photon detection at 62.5 fps and then allows direct bioluminescence observation with unprecedented sensitivity and without the need of an additional light source.

4. Methods and preliminary results

4.1. First measurement campaign and statistics

In October 2010, the LuSEApher camera has been installed at a depth of 2475 m (Latitude 42°48′N, Longitude 6°10′E) and

connected to the ANTARES SJB (Secondary Junction Box) thanks to an IFREMER ROV. The LuSEApher camera is fully operational for quiescent observation since middle of December 2010 and runs 24 h/24 h.

Results presented in this paper cover a 6 months period of continuous acquisition from January to June 2011. During this period, the camera system has been off only for few days due to power cuts or software upgrades (SJB, MII, camera system software) and 4813 trigger sequences have been recorded. Most of those events (81%—3915 events) are typical single frame sequences with more than 14 photoelectrons. Such events are mainly due to ion feedback or to statistical fluctuations above the threshold. This has been confirmed by a statistical analysis of this subset. The detected photon number versus time distribution does not show any bioluminescence decay curve after the triggered frame. The mean number of reconstructed photons contained in the triggered frame is close to the threshold of 14 photons. This is the lowest threshold we can put without overloading the camera system CPU keeping the most sensitivity on very brief bioluminescence phenomena with very low flux. With this selection criterion of bioluminescence events, we obtain a mean rate of 5 bioluminescence events/day. Of course, this mean value has to be taken carefully since the bioluminescence activity is far from being constant in time. As can be seen on the sequence number versus time plot (see Fig. 6), there are periods with high bioluminescence activity (few day duration) and quiet periods.

4.2. Time characteristics of bioluminescent events

Using the relatively high frame rate of the LuSEApher camera in combination with its single-photon sensitivity offers the possibility to monitor bioluminescence activity on time scales ranging from 16 milliseconds (one frame duration) to months or years (duration of the survey). In this section, we focus on the methods to study the bioluminescence sequences ranging from few frames (few hundred of milliseconds) to few hundreds of frames (few seconds). From the sequence statistics taken during these 6 months period mainly three types of bioluminescence have been isolated.

4.2.1. Bioluminescence single flash events: type I

Selection method: A sequence is considered as a bioluminescence single flash event (type I) if the number of photons per frame increases and decreases rapidly (5–50 frames) down to the mean dark count (0.78 phe⁻/frame). The peak search from the number of recorded photons versus time has been performed with a sliding window (sliding mean on 3 frames) on the sequence by smoothing the statistical fluctuations and performing an automatic search of strong positive and negative consecutive slopes (zero crossing of the derivative). This peak search has been optimized first on the least luminescent sequences.
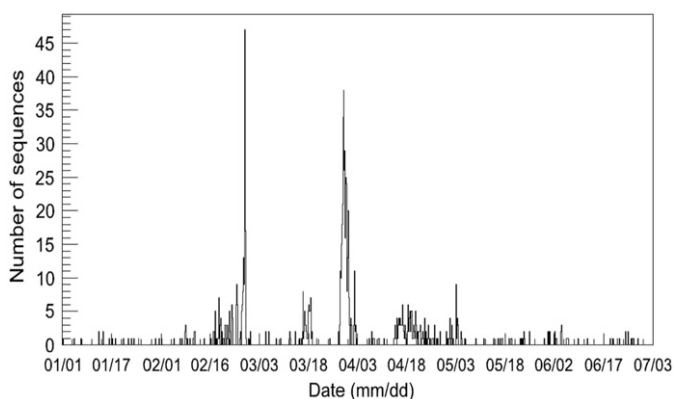
Analysis method: The single peak search method is applied on each triggered event. The 16 ms frame duration is sufficiently short to limit the jitter on time stamping of the bioluminescent flash.

The cumulative distribution of 175 single flash sequences is shown in Fig. 7. Three distinct parts can be defined. The first one is the tail of the distribution noted (1) in the plot. This part shows a constant photon activity. It is a precise measurement of the dark count rate. The mean number of photons per frame is 141.1 photoelectrons for 175 events stored. This value is consistent with the noise level already measured independently during calibration runs with a mean rate of 0.8 photons per frame. This tends to show that background is well understood.

The most interesting region of the curve is its exponential decays with two distinct decay constants. Zooms of each part are shown in Fig. 8. After background subtraction the fit of part (2) gives a decay constant of (255 ± 4) ms.

By subtracting the background and the exponential decay of (2), the shortest period can be fitted. A decay constant of (24.2 ± 0.7) ms is measured. Comparison of these bioluminescence decay constants with deep-sea bioluminescence organism taxonomy could lead to a possible identification of the sources of bioluminescence. Such bioluminescence decay studies have already been observed in laboratory for example in Refs. [8–10] with the dinoflagellates but never in quiescent conditions and in the natural environment.

The precision of the measurement shows the great potential of such a camera system for systematic studies of biodiversity in the deep-sea environment. Sequences showing a strong photon signal could also be used to study temporal and spatial correlations using "Single Photon Imaging" (SPI).

Parameters to extract for biological analysis: Since the aim of this paper is to show the potential that our smart camera system could provide for biological investigations, we summarize, which could be estimated from those type I events:

- Bioluminescence decay constants for identification
- Quantification through intensity measurement of the flash (absolute quantification if the distance is known, unfortunately this is not the case in this campaign)
- Appearance frequency versus oceanographic conditions
- Time correlation between single-flashes occurring in a short time

Fig. 6. Temporal distribution of the detected sequences during the 6 months period of data taking (January–June 2011).
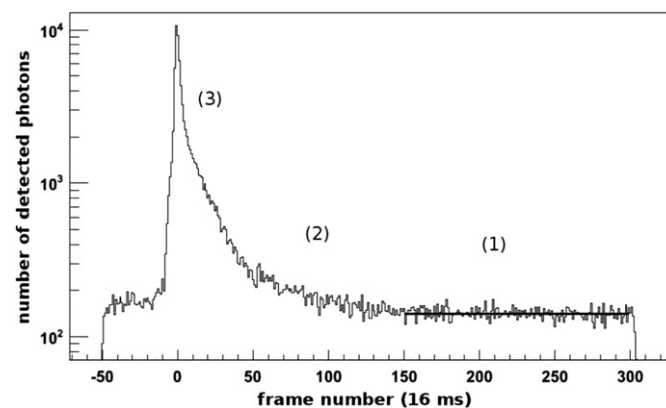
Fig. 7. Single-flash sequences. This graph shows the number of detected photoelectrons in function of the frame number (one frame=16 ms) for the 175 static sequences of type I.

period = (255 +/- 4) ms	hDecayTot	
	Entries	63294
	Mean	10.42
	RMS	12.16
	χ^2 / ndf	60.92 / 39
	Constant	7.815 ± 0.021
	Slope	-0.06281 ± 0.00096

period = (24.2 +/- 0.7) ms	hDecayTot	
	Entries	63613
	Mean	1.963
	RMS	1.245
	χ^2 / ndf	2.363 / 4
	Constant	8.919 ± 0.033
	Slope	-0.6604 ± 0.0183
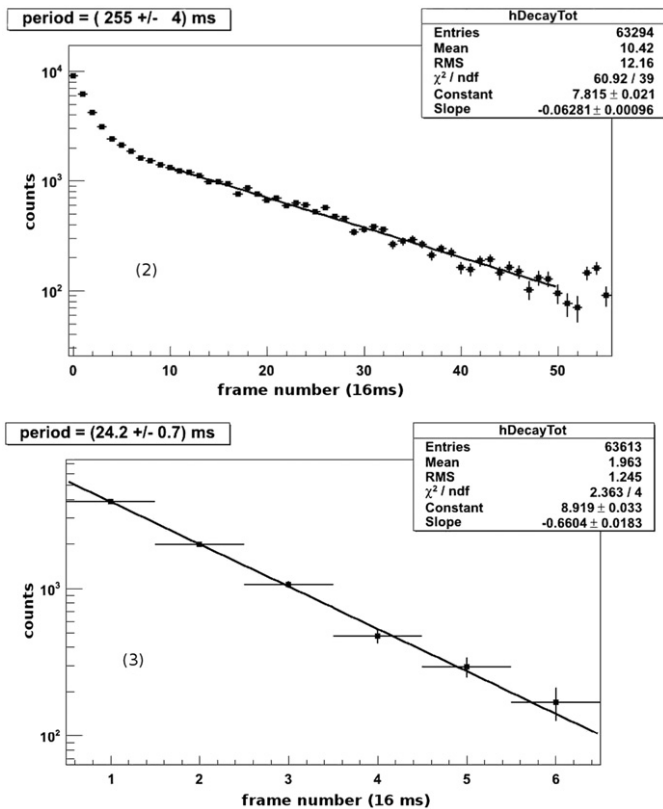
Fig. 8. Zoom on the decay part of Fig. 7. On the top the fit of the long period is shown after background subtraction. On the bottom the shortest period is fitted on the five first frames after the beginning of the flash.

4.2.2. Multiple pulsating events: type II

Selection method: Using the peak search method introduced above we extract sequences with more than one peak from the data. We call them pulsating events or type II sequences.

Analysis method: The duration of such sequences is of the order of few hundreds of frames (few seconds). In this case it is important to check first if the bioluminescence comes from the same source (SPI method). Then each sequence can be characterized in terms of the number of pulsations, their peak intensity (integral, maximum of the peak), the duration of each pulsation and the total duration of the pulsating sequence.

The inset of Fig. 9 gives an example of a pulsating event. Each peak has an intensity of more than 100 phe$^-$/frame. The distribution of the number of flashes for these pulsating events is shown on Fig. 9. A total of 630 sequences of type II have been recorded during the 6 months of observation. A completed study of multiple flash events is not in the scope of this paper and will be published soon. Some movie examples can be downloaded from our Website [11].

4.2.3. Non flashing bioluminescence events: type III

We observed in our data some sequences without strong flashes but with a persistent brightness. We call them type III events. Those 93 events can be classified by their duration and their mean intensity. The motion (velocity), the shape and the size of the bioluminescent source are obtained with a single photon imaging method described in the next section. Those sequences are interesting for biodiversity studies in correlation with oceanographic parameters such as the current velocity. Interactions between organisms could be also observed by a spatial and temporal analysis.
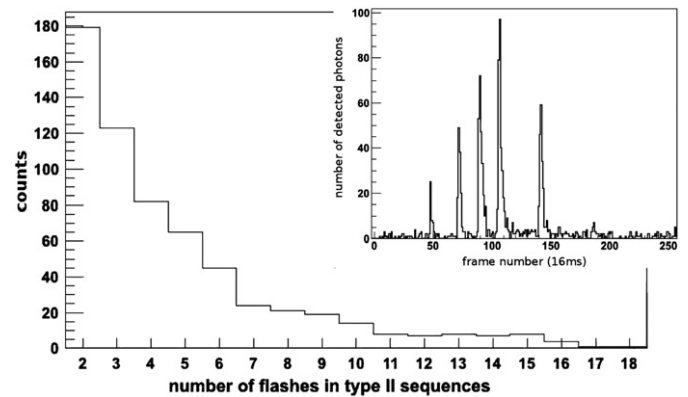
Fig. 9. Distribution of the number of flashes for pulsating sequences (type II). One example of a pulsating event (inset). Five distinct flashes can be observed with different intensity and comparable decay times.

The next table summarizes the statistics of bioluminescent sequences recorded from January to June 2011:

Number of triggered sequences	4813
Number of "single frame" sequences	3915
Number of bioluminescent candidates	898
• Number of type I sequences	175
• Number of type II sequences	630
• Number of type III sequences	93

4.3. Single photon imaging

We take advantage on the fact that our camera can reconstruct images based on single photon detection. The basic information provided by the camera system is the position of the single photon in the frame. When the photon flux is lower than 5, the number of photons per pixel can be evaluated. For higher intensity (ADC unit is used instead of photon number) a standard image processing is chosen. The frames containing more than 20 photons are used to extract topological parameters such as the position of the source or its "size". It is difficult to derive the exact shape of the bioluminescent source if the species remains unidentified because of the limited number of photons. This could be overcome using an active imaging with a light source on but it was not planned for this first prototype. Moreover, the optical part was not optimized for microscopic light sources. We observe a halo (off focus sources near the window) that could also prevent to deduce the exact shape of the bioluminescent source. However, we present in what follows a method to extract some information on the bioluminescence sources in the low photon regime.

4.3.1. Center of gravity and size of the light sources

Selection method: The position of the light source is obtained by computing its Center of Gravity (COG) from the impact distribution of the photons per frame. The COG is computed only for frames with more than 20 photons in order to avoid fluctuations of the COG due to statistical fluctuations in frames with a small number of detected photons. Then the "size" of the bioluminescence source can be obtained from the COG for each frame by computing the radius that contains 90% of the detected photons.

Analysis method: We can notice that all light sources exhibit a similar pattern: a quasi-circular halo as can be seen in Fig. 10 (left). From this graph, we extract a typical size of the light source on the sensor. The halo part is around 120 pixels and the central part around 15 pixels. We can deduce the size of the light source
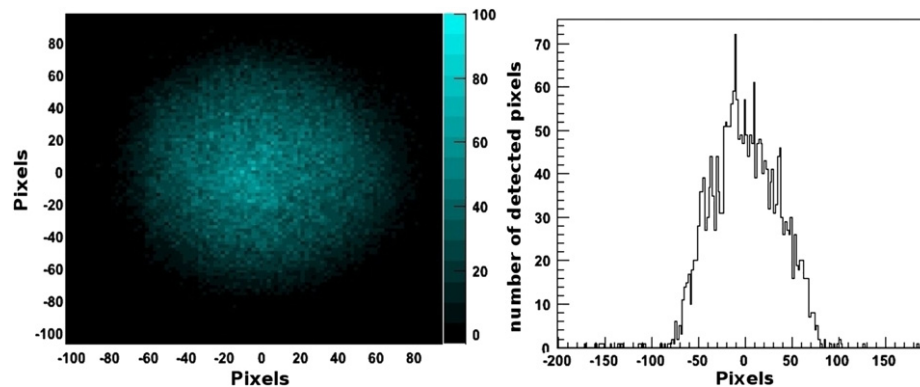
Fig. 10. Integrated image of recorded sequences by positioning the computed COG frame by frame at the center of the image (0,0) (left). Radial distribution of the photon number (right).
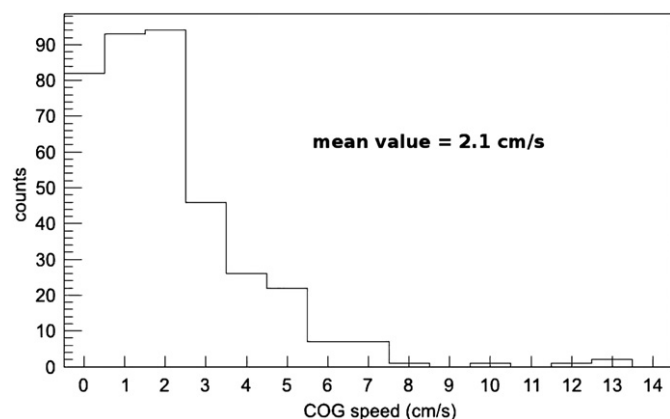
Fig. 11. Distribution of the velocities of the Center of Gravity for 383 moving sequences.

from the RMS value of the photoelectrons distribution reported on Fig. 10 (right). A typical RMS of 36 pixels is measured. Assuming an object situated in front of the glass window and taking into account the lens magnification for this distance (see Section 2.4), we can deduce an upper limit of the "size" of the source of 9.6 mm. To confirm those observations a 3D imaging is necessary.

4.3.2. COG velocity

The COG measurement and its time evolution can give access to the velocity of the light sources.

Selection method: The determination of the instantaneous velocity is difficult due to the natural fluctuation of the COG position because of the small photon statistics. This can be obtained only on the brightest recorded sequences. Therefore a mean velocity of the source is preferred. For small photon statistics a kind of velocity can be also computed from the distance between the positions of the COG at the start and at the end of the sequence versus the sequence duration.

Analysis method: Compare to statistical fluctuation of the COG reconstruction, we considered the source as moving if the distance between the start and the stop positions are longer than 40 pixels on the sensor plane. Fig. 11 shows the distribution of the COG velocities of 383 selected moving sources. A mean value of the COG velocity is estimated at 2 cm/s.

This analysis can provide an interesting parameter to be compared with oceanographic measurement on site such as current velocity. We already observed a correlation between the bioluminescence activity with fast moving sources and current velocity given by ANTARES Collaboration [3]. The standard

oceanographic conditions measured continuously by ANTARES gives a mean current velocity of around 5 cm/s and a South/West current direction. The moving events of type II or III have been measured when the current velocities reached a faster speed and a different direction. Fig. 12 shows the current velocity values up to 20 cm/s and the current angle, East/West, when moving events had been observed. This preliminary observation has to be confirmed by a systematic study.

5. Conclusion

In this paper, we presented the design and the fabrication of the LuSEApher prototype dedicated to quiescent bioluminescence observations. The acquisition system and the trigger threshold tuning have been discussed. A threshold of 14 photoelectrons has been set to trig the bioluminescence sequences, thanks to single photon sensitivity and to photon counting capability of the ebCMOS sensor [6]. The data acquisition system is monitored from the shore and can be modified remotely. Currently, the frame rate is 62.5 frames per second (16 ms/frame).

Since its immersion in October 2010 and after 2 months of calibration, dark count measurement and trigger threshold tuning, the LuSEApher prototype worked well and continues to survey the deep sea 24 h/24h. Almost 900 bioluminescence sequences have been recorded.

New analysis methods to sort different bioluminescence activity from the sequence statistics have been introduced. The information temporal and/or spatial extracted from the photon statistics allow to characterize the bioluminescence activity: duration, decays time, occurrence, intensity, localization, mean and instantaneous velocity of the source, simultaneous bioluminescence activity of two sources. Its temporal multi-scale ability allows observations from few milliseconds until few months.

We have shown in this paper that the camera LuSEApher is one of the most sensitive and fastest camera systems in the state of the art for quiescent bioluminescence observations. Despite an optical system not adapted to microscopic sources, it works in the same low photon regime than the ultra low light ICDeep (Image Intensified Charge Coupled Device) [12]. It would be interesting to complete the bioluminescence activity survey by oceanographic parameters such as temperature, water salinity, current velocity and direction, pressure and oxygen concentration

The first prototype fabricated in only 4 months has not been designed with an optical system dedicated to 3D imaging. A measure of the source distance would give an absolute quantification of the luminance of the bioluminescence sources. This last measurement could be of a great biological interest combined
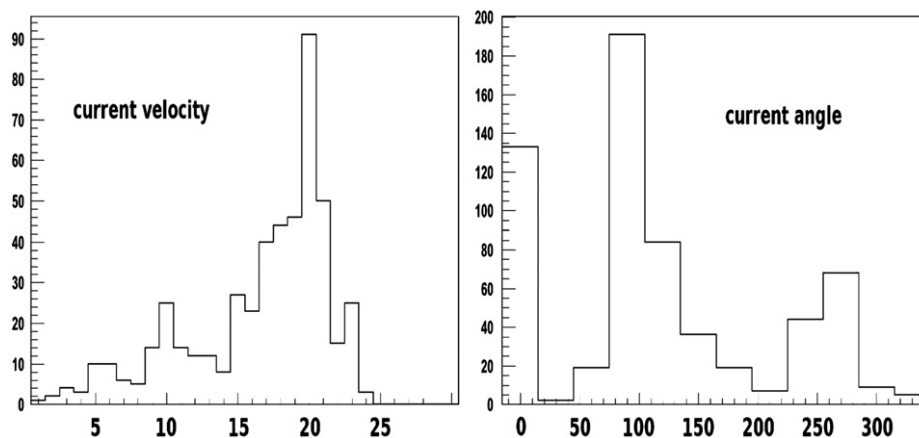
Fig. 12. Distribution of current velocities (cm/s) and current direction respect to North (0°) given by ANTARES when the fastest and brightest bioluminescent sequence has been recorded.

with all others parameters already measured. The next prototype should realize this break-through of 3D with low light photon flux.

Acknowledgment

References

[1] S.H.D. Haddock, M.A. Moline, J.F. Case, Annual Review of Marine Science 2 (2010) 443.
[2] I.G. Priede, et al., Deep Sea Research I 53 (2006) 1272.
[3] M. Ageron, ANTARES collaboration, et al., ANTARES: the First Undersea Neutrino Telescope Nuclear Instruments and Methods in Physics Research A 656 (2011) 11.
[4] H. Van Haren, et al., Deep-Sea Research I 58 (2011) 875.
[5] Juergen Brunner, Internal Communication.
[6] T. Cajgfinger, E. Chabanat, A. Dominjon, Q.T.Doan, C. Guerin, J. Houles, R. Barbier, Single-photon sensitive fast ebCMOS camera system for multiple-target tracking of single fluorophores, Application to Nano-Biophotonics IS&T/SPIE Electronic Imaging (2011).
[7] R. Barbier, et al., Nuclear Instruments and Methods in Physics Research A 648 (2011) 266.
[8] M.S. Webster, et al., Mechanical stimulation of bioluminescence in the deep Pacific Ocean Deep-Sea Research 38 (2) (1991) 201.
[9] E.A. Widder, J.F. Case, Journal of Comparative Physiology A 143 (1981) 43.
[10] A.-S. Cussatlegras, P. Le Gal, Journal of Experimental Marine Biology and Eclogy 343 (2007) 74.
[11] Bioluminescence movies can be seen on the Web page: ⟨http://www.ipnl.in2p3.fr/spip.php?article1297⟩.
[12] J. Craig, A.J. Jamieson, P.M. Bagley, I.G. Priede, Journal of Marine Systems 88 (2011) 563.

F.3 Publication sur l'acquisition 10 Gbits *IEEE NSS 2011*

An Acquisition system for CMOS imagers with a genuine 10 Gbit/s bandwidth

First C. Guérin, Second R. Barbier, J. Marhoug, W. Tromeur, J. Houles, Q. T. Doan, A. Dominjon, T. Cajgfinger

Abstract– **This paper presents a high data throughput acquisition system for pixel detector readout such as CMOS imagers. This CMOS acquisition board offers a genuine 10 Gbit/s bandwidth to the workstation and can provide an on-line and continuous high frame rate imaging capability. On-line processing can be implemented either on the Data Acquisition Board or on the multi-cores workstation depending on the complexity of the algorithms. The different parts composing the acquisition board have been design to be used first with a single-photon detector called LUSIPHER (800x800 pixels), developed in our Lab for scientific applications ranging from nano-photonics to adaptive optics. The architecture of the acquisition board is presented and the performances achieved by the produced boards are described. The future developments (hardware and software) concerning the on-line implementation of algorithms dedicated to single-photon imaging are tackled.**

I. Introduction

THE CMOS Image Sensors (CIS) are able to provide high-definition images at an ultra-fast frame rate, thanks to the reduction of the grid size (smaller pixels) and the parallelisation of the readout lines (column parallel). The further reduction in size trend is not completed and some new techniques for increasing compactness such as 3D integration technology for CIS will provide obviously a huge data flow that is today impossible to treat in-line. The temporary storage solution is more often used when the application allows a sequential readout with an allowed dead time. Nevertheless some real-time applications require an in-line and continuous processing. In this case, the good information has to be extracted from the pixel matrix by applying a data reduction. The CMOS imager such as the electro-bombarded CMOS (ebCMOS) belongs to this category of sensors. Nevertheless, a complicated reduction of data is not easy to implement into a System On Chip (SoC) while keeping versatility. This is true especially for R&D chip for which it is important to keep flexibility through the software of the acquisition system. Indeed, the acquisition system has to be open to different CMOS sensors with analogue or digital readout. Furthermore the main board has to sustain a high data throughput and propose an in-line processing. The acquisition system for CIS readout with a genuine 10 Gbit/s bandwidth presented in this

paper meets this challenge. This acquisition system is not a pure conceptual attempt on an acquisition system but is driven by low light imaging and single-particle tracking with the ebCMOS camera, LUSIPHER [1].

We present in section 2, the general architecture of the whole system and the main tasks of each part. Then the heart of the acquisition system, the acquisition boards, is described in section 3 from an architecture point of view. The implementation and the performances of the boards are discussed in the second part of this section. The software platform developed to overcome some possible limitations of the on board in-line processing is presented in section 4. To conclude, the future developments (hardware and software) concerning the in-line implementation of the algorithms are tackled.

II. Synoptic of the Data Acquisition System

The imaging system is composed of 3 main blocks (the ebCMOS camera, the acquisition board and the workstation) and is shown in Figure 1. In this paper we focus on the acquisition system (DAQ) that is composed of the two last blocks. The ebCMOS detector has been already presented in details in Ref. [1]. The acquisition board is connected to the workstation through a single 10 Gbit/s Ethernet link. It is used both for data taking that for the camera control. The DAQ board is connected on the other side to the ebCMOS camera with three different types of communication. The DAQ board receives the analog or digital raw data from the CMOS chip and generates the sequencing patterns to the CMOS chip (clocks, reset). It communicates with the microcontroller inside the camera for the management of the slow control parameters (the configurations of the chip, the reference voltages, the temperatures, the ebCMOS high voltage reference, the hygrometry measurement). In addition to I/O management, the DAQ board digitizes the 16 analogue signals in parallel (65 MHz/channel) and performs some simple imaging processing, the Correlated Double Sampling computation and the pedestal subtraction). The software, the third block, runs on a multi-core workstation equipped with a 10 Gbit/s Ethernet board and a Solid State Disk for data storage on the fly.

The software has also an interface to the end-user through a Graphical User Interface implemented in Qt language. The DAQ software implements algorithms for in-line pattern recognition dedicated to single particle tracking based on single-photon detection. The noise suppression algorithms are also implemented to increase the image quality. The DAQ system works continuously with the ebCMOS camera

F. C. Guérin is with the Université de Lyon, Université Lyon 1, Lyon, F-69003, France, CNRS/IN2P3, Institut de Physique Nucléaire de Lyon, Villeurbanne, F-69622, France (telephone: +33 4 72 44 84 71, e-mail: c.guerin@ipnl.in2p3.fr).

S. R. Barbier is with the Université de Lyon, Université Lyon 1, Lyon, F-69003, France, CNRS/IN2P3, Institut de Physique Nucléaire de Lyon, Villeurbanne, F-69622, France (telephone: +33 4 72 43 12 22, e-mail: r.barbier@ipnl.in2p3.fr).

LUSIPHER (800x800 pixels), at a frame rate of 500 Hz and all implemented algorithms in parallel.
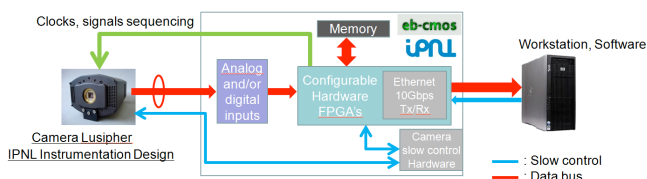
Fig. 1. The ebCMOS imaging system overview with its 3 main blocks: The ebCMOS camera, the acquisition board and the workstation.

III. DAQ BOARDS

The DAQ board has been designed to be modular and is opened to other CMOS chips than the LUSIPHER ebCMOS. It is composed of three electronic boards. The motherboard is dedicated to the digitization, to pattern generation and to raw data processing (CDS). One of the 2 daughter boards (ComEth10G) is the communication card to the workstation through two parallel 10 Gbit/s Ethernet links (2x10 Gbit/s bandwidth upgrade is possible). This board can be used in addition for data processing, thanks to memory banks connected to a powerful FPGA. The second daughter board is devoted to the slow control of the camera. The picture of the 3 boards assembly is shown in Figure 2.
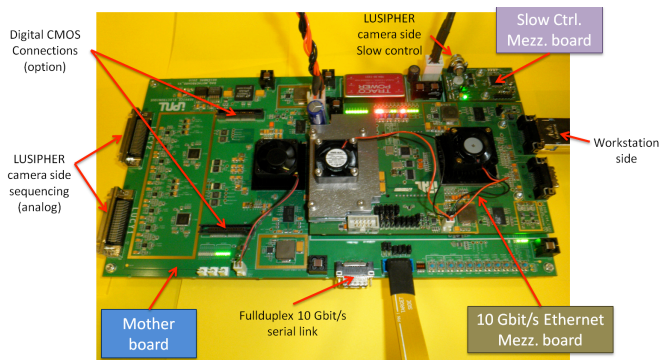
Fig. 2. The DAQ boards: The motherboard with the analog and digital parts, the ComEth10 board with the two parallel CX4 Ethernet links and the smaller board (top right) for the slow control.

A. Motherboard Architecture

The motherboard is connected to the LUSIPHER camera with two SCSI (50 pins). Those links allow on one hand to the transmission of the patterns generated by the FPGA such as the clocks and the resets required for the sequencing of the CMOS chip and on the other hand to the reception of the analogue signals coming from the pixel outputs. The board has 16 analogue inputs for a parallel digitisation by the 12 bit ADCs [2]. The sampling clock can be tuned on the pixel clock for an optimized sampling (40 MHz for the ebCMOS LUSIPHER) with a maximum sampling frequency of 65 MHz. In this last case the sampling rate is 1,040 GS/s. This corresponds to a maximum input data flow for the FPGA of 12.48 Gbit/s. In case of the LUSIPHER ebCMOS, the input data rate obtained for 800x800 pixels, 16 outputs in parallel

and a 40 MHz clock is 7.68 Gbit/s. The motherboard can also drive and read out a digital CMOS chip, thanks to a Mictor 76 point connection with LVDS links to the FPGA. All of these details are shown in Figure 3.
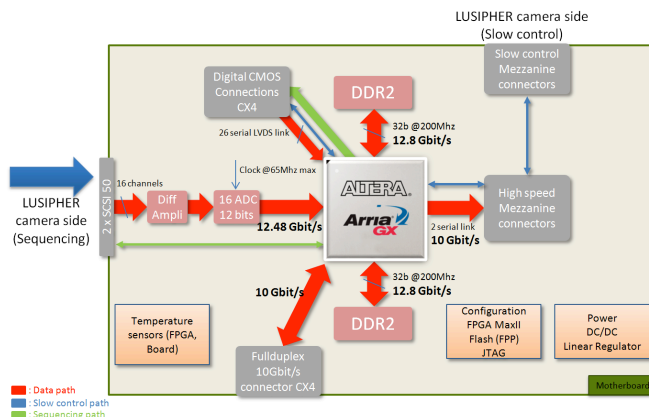
Fig. 3. The motherboard architecture, with bandwidth indications for inputs, outputs, and memory, between the FPGA.

The FPGA, an ARRIA GX from ALTERA [3], implements the following tasks: - pattern generator – ADC sequencing and tuning of the reference clock, image reconstruction from data packets– Correlated Double Sampling computation – configuration of the CMOS readout mode – Double Data Rate (DDR2) memory bank R/W controller [4]. Figure 4 illustrates the main FPGA architecture of the motherboard. Another smaller FPGA [5] is used on this board for configuration purposes (JTAG and FPP).
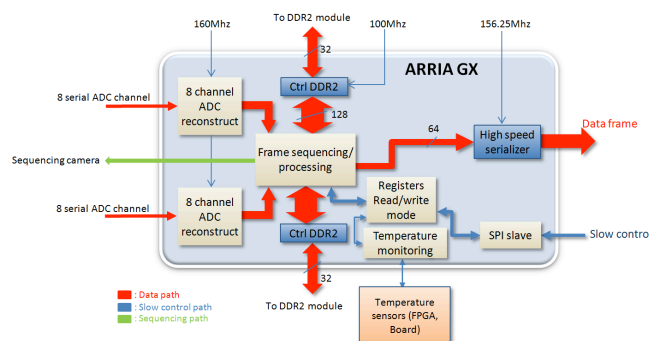
Fig. 4. The main architecture of the motherboard with a zoom in the DDR controller used for the in-line image reconstruction.

B. Daughter Board "ComEth 10G" Architecture

The Figure 5 shown the mezzanine architecture. It is quite similar than the Motherboard. The daughter board is mainly composed of a FPGA and of DDR memories. The tasks completed by the FPGA are divided into two groups: the communication and the processing. The most important block is the Ethernet link management in order to achieve a true bandwidth of 10Gbit/s. The chosen Ethernet protocol is UDP (User Datagram Protocol) instead of TCP/IP protocol, which is more bandwidth consuming.
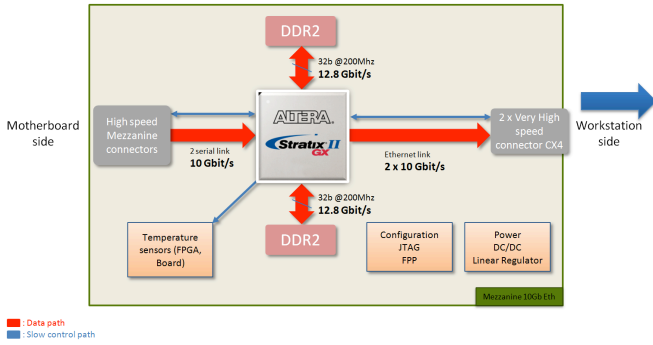
Fig 5. The Mezzanine board "ComEth 10G" architecture, with bandwidth indications.

Furthermore, the Ethernet link between the FPGA and the Ethernet board inside the workstation is a point-to-point link with a static IP address for each of them. The encapsulation of the Ethernet frame is performed by the FPGA [6] and corresponds to a custom implementation of the 10 Gbit Media Access Control (MAC). Figure 6 shows in more details the different blocks of the architecture implemented into the STRATIX FPGA. When the FPGA is powered on an ARP (Address Resolution Protocol) request is sent by the FPGA to verify if the Ethernet board of the workstation is on-line, then acquisition can start. Two communication ports are used, one for the slow control (transmission/reception) and the other for the transmission of the CDS frames (pixel values). The frames are received from the motherboard through two high-speed serial links (ALTERA Intellectual Property, Serial Light II). The bandwidth per link is 6.25 Gbit/s. The data used for the camera slow control are transmitted or received by a Serial Peripheral Interface (SPI) bus. See Figures 2 and 3 for more details.

The ComEth10G board used a DDR2 memory bank of 1Gb [4] for processing with two independent controllers (ALTERA Intellectual Property, DDR2 SDRAM controller). implemented into the FPGA. This combination of FPGA and memory banks offers an interesting processing capability before the data transmission. We use it for example to reconstruct the 800x800 image coming from 4 frames of 400x400 pixels in parallel. The power supply of the ComEth10G is independent from the motherboard therefore this board can work alone. Its total current consumption is 2.5 A with an input voltage of 9 Volts.
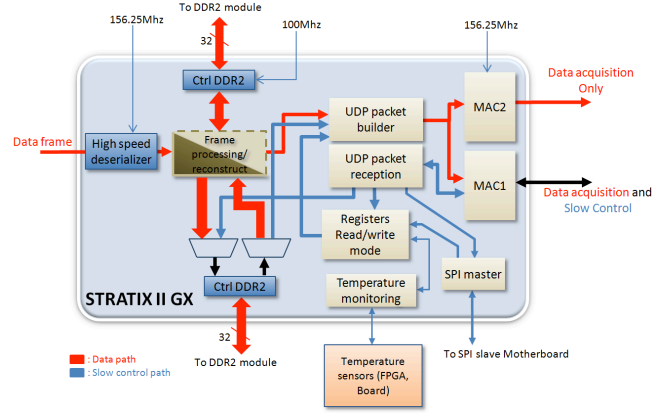
Fig. 6. The main architecture of the communication ComEth10 board. Notice that the two MACs offer a 2x10 Gbit/s data throughput. This daughter board has DDR memory banks connected to the FPGA for local computing of the data.

C. Slow Control daughter board

The slow control board performs the monitoring of the camera (see Figure 2). This board embeds a microcontroller (microchip) [7] to implement the monitoring functionalities and to communicate either to the FPGA or to the camera hardware (see [1] for more details). All data concerning the camera control is transmitted via the ComEth10G board for visualisation.

D. DAQ board performances

The simulation of the VHDL code has been performed with the ModelsSim software [8]. The synthesis of the firmware has been realised with Quartus II v9.0 from ALTERA [9]. To check the performance of the 10 Gbit/s Ethernet link a dedicated VHDL code has been developed to use the two MACs and the two CX4 Ethernet links connected together, as shown Figure 7.
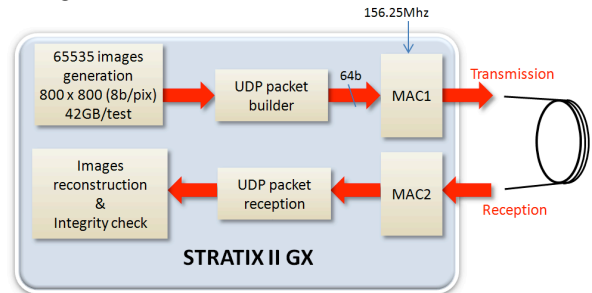
Fig. 7. FPGA architecture used to test the 10 Gbit/s Ethernet link.

One MAC is used for the emission of known frames with a true 10 Gbit/s rate and the other is used in reception. Figure 8 show the Ethernet packet transmission with no dead time. Each Ethernet packet is sent one after the other, to use the maximum bandwidth of the Ethernet link.

Fig. 8. Ethernet packet transmission, with no dead time.

A cross check of the data integrity is performed. In this configuration a true 10 Gbit/s data rate has been obtained without any error. A CX4 copper cable of 8 meters length (maximum) has been used for the tests.

An optical fibre link has been also produced and is under test. Then it will be possible to use this DAQ system for deported detectors (deep sea research for example).

The DAQ boards have been tested to read out the LUSIPHER camera. The maximum pixel clock of the chip (40 MHz) has been used to test the bandwidth. The bandwidth offered by the DAQ boards didn't show any saturation (buffer or FIFO full) even with the highest frame rate and an unlimited continuous readout is achieved.

IV. Software

A. The software platform

The computer is in charge of data reception, image processing and display. The flow is divided in two parts: one for the direct storage on hard disk, the other for the display. Many tasks are used on the second flow: image reconstruction from the received UDP packets, computation of the Signal to Noise Ratio (SNR) of each pixel, processing for the clustering, target tracking and display with slow motion or mean at 25 Hz. Therefore, the significant data flow between the DAQ board and the computer requires the use of a quite powerful hardware able to run a multithreaded application with optimized algorithms.

The choice fell on a Hewlett-Packard Z800 workstation with dual Intel Xeon X5660 multi-processors containing six 2.8 GHz cores each (QPI at 6.4 GT/s), 16 GB of memory (only in dual channel unfortunately) at 1333 MHz and a 10Gb Ethernet board from Mellanox Technologies [10]. The fast storage is done on a built-in RAID 512 GB SSD board from OCZ mounted on a PCIe 8X slot. A standard Linux Ubuntu 2.6.35 is used as operating system.

B. Implementation, optimization and performances

When working at 500 frames per second (maximum frame rate of LUSIPHER prototype), the whole processing chain must be covered in a 2 ms period. This is simply impossible for a single threaded application. Therefore multitasking is used. The most CPU consuming tasks are the SNR processing, clustering and display with processing (mean, auto-scaling, slow-motion viewing, target marker, target motion display). The CPU load for the most demanding computations has been reduced by a factor of four, thanks to the SSE (Streaming SIMD Extensions) instructions of the processors and to cache memory optimizations (use of aligned memory, unrolling, cache bypass, prefetching). The final performance after optimization, for an incoming flow of 2.56 Gbit/s (500 fps, 800*800 pixels, 8 bits/pixel), is 50% (600% of a core) of the CPU load for a real-time of about 1500 targets in the field of view.

The clustering tasks are spread on 7 cores, loaded at 55% each. The SNR computation and display tasks use one core each loaded at 60%. The CPU available (50%) can be used either to increase the number of targets to track in a frame or to increase the input data rate due.

We observed an interesting effect on the speedup of some tasks in spite of the high data rate of the QPI Bus by using NUMA for strategic memory allocation on specific nodes. The data storage task writes packets of 4 MB size and bypasses the Linux page cache to improve the write performance. It reaches a rate of 950 MB/s. The system is able to handle and compute a 6.7 Gbit/s rate without any loss of data. The next step consists of using GPU computing to prepare the next generation of DAQ board and Megapixels CIS.

V. Conclusion

We presented in this paper an acquisition system for CMOS imager with a true 10 Gbit/s bandwidth. The main components of the system are the acquisition boards. The design takes into account the need for the system to be opened for CIS sensors either with digital or analogue channels. Three boards composing the DAQ system, have been produced: a motherboard for the control and acquisition of the CMOS chip, the communication board for the encapsulation of the data before transmission to the workstation and a slow control board of the camera system. The architectures of the boards have been presented as well as the performances. The transmission rate shows a true 10 Gbit/s bandwidth. Memory banks have been added on each board to improve the imaging processing and simple algorithm implementation inside the FPGAs.

The acquisition software developed on a multiprocessor platform is able to sustain a 6.7 Gbit/s input rate. In the case of LUSIPHER ebCMOS (800 x 800 pixels), the 2.56 Gbit/s input rate is easily managed with a CPU load of 50% of the 12 cores. Figure 9 show a image capture of a film on the study of swimming bacteria E. Coli. Nevertheless more optimizations are foreseen to increase the bandwidth up to 40 Gbit/s. Indeed, it is the mandatory data rate for an acquisition of a megapixels CMOS at 1 kHz frame rate. A genuine bandwidth of 40 Gbit/s with in-line algorithm and a continuous acquisition of a megapixel CIS is now the target of this development.
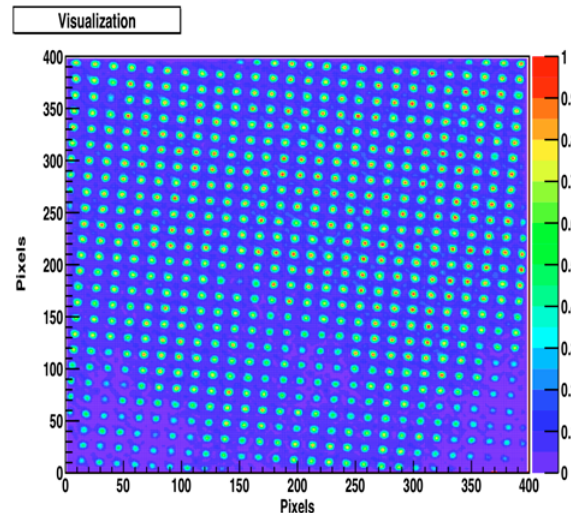
Fig. 9. Image capture of a film on the study of swimming bacteria E. Coli (Frame rate is 500 frame per second…)

REFERENCES

[1] R. Barbier et. al., A single-photon sensitive ebCMOS camera: The LUSIPHER prototype, Nucl. Instr. And Meth. A 648 (2011) 266–274.
[2] Analog Device AD9222.
[3] ALTERA EP1AGX90EF1152.
[4] Micron MT47H32M16; Micron -Micron « TN-47-16: Designing for High-Density DDR2 Memory»;
Micron « TN-47-19: DDR2 (Point-to-Point) Features and Functionality»;
Micron « TN-47-01 DDR2 DESIGN GUIDE FOR TWO-DIMM SYSTEMS».
[5] ALTERA MAX II EPM1270F256.
[6] ALTERA STRATIX II GX EP2SGX90FF1500.
[7] Microchip, Ref. PIC 18F4550.
[8] MentorGraphics, ModelsSim SE v6.3.
[9] ALTERA, QUARTUS II v9.0.
[10] Mellanox Ethernet Board MNEH29-XTC.

F.4   Publications sur l'ebMIMOSA5

**First Results from the development of a new generation of
Hybrid Photon Detector: EBCMOS** [1]

R. BARBIER[2], P. DEPASSE

Université de Lyon, Université Lyon 1, Lyon, F-69003, France ; Institut de
Physique Nucléaire de Lyon, CNRS/IN2P3, Villeurbanne, F-69622, France

J. BAUDOT, W. DULINSKI, M. WINTER

IPHC-IN2P3, Université Louis Pasteur Strasbourg, 23 rue du Loess, Strasbourg
F-67037, France

N. ESTRE*, N. LAURENT*, C.T. KAISER†

* PHOTONIS France SAS, avenue Roger Roncier BP 520, 19106 Brive cedex,
France; † PHOTONIS Netherlands BV, Roden B.O. Box 60, 9300 AB Roden, The
Netherlands

S. KATSANEVAS

IN2P3-CNRS, 3 Rue Michel Ange, Paris, 75016, France

Abstract

The proximity focusing Hybrid Photon Detector (HPD) concept is im-
plemented to develop a single photon sensitive Electron Bombarded CMOS
(EBCMOS). The first demonstrator has been produced by the collaboration
between the EBCMOS group of IPNL, the CMOS sensor group of IPHC and
the R&D department of PHOTONIS. The prototype characteristics (dark
current, gain, spatial and energy resolutions) are presented. The futur devel-
opments of this type of photo detector are discussed.

1   Introduction

This development is related to the design and the integration of a Monolithic Active
Pixel Sensor (MAPS) into a photosensitive proximity focusing vacuum-based tube.
This Hybrid Photo Detector is dedicated to the fluorescent and the bioluminescent
high speed imaging. The project is developed within the framework of the GIS
(Grouping of Scientific Interest) PHOTONIS-IN2P3.

The first goal of this project was to produce and characterize a demonstrator based
on a large scale back-thinned MAPS, sensitive to a single photon with a micrometric
spatial resolution.

2   The EBCMOS demonstrator

2.1   Demonstrator description

The Minimum Ionizing MOS Active sensor (MIMOSA [1]) chips are developed
by the IPHC team and are dedicated to the tracking of the charged particles in
HEP experiments. The first mega-pixel sensor (17 μm pitch, 1024x1024 pixels, 3.5
cm^2) of the MIMOSA chip family, named MIMOSA5[2], have been back-thinned
(MIMOSA5B[3]) and post-processed in order to be sensitive to low energy electrons.
This process has been done within the framework of the SUCIMA FP5 European
Project[4]. The precise characteristics of MIMOSA5B and his capabilities on low
energy electron detection are presented in Refs [3, 6, 5].

The back-thinned MIMOSA5B chip is mounted in the die cavity of a ceramic carrier.
The cathode-sensor gap is of the order of one millimeter. A tunable high voltage
is put on the cathode ($\leq$ 10 kV). The cathode is a standard multi-alkali S20 type

---

[1]Contribution to ICATPP 2007 Como 8-12 october 2007.
[2]Corresponding author: rbarbier@ipnl.in2p3.fr
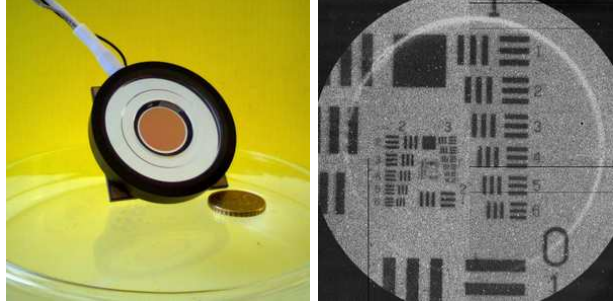
Figure 1: On the left, the demonstrator EBMIMOSA5 with S20 photocathode. On the right, example of a *1951 USAF* resolution test chart imaging. The USAF target is mounted on a binocular with a magnification factor equals to 1.3. The illumination is tuned to 200 μLux and the high voltage to 4 kV.
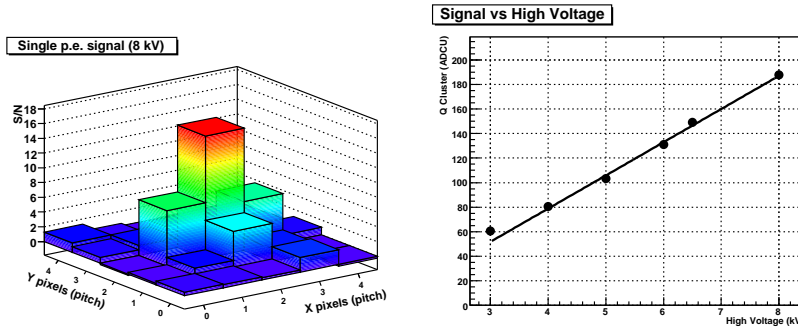
Figure 2: On the left, signal over noise ratio of 25 pixels for a single photo-electron event at HV=8 kV: the charge sharing around the central pixel (called *seed*) is clearly visible. On the right, linearity of the sensor response *w.r.t* the high voltage.

and provides a quantum efficiency equals to $15 \pm 2\%$ for a 520 nm wavelength. A picture of the first EBMIMOSA5 is presented in Fig. 1. The sensor encloses the cathode with a useful diameter of 18 mm.

2.2   Photo-electron response and gain linearity

The first characterization of the demonstrator is dedicated to single photo-electron energy measurement. The readout method and signal processing of MIMOSA5 are presented in Ref. [7]. The readout clock is fixed at 10 MHz which corresponds to 27 ms exposure time for one frame. The signal selection is performed on a seed pixel and the charge deposited by the photo-electron is measured by the charge sum over the 5x5 pixels. The figure 2 shows the *signal-over-noise* ratio of the 25 pixels for a single photo-electron event. In the same figure, the linearity of the response with respect to the high voltage (3-8 kV) is presented.

2.3   Dark Current measurement.

The drawback of proximity HPDs is the dark current from the cathode due to thermionic or field effects. The dark current obtained at 6 kV and 10°C is equal to 650 $\pm$ 25 photo-electrons per 27 ms per 2.5 cm^2. This corresponds to a dark current rate close to 100 Hz/mm^2. Cooling the EBCMOS window from 20°C to

2
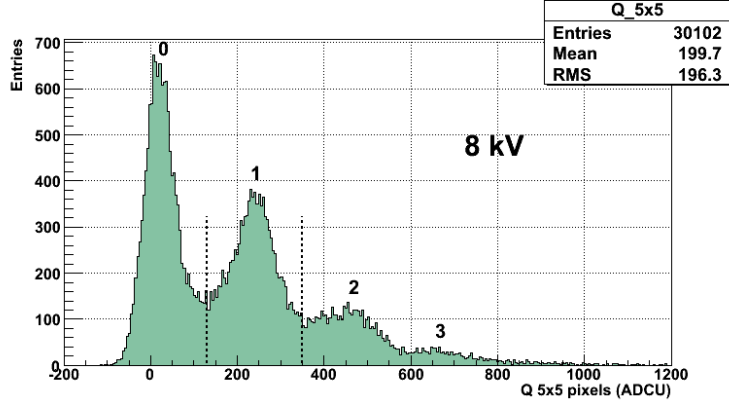
Figure 3: Multi-photo-electron spectrum in ADC unit for the 5x5 pixel cluster.

10°C reduces the dark current by a factor of 2. No real improvement is observed when cooling below 10°C.

2.4 Spatial resolution

The point-spread function (PSF) of the tube is characterized with an optical test bench which provides a 2 μm diameter spot[3] on the photocathode plane. The spot can be precisely positionned with a 3D micro-controlled displacement. The pulse duration of the LED source is calibrated and fixed to 500 ns in order to obtain an average of one photo-electron into a selected sub-window (5x5 pixels). The PSF is obtained by computing, for single photo-electron events, the distribution of the position of the seed pixel. A Full Width at Half Maximum equals to 27.1 $\pm$ 0.1 μm has been measured at HV=8 kV.

2.5 Photon counting capability

One of the strong advantage of EBCMOS against EMCCD is its capability to count the number of photo-electrons in the same cluster. Figure 3 presents the charge sum over the 5x5 sub-window without any seed selection. The histogram exhibits a well defined Poisson distribution of the photo-electrons peaks. The peaks corresponding to 0, 1, 2 and 3 photo-electron events are resolved.

3 Conclusion and Future plane

3.1 Tracking concept for bioluminescence and fluorescence imaging.

The first results obtained on the EBMIMOSA5 demonstrate the concept of proximity focusing vacuum-tube on a back-thinned CMOS sensor. Single photon and multi-photon sensitivity with 27 μm resolution (FWHM) has been obtained with a back-thinned chip which is not optimized for this application. The characterization of the demonstrators is now focused on the main goal of this project: the tracking of fluorescent molecules. Cross comparisons between existing devices on fluorescence

---

[3]The spot is obtained by imaging a 100 μm diameter pinhole through an inverted MITUTOYO long working distance 50X objective.

imaging of cell division (in zebrafish eggs) and on bioluminescence of calcium flow in drosophila brain are scheduled for the end of 2007.

3.2   Future plans

To overcome the limitation of the MIMOSA5 for the considered applications, we will produce in 2008 a Large-scale Ultra-fast SIngle PHoton trackER (LUSIPHER) with a dedicated back-thinned CMOS chip (medium-scale 400x800 pixels, 10 μm pitch, 8 analogue outputs and 40 MHz clock frequency, ST 0.25 μm process). A new acquisition ethernet board is currently developed to achieve 1000 frames per second (the equivalent data flow is equal to 3.6 Gb/s). LUSIPHER will be our first prototype dedicated to ultra-fast single photon tracking in fluorescence and bioluminescence experiments of single molecule tracking.

4   Acknowledgments

References

[1] R. Turchetta, et al., *Nucl. Instr. and Meth. A* **458** 677 (2001).

[2] Yu. Gornushkin, et al., *Nucl. Instr. and Meth. A* **513** 291 (2003).

[3] G. Deptuch, *Nucl. Instr. and Meth. A* **543** 537 (2005).

[4] M. Caccia, et al., *Nucl. Phys. B (Poc. Suppl.)* **125** 133 (2003).

[5] G. Deptuch, *Nucl. Instr. and Meth. A* **570** 165 (2007).

[6] W. Dulinski, *Nucl. Instr. and Meth. A* **546** 274 (2005).

[7] G. Claus, et al., *Nuclear Science Symposium Conference Record, 2004 IEEE 16-22 Oct.,* **Vol. 3** 1512 (2004).

Performance study of a MegaPixel single photon position sensitive photodetector EBCMOS

Rémi Barbier [a,*], J. Baudot [d,e], E. Chabanat [b,c], P. Depasse [b,c], W. Dulinski [d,e], N. Estre [b,c], C.T. Kaiser [f], N. Laurent [f], M. Winter [d,e]

[a] IPNL, 4 rue E. Fermi 69622 Villeurbanne Cedex, France
[b] Université de Lyon, Université Lyon 1, Lyon F-69003, France
[c] CNRS/IN2P3, Institut de Physique Nucléaire de Lyon, Villeurbanne F-69622, France
[d] Université Louis Pasteur Strasbourg, Strasbourg, France
[e] CNRS/IN2P3, Institut Pluridisciplinaire Hubert Curien, Strasbourg F-67037, France
[f] PHOTONIS SAS, 19106 Brive, France

ARTICLE INFO

ABSTRACT

This development is related to the design and the integration of a Monolithic Active Pixel Sensor (MAPS) into a photosensitive proximity focusing vacuum-based tube. This EBCMOS project is dedicated to the fluorescent and the bioluminescent high speed imaging. The results of the full characterization of the first prototype are presented. Comparative tests with different fluorescent dyes have been performed in biology laboratories. Preliminary conclusions on the ability of EBCMOS to perform fast single-molecule tracking will be given.

© 2009 Elsevier B.V. All rights reserved.

1. Introduction

Integrating an electron-bombarded back thinned Monolithic Active Pixel Sensor (MAPS) into a vacuum tube associated with a photocathode (EBCMOS) is one way to develop a new generation of single photon sensitive detector. Furthermore the MAPS, based on CMOS technology, are very promising pixel detectors for ultra-fast readout and real-time signal processing. Combining these advantages, photon counting ability at very high frame rate could push the EBCMOS detectors beyond the state of the art in multipixels single photon detection [1].

The first EBCMOS demonstrator has been produced by a collaboration consisting of the EBCMOS group (IPNL), the CMOS sensor group (IPHC) and the PHOTONIS company.

We report in the first section on the complete characterization of this prototype. The second one is devoted to tests of the device for imaging of fluorescent dyes. Images have been obtained on standard epifluorescence microscopes used in biology laboratories. Finally, the preliminary conclusions on the performances of the demonstrators and the future R&D plans are discussed.

2. Characterization of the EBCMOS demonstrator

2.1. Prototype description

The Minimum Ionizing MOS Active sensor (MIMOSA) chips, developed by the IPHC team, are dedicated to the tracking of charged particles in High Energy Physics experiments. The first mega-pixel sensor (17 μm pitch, 1024×1024 pixels, 3.5 cm^2) of the MIMOSA chip family, named MIMOSA5 (the chip design is presented in Refs. [2,3]), has been back-thinned and post-processed to be sensitive to low energy electrons [4,5]. The back-thinned MIMOSA5 chip is mounted in a die cavity of a ceramic carrier. A tunable high voltage (useable range is 5–10 kV) is set between the cathode (18 mm diameter) and the sensor over a sub-millimeter gap. The cathode is a standard multi-alkali S20 type and provides a quantum efficiency equal to $15 \pm 2\%$ for wavelength of 520 nm.

2.2. Characterization results

The first characterization of the demonstrator is dedicated to single photo-electrons energy measurement. The signal selection is performed on a seed pixel and the energy deposited by the photo-electron is obtained by the sum of the charge over the 5×5 pixels around the seed. The averaged sensitivity to photo-electrons, which is expressed in signal-over-noise-ratio units is equal to 18 on the seed pixel for HV = 8 kV (see Fig. 1).

* Corresponding author.
  E-mail address: rbarbier@ipnl.in2p3.fr (R. Barbier).
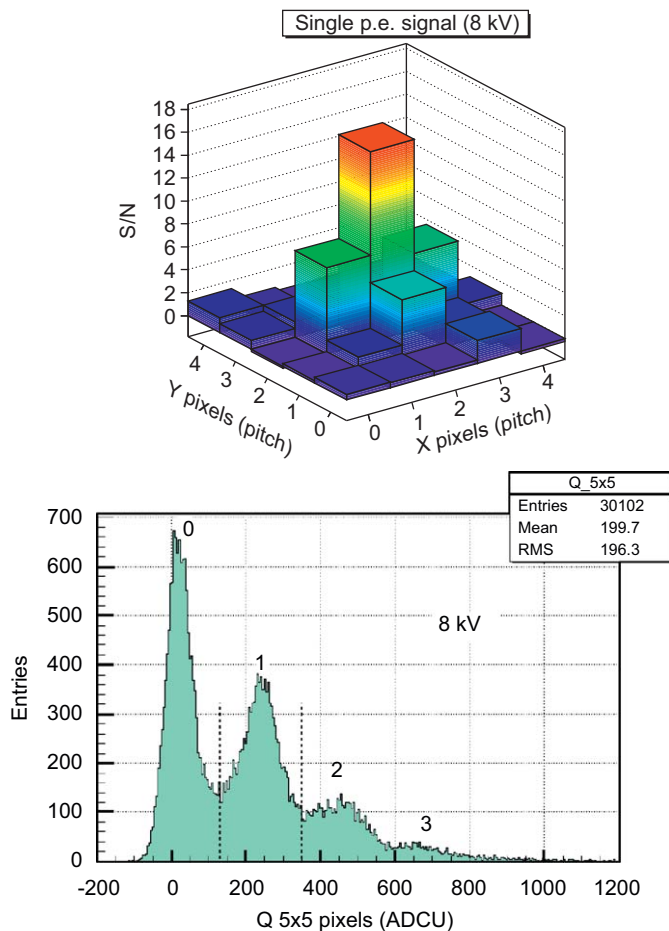
Fig. 1. 2D signal over noise distribution of a photo-electron event (top) and the multi-photo-electron spectrum in a 5×5 pixel cluster (bottom).

The dark count, due to the photocathode emission, has been measured for different temperatures and high voltages. Typical number of dark counts obtained at 6 kV and 10 °C is equal to 650 ± 25 photo-electrons per 27 ms per 2.5 cm^2. This corresponds to a dark count rate close to 100 Hz/mm^2. Cooling the EBCMOS window from 20 to 10 °C reduces the dark current by a factor of 2. No real improvement is observed when cooling below 10 °C.

The point-spread function (PSF) of the tube is characterized with an optical test bench which projects a 1 μm diameter spot on the photocathode. The pulse duration of the LED source is calibrated to obtain a Poisson distribution with an average of one photo-electron into a selected sub-window (5×5 pixels). The PSF is obtained by computing the distribution of the position of the seed pixel corresponding to a single photo-electron event. A Full Width at Half Maximum equal to 27.1 ± 0.1 μm has been measured at HV = 8 kV. A variation of 3 μm on the FWHM has been measured between 6 and 8 kV working points.

The photo-electrons counting ability is illustrated in Fig. 1: the histogram exhibits the Poisson distribution of the detected photo-electrons with peaks corresponding to 0–3 photo-electron events.

## 3. Imaging of fluorescent dyes with microscopes

Tests on fluorescence imaging have been performed at IGBMC [6] on a Leica DMRXA2 microscope and at ENS-LKB [7] on a Nikon Eclipse Ti microscope. Epifluorescence microscopy was tried varying the excitation wavelength as well as the intensity. Fluorescent dyes emitting in different wavelength from red to blue (GFP, mitotracker, Hoescht, and Sytogreen) were fixed into cells to be used for our sensitivity tests. Resolution has been studied with standard fluorescent beads deposited on glass. Imaging of CdSe Quantum Dots (QDs) fixed on the membrane of Hela Cells has been performed to give some hints on single molecule detection capabilities. The well-known blinking effect of a single QD has been observed.

The main goals of the fluorescence imaging tests were

- evaluate the sensitivity and the spatial resolution of the EBMI5 compared to Standard CCD and Electron Multiplying (EM) CCD (sensitivity, resolution, dark count) [8];
- evaluate EBMI5 under single photon experiment condition and extrapolate the signal processing strategy to work at least at 1 kHz frame rate (dynamics, occupancy rate, temporal filtering).

Our prototype EBMI5 has been compared to a standard cooled CCD (CoolSNAP HQ2) and EMCCD (Cascade 2) from Roper Scientist at IGBMC and with EMCCD Ixon DU 897 BI from ANDOR at ENS Biology laboratory.

The two cameras (EBMI5 and CCD or EMCCD) were put on the same microscope with the possibility to switch from one to the other. Therefore the imaging light condition was identical for the same field of view. The EMCCDs were used with different Electron Multiplication Gain (EMGain) up to the maximum for single photon condition imaging. Almost the same integration time than EBMI5 (27 ms) was set on EMCCD (25 ms).

We summarize the results obtained from the data analysis in what follows:

Sensitivity and dark count:

- The EBMI5 has a better sensitivity than standard cooled CCD in the whole VIS spectrum.
- The EBMI5 is competitive to EMCCD in the green spectrum where the QE is optimized. EBMI5 is less sensitive than EMCCD for CdSe emission at 605 nm and 8% of cathode QE. The next cathode production for EBCMOS prototype should be optimized between the red and the green part of the VIS spectrum.
- The background due to the dark count of the device is lower than 10% of the total background (mainly the photon noise coming from the microscopes and from off-focus fluorescent dyes).
- EBMI5 device has an equivalent (and for some cases better) contrast than EMCCD.
- In more intense light condition the HV can be lowered and keeping a good image quality. Since the CMOS is back illuminated with the photons which pass the cathode an image composed of photons and photo-electrons is obtained. We discover during our tests that this configuration could be used in biological experiment where high light condition should be used continuously with ultra low light or single molecule tracking.
- As can be expected, single photon imaging is very sensitive to photon background coming from off-focus dyes. Algorithm such as Kalman filter [9] has been implemented off-line to reduce dark count which is spatially and temporally randomly distributed on the CMOS.
- Ion feedback, a well-known effect of HPD [10], has been characterized and should be filtered in our next acquisition software.
- The limited dynamical range of the pixels (1–30 photo-electron at 8 kV) has to be be compensated by the increase of the frame rate. Furthermore the incoming number of photons has to be compatible with single molecule detection, therefore we

expect, for the next device, an occupancy rate of the pixels smaller than 10%.

Resolution:

- The resolution of the EBCMOS is related to the convolution of two point-spread functions: the photo-electron PSF of the tube itself and the PSF of the CMOS sensor due to charge sharing between pixels. The first one is dominant (see Section 2.1) because some clustering algorithm (Center of Gravity of pixel charges) can reduce the second down to few microns [2]. We tested deconvolution method with standard software [11] to improve the resolution. An example of the results obtained on GFP imaging of root of lily cells is shown in Fig. 2.
- The imaging of latex beads at the diffraction limit of the microscope shows a resolution on the beads: $\sigma = 245 \pm 30$ nm. This result has to be compared to the very good resolution of the coolSNAP HQ2, $\sigma = 130 \pm 15$ nm, due to a pitch of 6.5 μm.

Single molecule imaging and on-line processing:

- The blinking of a QD has been observed. The effect of the implemented filtering algorithm [9] is shown in Fig. 3. This first off-line results on QDs imaging is a good starting point to implement on-line QDs tracking into the future acquisition system based on FPGAs.

As a general conclusion we can say that EBCMOS is a device with very good single photon sensitivity-low noise and fast readout. It gives the possibility to improve the performances of target tracking on a large field of view by taking advantages from this intrinsic qualities by on-line signal processing. An improvement of background rejection and spatial resolution is expected from on-line software developments keeping in mind that ultra fast frame
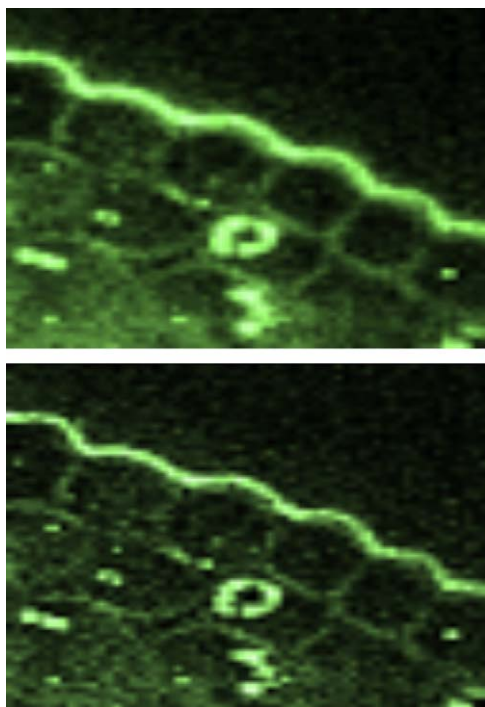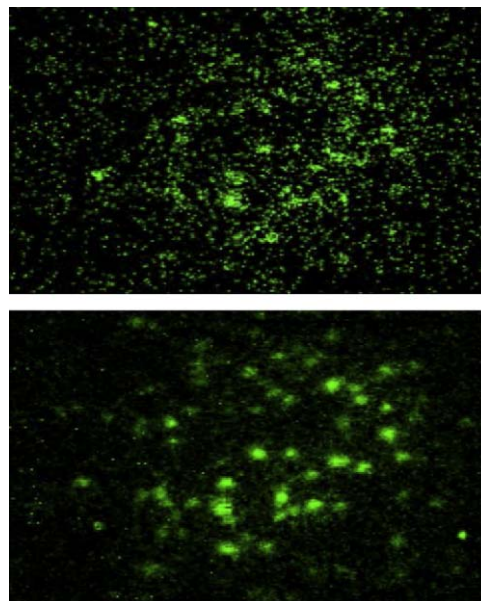
Fig. 3. Left: image of QDs fixed on Hela cell. Right: the same image with pixel-by-pixel Kalman filter. The two images correspond to a window of 200 × 200 pixels. Magnification of the microscope was set at ×100.

rate allows more processing to be performed at the level of the quantum basic element of an image: the single photon.

4. Future plans

To overcome the limitation of the MIMOSA5 for the considered applications, we will produce in 2009 a Large-scale Ultra-fast SIngle PHoton recordER (LUSIPHER) with a dedicated back-thinned CMOS chip (medium-scale 400 × 800 pixels, 10 μm pitch, 8 analogue outputs and 40 MHz clock frequency). A new acquisition ethernet board is currently developed to achieve 1000 frames per second (the equivalent data flow is equal to 3.6 Gb/s). LUSIPHER will be applied to single molecule tracking in fluorescence and bioluminescence experiments.

Acknowledgements

References

[1] R. Barbier, et al., in: Proceedings of the ICATTP Conference, Como, Italy, 8–12 October 2007.
[2] R. Turchetta, et al., Nucl. Instr. and Meth. A 458 (2001) 677.
[3] G. Deptuch, et al., Nucl. Instr. and Meth. A 511 (2003) 240;
Yu. Gornushkin, et al., Nucl. Instr. and Meth. A 513 (2003) 291.
[4] W. Dulinski, Nucl. Instr. and Meth. A 546 (2005) 274.
[5] M. Caccia, et al., Nucl. Phys. B (Poc. Suppl.) 125 (2003) 133.
[6] IGBMC stands for Institut de Génomique et de Biologie Moléculaire et Cellulaire, Unit Mixte de Recherches CNRS/Inserm/Universit Louis Pasteur Strasbourg.
[7] ENS stands for Ecole Normale Suprieure, LKB stands for Laboratoire Kastler Brossel, Paris.
[8] EMCCD from Roper can be found on roperscientific.fr and from Andor on ⟨www.andor.com⟩.
[9] R.E. Kalman, J. Basic Eng. 82 (1) (1960) 35.
[10] T. Gys, et al., Nucl. Instr. and Meth. A 355 (1995) 386.
[11] ImageJ software plugin for deconvolution ⟨http://piotr.wendykier.googlepages.com/spectraldeconvolution⟩.

Fig. 2. Top: zoom (200 × 150 pixels) on a raw image from lily cells tagged with GFP. Bottom: the same image after PSF deconvolution. Magnification of the microscope was set at ×40.

CONCLUSION

L E domaine de la détection aux photons uniques et les applications qui en découlent est particulièrement actif depuis quelques années et cette activité ne fera qu'augmenter dans les années à venir quelque soit le domaine de longueurs d'onde considéré, UV, VIS ou NIR. Les raisons de cette tendance peuvent être identifiées en partie :

- Evolution des technologies de détection et de multiplication du signal et de diminution des bruits de détection.

- Evolution du cahier des charges des capteurs vers une photodétection plus fine, c'est-à-dire limitée uniquement par le "shot-noise", avec des cadences d'images en augmentation.

- Evolution vers une sensibilité accrue par le fait que les phénomènes observés sont obtenus dans des conditions où la quantité de lumière émise par la source ne peut être augmentée. Je pense ici à la compatibilité des sources et de leur intensité d'excitation de fluorescence dans les milieux biologiques (dommages photoniques, photo-stabilité ...).

- Evolution vers une meilleure quantification de l'image observée avec génération d'informations supplémentaires à partir des données brutes des pixels (super-résolution, Shack-Hartmann...). La limite à atteindre est le comptage de photons. Celui-ci n'est pas compatible avec certains processus de multiplication de charges et nécessite, soit une augmentation de la fréquence d'acquisition soit une diminution du flux pour éviter la perte d'efficacité du comptage de photons véritables.

- Evolution vers un abaissement des seuils de détection de phénomènes soudains et transitoires pour une surveillance sans perte en condition de bruit minimum. Je pense bien évidemment aux phénomènes de bioluminescence.

- Evolution vers une augmentation du débit de données stockées mais aussi traitées en temps réel au plus proche du volume de détection.

- Evolution de la fréquence d'images pour permettre une imagerie 3D.

- Evolution vers une imagerie "quantique" où la corrélation entre photons permet la diminution du bruit en dessous du bruit de Poisson.

Je suis persuadé que la liste pourrait être allongée et s'enrichira d'ici peu.

Ce mémoire d'habilitation à diriger des recherches a tenté de donner quelques réponses ou quelques points de vue sur cette évolution constatée, pour laquelle j'ai également œuvré.

C'est pourquoi le premier chapitre, qui est divisé en deux parties, comporte d'une part une revue simplifiée, voir parfois synthétique, des différents concepts de détection utilisés pour atteindre la sensibilité aux photons uniques en imagerie et propose d'autre part une étude plus détaillée de l'ebCMOS qui va au delà de mon activité propre de R&D. Les perspectives d'évolution de ce capteur ont été abordées et n'engagent que ma compréhension du domaine. En effet, l'évolution de l'ebCMOS dans le domaine de l'imagerie scientifique dépend (force et faiblesse de cette R&D académique) de domaines industriels dont les choix stratégiques sont parfois obscurs ou uniquement guidés par un gain à très court terme.

Le deuxième chapitre est complètement dédié à la description des activités du groupe ebCMOS. Tout d'abord, cela concerne nos bancs de tests et nos méthodes de caractérisation que nous continurons de développer dans le cadre de projets collaboratifs avec des industriels des capteurs CMOS. L'évolution des technologies CMOS avec gain rend nécessaire l'évolution en parallèle des moyens de caractérisation et je pense qu'il est possible de progresser de manière significative dans les deux années à venir. J'ai ensuite présenté les deux prototypes produits avec de multiples partenaires. Une description précise de toutes les étapes de fabrication des prototypes fabriqués, ebMIMOSA5 et LUSIPHER, ne pouvait être faite dans le cadre de ce mémoire et restera finalement uniquement dans les esprits de ceux qui ont vécus cette aventure avec moi.

Ce chapitre se termine par la présentation des différentes applications que nous avons abordées dans nos tests sur site. Pour chacune d'elle, une publication, au minimum, doit être réalisée dans une revue du domaine considéré afin d'assurer le retour scientifique de notre R&D. Nous sommes sur la bonne voie. Mon investissement et celle de l'équipe sur la caractérisation de capteurs IR pour l'expérience du télescope spatiale EUCLID ne doit pas infléchir notre dynamique de production scientifique mais fait partie d'une évolution "naturelle" de nos activités. Néanmoins, il faut toujours ce méfier des arguments de "naturalité" dans la bouche d'un physicien...

Je n'ai jamais conçu mon engagement comme étant un exercice de style ou une R&D fondamentale permettant simplement de faire du management de projet sans lendemain. Notre activité du groupe ebCMOS ira le plus loin possible dans les applications testées.

Mais la question la plus sensible après celle du choix des collaborations scientifiques reste de savoir si le prolongement de cette activité, qui est d'une certaine manière allée "trop" loin dans l'élaboration d'un "concept-produit", est possible ou souhaitable dans un cadre académique.

Nous sommes ici sur une frontière mal définie où les intérêts de nombreux acteurs soci-économiques et scientifiques supplantent la prise en compte des contingences fortes subit par le chercheur alors que celui n'est qu'un catalyseur de la propriété intellectuelle diffuse d'un domaine de recherche. Le passage d'une valeur scientifique et technique à une valeur économique et financière est encore très empirique dans l'esprit des acteurs de ce domaine du transfert.

Plus nous avançons dans l'exploration des applications de l'ebCMOS plus l'intérêt scientifique croît et plus nous nous rapprochons d'une possible industrialisation. C'est un paradoxe pour le chercheur qui évitera la réponse rationnelle et binaire. Le plus longtemps

possible, il évitera le principe du tiers exclu.

Enfin je voudrais conclure par une description ironique, amusée et porteuse de sens, d'une vision introspective de la pratique de la recherche par la conduite de projets. Il s'agit de la propension des chercheurs "dynamiques" à déposer chaque année de nombreuses demandes de financement liées à l'évolution du pilotage de la recherche. La plupart ne sont pas couronnées de succès. Cela explique en partie la nécessité de l'augmentation du nombre de dépôts.

Dans quel état se trouve un chercheur "dynamique", lorsqu'il vient de déposer sa demande de budget, après un travail acharné pour la préparer avec ses partenaires ?

Il est au fond de lui heureux...

pas seulement par la satisfaction du travail bien fait (assez rare), mais plutôt par la sensation enivrante d'être "potentiellement millionnaire" (le plus souvent demi-millionnaire). Il restera dans cet état au moins six mois de l'année. Pendant cette période d'attente insoutenable, on a pris soin de l'occuper à expertiser d'autres demandes. En qualité d'expert et entre experts, c'est un devoir.

Puis, comme la majorité des porteurs de projets "dynamiques", il apprend qu'il n'est pas sélectionné... Non pas par manque d'excellence de celui-ci, dixit le rapport qu'il recevra plus tard, mais par ce que d'autres nombreux projets sont encore plus excellents.

Après l'abattement ressenti par la perte de "son" demi-million virtuel et de voir repoussé, d'un an au moins, ses perspectives scientifiques, qu'il a si difficilement chiffrées par des diagrammes de Gantt composés de centaines de tâches, il repartira sur la recherche de nouvelles alliances pour monter un dossier encore plus solide et plus ambitieux et plus couteux afin cette fois de décrocher le gros-lot... C'est la réponse positive à l'échec et c'est préférable au prozac !

Dans tous les cas, si l'on pouvait chiffrer la quantité d'énergie dépensée dans ce rituel annuel, tant dans le montage que dans l'expertise des projets, on serait vraisemblablement, en bon gestionnaire de la recherche, dans un constat d'efficacité quasi-nulle.

Ce constat n'est évidemment pas vrai pour les quelques "privilégiés" qui ont la chance de rentrer dans le scope de la politique nationale certainement justifiée de l'aménagement du territoire, ou des chercheurs qui, quelle que soit l'usine à gaz, sont brillants.

Qu'il s'agisse d'un effet collatéral ou d'une simple opportunité politique, la gestion de la pénurie que je ne considère non pas dans l'absolu mais en rapport du facteur de pression des projets, nous sommes arrivés à une situation où les acteurs de la recherche française s'occupent entre eux et à moindre "frais". Du moins jusqu'au minimum possible c'est-à-dire la masse salariale !

Cela nous permet de rester, sur le papier au moins, sur les demandes de financements surtout, dans la course à **l'excellence mondiale**.

Bibliographie

[1] G. Brida, M. Genovese, and I. Ruo Berchera, "Experimental realization of sub-shot-noise quantum imaging," *Nature Publishing Group*, vol. 4, pp. 227–230, Feb. 2010.

[2] R. J. McIntyre, "Multiplication Noise in Uniform Avalanche Diodes," *IEEE Transactions on Electron Devices*, vol. 13, pp. 164–168, Jan. 1966.

[3] R. J. McIntyre, "The distribution of gains in uniformly multiplying avalanche photodiodes : Theory ," *IEEE Transactions on Electron Devices*, vol. 19, pp. 7003–713, Jan. 1972.

[4] R. H. Haitz, . Goetzberger A, R. M. Scarlett, and S. W, "Avalanche Effects in Silicon p—n Junctions. I. Localized Photomultiplication Studies on Microplasmas ," *J. Appl. Phys.*, vol. 34, pp. 1581–1591, Apr. 1963.

[5] J. Ninković, L. Andriček, C. Jendrisyk, G. Liemann, G. Lutz, H.-G. Moser, R. Richter, and F. Schopper, "The first measurements on SiPMs with bulk integrated quench resistors," *Nuclear Inst. and Methods in Physics Research, A*, vol. 628, pp. 407–410, Feb. 2011.

[6] G. Q. Zhang, X. B. Hu, C. Z. Hu, D. P. Yin, K. Liang, R. Yang, and D. J. Han, "Demonstration of a silicon photomultiplier with bulk integrated quenching resistors on epitaxial silicon," *Nuclear Inst. and Methods in Physics Research, A*, vol. 621, pp. 116–120, Sept. 2010.

[7] E. Charbon, "CMOS integration enables massively parallel single-photon detection," *SPIE Newsroom*, Mar. 2011.

[8] L. Neri, S. Tudisco, L. Lanzanò, F. Musumeci, S. Privitera, A. Scordino, G. Condorelli, G. Fallica, M. Mazzillo, D. Sanfilippo, and G. Valvo, "Design and characterization of single photon avalanche diodes arrays," *Nuclear Inst. and Methods in Physics Research, A*, vol. 617, pp. 432–433, Apr. 2010.

[9] T. Frach, G. Prescher, C. Degenhardt, R. de Gruyter, A. Schmitz, and R. Ballizany, "The Digital Silicon Photomultiplier - Principle of Operation and Intrinsic Detector Performance," pp. 1–7, Nov. 2009.

[10] B. Fowler, C. Liu, S. Mims, J. Balicki, W. Li, H. Do, and P. Vu, "Proceedings of SPIE," in *SPIE Defense Security and Sensing ; Infrared Technology and Applications XXXV*, pp. 72981D–72981D–12, SPIE, 2009.

[11] M. S. Robbins and B. J. Hadwen, "The noise performance of electron multiplying charge-coupled devices," *IEEE Transactions on Electron Devices*, vol. 50, pp. 1227–1232, May 2003.

[12] J. N. Hollenhorst, "A theory of multiplication noise," *IEEE Transactions on Electron Devices*, vol. 37, pp. 781–788, Apr. 1990.

[13] R. Hartmann, W. Buttler, H. Gorke, S. Hermann, P. Holl, N. Meindinger, H. Soltau, and L. Strüder, "A high-speed pnCCD detector system for optical applications," *Nuclear Inst. and Methods in Physics Research, A*, vol. 568, pp. 118–123, Nov. 2006.

[14] T. Ohnuki, X. Michalet, W. S. Tripathi, A, and K. Arisaka, "Proceedings of SPIE," in *Proc. of SPIE Ultrasensitive and Single-Molecule Detection Technologies*, pp. 60920P–60920P–9, SPIE, 2006.

[15] X. Michalet, O. Siegmund, J. Vallerga, P. Jelinsky, J. Millaud, and S. Weiss, "Photon-counting H33D detector for biological fluorescence imaging," *Nuclear Inst. and Methods in Physics Research, A*, vol. 567, pp. 133–136, Nov. 2006.

[16] J. S. Lapington and T. Conneely, "Multi-channel picosecond photon timing with microchannel plate detectors," *Nuclear Inst. and Methods in Physics Research, A*, p. doi :10.1016/j.nima.2010.11.175, Mar. 2011.

[17] A. Ronzhin, M. G. Albrow, M. Demarteau, S. Los, S. Malik, A. Pronko, E. Ramberg, and A. Zatserklyaniy, "Development of a 10ps level time of flight system in the Fermilab Test Beam Facility," *Nuclear Inst. and Methods in Physics Research, A*, vol. 623, pp. 931–941, Nov. 2010.

[18] A. Suzuki, S. Aoki, J. Haba, M. Sakuda, and M. Suyama, "Novel large aperture EBCCD," *Nuclear Inst. and Methods in Physics Research, A*, vol. 628, pp. 260–263, Feb. 2011.

[19] C. D'Ambrosio and H. Leutz, "Hybrid photon detectors," *Nuclear Inst. and Methods in Physics Research, A*, vol. 501, pp. 463–498, Apr. 2003.

[20] M. Alemia, M. Campbell, T. Gys, B. Mikulec, D. Piedigrossi, E. Puertolas, D.and Rosso, R. Schomaker, W. Snoeys, and K. Wyllie, "First operation of a hybrid photon detector prototype with electrostatic cross-focussing and integrated silicon pixel readout," *Nuclear Inst. and Methods in Physics Research, A*, pp. 48–59, June 2000.

[21] A. Braem, E. Chesi, C. Joram, J. Séguinot, P. Weilhammer, M. Giunta, N. Malakhov, A. Menzione, R. Pegna, and A. PICCIOLI, "Design, fabrication and performance of the 10-in. TOM HPD," *Nuclear Inst. and Methods in Physics Research, A*, vol. 518, pp. 574–578, Feb. 2004.

[22] Hamamatsu, *Photomultiplier Tubes, Basics and Apllications, third edition.* Hamamatsu, Japan : Hamamatsu, 2011.

[23] K. Nakamura, Y. Hamana, Y. Ishigami, and T. Matsui, "Latest bialkali photocathode with ultra high sensitivity," *Nuclear Inst. and Methods in Physics Research, A*, vol. 623, pp. 276–278, Nov. 2010.

[24] P. Seitz and A. J. Theuwissen, *Single Photon Imaging.* Springer-Verlag Berlin Heidelberg : Springer Series in Optical Sciences, 2011.

[25] I. P. Csorba, *Image Tubes.* Indianapolis , Indiana, USA : The Howard W. Sams and Co., Inc., 1985.

[26] E. Eberhardt, "Image transfer properties of proximity focussed image tubes," *Applied Optics*, vol. 16, no. 8, p. 2127, 1977.

[27] R. Barbier and N. Estre, "Procédé de traitement pour un capteur sensible au photon unique et dispositif en faisant application," 2008.

[28] V. Delaubert, N. Treps, C. Fabre, H. A. Bachor, and P. Réfrégier, "Quantum limits in image processing," *Europhysics Letters*, vol. 81, p. 44001, Jan. 2008.

[29] J. Fade, N. Treps, C. Fabre, and P. Réfrégier, "Optimal precision of parameter estimation in images with local sub-Poissonian quantum fluctuations," *The European Physical Journal D*, vol. 50, pp. 215–227, Nov. 2008.

[30] R. Ober, S. Ram, and E. Ward, "Localization accuracy in single-molecule microscopy (vol 86, pg 1185, 2004)," *Biophysical Journal*, vol. 87, pp. 1399–1399, Aug. 2004.

[31] D. L. Snyder, C. W. Helstrom, A. D. L. Faisal, Mohammad, and R. L. White, "Compensation for readout noise in CCD images," *J. Opt. Soc. Am. A*, vol. 12, pp. 272–288, Jan. 1995.

[32] T. Cajgfinger, E. Chabanat, A. Dominjon, Q. T. Doan, C. Guerin, J. Houles, and R. Barbier, "Single-photon sensitive fast ebCMOS camera system for multiple-target tracking of single fluorophores : application to nano-biophotonics.," *SPIE IS&T/SPIE*, vol. 6, Dec. 2010.

[33] X. Michalet, "Mean square displacement analysis of single-particle trajectories with localization error : Brownian motion in an isotropic medium," *Physical Review E*, vol. 82, Oct. 2010.

[34] A. Berglund, "Statistics of camera-based single-particle tracking," *Physical Review E*, vol. 82, July 2010.

[35] G. Konstantatos and E. H. Sargent, "Nanostructured materials for photon detection," *Nature Nanotechnology*, vol. 5, pp. 391–400, May 2010.

[36] G. Konstantatos and E. H. Sargent, "Colloidal quantum dot photodetectors," *Infrared Physics and Technology*, vol. 54, pp. 278–282, May 2011.

[37] S. Burov, J.-H. Jeon, R. Metzler, and E. Barkai, "Single particle tracking in systems showing anomalous diffusion : the role of weak ergodicity breaking," *Physical Chemistry Chemical Physics*, vol. 13, no. 5, p. 1800, 2011.

[38] E. Betzig, G. Patterson, R. Sougrat, O. Lindwasser, S. Olenych, J. Bonifacino, M. Davidson, J. Lippincott-Schwartz, and H. Hess, "Imaging intracellular fluorescent proteins at nanometer resolution," *Science*, vol. 313, pp. 1642–1645, Sept. 2006.

[39] S. Manley, J. Gillette, G. Patterson, H. Shroff, H. Hess, E. Betzig, and J. Lippincott-Schwartz, "High-density mapping of single-molecule trajectories with photoactivated localization microscopy," *Nature Methods*, vol. 5, pp. 155–157, Feb. 2008.

[40] D. S. Grebenkov, "Time-averaged quadratic functionals of a Gaussian process," *Physical Review E*, vol. 83, June 2011.

[41] D. S. Grebenkov, "Probability distribution of the time-averaged mean-square displacement of a gaussian process," *Physical Review E*, vol. 84, p. 031124, Sep 2011.

[42] M. A. Thompson, M. D. Lew, M. Badieirostami, and W. E. Moerner, "Localizing and Tracking Single Nanoscale Emitters in Three Dimensions with High Spatiotemporal Resolution Using a Double-Helix Point Spread Function," *Nano Letters*, vol. 10, pp. 211–218, Jan. 2010.

[43] P. R. Pavani, S. R. P., "Three dimensional tracking of fluorescent microparticles using a photon-limited double-helix response system," *Optics Express*, pp. 3484–3489, 2008.

[44] B. McNally, A. Singer, Z. Yu, Y. Sun, Z. Weng, and A. Meller, "Optical Recognition of Converted DNA Nucleotides for Single-Molecule DNA Sequencing Using Nanopore Arrays," *Nano Letters*, vol. 10, pp. 2237–2244, June 2010.

[45] L. Zonia and D. Bray, "Swimming patterns and dynamics of simulated Escherichia coli bacteria," *Journal of The Royal Society Interface*, vol. 6, pp. 1035–1046, Sept. 2009.

[46] J. Yuan, K. A. Fahrner, L. Turner, and H. C. Berg, "Asymmetry in the clockwise and counterclockwise rotation of the bacterial flagellar motor," *Proceedings of the National Academy of Sciences*, vol. 107, pp. 12846–12849, July 2010.

[47] L. Turner, R. Zhang, N. C. Darnton, and H. C. Berg, "Visualization of Flagella during Bacterial Swarming," *Journal of Bacteriology*, vol. 192, pp. 3259–3267, June 2010.

[48] N. C. Darnton, L. Turner, S. Rojevsky, and H. C. Berg, "On Torque and Tumbling in Swimming Escherichia coli," *Journal of Bacteriology*, vol. 189, pp. 1756–1764, Feb. 2007.

[49] A. Berke, L. Turner, H. Berg, and E. Lauga, "Hydrodynamic Attraction of Swimming Microorganisms by Surfaces," *Physical Review Letters*, vol. 101, July 2008.

[50] B. T. Glindemann, Hippler S. and H. W. A., "Adaptive optics on large telescope," *Experimental Asrtronomy, Kluwer Academic Publishers*, vol. 10, pp. 5–47, 2010.

[51] S. H. D. Haddock, M. A. Moline, and J. F. Case, "Bioluminescence in the Sea," *Annual Review of Marine Science*, vol. 2, pp. 443–493, Jan. 2010.

[52] R. Cluzel, *Etude de la passivation du silicium dans des conditions d'irradiation électronique de faible énergie.* PhD thesis, Université Claude Bernard - Lyon 1, 2010.

[53] R. Barbier, J. Baudot, E. Chabanat, P. Depasse, W. Dulinski, N. Estre, C. Kaiser, N. Laurent, and M. Winter, "Performance study of a MegaPixel single photon position sensitive photodetector EBCMOS," *Nuclear Inst. and Methods in Physics Research, A*, vol. 610, pp. 54–56, Oct. 2009.

[54] R. Turchetta, J. Berst, B. Casadei, G. Claus, C. Colledani, W. Dulinski, Y. Hu, D. Husson, J. L. Normand, J. Riester, G. Deptuch, U. Goerlach, S. Higueret, and M. Winter, "A monolithic active pixel sensor for charged particle tracking and imaging using standard VLSI CMOS technology," *Nuclear Inst. and Methods in Physics Research, A*, vol. 458, pp. 677–689, Feb. 2001.

[55] M. Caccia, L. Badano, D. Berst, C. Bianchi, J. Bol, C. Cappellini, G. Claus, C. Colledani, L. Conte, and A. Czermak, "The SUCIMA project : A status report on high granularity dosimetry and proton beam monitoring," *Nuclear Inst. and Methods in Physics Research, A*, vol. 560, pp. 153–157, May 2006.

[56] W. Dulinski, A. Braem, M. Caccia, G. Claus, G. Deptuch, D. Grandjean, C. Joram, J. Seguinot, and M. Winter, "Tests of a backside illuminated monolithic CMOS pixel sensor in an HPD set-up," *Nuclear Inst. and Methods in Physics Research, A*, vol. 546, pp. 274–280, July 2005.

[57] G. Deptuch, W. Dulinski, M. Caccia, and M. Winter, "High-resolution, back-side illuminated monolithic active pixel sensor for low-energy electron imaging," *IEEE Transactions on Nuclear Science*, vol. 52, pp. 1745–1754, Oct. 2005.

[58] R. Barbier, T. Cajgfinger, P. Calabria, E. Chabanat, D. Chaize, P. Depasse, Q. T. Doan, A. Dominjon, C. Guerin, J. Houles, L. Vagneron, J. Baudot, A. Dorokhov, W. Dulinski, M. Winter, and C. T. Kaiser, "A single-photon sensitive ebCMOS camera : The LUSIPHER prototype," *Nuclear Inst. and Methods in Physics Research, A*, vol. 648, pp. 266–274, AUG 21 2011.

[59] T. Cajgfinger, E. Chabanat, A. Dominjon, Q. T. Doan, C. Guerin, J. Houles, and R. Barbier, "Single-photon sensitive fast ebCMOS camera system for multiple-target tracking of single fluorophores : application to nano-biophotonics," in *SENSORS, CAMERAS, AND SYSTEMS FOR INDUSTRIAL, SCIENTIFIC, AND CONSUMER APPLICATIONS XII* (Widenhorn, R and Nguyen, V, ed.), vol. 7875 of *Proceedings of SPIE*, 2011. Conference on Sensors, Cameras, and Systems for Industrial, Scientific, and Consumer Applications XII, San Francisco, CA, JAN 25-27, 2011.

[60] A. Dominjon, E. Chabanat, P. Depasse, R. Barbier, J. Baudot, W. Dulinski, A. Dorokhov, and M. Winter, "LUSIPHER Large-scale Ultra-fast SIngle PHoto-Electron trackeR," in *2009 IEEE NUCLEAR SCIENCE SYMPOSIUM CONFERENCE RECORD, VOLS 1-5* (Yu, B, ed.), IEEE Nuclear Science Symposium Conference Record, pp. 1527–1531, 2009. IEEE Nuclear Science Symposium Conference 2009, Orlando, FL, OCT 25-31, 2009.

[61] R. Barbier, J. Baudot, E. Chabanat, P. Depasse, W. Dulinski, N. Estre, C. T. Kaiser, N. Laurent, and M. Winter, "Performance study of a MegaPixel single photon position sensitive photodetector EBCMOS," *Nuclear Inst. and Methods in Physics Research, A*, vol. 610, pp. 54–56, OCT 21 2009.

[62] DELPHI-Collaboration, "Search for supersymmetric particles assuming R-parity non-conservation in e(+)e(-) collisions at root s = 192 to 208 GeV (vol 36, pg 1, 2004)," *European Physical Journal C*, vol. 37, pp. 129–131, SEP 2004.

[63] DELPHI-Collaboration, "Search for supersymmetric particles assuming R-parity non-conservation in e(+)e(-) collisions at root s=192 to 208 GeV," *European Physical Journal C*, vol. 36, pp. 1–23, JUL 2004.

[64] DELPHI-Collaboration, "Search for R-parity violation with a (U)over-bar(D)over-bar(D)over-bar coupling at root s approximate to 189 GeV," *Physics Letters B*, vol. 500, pp. 22–36, FEB 15 2001.

[65] R. Barbier, C. Berat, M. Besancon, M. Chemtob, A. Deandrea, E. Dudas, P. Fayet, S. Lavignac, G. Moreau, E. Perez, and Y. Sirois, "R-parity-violating supersymmetry," *Physics Reports-Review Section of Physics Letters*, vol. 420, pp. 1–195, NOV 2005.

[66] S. Jan, G. Santin, D. Strul, S. Staelens, K. Assie, D. Autret, S. Avner, R. Barbier, M. Bardies, P. Bloomfield, D. Brasse, V. Breton, P. Bruyndonckx, I. Buvat, A. Chatziioannou, Y. Choi, Y. Chung, C. Comtat, D. Donnarieix, L. Ferrer, S. Glick, C. Groiselle, D. Guez, P. Honore, S. Kerhoas-Cavata, A. Kirov, V. Kohli, M. Koole, M. Krieguer, D. van der Laan, F. Lamare, G. Largeron, C. Lartizien, D. Lazaro, M. Maas, L. Maigne, F. Mayet, F. Melot, C. Merheb, E. Pennacchio, J. Perez, U. Pietrzyk, F. Rannou, M. Rey, D. Schaart, C. Schmidtlein, L. Simon, T. Song, J. Vieira, D. Visvikis, R. de Walle, E. Wieers, and C. Morel, "GATE : a simulation toolkit for PET and SPECT," *Physics in Medecine and Biology*, vol. 49, pp. 4543–4561, OCT 7 2004.

[67] R. Barbier, Y. Declais, C. Dujardin, N. Garnier, M. Janier, I. Kamenskikh, G. Largeron, J. Marteau, C. Pedrini, and D. Marinier, "Two-head small animal PET prototype with LSO/LuAP coupled to a multi-anode PMT," *Nuclear Inst. and Methods in Physics Research, A*, vol. 527, pp. 175–179, JUL 11 2004. 2nd International Conference on Imaging Technologies in Biomedical Sciences, Athens, GREECE, MAY 26-30, 2003.

[68] R. Barbier, J. Meyer, and M. Kibler, "A U-QP(U(2)) rotor model for rotational bands of superdeformed nuclei," *International Journal of Modern Physics E Nuclear Physics*, vol. 4, pp. 385–410, JUN 1995.

[69] R. Barbier, J. Meyer, and M. Kibler, "A U-QP(U2) model for rotational bands of nuclei," *Journal of Physics G Nuclear and Particle Physics*, vol. 20, pp. L13–L19, JAN 1994.

Chapitre III

Autres travaux

A R&D sur un module de coïncidences pour μTEP, 2002-2004

A.1 Description du travail de R&D

C'est en 2002 que j'ai commencé à travailler sur deux types de détecteurs et leur système d'acquisition : les Multi-Anodes PMT d'Hamamatsu utilisés dans l'expérience OPERA et les capteurs CMOS de l'équipe de M. Winter à l'IPHC. Dans le premier cas il s'agissait de reprendre l'activité de R&D développée via un financement ACI technologies pour la santé, acronym IMHOTEP et de développer des partenariats académiques et industriels autour des micro tomographes par émission de positon (microTEP). Cette mission qui m'a conduit à soutenir une activité de recherche à part entière nécessitant un investissement important sur la coordination de l'activité. Je pense avoir énormément appris sur l'être humain pendant cette période au détriment certainement de progrès scientifiques claires sur ce domaine. A posteriori les moyens humains et techniques nécessaires pour la réalisation des objectifs scientifiques étaient disproportionnés et ma plus grosse erreur (ou qualité) a été d'y croire et de le défendre contre les évidences.

Un des objectifs du projet sur lequel j'ai particulièrement travaillé était d'obtenir un spectre de photons de 511 keV d'une source de sodium, de manière reproductible, avec une tête de détection comportant un MaPMT de 64 canaux ajusté et couplé au dixième de millimètre avec deux couches de matrices de cristaux, mode phoswitch LSO/LuAP (section de 2x2 mm2) et un système d'acquisition auto-déclenché sur Ethernet. Les points délicats que nous avons rencontrés dans cette première étape étaient les suivants :
- fabrication et tests de matrices (casiers à cristaux) de 8 par 8 avec des parois de 300 microns en téflon ou en tyvek (Figure 2 de la section A.2).
- réalisation d'un couplage optique uniforme pour optimiser la collection de lumière et éviter la disparition de certains canaux en dessous du seuil de déclenchement commun.

– mesure de la variation du « gain total» entre pixels. Cette variation (facteur 3 au maximum) compromet considérablement l'ajustement du seuil de trigger commun pour le mode d'acquisition auto-déclenché. Le gain total par pixel découle de l'efficacité de transfert du cristal, du couplage optique, de l'efficacité quantique de la photocathode et des gains du MaPMT. Ces points ont largement été étudiés (soutien décisif en mécanique et instrumentation à l'IPNL) et ont conduit à l'élaboration d'un prototype 2 têtes en coïncidence.

Les 2 têtes (128 canaux) ont été caractérisées en mode LSO tant au niveau de leur résolution en énergie (15 à 20%) qu'au niveau de la diaphonie optique inter-pixels (10 % au plus proche voisin). Ces résultats sont présentés dans l'article reproduit dans la section A.2.

La recherche des coïncidences a été effectuée off-line comme cela a été proposé à l'origine et a donc nécessité une synchronisation des compteurs locaux utilisés dans le marquage temporel de l'auto-déclenchement de l'acquisition. Dans l'objectif de validation de toute la chaîne d'acquisition (de la prise de données ou de la simulation Monte Carlo à l'image reconstruite) il a été nécessaire de mettre au point un formatage quasi-automatique des données brutes au Format Mode Liste de la Collaboration Crystal Clear. La chaîne d'acquisition Ethernet a été validée et a permis d'obtenir des images reconstruites d'une source ponctuelle (3 mm de diamètre) de Sodium 22.

A.2   Publications μTEP

From high energy physics large scale distributed optoelectronics readout to medical imaging applications : prototyping a 2-head readout system for micro-PET

Authors

Rémi Barbier, Jacques Marteau, E.Pennachio[*]

Abstract

This paper describes the experimental set-up designed for micro-PET detectors studies and presents the results. The prototype includes 2 smart detection heads composed with scintillating crystals, pixel photo-detector, auto-triggerable front-end electronics and Ethernet capable DAQ processor totally independent and configurable via Ethernet. The electronic readout system based on the "smart sensor" design is inspired by the OPERA experiment of neutrino oscillations detection currently under installation in the Gran Sasso underground laboratory. The two detection heads have been characterized. Different aspects of the development are presented : pulse shape discrimination (PSD) from two different crystals for depth of interaction (DOI) measurement, energy resolution, light sharing, multi- hit studies from Compton events, flood diagram and sodium 22 point source image reconstruction.

Introduction

Main requirements to a small animal PET system are spatial resolution (1.5 mm^3 expected) and sensitivity. Unfortunately increasing the sensitivity by decreasing the gantry radius implies increasing the parallax error which is drastically enhanced with the crystal size. One solution is to perform Depth of Interaction (DOI) measurement from pulse shape discrimination (PSD) of two crystals with different mean decay constants. The project described here has been developed in the Crystal Clear Collaboration (CCC) which promotes DOI measurement through PSD with the so-called "phoswitch" configuration. The phoswitch mode is obtained in our case with 2 different crystals putted one behind the other in the "pointing geometry". The purpose of this paper is to present the developments performed in 2002-2003 on a two head micro-PET prototypes. The main components of the prototype are:

- lutetium oxides crystals (LSO and LuAP),
- multi anode PMT HR7546 from Hamamatsu,
- electronic readout chain based on an Ethernet "smart sensor" concept[1].

The main goal of such prototype was the evaluation of the full optoelectronic chain performance: crystals light yields, reflectors and packaging performance in real micro-PET conditions, light sharing effects on the reconstructed energy, Compton events selection for image reconstruction. A point source Na image has been obtained to validate the full opto-electronic chain within the off-line coincidence sorting concept.

Experimental setup

-1/ Crystals

The crystals used for the tests were of LuAP type (LuAlO$_3$:Ce^{3+}) and LSO type (Lu$_2$SiO$_5$:Ce^{3+}), which have equivalent stopping power but different decay times: 40 ns for LSO and 20 ns for LuAP. On top of these fast components the LuAP has a slow component of about 400 ns. The crystals also differ by their light yields (LuAP/LSO ~ 10-50 % depending on the crystals quality). The light yields discrepancy is the major drawback for such phoswitch solution which suffers from single trigger electronic threshold. Details on the production of the LuAP crystals used for these tests can be found in the literature [1].

-2/ Crystal Matrix

The crystal dimension was 2mm×2mm×10mm to match the multi-anode photo-multiplier pixel size of the Hamamatsu HR7546. The 64 crystals were gathered in an 8×8 "matrix". The one-to-one mapping between crystals and pixels induces severe constraints on the light collection and on the matrices technologies.

The first arises from the relatively large surface/volume ratio, which implies that a lot of light is emitted through the lateral surfaces. Tests show that this represents roughly half of the emitted light. The second comes from the differences in the emission spectra of the 2 crystals (420nm at the emission peak for the LuAP vs. 480nm for the LSO). The reflective index depending on the wavelength, a good compromise has to be found in the type of material if one wants to have the same matrix material for both crystals, which is actually the third constraint. The last constraint comes from the mechanics of both the MaPMT, which imposes an inter-pixel pitch of 0.3mm and of the crystals, which requires the most possible regular shape.

---

[1] Patent WO2005081121

The first matrix prototype was done in stainless steel and the inner walls were cut with a 0.1mm diameter wire. This gives the best mechanical results (Fig.1, left picture) but a poor light collection. This prototype was then used to build a mould (Fig.2, left picture) in which matrices were then produced (Fig.1, right picture).

Different materials were tested in these matrices (TiO_2 loaded epoxy, Tyvek and Teflon). The best results for the light collection were obtained with Tyvek and Teflon (+40% and +30% respectively for LSO and +25% for LuAP). Matrices studies has been discussed in the paper [1].

Figure 1: Matrix pictures: stainless steel matrix (left) and Teflon matrix (right) obtained with the epoxy mould displayed in Fig.2 (left).
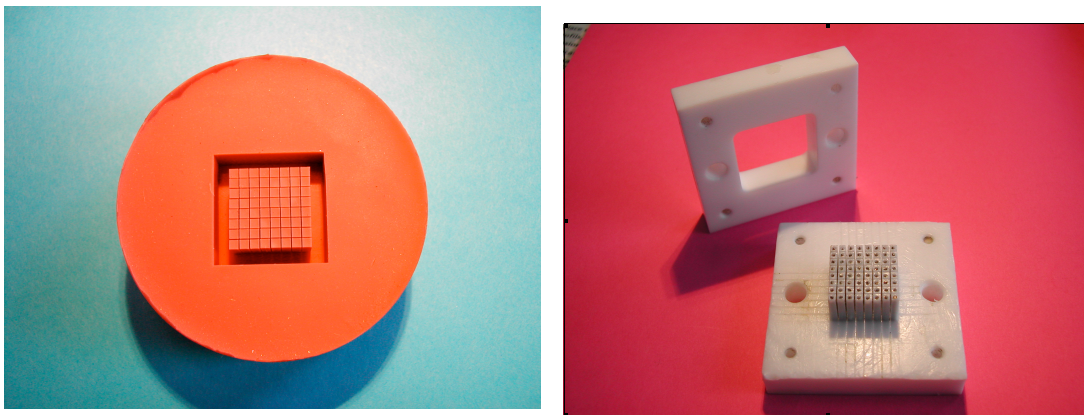
Figure 2: Different mounting system for matrix production: epoxy mould (left) obtained with the stainless steel matrix (Fig. 1) and Teflon template (right) used to gather Tyvek thin foils to wrap the 64 crystals.

-3/ Detection head production

The detection head was composed with one or two matrices (one with LSO crystals and/or one with LuAP crystals) depending on phoswich test was performed or not. The matrices were mechanically mapped on the HR7546 MaPMT. Optical grease was used to enhance the light collection, which was really critical for LuAP prototypes crystals.

The two detection heads with their electronics were aligned along a ring diameter. The ring dimension was set to simulate the final micro-PET gantry (~16 cm). The point Na source (diameter ~3mm) was placed in the centre of the ring. A mechanical rotation of the source

gave 10 data taking period with a 20-degree rotation step to simulate a data taking with a full ring of 18 MaPMT. Fig.3 shows the coincidence set-up that gave us the first image produce with this new auto triggered detection head with off-line coincidence sorting concept.
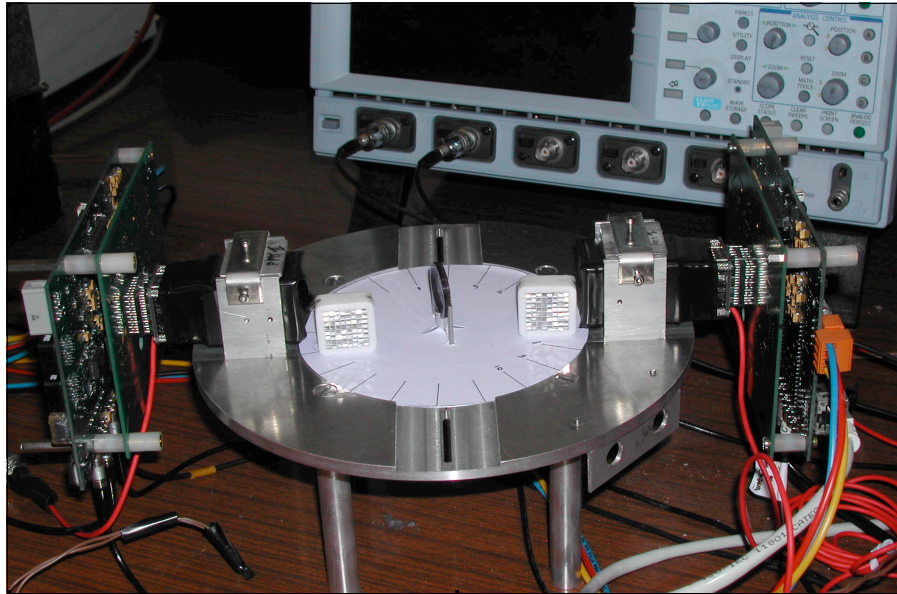
Figure 3: *Detection head set-up for matrix tests and off-line coincidence sorting demonstration. The Na source can be seen in the centre.*

Readout electronics

-1/ MaPMT tests using a BFOOT system

We perform tests of the MaPMT used in the OPERA experiment with a demonstrator DAQ board – using the BFOOT processor from Agilent – and a commercially available front-end electronics, the VA-TA system from IDEAS. Two board generations were produced and validated to readout HPDs (DEP proximity focusing 61 pixels) and MaPMTs (Hamamatsu) [2]. The 2 boards are shown in Fig.4 : 1st prototype (ORCA board, left) and 2nd prototype (right).
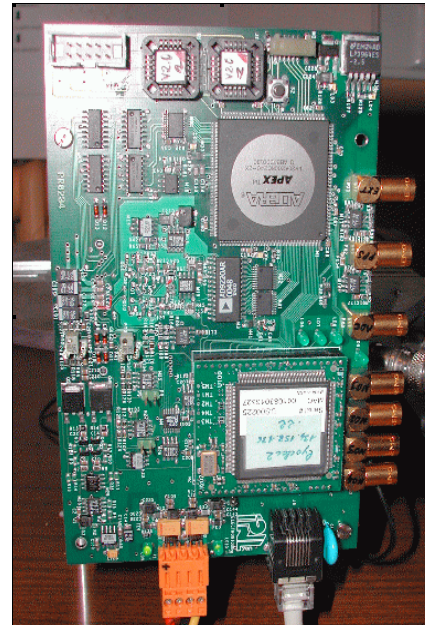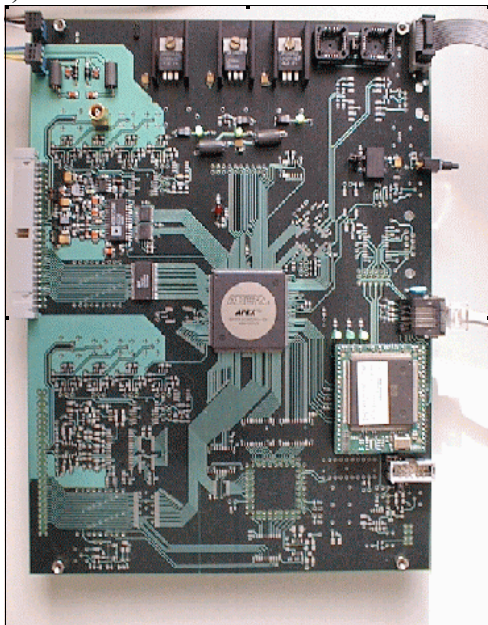
The readout sequence is independent of the photo detectors, which have a comparable ~4pF pixel output capacitance: the photo detector charge is readout through a slow shaping time chip – VA32c (low noise and high gain) for HPD readout, VA32hdr11 (High Dynamic Range chip) for MAPMT readout – after a sample/hold logic triggered by a fast shaping chip – TA32c in both cases – followed by a discriminator.

The system allows detailed tests on gain uniformity, gain linearity with applied voltage, photoelectron resolution – illustrated on Fig.5 with the Poisson spectrum seen by the HPD (left) and the single p.e. spectrum seen by the MaPMT (right) –, trigger efficiency (using a pulsed blue LED and its pulse as external trigger), dark current measurement (which indicates a dark current less than 3 Hz per pixel in the case of the MaPMT).
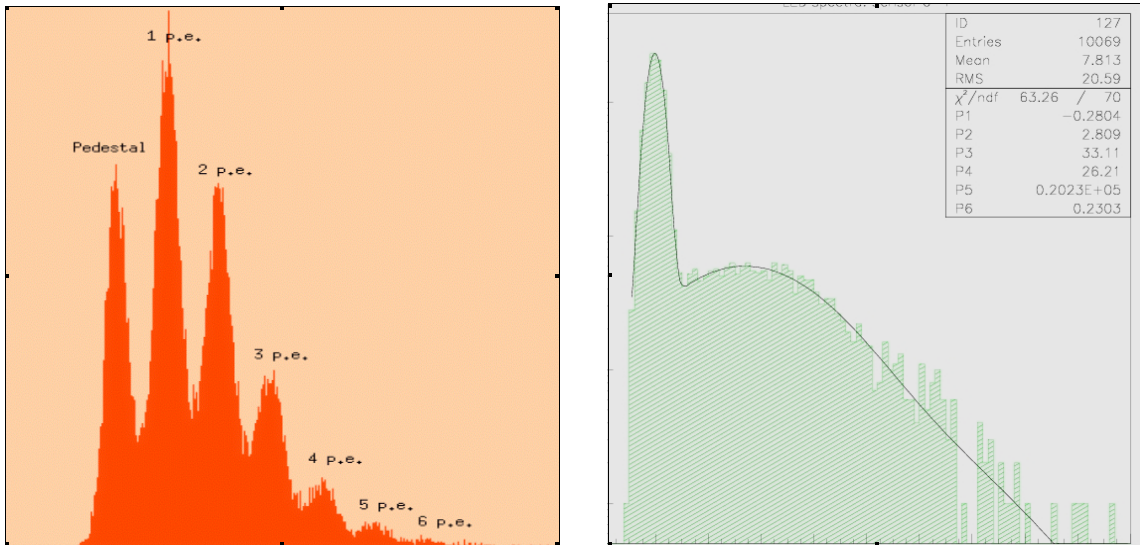
Figure 5: *photoelectron resolution obtained with the BFOOT readout system : HPD case (left) and MaPMT case (right).*

The results obtained on the HPD tests with the 1st version of BFOOT board lead to the development of an upgraded and compact system.

-2/ The BFOOT version 2 acquisition system

The second version of BFOOT Ethernet controller has been developed as a backup solution for the final R/O chain of the OPERA experiment, dedicated to the MaPMT R/O at the test facility in the OPERA scintillator module assembly site.

The R/O can be performed either in auto trigger mode, using the internal trigger generated by the TA chip, or in external trigger mode (NIM signal input). The system performance is limited by the 1Mbps data transfer capability of the BFOOT processor. This corresponds to roughly 100Hz per pixel data rate given the data format used for the tests.

The system specifications are listed below:
- R/O of VA-TA HDR11(PMT) (f_{max} = 5 MHz)
- 4 DACs: 1 for the threshold setting + 3 biases VA-TA
- 12 bits ADC (10 MHz) for the multiplexed output digitisation
- 7 NIM I/O connectors (trigger in/out, busy out, ADC out, PPS in)

- Ethernet controller: BFOOT
- 1 external trigger input
- 1 time reference input
- event timestamp: 10 ns resolution (typ.), 5 ns (min.)
- Read/Write register access through HTTP commands
- FIFO FPGA: 2048 x 32 bits words, buffer BFOOT: 1 Mbytes
- Data Streaming mode (1 Mbits / sec): TCP/IP

The block diagram of the R/O system is displayed below (Fig.6)
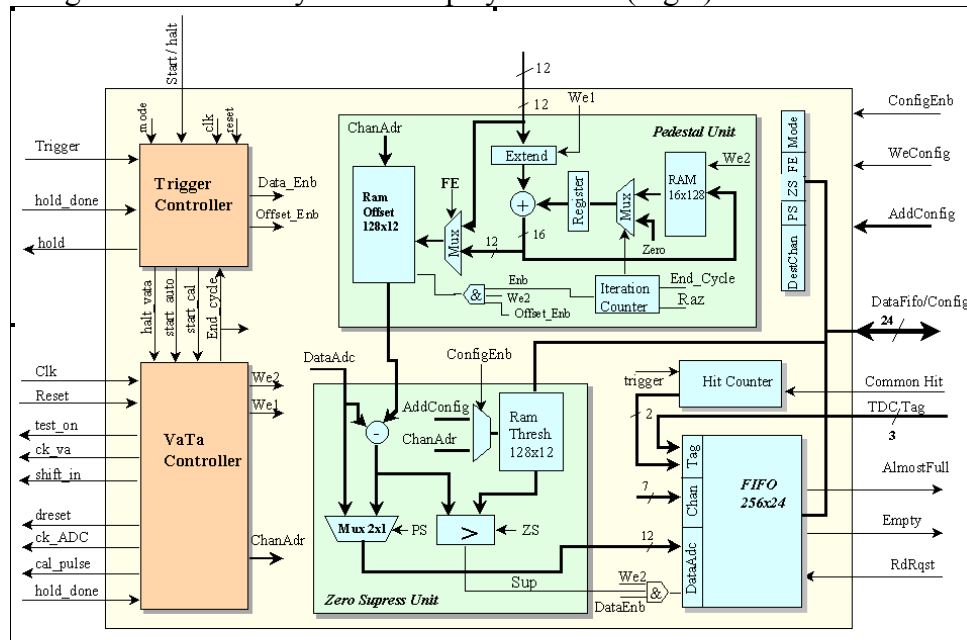
Figure 6: Block diagram of the BFOOT board.

The sequencer (FPGA APEX from Altera) manages the following operations:
- readout sequence,
- event timestamp,
- data formatting (including possible zero suppress),
- data temporary storage in a FIFO.

The BFOOT processor gets the data from the FIFO at a fixed and programmable frequency (min. refreshing period = 17ms).

The BFOOT processor is host on a daughter board (so-called "mezzanine" board) plugged on the main board. The VA-TA and the BFOOT boards have been directly connected through an ERNI 50 pins connector for all the required I/O signals. On Fig.7 one sees a picture of the readout electronics elements (VA-TA front-end board, BFOOT mezzanine and BFOOT mother board). The MaPMT is plugged directly on the front-end board.
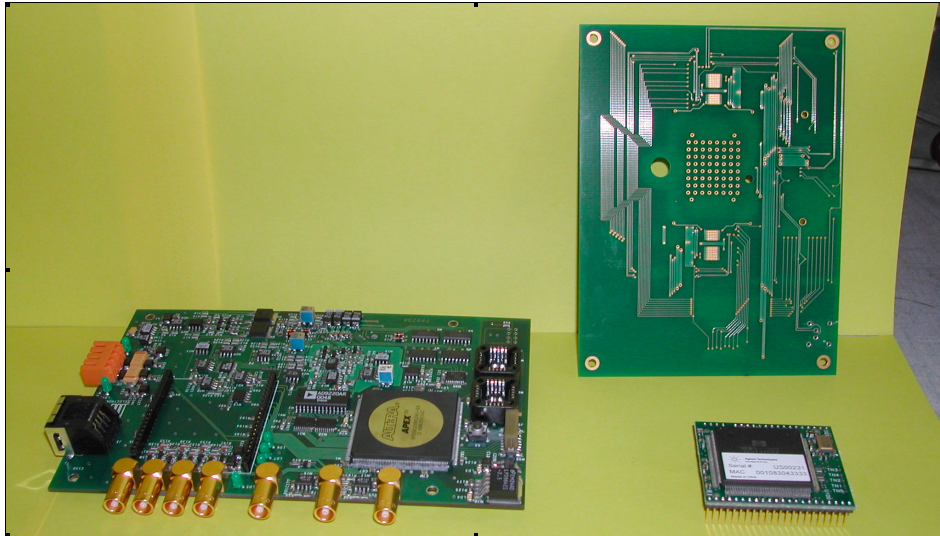
Figure 7 : *Picture of the readout electronics elements of BFOOT V2 acquisition system. The component on right is the Ethernet processor.*

-3/ Software control

The system is totally manageable through *http* commands, the processor hosting a *WEB* server (see its "applications homepage" below). A LabView interface has also been developed with all embedded commands in a more standard "user friendly" format. The program allows all the slow control, monitoring (front-end biases settings, acquisition mode, trigger source selection…) and acquisition commands.
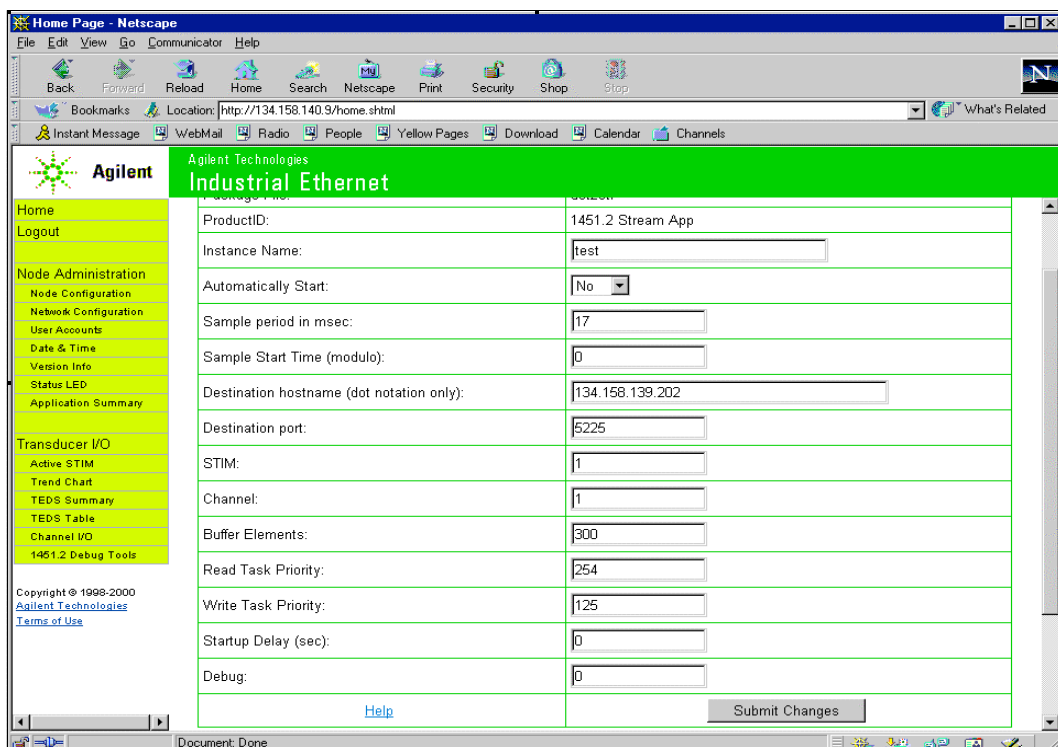
Figure 8: *Applications homepage running on the BFOOT WEB server.*

Results and Analysis

-1/ Pulse Shape Discrimination

To enhance the sensitivity of a Micro-PET system, longer crystals are required to improve the stopping power and therefore the sensitivity of the scanner. Nevertheless with longer crystals parallax error occurs when the region of interest is far from the center of the field of view. To perform DOI measurement, pulse shape discrimination can be achieved using the difference of pulse shape between two crystal types (LSO and LuAP in our test bench). The PSD can be performed either on the slow component or on the fast component of the LuAP (~20 ns). We evaluated the efficiency and the purity of the fast component discrimination. The pulses from the MaPMT were collected at the level of the last dynode (12th) by a numerical oscilloscope (Lecroy LT402) and each pulse was digitized with a maximum sampling rate of 1GHz and transferred to a computer. Pulse sampling allows to store pulse height spectra as function of time. For each value being in the photo-peak, the time gravity center of the pulse has been calculated (this corresponds more ore less to the mean decay time of the crystal) following the formula:

$$\tau = \frac{\sum_{t_i=t_0}^{t_{end}} t_i y(t_i)}{\sum_{t_i=t_0}^{t_{end}} y(t_i)}$$

where t_0 was set at the maximum of the decay and different t_{end} have been tried in order to estimate the best LSO/LuAP discrimination. Different values from t_{end}=10ns up to t_{end}=400ns were tried.

An event by event analysis has been performed using this PSD method with LuAP and LSO pure samples. Fig.10 shows the corresponding results. Efficiency and purity of the PSD has been estimated to be around 90 % with a 250 MHz sampling rate.
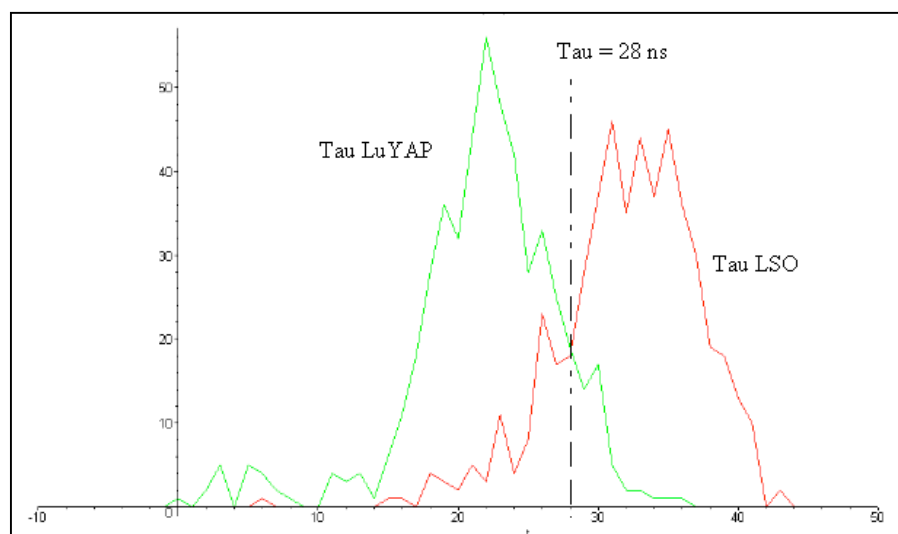
Figure 9: *PSD distribution example on real DATA between LuAP and LSO crystals. 90% of efficiency and purity has been achieved but at 250 MHz sampling rate.*

The PSD results versus the crystal quality have been extensively discussed in [1]. Nevertheless we conclude that the light emitted by the LuAP was two weak to perform a good PSD on his fast component and a Front-End electronic with a 250 MHz sampling would be necessary to perform a good PSD with an efficiency around 99%.

-2/ Single electron calibration method

The main drawback of the MaPMT vs. the HPD is the pixel to pixel gain spread, which can be as large as 1:3. On the other side, the gain of the MaPMT is sufficiently high (typ. 10^6) to avoid an extra pre-amplifier stage in the front-end electronics. The VA chips can not compensate the MaPMT's gain spread. The only "correction" of the system is applied at the level of the trigger mask where individual thresholds can be set for all the channels. It ensures a trigger efficiency equal for all the channels, although the recorded charge spectra differ. The off-line gain correction to be applied implies a good calibration of the MaPMT pixels gain.

The calibration method is derived from the so-called Bellamy method [3] which is a fitting procedure involving 11 individual parameters. In the case of this application, we retain only a sub-set of those parameters, all the individual crystals producing a intense light yield, far from the pedestal region where most of the fitting procedure difficulties are concentrated.

Therefore we adopted a fitting function taking into account:

- the Poisson fluctuation of the photoelectrons numbers: $P_k = e^{-\mu} \dfrac{\mu^k}{k!}$ where μ stands for the average number of photoelectrons,

- the Gaussian shape of pedestal and photoelectron peaks: $G_p = G(m_p, \sigma_p)$ where
  - $G()$ is standard normalized Gaussian distribution;
  - the position of each peak is computed as: $m_p = m_0 + p \times g$ $(p \in \mathbb{N})$, g being the single photoelectron gain and m_0 the position of the pedestal peak;
  - the width of each peak is given as: $\sigma_p{}^2 = \sigma_0{}^2 + p \times \sigma^2$ $(p \in \mathbb{N})$, σ being the width of a photoelectron peak without noise.

- a possible extra exponential component between the pedestal and the 1st p.e. peak

- an overall normalization constant.

The convergence of the fit depends very sensitively of the initial values given to all these parameters. The pedestals parameters (position and width) are fixed via an independent run done with the same high voltage applied on the MaPMT and an uncorrelated trigger. This gives the most realistic pedestals values between the pedestal and the LED runs.

The initial average number of p.e. value is taken directly from the Poisson statistics:

$\mu = \ln\left(\dfrac{P_{1...\infty}}{P_0} + 1\right)$, which implies to count the number of counts in the pedestal w.r.t. the total number of entries.

The individual gains are derived from the mean value of the spectrum $\bar{m}$:

$$g = \frac{\vec{m} - m_0}{\mu}$$

The width of each p.e. peak is taken in a reasonable range. The normalization constant depends directly of the number of entries of the run (usually 10^5 to 10^6).

All the pixels are illuminated by a diffusing system (segmented cylindrical plexiglass block with 3 LEDs at 120° of each other, all the LEDs driven by the same input signal). With a typical frequency of 500Hz the calibration of each MaPMT is a rather fast procedure. The light yield chosen to perform the fit is relatively large (2 to 5 p.e. in average) to minimize the weight of the pedestal region but to ensure that the pedestal is nevertheless still visible. Typical results are shown in the next Fig. with various values of μ for different channels:
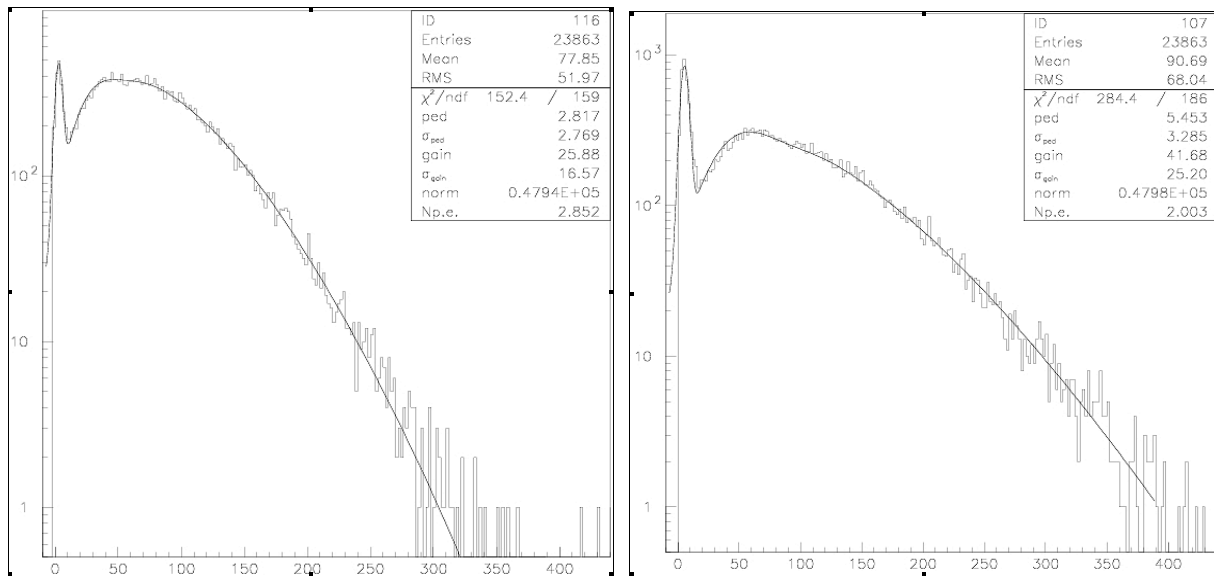
Figure 10: *LED spectra obtained with an average number of p.e. ranging from 2.8 (left) to 2.0 (right).*

Low light yield spectra (see Fig.11, left) exhibit strange behaviour in the pedestal definition which implies the use of an extended fit function. The gain distribution over the 64 pixels (Fig.11, right) shows the typ. 1:3 gain spread for the MaPMT between min. and max. values (20:60 ADC counts, mean value: 40 ADC counts).
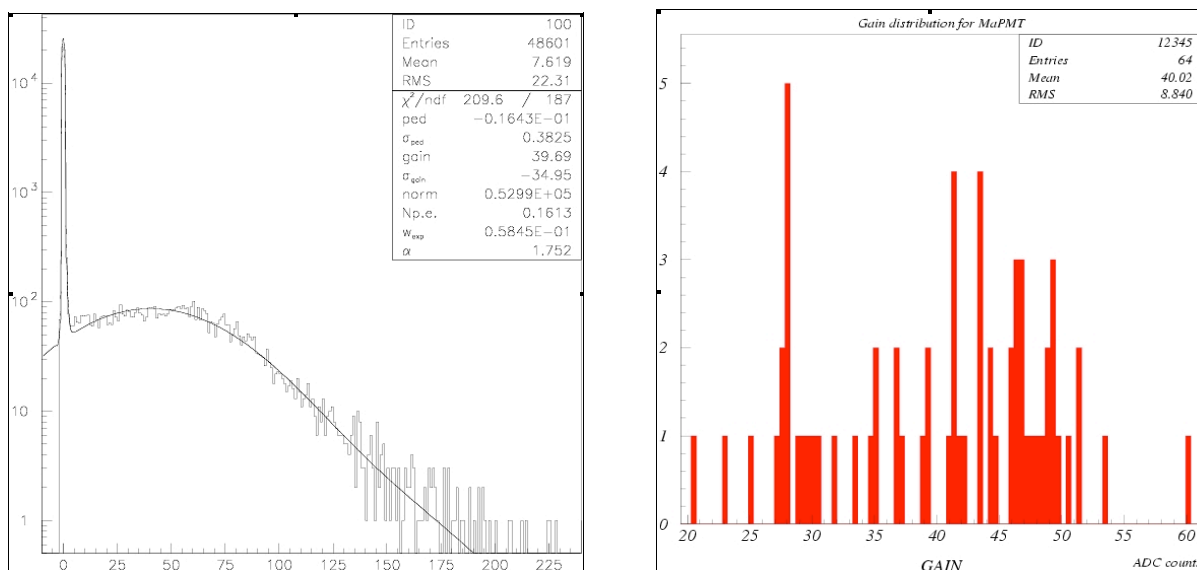
Figure 11 *: LED spectra obtained with a low number of p.e. (less than 0.2) (left). Also shown is the gain distribution over the 64 PMT pixels (right).*

-3/ Light sharing and matrices mapping

The readout electronics described in the previous section has the major advantage to store energy information (ADC values) of the 64 MaPMT channels for each triggered event. This information has been extensively used to characterize the two detection heads. Information giving only the position of the pulse (anger method) is completely blind to the effect of the trigger threshold adjustment, light sharing between pixels, off-axis displacement between the matrix and the MaPMT.

Selecting event triggered by one pixel allowed to perform specific event studies based on the 64 ADC values recorded. Such recorded events are shown in Fig.12.
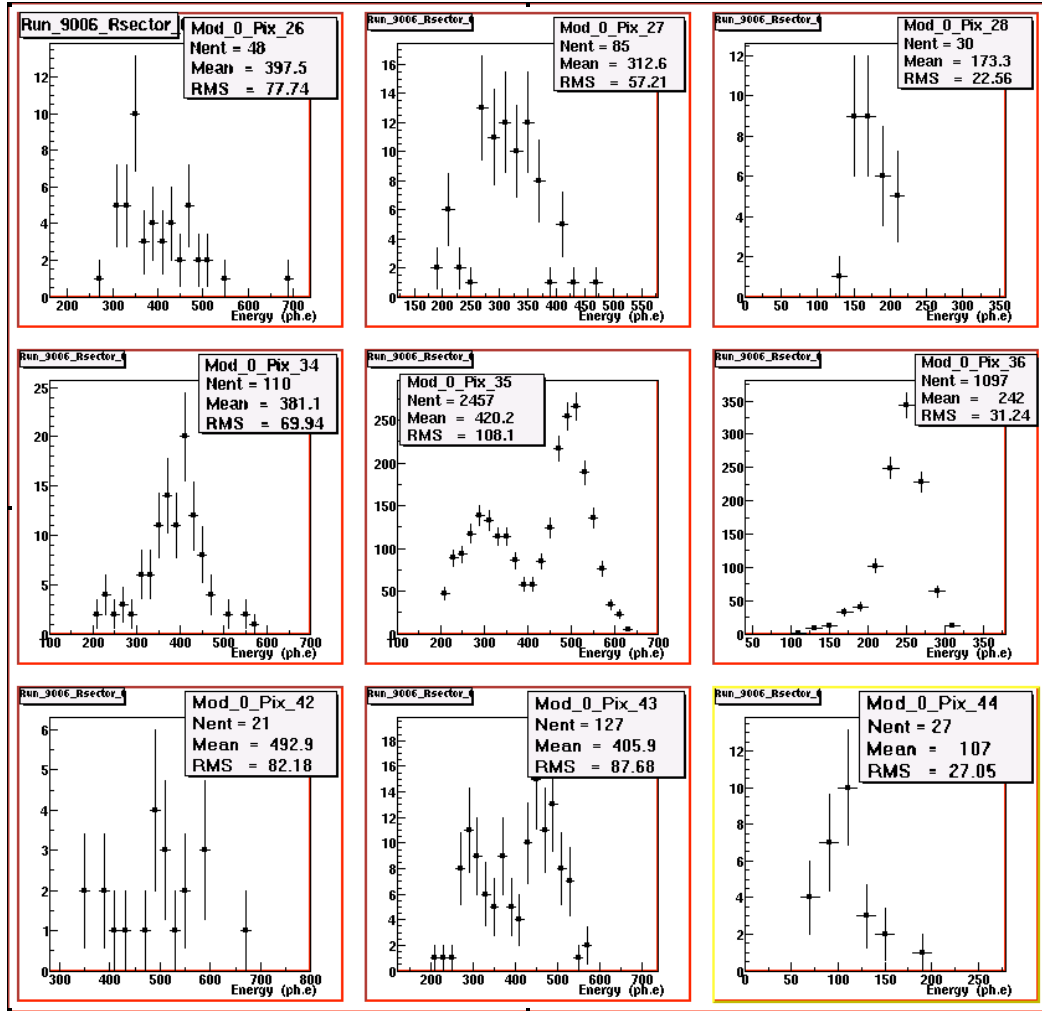
Figure 12: *Full spectrum obtained for nine pixels when the central pixel is auto-triggered and the nine ADC values are recorded. Light sharing between neighbour pixels is well seen.*

-3.1/ Energy resolution

The first study was dedicated to the photo-peak energy resolution taking into account the energy sum of the neighbour pixels. Fig.13 represents the evolution of the energy resolution as a function of the cluster size. The ratio FWHM/Mean decreased from 21% to 19%, 18% and to 16% when the sum is performed on 5, 9 and 21 neighbour pixels. We concluded from this study that energy resolution would be increasing by sampling the 20 neighbours of the triggered pixel. This feature has to be put in balance with the dead time due to the ADC sampling. The best solution to optimize in the same time the energy resolution and dead time should be a smart ASIC with a serial output of only 9 or 25 pixel values. The readout electronic developed here could be used with some logic implemented in the FPGA or in the Ethernet Processor.
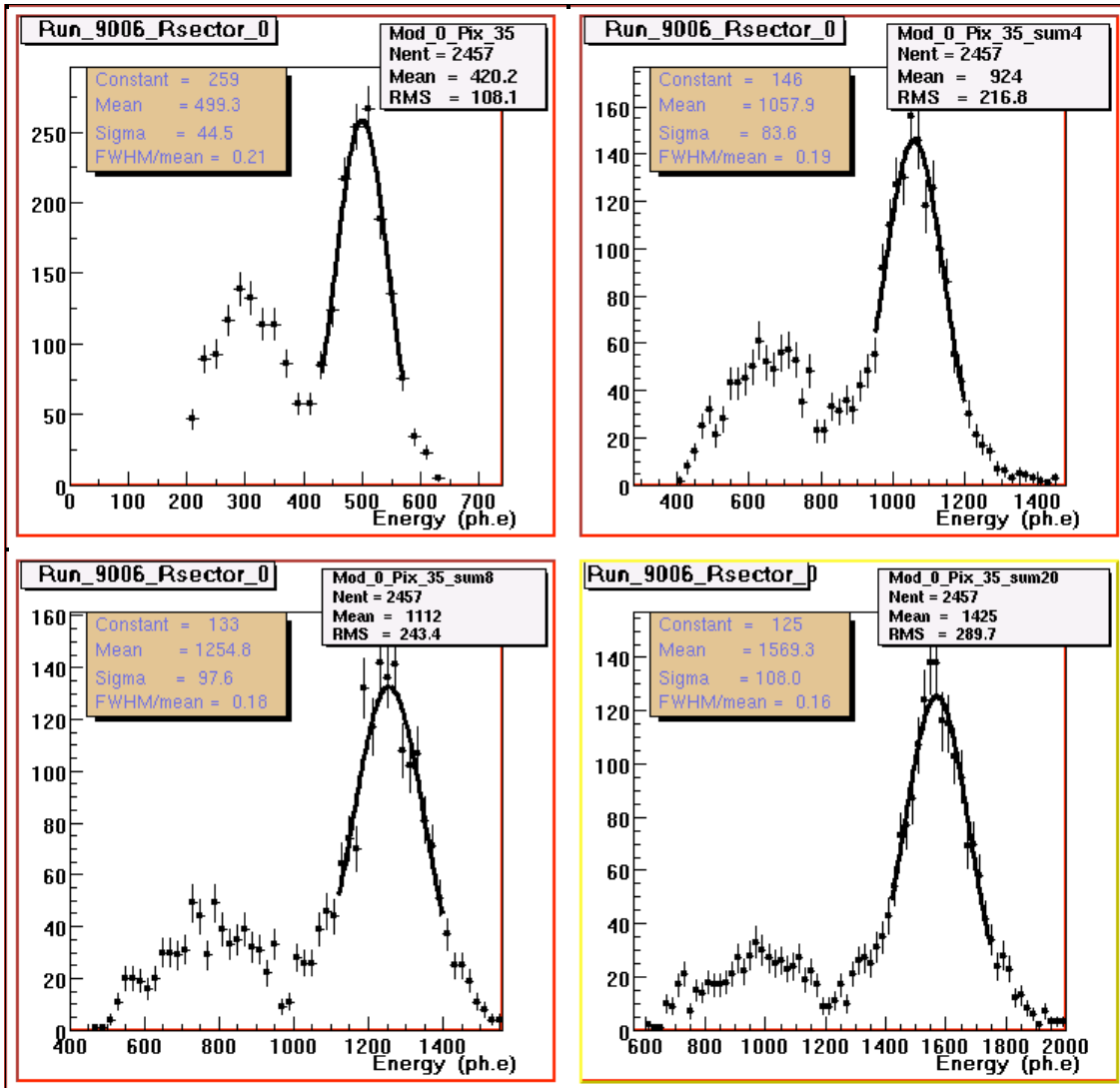
Figure 13: *The full spectrum obtained with Pixel 35 (upper left plot). The 5 pixel energy sum distribution (upper right plot). The 9 pixel energy sum distribution (lower left plot). The 21 pixel energy sum distribution (lower right plot).*

-3.2/ Matrices mapping control from light sharing.

Information obtained from light sharing has been used to perform a control of the mapping between crystal matrix and MaPMT grid. We computed the energy fraction of light loss in the neighbours. Fig.14 shows the results. We have shown that a mechanical mismatch (0.1 mm estimated) could be seen with this method (Fig. 15).
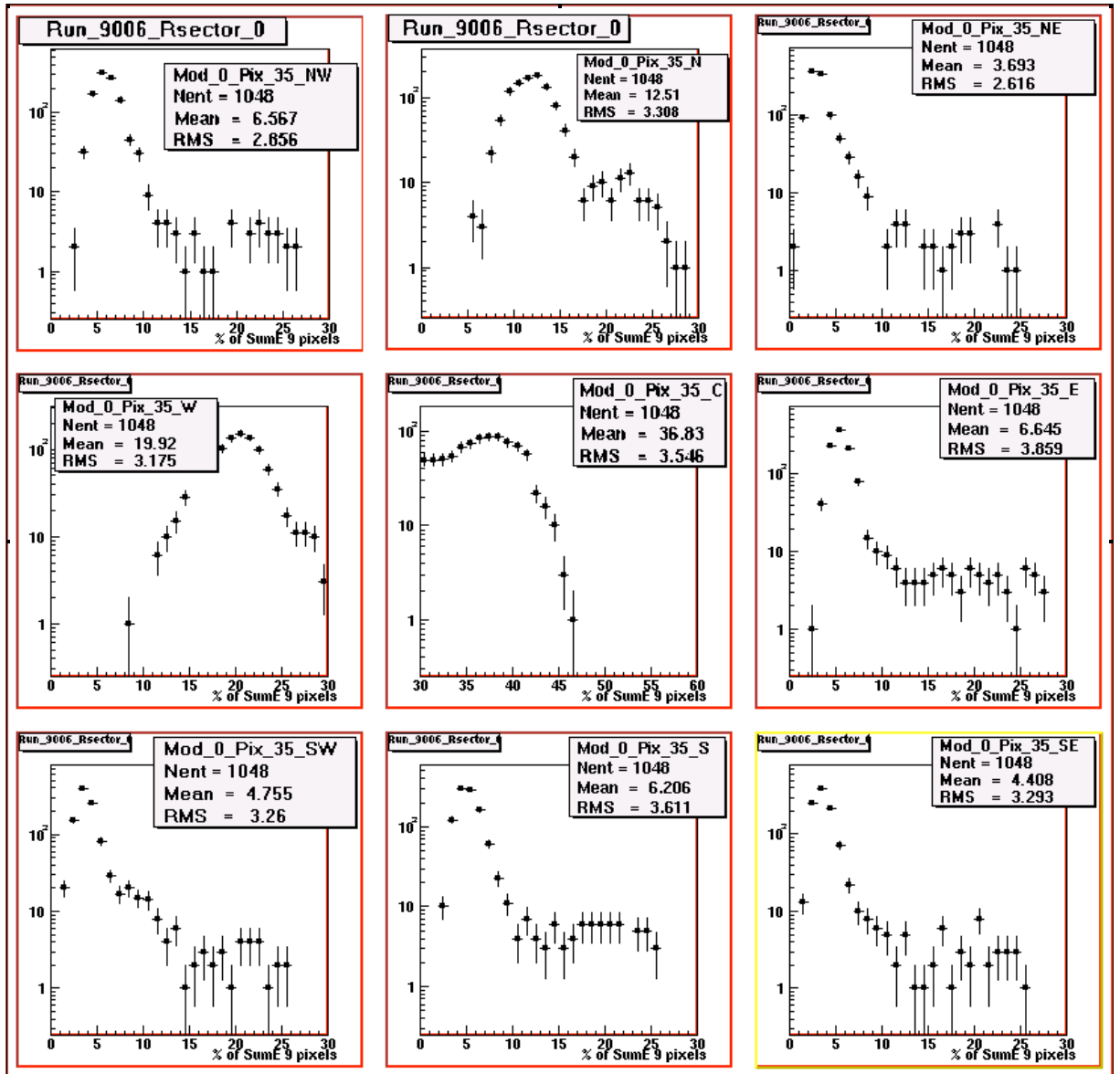
Figure 14 : *Energy fraction (in %) obtained after summation of the nine pixel energies. The central pixel number 35 has been triggered. Notice the deviation discrepancy between the values of the West and the East pixels.*
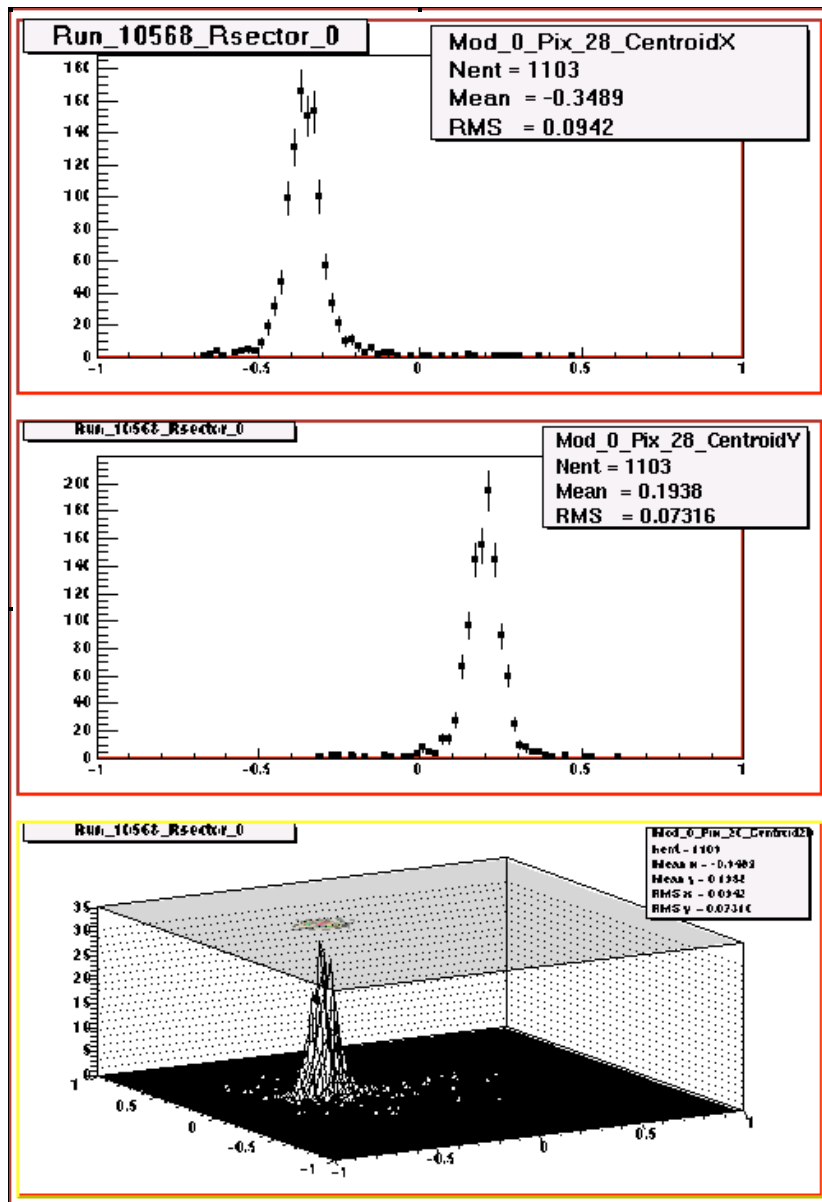
Figure 15*: Off axis centre of the crystal position estimated with real data from the discrepancy between West and East pixels light sharing for X direction and between North and South Pixels for Y direction. X and Y Axis are in mm. Bottom a 2D representation.*

-3.3/ Compton events studies

One way to increase the image resolution could be the use of information on the type of interaction occurred in the crystals (remind that a 250 keV cut is the common threshold in PET scanner). It could be really interesting to differentiate the Compton events occurred in

the crystals to the Compton events occurred in the mouse. For this purpose we selected only the off-peak events (Compton events). The Compton spectrum is shown in Fig. 16 for the nine pixels with the seed pixel in the center.
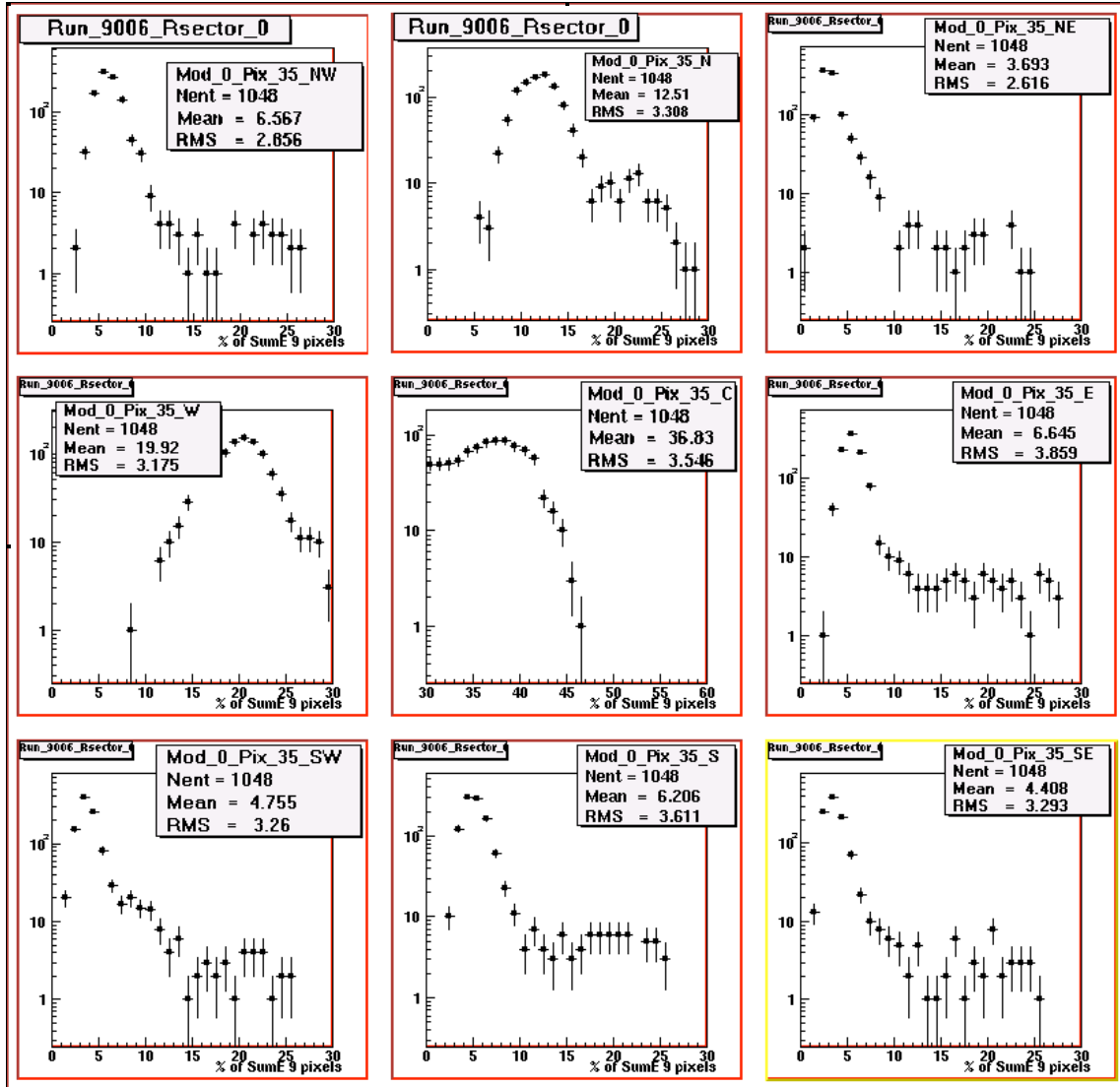
Figure 16 *: Energy fraction (in %) obtained after summation of the nine pixel energies. The central pixel has been auto-triggered. The selected events are the events with a 9 pixel energy sum below the full energy peak. This should corresponds to Compton events.*

The energy sum of 5, 9 and 21 neighbour pixels is shown in Fig.17. From this plot we can conclude that 50 % of selected events can be classified as Compton events in the crystal. And this information could be used by statistical algorithm for PET image reconstruction.
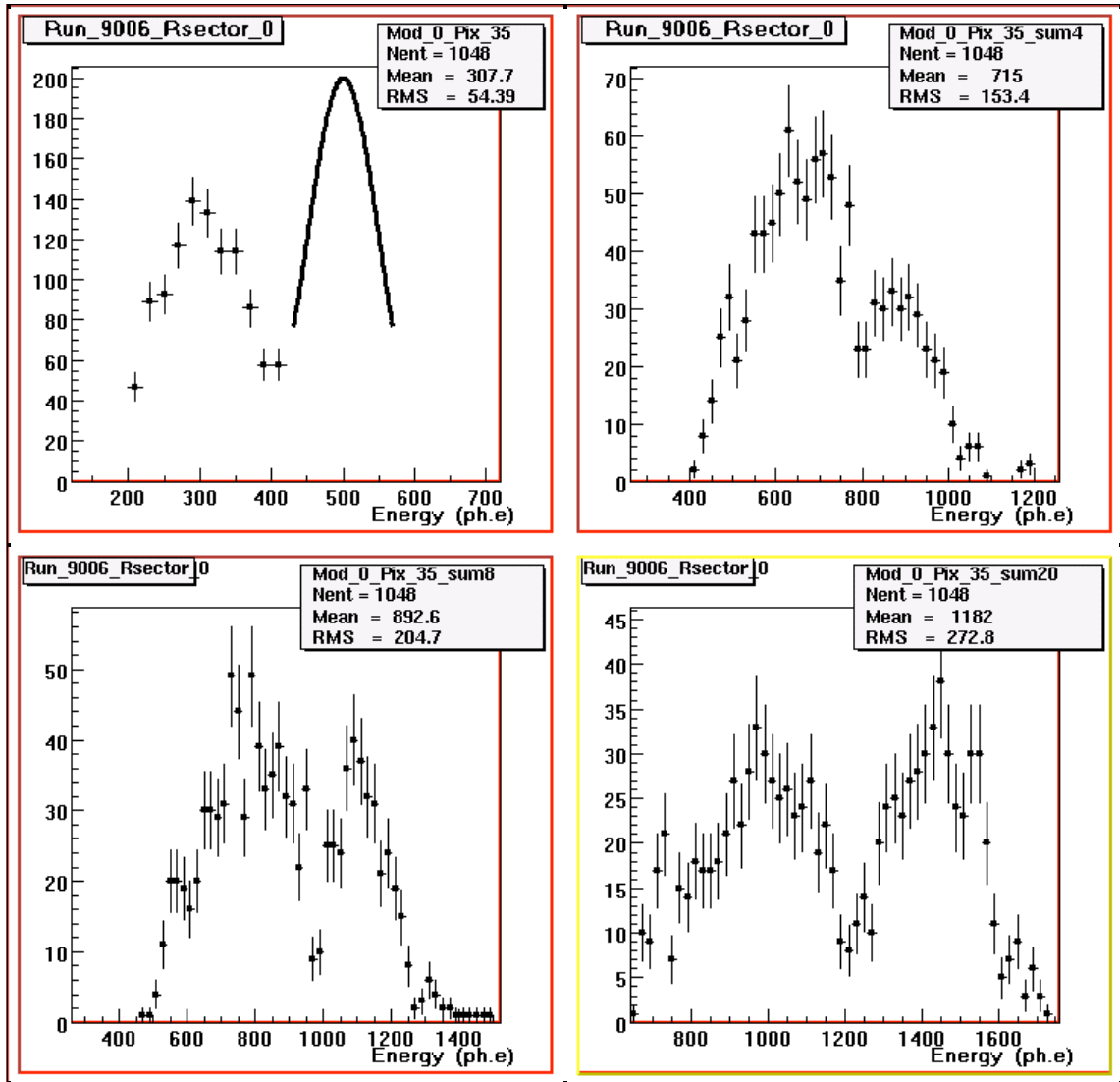
Figure 17: *Compton selected events obtained with one auto-triggered pixel (upper left). Energy sum distribution is shown for 5 pixels (upper right), 9 pixels (lower leftt) and 20 (lower right). We can see the photo-peak reconstruction for 50 % of the events with 20 or 9 pixel clusters.*

-3.4/ Flood diagram trigger rates

A crucial issue of the 64 crystal matrix and MaPMT mapping is the gain variation between the 64 channels since on trigger threshold is used. This can be seen with the flood diagram of

Fig.18. This exercise has been performed in order to show the interest of adjustable trigger level for each channel. This is a strong advantage of the new version of the ASIC developed for the OPERA experiment [4]. This effect has to be taken into account in the normalisation before the image reconstruction.
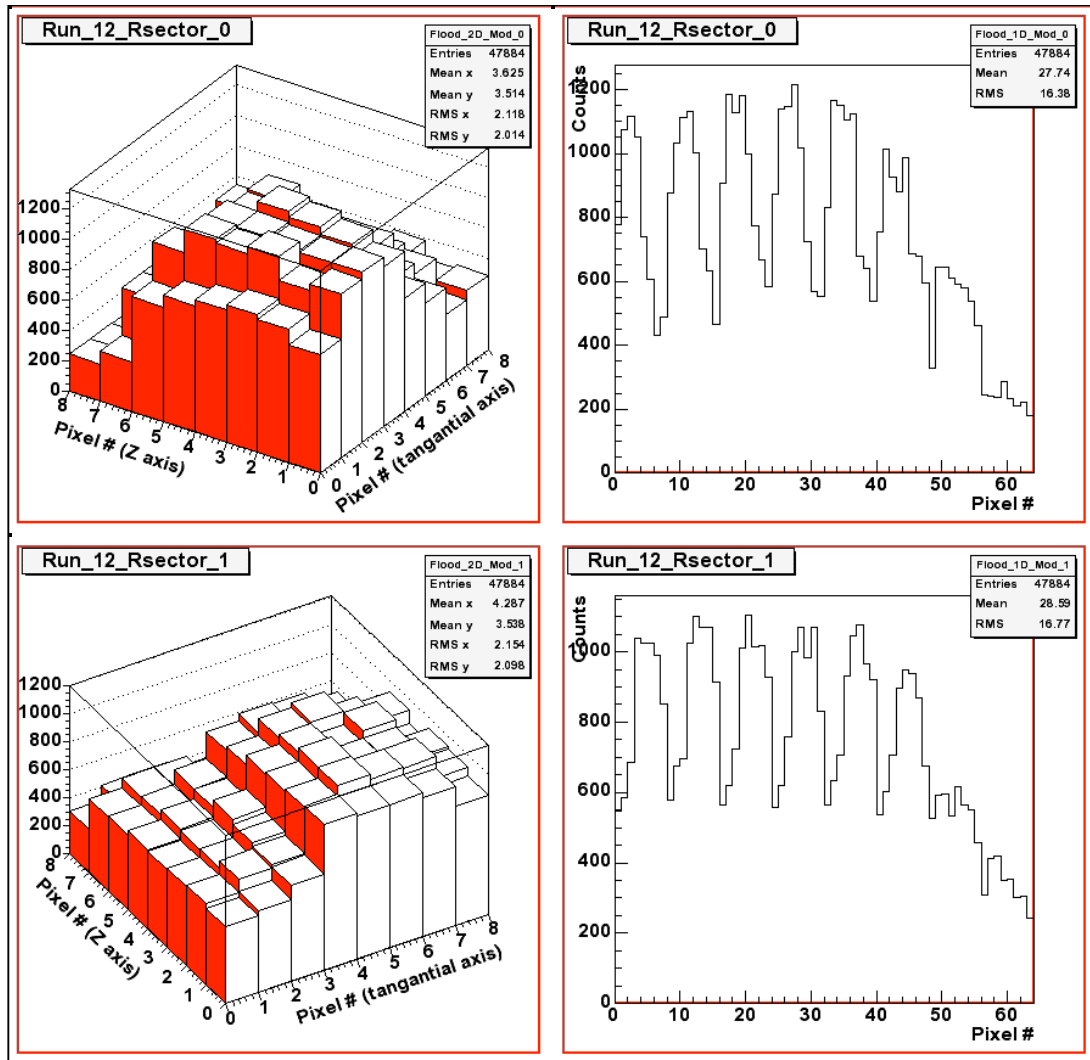
Figure 18 *: Flood diagram of the two detection heads used for the image reconstruction of the Sodium source. Notice the loss of events at the border of the matrix. The shift in the X and Y direction is also visible.*

-4/ Image reconstruction with off-line coincidence sorting

The major difference with classical acquisition PET system is that the coincidence is performed off-line with the event time stamping information. Although the prototype Ethernet board was not really optimised for this purpose from the dead time point of view, we recorded 9 positions of the two heads (20 degree rotation step) to simulate a full ring imaging of a sodium source. The raw data was processed in the List Mode Format of CCC [5]. To reconstruct the image of the source we used a private interface to the STIR software [6] developed by our CCC collaborators.

Fig.19 shows an image obtained by the two LSO detection head set-up of Fig.3.
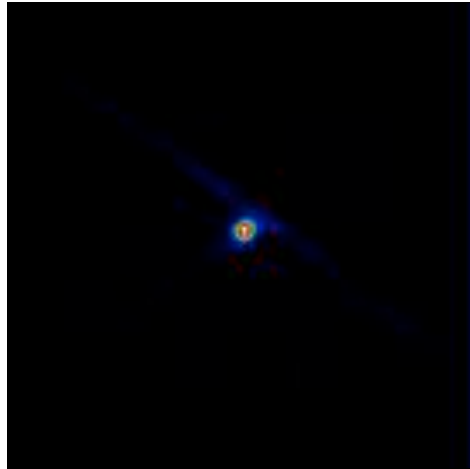
Figure 19: *The reconstructed image of the ^{22}Na source obtained with the coincidence set-up. The reconstruction software used is the STIR package. The Raw DATA has been first processed in LMF Crystal Clear Format.*

Conclusion

This paper describes the results obtained with a 2-heads micro-PET prototype using lutetium crystals (LSO/LuAP), MaPMTs and a dedicated, fully developed by IPNL, DAQ readout chain, completely driven through an Ethernet processor.
Detailed results have been obtained using this set-up in the overall prototype calibration (single p.e. resolution, trigger efficiencies, energy resolution) and in its tracking and imaging capabilities. The limitations of DOI reconstruction using the fast components of LSO/LuAP have been demonstrated together with the possibility to use part of the Compton events in the detection head.
The feasibility of producing images has also been given. Such a system is easily scalable and can be upgraded using different photo detectors (flat panel PMTs have been characterized with the same R/O chain) and more powerful electronic chain (for example à la OPERA where the front end chip allows the gain spread compensation and the Ethernet DAQ system allows a 100 larger bandwidth for data transfer).

References:

[1] R. Barbier, Y. Déclais, C. Dujardin, N. Garnie, M. Janier, I.A. Kamenskikh, G. Largeron, J. Marteau, C. Pedrini, D. Sappey Marinier, *Nucl. Instr. Meth*. **A 527** (2004) 175-179.

[2] C. Girerd, et al., *IEEE Nuclear Science Symposium and Nuclear Imaging Conference*, , Lyon, 15-20 October 2003. **Patent Id WO2005081121**.

[3] E.H. Bellamy et al, *Nucl. Instr. Meth.* **A 339** (1994) 468-476.

[4] S. Bondil et al. Performance of the 32-channels front-end electronic chip, OPERA internal note n°34 (2005).

[5] Ch. Morel et al. Clear PET Project List Mode Format Implementation V1.3.2, IPHE/UNIL 2002, private communication.

[6] C Labbé et al. Software for Tomographic Image Reconstruction, STIR package; *Proc. Of 3D99*, **June 1999**, Egmond aan Zee, The Netherlands.

Two-head small animal PET prototype with LSO/LuAP coupled to a multi-anode PMT

R. Barbier[a], Y. Déclais[a], C. Dujardin[b,*], N. Garnier[b], M. Janier[c], I.A. Kamenskikh[b], G. Largeron[a], J. Marteau[a], C. Pedrini[b], D. Sappey Marinier[c]

[a] *Institut de Physique Nucléaire de Lyon, UMR CNRS 5822, Université Lyon I, Villeurbanne, France*
[b] *Laboratoire de Physico-Chimie des Matériaux Luminescents, UMR CNRS 5620, Université Lyon I, 43 Bd. du 11 novembre 1918, Villeurbanne, Cedex 69622, France*
[c] *Centre D'Etudes et de Recherches Médicales en Emission de Positrons, Hôpital Cardio-Neurologique, Lyon, France*

Abstract

In the frame of the Crystal Clear Collaboration, a small animal PET prototype is presented. To measure the depth of interaction we have chosen a LSO/LuAP phoswich mode. Recent results on LuAP in terms of light yield and scintillation decay are presented. Multi-Anode PMT from Hamamatsu were used for the light detection. A dedicated acquisition electronics fully based on Ethernet was developed for the readout configuration and the data acquisition. In this note, we present the progress status and the perspectives of this work.
© 2004 Elsevier B.V. All rights reserved.

1. Introduction

Main requirements to a small animal PET system are spatial resolution and sensitivity [1]. Unfortunately increasing the spatial resolution implies reducing the parallax error which is drastically enhanced with the crystal size. One of the solutions is to perform Depth of Interaction (DOI) analysis which can be achieved using pulse shape discrimination (PSD). The purpose of this paper is to present the advance of a two-head prototype based on two different crystals (LSO and LuAP), a multi anode PMT and dedicated electronics based on Ethernet. The main goal of

such prototype is to be easily used to evaluate different components such as crystals, reflectors, packaging in real conditions of PET.

2. Crystals

$Lu_2SiO_5:Ce^{3+}$ (LSO) and $LuAlO_3:Ce^{3+}$ (LuAP) are known for their good scintillation properties for nuclear imaging [2]. Their stopping power is similar. The main difference is in the decay time. LSO has a decay time of 40 ns while LuAP has a fast component in the range of 20 ns and a slow component of about 400 μs. Depending on the crystal quality and geometry of the experiment, the light yield can vary from 10% to 50% of a standard LSO crystal. While LSO is commercially

*Corresponding author. Fax: +33-72-43-11-30.
E-mail address:* dujardin@pcml.univ-lyon1.fr (C. Dujardin).

available, research on LuAP is still in progress to improve mainly the light yield. Different ways are investigated. Substitution of Lu by Y (at a level over 10%) makes the crystal growth easier (mainly in terms of Ce^{3+} incorporation). This results in the decrease of the stopping power but a significant improvement of the yield has been observed. Up to now the origin of the improved properties of mixed crystals as compared to LuAP remains unclear since it is hard to identify which limitations on scintillator performance are inherent to the material and which are caused by the imperfection of crystal growth procedure. We have chosen to focus our attention on LuAP.

The LuAP crystals were grown by A. Petrosyan using Bridgmann technique [3]. Up to now, we received more than 200 pixels with dimensions of $2 \times 2 \times 10 \, mm^3$. The yield has been measured using the 662 keV γ-rays from a ^{137}Cs source. A 2020Q PMT and a shaping amplifier connected to a multichannel analyzer were used to measure the pulse height spectra. The crystals were measured without any wrapping in the vertical position. Actual cerium concentration has been evaluated from the absorption spectra in the energy region of the 4f–5d transition within the cerium ion. Due to the sample thickness we used the values of the absorption coefficient at 320 nm. Previous calibration on thin samples was performed elsewhere [4]. We deduced from these measurements the estimation of the Ce^{3+} concentration in the crystal. The former and the latter results joined together allow to plot the concentration dependence of the pixels yield (Fig. 1). The dependence looks linear when the same starting materials are used. Additional experiments are in progress to verify the dependence of the light yield on the starting material. An important factor is the transparency of the crystal in the range of the fluorescence (340–440 nm). Previously published studies are available [4,5]. Traps which are known to have a substantial effect on LuAP light yield offer additional competitive channels for the relaxation of excitations. The thermoluminescence glow curves exhibit some differences from crystal to crystal [6] but the correlation between traps and growth conditions is not clear yet apart from the case of specific traps introduced by co-doping.
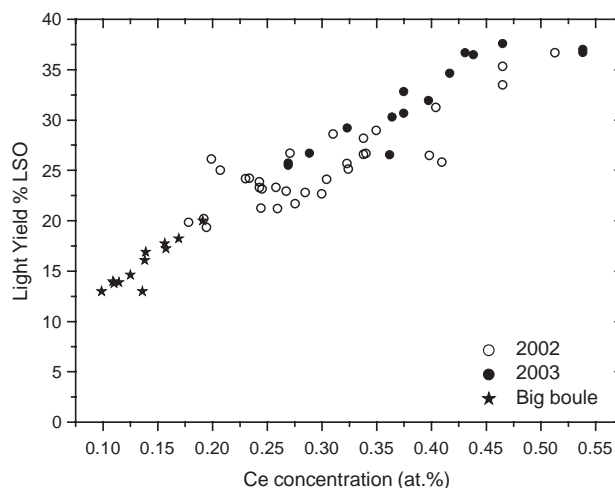
Fig. 1. Light yield measured on $2 \times 2 \times 10 \, mm^3$ LuAP naked pixels in vertical position as a function of the cerium content deduced from absorption.

3. Light collection

In the one to one coupling mode the light collection is a crucial point. In the "needle" shape, multiple reflections occur prior to the detection. We measured the light output of different crystals without any wrapping but with and without mask on the PMT. It was shown that for LSO and LuAP, nearly half of the light was emitted through the side faces. Even with a mask between the PMT and the "exit" face, a nice photopeak can be observed. To collect as much light as possible matrices made of different materials (stainless steel, epoxy, epoxy charged with TiO_2, Tyvek and Teflon) were made. Among all these materials only Tyvek and Teflon improve the light collection. Tyvek improves the observed LSO yield by 40% while Teflon gives 30% improvement. For LuAP, both materials improve the observed light output by 25%. From a mechanical point of view teflon is easier to work with. A full matrix filled with LSO pixels is shown in Fig. 2.

4. Pulse shape discrimination

To enhance the sensitivity of the system, longer crystals are required to improve the stopping power. But with longer crystals parallax error

Fig. 2. Matrix made of Teflon and filled with LSO pixels. Distance between the crystals is 300 μm.

occurs when the region of interest is far from the center of the field of view. To perform DOI analysis, pulse shape discrimination can be achieved using the difference of time shape between LSO and LuAP. This PSD can be performed on the slow component of LuAP or on its fast component. We did evaluate the efficiency of the fast component discrimination. The pulses from the PMT were collected by a numerical oscilloscope (LeCroy LT402) and each pulse was digitized (sampling: 1 GHz) and transferred to a computer. Histogramming each pulse allows to record pulse height spectra. For each value being in the photopeak, the time gravity center τ of the corresponding pulse has been calculated and histogrammed.

$$\tau = \frac{\sum_{t_i=t_0}^{t_{end}} t_i y(t_i)}{\sum_{t_i=t_0}^{t_{end}} y(t_i)}$$

t_0 was set at the maximum of the decay and different t_{end} have been tried in order to estimate the best LSO/LuAP discrimination. Different values from $t_{end} = 10$ ns up to $t_{end} = 400$ ns were tried and the results are presented in Fig. 3a. Position of the averaging value (τ_{av}) obtained for LSO and LuAP versus t_{end} is presented in Fig. 3b. It is clear that the best compromise is for t_{end} lying between 80 and 140 ns. For higher values of t_{end}, the slow component of the LuAP crystal shifts τ_{av}
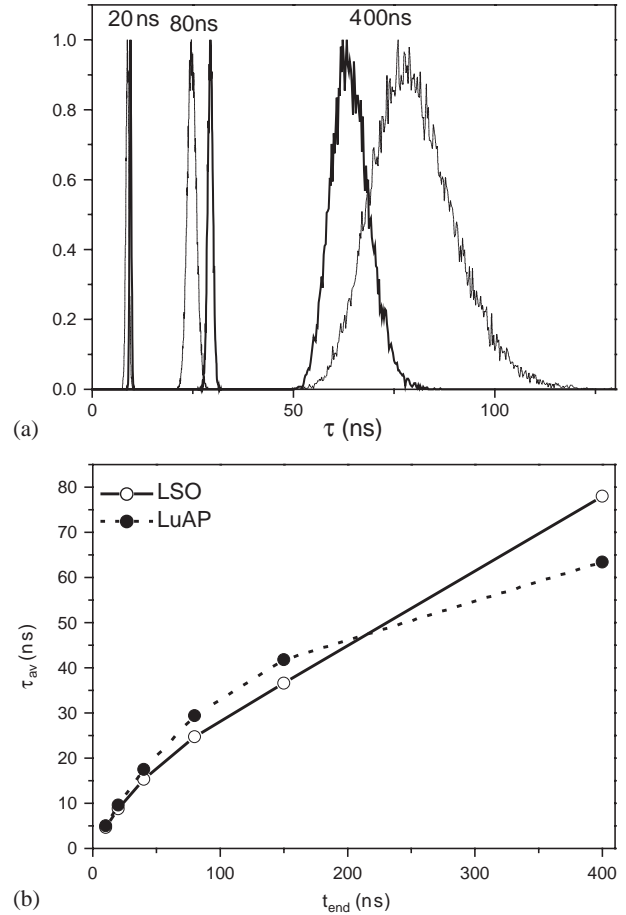
Fig. 3. (filled circle: LuAP; open circle: LSO). (a) Histogram of τ for $t_{end} = 20$, 80 and 400 ns. (b) Evolution of the histogram maximum position with t_{end} for LSO and LuAP.

towards higher values which deteriorate the LSO/LuAP discrimination.

Sampling effect has been checked as well. Same measurement with $t_{end} = 80$ ns but with sampling changing from 1 GHz to 100 MHz are presented in Fig. 4. It shows that with F-ADC running at 250 MHz the mismatch factor is in the range of 1%.

5. Electronics and experimental setup

5.1. Smart sensor and DAQ architecture

A new concept of Ethernet DAQ is demonstrated. The DAQ architecture is based on
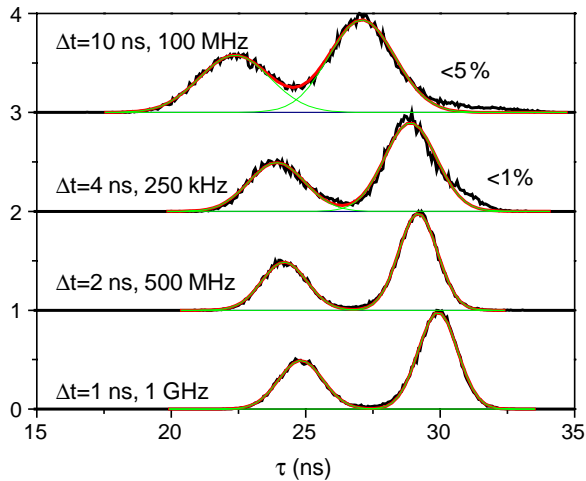
Fig. 4. Sampling effect measured with two crystals on the PMT.

Ethernet [7]. Each detector and associated electronics is a smart sensor controlled via the network. Data are also sent to the event builder via the network. Therefore no specific bus is needed with this architecture. Each detector head interface has an IP address and is a node on the network. First acquisition tests with off-line coincidence processing has been performed with the following configuration:

- Detector: LSO (section $2 \times 2\,mm^2$) matrices are mapped on a MaPMT R7600 (Hamamatsu).
- Front-end electronics: an auto-triggerable VAhdr11-TA32cg chip (IDEAS) is used to read out the 64 channels. Charge digitization of the 64 channels is performed by a 12 bits ADC at 5 MHz. The corresponding readout time is 12.4 μs.
- The sequencer: an FPGA performs the readout sequencing and the configuration of the front-end electronics. The time stamping precision of one single event is 20 ns for this first board version (this corresponds to the FPGA clock).
- Ethernet interface: an Ethernet processor, BFOOT (Agilent) is the detector head interface with the network. The processor sends the data on the network to the event builder PC and receives the configuration command. The bandwidth processor for this version was 1 Mbits/s. The event builder receives data via the network

and can be used for data processing and data formatting (LMF format).

5.2. Coincidence experimental setup

The experimental setup is composed of two detector heads. One smart sensor is working in an
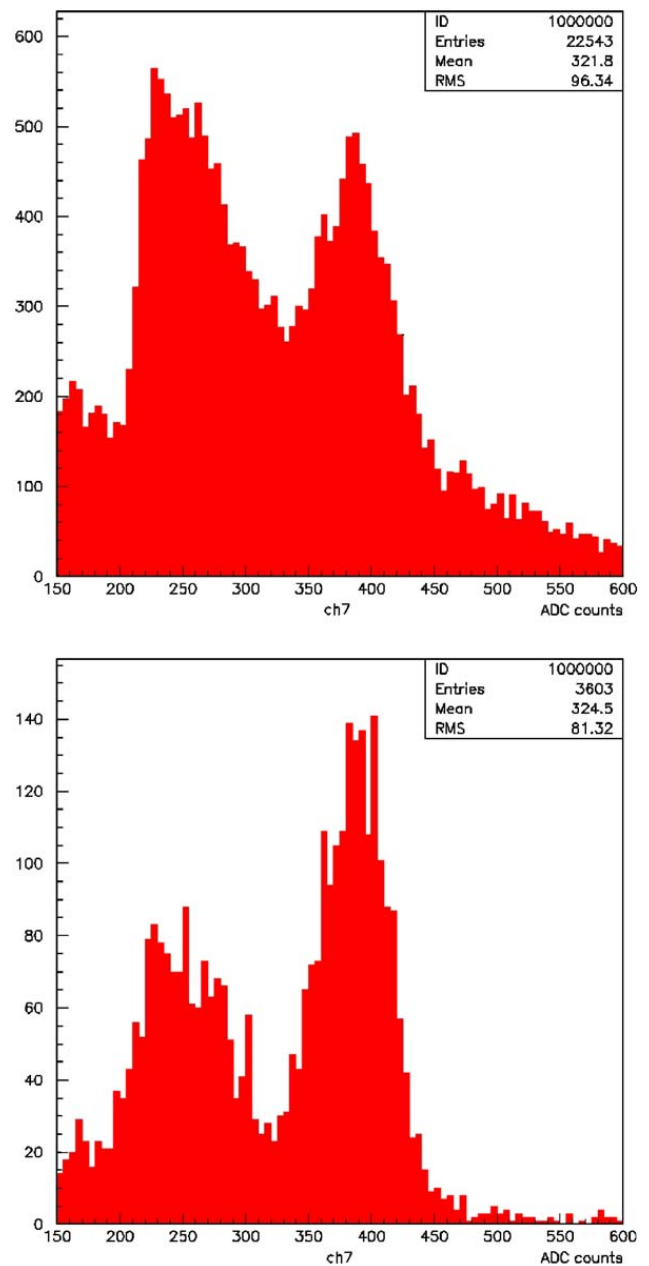
Fig. 5. Data obtained with a ^{22}Na source before and after coincidence sorting.

auto-triggerable mode and receives from the second head an external trigger. The same front-end electronics is used by the second detector head and the trigger of the fast shaper is used to generate the external trigger. The time stamp of the external trigger arrival is registered by the smart sensor and is sent via the network to the event builder PC with the charge ADC values of each pixel and the time stamp value of the triggered event.

5.3. Preliminary results

A Gaussian fit of the coincidence distribution (difference between the two time stamps) gives a FWHM of 75 ns. The energy spectra obtained for 1 pixel are shown in Fig. 5 before (top) and after (bottom) off-line coincidence selection. We can see that the random trigger due to natural crystal activity is suppressed. Cross-talk between neighboring pixels has been obtained from energy information of each pixel. We measured that 8% (2%) of the central pixel energy is received by the central (corner) neighbors. This cross-talk could be used for DOI determination with different crystal matrix layers corresponding to different optical cross-talks. This will be tested in a future work for DOI application. A new version of smart sensor with a better time stamp precision is under test. Two smart sensor heads with the same electronics will be tested and coincidence time resolution will be performed. A dedicated board to treat coincidence triggers will be used to decrease the time stamp of the triggers and the readout time due to charged digitization.

References

[1] S.R. Cherry, et al., IEEE Trans. Nucl. Sci. NS-44 (1997) 1161.
[2] C. Dujardin, J.C. Gacon, C. Pedrini, Encyclopedia of Materials: Science and Technology, Elsevier Science, Amsterdam, 2001, pp. 5325–5329.
[3] A. Petrosyan, et al., Cryst. Res. Technol. 33 (1998) 241, and related works.
[4] C. Dujardin, et al., J. Phys.: Condens. Matter 10 (1998) 3061.
[5] A. Lempicki, et al., Proceedings of the International Conference on Inorganic Scintillators and their Applications, SCINT95, 28 August–1 September 1995, Delft University Press, Delft, p. 340.
[6] A.J. Wojtowicz, et al., Radiat. Meas. 29 (3–4) (1998) 323.
[7] C. Girerd, et al., IEEE Nuclear Science Symposium and Nuclear Imaging Conference, LYCEN 2000-109, Lyon, 15–20 October 2003.

B   Recherche de la supersymétrie au LEP, 1996-2002

B.1   Description du contexte et du travail d'analyse

Je suis arrivé en 1996 dans l'expérience DELPHI sur le collisionneur e^+e^- du LEP situé au CERN. J'ai débuté ma première analyse des données, comme pouvait le faire un doctorant de l'époque, en recherchant les événements de production de paires de bosons W se désintégrant dans le canal 100% hadronique dit 4 jets dans l'état final. Il s'agissait dans ce travail d'optimiser la partie reconstruction de jets permettant une meilleur sélection des événements W^+W^- en vue de la reconstruction de la masse invariante du boson W.

La venue d'un responsable du groupe DEPHI à l'IPNL pour monter un groupe d'analyse sur une nouvelle thématique conduisit les doctorants et moi-même à se tourner vers la recherche de nouvelle physique et plus particulièrement vers la supersymétrie. L'activité du groupe DELPHI IPNL sur LEPI était dédiée aux mesures électrofaibles du modèle standard.

Lors de la montée en énergie du LEP 1.5 (1995) des excès d'événements avaient été observés dans les données par des analyses de l'expérience ALEPH dédiées à la recherche du boson de Higgs en 4-jets. Cette analyse utilisait comme veto aux "jets QCD", des éléments de matrice de diffusion de type QCD à 4 partons dans l'état final ($q\bar{q}gg$). Il y avait également un important travail sur l'étude de la combinatoire et la sélection des paires de jets pour calculer les masses invariantes recherchées. Nous avons mené ce type d'études dans l'expérience DELPHI et des analyses de données similaires.

C'est ainsi que nous avons été amenés à développer des analyses multi-jets où le nombre de jets pouvait être libre. Nous pouvions ainsi étudier les queues de distribution des événements à grands nombre de jets pour la recherche de la supersymétrie.

Pendant la même période des événements en excès (comme c'est souvent le cas) étaient observés dans l'expérience HERA sur le collisionneur H1. Ces événements pouvaient être interprétés comme la signature de supersymétrie avec brisure de la R-parité comme d'ailleurs les excès d'ALEPH en 4 jets.

En 1997 mon recrutement en tant que Maître de Conférences (Jean-Eudes Augustin directeur de l'IPNL) m'a permis de m'investir pleinement sur ce sujet. Nous avions à notre disposition le Générateur Monte Carlo Susygen qui fournissait une version de la supersymétrie avec la brisure de la R-parité (malheureusement sans les équations du groupe de renormalisation avec brisure de la R-parité).

C'est dans ce contexte qu'a débuté mon analyse pour la recherche de la supersymétrie avec brisure de la R-parité et la désintégration du neutralino via des couplages de type UDD. En cohérence avec mes premières études sur la masse du boson W dans le canal 4-jets, mes analyses ont consisté à rechercher des événements ayant des topologies à grands nombres de jets (6 et 10). Des techniques de clustering comme les algorithmes de Durham (spécialistes des études QCD) nous permettaient de caractériser la topologie des événements multi-jets.

Vu la quantité de canaux à couvrir (couplages LLE, LQD, UDD pour les neu-

tralinos, les charginos, les sleptons et les squarks) le travail était réparti entre l'équipe DELPHI du LPSC (IRSN à cette époque) et de l'IPNL.

J'ai effectué durant les premières années, la recherche des neutralinos et des charginos puis celle des squarks et des sleptons après que mon analyse initiale fut reprise par un doctorant de Saclay... La particularité de ces analyses résidait dans l'étude de la combinatoire de l'appariement des jets afin de reconstruire des masses invariantes des particules supersymétriques recherchées.

C'était à mon avis une stratégie intéressante (et pas complètement stupide) puisque complémentaire au recherche "standard" du Higgs en 4-jets. Notre analyse était plus ouverte à l'apparition de phénomènes exotiques. La contrepartie résidait dans la nécessité de produire ses propres échantillons de simulation complète (DELSIM) de tous ces canaux possibles (les connaisseurs apprécieront) sur les différentes fermes de calcul du CERN ou du CCIN2P3. Ce travail fastidieux et peu gratifiant, mais néanmoins nécessaire, a certainement nui à la qualité de nos analyses R-parité violée, n'ayant je le fais remarquer au passage pas de doctorant pour effectuer l'analyse alors que j'avais 280 heures d'enseignement en TP à assurer par an.

Un autre point important concernant l'analyse UDD menée par l'IPNL et le CEA Saclay est que nous n'utilisions qu'une modélisation simplifiée de l'hadronisation interfacée à PYTHIA lorsqu'un squark se désintégrait en paires de quarks avec une brisure du nombre baryonique B (pas prévue par le modèle des cordes de ce générateur). Sur le plan des méthodes d'analyse proprement dites nous étions déjà passés à l'utilisation de réseaux de neurones.

A cette période cela était encore décrié par une majorité des chercheurs qui utilisaient des coupures séquentielles. Il est assez amusant de voir l'utilisation systématique de ces techniques ("automatisées" sous ROOT) dans les différentes analyses au LHC.

J'ai poursuivi ces études deux années supplémentaires après la fin de la prise des données afin de publier l'analyse définitive et complète de l'ensemble des données pour la recherche de la supersymétrie avec brisure de la R-parité de la collaboration DELPHI (voir la section suivante). J'étais également coordonnateur de la "boîte" R-parity violation au CERN pour les semaines DELPHI mensuelles. Cela m'a permis de suivre deux autres articles de la collaboration sur le sujet.

Venant de la théorie, j'ai réalisé durant toutes ces années qu'il existait dans la physique des particules expérimentale un respect constant du travail même si celui-ci n'était pas toujours de très haut niveau. C'est certainement le premier moteur de la recherche collaborative et c'est à mon avis une marque de fabrique de ce domaine de recherche.

Mon investissement dans la recherche de la supersymétrie avec brisure de la R-parité m'a permis de participer en toute modestie à l'écriture d'un article de revue dans "Physics Report".

Je ne dois d'être en tête des signataires qu'à mon nom de famille. Ce papier relativement volumineux a tout de même nécessité un travail de plusieurs années à ses auteurs.

B.2 Publication DELPHI sur la recherche de la supersymétrie en R-parité violée

Search for supersymmetric particles assuming R-parity non-conservation in e$^+$e$^-$ collisions at $\sqrt{s} = 192$ to 208 GeV

The DELPHI Collaboration

J. Abdallah[25], P. Abreu[22], W. Adam[51], P. Adzic[11], T. Albrecht[17], T. Alderweireld[2], R. Alemany-Fernandez[8], T. Allmendinger[17], P. Allport[23], U. Amaldi[29], N. Amapane[45], S. Amato[48], E. Anashkin[36], A. Andreazza[28], S. Andringa[22], N. Anjos[22], P. Antilogus[25], W-D. Apel[17], Y. Arnoud[14], S. Ask[26], B. Asman[44], E. Augustin[25], A. Augustinus[8], P. Baillon[8], A. Ballestrero[46], P. Bambade[20], R. Barbier[27], D. Bardin[16], J. Barker[17], A. Baroncelli[39], M. Battaglia[8], M. Baubillier[25], K-H. Becks[53], M. Begalli[6], A. Behrmann[53], E. Ben-Haim[20], N. Benekos[32], A. Benvenuti[5], C. Berat[14], M. Berggren[25], L. Berntzon[44], D. Bertrand[2], M. Besancon[40], N. Besson[40], D. Bloch[9], M. Blom[31], M. Bluj[52], M. Bonesini[29], M. Boonekamp[40], L. Booth[23], G. Borisov[21], O. Botner[49], B. Bouquet[20], V. Bowcock[23], I. Boyko[16], M. Bracko[43], R. Brenner[49], E. Brodet[35], P. Bruckman[18], M. Brunet[7], L. Bugge[33], P. Buschmann[53], M. Calvi[29], T. Camporesi[8], V. Canale[38], F. Carena[8], N. Castro[22], F. Cavallo[5], M. Chapkin[42], Ph. Charpentier[8], P. Checchia[36], R. Chierici[8], P. Chliapnikov[42], J. Chudoba[8], U. Chung[8], K. Cieslik[18], P. Collins[8], R. Contri[13], G. Cosme[20], F. Cossutti[47], J. Costa[50], D. Crennell[37], J. Cuevas[34], J. D'Hondt[2], J. Dalmau[44], T. da Silva[48], W. Da Silva[25], G. Della Ricca[47], A. De Angelis[47], W. De Boer[17], C. De Clercq[2], B. De Lotto[47], N. De Maria[45], A. De Min[36], L. de Paula[48], L. Di Ciaccio[38], A. Di Simone[39], K. Doroba[52], J. Drees[53,8], M. Dris[32], G. Eigen[4], T. Ekelof[49], M. Ellert[49], M. Elsing[8], C. Espirito Santo[22], G. Fanourakis[11], D. Fassouliotis[11,3], M. Feindt[17], J. Fernandez[41], A. Ferrer[50], F. Ferro[13], U. Flagmeyer[53], H. Foeth[8], E. Fokitis[32], F. Fulda-Quenzer[20], J. Fuster[50], M. Gandelman[48], C. Garcia[50], Ph. Gavillet[8], E. Gazis[32], R. Gokieli[8,52], B. Golob[43], G. Gomez-Ceballos[41], P. Goncalves[22], E. Graziani[39], G. Grosdidier[20], K. Grzelak[52], J. Guy[37], C. Haag[17], A. Hallgren[49], K. Hamacher[53], K. Hamilton[35], S. Haug[33], F. Hauler[17], V. Hedberg[26], M. Hennecke[17], H. Herr[8], J. Hoffman[52], S-O. Holmgren[44], J. Holt[8], A. Houlden[23], K. Hultqvist[44], N. Jackson[23], G. Jarlskog[26], P. Jarry[40], D. Jeans[35], K. Johansson[44], D. Johansson[44], P. Jonsson[27], C. Joram[8], L. Jungermann[17], F. Kapusta[25], S. Katsanevas[27], E. Katsoufis[32], G. Kernel[43], P. Kersevan[8,43], U. Kerzel[17], A. Kiiskinen[15], T. King[23], J. Kjaer[8], P. Kluit[31], P. Kokkinias[11], C. Kourkoumelis[3], O. Kouznetsov[16], Z. Krumstein[16], M. Kucharczyk[18], J. Lamsa[1], G. Leder[51], F. Ledroit[14], L. Leinonen[44], R. Leitner[30], J. Lemonne[2], V. Lepeltier[20], T. Lesiak[18], W. Liebig[53], D. Liko[51], A. Lipniacka[44], H. Lopes[48], M. Lopez[34], D. Loukas[11], P. Lutz[40], L. Lyons[35], J. MacNaughton[51], A. Malek[53], S. Maltezos[32], F. Mandl[51], J. Marco[41], R. Marco[41], B. Marechal[48], M. Margoni[36], J-C. Marin[8], C. Mariotti[8], A. Markou[11], C. Martinez-Rivero[41], J. Masik[12], N. Mastroyiannopoulos[11], F. Matorras[41], C. Matteuzzi[29], F. Mazzucato[36], M. Mazzucato[36], R. Mc Nulty[23], C. Meroni[28], E. Migliore[45], W. Mitaroff[51], U. Mjoernmark[26], T. Moa[44], M. Moch[17], K. Moenig[8,10], R. Monge[13], J. Montenegro[31], D. Moraes[48], S. Moreno[22], P. Morettini[13], U. Mueller[53], K. Muenich[53], M. Mulders[31], L. Mundim[6], W. Murray[37], B. Muryn[19], G. Myatt[35], T. Myklebust[33], M. Nassiakou[11], F. Navarria[5], K. Nawrocki[52], R. Nicolaidou[40], M. Nikolenko[16,9], A. Oblakowska-Mucha[19], V. Obraztsov[42], A. Olshevski[16], A. Onofre[22], R. Orava[15], K. Osterberg[15], A. Ouraou[40], A. Oyanguren[50], M. Paganoni[29], S. Paiano[5], P. Palacios[23], H. Palka[18], D. Papadopoulou[32], L. Pape[8], C. Parkes[24], F. Parodi[13], U. Parzefall[8], A. Passeri[39], O. Passon[53], L. Peralta[22], V. Perepelitsa[50], A. Perrotta[5], A. Petrolini[13], J. Piedra[41], L. Pieri[39], F. Pierre[40], M. Pimenta[22], E. Piotto[8], T. Podobnik[43], V. Poireau[8], E. Pol[6], G. Polok[18], V. Pozdniakov[16], N. Pukhaeva[2,16], A. Pullia[29], J. Rames[12], A. Read[33], P. Rebecchi[8], J. Rehn[17], D. Reid[31], R. Reinhardt[53], P. Renton[35], F. Richard[20], J. Ridky[12], M. Rivero[41], D. Rodriguez[41], A. Romero[45], P. Ronchese[36], P. Roudeau[20], T. Rovelli[5], V. Ruhlmann-Kleider[40], D. Ryabtchikov[42], A. Sadovsky[16], L. Salmi[15], J. Salt[50], C. Sander[17], A. Savoy-Navarro[25], U. Schwickerath[8], A. Segar[35], R. Sekulin[37], M. Siebel[53], A. Sisakian[16], G. Smadja[27], O. Smirnova[26], A. Sokolov[42], A. Sopczak[21], R. Sosnowski[52], T. Spassov[8], M. Stanitzki[17], A. Stocchi[20], J. Strauss[51], B. Stugu[4], M. Szczekowski[52], M. Szeptycka[52], T. Szumlak[19], T. Tabarelli[29], C. Taffard[23], F. Tegenfeldt[49], J. Timmermans[31], L. Tkatchev[16], M. Tobin[23], S. Todorovova[12], B. Tome[22], A. Tonazzo[29], P. Tortosa[50], P. Travnicek[12], D. Treille[8], G. Tristram[7], M. Trochimczuk[52], C. Troncon[28], M-L. Turluer[40], A. Tyapkin[16], P. Tyapkin[16], S. Tzamarias[11], V. Uvarov[42], G. Valenti[5], P. Van Dam[31], J. Van Eldik[8], A. Van Lysebetten[2], N. van Remortel[2], I. Van Vulpen[8], G. Vegni[28], F. Veloso[22], W. Venus[37], P. Verdier[27], V. Verzi[38], D. Vilanova[40], L. Vitale[47], V. Vrba[12], H. Wahlen[53], J. Washbrook[23], C. Weiser[17], D. Wicke[8], J. Wickens[2], G. Wilkinson[35], M. Winter[9], M. Witek[18], O. Yushchenko[42], A. Zalewska[18], P. Zalewski[52], D. Zavrtanik[43], V. Zhuravlov[16], I. Zimin[16], A. Zintchenko[16], M. Zupan[11]

¹   Department of Physics and Astronomy, Iowa State University, Ames IA 50011-3160, USA
²   Physics Department, Universiteit Antwerpen, Universiteitsplein 1, 2610 Antwerpen, Belgium
     and IIHE, ULB-VUB, Pleinlaan 2, 1050 Brussels, Belgium
     and Faculté des Sciences, Univ. de l'Etat Mons, Av. Maistriau 19, 7000 Mons, Belgium
³   Physics Laboratory, University of Athens, Solonos Str. 104, 10680 Athens, Greece
⁴   Department of Physics, University of Bergen, Allégaten 55, 5007 Bergen, Norway
⁵   Dipartimento di Fisica, Università di Bologna and INFN, Via Irnerio 46, 40126 Bologna, Italy
⁶   Centro Brasileiro de Pesquisas Físicas, rua Xavier Sigaud 150, 22290 Rio de Janeiro, Brazil
     and Depto. de Física, Pont. Univ. Católica, C.P. 38071 22453 Rio de Janeiro, Brazil
     and Inst. de Física, Univ. Estadual do Rio de Janeiro, rua São Francisco Xavier 524, Rio de Janeiro, Brazil
⁷   Collège de France, Lab. de Physique Corpusculaire, IN2P3-CNRS, 75231 Paris Cedex 05, France
⁸   CERN, 1211 Geneva 23, Switzerland
⁹   Institut de Recherches Subatomiques, IN2P3 - CNRS/ULP - BP20, 67037 Strasbourg Cedex, France
¹⁰ Now at DESY-Zeuthen, Platanenallee 6, 15735 Zeuthen, Germany
¹¹ Institute of Nuclear Physics, N.C.S.R. Demokritos, P.O. Box 60228, 15310 Athens, Greece
¹² FZU, Inst. of Phys. of the C.A.S. High Energy Physics Division, Na Slovance 2, 180 40, Praha 8, Czech Republic
¹³ Dipartimento di Fisica, Università di Genova and INFN, Via Dodecaneso 33, 16146 Genova, Italy
¹⁴ Laboratoire de Physique Subatomique et de Cosmologie, IN2P3-CNRS, Université de Grenoble 1, 38026 Grenoble Cedex,
     France
¹⁵ Helsinki Institute of Physics, P.O. Box 64, 00014 University of Helsinki, Finland
¹⁶ Joint Institute for Nuclear Research, Dubna, Head Post Office, P.O. Box 79, 101 000 Moscow, Russian Federation
¹⁷ Institut für Experimentelle Kernphysik, Universität Karlsruhe, Postfach 6980, 76128 Karlsruhe, Germany
¹⁸ Institute of Nuclear Physics PAN,Ul. Radzikowskiego 152, 31142 Krakow, Poland
¹⁹ Faculty of Physics and Nuclear Techniques, University of Mining and Metallurgy, 30055 Krakow, Poland
²⁰ Université de Paris-Sud, Lab. de l'Accélérateur Linéaire, IN2P3-CNRS, Bât. 200, 91405 Orsay Cedex, France
²¹ School of Physics and Chemistry, University of Lancaster, Lancaster LA1 4YB, UK
²² LIP, IST, FCUL - Av. Elias Garcia, 14-1º, 1000 Lisboa Codex, Portugal
²³ Department of Physics, University of Liverpool, P.O. Box 147, Liverpool L69 3BX, UK
²⁴ Dept. of Physics and Astronomy, Kelvin Building, University of Glasgow, Glasgow G12 8QQ
²⁵ LPNHE, IN2P3-CNRS, Univ. Paris VI et VII, Tour 33 (RdC), 4 place Jussieu, 75252 Paris Cedex 05, France
²⁶ Department of Physics, University of Lund, Sölvegatan 14, 223 63 Lund, Sweden
²⁷ Université Claude Bernard de Lyon, IPNL, IN2P3-CNRS, 69622 Villeurbanne Cedex, France
²⁸ Dipartimento di Fisica, Università di Milano and INFN-MILANO, Via Celoria 16, 20133 Milan, Italy
²⁹ Dipartimento di Fisica, Univ. di Milano-Bicocca and INFN-MILANO, Piazza della Scienza 2, 20126 Milan, Italy
³⁰ IPNP of MFF, Charles Univ., Areal MFF, V Holesovickach 2, 180 00, Praha 8, Czech Republic
³¹ NIKHEF, Postbus 41882, 1009 DB Amsterdam, The Netherlands
³² National Technical University, Physics Department, Zografou Campus, 15773 Athens, Greece
³³ Physics Department, University of Oslo, Blindern, 0316 Oslo, Norway
³⁴ Dpto. Fisica, Univ. Oviedo, Avda. Calvo Sotelo s/n, 33007 Oviedo, Spain
³⁵ Department of Physics, University of Oxford, Keble Road, Oxford OX1 3RH, UK
³⁶ Dipartimento di Fisica, Università di Padova and INFN, Via Marzolo 8, 35131 Padua, Italy
³⁷ Rutherford Appleton Laboratory, Chilton, Didcot OX11 OQX, UK
³⁸ Dipartimento di Fisica, Università di Roma II and INFN, Tor Vergata, 00173 Rome, Italy
³⁹ Dipartimento di Fisica, Università di Roma III and INFN, Via della Vasca Navale 84, 00146 Rome, Italy
⁴⁰ DAPNIA/Service de Physique des Particules, CEA-Saclay, 91191 Gif-sur-Yvette Cedex, France
⁴¹ Instituto de Fisica de Cantabria (CSIC-UC), Avda. los Castros s/n, 39006 Santander, Spain
⁴² Inst. for High Energy Physics, Serpukov P.O. Box 35, Protvino, (Moscow Region), Russian Federation
⁴³ J. Stefan Institute, Jamova 39, 1000 Ljubljana, Slovenia and Laboratory for Astroparticle Physics, Nova Gorica Polytechnic,
     Kostanjeviska 16a, 5000 Nova Gorica, Slovenia,
     and Department of Physics, University of Ljubljana, 1000 Ljubljana, Slovenia
⁴⁴ Fysikum, Stockholm University, Box 6730, 113 85 Stockholm, Sweden
⁴⁵ Dipartimento di Fisica Sperimentale, Università di Torino and INFN, Via P. Giuria 1, 10125 Turin, Italy
⁴⁶ INFN,Sezione di Torino, and Dipartimento di Fisica Teorica, Università di Torino, Via P. Giuria 1, 10125 Turin, Italy
⁴⁷ Dipartimento di Fisica, Università di Trieste and INFN, Via A. Valerio 2, 34127 Trieste, Italy
     and Istituto di Fisica, Università di Udine, 33100 Udine, Italy
⁴⁸ Univ. Federal do Rio de Janeiro, C.P. 68528 Cidade Univ., Ilha do Fundão, 21945-970 Rio de Janeiro, Brazil
⁴⁹ Department of Radiation Sciences, University of Uppsala, P.O. Box 535, 751 21 Uppsala, Sweden
⁵⁰ IFIC, Valencia-CSIC, and D.F.A.M.N., U. de Valencia, Avda. Dr. Moliner 50, 46100 Burjassot (Valencia), Spain
⁵¹ Institut für Hochenergiephysik, Österr. Akad. d. Wissensch., Nikolsdorfergasse 18, 1050 Vienna, Austria
⁵² Inst. Nuclear Studies and University of Warsaw, Ul. Hoza 69, 00681 Warsaw, Poland
⁵³ Fachbereich Physik, University of Wuppertal, Postfach 100 127, 42097 Wuppertal, Germany

Abstract. Searches for pair-production of supersymmetric particles under the assumption of non-conservation of R-parity with a dominant $LL\bar{E}$ or $\bar{U}\bar{D}\bar{D}$ term have been performed using the data collected by the DELPHI experiment at LEP in e^+e^- collisions at centre-of-mass energies from 192 up to 208 GeV. No excess of data above Standard Model expectations was observed. The results were used to constrain the MSSM parameter space and to derive limits on the masses of supersymmetric particles.

1 Introduction

The R-parity (R_p) symmetry plays an essential role in the construction of supersymmetric theories, such as the Minimal Supersymmetric extension of the Standard Model (MSSM) [1]. The conservation of R_p is closely related to the conservation of lepton (L) and baryon (B) numbers and the multiplicative quantum number associated to the R_p symmetry is defined by $R_p = (-1)^{3B+L+2S}$ for a particle with spin S [2]. Standard model particles have even R_p, whereas the corresponding superpartners have odd R_p. The conservation of R_p guarantees that the spin-0 sfermions cannot be directly exchanged between standard fermions. It also implies that the sparticles $(R_p = -1)$ can only be produced in pairs, and that the decay of a sparticle leads to another sparticle, or an odd number of them. Therefore, it ensures the stability of the Lightest Supersymmetric Particle (LSP). In the MSSM, the conservation of R_p is assumed: this is phenomenologically justified by proton decay constraints, and by the fact that a neutral LSP could be a good dark matter candidate.

From a theoretical point of view, the conservation of R_p is not mandatory in supersymmetric extensions of the Standard Model (SM). Nevertheless, to be in agreement with the present experimental limit on proton lifetime, R_p violation can be introduced in MSSM either via the non-conservation of L or the non-conservation of B. One of the major consequences of the non-conservation of R_p is the allowed decay of the LSP into fermions; this modifies the signatures of supersymmetric particle production compared to the expected signatures in the case of R_p conservation.

In this paper, searches for pair-produced supersymmetric particles in the hypothesis of R_p violation via one dominant sparticle-particle coupling are presented. The data recorded in 1999 and 2000 by the DELPHI experiment have been analyzed, and no signal of R_p-violating decays was found in any of the channels. Previous results published by DELPHI on this subject can be found in [3,4]. Similar searches performed by the other three LEP experiments have also shown no evidence for R_p-violating effects [5].

The paper is organized as follows. Section 2 is dedicated to the R_p violation phenomenology considered in the present search. The data samples and simulated sets are presented in Sect. 3. Section 4 is devoted to the description of the analyses, and in Sect. 5 the search results are given and interpreted in order to constrain the mass spectrum of SUSY particles. A brief summary is given in the last section.

2 R_p non-conservation framework

In the presence of R_p violation the superpotential [6] contains three trilinear terms, two violating L conservation, and one violating B conservation. We consider here the $\lambda_{ijk}L_iL_j\bar{E}_k$ (non-conservation of L) and $\lambda''_{ijk}\bar{U}_i\bar{D}_j\bar{D}_k$ (non-conservation of B) terms [1], which couple the sleptons to the leptons and the squarks to the quarks, respectively. Since $\lambda_{ijk} = -\lambda_{jik}$ and $\lambda''_{ijk} = -\lambda''_{ikj}$, due to SU(2) and SU(3) symmetries, there are only 9 λ_{ijk} and only 9 λ''_{ijk} free couplings. In the present work, it is assumed that only one λ_{ijk} or λ''_{ijk} is dominant at a time. In the following, searches assuming R_p-violation via one dominant $\lambda_{ijk}L_iL_j\bar{E}_k$ term are referred as "$LL\bar{E}$", and those via one $\lambda''_{ijk}\bar{U}_i\bar{D}_j\bar{D}_k$ term as "$\bar{U}\bar{D}\bar{D}$". Searches assuming R_p-violation via one $\lambda'_{ijk}L_iQ_j\bar{D}_k$ term (non-conservation of both L and B) were not performed in DELPHI for data collected in 1999 and 2000.

In the pair-production of supersymmetric particles studied here, R_p is not conserved in the decay of the sparticles, but is conserved at the production vertex. The production cross-sections behave as in the MSSM with R_p conservation (see Sect. 2.3).

2.1 R_p-violating decays of sparticles via $LL\bar{E}$ or $\bar{U}\bar{D}\bar{D}$ terms

Two types of supersymmetric particle decays are considered: *direct decay* and *indirect decay*.

2.1.1 Direct decays

R_p violation allows the direct decay of a sfermion into two conventional fermions (Fig. 1a,b), or the direct decay of a neutralino or a chargino into a fermion and a virtual sfermion which then decays into two conventional fermions (Fig. 1c). A direct decay is the only possibility for the LSP.

Decays through $LL\bar{E}$ terms

Sleptons are coupled to leptons through the $\lambda_{ijk}L_iL_j\bar{E}_k$ term. In four-component Dirac notation, the $LL\bar{E}$ Yukawa

---

[1] i, j, k are generation indices, L denotes the lepton doublet superfields, $\bar{E}$ $(\bar{U}, \bar{D})$ denote the lepton (up and down quark) singlet superfields, λ_{ijk} and λ''_{ijk} are Yukawa couplings.
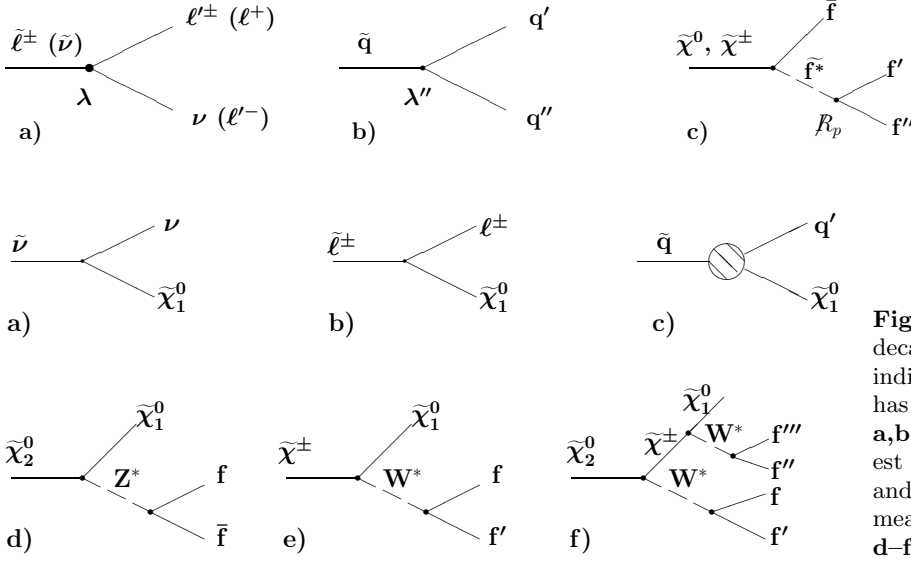
Fig. 1. Diagrams of sparticle direct decays. **a** slepton direct decay via LL$\bar{\text{E}}$ term; **b** squark direct decay via $\bar{\text{U}}\bar{\text{D}}\bar{\text{D}}$ term; **c** neutralino/chargino direct decay via any R_p-violating trilinear term
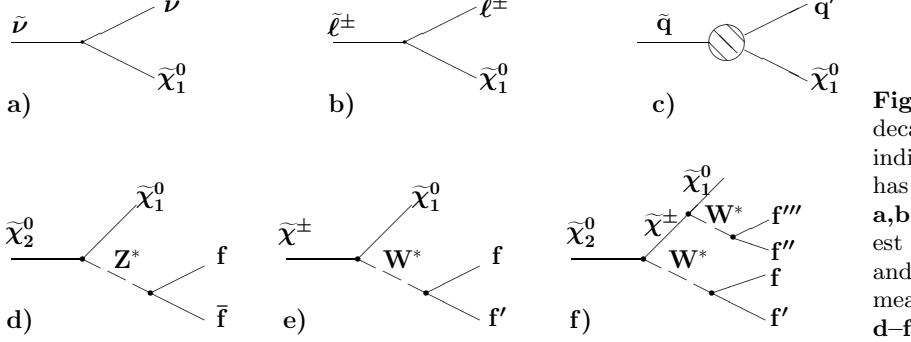
Fig. 2. Diagrams of sparticle R_p-conserving decays. To get the whole chain of the sparticle indirect decay, the LSP (lightest neutralino) has to undergo a direct R_p-violating decay. **a,b** slepton decays into a lepton and the lightest neutralino; **c** squark decay into a quark and the lightest neutralino, the hatched disk means decay beyond tree level for the stop case; **d–f** examples of gaugino decays

interaction terms are[2] [7]:

$$\lambda_{ijk} \left(\tilde{\nu}_{iL} \bar{\ell}_{kR} \ell_{jL} + \tilde{\ell}_{jL} \bar{\ell}_{kR} \nu_{iL} + \tilde{\ell}_{kR}^* (\overline{\nu}_{iL})^c \tilde{\ell}_{jL} - i \leftrightarrow j \right)$$
$$+ \text{ h.c.}$$

Considering the above expression, it can be deduced that the R_p-violating decay of a sfermion is possible only with specific indices i, j, k of the coupling which is considered to be dominant. The possible sparticle decays with such a dominant λ_{ijk} coupling are listed below.

- The sneutrino direct decay gives two charged leptons: via λ_{ijk} only the $\tilde{\nu}_i$ and $\tilde{\nu}_j$ are allowed to decay directly: $\tilde{\nu}_i \to \ell_{jL}^\pm \ell_{kR}^\mp$ and $\tilde{\nu}_j \to \ell_{iL}^\pm \ell_{kR}^\mp$ respectively.
- The charged slepton direct decay gives one neutrino and one charged lepton (the lepton flavour may be different from the slepton one). Among the supersymmetric partners of the right-handed leptons, only the one belonging to the kth generation can decay directly: $\tilde{\ell}_{kR}^- \to \nu_{iL} \ell_{jL}^- , \ell_{iL}^- \nu_{jL}$. For the supersymmetric partners of the left-handed leptons, the allowed direct decays are: $\tilde{\ell}_{iL}^- \to \bar{\nu}_{jL} \ell_{kR}^-$ and $\tilde{\ell}_{jL}^- \to \bar{\nu}_{iL} \ell_{kR}^-$.
- The neutralino decays via a virtual slepton and a lepton, and subsequently gives three-lepton final states (two charged leptons and one neutrino): $\tilde{\chi}^0 \to \ell_i^+ \bar{\nu}_j \ell_k^- , \ell_i^- \nu_j \ell_k^+ , \bar{\nu}_i \ell_j^+ \ell_k^- , \nu_i \ell_j^- \ell_k^+$.
- The chargino decays via a virtual slepton and gives either three charged leptons, or two neutrinos and one charged lepton: $\tilde{\chi}_1^+ \to \ell_i^+ \ell_j^+ \ell_k^- , \ell_i^+ \bar{\nu}_j \nu_k , \bar{\nu}_i \ell_j^+ \nu_k , \nu_i \nu_j \ell_k^+$.

Decays through $\bar{\text{U}}\bar{\text{D}}\bar{\text{D}}$ terms

The squarks are coupled to the quarks through the λ_{ijk}'' $\bar{\text{U}}_i \bar{\text{D}}_j \bar{\text{D}}_k$ term. The decays allowed via this term can be inferred by considering the Lagrangian for the trilinear Yukawa interactions written in expanded notation:

$$\lambda_{ijk}'' \left(\overline{(u_i)^c (d_j)^c} \tilde{d}_k^* + \overline{(u_i)^c} \tilde{d}_j^* \overline{(d_k)^c} + \tilde{u}_i^* \overline{(d_j)^c} \overline{(d_k)^c} \right) + \text{ h.c.}$$

From this Lagrangian, we can derive the following rules:

- The direct decays of squarks into two quarks are given by: $\tilde{u}_{i,R} \to \bar{d}_{j,R} \bar{d}_{k,R}$, $\tilde{d}_{j,R} \to \bar{u}_{i,R} \bar{d}_{k,R}$ and $\tilde{d}_{k,R} \to \bar{u}_{i,R} \bar{d}_{j,R}$.
- The neutralino decays via a virtual squark and a quark and subsequently gives a three-quark final state: $\tilde{\chi}^0 \to \bar{u}_j \bar{d}_j \bar{d}_k, u_j d_j d_k$
- Chargino decay is similar to the neutralino one, and then gives also a three quarks final state: $\tilde{\chi}_1^+ \to u_j d_j u_k$, $u_i u_j d_k, \bar{d}_i \bar{d}_j \bar{d}_k$

2.1.2 Indirect decays

Indirect decays are cascade decays through R_p-conserving vertices to on-shell supersymmetric particles, down to the lightest supersymmetric particle, which then decays via one LL$\bar{\text{E}}$ or $\bar{\text{U}}\bar{\text{D}}\bar{\text{D}}$ term (Fig. 2). A typical example is the R_p-conserving decay $\tilde{\chi}_1^+ \to \tilde{\chi}_1^0 + \text{W}^{*+}$ (see Fig. 2e) and the subsequent decay of $\tilde{\chi}_1^0$ through the R_p-violating couplings. The indirect decay mode usually dominates when there is enough phase space available in the decay between "mother" and "daughter" sparticles, for example, when the difference of masses between these two sparticles is larger than 5–10 GeV/c^2. Regions of the parameter space where there is a "dynamic" suppression of the R_p-conserving modes also exist. In this case, even if the sparticle is not the LSP, it decays through an R_p-violating mode. For example, if the field component of the two lightest neutralinos is mainly the photino, then the decay $\tilde{\chi}_2^0 \to \tilde{\chi}_1^0 \text{Z}^*$ is suppressed.

---

[2] Here ν ($\tilde{\nu}$) refer to neutrino (sneutrino) fields, ℓ ($\tilde{\ell}$) refer to charged lepton (slepton) fields, i,j,k are generation indices and the superfix c refers to a charge-conjugate field.

The sfermion indirect decay studied here is the decay through the lightest neutralino considered as the LSP ($\tilde{f} \rightarrow f' \tilde{\chi}_1^0$), followed by the R_p-violating decay of the LSP. With LL$\bar{E}$, the indirect decay of a sneutrino (charged slepton) through a neutralino and a neutrino (charged lepton) leads to two charged leptons and two neutrinos (three charged leptons and one neutrino). The squark decay into a quark and a gaugino leads to one quark and three leptons. With $\bar{U}\bar{D}\bar{D}$, the indirect decay of a squark (slepton) leads to four quarks (three quarks and one lepton).

2.2 R_p-violating coupling upper limits and LSP lifetime

Upper limits on the λ_{ijk} and λ''_{ijk} couplings can be derived mainly from indirect searches of R_p-violating effects [7,8], assuming that only one coupling is dominant at a time. They are dependent on the sfermion mass, and usually given for $m_{\tilde{f}} = 100 \text{ GeV}/c^2$. The upper bounds on λ_{ijk} are obtained from charged-current universality, lepton universality, $\nu_\mu - e$ scattering, forward-backward asymmetry in $e^+ e^-$ collisions, and bounds on ν_e-Majorana mass. Most present indirect limits are in the range of 10^{-3} to 10^{-1}; the most stringent upper limit is given for λ_{133} ($\simeq 6 \cdot 10^{-3}$). Upper limits on λ''_{ijk} couplings come from experimental measurements of double nucleon decays for λ''_{112} (10^{-6}), $n - \bar{n}$ oscillations for λ''_{113} (10^{-5}) and of $R_\ell = \Gamma_{had}(Z^0)/\Gamma_\ell(Z^0)$ in $e^+ e^-$ collisions for $\lambda''_{312}, \lambda''_{313}, \lambda''_{323}$ (0.43). The upper limits on the other λ''_{ijk} couplings are obtained from the requirement of perturbative unification at the Grand Unified Theory (GUT) scale of 10^{16} GeV. This gives a limit of 1.25.

In the present searches, the LSP lifetime was a crucial parameter since the analyses were valid only if the R_p-violating decays were close to the production vertex, which means a LSP flight path shorter than a few centimetres.

The LSP mean decay length is given by [9,10]:

$$\text{L(cm)} = 0.3 \; (\beta\gamma) \left(\frac{m_{\tilde{f}}}{100 \text{ GeV}/c^2}\right)^4 \left(\frac{1 \text{ GeV}/c^2}{m_{\tilde{\chi}}}\right)^5 \frac{1}{\Lambda^2} \quad (1)$$

if the neutralino or the chargino is the LSP with $\beta\gamma = P_{\tilde{\chi}}/m_{\tilde{\chi}}$ and with $\Lambda = \lambda_{ijk}$ or $\Lambda = \sqrt{3}\lambda''_{ijk}$. Considering the upper limits on the couplings described above and according to (1), the analyses are not sensitive to a light neutralino ($m_\chi \leq 15 \text{ GeV}/c^2$), due to the terms $m_{\tilde{\chi}}^{-5}$ and ($\beta\gamma$). Moreover, when studying neutralino decays, for the typical masses considered in the present study, the analyses are sensitivite to R_p-violating couplings greater than 10^{-4} to 10^{-5}, where the R_p-violating decay has a negligible decay length. For much lower values of the coupling strength, the LSP escapes the tracking devices before decaying and the results of the searches performed under the assumption of R_p conservation are recovered [11]. Between these two extreme cases, the LSP decay produces a displaced vertex topology[3].

---

[3] This particular topology, not considered in the present searches, has been studied in other searches performed by the DELPHI collaboration [12].

2.3 Pair-production of supersymmetric particles

Pair-production of supersymmetric particles in the MSSM assuming R_p violation is identical to pair-production in the case of R_p conservation, since the trilinear couplings are not present at the production vertex. The production of single supersymmetric particles via trilinear couplings has been studied in other searches performed by the DELPHI collaboration [13].

In the constrained MSSM scheme [1] considered in the present searches, the mass spectrum of neutralinos and charginos is determined by three parameters, with the assumption that both the gaugino and the sfermion masses are unified at the GUT scale. The relevant parameters are then: M_2, the SU(2) gaugino mass at the electroweak scale (it is assumed that $M_1 = \frac{5}{3}\tan^2\theta_W M_2$), m_0, the common sfermion mass at the GUT scale, μ, the mass-mixing term of the Higgs doublets at the electroweak scale and $\tan\beta$, the ratio of the vacuum expectation values of the two Higgs doublets. It is assumed that the running of the λ_{ijk} and λ''_{ijk} couplings from the GUT to the electroweak scales does not have a significant effect on the "running" of the gaugino and sfermion masses.

The charginos are produced in pairs in the s-channel via γ or Z exchange, or in the t-channel via $\tilde{\nu}_e$ exchange if the charginos have a gaugino component; the neutralinos are produced in pairs via s-channel Z exchange provided they have a higgsino component, or via t-channel $\tilde{e}$ exchange if they have a gaugino component. The t-channel contribution is suppressed when the slepton masses (depending on m_0) are high enough. When the $\tilde{e}$ mass is sufficiently small (less than $100 \text{ GeV}/c^2$), neutralino production can be enhanced, because of the t-channel contribution. On the contrary, if the $\tilde{\nu}_e$ mass is in the same range, the chargino cross-section can decrease due to destructive interference between the s- and t-channel amplitudes.

The pair-production cross-section of sfermions mainly depends on the sfermion masses. The $\tilde{e}$ and $\tilde{\nu}_e$ cross-sections are also very sensitive to the neutralino and chargino compositions (which are function of μ, M_2 and $\tan\beta$) via the t-channel exchange. The sfermion mass-eigenstates, $\tilde{f}_1$ and $\tilde{f}_2$ (where f is a quark or lepton and $\tilde{f}_1$ is lighter than $\tilde{f}_2$), are obtained from the two supersymmetric scalar partners $\tilde{f}_L$ and $\tilde{f}_R$ of the corresponding left and right-handed fermion [14, 15]:

$$\tilde{f}_1 = \tilde{f}_L \cos\Phi_{\text{mix}} + \tilde{f}_R \sin\Phi_{\text{mix}}$$
$$\tilde{f}_2 = -\tilde{f}_L \sin\Phi_{\text{mix}} + \tilde{f}_R \cos\Phi_{\text{mix}}$$

where Φ_{mix} is the mixing angle with $0 \leq \Phi_{\text{mix}} \leq \pi$. The supersymmetric partner of the left-handed fermions are likely to be heavier than their right-handed counterparts. The $\tilde{f}_L$–$\tilde{f}_R$ mixing is related to the off-diagonal terms of the scalar squared-mass matrix. It is proportional to the fermion mass, and is small compared to the diagonal terms, with the possible exception of the third family sfermion [16]. The lighter stop, $\tilde{t}_1$, is then probably the lightest squark. This is not only due to the mixing effect but also to the effect of the large Yukawa coupling of the top; both tend to

Table 1. Data collected by DELPHI in 1999 and 2000: the integrated luminosities correspond to the data actually used in the present analyses after the run selection. The last column refers to the integrated luminosity collected with one sector of the TPC off

$\sqrt{s}$ (GeV)	192	196	200	202	<204.9>	<206.6>	<206.6>
$\mathcal{L}$ (pb^{-1})	25.1	76.0	83.3	42.5	73.7	85.4	51.8

decrease the mass of $\tilde{t}_1$ [17]. Similarly the lightest charged slepton is probably the $\tilde{\tau}_1$. For small values of $\tan\beta$, $\tilde{\tau}_1$ is predominantly a $\tilde{\tau}_R$, and it is not so much lighter than $\tilde{e}_1$ and $\tilde{\mu}_1$. In the present slepton search, a no-mixing scenario is assumed. In the third squark generation searches two left-right mixing angle cases have been considered. The first one with mixing angle equal to zero and the second one with the mixing angle $\Phi_{\mathrm{mix}} = 56°$ ($\Phi_{\mathrm{mix}} = 68°$) corresponding to the minimum production cross-section of the stop (sbottom) via Z exchange [18].

3 Data and generated samples

3.1 Data samples

The data recorded in 1999 and 2000 by the DELPHI experiment at centre-of-mass energies from $\sqrt{s} = 192$ GeV to 208.8 GeV, correspond to a total integrated luminosity of around 450 pb^{-1}. The DELPHI detector has been described elsewhere [19]. An integrated luminosity of 386 pb^{-1} (Table 1) has been analysed, corresponding to high quality data, with the tracking detectors and the electromagnetic calorimeters in good working conditions. At the end of the data taking period in 2000, one sector (among twelve) of the Time Projection Chamber (TPC) failed beyond repair. This required modifications in the data treatment (pattern recognition), and a specific simulation of the detector with one TPC sector off has been performed. An integrated luminosity of 51.8 pb^{-1} recorded with one TPC sector off have been analysed.

3.2 Event generators

To evaluate background contaminations, different contributions coming from the SM processes were considered. The SM events were produced by the following generators:

- $\gamma\gamma$ *events:* BDK [20] for $\gamma\gamma \to \ell^+\ell^-$ processes, including radiative corrections for the $\mathrm{e^+e^-}\mu^+\mu^-$ and $\mathrm{e^+e^-}\tau^+\tau^-$ final states, and TWOGAM for $\gamma\gamma \to$ hadron processes.
- *two-fermion processes:* BHWIDE [21] for Bhabha scattering ($\mathrm{e^+e^-} \to \mathrm{e^+e^-}(\gamma)$), KORALZ [22] for $\mathrm{e^+e^-} \to \mu^+\mu^-(\gamma)$ and for $\mathrm{e^+e^-} \to \tau^+\tau^-(\gamma)$ and PYTHIA 6.143 [23] for $\mathrm{e^+e^-} \to \mathrm{q\bar{q}}(\gamma)$ events.
- *four-fermion processes:* EXCALIBUR [24] and GRC4F [25] for all types of four-fermion processes: non resonant ($\mathrm{f\bar{f}f'\bar{f}'}$), singly resonant ($\mathrm{Zf\bar{f}}$, $\mathrm{Wf\bar{f}'}$) and doubly resonant (ZZ, WW) (PYTHIA was used also for cross-checks on the final results).

Signal events were generated for all analyses with the SUSYGEN 3.00 program [26].

All generated background and signal events were passed through the full DELPHI simulation and reconstruction chain [19] and then processed in the same way as the real data. To treat the data taken with one sector of the TPC off, special background and signal event samples were generated, and the same treatment applied to them as to the real data.

3.3 Signal samples

Choice of the R_p-violating couplings

Among the nine λ_{ijk} couplings, λ_{122} (which leads to several muons in the final states) and λ_{133} (which leads to several taus in the final states) have been chosen for most of the signal generation. Their values were set for $m_{\tilde{\ell}} = 100$ GeV/c^2 at 0.04 and 0.003 respectively, below their upper bound derived from indirect searches of R_p-violating effects. Any value between 10^{-3} and 10^{-1} would not change the neutralino decay topologies. Simulations with other couplings have been also performed in order to check that the analyses developed for λ_{122} or λ_{133} were able to select the corresponding signal with an equal or better efficiency.

For the generation of all $\mathrm{U\bar{D}\bar{D}}$ signals, a λ''_{212} coupling of strength 0.1 (for $m_{\tilde{q}} = 100$ GeV/c^2) was used. Any value between 10^{-2} and 0.5 would not change the neutralino decay topologies.

Searches for decays through specific λ''_{ijk} couplings, leading to the production of one or several b quarks, can use b-tagging techniques to reach higher sensitivities, but at the cost of losing generality.

Generated signal sets

Two different procedures were applied to the signal generation for gaugino pair-production and subsequent decays through either $\mathrm{LL\bar{E}}$ or $\mathrm{U\bar{D}\bar{D}}$ terms in order to cover the MSSM parameter space.

For the $\mathrm{LL\bar{E}}$ term, the $\widetilde{\chi}^0_i$ and $\widetilde{\chi}^{\pm}_k$ pair-production processes were considered for different values of $\tan\beta$ (from 1 to 30), m_0 (between 90 GeV/c^2 and 500 GeV/c^2), μ (between -200 GeV/c^2 and 200 GeV/c^2) and M_2 (between 5 and 400 GeV/c^2), for centre-of-mass energies of 200 and 206 GeV. For the $\mathrm{U\bar{D}\bar{D}}$ term, pair-production of neutralinos was generated for several masses. The simulated masses started from 10 GeV/c^2 and were increased in steps of 10 GeV/c^2, as long as the mass of the chargino remained kinematically accessible. Masses corresponding to the kinematic limit were also simulated. To generate chargino pairs, the mass of the chargino was varied from 45 GeV/c^2 to 95 GeV/c^2 with a 10 GeV/c^2 step. Chargino masses were also simulated at the kinematic limit. The neutralino mass was varied from 10 GeV/c^2 to a mass difference with the chargino of 5 GeV/c^2 with a 10 GeV/c^2 step. For each mass pair, a set of the variables μ, M_2 and $\tan\beta$ was found for the chosen simulation.

Sfermion indirect decay signals were simulated at different masses with steps of $10\,\text{GeV}/c^2$ at centre-of-mass energies of 200 and $206\,\text{GeV}$, with $\tan\beta$ and μ fixed at 1.5 and $-200\,\text{GeV}/c^2$ respectively. M_2 was used to fix the neutralino mass at the required value. The points were simulated from 45 to $100\,\text{GeV}/c^2$ for the sfermion masses and from 15 to $95\,\text{GeV}/c^2$ for the $\widetilde{\chi}_1^0$ masses up to a mass difference between the sfermion and the LSP of $5\,\text{GeV}/c^2$.

Among the sfermions, only the sneutrino direct decay via $LL\bar{E}$ terms was studied. Specific signal sets have been produced with $\text{Br}(\tilde{\nu} \to \ell^+\ell^-) = 100\%$. The processes $\widetilde{\nu}_e\widetilde{\nu}_e \to 4\mu\ (\lambda_{122})$, $\widetilde{\nu}_e\widetilde{\nu}_e \to 4\tau\ (\lambda_{133})$, $\widetilde{\nu}_\mu\widetilde{\nu}_\mu \to 4\tau\ (\lambda_{233})$ and $\widetilde{\nu}_\tau\widetilde{\nu}_\tau \to 2e2\tau\ (\lambda_{133})$ have been generated for different values of the sneutrino mass up to $98\,\text{GeV}/c^2$, with $\tan\beta$ and μ fixed at 1.5 and $-200\,\text{GeV}/c^2$ respectively. In order to check that all final states from $\tilde{\nu}\tilde{\nu}$ decay were covered, signals obtained for other λ_{ijk} couplings and for sneutrino masses around $90\,\text{GeV}/c^2$ were also generated.

4 Description of the analyses

The analyses covering the decay of pair-produced sparticles were designed to cover multi-lepton final states for $LL\bar{E}$ coupling and multi-jet final states for $\bar{U}\bar{D}\bar{D}$ coupling. Different preselections were applied, one for the multi-lepton channels and one for the multi-jet channels. In each case, dedicated analyses were necessary to take into account the specific characteristics of the sparticle decay. The multi-jet analyses required a specific treatment based on neural network techniques.

The sensitivity of the searches for sparticle indirect decays depended on the mass difference (ΔM) between the sparticle being searched for and the LSP. The analyses were designed to be efficient for $\Delta M \geq 5\,\text{GeV}/c^2$. The multi-jet analyses required different signal selection optimisations to cover efficiently all ΔM regions; therefore they were divided into windows according to the value of ΔM.

No excess in the data appeared in these searches, therefore a working point optimization on the selection criteria was performed minimizing the expected excluded cross-section as a function of the average signal efficiency.

4.1 Description of the final states

4.1.1 Decays via $LL\bar{E}$

Direct and indirect decays of gauginos, direct and indirect decays of sneutrinos and indirect decays of charged sleptons and squarks were studied.

The direct decay of a pair of lightest neutralinos leads to two neutrinos and four charged leptons. For an indirect decay of chargino or heavier neutralino pairs the final state may contain some jets and/or leptons in addition to the four leptons and the missing energy from the decay of the LSP. The direct decay of a sneutrino pair gives final states with four charged leptons, in which the leptons can be of two different flavours. The direct decay of a charged slepton pair gives final states with two charged leptons, in which

the leptons can be of two different flavours, and missing energy. This final state has not been covered by the present analyses. In the indirect decay of any sfermion pair, the final states are composed of two fermions plus the decay products of the neutralinos.

Compared to other couplings the highest efficiencies and background reduction were obtained in analyses performed on the signal with a dominant λ_{122} coupling. For analyses dedicated to a λ_{133} coupling, due to the presence of several taus in the decay channels, the efficiencies and the rejection power were low. For final states produced by other λ_{ijk}, the detection efficiencies lay between these two limiting cases. Therefore conservative limits can be derived by considering the results of the analyses performed assuming a dominant λ_{133} coupling, and only these analyses will be described in Sect. 4.3.

The decay of pair-produced sparticles via a λ_{133} coupling leads to different types of final states, depending on the produced sparticles. The $\widetilde{\chi}_1^0\widetilde{\chi}_1^0$ decay via λ_{133} leads to $2\tau + \ell + \ell' + \not{E}$, where $\ell, \ell' = $ e or τ, and $\not{E}$ means missing energy. In addition, jets and/or leptons from the W or Z decays show up in the final state from $\widetilde{\chi}_i^0\widetilde{\chi}_j^0$ and $\widetilde{\chi}_1^+\widetilde{\chi}_1^-$ indirect decays. The indirect decay of a slepton pair gives $2\tau + \ell + \ell' + \not{E}$, with two additional charged leptons (same flavour, opposite charge) in the case of charged sleptons, and additional missing energy in the case of sneutrinos. A 4τ final state is produced by the direct decay of $\widetilde{\nu}_e\widetilde{\nu}_e$ via λ_{133}. The direct decay of $\widetilde{\nu}_\tau\widetilde{\nu}_\tau$ gives $2e2\tau$ and then, there is finally less missing energy coming from the taus decay than in the previous cases. The indirect decay of squarks adds exactly two jets to the $2\tau + \ell + \ell' + \not{E}$.

Four analyses have been performed to search for all these topologies. They are summarized in the first part of Table 2.

4.1.2 Decays via $\bar{U}\bar{D}\bar{D}$

Direct and indirect decays of gauginos, and indirect decays of charginos, charged sleptons and squarks were studied.

For each indirect decay of a chargino, squark or slepton pair there are at least six quarks in the final state. Therefore the most important feature of these decays is the number of quarks produced, which can be up to ten for the indirect decay of two charginos with the hadronic decays of the W bosons. The indirect decay channel presents the only possibility for the sleptons to decay through a $\bar{U}\bar{D}\bar{D}$ term. In this case, two leptons are produced in the R_p conserving decay of the slepton pair, and they add to the six jets coming from the decay of the two neutralinos: a 6 jets $+ 2\ell$, $\ell = $ e, μ final state is the signature of these signals. The indirect decay of a stop or sbottom pair produces 8 jets in the final state. Two b quarks are produced from the sbottom decay. The analysis of the different decay channels was organized on the basis of the number of hadronic jets in the final state (see Table 2).

Table 2. The multi-lepton and multi-jet visible final states which correspond to the analyses described in this paper, when one $LL\bar{E}$ or $\bar{U}\bar{D}\bar{D}$ term is dominant. The corresponding pairs of produced sparticles that may have given rise to them are indicated. For the $LL\bar{E}$ cases, only topologies produced with decays via λ_{133} are considered (see text), and for the $\bar{U}\bar{D}\bar{D}$ cases, $\ell = $ e or μ

	$LL\bar{E}$: multi-lepton topologies		
analysis name	final states	direct decays of	indirect decays of
gaugino	$2\tau + \text{n}\ell + \text{m}j + \not{E}$ (n≥2) (m≥0)	$\widetilde{\chi}_1^0\widetilde{\chi}_1^0$	$\widetilde{\chi}_1^+\widetilde{\chi}_1^-$ $\widetilde{\chi}_i^0\widetilde{\chi}_j^0$
slepton	$2\tau + 2\ell + \not{E} + \text{p}\ell$ (p = 0 or 2)		$\widetilde{\nu}\widetilde{\nu}$, $\widetilde{\ell}^+\widetilde{\ell}^-$
	$\tau\tau\tau$	$\widetilde{\nu}_e\widetilde{\nu}_e$	
sneutrino tau	ee$\tau\tau$	$\widetilde{\nu}_\tau\widetilde{\nu}_\tau$	
squark	$2\tau + 2\ell + \not{E} + 2j$		$\widetilde{q}\widetilde{\bar{q}}$
	$\bar{U}\bar{D}\bar{D}$: multi-jet topologies		
analysis name	final states	direct decays of	indirect decays of
neutralino	$6j$	$\widetilde{\chi}_1^0\widetilde{\chi}_1^0$, $\widetilde{\chi}_1^+\widetilde{\chi}_1^-$	
chargino	$10j$		$\widetilde{\chi}_1^+\widetilde{\chi}_1^-$
slepton	$6j + 2\ell$		$\widetilde{\ell}^+\widetilde{\ell}^-$
squark	$8j$		$\widetilde{q}\widetilde{\bar{q}}$

4.2 Analysis tools and techniques

4.2.1 Lepton identification

The identification of a muon or an electron, used in all λ_{ijk} analyses and several λ''_{ijk} ones, was based on standard DELPHI algorithms [19]. The identification could be "tight" if it was an unambiguous one, or "loose" otherwise. In the multi-lepton analyses described in this section a particle was considered as a well identified electron if it satisfied the tight conditions from the DELPHI electron identification algorithm, its momentum was greater than $8\,\text{GeV}/c$ and there was no other charged particle in a cone of half-angle $2°$ around it. A particle was considered as a well identified muon if its momentum was greater than $5\,\text{GeV}/c$ and it was tagged as a tight muon candidate by the DELPHI algorithm.

4.2.2 Jet reconstruction algorithms

Two different jet reconstruction algorithms have been used. The DURHAM algorithm [27] was used for the multi-lepton ($LL\bar{E}$ coupling) analyses, where jets were expected from τ or W boson decays. In case of multi-jet analyses, the CAMBRIDGE clustering algorithm [28] implemented in the CKERN package [29] was used.

The CAMBRIDGE algorithm was introduced to select soft jets, coming from quark-jets with gluon emission. The specific procedure of clusterization which extracts soft jets from the list of objects to be clustered, was particularly interesting for multi-jet analyses, where the jets (more than six) may not be well separated in momentum space. For each event, the two algorithms provided all possible configurations of jets between 2 and 10. They have the same definition of y_{cut} distance, but mainly differ in the iterative procedure of clustering. In this paper, the transition value of the y_{cut} in the DURHAM or CAMBRIDGE algorithm at which the event changes from a clustering with n jets, called n-jet configuration, to a clustering with $(n-1)$-jets, is denoted y_{nn-1}. In other words, the y_{nn-1} value is the y_{cut} value for which the number of particle clusters flips from n to $n-1$ for increasing y_{cut} distances. For example, the y_{43} value of one event is the highest value of y_{cut} to obtain 4 separated clusters of particles.

4.2.3 Neural networks

A neural network method was applied in order to distinguish signals from SM background events for all multi-jet analyses. The trainings of the neural networks were done in the standard back-propagation manner with one hidden layer on samples of simulated background ($q\bar{q}$ and four-fermion) and signal events. A feed-forward algorithm has been implemented to compute from the input discriminating variables a single discriminant variable (signal output node) which was used first to validate the training with different signal and background samples and then to select the final number of candidate events for each analysis. The exact configuration and the input discriminating variables of each neural network depended on the search channel. The working point on the signal ouput node value has been chosen to minimize the expected excluded cross-section at 95% confidence level (CL) when there is no signal.

4.3 Multi-lepton $LL\bar{E}$ channels

4.3.1 Preselection

The selections were based on the criteria already presented in [3], using mainly missing momentum, lepton identification and kinematic properties. The preselection requirements were:

- more than three charged particles and at least one of them with a polar angle between $40°$ and $140°$;
- at least one identified lepton (e or μ);
- a total energy greater than $0.1\cdot\sqrt{s}$;
- a missing momentum component transverse to the beam (p_t) greater than $5\,\text{GeV}/c$;
- a polar angle of the missing momentum (θ_{miss}) between $27°$ and $153°$;
- a thrust axis not close to the beam pipe, viz. $|\cos\theta_{\text{th}}|$ less than 0.9;
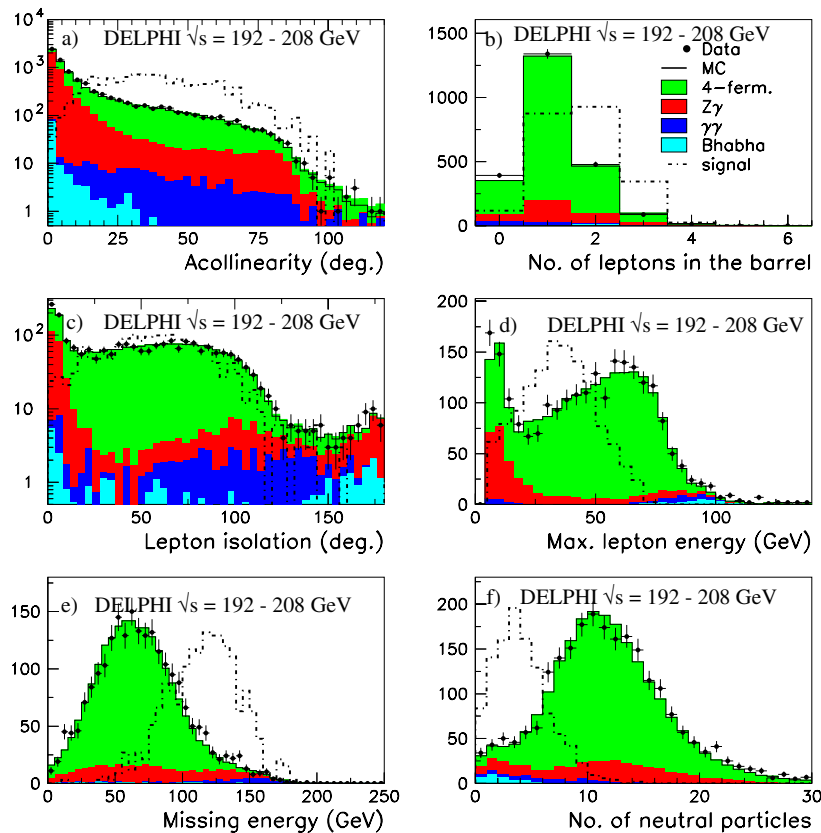
Fig. 3. LL$\bar{\text{E}}$: sparticle pair search in multi-lepton channels – Event variable (see text) distributions before the criteria applied on the acollinearity (preselection) **a** and after **b–f** the preselection. The simulated signal corresponds to $\tilde{\chi}_1^0 \tilde{\chi}_1^0$ production, with $\text{m}_{\chi_1^0} = 90\,\text{GeV}/c^2$ (the normalisation is arbitrary)

– an acollinearity[4] greater than $2°$, and greater than $7°$ for events with a charged particle multiplicity greater than 6.

The preselection was efficient in suppressing 99.9% of the backgrounds coming from Bhabha scattering and two-photon processes while removing 97% of the $\text{f}\bar{\text{f}}(\gamma)$ contribution. The preselection also reduced the four-fermion contamination by 75%. After this preselection stage, 2310 events (1220 for data at centre-of-mass energies between 192 and 202 GeV, and 1090 for those collected above 202 GeV) were selected to be compared to 2254 ± 6 expected from the background sources (1189 ± 5 at centre-of-mass energies between 192 and 202 GeV, 1065 ± 4 above 202 GeV). The corresponding efficiencies for the large majority of LL$\bar{\text{E}}$ signals lay between 60% and 80%. The distributions of several event variables at the hadronic preselection stage are shown in Fig. 3.

The above requirements had to be slightly modified for the stop analysis (see Sect. 4.3.5), in particular to take into account the fact that the final state always contains two jets. A minimum multiplicity of eight charged particles was required. No requirement was applied on the thrust axis. On the other hand, a stronger cut was applied on the polar angle of the missing momentum ($30° \leq \theta_{\text{miss}} \leq 150°$). After

this preselection stage, 2197 events were selected to be compared to 2208 ± 6 expected from the background sources.

4.3.2 Gaugino search

The gaugino analysis was designed to cover the $2\tau + \text{n}\ell + \text{m}j + \not{E}$ ($\text{n} \geq 2$, $\text{m} \geq 0$) final states, from direct or indirect decays of gauginos, and to be efficient for both low and high multiplicity cases.

The thrust had to be less than 0.9 and a lower limit on the missing energy was applied viz. E_{miss} greater than $0.3 \cdot \sqrt{s}$. The number of neutral (charged) particles had to be less than 20 (25) and the polar angle of at least one lepton had to be between $40°$ and $140°$.

The events were then separated in to two classes, according to their charged particle multiplicity.

– For events with a charged particle multiplicity from four to six, (mainly for neutralino direct decay topologies), the following criteria were applied:
  – the energy in a cone of $30°$ around the beam axis was required to be less than 50% of the total visible energy;
  – the energy of the most energetic lepton (e or μ) had to be between 2 and 70 GeV;
  – there should be no other charged particle in a cone of half angle of $20°$ ($6°$) around any identified lepton for a charged particle multiplicity equal to 4 (5 or 6).
– For events with a charged particle multiplicity greater than six, the previous criteria became:

---

[4] The acollinearity is computed between the two vectors corresponding to the sum of the particle momenta in each hemisphere of the event. The two hemispheres are defined by the plane orthogonal to the thrust axis.
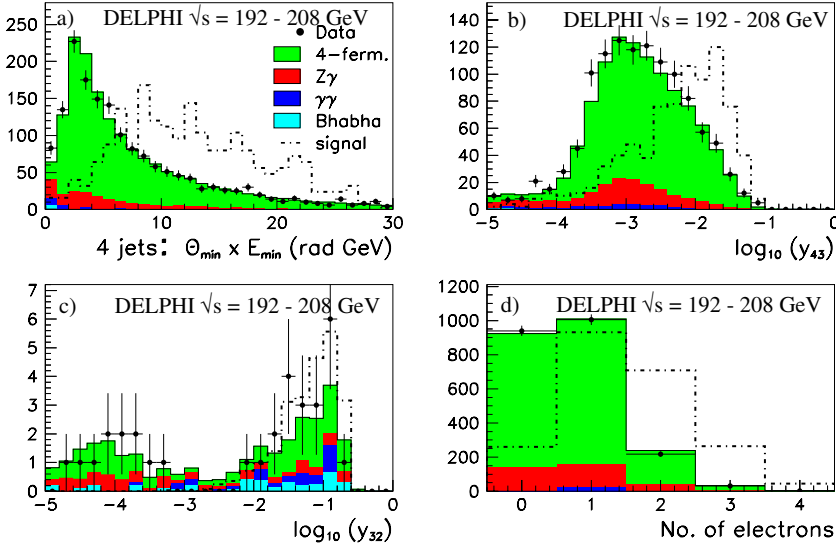
Fig. 4. LL$\bar{\text{E}}$: sparticle pair search in multi-lepton channels – Distributions of variables used in the four analyses, as described in the text: **a** gaugino, **b** slepton, **c** sneutrino tau, **d** squark. The simulated signals correspond to production of **a** $\widetilde{\chi}_2^0\widetilde{\chi}_1^0$ and $\widetilde{\chi}_1^+\widetilde{\chi}_1^-$ ($m_{\widetilde{\chi}_1^0} = 50\,\text{GeV}/c^2$, $m_{\widetilde{\chi}_2^0} = 85\,\text{GeV}/c^2$, $m_{\widetilde{\chi}_1^\pm} = 95\,\text{GeV}/c^2$), **b** $\widetilde{\nu}_e\widetilde{\nu}_e$ ($m_{\widetilde{\nu}_e} = 100\,\text{GeV}/c^2$), **c** $\widetilde{\nu}_\tau\widetilde{\nu}_\tau$ ($m_{\widetilde{\nu}_\tau} = 95\,\text{GeV}/c^2$), **d** $\widetilde{t}\widetilde{\bar{t}}$ ($m_{\widetilde{t}} = 95\,\text{GeV}/c^2$) (the signal normalisation is arbitrary)

– the energy in a cone of 30° around the beam axis was required to be less than 40% of the total visible energy;

– the energy of the most energetic lepton had to be between 5 and 60 GeV,

– if there was only one identified lepton; there should be no other charged particle in a cone with a half angle of 6° around it; if there was more than one identified lepton there should be no other charged particle in a cone with a half angle of 10° around at least two of them;

– at least one electron (loose identification) was required.

These criteria removed 95% of $f\bar{f}\gamma$, ZZ and W$^+$W$^-$ events.

A selection based on the jet characteristics and topologies was then applied, depending on the charged particle multiplicity, as mentioned above. First, constraints were imposed on the y_{32} and y_{43} values: they had to be greater than 0.002 and 0.0001 respectively for events with low charged particle multiplicity, and greater than 0.016 and 0.005 respectively for events whose charged particle multiplicity was above 7; these criteria eliminated 99% of the remaining $f\bar{f}\gamma$ contribution. In events with more than six charged particles, it was required that at least one jet had no more than two charged particles. In four or five-jet configurations, a minimum number of 4 jets with at least one charged particle was required. For a four-jet topology, a cut was applied on the value of $E_{min}^j \cdot \theta_{min}$ where E_{min}^j is the energy of the least energetic jet, and θ_{min} is the minimum di-jet angle (Fig. 4a). It had to be greater than 1 GeV·rad for events with low charged particle multiplicity, and greater then 5 GeV·rad for events with a charged particle multiplicity above 7. These requirements reduced the background from 4-fermion processes.

4.3.3 Slepton search

A slepton analysis, aimed to search for $2\tau + 2\ell + \not{E}$ $(+\,2\ell)$ was performed in order to study the following three channels:

– $\widetilde{\ell}_R^+\widetilde{\ell}_R^- \to \ell\widetilde{\chi}_1^0\ell\widetilde{\chi}_1^0$;
– $\widetilde{\nu}\widetilde{\bar{\nu}} \to \nu\widetilde{\chi}_1^0\nu\widetilde{\chi}_1^0$;
– $\widetilde{\nu}_e\widetilde{\nu}_e \to 4\tau$.

These final states have several taus, and most of them have missing energy. After the tau decays, all channels present a large amount of missing energy. The criteria used to eliminate almost all remaining $f\bar{f}\gamma$ events and most of the 4-fermion events were the following:

– the missing energy had to be greater than $0.3\cdot\sqrt{s}$;
– the energy in a cone of half-angle of 30° around the beam axis was required to be less than 40% of the total visible energy;
– the number of charged (neutral) particles had to be less than 8 (10);
– the energy of the most energetic lepton had to be between 2 and 70 GeV;
– at least one lepton should have a polar angle between 40° and 140°;
– there should be no other charged particle in a cone with a half-angle of 6° around at least one lepton;
– y_{32} and y_{43}, computed with the DURHAM algorithm, (Fig. 4b) had to be greater than $2 \cdot 10^{-3}$ and $4 \cdot 10^{-4}$ respectively;
– in a four-jet topology a minimum angle of 20° between any pair of jets was required.

4.3.4 $\widetilde{\nu}_\tau$ search

An analysis searching for $2e2\tau$ final states produced in the direct decay of $\widetilde{\nu}_\tau\widetilde{\nu}_\tau$ was performed. Compared to the selection described in 4.3.3, the most important change was the suppression of the criterion on the missing energy, and the introduction of the requirement of having at least one well identified electron:

– the energy in a cone of 30° around the beam axis was required to be less than 50% of the total visible energy;
– the number of charged (neutral) particles had to be less than 7 (10);

- there should be at least one electron;
- the energy of the most energetic lepton had to be between 25 and 80 GeV;
- at least one lepton should have a polar angle between 40° and 140°;
- there should be no other charged particle in a cone of half-angle of 6° around at least one lepton;
- y_{32} (Fig. 4c), computed with the DURHAM algorithm, had to be greater than $2 \cdot 10^{-3}$;
- in a four-jet topology, a minimum angle of 20° between any pair of jets was required.

This selection removed $f\bar{f}\gamma$ background and most of the 4-fermion events.

4.3.5 Stop search

In stop pair-production, each of the stops decays into a charm quark and a neutralino. The subsequent R_p-violating decay via the λ_{133} coupling of the neutralino into leptons, the final state: $2\tau + 2\ell + \not{E} + 2j$, $\ell =$e or τ.

After the preselection described in Sect. 4.3.1, the criteria used to select the final states of the stop pair indirect decay were:

- the missing energy greater than $0.3 \cdot \sqrt{s}$;
- the charged and neutral particle multiplicities below 25 and 20 respectively;
- the polar angle of at least one lepton between 40° and 140°;
- the energy of the most energetic identified lepton between 5 and 50 GeV;
- no other charged particle in a cone of half-angle of 6° around at least one lepton;
- at least one well identified electron (Fig. 4d);
- the y_{32} and y_{54} values constrained to be less than 0.016 and 10^{-3} respectively;
- in the four-jet configuration, at least one jet with less than three charged particles.

4.4 Multi-jet $\bar{U}\bar{D}\bar{D}$ channels

For all $\bar{U}\bar{D}\bar{D}$ channels the main SM backgrounds come from four-fermion processes except for the low neutralino mass channel where the hadronic Z decay is the dominant background. The following $\bar{U}\bar{D}\bar{D}$ analyses were based on neural network techniques since the optimisation of the signal selection over the four-fermion background was performed on topological variables, such as jet resolution parameters, which are extensively correlated.

4.4.1 Preselection

The multi-jet $\bar{U}\bar{D}\bar{D}$ signals have final states with a large hadronic activity, independent of the produced sparticles. Therefore a general hadronic preselection was performed with the aim of a high efficiency for the signal (especially for the gaugino analysis) and at the same time a good rejection of low particle multiplicity hadronic background events:

- the number of charged particles had to be greater than 15;
- the total energy was required to be greater than $0.6 \cdot \sqrt{s}$;
- the energy associated to charged particles was required to be greater than $0.3 \cdot \sqrt{s}$;
- the effective centre-of-mass energy [5] had to be greater than 150 GeV;
- the discriminating variable $d_\alpha = \alpha_{min} \cdot E_{min} - 0.5 \cdot \beta_{min} \cdot E_{max}/E_{min}$ (where the 0.5 energy factor is in GeV) had to be greater than -10 GeV.rad [6];
- the minimum jet invariant mass had to be greater than 500 MeV/c^2 when forcing the event into four jets;
- the $\ln(y_{32})$ had to be greater than -6.9;
- the $\ln(y_{43})$ had to be greater than -8.

After the hadronic preselection, the main remaining background events were the four-fermion events and the $q\bar{q}\gamma$ events with hard gluon radiation. We observed 3844 events in the data with 3869 ± 4 events expected from background processes for the year 2000 (4180 events in the data to be compared to 4096 ± 7 events in the simulation for the year 1999). Examples of the distributions of several event variables at the hadronic preselection level are shown in Fig. 5.

The efficiencies for the $\bar{U}\bar{D}\bar{D}$ signals varied from 60% to 99% depending on the simulated masses and ΔM. This preselection (sometimes with slight modifications, described in the following) was used for all the $\bar{U}\bar{D}\bar{D}$ analyses.

These requirements had to be slightly modified to be better optimised for slepton searches. The discriminating variable d_α was not used in the preselection, and the effective centre-of-mass energy was required to be above $0.6 \cdot \sqrt{s}$, because a tighter cut was set on y_{43} and a cut on y_{54} was applied.

Additional criteria to the basic hadronic preselection have been applied before the optimal neural network selection:

- the charged particle multiplicity had to be greater than 16;
- the total energy was required to be greater than $0.6 \cdot \sqrt{s}$;
- the energy of charged particles was required to be greater than $0.3 \cdot \sqrt{s}$;
- the $\ln(y_{43})$ had to be greater than -7;
- the $\ln(y_{54})$ had to be greater than -8;
- the thrust had to be lower than 0.94;
- the maximum di-jet mass in a four-jet configuration had to be greater than 10 GeV/c^2.

This selection was applied for the $\bar{U}\bar{D}\bar{D}$ sleptons ans squark analyses. After this selection the remaining number of events for all energies was 4245 for the data and 4378 ± 8 for the expected background from SM processes.

---

[5] the effective centre-of-mass energy is the centre-of-mass energy after the emission of one or more photons from the initial state.

[6] α_{min} is the minimum angle between two jets, β_{min} is the minimum angle between the most energetic jet and any other, E_{min} (E_{max}) is the minimum (maximum) jet energy from the four-jet topology of the event.
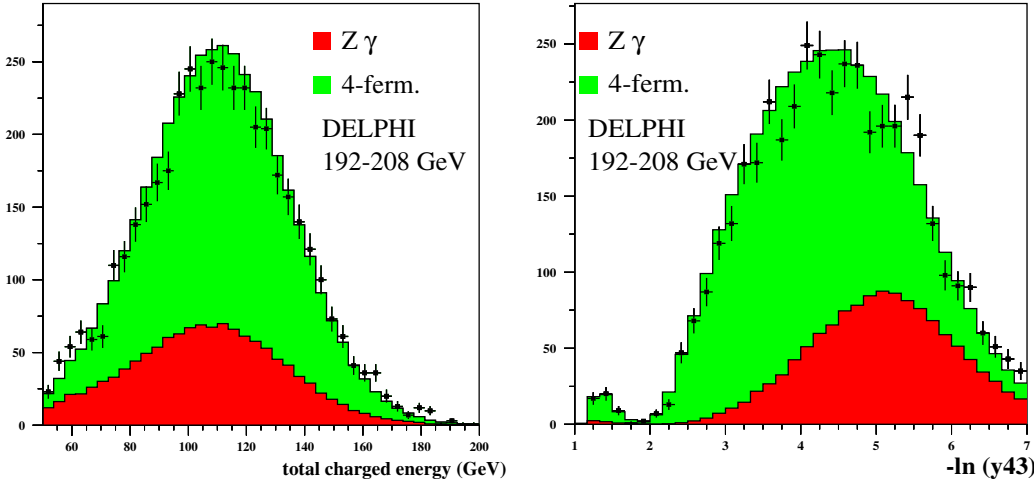
Fig. 5. $\bar{\text{U}}\bar{\text{D}}\bar{\text{D}}$: the total energy associated to charged particles (left) and -ln(y_{43}) (right) distributions in the multi-jet slepton analyses at the hadronic preselection level
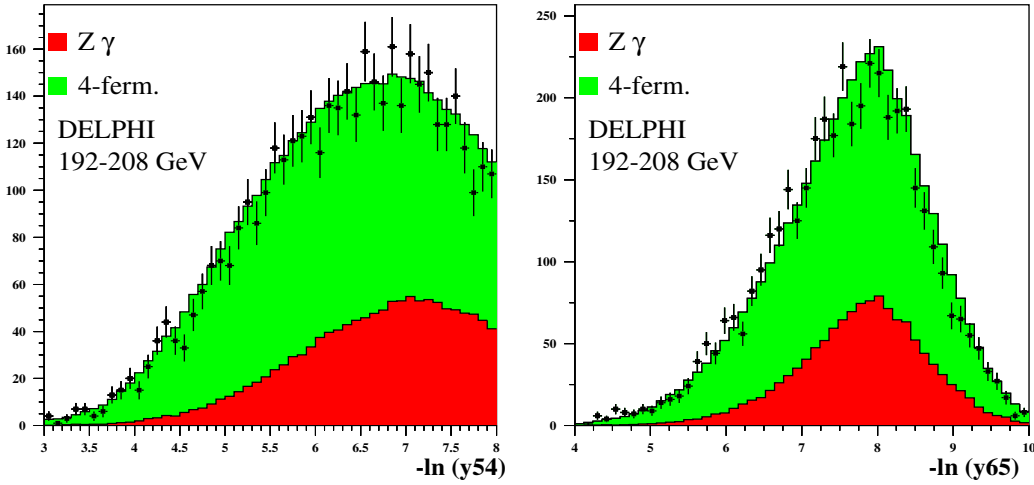
Fig. 6. $\bar{\text{U}}\bar{\text{D}}\bar{\text{D}}$: the -ln($y_{54}$) (left) and -ln($y_{65}$) (right) distributions in the multi-jet sfermion analyses at preselection level

The distributions of the variables $\ln(y_{54})$ and $\ln(y_{65})$ at this stage of the preselection level are shown in Fig. 6.

4.4.2 Neutralino search

The analysis described here was mainly designed to search for neutralino direct decays; it was also efficient in the search for chargino direct decays. The six-jet analyses were based on three different neural networks for the optimization of the background and signal discrimination. The neural network method used has been presented in Sect. 4.2.3.

Events with low gaugino mass have a large boost and look like di-jet events. On the contrary, events with heavy gauginos are almost spherical with six well separated jets. Therefore, we distinguished 3 mass windows to increase the sensitivity of each signal configuration:

- low mass window N1: $10 \leq m_{\tilde{\chi}} \leq 45 \,\text{GeV}/c^2$;
- medium mass window N2: $45 < m_{\tilde{\chi}} \leq 75 \,\text{GeV}/c^2$;
- high mass window N3: $m_{\tilde{\chi}} > 75 \,\text{GeV}/c^2$.

A mass reconstruction was performed using a method depending on the mass window. For the N1 analysis, the events were forced into two jets and the average of the two-jet masses was computed. For the other analyses, the events were forced into six jets and criteria on di-jet angles were applied to choose the optimum three-jet combinations corresponding to the decays of two neutralinos with the same mass. The minimum and maximum angles between the jets belonging to the same three-jet cluster (same neutralino) had to be in the intervals $[20°, 80°]$ and $[50°, 165°]$ for the medium mass window N2 ($[40°, 110°]$ and $[100°, 175°]$ for the high mass window N3). If more than one combination was selected, the combination with the minimum difference between the two energies of the three-jet clusters was chosen to compute the neutralino mass.

Three neural networks were used, one for each mass window, with the following variables as inputs:

- the thrust;
- $\text{dist}_{\text{WW}} = \sqrt{\frac{(\text{M}_1 - \text{M}_2)^2}{\sigma_-^2} + \frac{(\text{M}_1 + \text{M}_2 - 2\text{M}_\text{W})^2}{\sigma_+^2}}$, where M_1 and M_2 are the di-jet masses of the jet combination which minimized this variable (after forcing the event into 4 jets); we took $\text{M}_\text{W} = 80.4 \,\text{GeV}/c^2$ for the W mass, $\sigma_- = 9.5 \,\text{GeV}/c^2$ and $\sigma_+ = 4.8 \,\text{GeV}/c^2$ for the mass resolutions of the difference and the sum of the reconstructed di-jet masses respectively; this variable is peaked at 0 for WW events, allowing a good discrimination against this background;

– the energy of the least energetic jet multiplied by the minimum di-jet angle in four and five-jet configurations;
– the difference between the energies of the two combinations of three jets, after the mass reconstruction;
– the reconstructed neutralino mass;
– $y_{n\ n-1}$ with n=3 to 10.

It was observed that the modelling of the gluon emission was unable to describe the event distributions of $y_{n\ n-1}$ correctly for n greater than 5. To take into account this imperfect description, corrections were applied to the background distributions of the $y_{n\ n-1}$ variables (for n between 6 and 10) [30].

4.4.3 Chargino search

To take into account the effect of the mass difference between chargino and neutralino, ΔM, on the topology of the event, the ten-jet analysis was divided into two windows:

– low ΔM window C1: $5\leq \Delta M\leq 10\,\mathrm{GeV}/c^2$;
– high ΔM window C2: $\Delta M> 10\,\mathrm{GeV}/c^2$.

Two neural networks were trained with the following discriminating variables as inputs:

– the thrust;
– the variable dist$_{\mathrm{WW}}$ described above;
– the energy of the least energetic jet multiplied by the minimum di-jet angle in four and five-jet configurations;
– $y_{n\ n-1}$ with n=3 to 10 (for n=6 to 10, the corrected $y_{n\ n-1}$ were used); for the C1 analysis, the variables y_{87}, y_{98} and $y_{10\,9}$ were not used.

4.4.4 Slepton search

Three mass windows were defined to take into account the mass difference, ΔM, between the sfermion and the neutralino considered as the LSP:

– low ΔM window 1: $5 \leq \Delta M \leq 10\,\mathrm{GeV}/c^2$ with $m_{\widetilde{\chi}^0} > 55\,\mathrm{GeV}/c^2$;
– high ΔM window 2: $\Delta M > 10\,\mathrm{GeV}/c^2$ with $m_{\widetilde{\chi}^0} > 55\,\mathrm{GeV}/c^2$;
– low neutralino mass window 3: $m_{\widetilde{\chi}^0} \leq 55\,\mathrm{GeV}/c^2$.

Different selection criteria on the momentum of the tagged leptons were applied depending on the mass window.

Electron and muon momentum selection

In addition to the high rejection power of the topological jet variables, lepton identification has been used since two opposite sign leptons of the same flavour are produced in the final state (see Table 2). Therefore, an electron and positron, or two muons with opposite sign were required, with thresholds on the momentum which depended on ΔM, in order to discriminate the selectron or the smuon pair-production signal from the SM background:

– the momentum of the less energetic tagged lepton (electron or muon) had to be lower than $30\,\mathrm{GeV}/c$ (window 1), $70\,\mathrm{GeV}/c$ (windows 2 and 3);
– the momentum of the more energetic tagged electron had to be in the intervals [2,40] GeV/c (window 1), [10,70] GeV/c (window 2) and [10,90] GeV/c (window 3);
– the momentum of the more energetic tagged muon had to be in the intervals [2,40] GeV/c (window 1), [30,70] GeV/c (window 2) and [30,90] GeV/c (window 3).

Neural network signal selection optimisation

The following variables have been used as inputs to the neural networks:

– the clustering variables y_{43}, y_{54}, y_{65}, computed with the CAMBRIDGE algorithm;
– the minimum di-jet mass in the four, five and six-jet configurations;
– the energy of the least energetic jet · minimum di-jet angle in four and five-jet configurations;
– the thrust (only for window 3);
– the energy of the most energetic electromagnetic cluster (only for window 3).

The training was performed on signal samples of selectrons and smuons at centre-of-mass energies of 200 and 206 GeV for each analysis, and with the same statistics for two samples of the most important expected SM backgrounds (two and four-fermion events separately).

4.4.5 Squark search

Searches for stop and sbottom were performed in the case of indirect decays. The eight quarks event topology depends strongly on ΔM, the mass difference between the squark and the $\widetilde{\chi}_1^0$. The same mass windows as those defined for slepton analysis (Sect. 4.4.4) were used. After the preselection and before training the neural networks, additional criteria were applied to select high jet multiplicity events:

– the total multiplicity had to be lower than 40;
– the effective centre-of-mass energy had to be greater than $0.7 \cdot \sqrt{s}$;
– the total electromagnetic energy had to be lower than 20 GeV (window 3 only);
– the $\ln(y_{43})$ had to be greater than -6;
– the $\ln(y_{54})$ had to be greater than -6.5;
– the momentum of the less energetic tagged electron had to be lower than $16\,\mathrm{GeV}/c$ (windows 1 and 2), $20\,\mathrm{GeV}/c$ (window 3);
– the momentum of the most energetic tagged electron had to be lower than $40\,\mathrm{GeV}/c$;
– the energy of the most energetic electromagnetic cluster had to be lower than 40 GeV (window 3 only).

Sbottom decays produce b-quarks in the final state which may be identified with the impact parameter information provided by the micro-vertex detector. The event tagging

Table 3. Observed and expected numbers of events for all $LL\bar{E}$ and $\bar{U}\bar{D}\bar{D}$ analyses. Although not explicitly written, ΔM is always greater than $5\,\mathrm{GeV}/c^2$

	$LL\bar{E}$: multi-lepton topologies					
Analysis		192–202 GeV			203–208 GeV	
name		observed	expected		observed	expected
gaugino		15	13.4 $\pm$ 0.4		9	10.3 $\pm$ 0.4
slepton		4	4.2 $\pm$ 0.2		7	3.9 $\pm$ 0.2
sneutrino τ		3	3.5 $\pm$ 0.3		3	2.8 $\pm$ 0.2
squark		19	19.9 $\pm$ 0.5		16	15.5 $\pm$ 0.4
	$\bar{U}\bar{D}\bar{D}$: multi-jet topologies					
Analysis	Mass windows	192–202 GeV			203–208 GeV	
name	(GeV/c^2)	observed	expected		observed	expected
neutralino	$15 \leq \mathrm{m}_{\tilde{\chi}} \leq 45$	134	126.0 $\pm$ 13.0		121	119.3 $\pm$ 8.8
	$45 < \mathrm{m}_{\tilde{\chi}} \leq 75$	192	172.5 $\pm$ 8.2		167	164.7 $\pm$ 5.7
	$75 < \mathrm{m}_{\tilde{\chi}}$	97	103.3 $\pm$ 3.6		82	91.7 $\pm$ 2.3
chargino	$\Delta\mathrm{M} \leq 10$	187	181.1 $\pm$ 5.9		156	171.7 $\pm$ 5.2
	$\Delta\mathrm{M} > 10$	22	25.6 $\pm$ 1.1		20	23.5 $\pm$ 1.0
slepton	$\mathrm{m}_{\tilde{\chi}} > 55,\ \Delta\mathrm{M} \leq 10$	9	5.6 $\pm$ 0.2		1	6.2 $\pm$ 0.2
($\tilde{\mathrm{e}}$)	$\mathrm{m}_{\tilde{\chi}} > 55,\ \Delta\mathrm{M} > 10$	1	2.0 $\pm$ 0.1		5	2.3 $\pm$ 0.1
	$15 \leq \mathrm{m}_{\tilde{\chi}} \leq 55$	1	1.6 $\pm$ 0.1		0	1.8 $\pm$ 0.1
slepton	$\mathrm{m}_{\tilde{\chi}} > 55,\ \Delta\mathrm{M} \leq 10$	7	5.7 $\pm$ 0.2		5	6.4 $\pm$ 0.2
($\tilde{\mu}$)	$\mathrm{m}_{\tilde{\chi}} > 55,\ \Delta\mathrm{M} > 10$	4	3.3 $\pm$ 0.2		1	3.5 $\pm$ 0.2
	$15 \leq \mathrm{m}_{\tilde{\chi}} \leq 55$	2	2.0 $\pm$ 0.1		1	2.3 $\pm$ 0.1
squark	$\mathrm{m}_{\tilde{\chi}} > 55,\ \Delta\mathrm{M} \leq 10$	42	39.4 $\pm$ 0.6		38	40.4 $\pm$ 0.6
($\tilde{\mathrm{t}}$)	$\mathrm{m}_{\tilde{\chi}} > 55,\ \Delta\mathrm{M} > 10$	13	10.1 $\pm$ 0.3		8	9.5 $\pm$ 0.3
	$15 \leq \mathrm{m}_{\tilde{\chi}} \leq 55$	30	26.3 $\pm$ 0.5		25	25.2 $\pm$ 0.5
squark	$\mathrm{m}_{\tilde{\chi}} > 55,\ \Delta\mathrm{M} \leq 10$	10	11.9 $\pm$ 0.4		13	12.0 $\pm$ 0.4
($\tilde{\mathrm{b}}$)	$\mathrm{m}_{\tilde{\chi}} > 55,\ \Delta\mathrm{M} > 10$	4	5.4 $\pm$ 0.2		7	4.8 $\pm$ 0.2
	$15 \leq \mathrm{m}_{\tilde{\chi}} \leq 55$	6	4.6 $\pm$ 0.2		8	4.2 $\pm$ 0.2

obtained with the DELPHI algorithm for tagging events containing a b-quark [31] was therefore added as a sequential cut for the sbottom analysis.

The same input variables as in the selectron and smuon searches (Sect. 4.4.4) were used in the neural network, except for the low ΔM analysis, where the energy of the most energetic electromagnetic cluster was suppressed.

5 Results and limits

In this section, the number of selected and expected events after the final event selection, and the signal efficiencies obtained for each channel under study are presented. The results are in agreement with the SM expectation. Together with the signal efficiencies they were used to exclude at 95% CL possible regions of the MSSM parameter space. Unless otherwise stated, the limits were derived using the results from the centre-of-mass energies between 192 and 208 GeV.

As already mentioned, to obtain the most conservative constraints on the MSSM parameter values from $LL\bar{E}$ searches, only the analyses performed considering the λ_{133} coupling as the dominant one were used: in fact, if a different λ_{ijk} coupling is dominant, the exclusions would be at least as large as those from a dominating λ_{133} coupling.

After a presentation of the methods applied to derive limits, the efficiencies and the number of selected events are given for each channel, as well as the derived limits.

5.1 Limit computation

Limits on gaugino masses

An upper limit to the number of signal events, N_{95}, at 95% CL, was calculated according to the monochannel Bayesian method [32] from the number of events remaining in the data and those expected in the SM, summed over all centre-of-mass energies from 192 to 208 GeV.

The gaugino pair-production was considered for different values of $\tan\beta$ (from 0.5 to 30), m_0 (between $90\,\mathrm{GeV}/c^2$ and $500\,\mathrm{GeV}/c^2$), μ (between $-200\,\mathrm{GeV}/c^2$ and $200\,\mathrm{GeV}/c^2$) and M_2 (between 5 and $400\,\mathrm{GeV}/c^2$); for a given set of $\tan\beta$ and m_0 values the (μ, M_2) point was excluded at 95% CL if the expected number of signal, N_{exp} at this point was greater than N_{95}. The computations of N_{exp} were slightly different for $LL\bar{E}$ and $\bar{U}\bar{D}\bar{D}$ searches, as detailed below.

To obtain the limits on the gaugino masses with a good precision, special studies were performed to scan the regions of the parameter space from which the limits were
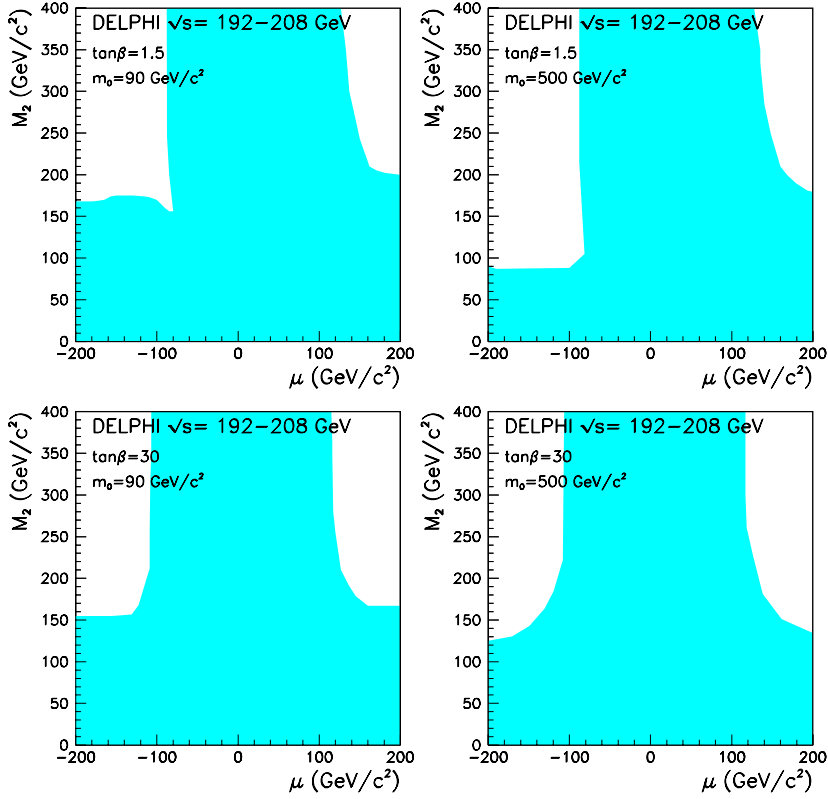
Fig. 7. LL$\bar{\text{E}}$: regions in μ, M$_2$ parameter space excluded at 95% CL by the neutralino and chargino searches for two values of $\tan\beta$ and two values of m$_0$
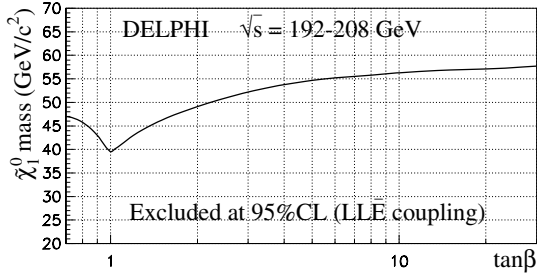
Fig. 8. LL$\bar{\text{E}}$: excluded lightest neutralino mass as a function of $\tan\beta$ at 95% CL. This limit is independent of the choice of the generation indices i,j,k of the λ_{ijk} coupling and is for values of m$_0$ between 90 and 500 GeV/c^2

determined: the steps in M$_2$ and μ were of 0.25 GeV/c^2 and 1 GeV/c^2, respectively.

Limits on sfermion masses

For all the sfermion searches the limits at 95% CL were derived using the modified frequentist likelihood ratio method [33]. Expected exclusion limits were obtained with the same algorithm where the number of observed events was set to the number of expected background events (absence of signal). To extract the mass limits, a branching ratio of 100% was assumed for the R_p-conserving decay of the sfermion into a neutralino and a fermion. The MSSM
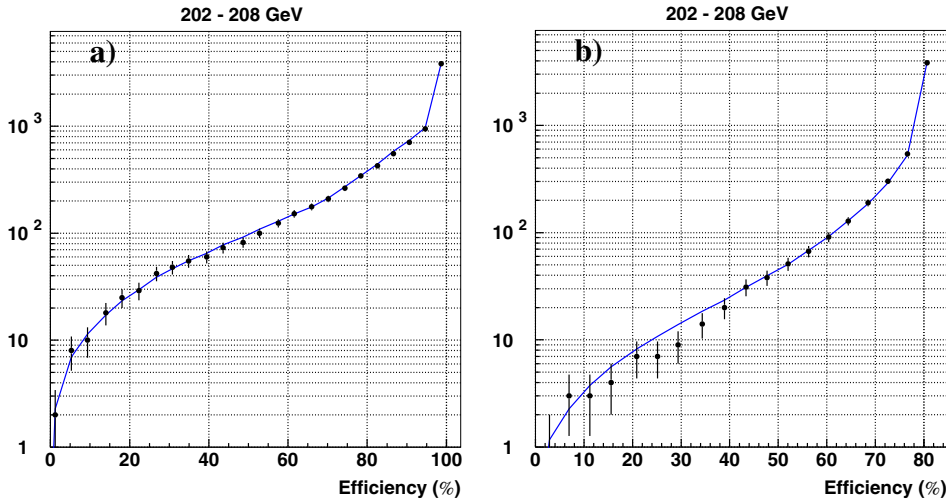
Fig. 9. $\bar{\text{U}}\bar{\text{D}}\bar{\text{D}}$: number of expected events (continuous line) and data events (black dots) versus average signal efficiency for the high neutralino mass search N3 (plot **a**) and for the large ΔM chargino search C2 (plot **b**) for centre-of-mass energies between 202 and 208 GeV
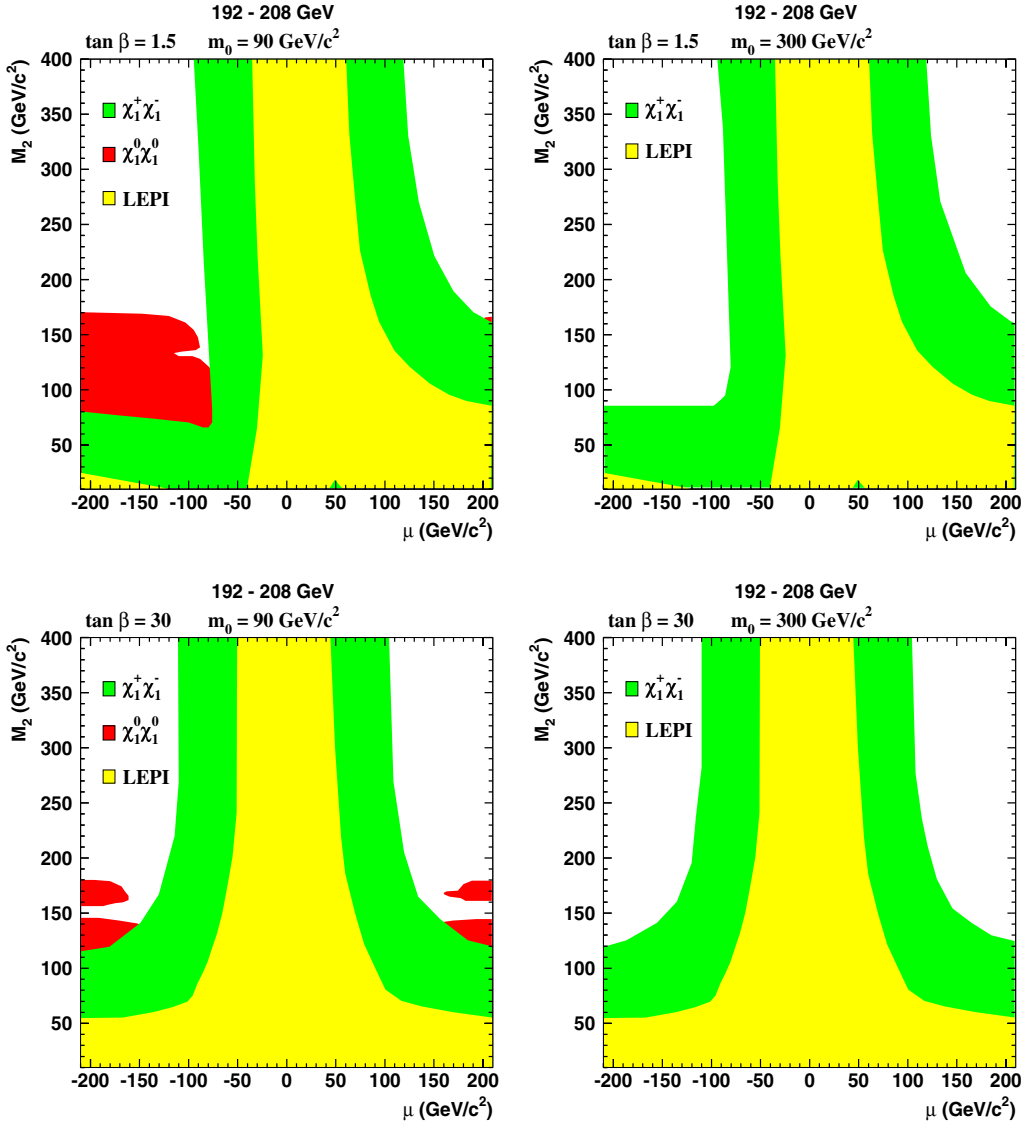
Fig. 10. $\bar{U}\bar{D}\bar{D}$: regions in μ, M_2 parameter space excluded at 95% CL by the neutralino and chargino searches for two values of $\tan\beta$ and two values of m_0
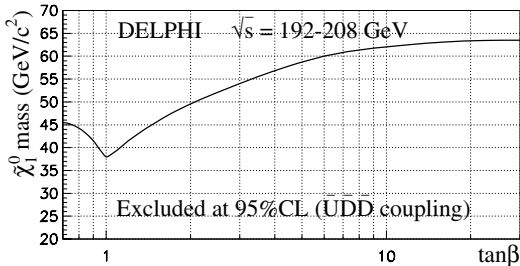
Fig. 11. $\bar{U}\bar{D}\bar{D}$: lightest neutralino mass excluded at 95% CL as a function of $\tan\beta$. This limit was obtained for $m_0 = 500\,\mathrm{GeV}/c^2$

the hard gluon radiation in the parton shower of the Monte Carlo $\bar{U}\bar{D}\bar{D}$ signal simulation is not implemented. Therefore this generates systematically events with background-like y_{mn} distributions. This is the reason why the $\bar{U}\bar{D}\bar{D}$ results of the present search are conservative.

5.2 Gaugino searches

5.2.1 LL$\bar{E}$ scenario

Efficiencies and selected events

The efficiency of the selection described in Sect. 4.3.2 was computed from simulated samples at different points of the MSSM parameter space. In order to benefit from the high centre-of-mass energies and luminosities, all $e^+e^- \to \widetilde{\chi}_i^0\widetilde{\chi}_j^0$ and $e^+e^- \to \widetilde{\chi}_1^+\widetilde{\chi}_1^-$ processes which contribute significantly have been simulated, at each MSSM point of this study. Then a global event selection efficiency was determined for each point. The efficiencies lay between 11% and 38%.

values chosen to present the exclusion plots were $\tan\beta = 1.5$ and $\mu = -200\,\mathrm{GeV}/c^2$.

The statistical errors on the efficiencies, which were between $\pm 1\%$ and $\pm 3\%$, and on the expected background were used in the limit computation, for gauginos and sfermions. The systematic uncertainties on the signal selection efficiencies were negligeable compared to statistical errors in the LL$\bar{E}$ analyses. In the case of $\bar{U}\bar{D}\bar{D}$ analyses, the systematic uncertainties on the signal efficiencies were larger. Indeed,

Fig. 12. LL$\bar{\text{E}}$: excluded regions at 95% CL in the $m_{\widetilde{\chi}^0}$ versus $m_{\widetilde{\ell}_R}$ planes for $\widetilde{\ell}_R$ pair-production, with BR($\widetilde{\ell}_R \rightarrow \widetilde{\chi}^0_1 \ell$) = 100% , and neutralino decay into leptons. The plots show the exclusion (filled area) for selectron, smuon and stau. The black contour is the corresponding expected exclusion at 95% CL

At each selection step of the gaugino analysis, good agreement between the number of observed and expected background events was obtained, and no excess was observed in the data; at the end, 24 candidates remained in the data from 192 to 208 GeV, compared to 23.7 ± 0.6 expected from SM background processes (see Table 3), mainly from W^+W^- events and the rest from other four-fermion processes.

Limits

The number of expected events corresponding to gaugino pair-production at each point of the explored MSSM parameter space was obtained by:

$$N_{exp} = \epsilon_{200} \cdot \sum_{E_{cm}=192}^{E_{cm}=202} \mathcal{L}_{E_{cm}} \cdot \sigma_{\chi\chi}$$
$$+ \epsilon_{206} \cdot \sum_{E_{cm}=203}^{E_{cm}=208} \mathcal{L}_{E_{cm}} \cdot \sigma_{\chi\chi}$$

where $\sigma_{\chi\chi} = \sum_{i,j=1}^{4} \sigma(e^+e^- \rightarrow \widetilde{\chi}^0_i \widetilde{\chi}^0_j) + \sigma(e^+e^- \rightarrow \widetilde{\chi}^+_1 \widetilde{\chi}^-_1)$, $\mathcal{L}_{E_{cm}}$ is the integrated luminosity collected at the centre-of-mass energy E_{cm}, and ϵ_{200} and ϵ_{206} are the global efficiencies determined as explained above at 200 and 206 GeV respectively. All points which satisfied $N_{exp} > N_{95}$ were excluded at 95% CL, and the corresponding excluded area in (μ, M_2) planes obtained with the present searches are presented in Fig. 7, for $m_0 = 90, 500 \, \text{GeV}/c^2$ and $\tan\beta = 1.5, 30$.

For each $\tan\beta$, the highest value of the mass of the lightest neutralino which can be excluded has been determined in the (μ, M_2) plane for several m_0 values from 90 to $500 \, \text{GeV}/c^2$; the most conservative mass limit was obtained for high m_0 values. The corresponding limit on neutralino mass as a function of $\tan\beta$ is shown in Fig. 8.

The same procedure has been applied to determine the most conservative lower limit on the chargino mass. The result is less dependent on $\tan\beta$, and almost reaches the kinematic limit for any value of $\tan\beta$. The lower limit obtained on
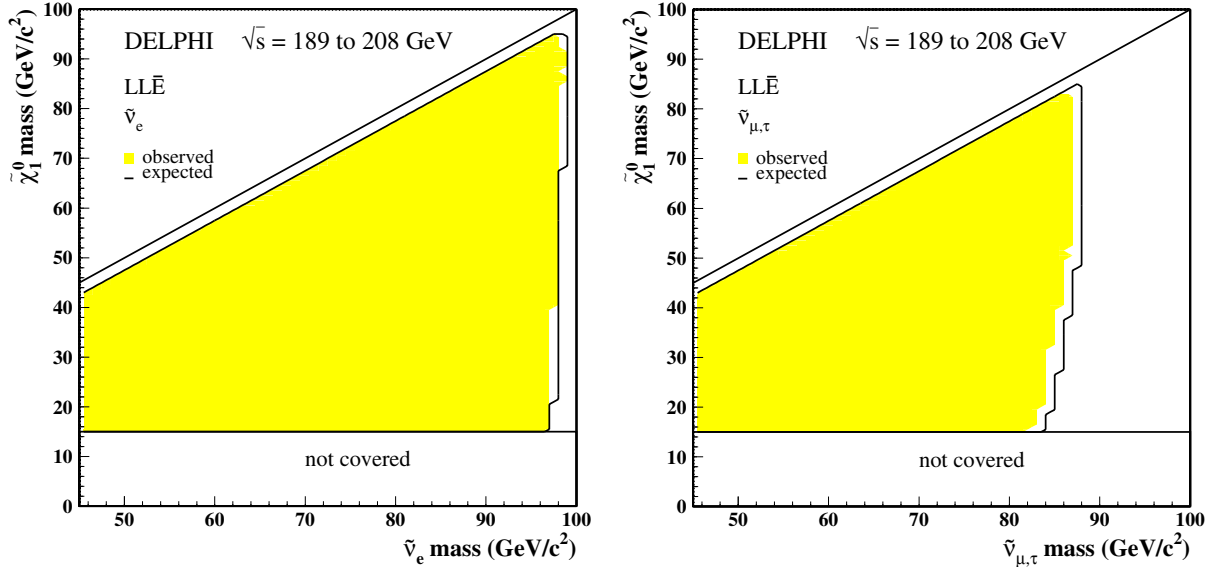
Fig. 13. LL$\bar{\mathrm{E}}$: excluded regions at 95% CL in the $m_{\tilde{\chi}^0}$ versus $m_{\tilde{\nu}}$ planes for $\tilde{\nu}_e$ (left) and $\tilde{\nu}_\mu, \tilde{\nu}_\tau$ (right) pair-production, with BR($\tilde{\nu} \to \tilde{\chi}_1^0 \nu$) = 100%, and neutralino decay into leptons. The black contour is the corresponding expected exclusion at 95% CL

the neutralino mass is $39.5\,\mathrm{GeV}/c^2$, and the one on the chargino mass is $103.0\,\mathrm{GeV}/c^2$.

5.2.2 $\bar{\mathrm{U}}\bar{\mathrm{D}}\bar{\mathrm{D}}$ scenario

Efficiencies and selected events

At the end of the analysis procedure to search for gauginos described in Sects. 4.4.2 and 4.4.3, no significant excess of events was seen in the data with respect to the SM expectations. Figure 9 shows the number of expected events from the SM and the number of observed events as a function of the average signal efficiency obtained with all simulated masses for the N3 and C2 analyses after a step-by-step cut on the neural network output.

For neutralino pair-production, the efficiencies were typically around 30–60% at the values of the optimized neural network outputs, depending on the simulated masses.

For chargino pair-production, the signal efficiencies were between 10% and 70%. The expected and observed numbers of events for both analyses are reported in Table 3 for each mass window.

Limits

The signal efficiency for any values of the $\tilde{\chi}_1^0$ and $\tilde{\chi}^\pm$ masses was interpolated using an efficiency grid determined with signal samples produced with the full DELPHI detector simulation. The number of expected events $\mathrm{N}_{\mathrm{exp}}$ has been computed separatly for neutralino and chargino pair productions.

$$\mathrm{N}_{\mathrm{exp}} = \epsilon_{200} \cdot \sum_{\mathrm{E_{cm}}=192}^{\mathrm{E_{cm}}=202} \mathcal{L}_{\mathrm{E_{cm}}} \cdot \sigma_{\chi\chi}$$
$$+ \epsilon_{206} \cdot \sum_{\mathrm{E_{cm}}=203}^{\mathrm{E_{cm}}=208} \mathcal{L}_{\mathrm{E_{cm}}} \cdot \sigma_{\chi\chi}$$
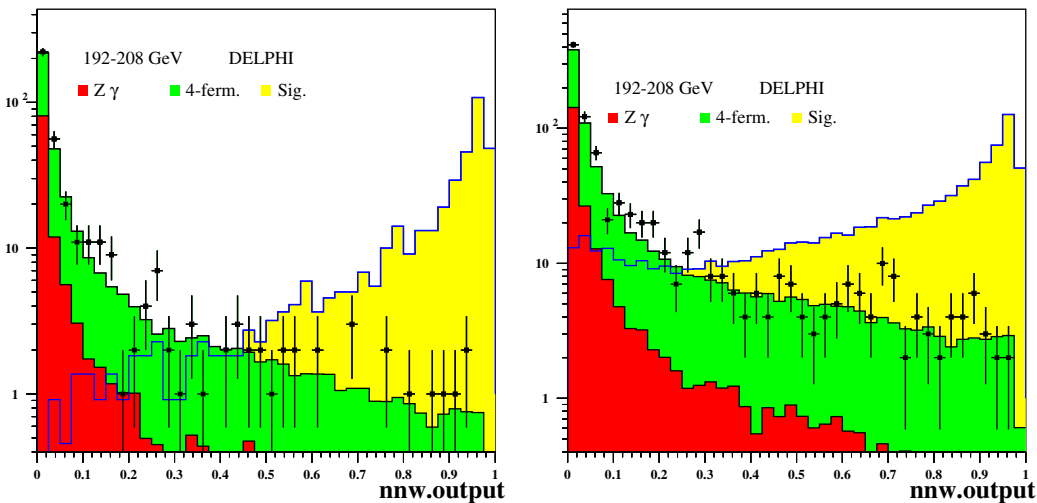
Fig. 14. $\bar{\mathrm{U}}\bar{\mathrm{D}}\bar{\mathrm{D}}$: the neural network signal output distributions for the selectron (left) and smuon (right) window 2 analyses. The cuts on the neural network output variable were chosen for the final selection at 0.83 (selectrons) and 0.92 (smuons)
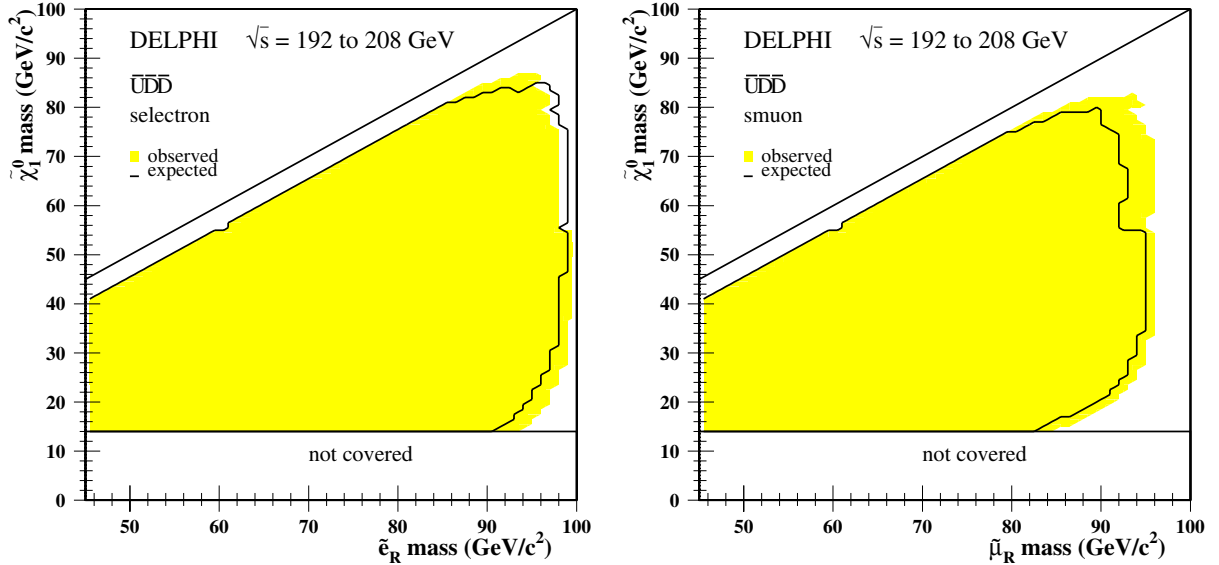
Fig. 15. $\overline{U}\overline{D}\overline{D}$: excluded domains at 95% CL in the $m_{\tilde\chi^0_1}$ versus $m_{\tilde\ell}$ planes for selectron (left) and for smuon (right) pair-production with $BR(\tilde\ell_R \to \tilde\chi^0_1 \ell) = 100\%$ and neutralino decay into jets (filled area). The superimposed contours show the expected exclusion at 95% CL

where $\sigma_{\chi\chi} = \sigma(e^+e^- \to \tilde\chi^0_1\tilde\chi^0_1)$ or $\sigma(e^+e^- \to \tilde\chi^+_1 \tilde\chi^-_1)$, and ϵ_{200} and ϵ_{206} are taken from the efficiency grids.

Using the six-jet and the ten-jet analysis results, an exclusion contours in the (μ, M_2) plane at 95% CL were derived for different values of m_0 (90 and 300 GeV/c^2) and $\tan\beta$ (1.5 and 30), as shown in Fig. 10. In the exclusion plots the main contribution comes from the study of the chargino indirect decays with the ten-jet analysis, due to the high cross-section. The six-jet analysis becomes crucial in the exclusion plot for low $\tan\beta$, low m_0 and negative μ. The lower limits on the mass of the lightest neutralino and chargino are obtained from the scan on $\tan\beta$ from 0.5 to 30. The lower limit on the neutralino mass of 38.0 GeV/c^2 is obtained for $\tan\beta = 1$ and $m_0 = 500$ GeV/c^2 (Fig. 11). The chargino is mainly excluded up to the kinematic limit at 102.5 GeV/c^2.

5.3 Slepton searches

5.3.1 LL$\overline{E}$ scenario

Efficiencies and selected events

The efficiencies of the slepton analysis described in Sect. 4.3.3 were between 18% and 38% for the sneutrino indirect decay channel, depending only on the neutralino mass. The efficiencies were higher for the final states obtained in indirect decay of charged slepton pairs, due to the presence of two additional leptons. They ranged from $\sim 20\%$ ($m_{\tilde\chi^0} = 15$ GeV/c^2) to 43% for stau pairs; they were of the same order but up to $\sim 5\%$ higher for selectron pairs, and ranged from $\sim 25\%$ ($m_{\tilde\chi^0} = 15$ GeV/c^2) to 64% for smuon pairs. For the direct decay of $\tilde\nu_e$, the analysis efficiencies lay in the range 27–36%, depending on the sneutrino mass.

At the end of the selection, 11 events remained in the data compared to 8.1 ± 0.3 expected from the SM processes (Table 3). The background was mainly composed of four-fermion events, in particular from W pair-production.

The efficiencies of the $\tilde\nu_\tau\tilde\nu_\tau$ direct decay analysis (see Sect. 4.3.4) varied with the $\tilde\nu_\tau$ mass and ranged from 45% to 51%. At the end of the selection, 6 candidates were obtained for 6.3 ± 0.4 expected (see Table 3).

Limits

To derive limits on slepton masses, the results of the search described above were combined with those obtained with data at $\sqrt{s} = 189$ GeV [3].

For charged slepton indirect decay, the areas excluded in the $m_{\tilde\chi^0}$ versus $m_{\tilde\ell_R}$ planes are plotted in Fig. 12.

As was explained in Sect. 2.3, a pair of selectrons can be produced in the t-channel via neutralino exchange. With the MSSM parameters fixed to derive limits, the $\tilde{e}^+\tilde{e}^-$ cross-section is higher than the $\tilde\mu^+\tilde\mu^-$ and $\tilde\tau^+\tilde\tau^-$ ones. So, though the analysis efficiencies for the smuon pair-production were higher, the excluded area in case of the selectron pair search is the largest; the smallest is obtained for the $\tilde\tau^+\tilde\tau^-$ production. For $\Delta M \geq 5$ GeV/c^2, the limits on the slepton mass are 94 GeV/c^2, 87 GeV/c^2 and 86 GeV/c^2 for the $\tilde{e}$, $\tilde\mu$ and $\tilde\tau$, respectively, and become 95 GeV/c^2, 90 GeV/c^2 and 90 GeV/c^2 if the neutralino mass limit is taken into account.

The results of the search for the indirect decay of the $\tilde\nu$ were used to exclude areas in the $m_{\tilde\chi^0}$ versus $m_{\tilde\nu}$ planes, as shown in Fig. 13. These exclusion areas are also valid for all the λ_{ijk} couplings. As already mentioned in Sect. 2.3, the $\tilde\nu_e\tilde\nu_e$ cross-section can be enhanced compared to the $\tilde\nu_\mu\tilde\nu_\mu$ and $\tilde\nu_\tau\tilde\nu_\tau$ cross-sections if production via a chargino exchange is possible and the excluded area depends on the chargino mass. For $\Delta M \geq 5$ GeV/c^2, the limit on the $\tilde\nu_\mu$
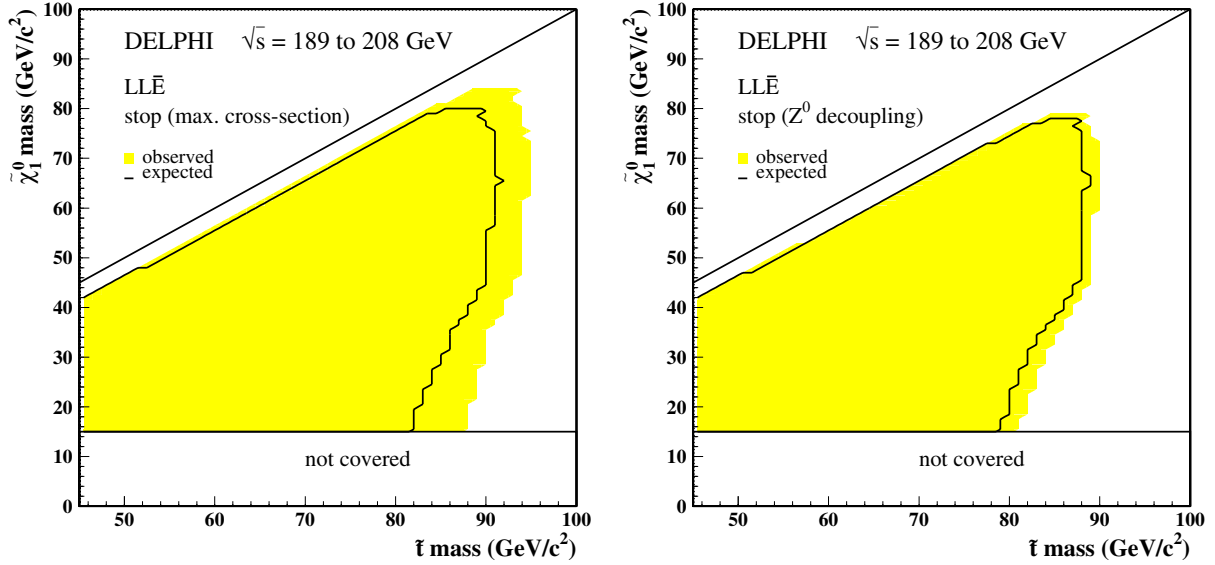
Fig. 16. LL$\bar{\text{E}}$: exclusion domains at 95% CL in the $m_{\tilde{\chi}^0}$ versus $m_{\tilde{t}}$ plane for the stop pair-production, with BR($\tilde{t} \to c\tilde{\chi}_1^0$) = 100% and neutralino decay into leptons. The plots show the exclusion (filled area) for the lightest stop for no mixing (left) and for the mixing leading to the maximal decoupling to the Z boson (right). The black contour is the corresponding expected exclusion at 95% CL
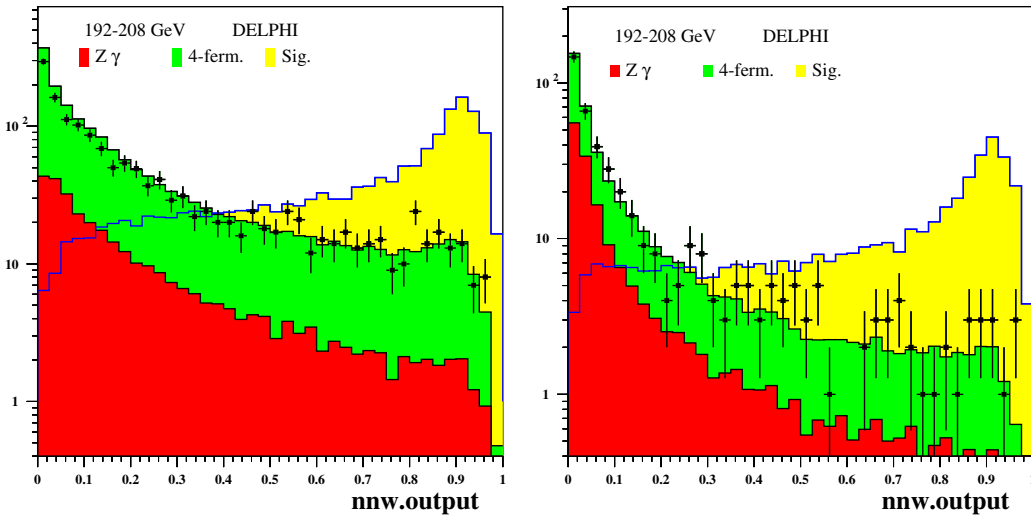
Fig. 17. $\bar{\text{U}}\bar{\text{D}}\bar{\text{D}}$: the neural network signal output distributions for the multi-jet stop (left) and sbottom (right) window 3 analyses. The cuts on the neural network output variable were chosen for the final selection at 0.86 and 0.75 for stop and sbottom, respectively

and $\tilde{\nu}_\tau$ mass is 82 GeV/c^2, and is 85 GeV/c^2 if the limit on the neutralino mass is taken into account. These limits are 96 and 98 GeV/c^2 respectively for $\tilde{\nu}_e$.

The results of the searches for 4τ and $2e2\tau$ final states, from sneutrino pair direct decays, were combined to obtain lower limits on the sneutrino mass. The results from the 4τ search were used to derive limits on $\tilde{\nu}_e$ and on $\tilde{\nu}_\mu$, those from the $2e2\tau$ to derive limits on $\tilde{\nu}_\tau$. The limits obtained are respectively 96 GeV/c^2, 83 GeV/c^2 and 91 GeV/c^2.

5.3.2 $\bar{\text{U}}\bar{\text{D}}\bar{\text{D}}$ scenario

Efficiencies and selected events

No significant excess has been observed in the output signal node distributions for any analyses. The signal output distributions for the selectrons and smuons analyses are

shown in Fig. 14 for the medium ΔM analyses. The signal efficiency of the slepton analyses described in Sect. 4.4.4 was evaluated at each of the simulated points for the two centre-of-mass energies (200 and 206 GeV). Efficiencies for the signal (selectron and smuon) were in the range from 5–40%, for small mass differences and small neutralino mass, and increased up to 60% for medium ΔM analyses. The 5% efficiency was obtained for the $\Delta M = 5$ GeV and for a neutralino mass of 45 GeV. This efficiency increased rapidly with ΔM and with the neutralino mass.

No excess of data with respect to the SM expectations was observed for the selectron and smuon analyses; the numbers of events observed and expected from background contributions are shown in Table 3. The remaining background comes mainly from four-fermion processes.
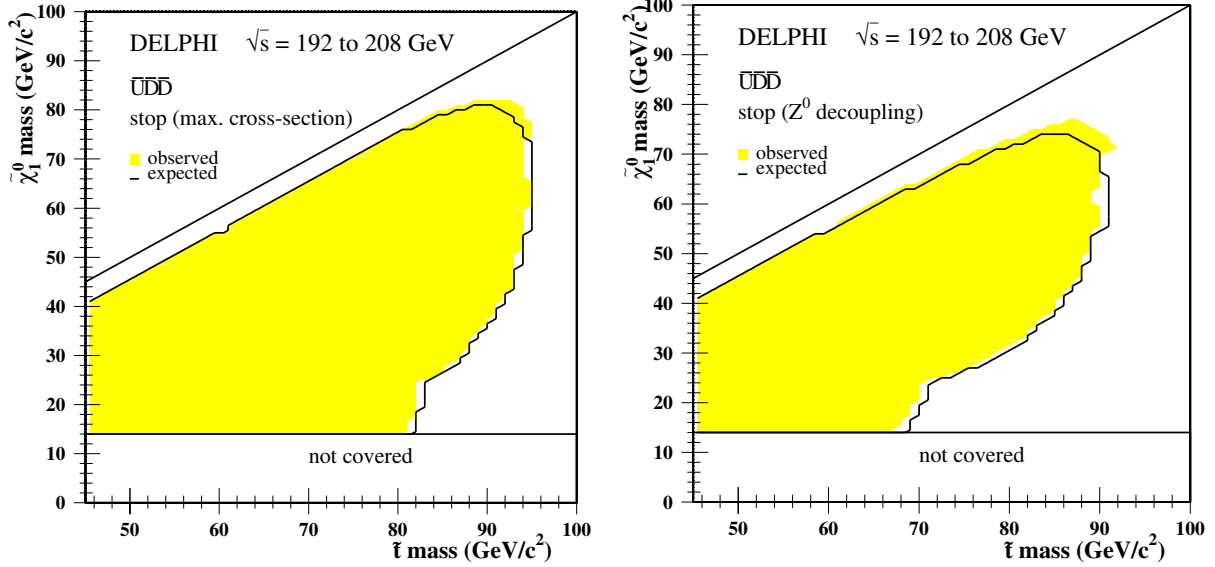
Fig. 18. $\bar{U}\bar{D}\bar{D}$: exclusion domains at 95% CL in the $m_{\tilde{\chi}_1^0}$ versus $m_{\tilde{t}}$ plane for the stop pair-production, with $\mathrm{BR}(\tilde{t} \to c\tilde{\chi}_1^0) = 100\%$ and neutralino decay into jets. The plots show the exclusion (filled area) for the lightest stop for no mixing (left) and for the mixing leading to the maximal decoupling to the Z boson (right). The black contour is the corresponding expected exclusion at 95% CL

Limits

From the selectron and smuon pair-production searches exclusion domains have been computed in the $m_{\tilde{\chi}^0}$ versus $m_{\tilde{\ell}_R}$ plane (Fig. 15). The M_2 value was fixed for each neutralino mass. For $\Delta M \geq 5\,\mathrm{GeV}/c^2$, the lower limit on the right-handed selectron mass was $92\,\mathrm{GeV}/c^2$, and the lower limit obtained for the right-handed smuon was $85\,\mathrm{GeV}/c^2$.

5.4 Squark searches

5.4.1 LL$\bar{E}$ scenario

Efficiencies and selected events

The selection efficiencies of the analysis described in 4.3.5 varied with the stop mass and with the mass difference between the stop and the lightest neutralino. They lay around 30% for most of cases, and around 18–20% for low neutralino masses.

After the selection procedure, 35 events remained with 35.4 ± 0.6 expected from background contributions, mostly coming from W^+W^- production.

The numbers of events observed and expected from SM processes are shown in Table 3.

Limits

From the study of the stop indirect decay, a lower limit on the stop pair-production cross-section was derived as a function of the stop and neutralino masses. Considering two cases of stop mixing (no mixing and mixing angle = 56°), the exclusion limit was derived in the $m_{\tilde{\chi}_1^0}$ versus $m_{\tilde{t}}$ plane, as shown in Fig. 16. With no mixing, the lower bound on

the stop mass is $88\,\mathrm{GeV}/c^2$, valid for $\Delta M > 5\,\mathrm{GeV}/c^2$. If the mixing angle is 56°, the lower bound on the stop mass is $81\,\mathrm{GeV}/c^2$, for $\Delta M > 5\,\mathrm{GeV}/c^2$, and becomes $87\,\mathrm{GeV}/c^2$, taking into account the lower limit on the mass of the lightest neutralino.

5.4.2 $\bar{U}\bar{D}\bar{D}$ scenario

Efficiencies and selected events

The final selection of candidate events was based on the signal output values of the neural networks for the stop and for the sbottom. The cut on the neural network variable has been relaxed for sbottom due to the effect of the b-tagging selection. The signal outputs of the neural network for the multi-jet stop and sbottom analyses (window 3) are shown in Fig. 17. The signal efficiencies of the neural network analyses described in 4.4.5 were evaluated at each of the evenly distributed simulated points in the plane of stop (sbottom) and neutralino masses. Efficiencies for the signal after the final selection were in the range from 10–20%, for small or large mass differences between squark and neutralino, up to around 50% for medium mass differences.

Limits

The resulting exclusion contours for stop and sbottom can be seen in Figs. 18 and 19. The lower limit on the mass of the left-handed stop, assuming the neutralino mass limit of $38\,\mathrm{GeV}/c^2$, is $87\,\mathrm{GeV}/c^2$ for $\Delta M \geq 5\,\mathrm{GeV}/c^2$. The lower limit on the stop mass with the mixing angle = 56° was $77\,\mathrm{GeV}/c^2$ under the same assumptions. The lower limit obtained for the left-handed sbottom assuming a neutralino mass limit of $38\,\mathrm{GeV}/c^2$, was $78\,\mathrm{GeV}/c^2$ for $\Delta M \geq 5\,\mathrm{GeV}/c^2$.

Table 4. Sparticle mass limits at 95% CL from the DELPHI R_p violation pair-production searches of supersymmetric particles; ×: the decay channel is not possible; –: the decay channel is not covered. These results are valid if $m_{\widetilde{\chi}_1^0} \geq 15\,\mathrm{GeV}/c^2$, except for the $\tilde{\nu}$ mass limits derived from the $\tilde{\nu}$ direct decay which does not depend on $m_{\widetilde{\chi}_1^0}$

SUSY particle	Comments about validity conditions	Mass limit (GeV/c^2) LL$\bar{\mathrm{E}}$	$\bar{\mathrm{U}}\bar{\mathrm{D}}\bar{\mathrm{D}}$
	Validity conditions for gauginos:		
$\widetilde{\chi}_1^0$	$90 < \mathrm{m}_0 < 500\,\mathrm{GeV}/c^2$, $0.7 < \tan\beta < 30$,	39.5	38.0
$\widetilde{\chi}_1^+$	$-200 < \mu < 200\,\mathrm{GeV}/c^2$ and $0 < \mathrm{M}_2 < 400\,\mathrm{GeV}/c^2$	103.0	102.5
	Validity conditions for sfermions:		
	$\mu = -200\,\mathrm{GeV}/c^2$ and $\tan\beta = 1.5$,		
	BR($\tilde{\mathrm{f}} \to$ f' $\widetilde{\chi}_1^0$)=1, ΔM$>5\,\mathrm{GeV}/c^2$		
$\widetilde{\mathrm{e}}_\mathrm{R}$	$\widetilde{\chi}_1^0$ mass limit not used	94	92
	$\widetilde{\chi}_1^0$ mass limit used	95	92
$\widetilde{\mu}_\mathrm{R}$	$\widetilde{\chi}_1^0$ mass limit not used	87	85
	$\widetilde{\chi}_1^0$ mass limit used	90	87
$\widetilde{\tau}_\mathrm{R}$	$\widetilde{\chi}_1^0$ mass limit not used	86	–
	$\widetilde{\chi}_1^0$ mass limit used	90	–
	$\widetilde{\chi}_1^0$ mass limit not used	96	–
$\widetilde{\nu}_\mathrm{e}$	$\widetilde{\chi}_1^0$ mass limit used	98	–
	direct decay only	96	×
	$\widetilde{\chi}_1^0$ mass limit not used	82	–
$\widetilde{\nu}_\mu$	$\widetilde{\chi}_1^0$ mass limit used	85	–
	direct decay only	83	×
	$\widetilde{\chi}_1^0$ mass limit not used	82	–
$\widetilde{\nu}_\tau$	$\widetilde{\chi}_1^0$ mass limit used	85	–
	direct decay only	91	×
	$\widetilde{\chi}_1^0$ mass limit not used, no mixing	88	81
$\tilde{\mathrm{t}}$	$\widetilde{\chi}_1^0$ mass limit used, no mixing	92	87
	$\widetilde{\chi}_1^0$ mass limit not used, minimal mixing	81	67
	$\widetilde{\chi}_1^0$ mass limit used, minimal mixing	87	77
$\tilde{\mathrm{b}}$	$\widetilde{\chi}_1^0$ mass limit not used, no mixing	–	78
	$\widetilde{\chi}_1^0$ mass limit used, no mixing	–	78
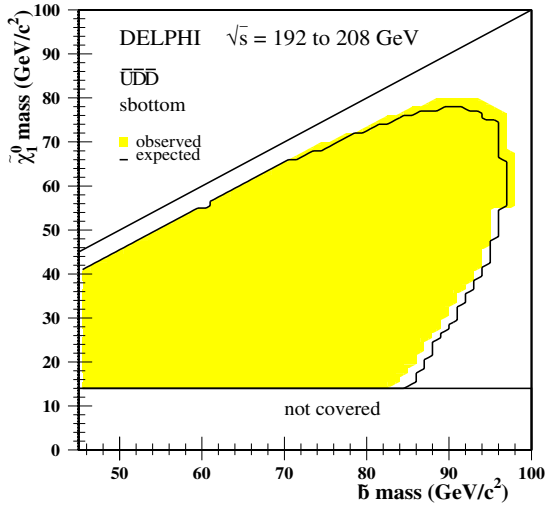
Fig. 19. $\bar{\mathrm{U}}\bar{\mathrm{D}}\bar{\mathrm{D}}$: exclusion contours at 95% CL in the $\mathrm{m}_{\widetilde{\chi}_1^0}$ versus $\mathrm{m}_{\tilde{\mathrm{b}}}$ plane for the sbottom pair-production, with BR($\tilde{\mathrm{b}} \to \mathrm{b}\widetilde{\chi}_1^0$) = 100% and neutralino decay into jets. The plot shows the obtained exclusion (filled area) for the lightest sbottom in the case of no mixing. The black contour is the expected exclusion at 95% CL

The sbottom pair-production cross-section in the case of the mixing angle corresponding to maximum decoupling from the Z boson (68° for sbottom) was too low to cover a significant region of the mass plane by the excluded cross-section of the sbottom analyses.

6 Summary

A large number of different searches for supersymmetric particles with the assumption of R_p violation via $\lambda_{ijk}\mathrm{L}_i\mathrm{L}_j\bar{\mathrm{E}}_k$ or $\lambda''_{ijk}\bar{\mathrm{U}}_i\bar{\mathrm{D}}_j\bar{\mathrm{D}}_k$ terms have been performed on the data recorded in 1999 and 2000 by the DELPHI experiment, at centre-of-mass energies between 192 and 208 GeV. No significant excess has been observed in any of the channels. Limits on the pair-production of sparticles have been derived. These limits were converted into limits on sparticle masses and excluded regions in the MSSM parameter space. Mass limits are summarized in Table 4, together with the assumptions under which these limits are valid.

References

1. For reviews, see e.g. H.P. Nilles, Phys. Rep. **110**, 1 (1984); H.E. Haber, G.L. Kane, Phys. Rep. **117**, 75 (1985)
2. P. Fayet, Phys. Lett. B **69**, 489 (1977); G. Farrar, P. Fayet, Phys. Lett. B **76**, 575 (1978)
3. P. Abreu et al. [DELPHI Collaboration], Eur. Phys. J. C **13**, 591 (2000); P. Abreu et al. [DELPHI Collaboration], Phys. Lett. B **487**, 36 (2000)
4. P. Abreu et al. [DELPHI Collaboration], Phys. Lett. B **500**, 22 (2001)
5. A. Heister et al. [ALEPH Collaboration], Eur. Phys. J. C **31**, 1 (2003); P. Achard et al. [L3 Collaboration], Phys. Lett. B **524**, 65 (2002); G. Abbiendi et al. [OPAL Collaboration], Eur. Phys. J. C **33**, 149 (2004)
6. S. Weinberg, Phys. Rev. D **26**, 287 (1982)
7. V. Barger, G.F. Giudice, T. Han, Phys. Rev. D **40**, 2987 (1989)
8. B.C. Allanach, A. Dedes, H.K. Dreiner, Phys. Rev. D **60**, 075014 (1999)
9. H. Dreiner, G.G. Ross, Nucl. Phys. B **365**, 597 (1991)
10. S. Dawson, Nucl. Phys. B **261**, 297 (1985)
11. J. Abdallah et al. [DELPHI Collaboration], CERN-EP-2003-007
12. J. Abdallah et al. [DELPHI Collaboration], Eur. Phys. J. C **27**, 153 (2003); P. Abreu et al. [DELPHI Collaboration], Phys. Lett. B **485**, 95 (2000)
13. J. Abdallah et al. [DELPHI Collaboration], Eur. Phys. J. C **28**, 15 (2003)
14. J. Ellis, S. Rudaz, Phys. Lett. B **128**, 248 (1983)
15. A. Bartl et al., Z. Phys. C **76**, 549 (1997)
16. M. Drees, An Introduction to Supersymmetry, Lectures given at Inauguration Conference of the Asia Pacific Center for Theoretical Physics (APCTP), Seoul, Korea, 4–19 Jun 1996; hep-ph/9611409
17. M. Drees, S.P. Martin, Implications of SUSY model building, hep-ph/9504324
18. M. Drees, K. Hikasa, Phys. Lett. B **252**, 127 (1990)
19. P. Aarnio et al., Nucl. Instr. Methods **303**, 233 (1991); P. Abreu et al., Nucl. Instr. Methods **378**, 57 (1996)
20. F.A. Berends, P.H. Daverveldt, R. Kleiss, Comput. Phys. Commun. **40**, 271, 285, and 309 (1986)
21. S. Jadach, W. Placzek, B.F.L. Ward, Phys. Lett. B **390**, 298 (1997)
22. S. Jadach, Z. Was, Comput. Phys. Commun. **79**, 503 (1994)
23. T. Sjostrand, Comput. Phys. Commun. **82**, 74 (1994)
24. F.A. Berends, R. Kleiss, R. Pittau, Comput. Phys. Commun. **85**, 437 (1995)
25. J. Fujimoto et al., Comput. Phys. Commun. **100**, 128 (1997)
26. S. Katsanevas, P. Morawitz, Comput. Phys. Commun. **112**, 227 (1998); N. Ghodbane, Proceedings of the Worldwide Study on Physics and Experiments with Future Linear e^+e^- Colliders, Sitges, Barcelona, Spain, 28 April–5 May 1999
27. S. Catani et al., Phys. Lett. B **269**, 432 (1991)
28. Yu.L. Dokshitzer, G.D. Leder, S. Moretti, B.R. Webber, J. High Energy Phys. 8 (1997) 1
29. S. Bentvelsen, I. Meyer, Eur. Phys. J. C **4**, 623 (1998)
30. V. Poireau, DAPNIA/SPP-01-01-T, PhD thesis (2001) in French
31. P. Abreu et al., Eur. Phys. J. C **10**, 415 (1999)
32. R.M. Barnett et al., Particle Data Group, Phys. Rev. D **54**, 1 (1996)
33. A. Read et al., 1st Workshop on Confidence Limits, CERN 2000-005, 81–103

Search for R-parity violation with a $\overline{U}\,\overline{D}\,\overline{D}$ coupling at $\sqrt{s} = 189$ GeV

DELPHI Collaboration

P. Abreu [u], W. Adam [ay], T. Adye [ak], P. Adzic [k], I. Ajinenko [aq], Z. Albrecht [q],
T. Alderweireld [b], G.D. Alekseev [p], R. Alemany [ax], T. Allmendinger [q], P.P. Allport [v],
S. Almehed [x], U. Amaldi [ab], N. Amapane [at], S. Amato [av], E.G. Anassontzis [c],
P. Andersson [as], A. Andreazza [aa], S. Andringa [u], P. Antilogus [y], W.-D. Apel [q],
Y. Arnoud [n], B. Åsman [as], J.-E. Augustin [w], A. Augustinus [i], P. Baillon [i],
A. Ballestrero [at], P. Bambade [i,s], F. Barao [u], G. Barbiellini [au], R. Barbier [y], D.Y. Bardin [p],
G. Barker [q], A. Baroncelli [am], M. Battaglia [o], M. Baubillier [w], K.-H. Becks [ba],
M. Begalli [f], A. Behrmann [ba], P. Beilliere [h], Yu. Belokopytov [i], N.C. Benekos [af],
A.C. Benvenuti [e], C. Berat [n], M. Berggren [w], L. Berntzon [as], D. Bertrand [b],
M. Besancon [an], M.S. Bilenky [p], M.-A. Bizouard [s], D. Bloch [j], H.M. Blom [ae],
M. Bonesini [ab], M. Boonekamp [an], P.S.L. Booth [v], G. Borisov [s], C. Bosio [ap], O. Botner [aw],
E. Boudinov [ae], B. Bouquet [s], C. Bourdarios [s], T.J.V. Bowcock [v], I. Boyko [p], I. Bozovic [k],
M. Bozzo [m], M. Bracko [ar], P. Branchini [am], R.A. Brenner [aw], P. Bruckman [i],
J.-M. Brunet [h], L. Bugge [ag], T. Buran [ag], B. Buschbeck [ay], P. Buschmann [ba], S. Cabrera [ax],
M. Caccia [aa], M. Calvi [ab], T. Camporesi [i], V. Canale [al], F. Carena [i], L. Carroll [v],
C. Caso [m], M.V. Castillo Gimenez [ax], A. Cattai [i], F.R. Cavallo [e], Ph. Charpentier [i],
P. Checchia [aj], G.A. Chelkov [p], R. Chierici [at], P. Chliapnikov [i,aq], P. Chochula [g],
V. Chorowicz [y], J. Chudoba [ad], K. Cieslik [r], P. Collins [i], R. Contri [m], E. Cortina [ax],
G. Cosme [s], F. Cossutti [i], M. Costa [ax], H.B. Crawley [a], D. Crennell [ak], G. Crosetti [m],
J. Cuevas Maestro [ah], S. Czellar [o], J. D'Hondt [b], J. Dalmau [as], M. Davenport [i],
W. Da Silva [w], G. Della Ricca [au], P. Delpierre [z], N. Demaria [at], A. De Angelis [au],
W. De Boer [q], C. De Clercq [b], B. De Lotto [au], A. De Min [i], L. De Paula [av], H. Dijkstra [i],
L. Di Ciaccio [al], J. Dolbeau [h], K. Doroba [az], M. Dracos [j], J. Drees [ba], M. Dris [af],
G. Eigen [d], T. Ekelof [aw], M. Ellert [aw], M. Elsing [i], J.-P. Engel [j], M. Espirito Santo [i],
G. Fanourakis [k], D. Fassouliotis [k], M. Feindt [q], J. Fernandez [ao], A. Ferrer [ax],
E. Ferrer-Ribas [s], F. Ferro [m], A. Firestone [a], U. Flagmeyer [ba], H. Foeth [i], E. Fokitis [af],
F. Fontanelli [m], B. Franek [ak], A.G. Frodesen [d], R. Fruhwirth [ay], F. Fulda-Quenzer [s],
J. Fuster [ax], A. Galloni [v], D. Gamba [at], S. Gamblin [s], M. Gandelman [av], C. Garcia [ax],
C. Gaspar [i], M. Gaspar [av], U. Gasparini [aj], Ph. Gavillet [i], E.N. Gazis [af], D. Gele [j],

T. Geralis [k], L. Gerdyukov [aq], N. Ghodbane [y], I. Gil [ax], F. Glege [ba], R. Gokieli [i,az],
B. Golob [i,ar], G. Gomez-Ceballos [ao], P. Goncalves [u], I. Gonzalez Caballero [ao],
G. Gopal [ak], L. Gorn [a], Yu. Gouz [aq], V. Gracco [m], J. Grahl [a], E. Graziani [am], P. Gris [an],
G. Grosdidier [s], K. Grzelak [az], J. Guy [ak], C. Haag [q], F. Hahn [i], S. Hahn [ba], S. Haider [i],
A. Hallgren [aw], K. Hamacher [ba], J. Hansen [ag], F.J. Harris [ai], F. Hauler [q], V. Hedberg [i,x],
S. Heising [q], J.J. Hernandez [ax], P. Herquet [b], H. Herr [i], E. Higon [ax], S.-O. Holmgren [as],
P.J. Holt [ai], S. Hoorelbeke [b], M. Houlden [v], J. Hrubec [ay], M. Huber [q], G.J. Hughes [v],
K. Hultqvist [i,as], J.N. Jackson [v], R. Jacobsson [i], P. Jalocha [r], R. Janik [g], Ch. Jarlskog [x],
G. Jarlskog [x], P. Jarry [an], B. Jean-Marie [s], D. Jeans [ai], E.K. Johansson [as], P. Jonsson [y],
C. Joram [i], P. Juillot [j], L. Jungermann [q], F. Kapusta [w], K. Karafasoulis [k], S. Katsanevas [y],
E.C. Katsoufis [af], R. Keranen [q], G. Kernel [ar], B.P. Kersevan [ar], Yu. Khokhlov [aq],
B.A. Khomenko [p], N.N. Khovanski [p], A. Kiiskinen [o], B. King [v], A. Kinvig [v], N.J. Kjaer [i],
O. Klapp [ba], P. Kluit [ae], P. Kokkinias [k], V. Kostioukhine [aq], C. Kourkoumelis [c],
O. Kouznetsov [p], M. Krammer [ay], E. Kriznic [ar], Z. Krumstein [p], P. Kubinec [g],
J. Kurowska [az], K. Kurvinen [o], J.W. Lamsa [a], D.W. Lane [a], V. Lapin [aq], J.-P. Laugier [an],
R. Lauhakangas [o], G. Leder [ay], F. Ledroit [n], L. Leinonen [as], A. Leisos [k], R. Leitner [ad],
G. Lenzen [ba], V. Lepeltier [s], T. Lesiak [r], M. Lethuillier [y], J. Libby [ai], W. Liebig [ba],
D. Liko [i], A. Lipniacka [as], I. Lippi [aj], B. Loerstad [x], J.G. Loken [ai], J.H. Lopes [av],
J.M. Lopez [ao], R. Lopez-Fernandez [n], D. Loukas [k], P. Lutz [an], L. Lyons [ai],
J. MacNaughton [ay], J.R. Mahon [f], A. Maio [u], A. Malek [ba], S. Maltezos [af], V. Malychev [p],
F. Mandl [ay], J. Marco [ao], R. Marco [ao], B. Marechal [av], M. Margoni [aj], J.-C. Marin [i],
C. Mariotti [i], A. Markou [k], C. Martinez-Rivero [i], S. Marti i Garcia [i], J. Masik [l],
N. Mastroyiannopoulos [k], F. Matorras [ao], C. Matteuzzi [ab], G. Matthiae [al], F. Mazzucato [aj],
M. Mazzucato [aj], M. Mc Cubbin [v], R. Mc Kay [a], R. Mc Nulty [v], G. Mc Pherson [v],
E. Merle [n], C. Meroni [aa], W.T. Meyer [a], E. Migliore [i], L. Mirabito [y], W.A. Mitaroff [ay],
U. Mjoernmark [x], T. Moa [as], M. Moch [q], R. Moeller [ac], K. Moenig [i,1], M.R. Monge [m],
D. Moraes [av], P. Morettini [m], G. Morton [ai], U. Mueller [ba], K. Muenich [ba], M. Mulders [ae],
C. Mulet-Marquis [n], L.M. Mundim [f], R. Muresan [x], W.J. Murray [ak], B. Muryn [r],
G. Myatt [ai], T. Myklebust [ag], F. Naraghi [n], M. Nassiakou [k], F.L. Navarria [e],
K. Nawrocki [az], P. Negri [ab], N. Neufeld [ay], R. Nicolaidou [an], B.S. Nielsen [ac],
P. Niezurawski [az], M. Nikolenko [j,p], V. Nomokonov [o], A. Nygren [x], V. Obraztsov [aq],
A.G. Olshevski [p], A. Onofre [u], R. Orava [o], G. Orazi [j], K. Osterberg [i], A. Ouraou [an],
A. Oyanguren [ax], M. Paganoni [ab], S. Paiano [e], R. Pain [w], R. Paiva [u], J. Palacios [ai],
H. Palka [r], Th.D. Papadopoulou [af], L. Pape [i], C. Parkes [i], F. Parodi [m], U. Parzefall [v],
A. Passeri [am], O. Passon [ba], T. Pavel [x], M. Pegoraro [aj], L. Peralta [u], M. Pernicka [ay],
A. Perrotta [e], C. Petridou [au], A. Petrolini [m], H.T. Phillips [ak], F. Pierre [an], M. Pimenta [u],
E. Piotto [aa], T. Podobnik [ar], V. Poireau [an], M.E. Pol [f], G. Polok [r], P. Poropat [au],
V. Pozdniakov [p], P. Privitera [al], N. Pukhaeva [p], A. Pullia [ab], D. Radojicic [ai], S. Ragazzi [ab],

H. Rahmani [af], J. Rames [l], P.N. Ratoff [t], A.L. Read [ag], P. Rebecchi [i], N.G. Redaelli [ab],
M. Regler [ay], J. Rehn [q], D. Reid [ae], P. Reinertsen [d], R. Reinhardt [ba], P.B. Renton [ai],
L.K. Resvanis [c], F. Richard [s], J. Ridky [l], G. Rinaudo [at], I. Ripp-Baudot [j], A. Romero [at],
P. Ronchese [aj], E.I. Rosenberg [a], P. Rosinsky [g], T. Rovelli [e], V. Ruhlmann-Kleider [an],
A. Ruiz [ao], H. Saarikko [o], Y. Sacquin [an], A. Sadovsky [p], G. Sajot [n], J. Salt [ax],
D. Sampsonidis [k], M. Sannino [m], A. Savoy-Navarro [w], Ph. Schwemling [w],
B. Schwering [ba], U. Schwickerath [q], F. Scuri [au], P. Seager [t], Y. Sedykh [p], A.M. Segar [ai],
N. Seibert [q], R. Sekulin [ak], G. Sette [m], R.C. Shellard [f], M. Siebel [ba], L. Simard [an],
F. Simonetto [aj], A.N. Sisakian [p], G. Smadja [y], N. Smirnov [aq], O. Smirnova [x],
G.R. Smith [ak], A. Sokolov [aq], A. Sopczak [q], R. Sosnowski [az], T. Spassov [i], E. Spiriti [am],
S. Squarcia [m], C. Stanescu [am], M. Stanitzki [q], K. Stevenson [ai], A. Stocchi [s], J. Strauss [ay],
R. Strub [j], B. Stugu [d], M. Szczekowski [az], M. Szeptycka [az], T. Tabarelli [ab], A. Taffard [v],
F. Tegenfeldt [aw], F. Terranova [ab], J. Timmermans [ae], N. Tinti [e], L.G. Tkatchev [p],
M. Tobin [v], S. Todorova [i], B. Tome [u], A. Tonazzo [i], L. Tortora [am], P. Tortosa [ax],
G. Transtromer [x], D. Treille [i], G. Tristram [h], M. Trochimczuk [az], C. Troncon [aa],
M.-L. Turluer [an], I.A. Tyapkin [p], P. Tyapkin [x], S. Tzamarias [k], O. Ullaland [i], V. Uvarov [aq],
G. Valenti [i,e], E. Vallazza [au], P. Van Dam [ae], W. Van den Boeck [b], J. Van Eldik [i,ae],
A. Van Lysebetten [b], N. van Remortel [b], I. Van Vulpen [ae], G. Vegni [aa], L. Ventura [aj],
W. Venus [ak,i], F. Verbeure [b], P. Verdier [y], M. Verlato [aj], L.S. Vertogradov [p], V. Verzi [aa],
D. Vilanova [an], L. Vitale [au], E. Vlasov [aq], A.S. Vodopyanov [p], G. Voulgaris [c], V. Vrba [l],
H. Wahlen [ba], A.J. Washbrook [v], C. Weiser [i], D. Wicke [i], J.H. Wickens [b],
G.R. Wilkinson [ai], M. Winter [j], M. Witek [r], G. Wolf [i], J. Yi [a], O. Yushchenko [aq],
A. Zalewska [r], P. Zalewski [az], D. Zavrtanik [ar], E. Zevgolatakos [k], N.I. Zimin [p,x],
A. Zintchenko [p], Ph. Zoller [j], G.C. Zucchelli [as], G. Zumerle [aj]

[a] *Department of Physics and Astronomy, Iowa State University, Ames, IA 50011-3160, USA*
[b] *Physics Department, Univ. Instelling Antwerpen, Universiteitsplein 1, B-2610 Antwerpen and IIHE, ULB-VUB, Pleinlaan 2,*
B-1050 Brussels and Faculté des Sciences, Univ. de l'Etat Mons, Av. Maistriau 19, B-7000 Mons, Belgium
[c] *Physics Laboratory, University of Athens, Solonos Str. 104, GR-10680 Athens, Greece*
[d] *Department of Physics, University of Bergen, Allégaten 55, NO-5007 Bergen, Norway*
[e] *Dipartimento di Fisica, Università di Bologna and INFN, Via Irnerio 46, IT-40126 Bologna, Italy*
[f] *Centro Brasileiro de Pesquisas Físicas, rua Xavier Sigaud 150, BR-22290 Rio de Janeiro and Depto. de Física, Pont. Univ. Católica,*
C.P. 38071 BR-22453 Rio de Janeiro, Brazil
and Inst. de Física, Univ. Estadual do Rio de Janeiro, rua São Francisco Xavier 524, Rio de Janeiro, Brazil
[g] *Comenius University, Faculty of Mathematics and Physics, Mlynska Dolina, SK-84215 Bratislava, Slovakia*
[h] *Collège de France, Lab. de Physique Corpusculaire, IN2P3-CNRS, FR-75231 Paris Cedex 05, France*
[i] *CERN, CH-1211 Geneva 23, Switzerland*
[j] *Institut de Recherches Subatomiques, IN2P3 - CNRS/ULP - BP20, FR-67037 Strasbourg Cedex, France*
[k] *Institute of Nuclear Physics, N.C.S.R. Demokritos, P.O. Box 60228, GR-15310 Athens, Greece*
[l] *FZU, Inst. of Phys. of the C.A.S. High Energy Physics Division, Na Slovance 2, CZ-180 40, Praha 8, Czech Republic*
[m] *Dipartimento di Fisica, Università di Genova and INFN, Via Dodecaneso 33, IT-16146 Genova, Italy*
[n] *Institut des Sciences Nucléaires, IN2P3-CNRS, Université de Grenoble 1, FR-38026 Grenoble Cedex, France*
[o] *Helsinki Institute of Physics, HIP, P.O. Box 9, FI-00014 Helsinki, Finland*
[p] *Joint Institute for Nuclear Research, Dubna, Head Post Office, P.O. Box 79, RU-101 000 Moscow, Russian Federation*
[q] *Institut für Experimentelle Kernphysik, Universität Karlsruhe, Postfach 6980, DE-76128 Karlsruhe, Germany*
[r] *Institute of Nuclear Physics and University of Mining and Metalurgy, Ul. Kawiory 26a, PL-30055 Krakow, Poland*

[s] *Université de Paris-Sud, Lab. de l'Accélérateur Linéaire, IN2P3-CNRS, Bât. 200, FR-91405 Orsay Cedex, France*
[t] *School of Physics and Chemistry, University of Lancaster, Lancaster LA1 4YB, UK*
[u] *LIP, IST, FCUL - Av. Elias Garcia, 14-1°, PT-1000 Lisboa Codex, Portugal*
[v] *Department of Physics, University of Liverpool, P.O. Box 147, Liverpool L69 3BX, UK*
[w] *LPNHE, IN2P3-CNRS, Univ. Paris VI et VII, Tour 33 (RdC), 4 place Jussieu, FR-75252 Paris Cedex 05, France*
[x] *Department of Physics, University of Lund, Sölvegatan 14, SE-223 63 Lund, Sweden*
[y] *Université Claude Bernard de Lyon, IPNL, IN2P3-CNRS, FR-69622 Villeurbanne Cedex, France*
[z] *Univ. d'Aix - Marseille II - CPP, IN2P3-CNRS, FR-13288 Marseille Cedex 09, France*
[aa] *Dipartimento di Fisica, Università di Milano and INFN-MILANO, Via Celoria 16, IT-20133 Milan, Italy*
[ab] *Dipartimento di Fisica, Univ. di Milano-Bicocca and INFN-MILANO, Piazza delle Scienze 2, IT-20126 Milan, Italy*
[ac] *Niels Bohr Institute, Blegdamsvej 17, DK-2100 Copenhagen Ø, Denmark*
[ad] *IPNP of MFF, Charles Univ., Areal MFF, V Holesovickach 2, CZ-180 00, Praha 8, Czech Republic*
[ae] *NIKHEF, Postbus 41882, NL-1009 DB Amsterdam, The Netherlands*
[af] *National Technical University, Physics Department, Zografou Campus, GR-15773 Athens, Greece*
[ag] *Physics Department, University of Oslo, Blindern, NO-1000 Oslo 3, Norway*
[ah] *Dpto. Fisica, Univ. Oviedo, Avda. Calvo Sotelo s/n, ES-33007 Oviedo, Spain*
[ai] *Department of Physics, University of Oxford, Keble Road, Oxford OX1 3RH, UK*
[aj] *Dipartimento di Fisica, Università di Padova and INFN, Via Marzolo 8, IT-35131 Padua, Italy*
[ak] *Rutherford Appleton Laboratory, Chilton, Didcot OX11 OQX, UK*
[al] *Dipartimento di Fisica, Università di Roma II and INFN, Tor Vergata, IT-00173 Rome, Italy*
[am] *Dipartimento di Fisica, Università di Roma III and INFN, Via della Vasca Navale 84, IT-00146 Rome, Italy*
[an] *DAPNIA/Service de Physique des Particules, CEA-Saclay, FR-91191 Gif-sur-Yvette Cedex, France*
[ao] *Instituto de Fisica de Cantabria (CSIC-UC), Avda. los Castros s/n, ES-39006 Santander, Spain*
[ap] *Dipartimento di Fisica, Università degli Studi di Roma La Sapienza, Piazzale Aldo Moro 2, IT-00185 Rome, Italy*
[aq] *Inst. for High Energy Physics, Serpukov P.O. Box 35, Protvino (Moscow Region), Russian Federation*
[ar] *J. Stefan Institute, Jamova 39, SI-1000 Ljubljana, Slovenia*
and Laboratory for Astroparticle Physics, Nova Gorica Polytechnic, Kostanjeviska 16a, SI-5000 Nova Gorica, Slovenia
and Department of Physics, University of Ljubljana, SI-1000 Ljubljana, Slovenia
[as] *Fysikum, Stockholm University, Box 6730, SE-113 85 Stockholm, Sweden*
[at] *Dipartimento di Fisica Sperimentale, Università di Torino and INFN, Via P. Giuria 1, IT-10125 Turin, Italy*
[au] *Dipartimento di Fisica, Università di Trieste and INFN, Via A. Valerio 2, IT-34127 Trieste and Istituto di Fisica, Università di Udine, IT-33100 Udine, Italy*
[av] *Univ. Federal do Rio de Janeiro, C.P. 68528 Cidade Univ., Ilha do Fundão BR-21945-970 Rio de Janeiro, Brazil*
[aw] *Department of Radiation Sciences, University of Uppsala, P.O. Box 535, SE-751 21 Uppsala, Sweden*
[ax] *IFIC, Valencia-CSIC, and D.F.A.M.N., U. de Valencia, Avda. Dr. Moliner 50, ES-46100 Burjassot (Valencia), Spain*
[ay] *Institut für Hochenergiephysik, Österr. Akad. d. Wissensch., Nikolsdorfergasse 18, AT-1050 Vienna, Austria*
[az] *Inst. Nuclear Studies and University of Warsaw, Ul. Hoza 69, PL-00681 Warsaw, Poland*
[ba] *Fachbereich Physik, University of Wuppertal, Postfach 100 127, DE-42097 Wuppertal, Germany*

Abstract

Searches for pair production of gauginos and squarks in e^+e^- collisions at a centre-of-mass energy of 189 GeV have been performed on data corresponding to an integrated luminosity of 158 pb^{-1} collected by the DELPHI detector at LEP. The data were analyzed under the assumption of non-conservation of R-parity through a single dominant $\overline{U}\,\overline{D}\,\overline{D}$ coupling between squarks and quarks. Typical final states contain between 4 and 10 jets with or without additional leptons. No excess of data above Standard Model expectations was observed. The results were used to constrain domains of the MSSM parameter space and derive limits on the masses of supersymmetric particles. The following mass limits at 95% CL were obtained from these searches: neutralino mass: $m_{\tilde{\chi}_1^0} \geqslant 32$ GeV; chargino mass: $m_{\tilde{\chi}_1^+} \geqslant 94$ GeV; stop and sbottom mass (indirect decay) with

---

[1] Now at DESY-Zeuthen, Platanenallee 6, D-15735 Zeuthen, Germany.

$\Delta M > 5$ GeV: $m_{\tilde{t}_1} \geqslant 74$ GeV for $\Phi_{\mathrm{mix}} = 0$ rad, $m_{\tilde{t}_1} \geqslant 59$ GeV for $\Phi_{\mathrm{mix}} = 0.98$ rad, $m_{\tilde{b}_1} \geqslant 72$ GeV for $\Phi_{\mathrm{mix}} = 0$ rad. The angle ϕ_{mix} is the mixing angle between left and right handed quarks.

1. Introduction

1.1. The R-parity violating Lagrangian

The most general way to write a superpotential, including the symmetries and particle content of the Minimal Supersymmetric extension of the Standard Model (MSSM) [1] is:

$$W = W_{\mathrm{MSSM}} + W_{\mathrm{RPV}}, \tag{1}$$

where W_{MSSM} represents interactions between MSSM particles consistent with $B - L$ conservation ($B =$ baryon number, $L =$ lepton number) and W_{RPV} describes interactions violating B or L conservation [2]. This latter term of the superpotential can explicitly be written as [2] [3]:

$$\lambda_{ijk} L_i L_j \overline{E}_k + \lambda'_{ijk} L_i Q_j \overline{D}_k + \lambda''_{ijk} \overline{U}_i \overline{D}_j \overline{D}_k, \tag{2}$$

where i, j and k are the generation indices; L and $\overline{E}$ denote the left-handed doublet lepton and the right-handed singlet charge-conjugated lepton superfields respectively, whereas Q, $\overline{U}$ and $\overline{D}$ denote the left-handed doublet quark and the right-handed singlet charge-conjugated up- and down-type quark superfields; λ_{ijk}, λ'_{ijk} and λ''_{ijk} are the Yukawa couplings. The first two terms violate L conservation, and the third term B conservation. Since $\lambda_{ijk} = -\lambda_{jik}$, $\lambda''_{ijk} = -\lambda''_{ikj}$, there are 9 λ_{ijk}, 27 λ'_{ijk} and 9 λ''_{ijk} leading to 45 additional couplings.

One major phenomenological consequence of R-parity violation ($\not{R}_p$) is that the Lightest Supersymmetric Particle (LSP) is allowed to decay into standard fermions. This fact modifies the signatures of the supersymmetric particle production compared to the expected signatures in case of R-parity conservation. First, the LSP may be a charged sparticle, for example a chargino (this case is considered in this Letter). Second, due to the LSP decay into fermions, multi-lepton and multi-jet topologies are expected. In this

Letter, searches for pair produced neutralinos ($\tilde{\chi}_i^0$), charginos ($\tilde{\chi}^{\pm}$) and squarks ($\tilde{q}$) were performed under the hypothesis of R-parity violation with one single dominant $\overline{U}\overline{D}\overline{D}$ coupling. The $\overline{U}\overline{D}\overline{D}$ terms couple squarks to quarks and the experimental signature of the $\not{R}_p$ events thus becomes multiple hadronic jets, in most of the cases without missing energy. These signatures with R-parity violation through $\overline{U}\overline{D}\overline{D}$ terms have been already performed by the other LEP2 experiments [5].

1.2. Pair production of gauginos and squarks

Pair production of supersymmetric particles in MSSM with $\not{R}_p$ is the same as R_p conserved pair production, since the $\overline{U}\overline{D}\overline{D}$ couplings are not present in the production vertex.

The mass spectrum and the pair production cross sections of neutralinos and charginos are fixed, in the analyses described in this Letter, by the three parameters of the MSSM theory assuming GUT scale unification of gaugino masses: M_2, the $SU(2)$ gaugino mass parameter at the electroweak scale, μ, the mixing mass term of the Higgs doublets at the electroweak scale and $\tan\beta$, the ratio of the vacuum expectation values of the two Higgs doublets. The cross section depends also on the common scalar mass at the GUT scale, m_0, due to selectron or sneutrino exchange in the t-channel for sufficiently low sfermions masses.

Pair production of squarks ($\tilde{q}$) is also studied in this Letter. Here the cross-section mainly depends on the squark masses. In the case of the third generation, the left–right mixing angle enters in the production cross-section as well. In the squark analysis two cases are considered: one with no mixing, the second with the mixing angle which gives the lowest production cross-section.

1.3. Direct and indirect decays of gauginos and squarks

The decay of the produced sparticles can either be direct or indirect. In a *direct decay* the sparticle decays

---

[2] An additional fourth term in Eq. (2), describing a bilinear coupling between the left handed lepton superfield and the up-type Higgs field, is assumed to be zero [4].
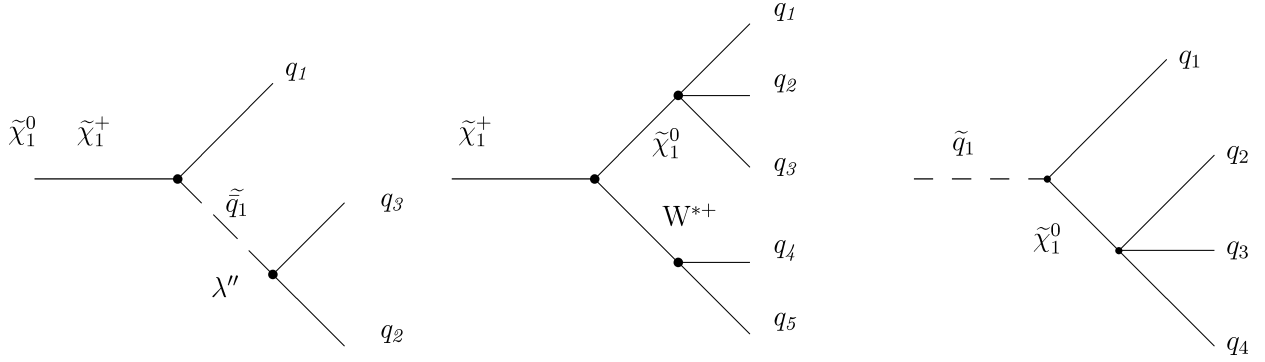
Fig. 1. $\tilde{\chi}_1^0$, $\tilde{\chi}_1^+$ direct decay (left), $\tilde{\chi}_1^+$ (center) and $\tilde{q}$ (right) indirect decay with a dominant $\overline{U}\,\overline{D}\,\overline{D}$ coupling. W^{*+} is an off-shell W^+ boson.

Table 1
The multijet final states in neutralino, chargino and squark pair production when one $\overline{U}\,\overline{D}\,\overline{D}$ coupling is dominant. The leptonic decays of W^* are not listed in these final states since only pure hadronic events are considered in this study

Final states	Direct decay of	Indirect decay of
$4j$	$\tilde{q}\tilde{q}$	
$6j$	$\tilde{\chi}_1^0\tilde{\chi}_1^0$, $\tilde{\chi}_2^0\tilde{\chi}_1^0$, $\tilde{\chi}_1^1\tilde{\chi}_1^-$	
$8j$		$\tilde{q}\tilde{q}$
$10j$		$\tilde{\chi}_1^+\,\tilde{\chi}_1^-$

Table 2
Upper limits on the $\overline{U}\,\overline{D}\,\overline{D}$ Yukawa couplings in units of $(m_{\tilde{f}}/100$ GeV), where $m_{\tilde{f}}$ is the appropriate squark mass [4]

ijk	λ''_{ijk}	ijk	λ''_{ijk}	ijk	λ''_{ijk}
$\lambda''_{uds}(112)$	10^{-6}	$\lambda''_{cds}(212)$	1.25	$\lambda''_{tds}(312)$	0.43
$\lambda''_{udb}(113)$	10^{-5}	$\lambda''_{cdb}(213)$	1.25	$\lambda''_{tdb}(313)$	0.43
$\lambda''_{usb}(123)$	1.25	$\lambda''_{csb}(223)$	1.25	$\lambda''_{tsb}(323)$	0.43

directly or via a virtual sparticle exchange to standard particles through an $\not{R}_p$ vertex. In an *indirect decay* the sparticle first decays through an R_p conserving vertex to a standard particle and an on-shell sparticle, which then decays through an $\not{R}_p$ vertex. The squark analysis is done considering only the indirect decay channels which are dominant for coupling values considered in the present studies.

Fig. 1 shows the direct and indirect decays of gauginos and the indirect decay of a squark via $\overline{U}\,\overline{D}\,\overline{D}$ couplings.

The most important features of these decays are the number of quarks in the final state which goes up to 10 for the indirect decay of two charginos. Table 1 displays the different event topologies from direct and indirect decays through $\overline{U}\,\overline{D}\,\overline{D}$ couplings of different pair produced sparticles. The 6-, 8-, 10-jet topologies of Table 1 correspond to the decay diagrams in Fig. 1.

1.4. $\overline{U}\,\overline{D}\,\overline{D}$ couplings

The $\overline{U}\,\overline{D}\,\overline{D}$ Yukawa coupling strength, corresponding to a squark decay into two quarks, can be bound from above by indirect limits.

Upper limits on $\overline{U}\,\overline{D}\,\overline{D}$ couplings come from Standard Model constraints with experimental measurements:

- double nucleon decays for λ''_{112} couplings [6],
- $n - \bar{n}$ oscillations for λ''_{113} [7],
- $R_l = \Gamma_{had}(Z^0)/\Gamma_l(Z^0)$ for λ''_{312}, λ''_{313}, λ''_{323} [8,9].

The upper limits on the other λ'' couplings do not come from experimental bounds. They are obtained from the requirement of perturbative unification at the GUT scale of 10^{16} GeV. This gives a limit of 1.25 for a sfermion mass of 100 GeV [6,10]. Upper limits on the $\overline{U}\,\overline{D}\,\overline{D}$ couplings are reported in Table 2.

Our analysis, which does not search for long lived sparticles in the detector (displaced vertices), has a limited sensitivity to weak coupling strengths. The coupling strength dependence of the mean decay

length of the LSP is given by [11,12]:

$$L \text{ (cm)} = 0.1 (\beta \gamma) \left(\frac{m_{\tilde{f}}}{100 \text{ GeV}} \right)^4 \left(\frac{1 \text{ GeV}}{m_{\tilde{\chi}}} \right)^5 \frac{1}{\lambda''^2} \quad (3)$$

if the neutralino or the chargino is the LSP with $\beta \gamma = P_{\tilde{\chi}} / m_{\tilde{\chi}}$. The typical lower limit of sensitivity for this analysis ($L \lesssim 1$ cm) is of the order of 10^{-4} (10^{-3}) in case of a $\tilde{\chi}^0$ or a $\tilde{\chi}^{\pm}$ of 30 GeV (10 GeV), with a squark mass of 100 GeV.

For the generation of all the signals a λ''_{212} coupling of the strength 0.1 was used. A different choice between 10^{-2} and 0.5 would not change the neutralino decay topologies. The choice of this specific coupling was arbitrary, since all the analyses in this Letter were coupling independent. Searches for decays through specific λ'' couplings, leading to the production of one or several b quarks, may indeed use the advantage of b-tagging techniques to reach higher sensitivities, but at the cost of lost generality. The aim of this paper was instead to perform a general coupling independent analysis for each of the search channels.

2. Data and MC samples

The analysis was performed on the data corresponding to an integrated luminosity of 158 pb^{-1} collected during 1998 by the DELPHI detector [13] at centre-of-mass energies around 189 GeV.

The contributions to the background coming from the Standard Model processes: four-fermion final states (WW, ZZ) and $Z\gamma \rightarrow q\tilde{q}(\gamma)$ were considered. The contribution from $\gamma\gamma$ events after preselection was found to be negligible, due to the high detected energy fraction and multiplicities of the studied signals. For the $Z\gamma \rightarrow q\tilde{q}(\gamma)$ backgrounds, the PYTHIA [14] generator was used whereas the four-fermion final states were generated with EXCALIBUR [15].

To evaluate signal efficiencies, sparticle production was generated using SUSYGEN [16]. All generated signal and background events were processed with the DELPHI detector simulation program (DELSIM).

3. Analyses

3.1. Topologies and analysis strategy

The present study covers the search for $\tilde{\chi}_1^0$, $\tilde{\chi}_1^1$ and $\tilde{q}$ pair production. The analysis of the different decay channels can be organized on the basis of the number of hadronic jets in the final state.

For each multijet analysis, the clustering of hadronic jets was performed by the *ckern* package [17] based on the Cambridge clustering algorithm [18]. The choice of this clustering algorithm was motivated by its good performance for configurations with a mixture of soft and hard jets, the expected case for $\overline{U}\overline{D}\overline{D}$ events. Moreover, the algorithm provides a good resolution for the jet substructure which is present in $\overline{U}\overline{D}\overline{D}$ indirect decays. For each event, *ckern* provides all possible configurations between two and ten jets. The value of the variable y_{i+1} (for i between 1 and 9), that is the transition value of the DURHAM resolution variable y_{cut} for a given i, which changes the characterization of an event from an i to an $i + 1$ jet configuration, constitutes a powerful tool to identify the topologies in multijet signals.

A neural network method was applied in order to distinguish signals from Standard Model background events. The SNNS [19] package was used for the training and validation of the neural networks. The training was done on samples of simulated background and signal. The exact configuration and input variables of each neural network depended on the search channel. Each neural network provided a discriminant variable which was used to select the final number of candidate events for each analysis.

3.2. Hadronic preselection

Preselection of pure hadronic events was performed at the starting point of the gaugino and squark analyses.

The following preselection criteria were applied for the gaugino (squark) analyses:

- the charged multiplicity had to be greater or equal to 15 (20),
- the total energy from charged particles was required to be greater than $0.30 \times \sqrt{s}$,
- the total energy was required to be greater than $0.55(0.53) \times \sqrt{s}$,
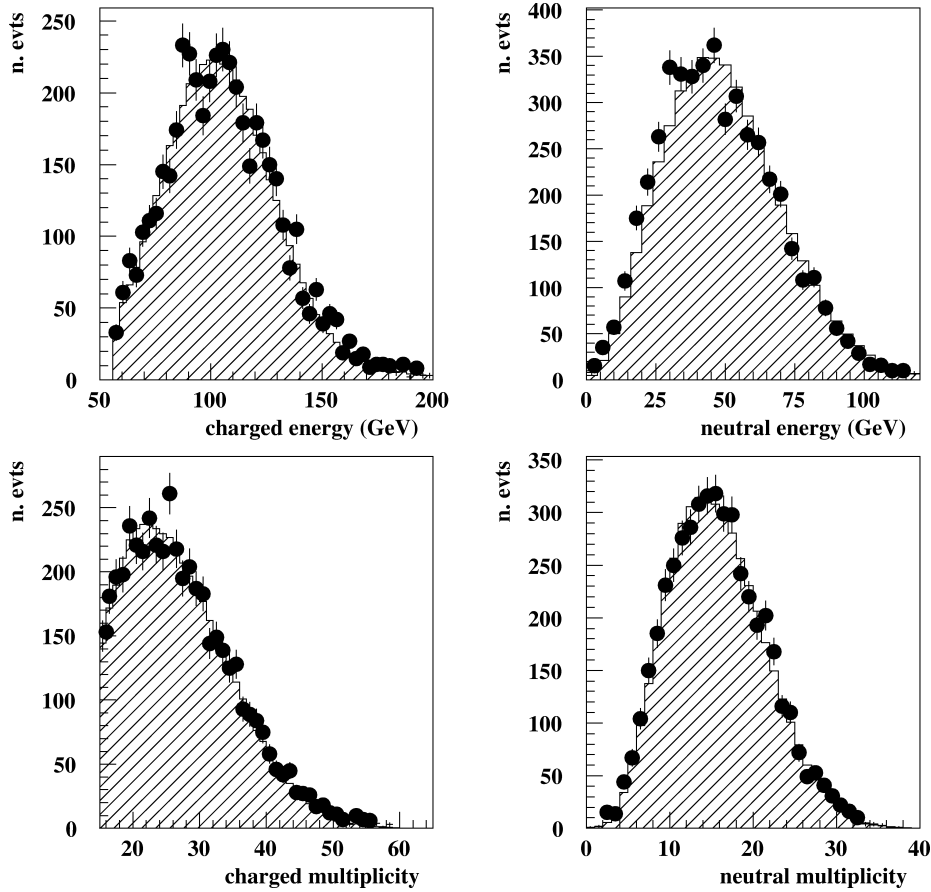
Fig. 2. Charged (upper left), neutral (upper right) energy distributions and charged (lower left) and neutral (lower right) multiplicity distributions after hadronic preselection of gaugino analyses for data (black dots), expected SM background (hatched histograms).

- the total energy from neutral particles was required to be less than $0.50(0.47) \times \sqrt{s}$.

With these preselections most of the $\gamma\gamma$ background was suppressed. Tighter requirements on charged multiplicity included in each analysis made this background negligible. Therefore in what follows the main background events will be the four-fermion events like W^+W^- and the $Z\gamma$ QCD events with hard gluon radiation. Signal efficiency at the level of hadronic preselection was between 80% and 90% for high and medium mass of pair-produced sparticles. The preselection efficiency for the lowest neutralino mass was around 70%. After the hadronic gaugino preselection the agreement between the number of observed events (4722) in data and the number of expected events (4736) from SM processes was rather

good. Fig. 2 shows the distributions of several variables after this hadronic preselection.

3.3. Charginos and neutralinos, 6- and 10-jet analyses

To be efficient for all possible neutralino and chargino masses, the 6- (10-) jet analysis was divided into 3 (2) different mass windows.

The signal selection in both channels was performed in two steps. First, we applied soft sequential criteria against mainly $Z\gamma \to q\bar{q}(\gamma)$ QCD events, except in the case of the low neutralino mass window:

- the effective centre-of-mass energy had to be greater than 150 GeV,
- the energy of the most energetic photon had to be less than 30 GeV,

- the sphericity had to be greater than 0.05, the thrust lower than 0.92 and $-\log(y_3)$ was required to be lower than 6.

Thereafter, a neural network method was used to select the signal against the $Z\gamma \to q\bar{q}(\gamma)$ QCD and the four-fermion backgrounds. For each analysis window a specific neural network was trained. Topological variables used as inputs to the network were:

- oblateness,
- $-\log(y_n)$ with $n = 4$ to 10,
- minimum di-jet mass in 4-, 5- and 6-jet configurations,
- energy of the least energetic jet $\times$ minimum di-jet angle in 4 and 5 jet configurations.

The training was performed in a standard backpropagation manner using the SNNS package [19]. The network configuration had 13 input nodes, 13 hidden nodes and 3 output nodes. The 3 output nodes correspond to the signal, the $Z\gamma \to q\bar{q}(\gamma)$ background and the four-fermion background. This choice was motivated by the fact that we were looking for different signal topologies which were either similar to $Z\gamma \to q\bar{q}(\gamma)$ or to four-fermion events depending on the analysis window.

3.3.1. Direct decay of $\tilde{\chi}_1^0 \tilde{\chi}_1^0$ or $\tilde{\chi}_1^+ \tilde{\chi}_1^-$ into 6 jets

The 6-jet analysis was divided into 3 mass windows to take into account the magnitude of the gaugino boost depending on its mass:

- window N1; low gaugino mass: $10 \leqslant m_{\tilde{\chi}} \leqslant 30$ GeV,
- window N2; medium gaugino mass: $30 < m_{\tilde{\chi}} \leqslant 70$ GeV,
- window N3; high gaugino mass: $70 < m_{\tilde{\chi}} \leqslant 94$ GeV.

The comparison between the number of expected SM background and the number of data events was performed for all neural network output values as is shown in Fig. 3 for the medium gaugino N2 mass analysis window. Signal efficiencies were calculated only from signal validation events (signal training events were not used at this level) for each neural network output value. Then the expected and obtained number of data events as a function of the signal efficiency was plotted as for example in Fig. 4 for the N2 analysis window.

Fig. 3. Neural network signal output for data (black dots), expected SM background (tight hatched) and the unweighted signals (loose hatched) corresponding to the medium gaugino mass search N2.
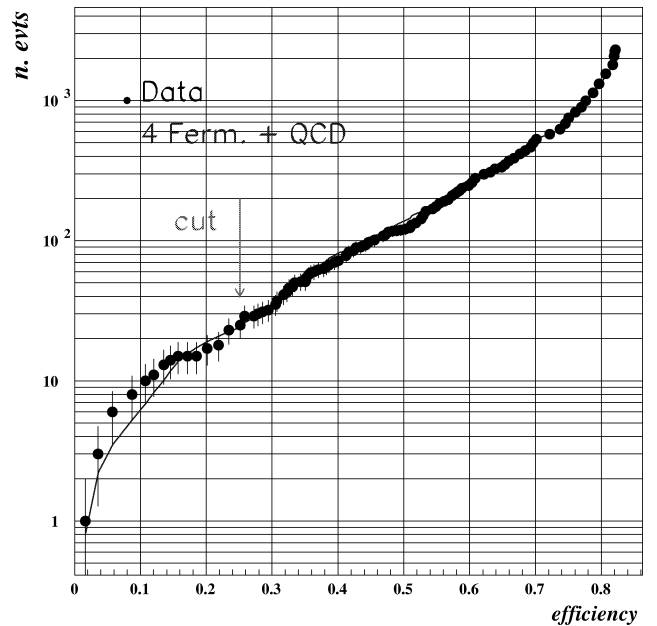
Fig. 4. Number of expected events (continuous line) data events (black dots) versus signal efficiency for a 60 GeV neutralino mass in the medium gaugino mass search N2. The arrow shows the efficiency corresponding to the working point.

No excess in the data appeared in these distributions, therefore a working point optimization on the neural network output was performed minimizing the

Table 3
The numbers of events seen and expected from backgrounds for the three mass windows of the 6-jet analysis

Window	Data	Backgrounds	$Z\gamma$ background	Four-fermion backgrounds
N1	13	11.5 ± 0.4	10	1.5
N2	25	23.8 ± 0.5	2.6	21.2
N3	9	6.3 ± 0.3	0.4	5.9

expected excluded cross-section as a function of the average signal efficiency of the mass window. The working points of the neural network output were 0.953, 0.852 and 0.966 for mass windows N1, N2 and N3, respectively. The corresponding signal efficiencies which increase with the neutralino mass were around 10–15%, 25–30% and 20–30% for the mass windows N1, N2 and N3, respectively. To obtain signal efficiencies, the full detector simulation was performed on neutralino pair production with a 10 GeV step grid in the neutralino mass (10 to 94 GeV). The statistical errors on the efficiencies was typically 2%.

No excess of data over background was observed for any working point. The numbers of events seen and expected from backgrounds are shown in Table 3.

3.3.2. Indirect decay of $\tilde{\chi}_1^+ \tilde{\chi}_1^-$ into 10 jets

The 10-jet analysis was more sensitive to the mass difference between the chargino and the neutralino than to the neutralino mass. To take into account this mass difference we divided the 10-jet analysis into 2 windows:

- window C1; low chargino neutralino mass difference: $\Delta M \leqslant 10$ GeV,
- window C2; high chargino neutralino mass difference: $\Delta M > 10$ GeV.

The same neural network method was applied to select 10-jet events coming from indirect chargino decays. Two neural networks for the two different windows were produced. The distributions from expected SM events and data events were in good agreement. The neural network output of the C2 mass analysis is given in Fig. 5 as an example. Fig. 6 shows the number of expected events and data events as a function of the signal efficiency for the C2 mass window.

The optimal working points have been found with the same procedure as for the 6-jet analysis. The neural

network output values were 0.894 and 0.956 for two mass windows (C1 and C2). The corresponding signal efficiencies were around 15–25% and 10–50% for the two mass windows. The statistical errors on the signal efficiency was 2%.

In Fig. 6 it can be seen that the background is not perfectly reproduced by the simulation in the high efficiency region dominated by $Z\gamma$ background, i.e., at the preselection level. This region of high efficiency is not considered in the final signal selection which is in the 10–50% efficiency region. The signal region is mainly dominated by four-fermion background. Therefore, an increase of the uncertainty of the $Z\gamma$ background does not drastically affect the uncertainty
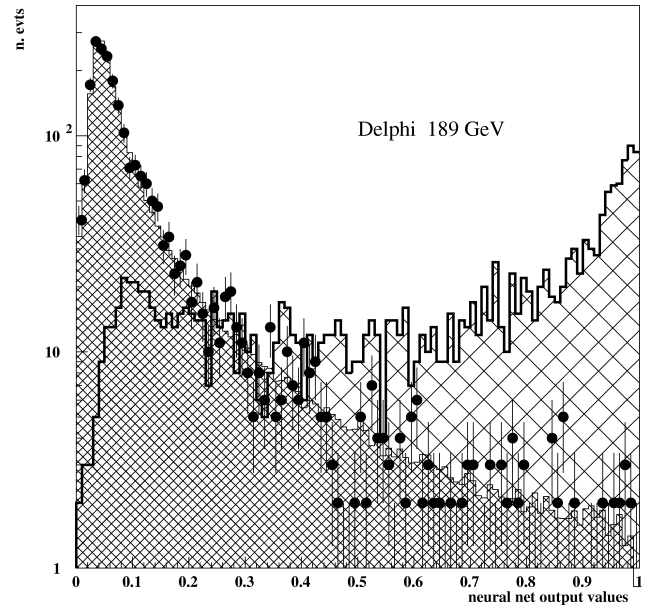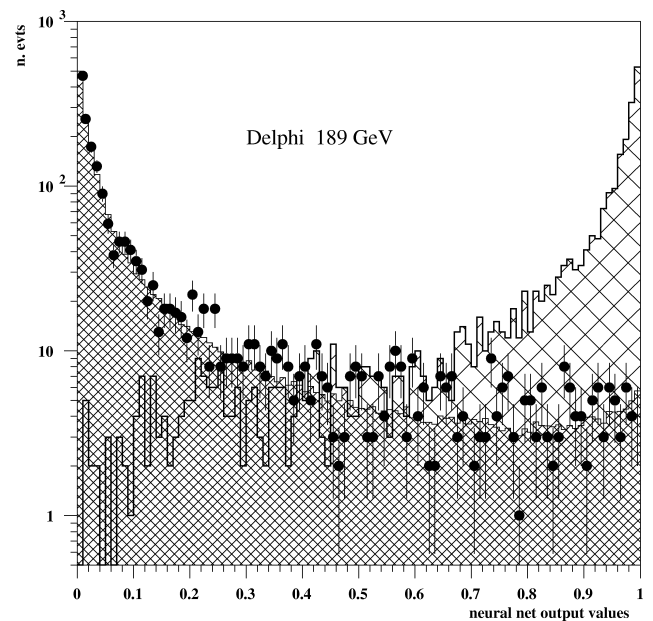

Fig. 5. Neural network signal output for data (black dots), expected SM background (tight hatched) and the unweighted signals (loose hatched) corresponding to the analysis applied in case of large ΔM between chargino and neutralino (window C2).

Table 4
The numbers of events seen and expected from backgrounds for the three mass windows of the 10-jet analysis

Window	Data	Backgrounds	$Z\gamma$ background	Four-fermion backgrounds
C1	28	25.3 ± 0.6	3.1	22.2
C2	18	21.0 ± 0.5	1.8	19.3
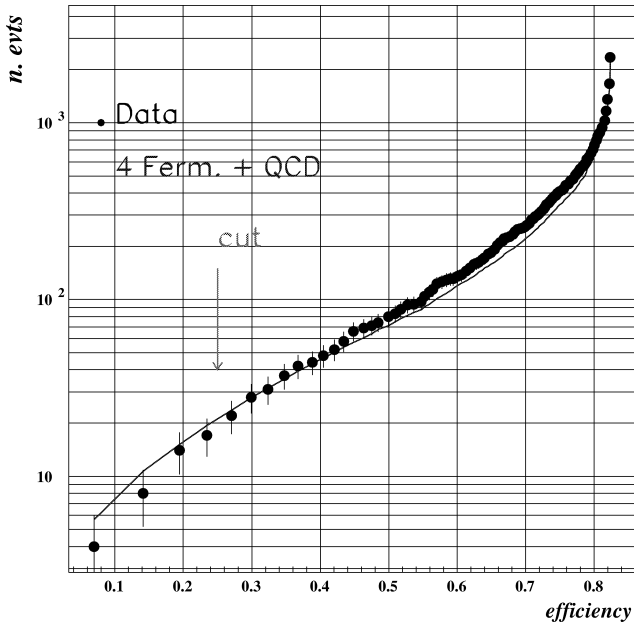
Fig. 6. Number of expected events (continuous line) data events (black dots) versus signal efficiency for a chargino mass of 80 GeV and a neutralino mass of 50 GeV in the analysis applied in case of large ΔM between chargino and neutralino (window C2). The arrow shows the efficiency corresponding to the working point.

on the expected background in the vicinity of the working point.

No excess was found in observed events compared to expected background for any working point. The numbers of events seen and expected from backgrounds are shown in Table 4.

3.4. Squark 8-jet analysis

Searches for squarks were performed in the case of indirect decays through a dominant R-parity violating $\overline{U}\,\overline{D}\,\overline{D}$ coupling. The final states in the indirect decay channel contain eight quarks of any flavour, but the topology of the signal strongly depends on the mass of the $\tilde{\chi}_1^0$, through which the decay proceeds. SUSY

signals were therefore simulated at different squark masses in the range 50–90 GeV with $\tilde{\chi}_1^0$ masses between 10–80 GeV. The simulated decay actually used for the studies and efficiency evaluation was $\tilde{b} \to b\tilde{\chi}_1^0$.

The general analysis methods based on a neural network background rejection were adopted for the analysis. The analysis was aimed at a good sensitivity for R-parity violating $\overline{U}\,\overline{D}\,\overline{D}$ signals all over the plane of kinematically available squark and $\tilde{\chi}_1^0$ masses. First a general preselection, in addition to the one presented in Section 3.2, was made with the aim of a high general efficiency for the signal and at the same time a good rejection of low multiplicity hadronic background events. The selection criteria were optimized for the 8-jet squark analysis with the following variables:

- the energy of the most energetic photon in the event had to be less than 45 GeV,
- the missing momentum of the event had to be less than 76 GeV,
- the oblateness of the event had to be less than 0.5.

A neural network was thereafter trained to calculate a discriminant variable for each event, in order to distinguish a possible signal from Standard Model background. The following quantities were used as input to the neural network:

- the total energy from neutral particles, the total event energy, the total number of charged particles, the energy of the most energetic photon in the event, the missing momentum of the event, the oblateness of the event,
- $-\log(y_n)$ with $n = 2$ to 10,
- the reconstructed mass from a 5 constraint kinematic fit (the fifth constraint is the equal mass constraint on the di-jet masses) performed on the 4 jet topology of the event and the χ^2 value of this fit,

Table 5
The numbers of events seen and expected from backgrounds for the three mass windows of the 8-jet analysis

Data	Backgrounds	$Z\gamma$ background	Four-fermion backgrounds
22	18.4 ± 0.7	3.8	14.6

- the minimum angle between two jets times the minimum jet energy from the 5 jet topology of the event.

Note that some of the input variables for the neural network were also used for the preselection, i.e., the preselection was used to eliminate the signal free regions and thereby unnecessary background from the analysis, whereas the neural network served to discriminate the signal from the background, in the remaining regions with overlapping values of the variables. The final selection of candidate events was made based on the output value of the neural network. The working point optimization on the neural network output was performed minimizing the expected excluded cross-section as a function of the average signal efficiency of the mass window. No excess of data over Standard Model backgrounds was observed. The numbers of events seen and expected from backgrounds are shown in Table 5.

The signal efficiency was evaluated at each of the 30 evenly distributed simulated points in the plane of squark and neutralino masses and interpolated in the regions between. Efficiencies for the signal after the final selection range from 10–20%, for small or large mass differences between squark and neutralino, up to 50% for medium mass differences. The statistical errors on signal efficiencies were typically 2%.

4. MSSM interpretation of the results

No excess was seen in the data with respect to the expected background in any of the channels of these analyses. Therefore, limits at 95% confidence level on the cross-section of each process were obtained. Mass limits were derived for supersymmetric particles in the MSSM frame with $\not{R}_p$. The cross-section (σ_{95}) that can be excluded experimentally at 95% confidence level, was calculated from data and SM event numbers obtained at the end of each analysis [20].

4.1. Chargino and neutralino multi-jet searches

The excluded cross-sections, which is the σ_{95} divided by the signal efficiency, are in the range [0.5, 0.7] pb, [0.2, 0.3] pb and [0.3, 0.4] pb for the N1, N2 and N3 neutralino analysis mass windows respectively and in the range [0.3, 0.6] pb and [0.1, 0.2] pb for the C1 and C2 indirect chargino decay analysis mass windows.

The signal efficiency for any value of $\tilde{\chi}_1^0$ and $\tilde{\chi}^\pm$ masses was interpolated using an efficiency grid determined with signal samples produced with the full DELPHI detector simulation. For typical values of $\tan\beta$ and m_0, a (μ, M_2) point was excluded at 95% confidence level if the signal cross-section times the efficiency at this point was greater than the cross-section (σ_{95}).

Adding the 6-jet analysis (used for the direct decay of $\tilde{\chi}_1^+ \tilde{\chi}_1^-$ or $\tilde{\chi}_1^0 \tilde{\chi}_1^0$) and the 10-jet analysis (used for indirect decay of $\tilde{\chi}_1^+ \tilde{\chi}_1^-$) results, an exclusion contour in the μ, M_2 plane at 95% confidence level was derived for different values of m_0 (90 and 300 GeV) and $\tan\beta$ (1.5 and 30). These exclusion contours in the μ, M_2 plane are shown in Fig. 7. In the exclusion plots the main contribution comes from the study of the chargino indirect decays with the 10-jet analysis, due to the high cross-section. The 6-jet analysis becomes crucial in the exclusion plot for low $\tan\beta$ value, low m_0 values and negative μ values. A 95% CL lower limits on the mass of lightest neutralino and chargino are obtained from the μ, M_2 plane for different values of $\tan\beta$ between 0.5 and 30 and for $m_0 = 500$ GeV. The result on the lightest neutralino as a function of $\tan\beta$ is shown in Fig. 8. A lower limit on neutralino mass of 32 GeV is obtained. The chargino is mainly excluded up to the kinematic limit at 94 GeV.

4.2. Indirect squark multi-jet searches

Exclusion domains were obtained by calculating σ_{95} divided by the signal efficiency for each 1 GeV × 1 GeV bin in the neutralino mass versus squark mass plane and comparing them to the cross-section for pair-produced squarks. The excluded cross-section varies between 0.2 and 0.9 pb depending on the efficiency. The resulting exclusion contours for stop and sbottom can be seen in Fig. 9. A 100% branching ratio of indirect decays in the neutralino channel was as-
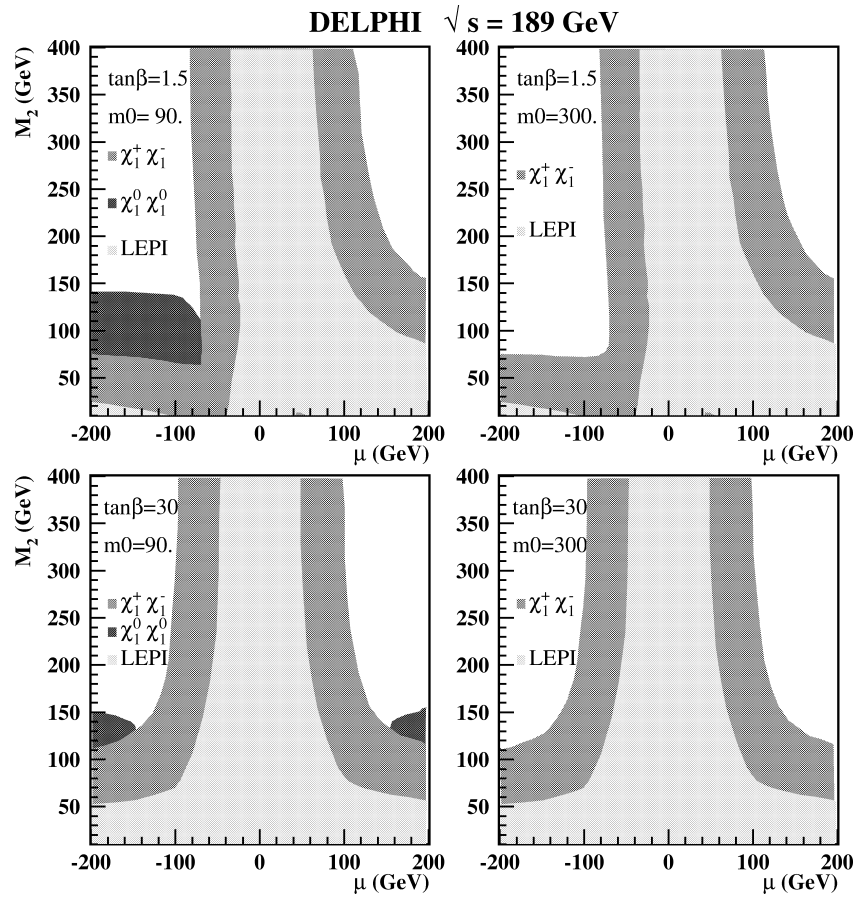
Fig. 7. Exclusion plot in μ, M_2 plane for $\tilde{\chi}_1^0 \tilde{\chi}_1^0$ and $\tilde{\chi}_1^+ \tilde{\chi}_1^-$ production in the case of a dominant $\overline{U}\,\overline{D}\,\overline{D}$ R-parity violation coupling. The 6- and 10-jets analyses are treated separately for this exclusion. The shaded areas are excluded.
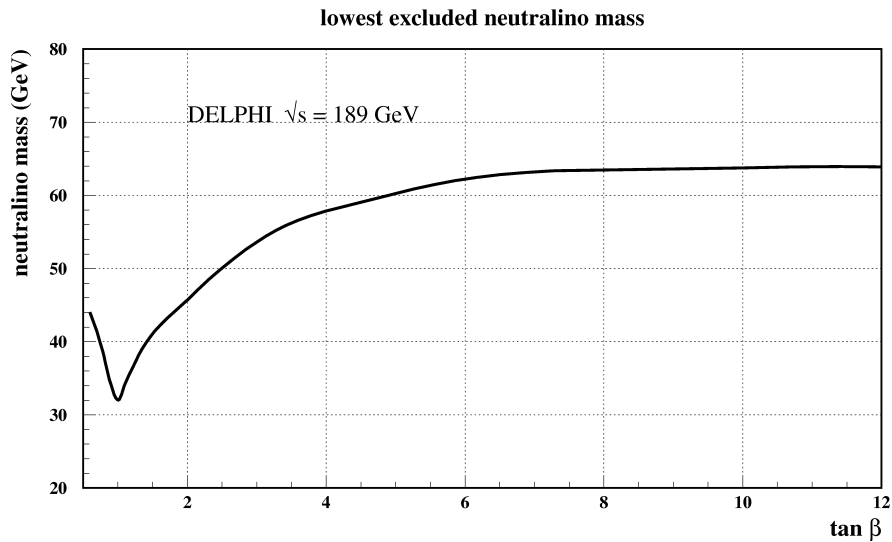
Fig. 8. The excluded lightest neutralino mass as a function of tan β at 95% confidence level.
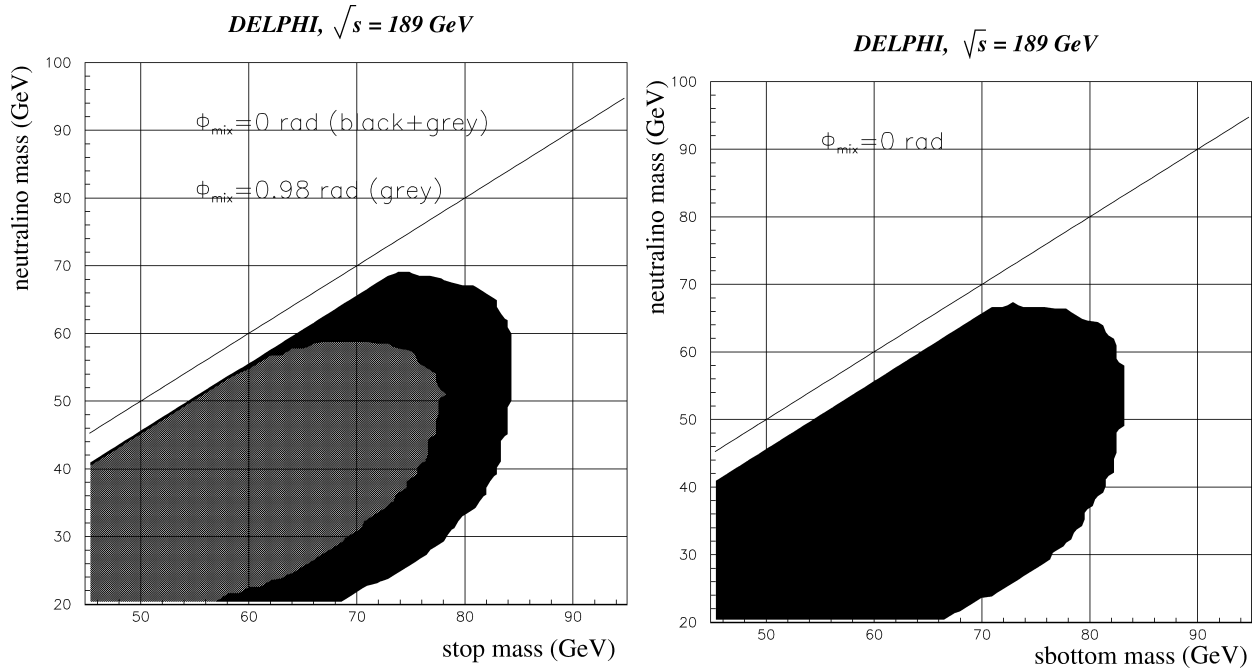
Fig. 9. Exclusion domains at 95% confidence level in the $M(\tilde{\chi}_1^0)$, $M(\tilde{q})$ plane for indirect squark decays in the case of a 100% branching ratio in the neutralino channel. The left plot shows the exclusion for a stop in the case of no mixing and with the mixing angle Φ_{mix} which gives a minimum cross-section. For sbottom the minimum cross-section is too low to extract any exclusion with the present analysis. The diagonal lines indicate the degenerate mass limit above which indirect squark decays are forbidden.

sumed for this exclusion. The mixing angle 0.98 rad corresponds to the minimal lightest stop cross-section due to a maximal decoupling from the Z boson.

By combining the exclusion contours from the squark searches with the constraint on the neutralino mass from the gaugino searches, lower bounds on the squark masses with $\Delta M > 5$ GeV are achieved. The lower mass limit on the stop is 74 GeV in the case of no mixing, and 59 GeV in the case of maximal Z-decoupling. The lower mass limit on the sbottom is 72 GeV in the case of no mixing. For sbottom the minimum cross-section is too low to extract any exclusion with the present analysis.

5. Summary

Searches for pair-produced gauginos and squarks, in the case of a single dominant R-parity violating $\overline{U}\,\overline{D}\,\overline{D}$ coupling, were performed on data collected by the DELPHI detector at a centre-of-mass energy of 189 GeV. The analysis of the hadronic multijet final-states was performed by means of a neural network method and the results were interpreted within the framework of the MSSM. No excess of data over the expected Standard Model events was found in any of the investigated search channels. The result of the analysis implies the following lower mass limits, at a 95% confidence level, on supersymmetric particles:

- neutralino mass: $m_{\tilde{\chi}_1^0} \geqslant 32$ GeV,
- chargino mass: $m_{\tilde{\chi}_1^+} \geqslant 94$ GeV,
- stop and sbottom mass (indirect decay) with $\Delta M > 5$ GeV: $m_{\tilde{t}_1} \geqslant 74$ GeV, for $\Phi_{mix} = 0$ rad, $m_{\tilde{t}_1} \geqslant 59$ GeV, for $\Phi_{mix} = 0.98$ rad, $m_{\tilde{b}_1} \geqslant 72$ GeV, for $\Phi_{mix} = 0$ rad.

These mass limits were obtained under the following assumptions:

- One $\overline{U}\,\overline{D}\,\overline{D}$ term is dominant.
- The limit on the neutralino and chargino masses were obtained for any m_0, $\tan\beta$ values and for $-200 < \mu < 200$ GeV and $0 < M_2 < 400$ GeV.
- The strength of the λ'' coupling was assumed to be greater than 10^{-3}, limited by a mean LSP

decay length smaller than 1 cm. Smaller coupling strengths lead to a region between dominant R-parity violation and R-parity conservation, which is not covered by these analyses.

- Stop and sbottom mass limits are valid for $\Delta M > 5$ GeV. They were obtained for $\mu = -200$ GeV and $\tan\beta = 1.5$. A branching ratio of 100% into quark-neutralino was assumed.

Acknowledgement

References

[1] For reviews, see, e.g., H.P. Nilles, Phys. Rep. 110 (1984) 1;
H.E. Haber, G.L. Kane, Phys. Rep. 117 (1985) 75.

[2] P. Fayet, Phys. Lett. B 69 (1977) 489;
G. Farrar, P. Fayet, Phys. Lett. B 76 (1978) 575.

[3] S. Weinberg, Phys. Rev. D 26 (1982) 287.

[4] H. Dreiner, in: G.L. Kane (Ed.), Perspectives on Supersymmetry, World Scientific, Singapore, 1997, pp. 462–479, hep-ph/9707435.

[5] ALEPH Collaboration, R. Barate et al., Eur. Phys. J. C 7 (1999) 383;
L3 Collaboration, M. Acciari et al., Phys. Lett. B 459 (1999) 354;
OPAL Collaboration, G. Abbiendi et al., Eur. Phys. J. C 11 (1999) 619.

[6] J.L. Goity, M. Sher, Phys. Lett. B 346 (1995) 69;
J.L. Goity, M. Sher, Phys. Lett. B 385 (1996) 500, Erratum.

[7] F. Zwirner, Phys. Lett. B 132 (1983) 103.

[8] G. Bhattacharyya, J. Ellis, K. Sridhar, Mod. Phys. Lett. A 10 (1995) 1583;
G. Bhattacharyya, D. Choudhury, K. Sridhar, Phys. Lett. B 355 (1995) 193;
J. Ellis, S. Lola, K. Sridhar, Phys. Lett. B 408 (1997) 252.

[9] G. Bhattacharyya, Nucl. Phys. Proc. Suppl. 52A (1997) 83.

[10] B. Brahmachari, P. Roy, Phys. Rev. D 50 (1994) 39;
B. Brahmachari, P. Roy, Phys. Rev. D 51 (1995) 3974, Erratum.

[11] S. Dawson, Nucl. Phys. B 261 (1985) 297.

[12] H. Dreiner, G.G. Ross, Nucl. Phys. B 365 (1991) 597.

[13] P. Abreu et al., Nucl. Instrum. Methods A 378 (1996) 57.

[14] T. Sjöstrand, Comput. Phys. Commun. 39 (1986) 347.

[15] F.A. Berends, R. Kleiss, R. Pittau, Comput. Phys. Commun. 85 (1995) 437.

[16] S. Katsanevas, P. Morawitz, Comput. Phys. Commun. 112 (1998) 227.

[17] S. Bentvelsen, I. Meyer, Eur. Phys. J. C 4 (1998) 623.

[18] Yu.L. Dokshitzer, G.D. Leder, S. Moretti, B.R. Webber, J. High Energy Phys. 08 (1997) 001.

[19] A. Zell et al., SNNS User manual, Version 4.1, Report N 6/95, Institute for Parallel and Distributed High-Performance Systems (IPVR), University of Stuttgart, Breitwiesenstrasse 20–22, 70565 Stuttgart, Germany.

[20] Particle Data Group, Phys. Rev. D 54 (1996) 1;
F. James, M. Roos, Phys. Rev. D 44 (1991) 299.

B.3 Physics Report sur la *R*-Parité violée

Ma contribution à ce *Physics Report* réside dans l'écriture d'une partie du chapitre 7, dans un travail de relecture de certaines parties du chapitre 6 (le chapitre le plus "lourd" et complexe) et à l'édition de tous les diagrammes de Feynman (supervisé par Pierre et Emmanuelle). Je n'inclue dans ce mémoire que l'introduction de Pierre et le chapitre 7.

R-Parity-violating supersymmetry

R. Barbier[a], C. Bérat[b], M. Besançon[c,*], M. Chemtob[d], A. Deandrea[a], E. Dudas[e,f], P. Fayet[g], S. Lavignac[d,h], G. Moreau[i], E. Perez[c], Y. Sirois[j]

[a]IPNL, Université Claude Bernard, IN2P3-CNRS, 69622 Villeurbanne, France
[b]LPSC, Université de Grenoble 1, IN2P3-CNRS, 38026 Grenoble, France
[c]DAPNIA/Service de Physique des Particules, CEA-Saclay, 91191 Gif-sur-Yvette, France
[d]Service de Physique Théorique, CEA-Saclay, 91191 Gif-sur-Yvette, France
[e]Laboratoire de Physique Théorique, Université de Paris-Sud, 91405 Orsay, France
[f]Centre de Physique Théorique, Ecole Polytechnique, 91128 Palaiseau, France
[g]Laboratoire de Physique Théorique, Ecole Normale Supérieure, 75005 Paris, France
[h]CERN Theory Division, CH-1211 Genève, Switzerland
[i]Service de Physique Théorique, Université Libre de Bruxelles, 1050 Brussels, Belgium
[j]Laboratoire Leprince-Ringuet, Ecole Polytechnique, IN2P3-CNRS, 91128 Palaiseau, France

Abstract

Theoretical and phenomenological implications of R-parity violation in supersymmetric theories are discussed in the context of particle physics and cosmology. Fundamental aspects include the relation with continuous and discrete symmetries and the various allowed patterns of R-parity breaking. Recent developments on the generation of neutrino masses and mixings within different scenarios of R-parity violation are discussed. The possible contribution of R-parity-violating Yukawa couplings in processes involving virtual supersymmetric particles and the resulting constraints are reviewed. Finally, direct production of supersymmetric particles and their decays in the presence of R-parity-violating couplings is discussed together with a survey of existing constraints from collider experiments.
© 2005 Elsevier B.V. All rights reserved.

Contents

* Corresponding author.
  E-mail address: besanco@hep.saclay.cea.fr (M. Besançon).

Introductory remarks

The possible appearance of *R*-parity-violating couplings, and hence the question of the conservation or non-conservation of baryon and lepton numbers (*B* and *L*) in supersymmetric theories, has been emphasized for a long time. The rich phenomenology implied by *R*-parity violation has gained full attention in the search for supersymmetry. We shall discuss here the theoretical as well as phenomenological aspects of $\mathcal{R}_p$ supersymmetry in particle and astroparticle physics.

In Section 1 we introduce fundamental aspects of supersymmetry, having in mind the question of the definition of conserved baryon and lepton numbers in supersymmetric theories. In supersymmetric extensions of the Standard Model *R*-parity has emerged as a discrete remnant of a group of continuous $U(1)$ *R*-symmetry transformations acting on the supersymmetry generator. *R*-parity is intimately connected with baryon and lepton numbers, its conservation naturally allowing for conserved baryon and lepton numbers in supersymmetric theories. Conversely, the violation of *R*-parity requires violations of *B* and/or *L* conservation laws. This generally leads to important phenomenological difficulties, unless *R*-parity-violating interactions are sufficiently small. How small they have to be, and how these difficulties may be turned into opportunities in some specific cases, concerning for example neutrino masses and mixings, constitute important aspects of this review.

Section 2 is devoted to the discussion of *how R-parity may be broken*. The corresponding superpotential couplings (and resulting Lagrangian terms) and soft supersymmetry-breaking terms are recalled. Various possible patterns of *R*-parity breaking are discussed, including bilinear breaking as well as spontaneous breaking. Further theoretical insights on the possible origin of such terms violating *B* and/or *L* as well as the *R*-parity symmetry are reviewed. This includes more recent developments on abelian family symmetries, grand-unified gauge symmetries, and other discrete symmetries, and what they could tell us about possible $\not{R}_p$ terms.

The high-energy convergence of the gauge couplings obtained by renormalization-group evolution of low-energy measurements gets remarkably improved once supersymmetry is introduced. More generally, the renormalization group equations governing the evolutions of the coupling and mass parameters between two energy scales provide a way to test, at lower energies, physical assumptions postulated at a much higher energy scale; or conversely to translate available experimental data into quantities at a higher energy scale. In Section 3 we consider *the effects of the renormalization group equations*, in the presence of *R*-parity-violating interactions. We focus in particular, within the supergravity framework, on the evolution of the constraints associated with perturbative unitarity, the existence of infrared fixed points and the tests of grand-unification schemes. The additional effects of the new soft supersymmetry-breaking terms associated with R_p-violations are also discussed.

Supersymmetric theories with conserved *R*-parity naturally provide a (color and electrically neutral) stable lightest supersymmetric particle (LSP), i.e. a weakly-interacting massive particle which turns out to be a very good Dark Matter candidate. In contrast, one of the most striking features of supersymmetric theories with *R*-parity-violating interactions stems from the fact that *the LSP can now decay into Standard Model particles only*. We discuss in Section 4 how such an unstable LSP might still remain (if its lifetime is sufficiently long) a possible Dark Matter candidate. We also discuss the gravitino relic issue, and the origin of the cosmological baryon asymmetry, reviewing several attempts at generating this asymmetry, as well as how it could survive in the presence of *R*-parity-violating interactions.

The most dramatic implication of *L*-violating interactions from *R*-parity violations is the automatic generation of *neutrino masses and mixings*. The possibility that the results of atmospheric and solar neutrino experiments be explained by neutrino masses and mixings originating from *R*-parity-violating interactions has motivated a large number of studies and models. *R*-parity violation in the lepton sector also leads to many new phenomena related to neutrino and sneutrino physics. These aspects of neutrino physics related to *L*-violating interactions are reviewed in Section 5.

In Section 6 we discuss the possible contribution of *R*-parity violating couplings to processes involving the *virtual effects* of supersymmetric particles. Indeed *R*-parity-violating couplings in the Supersymmetric Standard Model introduce new interactions between ordinary and supersymmetric particles which can contribute to a large variety of low, intermediate and high-energy processes, not involving the direct production of supersymmetric particles in the final state. The requirement that the *R*-parity-violating contribution to a given observable avoids conflicting with actual experimental measurements leads to upper bounds on the *R*-parity-violating couplings possibly involved. These bounds are extensively discussed, the main ones being summarized at the end, in Section 6.5. Their robustness as well as phenomenological implications are also discussed at the end of this section.

The search for $\not{R}_p$-supersymmetry processes has been a major analysis activity at high-energy colliders over the past 15 years, and is likely to be pursued at existing and future colliders. Section 7.1 is dedicated to the phenomenology and *direct searches*, at colliders, for supersymmetric particles involving *R*-parity-violating couplings. The essential ingredients of the corresponding phenomenology at colliders, including discussions on the magnitude of *R*-parity-violating couplings and the subsequent decay of supersymmetric particles, are reviewed.

We then discuss the main and generic features of the *R*-parity-violating phenomenology for *gaugino–higgsino pair production* and *sfermion pair production*, both at leptonic and hadronic colliders. Furthermore, a remarkable specificity of the phenomenology of $\not{R}_p$ at colliders comes from possibility of producing *a single supersymmetric particle*. (This is also discussed in Section 7 for leptonic, lepton–hadron and hadronic colliders.) The phenomenology of $\not{R}_p$ at colliders also covers virtual effects such as those concerning fermion pair production, contributions to flavor-changing neutral currents and to *CP* violation. These aspects are also met in Section 7.1.

Altogether, many direct experimental limits have accumulated during the last 15 years of searches for $\not{R}_p$ processes at colliders. We do not aim here at an exhaustive (and possibly tedious) catalog of all these searches with the corresponding limits. We rather choose to refer the reader interested in specific limits and details of experimental analyses to the relevant

literature and emphasize only the description of generic features of the phenomenology of *R*-parity-violating processes at colliders, illustrated by examples from the literature.

Conclusions and prospects for supersymmetry with R_p-violating couplings are given in Section 8. Finally, notations and conventions are summarized in Appendix A. The Yukawa-like $\not{R}_p$ interactions associated with the trilinear $\not{R}_p$ superpotential couplings are derived in Appendix B. Useful formulae for the production and decays of sfermions, neutralinos and charginos are given in Appendix C.

1. What is *R*-parity?

In this section, we recall how *R*-parity emerged, in supersymmetric extensions of the Standard Model, as a discrete remnant of a continuous $U(1)$ *R*-symmetry group acting on the supersymmetry generator, necessarily broken so as to allow for the gravitino and gluinos to acquire masses. *R*-parity naturally forbids unwanted squark and slepton exchanges, allowing for conserved baryon (*B*) and lepton (*L*) numbers in supersymmetric theories. It guarantees the stability of the "lightest supersymmetric particle", which is, also, a very good candidate for the non-baryonic Dark Matter of the universe. *A contrario*, *R*-parity violations are necessarily accompanied by *B* and/or *L* violations. This is, usually, a source of phenomenological difficulties, unless *R*-parity-violating ($\not{R}_p$) interactions are sufficiently small, as we shall discuss in this review article. *R*-parity violations, on the other hand, could also appear as a desired feature, since they may provide a source of Majorana masses for neutrinos. Whether *R*-parity turns out to be absolutely conserved, or not, it plays an essential rôle in the phenomenology of supersymmetric theories, and the experimental searches for the new sparticles.

1.1. What is R-parity, and how was it introduced?

Among the problems one had to solve before thinking of applying supersymmetry to the real world, was the question of the definition of conserved quantum numbers, like baryon number *B* and lepton number *L*. These are carried by Dirac fermions, the spin-$\frac{1}{2}$ quarks and leptons. But supersymmetric theories make a systematic use of *Majorana* fermions, in particular the fermionic partners of the spin-1 gauge bosons (now called gauginos). This makes it very difficult, even in general practically impossible, for them to carry additive conserved quantum numbers like *B* and *L*, in a supersymmetric theory.

Still, even Majorana fermions may be arranged into (chiral or non-chiral) Dirac fermions so as to carry non-zero values of a new additive quantum number, called *R*. In an early $SU(2) \times U(1)$ supersymmetric electroweak model with two chiral doublet Higgs superfields, now called H_d and H_u (or H_1 and H_2), the definition of a continuous *R*-symmetry acting on the supersymmetry generator allowed for an additive conserved quantum number, *R*, one unit of which is carried by the supersymmetry generator [1]. The values of *R* for bosons and fermions differ by ± 1 unit inside the multiplets of supersymmetry, the photon, for example, having $R = 0$ while its spin-$\frac{1}{2}$ partner, constrained from the continuous *R*-invariance to remain massless, carries $R = \pm 1$. Such a quantum number might tentatively have been identified as a lepton number, despite the Majorana nature of the spin-$\frac{1}{2}$ partner of the photon, if the latter could have been identified as one of the neutrinos. This, however, is not the case. The fermionic partner of the photon should be considered as a neutrino of a new type, a "photonic neutrino", called in 1977 the *photino*.

This still leaves us with the question of how to define, in such theories, Dirac spinors carrying conserved quantum numbers like *B* and *L*. Furthermore, these quantum numbers, presently known to be carried by fundamental fermions only, not by bosons, seem to appear as *intrinsically fermionic* numbers. Such a feature cannot be maintained in a supersymmetric theory (in the usual framework of the "linear realizations" of supersymmetry), and one had to accept the (then rather heretic) idea of attributing baryon and lepton numbers to fundamental bosons, as well as to fermions. These new bosons carrying *B* or *L* are the superpartners of the spin-$\frac{1}{2}$ quarks and leptons, namely the now-familiar, although still unobserved, spin-0 *squarks* and *sleptons*. Altogether, all known particles should be associated with new *superpartners* [2].

This introduction of squarks and sleptons now makes the definition of baryon and lepton numbers in supersymmetric theories a quasi-triviality — these new spin-0 particles carrying *B* and *L*, respectively, almost by definition — to the point that this old problem is now hardly remembered, since we are so used to its solution. This does not mean, however, that these newly-defined *B* and *L* should *necessarily* be conserved, since new interactions that could be present

in supersymmetric theories might spoil our familiar baryon and lepton-number conservation laws, even without taking into account the possibility of grand unification!

In fact the introduction of a large number of new bosons has a price, and carries with it the risk of potential difficulties. Could these new bosons be exchanged between ordinary particles, concurrently with the gauge bosons of electroweak and strong interactions? But known interactions are due to the exchanges of spin-1 gauge bosons, not spin-0 particles! Can we then construct supersymmetric theories of weak, electromagnetic and strong interactions, which would be free of this potential problem posed by unwanted interactions mediated by spin-0 particles? Fortunately, the answer is yes. As a matter of fact the above problem, related with the conservation or non-conservation of B and L, comes with its own natural solution, namely R-invariance or, more precisely, a discrete version of it, known as R-parity. This one is closely related, of course, with the definitions of B and L, once we have decided, and accepted, to attribute B and L to the new squarks and sleptons, as well as to the ordinary quarks and leptons.

R-parity is associated with a Z_2 subgroup of the group of continuous $U(1)$ R-symmetry transformations — often referred to as $U(1)_R$ — acting on the gauge superfields and the two chiral doublet Higgs superfields H_d and H_u responsible for electroweak symmetry breaking [1], with their definition extended to quark and lepton superfields so that quarks and leptons carry $R = 0$, and squarks and sleptons, $R = \pm 1$ [2]. As we shall see later, R-parity appears in fact as the discrete remnant of this continuous $U(1)$ R-invariance when gravitational interactions are introduced [3], in the framework of local supersymmetry (supergravity), in which the gravitino must at some point acquire a mass $m_{3/2}$ (which breaks the continuous R-invariance). In addition, either the continuous R-invariance, or simply its discrete version of R-parity, if imposed, naturally forbid the unwanted direct exchanges of the new squarks and sleptons between ordinary quarks and leptons. It is, therefore, no surprise if the re-introduction of (unnecessary) $\not{R}_p$ terms in the Lagrangian density generally introduces again, most of the time, the problems that were elegantly solved by R-parity.

The precise definition of R-invariance, which acts chirally on the anticommuting Grassmann coordinate θ appearing in the definition of superspace and superfields, will be given later (see Table 1.3 in Section 1.4). R-transformations are defined so as not to act on ordinary particles, which all have $R = 0$, their superpartners having, therefore, $R = \pm 1$. This allows one to distinguish between two separate sectors of R-even and R-odd particles. R-even particles (having R-parity $R_p = +1$) include the gluons, the photon, the $W^\pm$ and Z gauge bosons, the quarks and leptons, the Higgs bosons originating from the two Higgs doublets (required in supersymmetry to trigger the electroweak breaking and to generate quark and lepton masses) — and the graviton. R-odd particles (having R-parity $R_p = -1$) include their superpartners, i.e. the gluinos and the various neutralinos and charginos, squarks and sleptons — and the gravitino. According to this first definition, R-parity simply corresponds to the parity of the additive quantum number R associated with the above continuous $U(1)$ R-invariance, as given by the expression [4]:

$$R\text{-parity} \quad R_p = (-1)^R = \begin{cases} +1 \text{ for ordinary particles}\,, \\ -1 \text{ for their superpartners}\,. \end{cases} \tag{1.1}$$

But should we limit ourselves to the discrete R-parity symmetry, rather than considering its full continuous parent R-invariance? This *continuous* $U(1)$ R-invariance, from which R-parity has emerged, is indeed a symmetry of all four necessary basic building blocks of the Supersymmetric Standard Model [2]:

(1) the Lagrangian density for the $SU(3) \times SU(2) \times U(1)$ gauge superfields responsible for strong and electroweak interactions;

(2) the $SU(3) \times SU(2) \times U(1)$ gauge interactions of the quark and lepton superfields;

(3) the $SU(2) \times U(1)$ gauge interactions of the two chiral doublet Higgs superfields H_d and H_u responsible for the electroweak breaking;

(4) and the "super-Yukawa" interactions responsible for quark and lepton masses, through the trilinear superpotential couplings of quark and lepton superfields with the Higgs superfields H_d and H_u,

$$W = \lambda^e_{ij} \; H_d \, L_i E^c_j + \lambda^d_{ij} \; H_d \, Q_i D^c_j - \lambda^u_{ij} \; H_u \, Q_i U^c_j \,, \tag{1.2}$$

in which chiral quark and lepton superfields are all taken as left-handed and denoted by Q_i, U^c_i, D^c_i and L_i, E^c_i, respectively (with $i = 1, 2$ or 3 being the generation index).

Since all the corresponding contributions to the Lagrangian density are invariant under this continuous R-symmetry, why not simply keep it instead of abandoning it in favor of its discrete version, R-parity? But an unbroken continuous

R-invariance, which acts chirally on *gluinos*, would constrain them to remain massless, even after a spontaneous breaking of the supersymmetry. We would then expect the existence of relatively light "*R*-hadrons" [5,6] made of quarks, antiquarks and gluinos, which have not been observed. Once the continuous *R*-invariance is abandoned, and supersymmetry is spontaneously broken, radiative corrections do indeed allow for the generation of gluino masses [7], a point to which we shall return later. Furthermore, the necessity of generating a mass for the Majorana spin-$\frac{3}{2}$ *gravitino*, once *local* supersymmetry is spontaneously broken, also forces us to abandon the continuous *R*-invariance in favor of the discrete *R*-parity symmetry, thereby automatically allowing for gravitino, gluino, and other gaugino masses [3].

Once we drop the continuous *R*-invariance in favor of its discrete *R*-parity version, it is legitimate to look back and ask: how general is this notion of *R*-parity, and, correlatively, are we *forced* to have this *R*-parity conserved? As a matter of fact, there is from the beginning a close connection between *R*-parity and baryon and lepton-number conservation laws, which has its origin in our desire to get supersymmetric theories in which *B* and *L* could be conserved, and, at the same time, to avoid unwanted exchanges of spin-0 particles.

Actually the superpotential of the supersymmetric extensions of the Standard Model discussed in Ref. [2] was constrained from the beginning, for that purpose, to be an *even* function of the quark and lepton superfields. In other terms, *odd* gauge-invariant superpotential terms (W', also denoted $W_{\not R_p}$), which would have violated the "matter-parity" symmetry $(-1)^{(3B+L)}$, were then excluded from the beginning, to be able to recover *B* and *L* conservation laws, and avoid direct Yukawa exchanges of spin-0 squarks and sleptons between ordinary quarks and leptons.

Tolerating unnecessary superpotential terms which are *odd* functions of the quark and lepton superfields (i.e. $\not R_p$ terms, precisely those that we are going to discuss in this review), does indeed create, in general, immediate problems with baryon- and lepton-number conservation laws [8]. Most notably, a squark-induced proton instability with a much too fast decay rate, if both *B* and *L* violations are simultaneously allowed; or neutrino masses (and other effects) that could be too large, if *L* violations are allowed so that ordinary neutrinos can mix with neutral higgsinos and gauginos. The aim of this review is to discuss in detail how much of these $\not R_p$ contributions — parametrized by sets of coefficients λ_{ijk}, λ'_{ijk}, λ''_{ijk} (and possibly μ_i, etc.) — may be tolerated in the superpotential and in the various supersymmetry-breaking terms.

The above intimate connection between *R*-parity and *B* and *L* conservation laws can be made explicit by re-expressing the *R*-parity (1.1) in terms of the spin *S* and a matter-parity $(-1)^{3B+L}$, as follows [5]:

$$R\text{-parity} = (-1)^{2S}\,(-1)^{3B+L}\;. \tag{1.3}$$

To understand the origin of this formula we note that, for all ordinary particles, $(-1)^{2S}$ coincides with $(-1)^{3B+L}$, expressing that among Standard Model fundamental particles, *leptons and quarks*, *and only them*, *are fermions*, i.e. that *B* and *L* normally appear as intrinsically-fermionic numbers. The quantity $(-1)^{2S}\,(-1)^{3B+L}$ is always, trivially, identical to unity for all known particles (whether fundamental or composite) and for Higgs bosons as well, all of them previously defined as having *R*-parity $+1$. (Indeed expression (1.1) of *R*-parity comes from the fact that the (additive) quantum number *R* was defined so as to vanish for ordinary particles, which then have *R*-parity $+1$, their superpartners having, therefore, *R*-parity -1.) This immediately translates into the equivalent expression (1.3) of *R*-parity.

R-parity may also be rewritten as $(-1)^{2S}\,(-1)^{3\,(B-L)}$, showing that this discrete symmetry (now allowing for gravitino and gluino masses) may still be conserved even if baryon and lepton numbers are separately violated, as long as their difference $(B-L)$ remains conserved, even only modulo 2. Again, it should be emphasized that the conservation (or non-conservation) of *R*-parity is closely related with the conservation (or non-conservation) of baryon and lepton numbers, *B* and *L*. Abandoning *R*-parity by tolerating both *B* and *L* violations, simultaneously, would allow for the proton to decay, with a very short lifetime!

The *R*-parity operator plays an essential rôle in the construction of supersymmetric theories of interactions, and the discussion of the experimental signatures of the new particles. *R*-invariance, or simply its discrete version of *R*-parity, guarantees that *the new spin-0 squarks and sleptons cannot be directly exchanged* between ordinary quarks and leptons. It ensures that the new *R*-odd sparticles can only be pair-produced, and that the decay of an *R*-odd sparticle should always lead to another one (or an odd number of them). Conserved *R*-parity also ensures the stability of the "Lightest

Supersymmetric Particle" (or LSP), a neutralino for example (or conceivably a sneutrino, or gravitino),[1] which appears as an almost ideal candidate to constitute the non-baryonic Dark Matter that seems to be present in our universe.

Expression (1.3) of R-parity in terms of B and L makes very apparent that imposing R-parity is equivalent to imposing a matter-parity symmetry. Still the definition of R-parity offers the additional advantage of identifying the two separate sectors of $R_p = +1$ particles and $R_p = -1$ sparticles, making apparent the pair-production law of the new R-odd sparticles, and the stability of the LSP, if R-parity is conserved. Considering "matter-parity" alone would only imply directly the stability of the lightest "matter-odd" particle, not a very useful result!

Obviously, in the presence of R-parity violations, the LSP is no longer required to be stable, superpartners being allowed to decay into ordinary particles.

1.2. Nature does not seem to be supersymmetric!

The algebraic structure of supersymmetry involves a spin-$\frac{1}{2}$ fermionic symmetry generator Q satisfying the (anti) commutation relations in four dimensions [9–11]:

$$\{Q, \bar{Q}\} = -2\gamma_\mu P^\mu \,,$$
$$[Q, P^\mu] = 0 \,. \tag{1.4}$$

This spin-$\frac{1}{2}$ supersymmetry generator Q, here written as a 4-component Majorana spinor, was originally introduced as relating fermionic with bosonic fields, in relativistic quantum field theories. The presence of the generator of space-time translations P^μ on the right-hand side of the anticommutation relations (1.4) is at the origin of the relation of supersymmetry with general relativity and gravitation, since a locally supersymmetric theory must be invariant under local coordinate transformations [12].

The supersymmetry algebra (1.4) was introduced with quite different motivations: in connection with parity violation, with the hope of understanding parity violation in weak interactions as a consequence of a (misidentified) intrinsically parity-violating nature of the supersymmetry algebra [9]; in an attempt to explain the masslessness of the neutrino from a possible interpretation as a spin-$\frac{1}{2}$ Goldstone particle [10]; or by extending to four dimensions the supersymmetry transformations acting on the two-dimensional string worldsheet [11]. However, the mathematical existence of an algebraic structure does not mean that it could play a rôle as an invariance of the fundamental laws of Nature.[2]

Indeed many obstacles seemed, long ago, to prevent supersymmetry from possibly being a fundamental symmetry of Nature. Is spontaneous supersymmetry breaking possible at all? Where is the spin-$\frac{1}{2}$ Goldstone fermion of supersymmetry, if not a neutrino? Can we use supersymmetry to relate directly known bosons and fermions? And, if not, why? If known bosons and fermions cannot be directly related by supersymmetry, do we have to accept this as the sign that supersymmetry is *not* a symmetry of the fundamental laws of Nature? Can one define conserved baryon and lepton numbers in such theories, although they systematically involve *self-conjugate* Majorana fermions, (so far) unknown in Nature? And finally, if we have to postulate the existence of new bosons carrying B and L — the new spin-0 squarks and sleptons — can we prevent them from mediating new unwanted interactions?

While bosons and fermions should have equal masses in a supersymmetric theory, this is certainly not the case in Nature. Supersymmetry should clearly be broken. But it is a special symmetry, since the Hamiltonian, which appears on the right-hand side of the anticommutation relations (1.4), can be expressed proportionally to the sum of the squares of the components of the supersymmetry generator, as $H = \frac{1}{4} \sum_\alpha Q_\alpha^2$. This implies that a supersymmetry-preserving vacuum state must have vanishing energy, while a state which is not invariant under supersymmetry could naïvely be expected to have a larger, positive, energy. As a result, potential candidates for supersymmetry-breaking vacuum states seemed to be necessarily unstable. This led to the question

> Q1:   *Is spontaneous supersymmetry breaking possible at all?* $\tag{1.5}$

---

[1] The possibility of a *charged* or *colored* LSP may also be considered, although it seems rather strongly disfavored, as it could lead to new heavy isotopes of hydrogen and other elements, which have not been observed (cf. Section 4.1.1).

[2] Incidentally while supersymmetry is commonly referred to as "relating fermions with bosons", its algebra (1.4) does not even require the existence of fundamental bosons! With non-linear realizations of supersymmetry a fermionic field can be transformed into a *composite* bosonic field made of fermionic ones [10].

As it turned out, and despite the above argument, several ways of breaking spontaneously global or local supersymmetry have been found [13,14]. But spontaneous supersymmetry breaking remains in general rather difficult to obtain, at least in global supersymmetry (and even without addressing yet the issue of how this breaking could lead to a realistic theory), since theories tend to prefer systematically, for energy reasons, supersymmetric vacuum states. Only in very exceptional situations can the existence of such states be avoided! In local supersymmetry, which includes gravity, one also has to arrange, at the price of a very severe fine-tuning, for the energy density of the vacuum to vanish exactly, or almost exactly, to an extremely good accuracy, so as not to generate an unacceptably large value of the cosmological constant Λ.

We still have to break supersymmetry in an acceptable way, so as to get — if this is indeed possible — a physical world which looks like the one we know! Of course just accepting explicit supersymmetry-breaking terms without worrying too much about their possible origin would make things much easier (unfortunately also at the price of introducing a large number of arbitrary parameters). But such terms must have their origin in a spontaneous supersymmetry-breaking mechanism, if we want supersymmetry to play a fundamental rôle, especially if it is to be realized as a local fermionic gauge symmetry, as it should in the framework of supergravity theories.

But the spontaneous breaking of the global supersymmetry must generate a massless spin-$\frac{1}{2}$ Goldstone particle, leading to the next question,

Q2 :   *Where is the spin-$\frac{1}{2}$ Goldstone fermion of supersymmetry?*   (1.6)

Could it be one of the neutrinos [10]? A first attempt at implementing this idea within a $SU(2) \times U(1)$ electroweak model of "leptons" [1] quickly illustrated that it could not be pursued very far. The "leptons" of this model were soon to be reinterpreted as the "charginos" and "neutralinos" of the Supersymmetric Standard Model.

If the Goldstone fermion of supersymmetry is not one of the neutrinos, why hasn't it been observed? Today we tend not to think at all about the question, since: (1) the generalized use of soft terms breaking *explicitly* the supersymmetry seems to render this question irrelevant; (2) since supersymmetry has to be realized locally anyway, within the framework of supergravity [12], the massless spin-$\frac{1}{2}$ Goldstone fermion ("goldstino") should in any case be eliminated in favor of extra degrees of freedom for a massive spin-$\frac{3}{2}$ gravitino [3,14].

But where is the gravitino, and why has no one ever seen a fundamental spin-$\frac{3}{2}$ particle? To discuss this properly we need to know which bosons and fermions could be associated under supersymmetry. Still, even before addressing this crucial question we might already anticipate that the interactions of the gravitino, with amplitudes proportional to the square root of the Newton constant $\sqrt{G_N} \simeq 10^{-19}\,\text{GeV}^{-1}$, should in any case be absolutely negligible in particle physics experiments, so that we don't have to worry about the fact that no gravitino has been observed.

This simple but naïve answer is, however, not true in all circumstances! It could be that the gravitino is light, possibly even extremely light, so that it would still interact very much like the massless Goldstone fermion of global supersymmetry, according to the "equivalence theorem" of supersymmetry [3]. Its interaction amplitudes are then determined by the ratio $\sqrt{G_N}/m_{3/2}$ (i.e. are inversely proportional to the square of the "supersymmetry-breaking scale" Λ_{ss}). As a result a sufficiently light gravitino could have non-negligible interactions, which might even make it observable in particle physics experiments, provided that the supersymmetry-breaking scale parameter fixing the value of its mass $m_{3/2}$ is not too large [3,15]! Because of the conservation of R-parity, at least to a good approximation, in the Supersymmetric Standard Model, the R-odd gravitino should normally be produced in association with another R-odd superpartner, provided the available energy is sufficient. Gravitinos could also be pair-produced, although these processes are normally suppressed at lower energies. But they would remain essentially "invisible" in particle physics, as soon as the supersymmetry-breaking scale is large enough (compared to the electroweak scale), which is in fact the most plausible and widely considered situation.

In any case, much before getting to the Supersymmetric Standard Model, the crucial question to ask, if supersymmetry is to be relevant in particle physics, is

Q3 :   *Which bosons and fermions could be related by supersymmetry?*   (1.7)

But there seems to be no answer since known bosons and fermions do not appear to have much in common (excepted, maybe, for the photon and the neutrino). In addition the number of (known) degrees of freedom is significantly larger for fermions than for bosons. And these fermions and bosons have very different gauge symmetry properties! Furthermore,

as discussed in Section 1.1, the question

$$Q4 : \qquad \begin{array}{c} \textit{How could one define (conserved)} \\ \textit{baryon and lepton numbers, in a supersymmetric theory?} \end{array} \qquad (1.8)$$

once appeared as a serious difficulty, owing in particular to the presence of *self-conjugate* Majorana fermions in supersymmetric theories. Of course nowadays we are so used to dealing with spin-0 squarks and sleptons, carrying baryon and lepton numbers almost by definition, that we can hardly imagine this could once have appeared as a problem. Its solution required accepting the idea of attributing baryon or lepton numbers to a large number of new fundamental bosons. Even then, if such new spin-0 squarks and sleptons are introduced, their direct (Yukawa) exchanges between ordinary quarks and leptons, if allowed, could lead to an immediate disaster, preventing us from getting a theory of electroweak and strong interactions mediated by spin-1 gauge bosons, and not spin-0 particles, with conserved B and L quantum numbers! This may be expressed by the question

$$Q5 : \qquad \begin{array}{c} \textit{How can we avoid unwanted interactions} \\ \textit{mediated by spin- 0 squark and slepton exchanges?} \end{array} \qquad (1.9)$$

Fortunately, we can naturally avoid such unwanted interactions, thanks to R-parity, which, if present, guarantees that squarks and sleptons can *not* be directly exchanged between ordinary quarks and leptons, allowing for conserved baryon and lepton numbers in supersymmetric theories.

1.3. Continuous R-invariance, and electroweak breaking

The definition of the continuous R-invariance we are using arose from an early attempt at relating known bosons and fermions together, in particular the spin-1 photon with a spin-$\frac{1}{2}$ neutrino. If we want to try to identify the companion of the photon as being a "neutrino", although it initially appears as a self-conjugate Majorana fermion, we need to understand how it could carry a conserved quantum number that we might attempt to interpret as a "lepton" number. This led to the definition of *a continuous $U(1)$ R-invariance* [1], which also guaranteed the masslessness of this "neutrino" ("ν_L", carrying $+1$ unit of R), by acting chirally on the Grassmann coordinate θ which appears in the expression of the various gauge and chiral superfields.[3]

Attempting to relate the photon with one of the neutrinos could only be an exercise of limited validity. The would-be "neutrino", in particular, while having in this model a $V - A$ coupling to its associated "lepton" and the charged $W^\pm$ boson, was in fact what we would now call a "photino", not directly coupled to the Z! Still this first attempt, which became a part of the Supersymmetric Standard Model, illustrated how one can break spontaneously a $SU(2) \times U(1)$ electroweak gauge symmetry in a supersymmetric theory, using *a* pair *of chiral doublet Higgs superfields*, now known as H_d and H_u! Using only a single doublet Higgs superfield would have left us with *a massless charged chiral fermion*, which is, evidently, unacceptable. Our previous charged "leptons" were in fact what we now call two winos, or charginos, obtained from the mixing of charged gaugino and higgsino components, as given by the mass matrix

$$M_C = \begin{pmatrix} (M_2 = 0) & \dfrac{g v_u}{\sqrt{2}} = M_W \sqrt{2} \sin \beta \\[2mm] \dfrac{g v_d}{\sqrt{2}} = M_W \sqrt{2} \cos \beta & \mu = 0 \end{pmatrix} \qquad (1.10)$$

in the absence of a direct higgsino mass originating from a $\mu\, H_u H_d$ mass term in the superpotential.[4] The whole construction showed that one could deal elegantly with elementary spin-0 Higgs fields (not a very popular ingredient at the time), in the framework of spontaneously-broken supersymmetric theories. Quartic Higgs couplings are no

---

[3] This R-invariance itself originates from an analogous Q-invariance used, in a two-Higgs-doublet presupersymmetry model, to restrict the allowed Yukawa and φ^4 interactions, in a way which prepared for the two Higgs doublets and chiral fermion doublets to be related by supersymmetry [16]. Q-transformations were then modified into R-symmetry transformations, which survive the electroweak breaking and allow for massive Dirac fermions carrying the new quantum number R. Transformations similar to R-transformations were also considered in [17], but acted differently on two disconnected sets of chiral superfields ϕ_+ and ϕ_-, with no mutual interactions; i.e. they acted differently on the Grassmann coordinate θ, depending on whether the superfields considered belonged to the first or second set.

[4] This μ term initially written in [1] (which would have broken explicitly the continuous $U(1)$ R-invariance) was immediately replaced by a $\lambda\, H_u H_d N$ trilinear coupling involving an *extra neutral singlet chiral superfield N*: $\mu\, H_u H_d \longmapsto \lambda\, H_u H_d N$, as in the so-called Next-to-Minimal Supersymmetric Standard Model (NMSSM).

longer completely arbitrary, but fixed by the values of the electroweak gauge couplings g and g' through the following "D-terms" in the scalar potential given [5] in Ref. [1]:

$$V_{\text{Higgs}} = \frac{g^2}{8}(h_d^\dagger \, \vec{\tau} \, h_d + h_u^\dagger \, \vec{\tau} h_u)^2 + \frac{g'^2}{8}(h_d^\dagger h_d - h_u^\dagger h_u)^2 + \cdots$$
$$= \frac{g^2 + g'^2}{8}(h_d^\dagger h_d - h_u^\dagger h_u)^2 + \frac{g^2}{2}|h_d^\dagger h_u|^2 + \cdots. \tag{1.11}$$

This is precisely the quartic Higgs potential of the "minimal" version of the Supersymmetric Standard Model, the so-called Minimal Supersymmetric Standard Model (MSSM). Further contributions to this quartic Higgs potential also appear in the presence of additional superfields, such as the neutral singlet chiral superfield N already introduced in the previous model, which plays an important rôle in the NMSSM, i.e. in "next-to-minimal" or "non-minimal" versions of the Supersymmetric Standard Model. Charged Higgs bosons (called $H^\pm$) are always present in this framework, as well as several neutral ones, three of them at least. Their mass spectrum depends on the details of the supersymmetry-breaking mechanism considered: soft-breaking terms, possibly "derived from supergravity", presence or absence of extra $U(1)$ gauge fields and/or additional chiral superfields, rôle of radiative corrections, etc.

1.4. R-Invariance and R-parity in the Supersymmetric Standard Model

These two Higgs doublets H_d and H_u are precisely those used to generate the masses of charged leptons and down quarks, and of up quarks, in supersymmetric extensions of the Standard Model [2]. Note that at the time having to introduce Higgs fields was generally considered as rather unpleasant. While one Higgs doublet was taken as probably unavoidable to get to the Standard Model or at least simulate the effects of the spontaneous breaking of the electroweak symmetry, having to consider two doublets, necessitating charged Higgs bosons as well as several neutral ones, in addition to the "doubling of the number of particles", was usually considered as further indication of the irrelevance of supersymmetry. As a matter of fact, considerable work was devoted for a while on attempts to avoid fundamental spin-0 Higgs fields (and extra sparticles), before returning to fundamental Higgs bosons, precisely in this framework of supersymmetry.

In the previous $SU(2) \times U(1)$ model [1], it was impossible to view seriously for very long "gaugino" and "higgsino" fields as possible building blocks for our familiar lepton fields. This led to consider that all quarks, and leptons, ought to be associated with new bosonic partners, the *spin-0 squarks and sleptons*. Gauginos and higgsinos, mixed together by the spontaneous breaking of the electroweak symmetry, correspond to a new class of fermions, now known as "charginos" and "neutralinos". In particular, the partner of the photon under supersymmetry, which cannot be identified with any of the known neutrinos, should be viewed as a new "photonic neutrino", the *photino*; the fermionic partner of the gluon octet is an octet of self-conjugate Majorana fermions called *gluinos* (although at the time *colored fermions* belonging to *octet* representations of the color $SU(3)$ gauge group were generally believed not to exist), etc.

The two doublet Higgs superfields[6] H_d and H_u generate quark and lepton masses [2], in the usual way, through the familiar trilinear superpotential of Eq. (1.2). The vacuum expectation values of the two corresponding spin-0 Higgs doublets h_d and h_u generate charged-lepton and down-quark masses, and up-quark masses, with mass matrices given by $m_{ij}^e = \lambda_{ij}^e \, v_d/\sqrt{2}$, $m_{ij}^d = \lambda_{ij}^d \, v_d/\sqrt{2}$ and $m_{ij}^u = \lambda_{ij}^u \, v_u/\sqrt{2}$, respectively. This constitutes the basic structure of the *Supersymmetric Standard Model*, which involves, at least, the basic ingredients shown in Table 1.1. Other ingredients, such as a $\mu \, H_u H_d$ direct Higgs superfield mass term in the superpotential, or an extra singlet chiral superfield N with a trilinear superpotential coupling $\lambda \, H_u H_d N + \cdots$ possibly acting as a replacement for a direct $\mu \, H_u H_d$ mass term

---

[5] With a different denomination for the two Higgs doublets, such that $\varphi'' \mapsto$ Higgs doublet h_d, $(\varphi')^c \mapsto$ Higgs doublet h_u, $\tan \delta = v'/v'' \mapsto \tan \beta = v_u/v_d$.

[6] The correspondence between earlier notations and modern ones is as follows:

$$S = \begin{pmatrix} S^0 \\ S^- \end{pmatrix} \text{ and } T = \begin{pmatrix} T^0 \\ T^- \end{pmatrix} \mapsto H_d = \begin{pmatrix} H_d^0 \\ H_d^- \end{pmatrix} \text{ and } H_u = \begin{pmatrix} H_u^+ \\ H_u^0 \end{pmatrix}.$$

(left-handed)   (right-handed)   (both left-handed)

Table 1.1
The basic ingredients of the Supersymmetric Standard Model

(1) the three $SU(3) \times SU(2) \times U(1)$ gauge superfields;
(2) chiral superfields for the three quark and lepton families;
(3) the two doublet Higgs superfields H_d and H_u responsible for the spontaneous electroweak breaking, and
    the generation of quark and lepton masses;
(4) the trilinear superpotential of Eq. (1.2).

Table 1.2
Minimal particle content of the Supersymmetric Standard Model

Spin 1	Spin 1/2	Spin 0	
Gluons g	Gluinos $\tilde{g}$		
Photon γ	Photino $\tilde{\gamma}$		
$W^\pm$	Winos $\tilde{W}^\pm_{1,2}$	$H^\pm$	Higgs
Z	Zinos $\tilde{Z}_{1,2}$	H	bosons
	Higgsino $\tilde{h}^0$	h, A	
	Leptons l	Sleptons $\tilde{l}$	
	Quarks q	Squarks $\tilde{q}$	

Table 1.3
Action of a continuous $U(1)$ R-symmetry transformation on the gauge and chiral superfields of the Supersymmetric Standard Model

$V(x, \theta, \bar{\theta}) \to V(x, \theta e^{-i\alpha}, \bar{\theta} e^{i\alpha})$	for the $SU(3) \times SU(2) \times U(1)$ gauge superfields
$H_{d,u}(x, \theta) \to H_{d,u}(x, \theta e^{-i\alpha})$	for the left-handed doublet Higgs superfields H_d and H_u
$S(x, \theta) \to e^{i\alpha} S(x, \theta e^{-i\alpha})$	for the left-handed (anti)quark and (anti)lepton superfields $Q_i, U^c_i, D^c_i, L_i, E^c_i$

[1], and/or extra $U(1)$ factors in the gauge group, may or may not be present, depending on the particular version of the Supersymmetric Standard Model considered.

In any case, independently of the details of the supersymmetry-breaking mechanism ultimately considered and of the absence or presence of $\displaystyle{\not}R_p$ interactions, we obtain the following minimal particle content of the Supersymmetric Standard Model, as summarized in Table 1.2. Each spin-$\frac{1}{2}$ quark q or charged lepton l^- is associated with *two* spin-0 partners collectively denoted by $\tilde{q}$ or $\tilde{l}^-$, while a left-handed neutrino v_L is associated with a *single* spin-0 sneutrino $\tilde{v}_L$. We have ignored for simplicity, in this table, further mixing between the various "neutralinos" described by neutral gaugino and higgsino fields, schematically denoted by $\tilde{\gamma}$, $\tilde{Z}_{1,2}$, and $\tilde{h}^0$. More precisely, all such models include four neutral Majorana fermions at least, mixings of the fermionic partners of the two neutral $SU(2) \times U(1)$ gauge bosons (usually denoted by $\tilde{Z}$ and $\tilde{\gamma}$, or $\tilde{W}_3$ and $\tilde{B}$) and of the two neutral higgsino components ($\tilde{h}^0_d$ and $\tilde{h}^0_u$). Non-minimal models also involve additional gauginos and/or higgsinos.

Let us return to the definition of the continuous $U(1)$ R-symmetry, and discrete R-parity, transformations. As explained earlier, the new *additive* quantum number R associated with this continuous $U(1)$ R-symmetry is carried by the supersymmetry generator, and distinguishes between bosons and fermions within the multiplets of supersymmetry [1]. Gauge bosons and Higgs bosons have $R = 0$ while their partners under supersymmetry, now interpreted as gauginos and higgsinos, have $R = \pm 1$. This definition is extended to the chiral quark and lepton superfields, spin-$\frac{1}{2}$ quarks and leptons having $R = 0$, and their spin-0 superpartners, $R = +1$ (for $\tilde{q}_L, \tilde{l}_L$) or $R = -1$ (for $\tilde{q}_R, \tilde{l}_R$) [2]. The action of these R-symmetry transformations, which survive the spontaneous breaking of the electroweak symmetry (see also footnote 3 in Section 1.3), is given in Table 1.3 .

This continuous $U(1)$ R-symmetry ($U(1)_R$) is indeed a symmetry of the four basic building blocks of the Supersymmetric Standard Model (cf. Table 1.1). This includes the self-interactions of the $SU(3) \times SU(2) \times U(1)$ gauge superfields, and their interactions with the chiral quark and lepton superfields, and the two doublet Higgs superfields

Table 1.4
R-parities in the Supersymmetric Standard Model

Bosons	Fermions
Gauge and Higgs bosons, graviton ($R = 0$) *R*-parity +	Gauginos and higgsinos, gravitino ($R = \pm 1$) *R*-parity −
Sleptons and squarks ($R = \pm 1$) *R*-parity −	Leptons and quarks ($R = 0$) *R*-parity +

H_d and H_u. Also invariant under the continuous $U(1)$ *R*-symmetry are the super-Yukawa interactions of H_d and H_u, responsible for the generation of quark and lepton masses through the superpotential (1.2). Indeed it follows from Table 1.3 that this trilinear superpotential W transforms under the continuous *R*-symmetry with "*R*-weight" $n_W = \sum_i n_i = 2$, i.e. according to

$$W(x, \theta) \to \mathrm{e}^{2\mathrm{i}\alpha} \, W(x, \theta \mathrm{e}^{-\mathrm{i}\alpha}) \, . \tag{1.12}$$

Its auxiliary "*F*-component", obtained from the coefficient of the bilinear $\theta\theta$ term in the expansion of this superpotential W, is therefore *R*-invariant, generating *R*-invariant interaction terms in the Lagrangian density. Note, however, that a direct Higgs superfield mass term $\mu \, H_u H_d$ in the superpotential, which has *R*-weight $n = 0$, does *not* lead to interactions invariant under the continuous *R*-symmetry (see also footnote 4 in Section 1.3 and [1] for a replacement of the μ term by a trilinear coupling with an extra singlet chiral superfield, as in the NMSSM). But it gets in general re-allowed as soon as the continuous *R*-symmetry gets reduced to its discrete version of *R*-parity.

This *R*-invariance led us to distinguish between a sector of *R-even particles*, which includes all those of the Standard Model, with $R = 0$ (and therefore $R_p = (-1)^R = +1$); and their *R-odd superpartners*, gauginos and higgsinos, sleptons and squarks, with $R = \pm 1$ (and $R_p = -1$), as indicated in Table 1.4.

More precisely the necessity of generating masses for the (Majorana) spin-$\frac{3}{2}$ gravitino [3] and the spin-$\frac{1}{2}$ gluinos did not allow us to keep a distinction between $R = +1$ and $R = -1$ particles, forcing us to abandon the continuous *R*-invariance in favor of its discrete version, *R*-parity. The — even or odd — parity character of the (additive) *R* quantum number corresponds to the well-known *R-parity*, first defined as $+1$ for the ordinary particles and -1 for their superpartners, simply written as $(-1)^R$ in (1.1) [4], then re-expressed as $(-1)^{2S}(-1)^{3B+L}$ in (1.3) as an effect of the close connection between *R*-parity and baryon and lepton-number conservation laws.

This *R*-parity symmetry operator may also be viewed as a non-trivial geometrical discrete symmetry associated with a reflection of the anticommuting fermionic Grassmann coordinate, $\theta \to -\theta$, in superspace [18]. This *R*-parity operator plays an essential rôle in the construction of supersymmetric theories of interactions, and in the discussion of the experimental signatures of the new particles. A conserved *R*-parity guarantees that *the new spin-0 squarks and sleptons cannot be directly exchanged* between ordinary quarks and leptons, as well as the absolute stability of the LSP. But let us discuss more precisely the reasons which led to discarding the continuous *R*-invariance in favor of its discrete version, *R*-parity.

1.5. Gravitino and gluino masses: from R-invariance to R-parity

There are two strong reasons, at least, to abandon the continuous *R*-invariance in favor of its discrete Z_2 subgroup generated by the *R*-parity transformation. One is theoretical, the necessity — once gravitation is introduced — of generating a mass for the (Majorana) spin-$\frac{3}{2}$ *gravitino* in the framework of spontaneously-broken locally supersymmetric theories [3]. The other is phenomenological, the non-observation of massless (or even light) *gluinos*. Both particles would have to stay massless in the absence of a breaking of the continuous $U(1)$ *R*-invariance, thereby preventing, in the case of the gravitino, supersymmetry from being spontaneously broken. (A third reason could now be the non-observation at LEP of a charged *wino* — also called *chargino* — lighter than the $W^\pm$, that would exist in the case of a continuous $U(1)$ *R*-invariance [1,2], as shown by the mass matrix M_C given in Eq. (1.10).)

constants by the order of magnitude relation, $\hat{\lambda}^2/\tilde{m}^2 \approx 4\pi/\Lambda^2$. More quantitatively, an identification with the neutral current interactions, for instance, yields [427],

$$C_1(q) = \frac{\sqrt{2}\pi}{G_F} \left(\frac{\eta_{RL}^q}{\Lambda_{RL}^{q2}} - \frac{\eta_{LL}^q}{\Lambda_{LL}^{q2}} - \frac{\eta_{LR}^q}{\Lambda_{LR}^{q2}} + \frac{\eta_{RR}^q}{\Lambda_{RR}^{q2}} \right) \ .$$

An important observation here is that the high energy collider experimental data favor low values of the energy scales. Some currently quoted experimental bounds are, $\Lambda_{[LR,RL]}^{[-,+]d} > [1.4, 1.6]$ TeV, from the dijet production data [428], $\Lambda_{[LR,RL]}^{[+,+]u} > [2.5, 2.5]$ TeV from the Drell–Yan production data [429] and $\Lambda \approx 1$ TeV from the anomalous deep inelastic scattering events data [277,430,431]. In contrast to these results, it appears that the low energy experimental data consistently favors larger values of the energy scales. This is most explicit in the Cesium atom APV data, where assuming that no cancellations occur between the different terms in $C_1(q)$, leads to the strong bound, $\Lambda > 10$ TeV. More quantitatively, the simultaneous fits of the flavor diagonal $eeqq$ contact interactions to both low and high energy experimental data, as completed by incorporation of the HERA high Q^2 data [286], infer large values of the scale parameters with a non-trivial trend of relative signs between the different interactions. Quoting from [286] one finds the fitted values:

$$\Lambda_{LL}^{-eu} = 12.4 \begin{pmatrix} +50.6 \\ -34.8 \end{pmatrix} \text{ TeV}, \ \ \Lambda_{LR}^{+eu} = 3.82 \begin{pmatrix} +0.93 \\ -1.62 \end{pmatrix} \text{ TeV}, \ \ \Lambda_{RL}^{+eu} = 5.75 \begin{pmatrix} +5.06 \\ -6.88 \end{pmatrix} \text{ TeV} \ .$$

These quantitative analyzes indicate that cancellation effects are taking place at low energies between the contributions from different interactions. Such cancellations would clearly pass unnoticed within analyzes based on a single coupling constant dominance hypothesis. Tentative explanations have been sought in terms of a short distance parity conserving interaction [427], implying the relations $\frac{\eta_{iL}^q}{(\Lambda_{iL}^q)^2} = -\frac{\eta_{iR}^q}{(\Lambda_{iR}^q)^2}$, or an extended global flavor symmetry group [432]. Applied to the $\not{R}_p$ interactions, the implications would be in the existence of degeneracies amongst the subset of relevant $\not{R}_p$ coupling constants.

The Lorentz vector component of the charged current (CC) electron–quark four fermions contact interactions appears also to lead to similar conclusions. The fits to the leptonic or hadronic colliders data based on the conventional parametrization of the effective Lagrangian,

$$\mathcal{L}_{CC} = \frac{4\pi\eta}{\Lambda_{CC}^2} \bar{e}_L \gamma_\mu \nu_L \bar{u}_L \gamma_\mu d'_L$$

yield the typical bounds, $\Lambda_{CC}^- > 1.5$ TeV. The recent deep inelastic scattering events observed at HERA also favor low scales, $\Lambda_{CC} = (0.8–1)$ TeV [277,431]. By contrast, the fits to the low energy experimental data associated with the leptons universality or for meson decays favor larger scales [431], $\Lambda_{CC} \approx (10.–30.)$ TeV. A recent study of the non $V - A$ charged current interactions, based on the high precision measurements of the muon decay rate differential distributions, also predicts strong bounds for the scales [433], $\Lambda_{CC}^{\pm ll} > [7.5, 10.2]$ TeV, for the four lepton interactions and $\Lambda_{CC}^{\pm lq} > [5.8, 10.1]$ TeV for the two lepton two quark interactions.

7. Phenomenology and searches at colliders

7.1. Introduction

The search for $\not{R}_p$ supersymmetry processes has been a major analysis activity at high energy colliders over the past decade, and is likely to remain so at existing and future colliders unless the idea of supersymmetry itself somehow becomes falsified.

We have seen in Sections 1 and 2 that on the theory side, $\not{R}_p$ is (and will) remain a central issue since gauge invariance and renormalizability do not ensure lepton- and baryon-number conservation in supersymmetric extensions of the Standard Model. A consequence is that a general superpotential allows for trilinear terms corresponding to $\not{R}_p$ fermion–fermion–sfermion interactions involving λ, λ' or λ'' Yukawa couplings. It moreover possibly allows for additional *explicit* (bilinear) or *spontaneous* sources of lepton-number violation.

Table 7.1
Main contemporary and future collider facilities which are considered in the search analyzes and prospective studies described in this section

Collider	Beams	$\sqrt{s}$	$\int L\,dt$	Years
LEP 1	e^+e^-	M_Z	$\sim 160\,\text{pb}^{-1} \otimes 4$	1989–95
LEP 2	e^+e^-	$> 2 \times M_W$	$\sim 620\,\text{pb}^{-1} \otimes 4$	1996–00
HERA Ia	$e^- p$	300 GeV	$\mathcal{O}(1\,\text{pb}^{-1}) \otimes 2$	1992–93
HERA Ib	$e^\pm p$	$\lesssim 320$ GeV	$\mathcal{O}(100\,\text{pb}^{-1}) \otimes 2$	1994–00
Tevatron Run Ia	$p\bar{p}$	1.8 TeV	$\mathcal{O}(10\,\text{pb}^{-1})$	1987–89
Tevatron Run Ib	$p\bar{p}$	1.8 TeV	$\mathcal{O}(100\,\text{pb}^{-1}) \otimes 2$	1992–96
HERA II	$e^\pm_{L,R} p$	~ 320 GeV	$\sim 1\,\text{fb}^{-1} \otimes 2$	$\geqslant 2002$
Tevatron Run II	$p\bar{p}$	~ 2.0 TeV	1–$10\,\text{fb}^{-1} \otimes 2$	$\geqslant 2002$
LHC	pp	14.0 TeV	10–$100\,\text{fb}^{-1} \otimes 2$	$\gtrsim 2007$
Future LC	e^+e^-	~ 0.5–1.0 TeV	$50\,\text{fb}^{-1}$	. . . NLC [434]
		~ 0.5–1.0 TeV	$500\,\text{fb}^{-1}$	. . . TESLA [435]
Future μC	$\mu^+\mu^-$	~ 0.35–0.5 TeV	$10\,\text{fb}^{-1}$	. . . FMC [436]
		~ 1.0–3.0 TeV	$1000\,\text{fb}^{-1}$	. . . NMC [436]

The facilities are listed together with the nature of the colliding beams, the available center-of-mass energies $\sqrt{s}$, and the integrated luminosities $\mathcal{L} = \int L\,dt$ accumulated (or the range of $\mathcal{L}$ expected) per experiment. The multiplicative factors after the $\otimes$ sign denotes the number of multi-purpose collider experiments operating (or expected to be operating) simultaneously around each collider.

The presence of $\not{R}_p$ interactions could have important consequences on the phenomenology relevant for supersymmetry searches at high energy colliders. This is because $\not{R}_p$ entails a fundamental instability of supersymmetric matter, thus opening up new decay channels for sparticles. Especially crucial in this respect will be the fate of the lightest supersymmetric particle (LSP). Even for relatively weak $\not{R}_p$ interaction strengths, the decay of the LSP will lead to event topologies departing considerably from the characteristic "missing momentum" signal of R_p conserving theories. But $\not{R}_p$ could be more than a mere observational complication. It could also enlarge the discovery reach for supersymmetry itself as it allows for the creation or exchange of single sparticles.

In this section, essential ingredients of the phenomenology and search strategies for $\not{R}_p$ physics at colliders are presented. Extensive references to related detailed studies for specific supersymmetry models are provided. Existing experimental constraints established at LEP e^+e^-, HERA ep and Tevatron $p\bar{p}$ colliders are reviewed and discovery prospects in future collider experiments are discussed. The analyzes and prospective studies in the literature have generally been carried in the context of a given existing of future collider project. The Table 7.1 gives a list of the machine parameters considered in the studies reviewed in this section.

7.2. Interaction strength and search strategies

The way supersymmetry could become manifest at colliders crucially depends both on the structure and parameters of the model followed by Nature and on the a priori unknown magnitudes (individual and relative) of the new $\not{R}_p$ couplings. The weakest $\not{R}_p$ coupling values are likely to be felt mostly through the decay of sparticles otherwise pair produced via gauge couplings. The strongest $\not{R}_p$ coupling values could contribute to direct or indirect single sparticle production. The best search strategy at a given collider will ultimately depend on the specific signal and background environment.

In the absence of definite theoretical predictions for the values of the 45 independent trilinear Yukawa couplings Λ (λ_{ijk}, λ'_{ijk} and λ''_{ijk}), and facing the formidable task of testing $2^{45} - 1$ possible non-vanishing coupling combinations, it is necessary in practice to assume a strong hierarchy among the couplings. For the "hierarchy" between different types of couplings this is an arbitrary choice since λ, λ' and λ'' appear fundamentally independent. Empirically, it can be partially justified by the fact that indirect bounds are particularly stringent on non-vanishing coupling products

involving a $\not{L}$ and a $\not{B}$ coupling as was seen in Section 6.4.4. For example, the lower limit on the proton lifetime translates [406] into very stringent bounds on the $\lambda' \times \lambda'' < \mathrm{O}(10^{-9})$ applicable to all possible flavor combinations. Restrictions on combinations of couplings of a given type can be legitimized by analogy with the strong hierarchy of the Higgs Yukawa couplings structure in the Standard Model [255,261]. It may also be empirically justified by the fact that indirect bounds (Section 6) are generally more stringent on the product of two different couplings than on the square of individual λ, λ' or λ'' couplings.

Thus, a reasonable simplifying assumption for the search strategy at colliders is to postulate the existence of a single (dominant) $\not{R}_p$ coupling. Most of the prospective studies on $\not{R}_p$ and actual search analyzes at colliders rely on this assumption, i.e. that only one $\not{R}_p$ coupling exists which can connect sleptons or squarks to ordinary fermions. By doing so, it is in addition assumed implicitly or explicitly (through some mixing angles [255] connecting the squark current and mass basis) that flavor mixing relating various couplings (see Section 2.1.4) is suppressed.

Having chosen (somehow) a single dominant coupling Λ, the next question is that of the range of coupling values relevant for collider physics. As to what concerns lower bounds, cosmology considerations do not provide much help. As discussed in Section 4.1.1, a lightest supersymmetric particle (LSP) can no more be considered as a cold dark matter candidate in presence of a single non-vanishing $\not{R}_p$ Yukawa coupling with values even as small as $\mathcal{O}(10^{-20})$. Strengthened lower bounds of $[\lambda, \lambda', \lambda''] > \mathcal{O}(10^{-12})$ are obtained from the argument (Section 4.1.1) that an unstable LSP ought to decay fast enough in order not to disrupt nucleosynthesis. But even these still lie many orders of magnitude below the sensitivity reach of collider experiments. For Λ coupling values below $\mathcal{O}(10^{-8}$–$10^{-6})$ (depending in detail on model parameters), the lifetime of the LSP is so large that it is likely to completely escape detection in a typical $\mathcal{O}(10)$m diameter collider experiment. An immediate consequence is that for a wide range of coupling values, the phenomenology at colliders would appear indistinguishable from that of R_p conserving theories. Only a discovery that the LSP turns out to be colored or charged, a fact forbidden by cosmological constraints for a stable LSP, could be an indirect hint of the existence of $\not{R}_p$ interactions beyond the collider realm. Otherwise, there exist no known direct observational tests for such *very long-lived* LSPs [259]. This inaccessible coupling range will not be discussed further in this section.

In case a non-vanishing $\not{R}_p$ coupling does exist with a magnitude leading to distinct phenomenology at colliders, the optimal search strategy will then depend on the absolute coupling value and the relative strength of the $\not{R}_p$ and gauge interactions, as well of course on the nature of the supersymmetric model considered (sparticle spectrum and parameter space depending on the supersymmetry breaking mechanism, etc.). Sparticle direct and indirect $\not{R}_p$ decay topologies will be discussed on general grounds in Section 7.3. Anticipating this discussion, a direct sensitivity to a *long-lived* LSP might be provided by the observation of displaced vertices in an intermediate range of coupling values up to $\mathcal{O}(10^{-5}$–$10^{-4})$.

For even larger Λ values, the presence of $\not{R}_p$ supersymmetry could become trivially manifest through the decay of *short-lived* sparticles pair produced via gauge couplings. A possible search strategy in such cases consists of neglecting $\not{R}_p$ contributions at production (in non-resonant processes). This is valid provided that the $\not{R}_p$ interaction strength remains sufficiently small compared to electromagnetic or weak interaction strengths, i.e. for Λ values typically below $\mathcal{O}(10^{-2}$–$10^{-1})$. Such a strategy has been thoroughly explored at existing colliders to study how the experimental constraints on basic model parameters in specific supersymmetry models be affected by the presence of $\not{R}_p$ interactions. This and the question of whether and how different types of couplings could be distinguished at colliders in such a scenario will be discussed in Section 7.4.

In a similar range of (or for larger) coupling values, $\not{R}_p$ could manifest itself most strikingly at colliders via single resonant or non-resonant production of supersymmetric particles. Single sparticle production involving $\not{R}_p$ couplings and how it allows the extension of the discovery mass reach for supersymmetric matter at a given collider is discussed in Section 7.5.

Coupling values corresponding to interactions stronger than the electromagnetic interaction might still be allowed for sufficiently large masses. For masses beyond the kinematic reach of a given collider, $\not{R}_p$ could contribute to observable processes through virtual sparticle exchange. This is discussed in Section 7.6.

Realistic search strategies at colliders must take into account the upper bounds on the Λ couplings derived from indirect processes. As was seen in Section 6, these bounds all become weaker with increasing scalar masses but each possibly with a specific functional mass-dependence and each depending on a specific type of scalar [259].

Ultimately, the question of whether or not a given $\not{R}_p$ process is truly allowed by existing constraints must be answered at each point of the parameter space of a given supersymmetry model. A review of the huge number of publications

Table 7.2
Direct decays of sleptons and squarks via trilinear $\not{R}_p$ operators $\lambda_{ijk} L_i L_j \bar{E}_k$, $\lambda'_{ijk} L_i Q_j \bar{D}_k$ and $\lambda''_{ijk} \bar{U}_i \bar{D}_j \bar{D}_k$

Supersymmetric particles	Couplings		
	λ_{ijk}	λ'_{ijk}	λ''_{ijk}
$\tilde{v}_{i,L}$	$\ell^+_{j,L} \ell^-_{k,R}$	$\bar{d}_{j,L} d_{k,R}$	
$\tilde{\ell}^-_{i,L}$	$\bar{v}_{j,L} \ell^-_{k,R}$	$\bar{u}_{j,L} d_{k,R}$	
$\tilde{v}_{j,L}$	$\ell^+_{i,L} \ell^-_{k,R}$		
$\tilde{\ell}^-_{j,L}$	$\bar{v}_{i,L} \ell^-_{k,R}$		
$\tilde{\ell}^-_{k,R}$	$v_{i,L} \ell^-_{j,L} , \ell^-_{i,L} v_{j,L}$		
$\tilde{u}_{i,R}$			$\bar{d}_{j,R} \bar{d}_{k,R}$
$\tilde{u}_{j,L}$		$\ell^+_{i,L} d_{k,R}$	
$\tilde{d}_{j,L}$		$\bar{v}_{i,L} d_{k,R}$	
$\tilde{d}_{j,R}$			$\bar{u}_{i,R} \bar{d}_{k,R}$
$\tilde{d}_{k,R}$		$v_{i,L} d_{j,L}, \ell^-_{i,L} u_{j,L}$	$\bar{u}_{i,R} \bar{d}_{j,R}$

dealing with specific aspects of $\not{R}_p$ in specific supersymmetry models would clearly be beyond the scope of this section. In the following, essential aspects of the phenomenology will be discussed and references to detailed studies provided.

7.3. Decay of sparticles involving $\not{R}_p$ couplings

In the scenario with $\not{R}_p$ due to the trilinear terms, the supersymmetric particles are allowed to decay into standard particles through one $\not{R}_p$ coupling. For sparticles other than the LSP, these $\not{R}_p$ decays will in general compete with "cascade decays" initiated by standard gauge couplings. The review of possibly allowed direct and cascade $\not{R}_p$-decays for sfermions and gauginos–higgsinos is presented in this section. This will later on allow us to easily characterize the essential event topologies expected in $\not{R}_p$-SUSY searches. Direct decays are discussed in Sections 7.3.1 and 7.3.2. Indirect cascade decays are discussed in Section 7.3.3. For completeness, decays involving bilinear interactions are discussed in Section 7.3.4.

7.3.1. Direct $\not{R}_p$ decays of sfermions
The $LL\bar{E}$, $LQ\bar{D}$, or $\bar{U}\bar{D}\bar{D}$ couplings allow for a $\not{R}_p$ direct decay into two standard fermions of, respectively, sleptons, sleptons and squarks, or squarks. The allowed decays become evident when considering the Lagrangian for the trilinear Yukawa interactions written in expended notations in Eq. (2.7) to Eq. (2.9) and discussed in more details in Appendix B. For convenience the corresponding list of decay channels is given in Table 7.2. The $\not{R}_p$ decay of a sfermion of a particular family will be possible only for specific indices i, j, k of the relevant Yukawa coupling.

The partial widths of $\tilde{v}_i$'s when decaying via $\lambda_{ijk} LL\bar{E}$ or $\lambda'_{ijk} LQ\bar{D}$ are given (neglecting lepton and quark masses) by [437]:

$$\Gamma(\tilde{v}_i \to \ell^+_j \ell^-_k) = \frac{1}{16\pi} \lambda^2_{ijk} m_{\tilde{v}_i} , \tag{7.1}$$

$$\Gamma(\tilde{v}_i \to \bar{d}_j d_k) = \frac{3}{16\pi} \lambda'_{ijk}{}^2 m_{\tilde{v}_i} , \tag{7.2}$$

where the factor 3 between Eqs. (7.1) and (7.2) is a color factor. For sneutrinos undergoing direct decays, the mean decay length L in centimetres can then be numerically estimated from:

$$L(\text{cm}) = 10^{-12} (\beta\gamma) \left(\frac{1\text{GeV}}{m_{\tilde{v}_i}} \right) \frac{1}{\lambda^2_{ijk}, 3\lambda'_{ijk}{}^2} . \tag{7.3}$$

Similar formulae hold for charged sleptons in absence of mixing.

Table 7.3
Direct decays of neutralinos and charginos with trilinear $\not{R}_p$ operators $\lambda_{ijk} L_i L_j \bar{E}_k$, $\lambda'_{ijk} L_i Q_j \bar{D}_k$ and $\lambda''_{ijk} \bar{U}_i \bar{D}_j \bar{D}_k$

Supersymmetric particles	Couplings		
	λ_{ijk}	λ'_{ijk}	λ''_{ijk}
$\tilde{\chi}^0$	$\ell_i^+ \bar{v}_j \ell_k^-, \ell_i^- v_j \ell_k^+,$ $\bar{v}_i \ell_j^+ \ell_k^-, v_i \ell_j^- \ell_k^+$	$\ell_i^+ \bar{u}_j d_k, \ell_i^- u_j \bar{d}_k,$ $\bar{v}_i \bar{d}_j d_k, v_i d_j \bar{d}_k$	$\bar{u}_i \bar{d}_j \bar{d}_k, u_i d_j d_k$
$\tilde{\chi}^+$	$\ell_i^+ \ell_j^+ \ell_k^-, \ell_i^+ \bar{v}_j v_k$ $\bar{v}_i \ell_j^+ v_k, v_i v_j \ell_k^+$	$\ell_i^+ \bar{d}_j d_k, \ell_i^+ \bar{u}_j u_k$ $\bar{v}_i \bar{d}_j u_k, v_i u_j \bar{d}_k$	$u_i d_j u_k, u_i u_j d_k$ $\bar{d}_i \bar{d}_j \bar{d}_k$
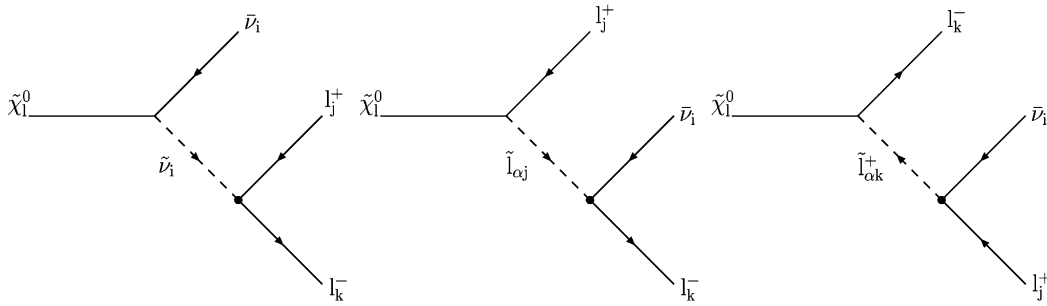
Fig. 7.1. Diagrams for the direct decays of the neutralino $\tilde{\chi}_l^0$ via the coupling λ_{ijk} of the $\not{R}_p$ trilinear $L_i L_j E_k^c$ interaction. The index $l = 1 \ldots 4$ determines the mass eigenstate of the neutralino. The indices $i, j, k = 1, 2, 3$ correspond to the generation. Gauge invariance forbids $i = j$. The index $\alpha = 1, 2$ gives the slepton mass eigenstate (i.e. the chirality of the Standard Model lepton partner in absence of mixing).

In the case of squarks or sleptons of the third generation, a possible mixing between supersymmetric partners of left-and right-handed fermions has to be taken into account. For instance, the width of the lightest stop $\tilde{t}_1$ writes [438]:

$$\Gamma(\tilde{t}_1 \to \ell_i^+ d_k) = \frac{1}{16\pi} \lambda'_{ijk}{}^{'2} \cos^2(\theta_t) m_{\tilde{t}_1} , \qquad (7.4)$$

where θ_t is the mixing angle of top squarks. The case of the stop is somewhat special. The typical decay time of a 100 GeV stop via a $\not{R}_p$ decay mode is roughly 3×10^{-23} s for a coupling value of 10^{-1}, and 3×10^{-21} s for a coupling value of 10^{-2}. So the stop $\not{R}_p$ decay time is of the same order or even greater than its hadronization time which from the strong interaction is $\mathcal{O}(10^{-23})$ s. Thus, the stop may hadronize before it decays.

7.3.2. Direct $\not{R}_p$ decays of gauginos–higgsinos

In a direct $\not{R}_p$ decay, the neutralino (chargino) decays into a fermion and a virtual sfermion with this virtual sfermion subsequently decaying to standard fermions via a $\not{R}_p$ coupling. Thus, direct $\not{R}_p$ decays of gauginos–higgsinos are characterized by three fermions in the final state with the fermion type depending on the dominant coupling. The possible decays are listed in Table 7.3. The corresponding diagrams are shown for the $L_i L_j E_k^c$ interactions in Figs. 7.1 and 7.2.

A collection of general expressions for three-body decays and matrix elements entering in the calculation of partial widths can be found in Appendix C. In the case of a pure photino neutralino decaying with λ_{ijk}, the expression for the partial width simplifies [34] to

$$\Gamma = \lambda_{ijk}^2 \frac{\alpha}{128\pi^2} \frac{m_{\tilde{\chi}_1^0}^5}{m_{\tilde{f}}^4} \qquad (7.5)$$

with $m_{\tilde{f}}$ the mass of the virtual slepton in the decay. Further details can be found in Ref. [439].

In practice, the LSP lifetime is a crucial observable when discussing the final state topology to be expected for supersymmetric events. The experimental sensitivity of collider experiments is often optimal if the LSP has a negligible
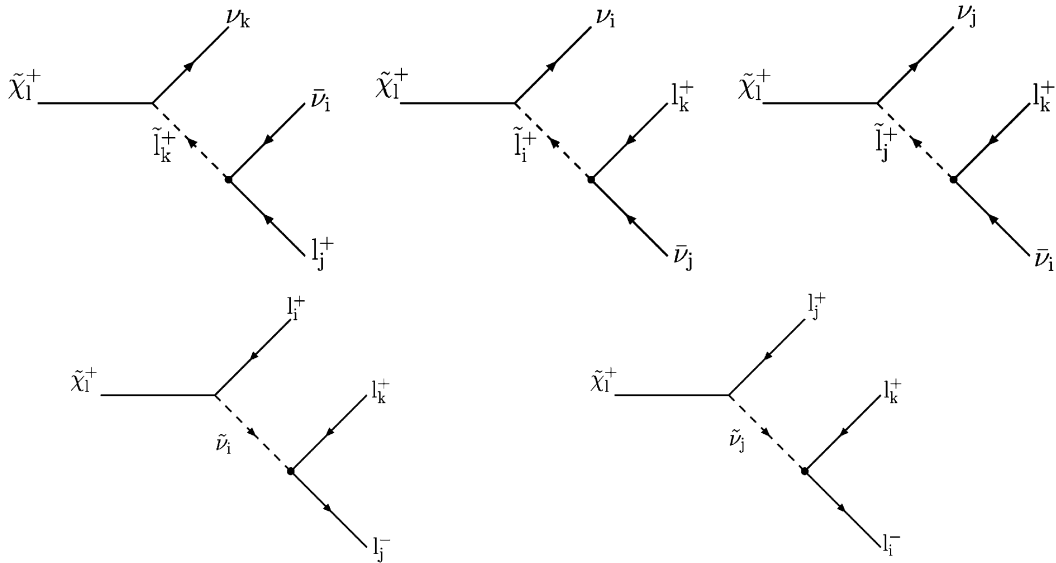
Fig. 7.2. Diagrams for the direct decays of the chargino $\tilde{\chi}_1^+$ via the coupling λ_{ijk} of the $\not{R}_p$ trilinear $L_i L_j E_k^c$ interaction. The index $l = 1 \ldots 4$ determines the mass eigenstate of the neutralino. The indices $i, j, k = 1, 2, 3$ correspond to the generation. Gauge invariance forbids $i = j$. The index $\alpha = 1, 2$ gives the slepton mass eigenstate (i.e. the chirality of the Standard Model lepton partner in absence of mixing).

lifetime so that the production and decay vertices coincide. Otherwise the LSP decay vertex is displaced. If the lifetime is sufficiently large, the LSP decays may occur outside the detector, giving rise to final states characteristic of R_p conserving models.

The mean decay length L in centimetres for the lightest neutralino can be numerically estimated [255] from

$$L(\text{cm}) = 0.3(\beta\gamma)\left(\frac{m_{\tilde{f}}}{100\,\text{GeV}}\right)^4\left(\frac{1\,\text{GeV}}{m_{\tilde{\chi}_1^0}}\right)^5\left[\frac{1}{\lambda_{ijk}^2}, \frac{3}{\lambda'_{ijk}{}'^2}, \frac{3}{\lambda''_{ijk}{}''^2}\right]. \tag{7.6}$$

Fig. 7.3 illustrates the behavior of the LSP lifetime as presented in M_2 versus μ planes for different values of $\tan\beta$ and m_0, and considering a dominant λ_{133} coupling. A translation in terms of L as a function of $m_{\tilde{\chi}_1^0}$ for a fixed $m_{\tilde{f}}$ is shown in Fig. 7.4. Measurements of $\not{R}_p$ coupling values can be performed through displaced vertex associated to the $\not{R}_p$ decay of the LSP.

The sensitivities on the $\not{R}_p$ couplings obtained via a displaced vertex depend of course on the specific detector geometry and performances. Let us estimate the largest values of the $\not{R}_p$ coupling constants that can be measured via the displaced vertex analysis. The LSP is assumed to be the lightest neutralino ($\tilde{\chi}_1^0$). Since a displaced vertex analysis is an experimental challenge at hadron colliders, the performance typically achievable at a future e^+e^- linear collider is considered here. Assuming that the minimum distance between two vertices necessary to distinguish them experimentally is of order $\mathcal{O}(2 \times 10^{-5})$m, it can be seen from Eq. (7.6) that the $\not{R}_p$ couplings can be measured up to the values,

$$\Lambda < 1.2 \times 10^{-4}\gamma^{1/2}\left(\frac{m_{\tilde{f}}}{100\,\text{GeV}}\right)^2\left(\frac{100\,\text{GeV}}{m_{\tilde{\chi}_1^0}}\right)^{5/2}. \tag{7.7}$$

where $\Lambda = \lambda$, $\lambda'/\sqrt{3}$ or $\lambda''/\sqrt{3}$, and γ is the Lorentz boost factor.

There is a gap between these values and the sensitivity of low-energy experiments which requires typically $\not{R}_p$ coupling values in the range $\Lambda \sim \mathcal{O}(10^{-1}\text{–}10^{-2})$ for superpartners masses of $100\,\text{GeV}$. However, the domain above the values of Eq. (7.7) can be tested through the study of the single production of supersymmetric particles as will be discussed in Section 7.5. Indeed, the cross-sections of such reactions are directly proportional to a power of the relevant $\not{R}_p$ coupling constant(s), which allows the determination of the values of the $\not{R}_p$ couplings. Therefore, there exists a
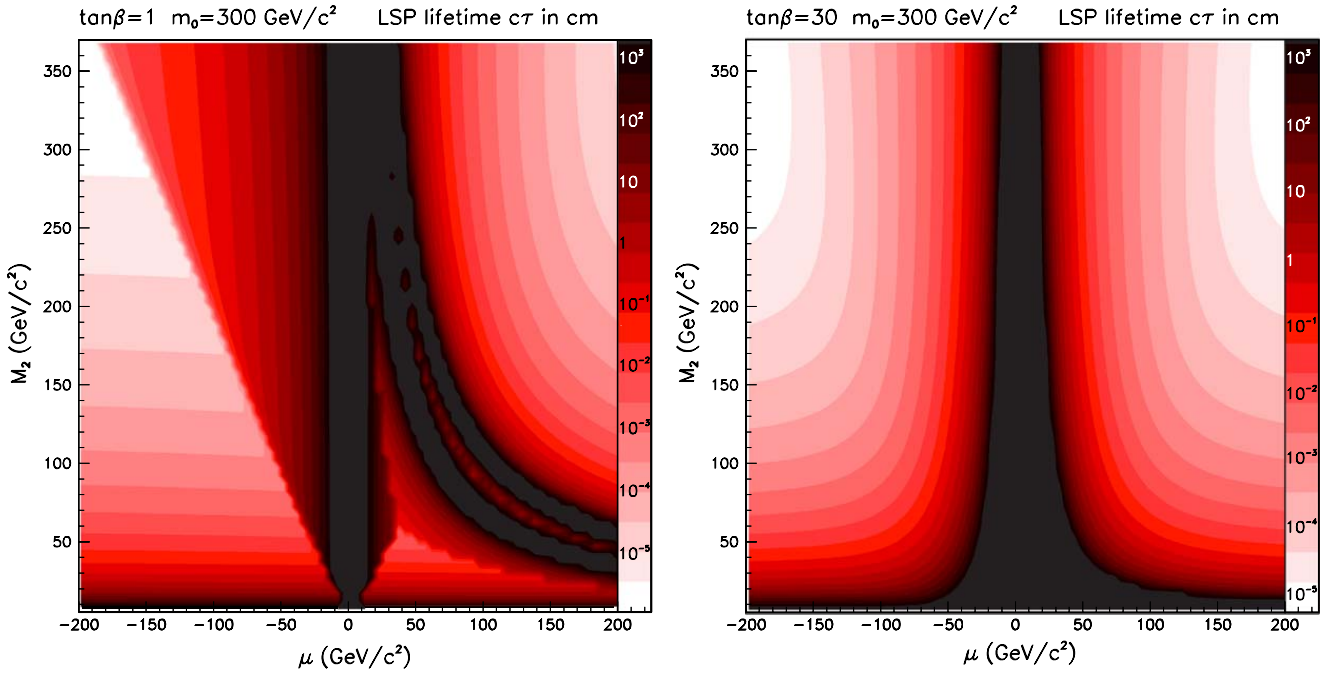
Fig. 7.3. LSP lifetime for different values of the MSSM parameters, and with a dominant λ_{133} coupling; for this illustration, the coupling has been set to $\lambda_{133} = 0.004$.
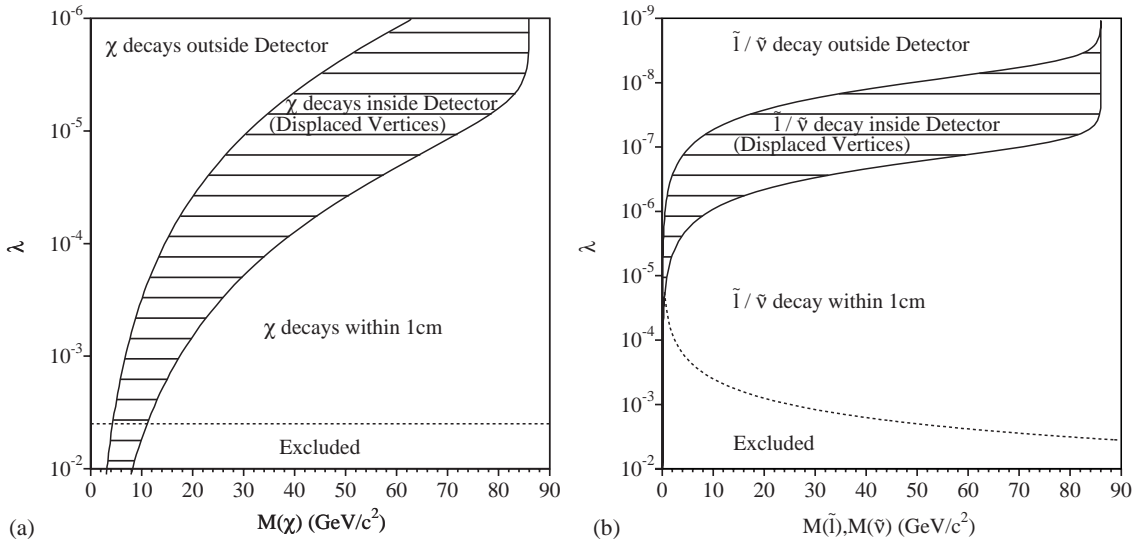
Fig. 7.4. Regions in the λ versus sparticle mass plane where the sparticle has a mean decay length of $L < 1\,\mathrm{cm}$, $1 < L < 3\,\mathrm{m}$ (displaced vertices), and $L > 3\,\mathrm{m}$ (decay outside a typical HEP detector) for (a) $\tilde{\chi}_1^0$ assuming $m_{\tilde{f}} = 100\,\mathrm{GeV}$ and (b) sleptons and sneutrinos. The dashed lines show an indirect limit on λ_{133} [440].

complementarity between the displaced vertex analysis and the study of singly produced sparticles, since these two methods allow to investigate different ranges of values of the $\not{R}_p$ coupling constants.

7.3.3. Cascade decays initiated by gauge couplings

In an indirect decay, the supersymmetric particle first decays through a R_p conserving vertex (i.e. through gauge couplings) to an on-shell supersymmetric particle, thus initiating a cascade which continues till reaching the LSP. The LSP then decays as described above via one $\not{R}_p$ coupling.
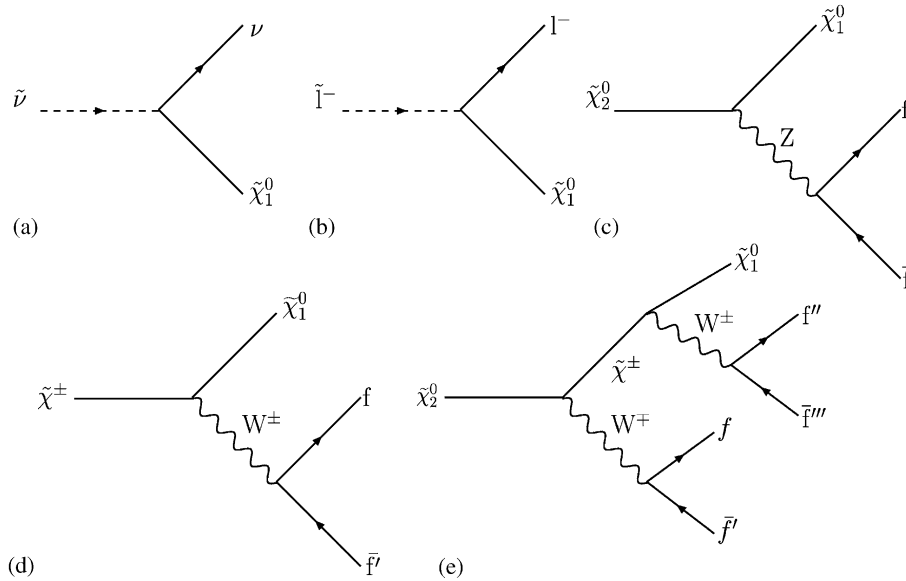
Fig. 7.5. Slepton (a), (b) and gauginos (c), (d), (e) indirect decay diagrams.

The sfermions may for example decay indirectly (i.e. undergo first a gauge decay) into a fermion plus a $\tilde{\chi}_1^0$ if the lightest neutralino $\tilde{\chi}_1^0$ is the LSP, as shown for example in the case of sleptons in Fig. 7.5 a and b. The $\tilde{\chi}_1^0$ will subsequently undergo a $\not{R}_p$ decay via one of the trilinear couplings. In the squark sector, such decays have mainly been considered for the stop and sbottom in actual searches at colliders as they possess a mass eigenstate which can be among the lightest for squarks. If the lightest stop mass eigenstate $\tilde{t}_1$ is not the LSP but the lightest charged supersymmetric particle, the cascade will be initiated through a decay to $\tilde{t}_1 \to c\tilde{\chi}_1^0$. If $m_{\tilde{t}_1} > m_{\tilde{\chi}^\pm} + m_b$ then the decay $\tilde{t}_1 \to b\tilde{\chi}^\pm$ is possible. In the case of the sbottom, the indirect decay $\tilde{b}_1 \to b\tilde{\chi}_1^0$ is generally treated as the dominant one.

In the gaugino–higgsino sector, the heavy neutralino and chargino mass eigenstates can decay, depending on their mass difference with the $\tilde{\chi}_1^0$, either directly into three standard fermions, or indirectly to $\tilde{\chi}_1^0$ via a virtual Z or W, as illustrated in Fig. 7.5c, d and e.

Assuming a small value for the $\not{R}_p$ coupling, the indirect decay mode will generally dominate as soon as there is enough phase space available between "mother" and "daughter" sparticles. For searches at existing colliders this happens when the mass difference between these two sparticles is larger than about 5 to 10 GeV. As an example, the Fig. 7.6 shows the $\not{R}_p$ decay branching fraction of the $\tilde{\tau}_R$ via the λ_{133} coupling as a function of the stau mass, for different values of the neutralino mass. If the slepton is lighter than the neutralino, only the $\not{R}_p$ mode is opened. As soon as the indirect decay mode is possible, it dominates.

Nevertheless, there exist regions of the SUSY parameter space where the R_p conserving decay (initiating the cascade) suffers from a "dynamic" suppression. This is the case for example if the field component of the two lightest neutralinos is mainly the photino, in which case the indirect decay $\tilde{\chi}_2^0 \to \tilde{\chi}_1^0 Z^*$ is suppressed. In these regions, even if the sparticle is not the LSP it will decay through a direct $\not{R}_p$ mode.

It should be emphasized here that the indirect decays lead to final state topologies which differ strongly from direct $\not{R}_p$ decays. For example, the direct decay of a neutralino via a $LL\bar{E}$ coupling leads to a purely leptonic final state, while the indirect decay adds (mainly) jets to such final state. The allowed indirect decays and their branching ratios depend on the parameters values for the specific supersymmetry model (e.g. MSSM, mSUGRA, . . .) as well as on the value of the $\not{R}_p$ coupling considered.

Detailed strategies for practical searches at colliders will be discussed starting in Section 7.4.

7.3.4. Decays through mixing involving bilinear interactions

For completeness, the effects of the $\mu_i L_i H_u$ bilinear terms in the superpotential which violate lepton-number conservation must be discussed in the context of collider physics. The theoretical motivations for the appearance of such terms in the superpotential of supersymmetric models were discussed in detail in Section 2. They appear for instance
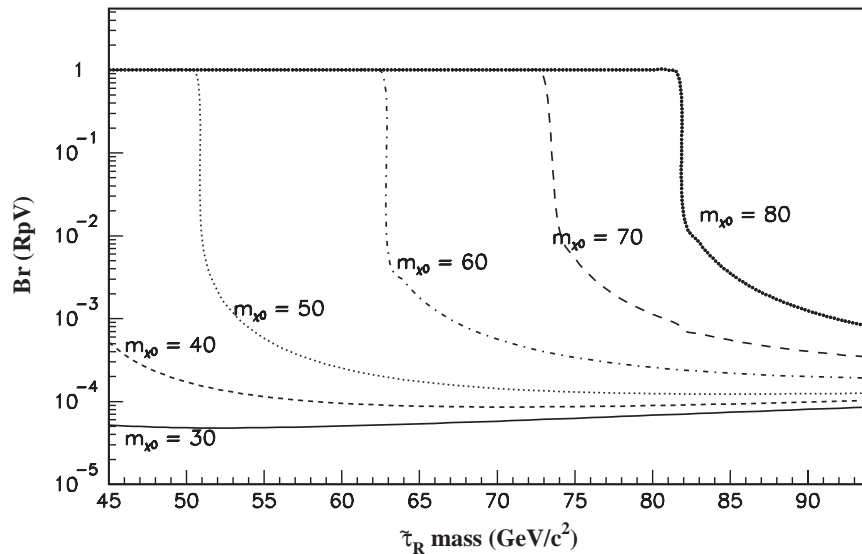
Fig. 7.6. Branching ratio of the $\not{R}_p$ decay $\tilde{\tau}_R \rightarrow ee, e\tau, \tau\tau + \not{E}$ as a function of the mass of the $\tilde{\tau}_R$ and for different values of the neutralino mass.

as a consequence of non-zero right handed sneutrino vacuum expectation values in models with spontaneous *R*-parity violation, or in models with explicitly broken *R*-parity.

As discussed in Section 2.3, there are strong constraints on the bilinear $\not{R}_p$ parameters from the neutrino sector. For this reason, the μ_i are often considered to be suppressed [259] and thus neglected in collider analyzes, with the notable exception of the LSP decays, where the LSP is not necessarily a neutralino in this context. Indeed, values of the μ_i suggested by the solar and atmospheric neutrino experiments can lead to observable decays of the LSP at colliders, with correlations between the neutrino mixing angles and the branching ratios into different lepton flavors [50–52,54,231] (see Section 5.2.2).

However, exotic scenarios with non-negligible μ_i parameters have been considered, in particular in the context of spontaneous *R*-parity violation [63–65]. Although these scenarios are disfavored by neutrino oscillation data, we mention for completeness the expected effect of e.g. a non-negligible μ_3. Such a term introduces a tau component in the chargino mass eigenstate. As a consequence, the tree level decay $Z \rightarrow \tilde{\chi}^- \tau^+$ becomes for instance possible. In the top sector, bilinear terms could rise to additional decay modes for top-quarks and stop-squarks such as $t \rightarrow \tilde{\tau}_1^+ + b$ or $\tilde{t}_1 \rightarrow \tau^+ + b$. Most of these new decay modes result, through cascade decays, in final states with two τ's and two *b*-quarks plus the possibility of additional jets and leptons. B-tagging and τ identification are therefore important tools for the analysis. Note that the $\tilde{t} \rightarrow \tau + b$ decay could also occur via a trilinear λ'_{333} coupling.

Spontaneous *R*-parity violation has been studied in the context of a single tau-lepton-number-violating bilinear term at the Tevatron $p\bar{p}$ collider in Ref. [441] and the $\tilde{t} \rightarrow \tau + b$ decay was found to be competitive with the decay in $c\tilde{\chi}_1^0$ for a discovery of the $\tilde{t}$. For the LHC pp collider, the possibility to observe spontaneous *R*-parity violation through multilepton and same sign dilepton signatures in gluino pair-production has been considered in Ref. [442].

7.4. Phenomenology from pair-produced sparticles

In this section, we are interested in the way the collider phenomenology for Supersymmetric Models is affected by the presence of an individual $\not{R}_p$ coupling with a value $\Lambda^2 \ll 4\pi\alpha$ such that $\not{R}_p$ contributions can be neglected at production.

In such a configuration, a first question of interest for searches at colliders is whether or not the nature of a specific non-vanishing $\not{R}_p$ coupling can be identified (within a range of allowed values) starting from the characteristics of the observed final states. Assuming that the presence of specific $\not{R}_p$ interactions is eventually established, a next important question is to understand whether and how the sensitivity to the fundamental parameters of a given supersymmetric theory is affected.

7.4.1. Gaugino–higgsino pair production

7.4.1.1. Production and final states. Gaugino–higgsino pair production via standard gauge couplings at colliders has been thoroughly studied in the literature and a detailed review is clearly outside the scope of this paper. Here, only the key ingredients shall be summarized. Otherwise we concentrate on the phenomenology associated with the presence of $\not{R}_p$ interactions.

At l^+l^- lepton colliders, the neutralinos are produced by pairs via s-channel Z exchange (provided they have a higgsino component), or via t-channel $\tilde{l}^{\pm}$ exchange (provided they have a gaugino component). The charginos are produced by pairs in the s-channel via γ or Z exchange, or in the t-channel via sneutrino ($\tilde{\nu}_l$) exchange if the charginos have a gaugino component. Of course, the t-channel contributions are suppressed for high slepton masses.

In the case of neutralinos, the t-channel exchange contributes to an enhancement which can be significant for slepton masses typically below $\sqrt{s_{ll}}/2$ (i.e. $m_{\tilde{e}} \lesssim 100\,\mathrm{GeV}$ in the case of selectron exchange at LEP 2 e^+e^- collider). In contrast, the chargino pair production cross-section can decrease due to destructive interference between the s- and t-channel amplitudes (i.e. between $\tilde{e}$ and $\tilde{\nu}_e$ exchange at a e^+e^- collider) if the $\tilde{l}^{\pm}$ and $\tilde{\nu}_l$ masses are comparable.

As an example, one can consider pair production in the framework of the MSSM, assuming in addition that scalars have a common mass m_0 at the GUT scale. In such a case m_0 determines the slepton masses at EW scale and the relevant MSSM parameters are M_2, μ, $\tan\beta$ and m_0. In such a framework the production cross-sections are generally found to be large. If the dominant component of neutralinos and charginos is the higgsino ($|\mu| \ll M_2$) the production cross-sections are also insensitive to slepton masses. Over a wide range of MSSM parameter values, the pair production cross-sections at LEP 2 for $\sqrt{s_{ee}} \simeq 200\,\mathrm{GeV}$ is found to vary typically from 0.1 to 10 pb. Investigations of gaugino pair production in a similar constrained MSSM framework and in presence of $\not{R}_p$ have been performed for the case of a future $500\,\mathrm{GeV}\,e^+e^-$ collider in Ref. [443].

At $p\bar{p}$ and pp hadron colliders, the main production process which has been studied for neutralinos and charginos is the associated production $q\bar{q}' \to \tilde{\chi}^{\pm}\tilde{\chi}^0$. In R_p-conserving theories like the MSSM or mSUGRA, measurable rates are expected mainly in the case of $\tilde{\chi}_1^{\pm}\tilde{\chi}_2^0$ and only for certain regions of the parameter space. In presence of $\not{R}_p$ interactions of course, the process $q\bar{q}' \to \tilde{\chi}_1^{\pm}\tilde{\chi}_1^0$ involving the lowest $\tilde{\chi}^0$ mass eigenstate could also become observable. In addition, $\not{R}_p$ could allow for pair production of neutralinos and charginos in $q\bar{q} \to \gamma$, Z annihilation processes to become observable. The production cross-sections would then depend on the gaugino and higgsino components as discussed above for l^+l^- annihilation.

The final states resulting from the decay of pair-produced neutralinos or charginos are listed in Table 7.4 for the three different couplings $LL\bar{E}$, $LQ\bar{D}$ and $\bar{U}\bar{D}\bar{D}$.

At first approximation, with $\lambda \neq 0$ the final states are characterized by multi-lepton (charged leptons and escaping neutrinos) event topologies. In contrast, with $\lambda' \neq 0$, the final states are likely to contain multi-jets and several more or less isolated leptons. One exception concerns here slepton pair production which could lead to four jet final states. Finally $\lambda'' \neq 0$, leads to final states with very high jet multiplicities. Thus, the existence of either a non-vanishing λ ($LL\bar{E}$), λ' ($LQ\bar{D}$), or λ'' ($\bar{U}\bar{D}\bar{D}$) can indeed be readily distinguished.

Of course such a simple picture applies essentially in the framework of MSSM of mSUGRA models where the $\tilde{\chi}_1^0$ is likely to be the lightest supersymmetric particle. It moreover has to be modulated in the presence of indirect (cascade) decays. For instance indirect gaugino decays when involving an intermediate Z^* or W^* might lead to final states containing jets for $LL\bar{E}$ interactions or, symmetrically, containing leptons and neutrinos for $\bar{U}\bar{D}\bar{D}$ interactions.

7.4.1.2. Searches for gaugino pair production at e^+e^- colliders. It is interesting to review what has been learned from studies by the experiments at the LEP collider. The analyzes have been performed assuming "short lived" sparticles such that the $\not{R}_p$ decays occur close enough to the production vertex and are not observable. In practice this implies a LSP flight path of less than $\mathcal{O}(1)$ cm. Considering the upper limits on the λ_{ijk} derived from low energy measurements (Section 6), and according to Eq. (7.6), the analyses are thus insensitive to a light $\tilde{\chi}$ of mass $M_{\chi_{\mathrm{LSP}}} \leqslant 10\,\mathrm{GeV}$ (due first to the term $m_{\tilde{\chi}}^{-5}$ and second to the term $(\beta\gamma)$ which becomes important). When studying $\tilde{\chi}$ decays, for typical masses considered, the LEP analyzes have a lower limit in sensitivity on the λ coupling of the order of 10^{-4} to 10^{-5}.

In most of the $\not{R}_p$ analyzes, the main background contributions come from the four-fermion processes and $f\bar{f}\gamma$ events. A discussion of such SM background contributions can be found in Ref. [444]. The $f\bar{f}\gamma$ cross-section decreases with the increase of the center-of-mass energy; on the other hand, the cross-sections of the four-fermion processes increase;

Table 7.4

Neutralino and chargino pair production final states in case of R_p decays

Gauginos	Decay mode	$LL\bar{E}$	$LQ\bar{D}$	$\bar{U}\bar{D}\bar{D}$
$\tilde{\chi}_1^0\,\tilde{\chi}_1^0$	Direct	$4\ell + \not{E}$	$1\ell + 4j + \not{E}$ $2\ell + 4j$ $4j + \not{E}$	$6j$
$\tilde{\chi}_1^+\,\tilde{\chi}_1^-$	Direct	$2\ell + \not{E}$ $4\ell + \not{E}$ 6ℓ	$1\ell + 4j + \not{E}$ $2\ell + 4j$ $4j + \not{E}$	$6j$
$\tilde{\chi}_2^0\,\tilde{\chi}_1^0$	Indirect	$4\ell + \not{E}$ $4\ell + 2j + \not{E}$ $6\ell + \not{E}$	$1\ell + 4j + \not{E}$ $1\ell + 6j + \not{E}$ $2\ell + 4j + \not{E}$ $2\ell + 6j$ $3\ell + 4j + \not{E}$ $4\ell + 4j$ $6\ell + \not{E}$	$8j$ $6j + 2\ell$ $6j + \not{E}$
$\tilde{\chi}_1^+\,\tilde{\chi}_1^-$	Indirect	$4\ell + 4j + \not{E}$ $5\ell + 2j + \not{E}$ $6\ell + \not{E}$	$1\ell + 6j + \not{E}$ $1\ell + 8j + \not{E}$ $2\ell + 4j + \not{E}$ $2\ell + 6j + \not{E}$ $2\ell + 8j$ $3\ell + 4j + \not{E}$ $3\ell + 6j + \not{E}$ $4\ell + 4j + \not{E}$ $8j + \not{E}$	$10j$ $8j + 1\ell + \not{E}$ $6j + 2\ell + \not{E}$

The notations l, $\not{E}$ and j correspond, respectively, to charged lepton, missing energy from at least one neutrino and jet final states.

in particular beyond the W^+W^- and the ZZ thresholds, these processes contribute significantly to the background, and lead to final states very similar to several R_p signal event topologies.

The $LL\bar{E}$ searches at LEP were mainly multi-lepton analyzes, with the missing energy in the final states most often coming from neutrinos. However, the indirect decay topologies may also contain hadronic jets (indirect decay of gauginos, see Table 7.4). The number of charged leptons in the final state varied between 4 and 6 except for direct decays of charginos with two neutrinos which lead to 2 charged leptons in the final state. Therefore, the crucial step in the selection of the signal events was the electron, muon or tau identification. Electrons and muons are typically identified by well isolated charged tracks in combination with either dE/dx measurements and deposits in the electromagnetic calorimeters (e) or information from hadron calorimeters and muon chambers (μ, τ) of the experiments. Tau decays may also be identified through isolated thin hadronic jets. In case of W or tau jets, signal selection has been performed with the additional discrimination provided by topological variables like the y_{cut} jet resolution variable. The two-lepton final states are difficult to separate from the SM background mainly coming from $f\bar{f}\gamma$ and $\gamma\gamma$ events and have been considered in the analyzes. The other multi-lepton final states on the other hand, provided almost background free analyzes with efficiencies typically between 20 and 60%. The decays producing taus in the final states were found to have lower efficiencies and rejection power. The analyses designed for signals produced with a dominant λ_{133} can be applied to signals produced with other λ_{ijk}, and the efficiencies are either of the same order or higher. Therefore, the weakest limits which have been derived are those resulting from analyzes performed assuming a dominant λ_{133} coupling [445].

For the $LQ\bar{D}$ searches at LEP, the analyzes of gaugino decays all included hadronic activity in the final state (at least 4 hadronic jets, see Table 7.4) such that topological variables like jet resolution and thrust were used to select events in combination with missing energy and/or one or two identified leptons. For the topologies with missing energy the polar angle of the missing momentum has also been used to select candidate events. The analysis of gaugino decays via the couplings λ'_{i3k} and λ'_{ij3} also benefits from the presence of b-quarks, and thereby from possible background reduction via b-tagging. The topologies of the indirect chargino decays depend heavily on the mass difference between chargino and neutralino, which is a free parameter in the model. Sensitivity to a large range of topologies is hence

needed in order to completely cover all possible $LQ\bar{D}$ scenarios. Several of the gaugino final state topologies closely resemble those of $\not{R}_p$ sfermion decays and the same event selection may therefore be used to cover these channels too, e.g. sneutrino and slepton decays. The SM background consists mainly of four-fermion events decaying either to hadronic or semileptonic final states. Signal efficiencies typically range from over 50% down to a few %, depending on topology and selection criteria. The worst efficiency is generally obtained for decays into taus and light quarks. The couplings generating these final states (e.g. λ'_{311}) are therefore used to evaluate conservative constraints on the production cross-sections. The excluded $LQ\bar{D}$ gaugino cross-sections at a 95% confidence level are typically of the order of 0.5 pb [446].

For the LEP searches in the case of a single dominant $\bar{U}\bar{D}\bar{D}$ coupling, the gauginos decay into mainly hadronic final states, however, the indirect gaugino decays may also include leptons and missing energy, depending on the decay mode of the W. As seen from Table 7.4, the number of jets expected in the final states varies between six and ten. The selection of candidate events typically depends on topological variables like jet resolution, thrust and jet angles, thereby rejecting the major part of the SM $f\bar{f}\gamma$, W^+W^- and ZZ background events. The absence of neutrinos and missing energy in the fully hadronic final states also enables direct reconstruction of the gaugino masses. The mass reconstruction consists of assigning each reconstructed jet to its parent gaugino and thereafter applying a kinematic fitting algorithm. These algorithms are also used to reconstruct the mass of the W bosons produced at LEP 2 and impose constraints on conserved energy and momenta in combination with equal masses of the pair produced gauginos. The indirect chargino decays, again, strongly depend on the mass difference between chargino and neutralino, thereby making it difficult to use the same event selection to cover all possible scenarios. Decays into light quarks (λ''_{112} and λ''_{122} couplings) generally have lower efficiencies and are therefore used to derive conservative cross-section limits at a 95% CL [445].

Since none of the $\not{R}_p$ gaugino searches at LEP 2 show any excess of data above the Standard Model expectations, the results are interpreted in terms of exclusions of the MSSM parameters. The gaugino pair production cross-sections are, as previously discussed, mainly determined by the MSSM parameters μ, M_2, m_0 and $\tan\beta$. The excluded gaugino cross-section at a 95% CL for each experimental search channel is therefore compared to the production cross-section provided by the MSSM for each set of these four parameters. Hereby an exclusion of experimentally disproved combinations of the parameters is obtained for each of the performed search channels. This exclusion is then typically presented as contours in the μ, M_2 plane for different fixed values of $\tan\beta$ and m_0 [445–448]. The LEP 1 excluded region of the (μ, M_2) contours is obtained from the Z line-shape measurement. Examples of such (μ, M_2) exclusion contours are shown in Figs. 7.7, 7.8 and 7.9. The dominant contribution to the exclusion contours comes from the chargino pair production analyzes in any $\not{R}_p$ couplings. The neutralino pair production analysis becomes relevant in case of low $\tan\beta$, low m_0, small M_2 and negative μ values (Fig. 7.9) which means when the chargino pair production cross-section is suppressed by destructive interferences between s- and t-channels.

From the exclusion plots in the (μ, M_2) plane the extraction of the minimum gaugino masses which is not excluded for the investigated range of parameters within the MSSM is performed. These limits on the lightest chargino and neutralino are obtained for high m_0 value which corresponds to the disappearance of neutralino pair production contribution. The mass of the lightest non-excluded gaugino is naturally shifted when $\tan\beta$ is changed. In Fig. 7.10, the lightest non-excluded neutralino mass as a function of $\tan\beta$ for the $LL\bar{E}$ searches in DELPHI is shown. It has been checked that this result is independent of m_0 values.

In this context, one of the most important results in the searches for supersymmetry obtained with data taken up to a center-of-mass energy of 208 GeV at LEP 2 by the four LEP experiments is that the lightest chargino mass is excluded at 95% CL up to 103 GeV and the lightest neutralino mass is excluded at 95% CL up to 39 GeV in the framework of the MSSM with $\not{R}_p$ assuming that the $\tilde{\chi}_1^0$ decays in the detector. These results are formally only valid in the scanned MSSM parameter space, i.e. for $1 \leqslant \tan\beta \leqslant 35$, $m_0 \leqslant 500$ GeV, $|\mu| \leqslant 200$ GeV, $M_2 \leqslant 500$ GeV, and for any coupling value from 10^{-4} up to the existing limits.

We hinted above of situations where indirect (cascade) decays could play a significant role. This could be the case for instance at future lepton colliders where center-of-mass energies far beyond the current lower mass limits on the LSP are being contemplated. In view of the constraints established at LEP 2, the possibility of opening up large production of heavier neutralinos and charginos at a future 500 GeV e^+e^- linear collider (LC) has been studied in Ref. [443] assuming that the lightest neutralino is the LSP and in presence of $\not{R}_p$. The study showed in this case (for a representative but finite number of points in the constrained MSSM parameter space) that only the production modes involving the $\tilde{\chi}_1^0$, $\tilde{\chi}_2^0$, $\tilde{\chi}_1^\pm$ need to be considered. The $\tilde{\chi}_3^0$, $\tilde{\chi}_4^0$, and $\tilde{\chi}_2^\pm$ being almost always beyond the reach of a 500 GeV
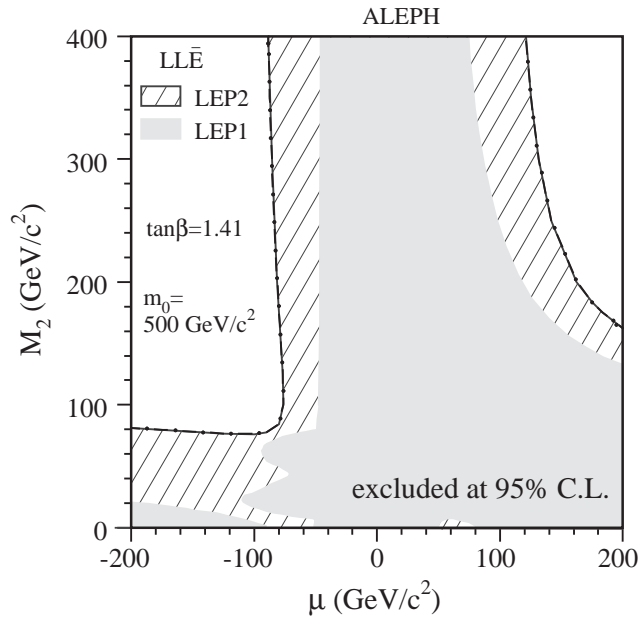
Fig. 7.7. Regions in the (μ, M_2) plane excluded at 95% *CL* at $\tan \beta = 1.41$ and $m_0 = 500$ GeV for $LL\bar{E}$ coupling [446]. The dotted line is the kinematic limit for pair production of the lightest chargino.
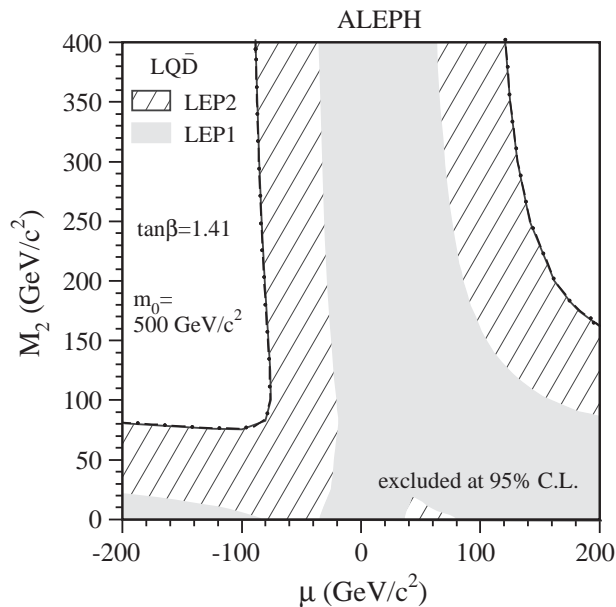
Fig. 7.8. Regions in the (μ, M_2) plane excluded at 95% *CL* for $\tan \beta = 1.41$ and $m_0 = 500$ GeV in the case of the dominant $LQ\bar{D}$ coupling [446]. The black line is the kinematic limit for pair production of the lightest chargino.

machine. As a consequence, the analysis would remain relatively simple, with a limited amount of cascade decays to take into account. Moreover, for a large part of the parameter space, the $\tilde{\chi}_2^0$ is nearly degenerate with the lighter chargino, and then, the number of decay chains to be considered is further reduced. The signals produced by $LL\bar{E}$, $LQ\bar{D}$, $\bar{U}\bar{D}\bar{D}$ operators have been studied in Ref. [443] and retain the basic characteristics listed above. For $LL\bar{E}$ the dominating signal remains an excess of multi-lepton final states, with possibly substantial missing energy. For $LQ\bar{D}$ the final states contain again leptons and jets. In this case, an algorithm to reconstruct the LSP and higher neutralino masses enables to identify the signal as due to supersymmetry with specific $\not{R}_p$ operators. The existence of like-sign dilepton final states, originating from the Majorana nature of neutralinos, appears to be a very promising signal practically
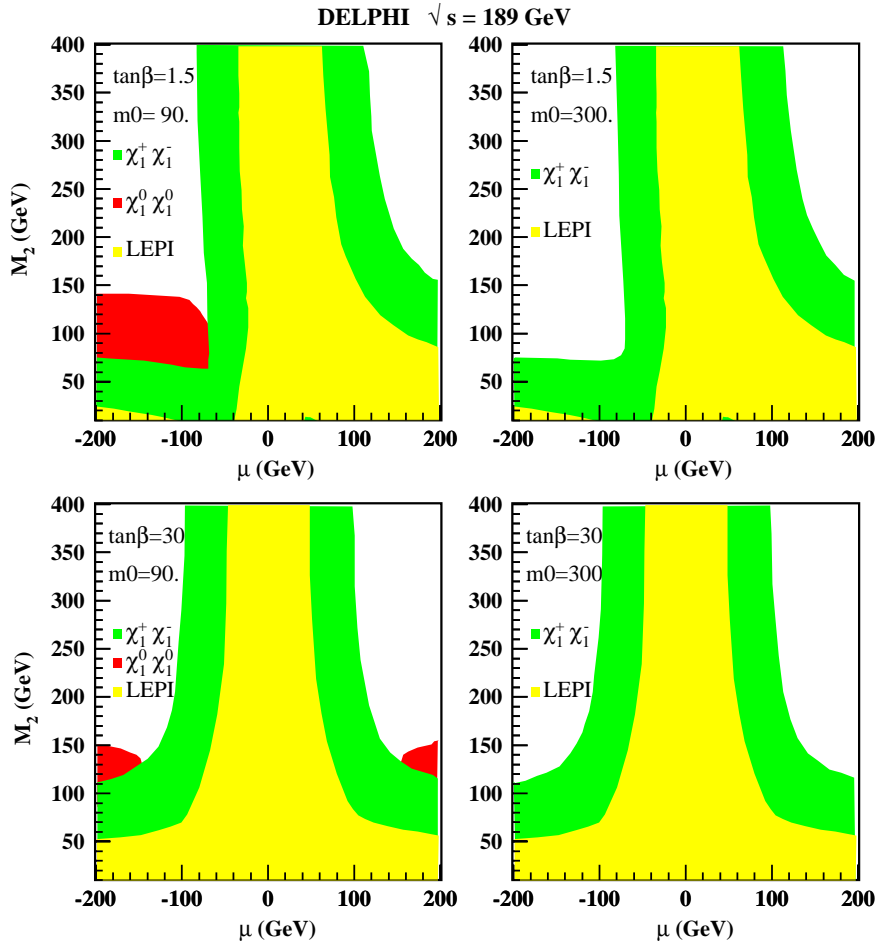
Fig. 7.9. Regions in the (μ, M_2) plane excluded at 95% *CL* for $\tan\beta = 1.5, 30$ and $m_0 = 90, 300$ GeV in the case of a dominant $\bar{U}\bar{D}\bar{D}$ coupling [445].
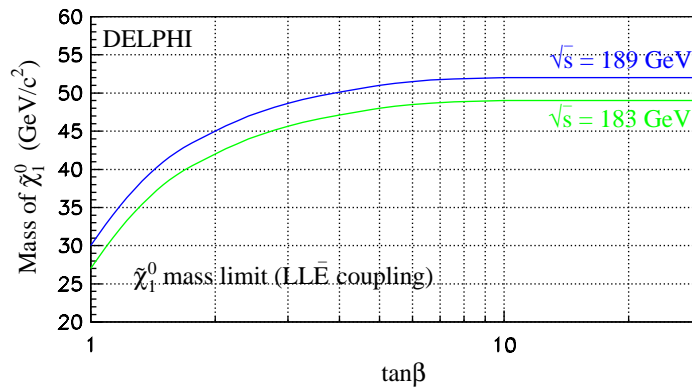
Fig. 7.10. The lightest non-excluded neutralino mass as a function of $\tan\beta$ at 95% *CL*. This limit is independent of the choice of m_0 in the explored range and of the generation indices i, j, k of the λ_{ijk} coupling [445] and it assumes that the $\tilde{\chi}_1^0$ in the detector.

free of true Standard Model background sources. For $\bar{U}\bar{D}\bar{D}$ the final states consist again of multiple jets which are more difficult to disentangle from a large number of Standard Model background sources. Mass reconstruction nevertheless appears promising here also to allow to identify the signal as due to supersymmetry with specific $\not{R}_p$ operators.

7.4.1.3. Searches for gaugino pair production at hadron colliders. Cascade decays involving trilinear $\not{R}_p$ couplings could also play a major rôle at future hadron colliders.

Outstanding multi-lepton event signatures are expected in the presence of a λ Yukawa coupling. The case of gaugino pair production with a trilepton signature has been investigated for the $D\emptyset$ experiment at the Tevatron collider in Ref. [449], in the framework of mSUGRA.

$D\emptyset$ [450] also considered the dimuon and four-jets channel occurring after $\tilde{\chi}_1^0$ decay via the λ'_{2jk} coupling ($j = 1, 2$; $k = 1, 2, 3$) where the $\tilde{\chi}_1^0$ can be produced either directly in pair or through cascade decays from squarks or gluinos. Gluinos masses below 224 GeV (for all squark masses and for $tan\beta = 2$) are excluded. For equal masses of squarks and gluinos the mass limit is 265 GeV.

The λ'' coupling implies multi-jet final states for sparticle decays which severely challenges the sensitivity at $p\bar{p}$ and pp colliders.

However the 1-lepton and various dileptons and multi-lepton event topologies that result from simultaneous production of all sparticles at the Tevatron assuming the LSP decays via baryon number violating operators have been studied in [451] giving reaches on the gluino mass from 150 GeV up to 360 GeV depending on the specific topology.

The study of the decay chain $\tilde{q}_L \rightarrow \tilde{\chi}_2^0 q \rightarrow \tilde{l}_R lq \rightarrow \tilde{\chi}_1^0 llq$ followed by the decay of the $\tilde{\chi}_1^0$ into three quarks assuming a non-zero λ''_{212} at the LHC has been performed in [452]. This study shows that even in the choice of a non-zero λ''_{212}, which is considered as the hardest choice, the $\tilde{\chi}_2^0$, $\tilde{\chi}_2^0$ and $\tilde{q}_L$ can be detected and their masses measured and that the mass of the $\tilde{l}_R$ can be obtained in much of the parameter space.

7.4.2. Sfermion pair production

7.4.2.1. Production and final states. As for the gaugino–higgsino production discussed above, we shall concentrate in this section on the phenomenology associated with the presence of $\not{R}_p$ interactions. But we shall first briefly review the key ingredients for sfermion pair production via standard gauge couplings at colliders.

The sfermion mass eigenstates, $\tilde{f}_1$ and $\tilde{f}_2$ (f: q or ℓ, $\tilde{f}_1$ lighter than $\tilde{f}_2$), are obtained from the two supersymmetric scalar partners $\tilde{f}_L$ and $\tilde{f}_R$ of the corresponding left and right-handed fermion [453,454]:

$$\tilde{f}_1 = \tilde{f}_L \ \cos\theta_{\tilde{f}} \ + \tilde{f}_R \ \sin\theta_{\tilde{f}} \ ,$$

$$\tilde{f}_2 = -\tilde{f}_L \ \sin\theta_{\tilde{f}} \ + \tilde{f}_R \ \cos\theta_{\tilde{f}} \ ,$$

where $\theta_{\tilde{f}}$ is the mixing angle with $0 \leqslant \theta_{\tilde{f}} \leqslant \pi$. According to the equations which give the sfermion masses (see for example in [455]), the left-handed sfermions are most often heavier than their right-handed counterparts. The $\tilde{f}_L$–$\tilde{f}_R$ mixing is related to the off-diagonal terms of the scalar squared-mass matrix. It is proportional to the fermion mass, and is small compared to the diagonal terms, with the possible exception of the third family sfermion [456]. The lightest squark is then probably the lighter stop $\tilde{t}_1$. This is due not only to the mixing effect but also to the effect of the large top Yukawa coupling; both tend to decrease the mass of $\tilde{t}_1$ [457]. The lightest charged slepton is probably the $\tilde{\tau}_1$. For small values of $tan\beta$, $\tilde{\tau}_1$ is predominantly a $\tilde{\tau}_R$, and it is not so much lighter than $\tilde{e}_R$ and $\tilde{\mu}_R$.

Sleptons and squarks can be pair produced in e^+e^- collisions via the ordinary gauge couplings of supersymmetry with conserved R-parity provided that their masses are kinematically accessible. They can be produced via s-channel Z or γ exchange with a cross-section depending on the sfermion mass. The $\tilde{\nu}_e$ ($\tilde{e}$) can also be produced via the exchange of a chargino (neutralino) in the t-channel, provided that the gaugino component of the chargino (neutralino) is the dominant one. The t-channel contributes if the chargino (neutralino) mass is sufficiently low, and then the cross-section depends also on the $\tilde{\chi}^\pm$ ($\tilde{\chi}^0$) mass and field composition and thereby on the relevant parameters of the supersymmetric model. The coupling between the squarks and the Z boson depends on the mixing angle $\theta_{\tilde{q}}$, and it is minimal for a particular angle value. For example in the case of the stop, the decoupling between the $\theta_{\tilde{t}}$ and the Z is maximal for $\theta_{\tilde{t}} = 0.98$ rad such that the stop pair production cross-section is minimal.

In general, both direct and indirect decays of sfermions can be studied in sparticle pair production at colliders. The direct decay of a sfermion via a given $\not{R}_p$ coupling involves specific standard fermions and can be (e.g. when involving the top quark) kinematically closed. The final states resulting from the decay of pair-produced sleptons or squarks are listed in Tables 7.5 and 7.6 for the three different couplings λ ($LL\bar{E}$), λ' ($LQ\bar{D}$), or λ'' ($\bar{U}\bar{D}\bar{D}$).

When considering sfermion pair production and the decays of Tables 7.5 and 7.6 relevant for e^+e^- colliders, it should be noticed that in general the indirect decays into a chargino will not be considered. This is because the chargino search

Table 7.5
Sfermion pair production final states in case of direct $\not\!\!R_p$ decays

Sfermions	$LL\bar{E}$	$LQ\bar{D}$	$\bar{U}\bar{D}\bar{D}$
$\tilde{\nu}\bar{\tilde{\nu}}$	$4\,\ell$	$4\,j$	Not possible
$\tilde{\ell}_R^+\tilde{\ell}_R^-$	$\ell\ell' + \not\!\!E$	Not possible	Not possible
$\tilde{\ell}_L^+\tilde{\ell}_L^-$	$2\,\ell + \not\!\!E$	$4\,j$	Not possible
$\tilde{u}_L\bar{\tilde{u}}_L,\ \tilde{d}_R\bar{\tilde{d}}_R$	Not possible	$2\ell + 2j$	$4\,j$
$\tilde{d}_R\bar{\tilde{d}}_R$		$1\ell + 2j + \not\!\!E$	
$\tilde{d}_L\bar{\tilde{d}}_L,\ \tilde{d}_R\bar{\tilde{d}}_R$		$2j + \not\!\!E$	

The notations l, $\not\!\!E$ and j correspond respectively to charged lepton, missing energy from at least one neutrino and jet final states.

Table 7.6
Sfermion pair production final states in case of indirect decays when the LSP is the lightest neutralino

Sfermions	$LL\bar{E}$	$LQ\bar{D}$	$\bar{U}\bar{D}\bar{D}$
$\tilde{\nu}\bar{\tilde{\nu}}$	$4\ell + \not\!\!E$	$2\ell + 4j + \not\!\!E$	$6j + \not\!\!E$
		$2\ell + 4j + \not\!\!E$	
		$4j + \not\!\!E$	
$\tilde{\ell}^+\tilde{\ell}^-$	$6\ell + \not\!\!E$	$4\ell + 4j$	$2\ell + 6j$
		$3\ell + 4j + \not\!\!E$	
		$2\ell + 4j + \not\!\!E$	
$\tilde{q}\bar{\tilde{q}}$	$4\ell + 2j + \not\!\!E$	$2\ell + 6j$	$8j$
		$\ell + 6j + \not\!\!E$	
		$6j + \not\!\!E$	

The notations l, $\not\!\!E$ and j correspond respectively to charged lepton, missing energy from at least one neutrino and jet final states.

itself provides a mass limit close to the kinematic limit. There is no phase space left for the production of (e.g.) two sleptons followed by decays involving charginos. This explains why for instance at LEP, the most general sfermion indirect decay studied has been the decay into the lightest neutralino considered as the LSP ($\tilde{\nu} \to \nu\tilde{\chi}_1^0$, $\tilde{\ell} \to \ell\tilde{\chi}_1^0$, $\tilde{q} \to q'\tilde{\chi}_1^0$). The final states are then composed of two fermions plus the decay products of the $\not\!\!R_p$ decay of the neutralino pair (see Table 7.6).

7.4.2.2. Slepton searches at lepton colliders.
Here again one can profit from what has been learned from actual studies by the experiments at LEP collider where both productions of sneutrino and charged slepton pairs have been searched for.

Early discussions on several *R*-parity-violating processes at e^+e^- colliders including charged slepton pairs can be found in [458,459].

Lets first consider the case of sneutrino pair production. In the presence of $LL\bar{E}$ interactions, searches for four charged lepton final states are performed. The six possible configurations are listed in Table 7.7. Event topologies containing muons and electrons allow for a high selectivity by applying conditions on two lepton invariant masses. The highest efficiencies are obtained when there are at least two muons in the final states, and the lowest when there are taus. In the latter case, a certain amount of energy is missing in the final state, due to the neutrinos produced in the tau decays. Then, most often, two extreme cases in the coupling choice are studied: the first one considering that the λ_{122} or λ_{232} is dominant, leading to the most efficient analyzes, the second considering that the λ_{133} or λ_{233} is dominant, leading to the least efficient analyzes. With these two analysis types, all the possible final states are probed.

In the presence of $LQ\bar{D}$ interactions, searches for four jets final states are performed. Here also, the absence of missing energy in the final state offers the possibility to reconstruct the sneutrino mass. Depending on the generation indices, 0, 2, and 4 jets can contain a *b*-quark (Table 7.8). With the possibility to tag the jets generated by *b*-quarks, the analyzes are very efficient.

Table 7.7
Four lepton final states produced by the direct decay via a $LL\bar{E}$ term of a sneutrino pair

Final states	Processes and couplings		
	$\tilde{v}_e \bar{\tilde{v}}_e$	$\tilde{v}_\mu \bar{\tilde{v}}_\mu$	$\tilde{v}_\tau \bar{\tilde{v}}_\tau$
$eeee$		λ_{121}	λ_{131}
$ee\mu\mu$	λ_{121}	λ_{122}	$\lambda_{132}, \lambda_{231}$
$ee\tau\tau$	λ_{131}	$\lambda_{123}, \lambda_{231}$	λ_{133}
$\mu\mu\mu\mu$	λ_{122}		λ_{232}
$\mu\mu\tau\tau$	$\lambda_{123}, \lambda_{132}$	λ_{232}	λ_{233}
$\tau\tau\tau\tau$	λ_{133}	λ_{233}	

Table 7.8
Four jet final states produced by the direct decay via a $LQ\bar{D}$ term of a sneutrino pair

Final states	Processes and couplings		
	$\tilde{v}_e \bar{\tilde{v}}_e$	$\tilde{v}_\mu \bar{\tilde{v}}_\mu$	$\tilde{v}_\tau \bar{\tilde{v}}_\tau$
$4q$ (no b-quarks)	$\lambda'_{1jk, j,k\neq3}$	$\lambda'_{2jk, j,k\neq3}$	$\lambda'_{3jk, j,k\neq3}$
$2q2b$	$\lambda'_{1j3, j\neq3}, \lambda'_{13k, k\neq3}$	$\lambda'_{2j3, j\neq3}, \lambda'_{23k, k\neq3}$	$\lambda'_{3j3, j\neq3}, \lambda'_{33k, k\neq3}$
$4b$	λ'_{133}	λ'_{233}	λ'_{333}

Table 7.9
Final states produced by the direct decay via a $LL\bar{E}$ term of a pair of supersymmetric partners of the right-handed leptons

Final states	Processes and couplings		
	$\tilde{e}_R \tilde{e}_R$	$\tilde{\mu}_R \tilde{\mu}_R$	$\tilde{\tau}_R \tilde{\tau}_R$
$ee, e\mu, \mu\mu + \not{E}$	λ_{121}	λ_{122}	λ_{123}
$ee, e\tau, \tau\tau + \not{E}$	λ_{131}	λ_{132}	λ_{133}
$\mu\mu, \mu\tau, \tau\tau + \not{E}$	λ_{231}	λ_{232}	λ_{233}

The LEP experiments have presented results on the lower limit on the sneutrino electron mass derived by searching for the direct decay of sneutrinos in the data collected in 1999 and 2000 up to a center-of-mass energy of 208 GeV. With a $LL\bar{E}$ ($LQ\bar{D}$) coupling, the most conservative lower limits are 98 (91) GeV [446,445,448]. For the derivation of limits, efficiencies are determined as function of the sneutrino mass. In case of $\tilde{v}_e$, due to the possible t-channel contribution, they are considered for a specific set of MSSM parameters, generally for $\mu = -200$ GeV, $M_2 = 100$ GeV. When the contribution of the t-channel becomes negligible, the $\tilde{v}_e \bar{\tilde{v}}_e$ production cross-section is similar to the $\tilde{v}_\mu \bar{\tilde{v}}_\mu$ or $\tilde{v}_\tau \bar{\tilde{v}}_\tau$ ones. Taking into account the number of expected events from the Standard Model processes, the number of observed events, and the analysis efficiencies, upper limits at 95% of confidence level on the sneutrino cross-section are obtained as function of the sneutrino mass. Comparing these upper limits to the expected MSSM cross-section, limits on the sneutrino mass have been derived, as illustrated in Fig. 7.11. The limits obtained are much stronger that those existing in the hypothesis of R-parity conservation, in which the sneutrino pair production is invisible.

Right-handed charged sleptons are mainly studied, because their production cross-section, for a given slepton mass, is lower than for the left-handed ones, therefore leading to more conservative results. The direct decay of a pair of charged sleptons lead to two charged leptons and some missing energy. This low multiplicity final state is difficult to analyze due to the high background of low multiplicity processes. With a dominant λ_{ijk} coupling constant, only the pair produced $\tilde{\ell}_{kR}$ and $\tilde{\ell}_{iL}$ or $\tilde{\ell}_{jL}$ are allowed to directly decay. The decay of $\tilde{\ell}_{kR}^+ \tilde{\ell}_{kR}^-$ gives $\ell_i \ell_i, \ell_i \ell_j, \ell_j \ell_j + \not{E}$, and since $i \neq j$ two lepton flavors are mixed in the final state (see Table 7.9). It is not the case in the direct decay of the supersymmetric partners of the left-handed charged leptons, for which there is only one lepton flavor in the $2\ell + \not{E}$ final state (Table 7.10). In case of selectrons, the $\tilde{e}_L \tilde{e}_R$ production is possible in the t-channel; direct decay of both selectrons is possible only via λ_{121} ($ee, e\mu + \not{E}$ final state) or via λ_{131} ($ee, e\tau + \not{E}$ final state).
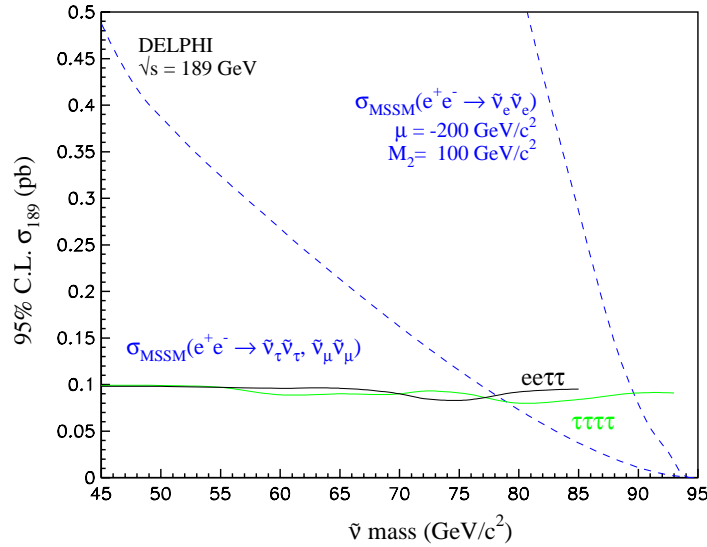
Fig. 7.11. Sneutrino direct decay searches with $LL\bar{E}$ coupling: limit on the $\tilde{\nu}\tilde{\nu}$ production cross-section as a function of the mass for two different final states. The MSSM cross-sections are reported in order to derive a limit on the sneutrino mass in the case of direct $\not{R}_p$ decay. The dashed lower curve corresponds to both $\tilde{\nu}_\mu\tilde{\nu}_\mu$ and $\tilde{\nu}_\tau\tilde{\nu}_\tau$ cross-sections, which depend only on the sneutrino mass. The dashed upper curve on the plot is the $\tilde{\nu}_e\tilde{\nu}_e$ cross-section obtained for $\mu = -200$ GeV and $M_2 = 100$ GeV, the corresponding chargino mass lies between 90 and 120 GeV [445].

Table 7.10
Two lepton with missing energy final states produced by the direct decay via a $LL\bar{E}$ term of a pair of supersymmetric partners of left-handed charged leptons

Final states	Processes and couplings		
	$\tilde{e_L}\tilde{e_L}$	$\tilde{\mu}_L\tilde{\mu}_L$	$\tilde{\tau}_L\tilde{\tau}_L$
$ee + \not{E}$	$\lambda_{121,131}$	$\lambda_{121,231}$	$\lambda_{131,231}$
$\mu\mu + \not{E}$	$\lambda_{122,132}$	$\lambda_{122,232}$	$\lambda_{132,232}$
$\tau\tau + \not{E}$	$\lambda_{123,133}$	$\lambda_{123,233}$	$\lambda_{133,233}$

Similarly to the sneutrino decay, the search for final states containing mainly taus is the least efficient one. An upper limit on the cross-section is obtained as a function of the slepton mass. Comparing this upper limit to the expected MSSM cross-section, limits on the slepton mass is deduced. In case of selectron production, the limit depends also on the chosen MSSM parameters, since the neutralino exchange in the t-channel may also contribute to the cross-section. From the data collected at LEP 2, the ALEPH experiment derived a lower limit of 96 GeV on the $\tilde{\mu}_R$ [446], and OPAL obtained a limit of 74 GeV for the same slepton mass [448], when a $LL\bar{E}$ coupling is considered to be dominant (Fig. 7.12).

From exclusion contours in the μ–M_2 plane, determined with the MSSM interpretation of the gaugino pair production results, after the analysis of the data collected up to 189 GeV, the L3 experiment sets indirect lower limit on the scalar lepton masses [447]. Fig. 7.13 shows how the lower limits on the mass of the supersymmetric partner of the right-handed electron are derived, taking into account the limits on M_2 as a function of m_0.

Contrary to the direct decays, the slepton indirect decays can be studied in any choice of the dominant coupling. As previously said, mainly the indirect decay into a neutralino (LSP) is searched for:

- indirect decay $\tilde{\nu} \to \nu\tilde{\chi}_1^0$, $\tilde{\chi}_1^0$ $\not{R}_p$ decay via any coupling,
- indirect decay $\tilde{\ell} \to \ell\tilde{\chi}_1^0$, $\tilde{\chi}_1^0$ $\not{R}_p$ decay via any coupling.

Then the final state depends on the slepton type (and flavor in case of charged sleptons), and mainly on the $\tilde{\chi}_1^0$ LSP decay. The efficiencies are determined in a $m_{\tilde{\chi}}$ versus $m_{\tilde{\nu}}$ ($m_{\tilde{\ell}}$) plane as well as the upper limit on the cross-section,
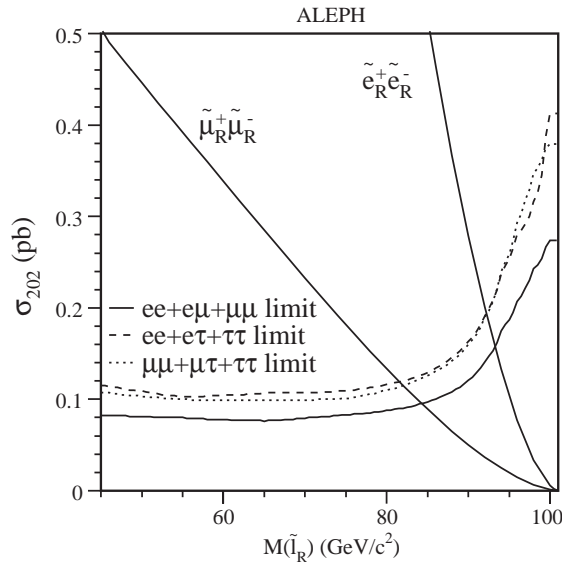
Fig. 7.12. Charged slepton direct decay searches with $LL\bar{E}$ couplings: the 95% *CL* exclusion cross-sections for sleptons. The MSSM cross-section for pair production of right-handed selectrons and smuons are superimposed [446].
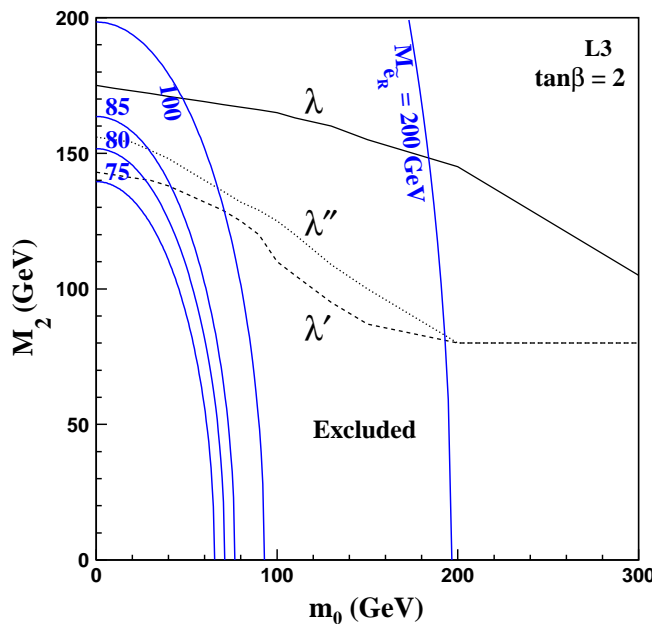
Fig. 7.13. Exclusion contours in the m_0-M_2 plane, for $\tan \beta = 2$, at 95% *CL*. The lines represent the isomasses of the supersymmetric partner of the right-handed electron (labelled with the corresponding value in GeV). The solid and dotted curves show the 95% *CL* lower limits on M_2 as a function of m_0 from which the limits on the scalar electron mass were derived [447].

which is compared to the MSSM cross-section, in order to exclude domains in the same $m_{\tilde{\chi}}$ versus $m_{\tilde{\nu}}$ ($m_{\tilde{l}}$) plane (see Fig. 7.14). The limit on the neutralino mass is used to set the limit on the sneutrino (slepton) mass in case of indirect decay. The results obtained on data collected in 1998, 1999 and 2000 [445–448] are summarized in Table 7.11.

The pair production of right selectrons followed by their decay in the presence of *R*-parity-violating couplings has been investigated for a 500 GeV e^-e^- linear collider (with possibly highly polarized beams) in Ref. [460].

At such a collider, a very strong suppression of the Standard Model background is expected and this could be further reduced by exploiting specific beam polarizations. The conservation of electric charge and lepton number actually forbid the pair production of most of supersymmetric particles at a e^-e^- collider: only selectrons can be produced via
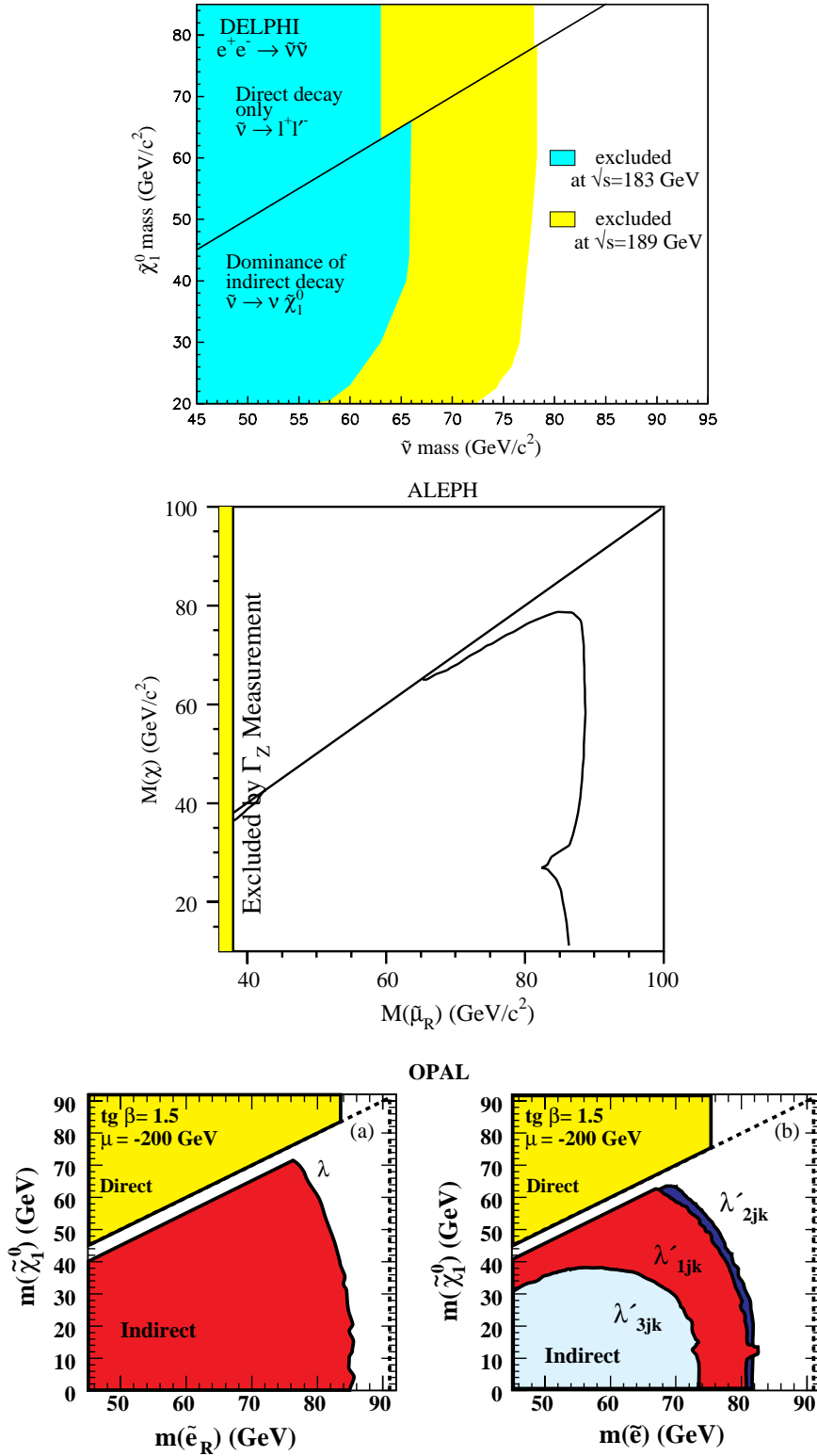
Fig. 7.14. Top: search for sneutrino decaying via a dominant $LL\bar{E}$ coupling in DELPHI; excluded region at 95% *CL* in $m_{\tilde{\nu}}$, $m_{\tilde{\chi}^0}$ plane by $\tilde{\nu}$ pair production for direct and indirect decays. The dark gray area shows the part excluded by the searches at $\sqrt{s} = 183$ GeV, the light gray area the one excluded by the searches at $\sqrt{s} = 189$ GeV. Middle: search for smuon decaying via a dominant $\bar{U}\bar{D}\bar{D}$ coupling in ALEPH; excluded region at 95% *CL* in $m_{\tilde{\chi}^0}$, $m_{\tilde{\mu}_R}$ plane. Bottom: search for selectron decaying indirectly via a dominant $LL\bar{E}$ (left) and $LQ\bar{D}$ (right) coupling in OPAL; MSSM exclusion region for selectron pair production in the $(m_{\tilde{\chi}^0}, m_{\tilde{\ell}})$ plane at 95% *CL*.

Table 7.11
95% *CL* lower limits (in GeV) on the slepton mass, considering the slepton indirect decay in lepton and lightest neutralino only

Experiments		ALEPH	DELPHI	L3	OPAL
DATA		1998–2000	1998–2000	1998–2000	1998–2000
$\tilde{\nu}_{\mu,\tau}$	$LL\bar{E}$	89	85	78	81
	$LQ\bar{D}$	78			
	$\bar{U}\bar{D}\bar{D}$	65		70	
$\tilde{e}_R$	$LL\bar{E}$	96	95	79	99
	$LQ\bar{D}$	93			92
	$\bar{U}\bar{D}\bar{D}$	94	92	96	
$\tilde{\mu}_R$	$LL\bar{E}$	96	90	87	94
	$LQ\bar{D}$	90			87
	$\bar{U}\bar{D}\bar{D}$	85	87	86	
$\tilde{\tau}_R$	$LL\bar{E}$	95		86	92
	$LQ\bar{D}$	76			
	$\bar{U}\bar{D}\bar{D}$	70		75	

the t-channel exchange of a neutralino. The pair production of selectrons has been studied in the hypothesis of *R*-parity violation. In case of $LL\bar{E}$ operator, the decay of the pair produced right selectrons will lead to final state consisting in $e^-e^- + 4\ell^\pm + E_{\text{miss}}$, where the flavor of $\ell^\pm$ depend on the particular type of coupling. This kind of final state is free from Standard Model background and permit an easy detection at a 500 GeV e^-e^- collider. In case of a dominant $LQ\bar{D}$ operator, the final state consists of charged leptons, multiple jets and/or missing energy, and in addition, the Majorana nature of the LSP gives rise to like-sign dilepton signal, with almost no background from Standard Model. In case of a dominant $\bar{U}\bar{D}\bar{D}$ operator, the final state consists of multiple jets associated to like-sign dielectrons. In both $LQ\bar{D}$ and $\bar{U}\bar{D}\bar{D}$ cases, it might be possible to give an estimate for the LSP mass from invariant mass reconstruction.

7.4.2.3. Squark searches at lepton colliders. $\not{R}_p$ decays of pair-produced squarks have been searched for in e^+e^- collisions at LEP 2. Special emphasis has been given to the $\tilde{t}$ and $\tilde{b}$ as they could possibly be the lightest squarks.

For squarks of the third generation, the $\tilde{f}_L$–$\tilde{f}_R$ mixing cannot be neglected. Hence a mixing angle must be taken into account for the pair production cross-section. This parameter will consequently enter as a free parameter when deriving experimental squark mass limits.

The results obtained at LEP 2 for the searches of both squark direct and indirect decays are reviewed in the following.

For small couplings ($< \mathrm{O}(10^{-1})$) the $\tilde{t}$ hadronises into colorless bound states before decaying (see Section 7.3.1), producing additional hadronic activity in the decay. Another consequence of the small width of the $\tilde{t}$ indirect decay ($\tilde{t} \to c\tilde{\chi}_1^0$) is that, unusually, the direct decay dominates over the indirect decay for a large range of coupling values ($> \mathrm{O}(10^{-5})$). On the contrary the indirect decay of the $\tilde{b}$ ($\tilde{b} \to b\tilde{\chi}_1^0$) dominates whenever kinematically possible.

As no quark superfield enters in the $LL\bar{E}$ term of the $\not{R}_p$ superpotential, there is no direct two-body decay of squark via a λ coupling. The $LQ\bar{D}$ and $\bar{U}\bar{D}\bar{D}$ terms can be responsible for squark direct decays. In the first case, the final states consist of two jets and charged lepton(s) and/or missing energy: the three possibilities are listed in Table 7.6. In the stop pair production searches, only the channels with two charged leptons were considered. Highest efficiencies are obtained for final states containing electrons (λ'_{13k}) or muons (λ'_{23k}); final states with two taus (λ'_{33k}) are more problematic and consequently have lower efficiency and lead to weakest limits. Using the efficiencies determined for different stop masses, an upper limit on the stop pair production cross-section can be set at 95% *CL* as a function of the stop mass. Then, considering the cross-section for the stop pair production (e.g. in the framework of the MSSM) and in case of no mixing and maximal decoupling to the *Z* boson, a lower limit on the stop mass can be derived. In the tau channel, a stop mass lower than 96 GeV has been excluded by OPAL [448] for any mixing angle using the data recorded in 1999 and 2000. At a center-of mass energy from 189 to 209 GeV, considering also the tau channel, but in a no mixing scenario, stop masses lower than 97 GeV are excluded by ALEPH [446].

Via a $\bar{U}\bar{D}\bar{D}$ term, the stop decays directly into two down quarks and the sbottom into an up and a down quark. The signature for the pair production of squarks is therefore four hadronic jets. Selections for these types of topologies rely

mainly on reconstructing the mass of the decaying squark by forcing the event to four jets and forming the invariant masses between pairs of jets. For couplings involving a *b*-quark in the final state "*b*-tagging" algorithms based on requiring large impact parameter tracks are also helpful to separate signal from the large background coming from two-quark and four-quark Standard Model processes. In "flavor blind" searches, the cross-section limits degraded in the range of W mass. For direct decay via a $\bar{U}\bar{D}\bar{D}$ interaction (λ'' coupling), stop masses lower than 77 GeV have been excluded by OPAL [448] for any mixing angle using the data recorded in 1999 and 2000.

Assuming that the lightest neutralino $\tilde{\chi}_1^0$ is the LSP, the squark indirect decay into a quark and a neutralino with the subsequent $\not{R}_p$ decay of the neutralino, has been studied. As any squark field can couple to the $\tilde{\chi}_1^0$, there are no restrictions related to the squark "chirality". Final states for each coupling consist of the corresponding fermions from the neutralino pair decay plus two jets.

In case of $LL\bar{E}$ coupling, the relevant final states are two hadronic jets +4 leptons + missing energy. Six jets are expected with a $LQ\bar{D}$ coupling, together with two charged leptons and no missing energy or 0–1 lepton + missing energy. Pure hadronic final states consisting of eight jets are expected in case of $\bar{U}\bar{D}\bar{D}$ couplings.

Using the efficiencies determined in the ($m_{\tilde{t}}$, $m_{\tilde{\chi}_1^0}$) plane, upper limit on the stop pair production cross-section can be derived as a function of the stop and neutralino masses (taking $\mu = -200$ GeV and $\tan\beta = 1.5$). Considering the MSSM cross-section for the stop pair production in case of no mixing and in case of a maximal decoupling to the Z boson exclusion contours were derived in the $m_{\tilde{t}}$, $m_{\tilde{\chi}_1^0}$ plane. By combining the exclusion contours with the result on the neutralino mass limit, a lower bound on stop mass can be derived.

From the analysis of the events collected at a center-of-mass energy from 189 GeV to 209 GeV, in the hypothesis of a dominant $LL\bar{E}$ coupling, a left-handed stop lighter than 91 GeV at 95% *CL* has been excluded by ALEPH [446]. ALEPH, DELPHI and L3 have performed the search for stop and sbottom indirect decays in the hypothesis of a dominant $\bar{U}\bar{D}\bar{D}$ coupling. Using the limit on the neutralino mass (32 GeV) from the gaugino searches, DELPHI set lower bounds on the squark masses with $m_{\tilde{q}} - m_{\tilde{\chi}_1^0} > 5$ GeV (Fig. 7.15). The lower mass limit on the stop (sbottom) is 87 GeV (78 GeV) in case of no mixing, and 77 GeV in case of maximal Z-decoupling. The study of indirect decay of left-handed stop and sbottom by ALEPH lead to exclude stop and sbottom lighter than 71 GeV at 95% *CL* (Fig. 7.15).

In view of the limitations posed on center-of-mass energies and luminosities by e^+e^- collider technologies, the case of a high energy $\mu^+\mu^-$ collider using storage rings has been considered. The phenomenology of supersymmetry with $\not{R}_p$ at a $\mu^+\mu^-$ collider resembles very much to the one at a e^+e^- collider. *R*-parity violation can manifest itself via either (a) pair-production of supersymmetric particles followed by $\not{R}_p$ decays or (b) resonant and non-resonant production of a single supersymmetric particle or finally (c) virtual effects in four fermions processes. The case (a) is discussed below. Cases (b) and (c) will be discussed in Sections 7.5–7.6.

The discussion of pair-production of supersymmetric particles followed by $\not{R}_p$ decays for $\mu^+\mu^-$ colliders is analogous in most of the aspects to the one for e^+e^- colliders and can be found in 7.3. However, unlike e^+e^- colliders, a particular feature of $\mu^+\mu^-$ colliders stems from the possible s-channel production of the *CP*-even (h^0 and H^0) or *CP*-odd (A^0) Higgs bosons of e.g. the MSSM. The Higgs boson produced would then decay into a pair of supersymmetric particles in processes like $h^0(H^0, A^0) \to \tilde{\chi}^+\tilde{\chi}^-$, $\tilde{\chi}^o\tilde{\chi}^o$, $\tilde{u}^c\tilde{u}$, $\tilde{d}^c\tilde{d}$, $\tilde{l}^c\tilde{l}$, etc, where $\tilde{u}$ and $\tilde{d}$ denote generically up-type down-type squarks respectively. The supersymmetric particles themselves would then undergo $\not{R}_p$ decays according to Tables 7.2 and 7.3. The analysis of these specific pair production of supersymmetric particles is governed by the analysis of the Higgs bosons decay widths with respect to the parameters of the minimal supersymmetric extension of the Standard Model into consideration [461]. The results of this analysis have then to be merged with the more familiar analysis of pair production of supersymmetric particles from ordinary processes arising from $\mu^+\mu^-$ annihilation (either γ and Z in the s-channel or sfermions or gauginos in the t-channel) as in the case of e^+e^- annihilation.

Additional Higgs bosons decays may also come into consideration such as $H^\pm \to W^\pm h^0$, $A^0 \to Zh^0$, $H^0 \to h^0h^0$ and $H^0 \to A^0A^0$ which may lead to the production of a pair of supersymmetric particles in association with a gauge boson or to the production of four supersymmetric particles and thus to more complicated signature when $\not{R}_p$ decays are switched on. We refer the reader to [461] for the calculation of the cross-section $\mu^+\mu^- \to higgs$ as well as the Higgs bosons total width.

7.4.2.4. Sfermion and Gluino pair production at Hadron colliders. Following the observation of an excess of high Q^2 events at HERA experiments [462,463], the CDF collaboration examined two scenarii with $\lambda'_{121} \neq 0$ using 107 pb^{-1}
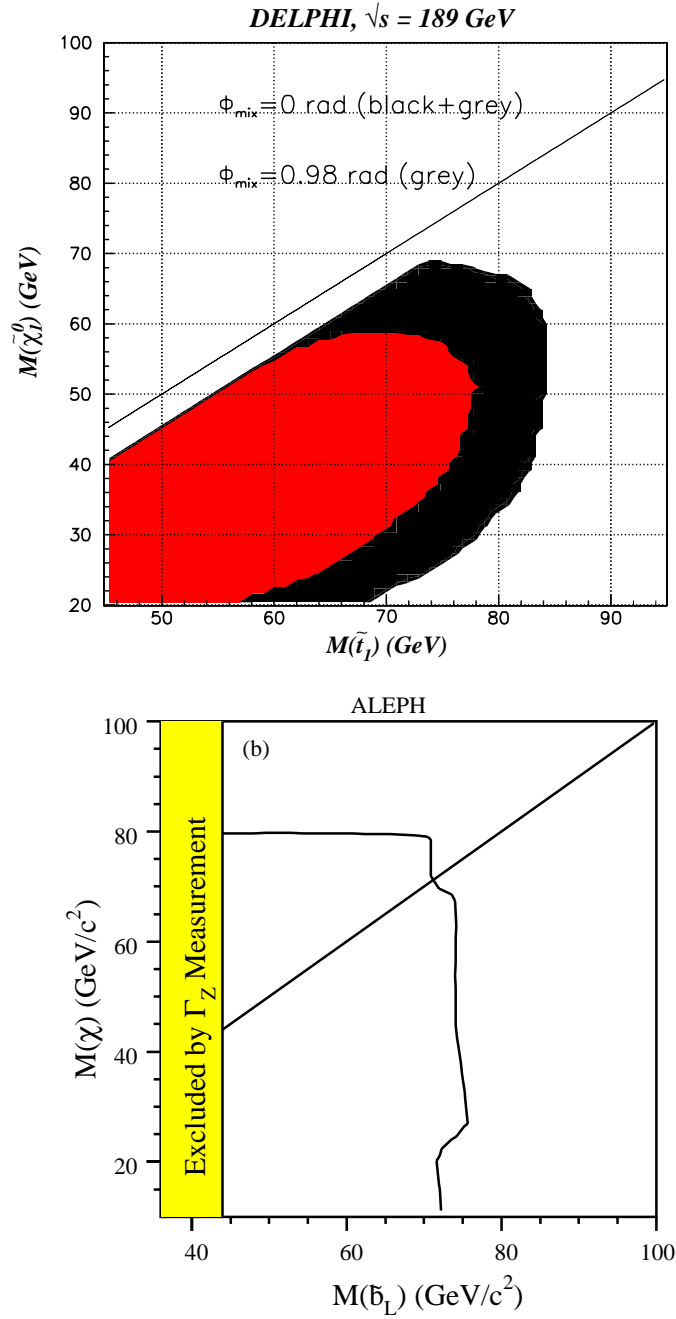
Fig. 7.15. Top: search for stop decaying indirectly via a dominant $\bar{U}\bar{D}\bar{D}$ operator in *DELPHI*; excluded region at 95% *CL* in $m_{\tilde{\chi}^0}$ versus $m_{\tilde{t}}$ plane; the largest excluded area corresponds to the case of no mixing and the smallest one to the case with the mixing angle which gives a minimum cross-section. Bottom: search for left-handed sbottom decaying indirectly via a dominant $\bar{U}\bar{D}\bar{D}$ operator in ALEPH; the 95% *CL* exclusion cross-sections is shown in the $m_{\tilde{\chi}^0}$ versus $m_{\tilde{b}_L}$ plane.

of data [464]:

$$p\overline{p} \to \tilde{g}\tilde{g} \to (c\tilde{c}_L)(c\tilde{c}_L) \to c(e^{\pm}d)c(e^{\pm}d) \tag{7.8}$$

and

$$p\overline{p} \to \tilde{q}\tilde{\bar{q}} \to (q\tilde{\chi}_1^0)(\overline{q}\tilde{\chi}_1^0) \to q(dce^{\pm})\overline{q}(dce^{\pm}) \ . \tag{7.9}$$
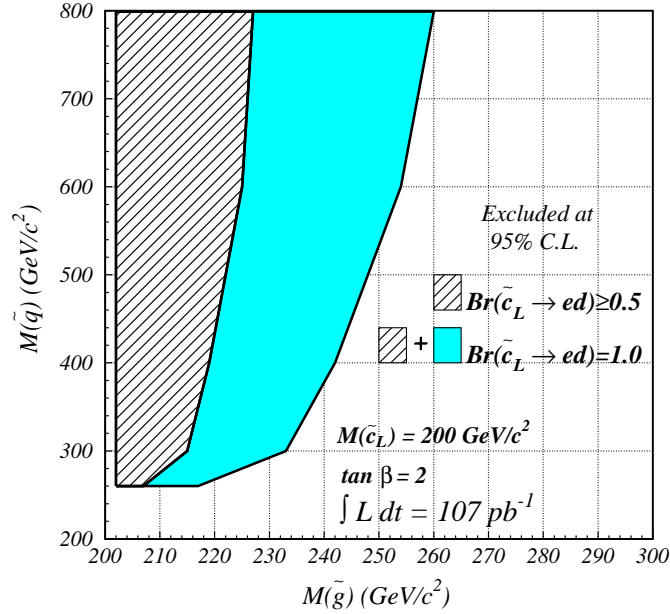
Fig. 7.16. Exclusion region in the plane $m_{\tilde{g}}$–$m_{\tilde{q}}$ for the charm squark analysis of the CDF collaboration.

For process (7.8) assumptions made were $m_{\tilde{q}} > m_{\tilde{g}} > m_{\tilde{c}_L} = 200$ GeV, where degenerate mass for all up-type squarks (except $\tilde{c}_L$) and all right-handed down-type squarks is denoted by $m_{\tilde{q}}$. The masses of all left-handed down-type squarks were obtained by using the HERA motivated relations given in [465]. For analysing process (7.9) assumptions made were $m_{\tilde{\chi}_1^\pm} > m_{\tilde{q}} > m_{\tilde{\chi}_0}$ and $m_{\tilde{\chi}_1^\pm} \simeq 2m_{\tilde{\chi}_0}$. Five degenerate squarks and the stop were treated separately. In the case of the process involving stop to ensure 100% branching ratio for the decay $\tilde{t}_1 \rightarrow c\tilde{\chi}_1^0$ when $m_{\tilde{t}_1} < m_t$, an additional condition that $m_{\tilde{\chi}_1^\pm} > m_{\tilde{t}_1} - m_b$ was imposed.

The Majorana nature of gluino and neutralino implies processes (7.8) and (7.9) each yield like sign dielectron and opposite sign dielectron with equal probability. Since the like-sign dilepton signature has very little SM background, for both processes (7.8) and (7.9) CDF searched for events with like sign dielectrons and at least two jets.

Analysis of 107 pb^{-1} data yields no event with an expected contribution of 0.3 ± 0.3 events from backgrounds. Exclusion contours obtained for process (7.8) are shown in Fig. 7.16 in the $m_{\tilde{g}}$–$m_{\tilde{q}}$ plane for different assumptions for the $Br(\tilde{c}_L \rightarrow ed)$. The region below $m_{\tilde{q}} \leqslant 260$ GeV is not excluded because in this region $\tilde{b}_L$ becomes lighter than $\tilde{c}_L$, hence suppressing the decay $\tilde{g} \rightarrow c\tilde{c}_L$. Fig. 7.17 (bottom) shows the 95% CL upper limit on the cross-section times branching ratios (obtained for process (7.9)) along with the NLO prediction [466] for the cross-section, as a function of squark masses. 95% CL lower limits are given for two different masses of the lightest neutralino.

A lower limit on the degenerate squark mass was found to be in the range of 200–260 GeV depending on the mass of the lightest neutralino and gluino (range of gluino mass considered was 200–1000 GeV). Fig. 7.17 (top) shows also a similar plot in the case of the stop. The mass of the stop was excluded below 135(120) GeV for a heavy (light) neutralino. The analysis for process (7.9) has been performed for the Tevatron Run II in [467]: it shows that squark masses up to 380 GeV should be tested. Finally, one point to note here is that, although the analysis for process (7.9) assumed only one $\not{R}_p$ coupling λ'_{121} to be non-zero, as the analysis does not depend on the quark flavors, the results are equally valid for any λ'_{1jk} ($j = 1, 2$ and $k = 1, 2, 3$) couplings.

DØ [468] considered squark pair production leading in $\not{R}_p$-SUGRA to like-sign dielectron events accompanied by jets, and has ruled out $M_{\tilde{q}} < 243$ GeV (95% CL) when assuming five degenerate squark flavors. The DØ analysis covers all λ'_{1jk} couplings. From a similar analysis by CDF [469] but restricted to $\lambda'_{121} \neq 0$, one can infer that a cross-section five times smaller would lead to a $M_{\tilde{q}}$ limit of $\simeq 150$ GeV depending on the gluino and $\tilde{\chi}_0$ masses.

CDF also considered separately [469,464] the pair production of a light stop $\tilde{t}_1$ assuming a decay into $c\tilde{\chi}_1^0$ and excluded $M_{\tilde{t}} < 135$ GeV. To translate this constraint in one relevant for $\lambda'_{13k} \neq 0$, it should be noted that in this latter case, $\not{R}_p$-decays of the $\tilde{t}$ would dominate over loop decays into $c\tilde{\chi}_1^0$. Moreover, $\not{R}_p$-decays would themselves be negligible compared to $\tilde{t} \rightarrow b\tilde{\chi}_1^+$ decays as soon as this becomes allowed, i.e. if $M(\tilde{t}_1) > M(\tilde{\chi}_1^+)$ and if the $\tilde{t}_1$ eigenstate possesses
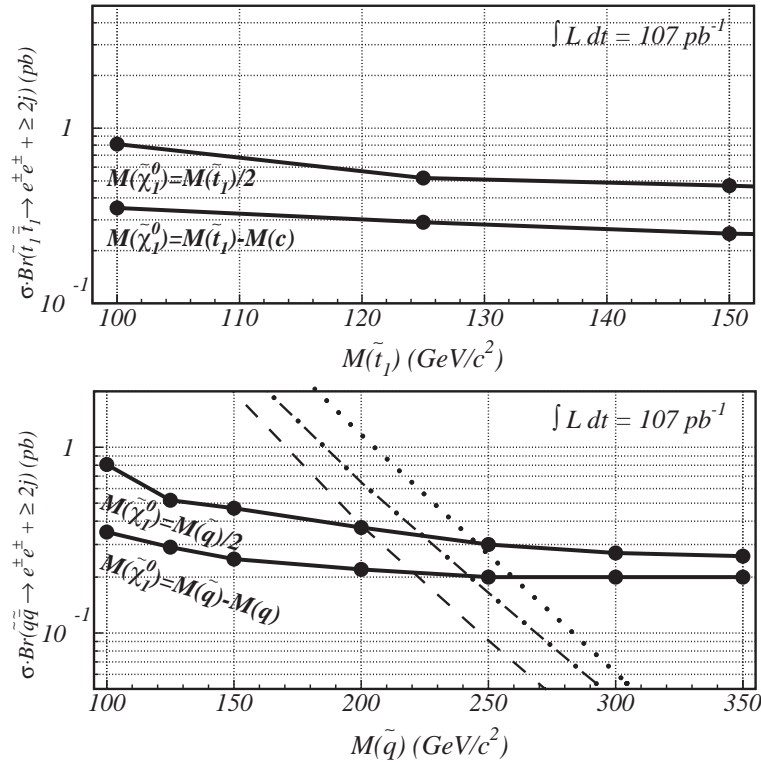
Fig. 7.17. Bottom: upper limits on the cross-section times branching ratio for the production of 5 degenerate squark flavors decaying to electrons and jets via neutralinos (solid lines). Also shown is the theoretical prediction for $\sigma \cdot Br$ for three values of the gluino mass: 200 GeV (dotted line), 500 GeV (dot–dashed line), and 1 TeV (dashed line). Top: upper limits on the cross-section times branching ratio for stop pair production decaying to electrons and jets via neutralinos (solid lines). The dashed curve is the theoretical prediction.

a sizeable admixture of $\tilde{t}_L$. The subsequentdecays of the $\tilde{\chi}_1^+$ would then lead to final states similar to those studied by CDF for $\tilde{t}_1 \to c\tilde{\chi}_1^0$. Thus, $130 - 150$ GeV appears to be reasonable rough estimate of the Tevatron sensitivity to a light $\tilde{t}$ for $\lambda'_{13k} \neq 0$. In summary, Tevatron and HERA sensitivities are competitive in $\not{R}_p$-SUSY models with five degenerate squarks, but models predicting a light $\tilde{t}$ are better constrained at HERA provided that λ'_{13j} is not too small.

In the above mentioned search by the $D\emptyset$ experiment [450] in the dimuon plus four-jets channel (occurring after $\tilde{\chi}_1^0$decay via the λ' coupling, see Section 7.4.1), it was seen that squark masses below 240 GeV (for all gluino masses and for $\tan\beta = 2$) are excluded. For equal masses of squarks and gluinos the mass limit is 265 GeV.

In contrast with the above studies of the λ' coupling constants which were based on the analysis of a given superpartner pair production, the $D\emptyset$ Collaboration has performed a study of the λ'_{1jk} and λ'_{2jk} ($j = 1, 2$ and $k = 1, 2, 3$) couplings based on the Monte Carlo simulation of all the superpartner pair productions [467,470]. In this work, it was assumed that the LSP is the lightest neutralino. The exclusion plot obtained in [467,470] in the case of a single dominant $\not{R}_p$ coupling of type λ'_{1jk} is presented in Fig.7.18. In this case, the studied final state is composed of 2 $e^\pm$ and at least 4 jets. We observe in Fig.7.18 that the $D\emptyset$ Collaboration is expected to search for squarks of mass up to 575 GeV and gluinos of mass up to 520 GeV. In the case of a single dominant $\not{R}_p$ coupling of type λ'_{2jk}, it was shown in [467,470] that the analysis of the dimuon plus four jets signature leads to the expectation that squarks of mass up to 640 GeV and gluinos of mass up to 560 GeV will be tested by the $D\emptyset$ Collaboration during the Tevatron Run II.

7.4.3. Effects of bilinear $\not{R}_p$ interactions

Search for spontaneous $\not{R}_p$ violation has been performed at LEP 2 by the DELPHI experiment [471].

This search is based on the model described in Refs. [63,64], in which $\not{R}_p$ breaking is parametrized by effective bilinear terms $\mu_i L_i H_u$ (see Section 2.4 for a theoretical review of this model). The most important phenomenological implication of the model is the existence of a massless Majoron J which is the LSP. Therefore the Majoron enters in the chargino and neutralino decays and the branching ratios of these new processes depend on an effective bilinear term parameter denoted by ϵ in Refs. [63,64,471]. In the case where the ϵ parameter is sufficiently high, roughly for $\epsilon > 10$ GeV the
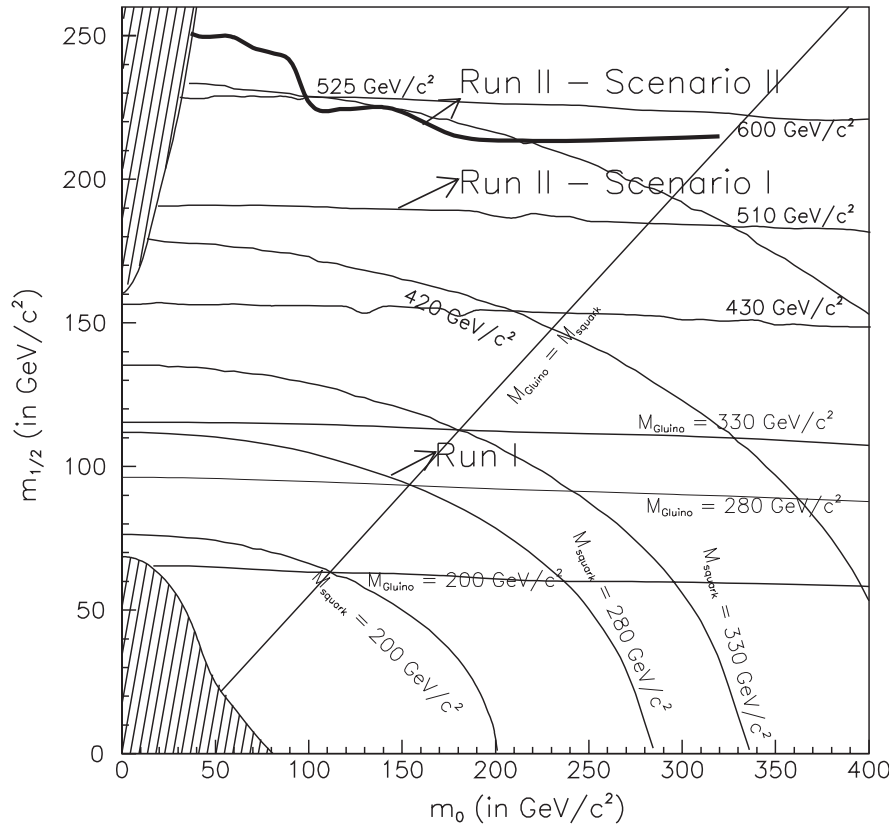
Fig. 7.18. Estimated exclusion contour for Tevatron Run I and II, within the mSUGRA framework, in the $(m_0, m_{1/2})$ plane for $\tan\beta = 2$, $A_0 = 0$ and $\mu < 0$, from the dielectron and four jets channel. Scenario I corresponds to a background of $36 \pm 4 \pm 6$ events (direct scaling from Run I) while scenario II uses the background of $15 \pm 1.5 \pm 1.5$ events (scaling, but with improvements in the detector taken into account).

chargino decay is fully dominated by the Majoron channel: $\tilde{\chi}^{\pm} \to \tau^{\pm} J$. Therefore, the experimental signature of the chargino pair production in this scenario is two acoplanar taus and missing momentum from the undetected Majorons. One should note, however, that such values of the ϵ parameter are incompatible with the cosmological bound on stable neutrino masses, and can arise only in the context of exotic scenarios with a heavy decaying neutrino ($m_\nu \sim 1\,\text{MeV}$).

The search for spontaneous $\not{R}_p$ violation in DELPHI was performed in the MSSM framework [471]. An upper limit at 95% CL on the chargino production cross-section of 0.3 pb and on the chargino mass of 94 GeV (close to the kinematic limit for 1998 data) has been obtained.

Before closing the discussion on the possible effects of bilinear $\not{R}_p$ interactions at lepton colliders, it is interesting to come back to the case of resonant higgs production at $\mu^+\mu^-$ colliders discussed above in the presence of trilinear $\not{R}_p$ interactions. The effects of bilinear terms from spontaneously broken R-parity would lead to invisible signature when $h^0 \to JJ$ where J stands for the Majoron. Furthermore, possible signatures with missing energies, when for example $\mu^+\mu^- \to H^0 \to h^0 h^0$, followed by $h^0 \to JJ$ for one of the h^0 and by $h^0 \to \tilde{\chi}_1^+ \tilde{\chi}_1^-$ for the other h^0, with the subsequent decay $\tilde{\chi}_1^+ \to \tau^+ J$, deserve further studies.

Effects of bilinear $\not{R}_p$ interactions could be observed already at existing hadron colliders. Current data from Tevatron Run I are already sensitive to these decays and effectively limits the total branching ratio of top decays in different channels than $t \to W^+ b$ to approximately 25%. The Tevatron Run II data will enhance the sensitivity for alternative top decays to branching ratios of 10^{-3}–10^{-2} depending on the decay mode. If the stop is lighter than the lightest chargino it may decay dominantly through $\tilde{t}_1 \to \tau^+ + b$. By interpreting the stop as a third generation leptoquark, the exclusion obtained from leptoquark searches can in this case be applied [472,473]. This leads to an exclusion of scalar-stop masses below 80–100 GeV from the Run I data. Here too, the Run II data will improve the sensitivity to a wider region of the SUSY parameter space.

Table 7.12
Sfermions s-channel resonant production at colliders

Resonant production of sfermions at colliders (Lowest-order processes)				
Collider	Coupling	Sfermion type	Elementary process	
e^+e^-	λ_{1j1}	$\tilde{\nu}_\mu, \tilde{\nu}_\tau$	$l_i^+ l_k^- \to \tilde{\nu}_j$	$i=k=1, \ j=2,3$
$pp, p\bar{p}$	λ'_{ijk}	$\tilde{\nu}_e, \tilde{\nu}_\mu, \tilde{\nu}_\tau$	$d_k \bar{d}_j \to \tilde{\nu}_i$	$i, j, k = 1, \ldots, 3$
		$\tilde{e}, \tilde{\mu}, \tilde{\tau}$	$u_j \bar{d}_k \to \tilde{l}_{iL}$	$i, k = 1, \ldots, 3, \ j = 1, \ldots, 2$
	λ''_{ijk}	$\tilde{d}, \tilde{s}, \tilde{b}$	$\bar{u}_i \bar{d}_j \to \tilde{d}_k$	$i, j, k = 1, \ldots, 3, \ j \neq k$
		$\tilde{u}, \tilde{c}, \tilde{t}$	$\bar{d}_j \bar{d}_k \to \tilde{u}_i$	$i, j, k = 1, \ldots, 3, \ j \neq k$
ep	λ'_{1jk}	$\tilde{d}_R, \tilde{s}_R, \tilde{b}_R$	$l_1^- u_j \to \tilde{d}_{kR}$	$j = 1, 2$
	λ'_{1jk}	$\tilde{u}_L, \tilde{c}_L, \tilde{t}_L$	$l_1^+ d_k \to \tilde{u}_{jL}$	$i, j, k = 1, \ldots, 3$

Charge conjugate processes (not listed here) are also possible. Real $\tilde{\nu}$ production at an e^+e^- collider can only proceed via λ_{121} or λ_{131}. In $e\gamma$ collisions all λ_{ijk} couplings where i, j or k is equal to one can be probed. The $e\gamma$ collision mode opens new possibilities, such as the single production of the $\tilde{\nu}_e$ via λ_{i11} or the single slepton production. Single squark production is also possible via a λ'_{1jk} coupling. Real $\tilde{q}$ production at an ep collider is possible via any of the nine λ'_{1jk} couplings.

7.5. Single sparticle production

New $\not{R}_p$ trilinear interactions enter directly in sparticle production and decays via basic tree diagrams as was illustrated in Fig. 2.1. The corresponding complete interaction Lagrangian is discussed in detail in Section 2.1 and Appendix B. The most striking feature of $\not{R}_p$ is to allow for single production of supersymmetric particles. For given center-of-mass collider energies, this extends the discovery mass reach for supersymmetric matter beyond that of superpartner pair production in R-parity conserving models.

A list of the s-channel processes allowed at lowest order in e^+e^-, ep and $p\bar{p}$ collisions is given in Table 7.12. The L-violating ($\not{L}$) term $LL\bar{E}$ couples sleptons and leptons (Fig. 2.1a). It allows for resonant production of $\tilde{\nu}$ at l^+l^- colliders and for the direct $\not{R}_p$-decay of sleptons $\tilde{l}^\pm \to l'^\pm \nu$ and $\tilde{\nu} \to l^+ l'^-$. The $\not{L}$ term $LQ\bar{D}$ couples squarks to lepton–quark pairs (Fig. 2.1b) and sleptons to quark pairs. It allows for resonant production of $\tilde{q}$ at ep colliders and $\tilde{\nu}$ or $\tilde{l}^\pm$ at pp colliders. Direct $\not{R}_p$-decay of squarks via $\tilde{q} \to lq'; \nu q''$ or sleptons via $\tilde{l}^\pm$ or $\tilde{\nu} \to qq'$ are made possible. The B-violating ($\not{B}$) term $\bar{U}\bar{D}\bar{D}$ couples squarks to quark pairs (Fig. 2.1c). It allows for resonant production of $\tilde{q}$ at pp colliders and direct $\not{R}_p$-decay of squarks via $\tilde{q} \to q'q''$.

Moreover, as seen in Sections 7.3.1 and 7.3.2, there is a gap between the constraints obtained via the detection of the displaced vertex and the low-energy experimental constraints on the $\not{R}_p$ couplings. This domain can be tested through the study of the single production of supersymmetric particles. Indeed, the cross-sections of such reactions are directly proportional to a power of the relevant $\not{R}_p$ coupling constant(s), which allows to determine the values of the $\not{R}_p$ couplings. Therefore, there exists a complementarity between the displaced vertex analysis and the study of singly produced sparticles, since these two methods allow to investigate different ranges of values of the $\not{R}_p$ coupling constants.

For values beyond $\mathcal{O}(10^{-4})$, single sparticle production will allow in favorable cases to determine or constrain specific λ, λ' or λ'' couplings as will be discussed in more details in Sections 7.5.1 and 7.5.2. Otherwise, the presence of such a large $\not{R}_p$ coupling will become trivially manifest through the decay of pair produced sparticles.

7.5.1. Single sparticle production at leptonic colliders

At leptonic colliders resonant (as well as non-resonant) production of single supersymmetric particles involve the λ_{ijk} couplings.

Early discussions on several R_p-violating processes at e^+e^- colliders including single supersymmetric particles production can be found in [458,459].

At a e^+e^- leptonic colliders, the sneutrinos $\tilde{\nu}_\mu$ and $\tilde{\nu}_\tau$ can be produced at resonance through the couplings λ_{211} and λ_{311}, respectively. The sneutrino may then decay either via an $\not{R}_p$ interaction [261], for example through λ_{ijk} as, $\tilde{\nu}^i \to \bar{l}_j l_k$, or via gauge interaction as, $\tilde{\nu}_L^i \to \tilde{\chi}_a^+ l^i$, or, $\tilde{\nu}_L^i \to \tilde{\chi}_a^0 \nu_L^i$. The sneutrino partial width is given in Eq. (7.1) for

the leptonic decay channel and is given in the following equation for the gauge decay channel [254]:

$$\Gamma(\tilde{v}_L^i \rightarrow \tilde{\chi}_a^+ l^i, \; \tilde{\chi}_a^0 v_L^i) = \frac{C g^2}{16\pi} m_{\tilde{v}_L^i} \left(1 - \frac{m_{\tilde{\chi}_a^+}^2}{m_{\tilde{v}_L^i}^2} \right)^2 , \tag{7.10}$$

where $C = |V_{a1}|^2$ for the decay into chargino and $C = |N_{a2}|^2$, for the neutralino case, with V_{a1} and N_{a2} the mixing matrix elements written in the notations of [25]. For reasonable values of λ_{ijk} ($\leqslant 0.1$) and most of the region of the supersymmetric parameter space, the decay modes of Eq. (7.10) are dominant, if kinematically accessible [474,254]. In the SUGRA parameter space, if $m_{\tilde{v}_L^i} > 80$ GeV, with $M_2 = 80$ GeV, $\mu = 150$ GeV and $\tan \beta = 2$, the total sneutrino width is higher than 100 MeV which is comparable to or greater than the typical expected experimental resolutions. The cross-section formula, for the sneutrino production in the s-channel, is the following [254]:

$$\sigma(e^+ e^- \rightarrow \tilde{v}_L^i \rightarrow X) = \frac{4\pi s}{m_{\tilde{v}_L^i}^2} \frac{\Gamma(\tilde{v}_L^i \rightarrow e^+ e^-)\Gamma(\tilde{v}_L^i \rightarrow X)}{(s - m_{\tilde{v}_L^i}^2)^2 + m_{\tilde{v}_L^i}^2 \Gamma_{\tilde{v}_L^i}^2} , \tag{7.11}$$

where $\Gamma(\tilde{v}_L^i \rightarrow X)$ generally denotes the partial width for the sneutrino decay into the final state X. At sneutrino resonance, Eq. (7.11) takes the form

$$\sigma(e^+ e^- \rightarrow \tilde{v}_L^i \rightarrow X) = \frac{4\pi}{m_{\tilde{v}_L^i}^2} B(\tilde{v}_L^i \rightarrow e^+ e^-) B(\tilde{v}_L^i \rightarrow X) , \tag{7.12}$$

where $B(\tilde{v}_L^i \rightarrow X)$ generally denotes the branching ratio for sneutrino decay into a final state X.

Diagrams for the single sparticle production at leptonic colliders are shown in Fig. 7.19.

The case of resonant production of single supersymmetric particles at $\mu^+ \mu^-$ colliders resembles very much the one of $e^+ e^-$ colliders described above. The relevant decay widths and cross-section formulae are obtained respectively from Eqs. (7.10), (7.11) and (7.12) by replacing e^+ and e^- by μ^+ and μ^-.

The gauge decays of a resonantly produced sneutrino at leptonic colliders lead to single chargino or neutralino production, or to the production of a lighter slepton in association with an electroweak gauge boson when this is kinematically allowed. Away from the sneutrino resonance, other diagrams contribute to the single production of sparticles. The t-channel exchange of a slepton can lead to single chargino or neutralino production, and the t- or u-channel exchange of a lepton allows for single slepton production.

Single chargino and neutralino productions both receive contributions from the resonant sneutrino production at $e^+ e^-$ colliders (see Fig. 7.19a and b). The single production of a chargino, $e^+ e^- \rightarrow \tilde{\chi}_a^\pm l_j^\mp$ (via λ_{1j1}), receives a contribution from the s-channel exchange of a $\tilde{v}_{jL}$ sneutrino and another one from the exchange of a $\tilde{v}_{eL}$ sneutrino in the t-channel (see Fig. 7.19a). The single neutralino production, $e^+ e^- \rightarrow \tilde{\chi}_a^0 v_j$ (via λ_{1j1}), occurs through the s-channel $\tilde{v}_{jL}$ sneutrino exchange and also via the exchange of a $\tilde{e}_L$ slepton in the t-channel or a $\tilde{e}_R$ slepton in the u-channel (see Fig. 7.19b). The single $\tilde{\chi}_1^\pm$ ($\tilde{\chi}_1^0$) production rate is reduced in the higgsino dominated region $|\mu| \ll M_1, M_2$ where the $\tilde{\chi}_1^\pm$ ($\tilde{\chi}_1^0$) is dominated by its higgsino component, compared to the wino dominated domain $|\mu| \gg M_1, M_2$ in which the $\tilde{\chi}_1^\pm$ ($\tilde{\chi}_1^0$) is mainly composed by the higgsino [475]. In addition, the single $\tilde{\chi}_1^\pm$ ($\tilde{\chi}_1^0$) production cross-section depends weakly on the sign of the μ parameter at large values of $\tan \beta$. However, as $\tan \beta$ decreases the rates increase (decrease) for $sign(\mu) > 0$ (< 0). This evolution of the rates with the $\tan \beta$ and $sign(\mu)$ parameters is explained by the evolution of the $\tilde{\chi}_1^\pm$ and $\tilde{\chi}_1^0$ masses in the supersymmetric parameter space [475].

For $\lambda_{1j1} = 0.05$, 50 GeV $< m_0 < 150$ GeV and 50 GeV $< M_2 < 200$ GeV in a SUGRA parameter space, the off-pole values of the cross-sections are typically [475] of the order of 100 fb (10 fb) for the single chargino production and of 10 fb (1 fb) for the single neutralino production at $\sqrt{s} = 200$ GeV (500 GeV) (see Fig. 7.20).

At the sneutrino resonance, the cross-sections of the single gaugino production are important: using Eq. (7.12), the rate for the neutralino production in association with a neutrino is of the order of 3×10^3 in units of the QED point cross-section, $R = \sigma_{pt} = 4\pi\alpha^2/3s$, for $M_2 = 200$ GeV, $\mu = 80$ GeV, $\tan \beta = 2$ and $\lambda_{1j1} = 0.1$ at $\sqrt{s} = m_{\tilde{v}_L^j} = 120$ GeV [254]. The cross-section for the single chargino production reaches 2×10^{-1} pb at $\sqrt{s} = m_{\tilde{v}_L^j} = 500$ GeV, for $\lambda_{1j1} = 0.01$ and $m_{\tilde{\chi}^\pm} = 490$ GeV [458,476]. The initial state radiation (ISR) lowers the single gaugino production cross-section at
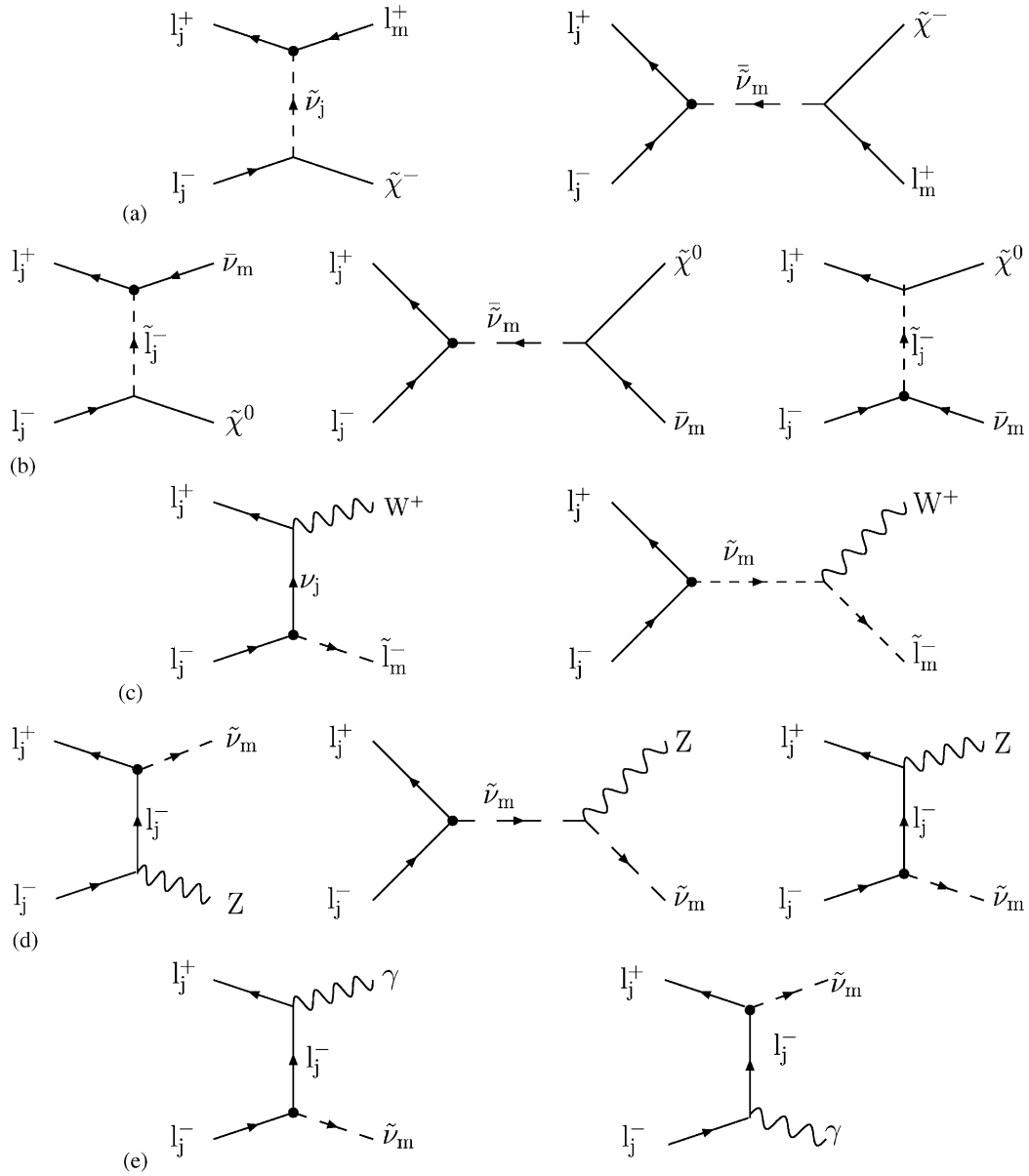
Fig. 7.19. Diagrams for the single production processes at leptonic colliders, namely, $l_j^+ l_j^- \to \tilde{\chi}^- l_m^+$ (a), $l_j^+ l_j^- \to \tilde{\chi}^0 \bar{\nu}_m$ (b), $l_j^+ l_j^- \to \tilde{l}_{mL}^- W^+$ (c), $l_j^+ l_j^- \to \tilde{\nu}_{mL} Z$ (d) and $l_j^+ l_j^- \to \tilde{\nu}_{mL} \gamma$ (e). The circled vertex corresponds to the $\not{R}_p$ interaction, with the coupling constant λ_{mjj}, and the arrows indicate the flow of the lepton number.

the $\tilde{\nu}$ pole but increases greatly the single gaugino production rate in the domain $m_{\text{gaugino}} < m_{\tilde{\nu}} < \sqrt{s}$. This ISR effect can be observed in Fig. 7.21 which shows the single charginos and neutralinos productions cross-sections as a function of the center-of-mass energy for a given MSSM point [474].

The experimental searches of the single chargino and neutralino productions have been performed at the LEP collider at various center-of-mass energies [477–479]. The off-pole effects of the single gaugino productions rates are at the limit of observability at the LEP collider even with the integrated luminosity of LEP 2. Therefore, the experimental analyzes of the single gaugino productions have excluded values of the λ_{1j1} couplings smaller than the low-energy bounds only at the sneutrino resonance point $\sqrt{s} = m_{\tilde{\nu}}$ and, due to the ISR effect, in a range of typically $\Delta m_{\tilde{\nu}} \sim 50\,\text{GeV}$ around the $\tilde{\nu}$ pole. Finally, for the various sneutrino resonances, the sensitivies on the λ_{1j1} couplings which have been derived from the LEP data reach values of order 10^{-3}. The experimental analyzes of the single chargino and neutralino productions will be continued at the future linear collider. Using its polarization capability as well as the specific kinematics of the single chargino production allows to reduce the expected background from pair productions
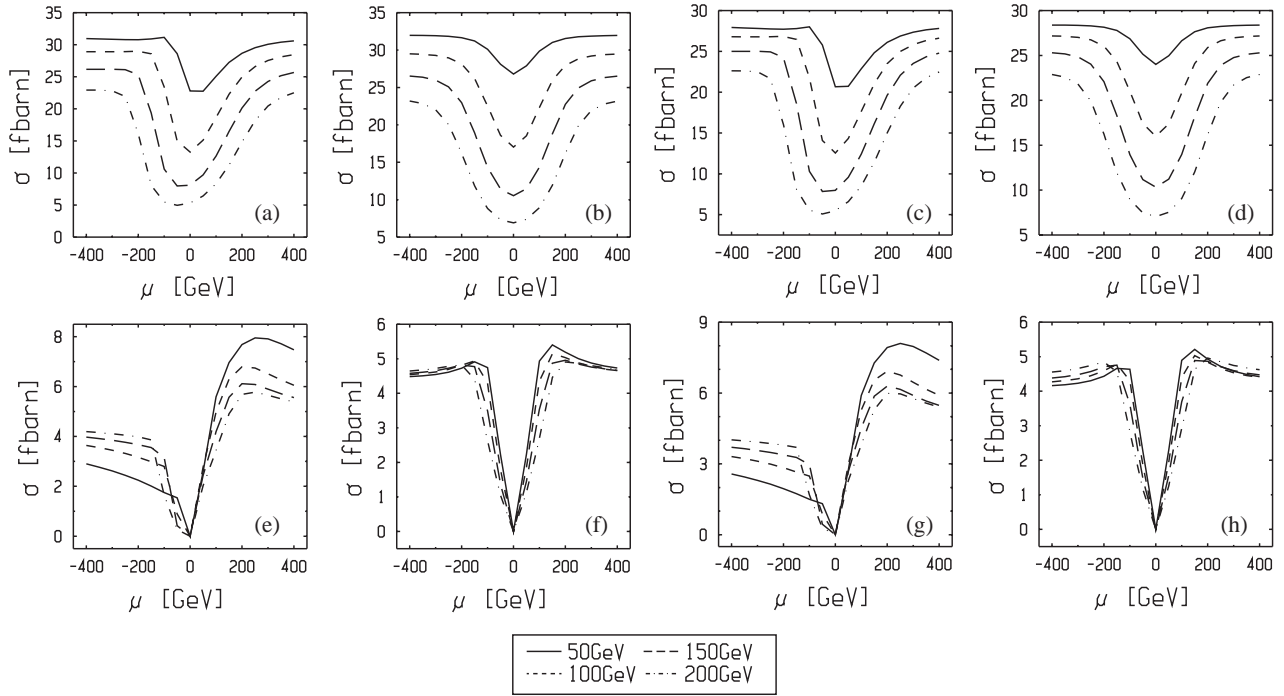
Fig. 7.20. The integrated cross-sections [475] for the processes (a, b, c and d) $e^+e^- \to \tilde{\chi}_1^- l_j^+$ and (e, f, g and h) $e^+e^- \to \tilde{\chi}_1^0 \bar{v}_j$, at a center-of-mass energy of 500 GeV, are shown as a function of μ for discrete choices of the remaining parameters: (a, e) $\tan\beta = 2$, $m_0 = 50$ GeV, (b, f) $\tan\beta = 50$, $m_0 = 50$ GeV, (c, g) $\tan\beta = 2$, $m_0 = 150$ GeV, and (d, h) $\tan\beta = 50$, $m_0 = 50$ GeV, with $\lambda_{1j1} = 0.05$. The windows conventions are such that $\tan\beta = 2$, 50 horizontally and $m_0 = 50$, 150 GeV vertically. The different curves refer to the value of M_2 of 50 GeV (continuous line), 100 GeV (dot–dashed line), 150 GeV (dotted line), as indicated at the bottom of the figure.

of supersymmetric particles. As an example, this background reduction allows to improve the sensitivity to the λ_{121} coupling obtained from the $\tilde{\chi}_1^\pm \mu^\mp$ production study at linear colliders [435] for $\sqrt{s} = 500$ GeV and $\mathscr{L} = 500$ fb^{-1} which then amounts to values of the order of 10^{-4} at the sneutrino resonance and can improve the low-energy constraint over a range of $\Delta m_{\tilde{v}} \approx\sim 500$ GeV around the $\tilde{v}$ pole [480]. Due to the high luminosities reached at linear colliders, the off-resonance contributions to the cross-section play an important role in the single $\tilde{\chi}_1^\pm$ production analysis.

The slepton and the sneutrino can also be singly produced via the coupling λ_{1j1} in the (non-resonant) reactions $e^+e^- \to \tilde{l}_{jL}^\mp W^\pm$, $e^+e^- \to \tilde{v}_L^j Z^0$ and $e^+e^- \to \tilde{v}_L^j \gamma$. Those reactions receive contributions from the exchange of a charged or neutral lepton of the first generation in the t- or u-channel (see Fig. 7.19). The single productions of a sneutrino accompanied by a Z or a W boson also occur through the exchange in the s-channel of a $\tilde{v}_L^j$ sneutrino which cannot be produced on-shell. When kinematically allowed, these processes have some rates of order 100 fb at $\sqrt{s} = 200$ GeV and 10 fb at $\sqrt{s} = 500$ GeV, for $\lambda_{1j1} = 0.05$ and various masses of the scalar supersymmetric particles [475].

The production of single gaugino and the non-resonant production of single slepton (either charged or neutral) similar to those in Fig 7.21 are relevant at $\mu^+\mu^-$ colliders. The only difference stems from the initial states particles which, being muons instead of electrons, allows to test different λ couplings as given in Table 7.13.

Leptonic colliders allow also for lepton–photon collisions in which sleptons and squarks can also be singly produced thus opening additional perspectives for $\not{R}_p$ coupling studies. For example [481] the processes $e^\pm \gamma \to l^\pm \tilde{v}, \tilde{l}^\pm v$, involving an on-shell photon radiated from one of the colliding leptons, allow to probe the $\lambda_{122}, \lambda_{123}, \lambda_{132}, \lambda_{133}$ and λ_{231} $\not{R}_p$ couplings which are otherwise not involved in the single sparticle productions from e^+e^- reactions.

The slepton or sneutrino production occurs either via the exchange of a charged lepton in the s-channel or the exchange of a charged slepton or lepton in the t-channel. Since the t-channel is dominant and $m_{\tilde{l}} \gg m_l$, the slepton production is about two order of magnitude less than the sneutrino production which is $\sigma(e^+e^- \to \tilde{v}_j e\tau) = 300$ fb at $\sqrt{s} = 500$ GeV.
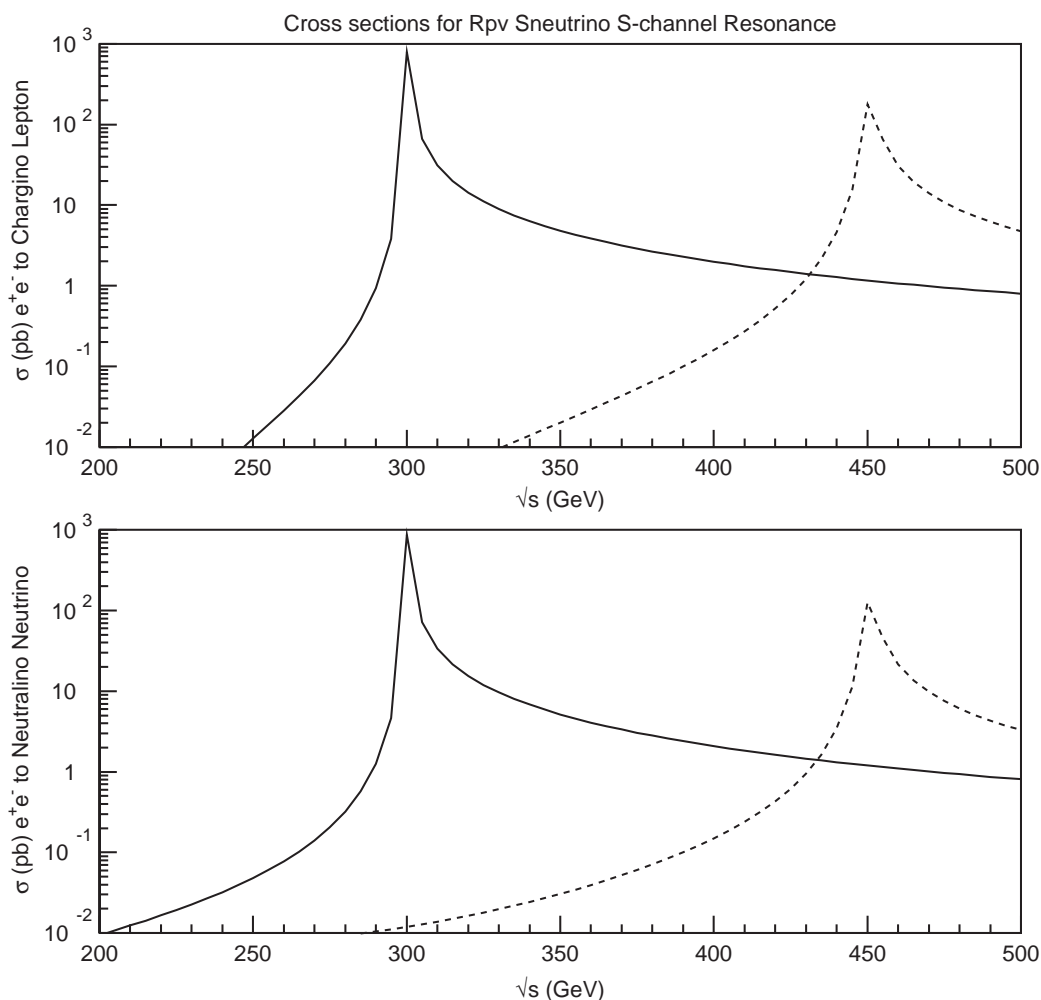
Fig. 7.21. Cross-sections of the single charginos and neutralinos productions as a function of the center-of-mass energy for $m_{\tilde{\nu}} = 300\,\text{GeV}$ (full curves) and $m_{\tilde{\nu}} = 450\,\text{GeV}$ (dashed curves) with $m_{\tilde{e}} = 1\,\text{TeV}$, $M_2 = 250\,\text{GeV}$, $\mu = -200\,\text{GeV}$, $\tan\beta = 2$ and $\lambda_{1j1} = 0.1$. The rates values are calculated by including the ISR effect and by summing over the productions of the different $\tilde{\chi}_i^{\pm}$ and $\tilde{\chi}_j^0$ eigenstates which can all be produced for this MSSM point.

In lepton–photon collisions, single squark production occurs via λ' couplings as shown for example in Fig. 7.22 for $e\gamma$ collisions. When the produced squark directly decays via λ' into a lepton and a quark the final state consists of one hard mono-jet with one well isolated energetic electron, and eventually a soft jet in the forward region of the detector in the case where the initial electron which scatters the quasi real photon escapes detection.

7.5.2. Single sparticle production at lepton–hadron colliders

An lp collider provides both leptonic and baryonic quantum numbers in the initial state and is thus ideally suited for $\not{R}_p$ SUSY searches involving λ'_{ijk}. Among the twenty-seven possible λ'_{ijk} couplings, each of the nine couplings with $i = 1$ can lead to direct squark resonant production through e-q fusion at an ep collider such as HERA. The phenomenology of such processes was first investigated theoretically in Refs. [482–485]. Search strategies taking into account in general the indirect $\not{R}_p$ squark decay modes were discussed in Refs. [485–487].

The production processes are listed in Table 7.14 in the case of an incident e^+ beam.

In $e^+ p$ collisions, the production of $\tilde{u}_L^j$ squarks of the jth generation via λ'_{1j1} is especially interesting as it involves a valence d quark of the incident proton. In contrast, for $e^- p$ collisions where charge conjugate processes are accessible, the λ'_{11k} couplings become of special interest as they allow for the production, involving a valence u quark, of $\tilde{d}_R^k$ squarks of the kth generation. As an illustration, the Fig. 7.23 shows the production cross-sections in $e^{\pm} p$ collisions for

Table 7.13
Resonant and non-resonant single production of gauginos and sleptons at e^+e^- colliders and $\mu^+\mu^-$ colliders

e^+e^- colliders				$\mu^+\mu^-$ colliders			
Coupling	Final state	Exchange	Channel	Coupling	Final state	Exchange	Channel
λ_{121}	$\tilde{\chi}_a^\pm\,\mu^\mp$	$\tilde{\nu}_e$	t	λ_{212}	$\tilde{\chi}_a^\pm\,e^\mp$	$\tilde{\nu}_\mu$	t
	$\tilde{\chi}_a^\pm\,\mu^\mp$	$\tilde{\nu}_\mu$	s		$\tilde{\chi}_a^\pm\,e^\mp$	$\tilde{\nu}_e$	s
	$\tilde{\chi}_b^0\,\nu_\mu$	$\tilde{e}$	t+u		$\tilde{\chi}_b^0\,\nu_e$	$\tilde{\mu}$	t+u
	$\tilde{\chi}_b^0\,\nu_\mu$	$\tilde{e}$	s		$\tilde{\chi}_b^0\,\nu_e$	$\tilde{\mu}$	s
	$\tilde{\mu}^\pm W^\mp$	ν_e	t		$\tilde{e}^\pm W^\mp$	ν_μ	t
	$\tilde{\mu}^\pm W^\mp$	$\tilde{\nu}_\mu$	s		$\tilde{e}^\pm W^\mp$	$\tilde{\nu}_e$	s
	$\tilde{\nu}_\mu Z$	e	t+u		$\tilde{\nu}_e Z$	μ	t+u
	$\tilde{\nu}_\mu Z$	$\tilde{\nu}_\mu$	s		$\tilde{\nu}_e Z$	$\tilde{\nu}_e$	s
	$\tilde{\nu}_\mu \gamma$	e	t+u		$\tilde{\nu}_e \gamma$	μ	t+u
λ_{131}	$\tilde{\chi}_a^\pm\,\tau^\mp$	$\tilde{\nu}_e$	t	λ_{232}	$\tilde{\chi}_a^\pm\,\tau^\mp$	$\tilde{\nu}_\mu$	t
	$\tilde{\chi}_a^\pm\,\tau^\mp$	$\tilde{\nu}_\tau$	s		$\tilde{\chi}_a^\pm\,\tau^\mp$	$\tilde{\nu}_\tau$	s
	$\tilde{\chi}_b^0\,\nu_\tau$	$\tilde{e}$	t+u		$\tilde{\chi}_b^0\,\nu_\tau$	$\tilde{\mu}$	t+u
	$\tilde{\chi}_b^0\,\nu_\tau$	$\tilde{\tau}$	s		$\tilde{\chi}_b^0\,\nu_\tau$	$\tilde{\tau}$	s
	$\tilde{\tau}^\pm W^\mp$	ν_e	t		$\tilde{\tau}^\pm W^\mp$	ν_μ	t
	$\tilde{\tau}^\pm W^\mp$	$\tilde{\nu}_\tau$	s		$\tilde{\tau}^\pm W^\mp$	$\tilde{\nu}_\tau$	s
	$\tilde{\nu}_\tau Z$	e	t+u		$\tilde{\nu}_\tau Z$	μ	t+u
	$\tilde{\nu}_\tau Z$	$\tilde{\nu}_\tau$	s		$\tilde{\nu}_\tau Z$	$\tilde{\nu}_\tau$	s
	$\tilde{\nu}_\tau \gamma$	e	t+u		$\tilde{\nu}_\tau \gamma$	μ	t+u

The indices a and b run as follow $a = 1, 2$ and $b = 1, 4$. The $\tilde{\chi}_a^\pm$ and the $\tilde{\chi}_b^0$ can further cascade decay through ordinary gauge decays till either the $\tilde{\chi}_1^\pm$ or the $\tilde{\chi}_1^0$ is reached. The $\tilde{\chi}_1^\pm$ can either decay into $W^\pm\tilde{\chi}_1^0$ or via virtual sfermion exchange and then with the λ coupling involved in the single production. The $\tilde{\chi}_1^0$ can also further decay with the λ coupling involved in the single production. The sleptons can also decay either directly via the λ coupling involved in their single production or into leptons and gauginos followed by the gauginos decay via the same λ coupling. The multilepton final state can then be deduced using Tables 7.2 and 7.3.
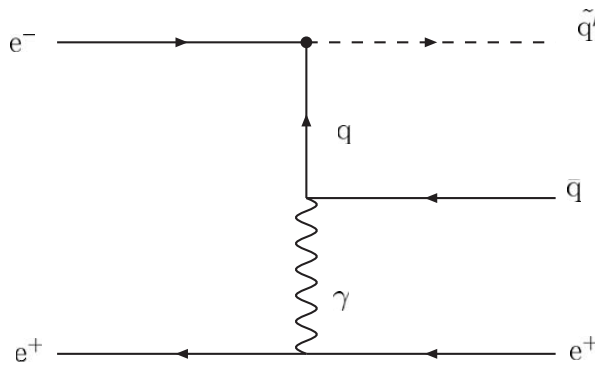
Fig. 7.22. Example diagram for single squark production in electron-photon collisions.

the "up"-like squarks $\tilde{u}_L^j$ via λ'_{1j1} ($j = 1\ldots 3$) compared to that for the "down"-like squarks $\bar{\tilde{d}}_R^k$ via λ'_{11k} ($k = 1\ldots 3$). The cross-sections are calculated [487] for coupling values of $\lambda' = 0.1$ and for an available center-of-mass energy of $\sqrt{s_{ep}}$ of 300 GeV characteristic of the HERA collider. By gauge symmetry, only $\tilde{u}_L$-like or $\tilde{d}_R$-like squarks (or their charge conjugates) can be produced in ep collisions. Since superpartners of left- and right-handed fermions may have different allowed or dominant decay modes, the dichotomy between the resonant production of $\tilde{u}_L$-like squarks in e^+p collisions and that of $\tilde{d}_R$-like squarks in e^-p collisions implies that the detailed analysis will differ between e^- and e^+ incident beams.

In the case of a direct $\not{R}_p$ decay through a λ' coupling, the squarks which have been resonantly produced in ep collisions behave as leptoquarks [488]. The $\tilde{u}_L$ may couple to an $e^+ + d$ pair via a Yukawa coupling λ'_{111} in a way

Table 7.14
Direct resonant production of squarks at an *ep* collider via a $\not{R}_p \lambda'_{1jk}$ coupling

λ'_{1jk}	Production process	
111	$e^+ + \bar{u} \to \bar{\tilde{d}}_R$	$e^+ + d \to \tilde{u}_L$
112	$e^+ + \bar{u} \to \bar{\tilde{s}}_R$	$e^+ + s \to \tilde{u}_L$
113	$e^+ + \bar{u} \to \bar{\tilde{b}}_R$	$e^+ + b \to \tilde{u}_L$
121	$e^+ + \bar{c} \to \bar{\tilde{d}}_R$	$e^+ + d \to \tilde{c}_L$
122	$e^+ + \bar{c} \to \bar{\tilde{s}}_R$	$e^+ + s \to \tilde{c}_L$
123	$e^+ + \bar{c} \to \bar{\tilde{b}}_R$	$e^+ + b \to \tilde{c}_L$
131	$e^+ + \bar{t} \to \bar{\tilde{d}}_R$	$e^+ + d \to \tilde{t}_L$
132	$e^+ + \bar{t} \to \bar{\tilde{s}}_R$	$e^+ + s \to \tilde{t}_L$
133	$e^+ + \bar{t} \to \bar{\tilde{b}}_R$	$e^+ + b \to \tilde{t}_L$

The processes are listed for an incident e^+ beam. Charge conjugate processes are accessible for an incident e^- beam.
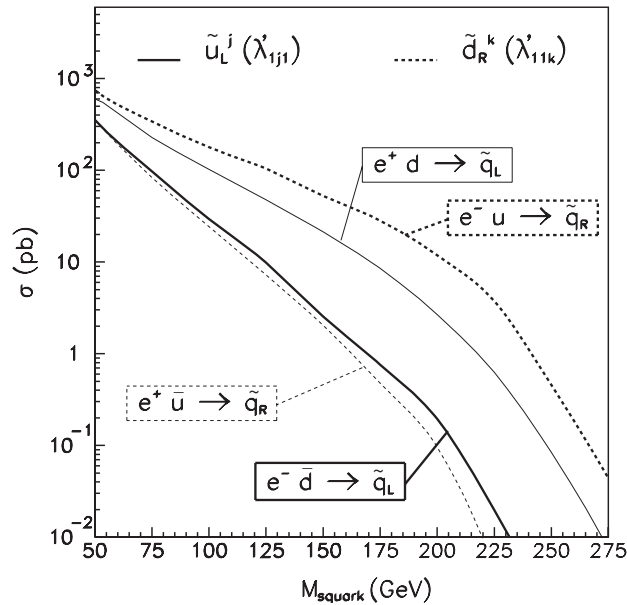
Fig. 7.23. Squark production cross-sections in $e^\pm p$ collisions calculated [487] for a coupling $\lambda' = 0.1$ and a collider center-of-mass energy of $\sqrt{s_{ep}} = 300$ GeV.

similar to the coupling of the first generation $\tilde{S}_{1/2,L}$ leptoquark of charge $|Q_{em}| = 2/3$. Via the same coupling, the $\tilde{d}_R$ couples to $e^- + u$ or $\nu_e + d$ pairs, thus behaving like the first-generation $S_{0,L}$ leptoquark of charge $|Q_{em}| = 1/3$. As a general consequence, it is possible to translate constraints on the λ couplings of leptoquarks into constraints on the λ'_{1jk} couplings of squarks in R_p-violating supersymmetry. For real squark production, this translation is limited to coupling values $\lambda' \gtrsim \sqrt{4\pi\alpha}$. For smaller values, the branching ratio into leptoquark-like final states rapidly drops as squarks will prefer indirect $\not{R}_p$ decays. Such a re-interpretation of leptoquark constraints from early HERA data has been performed in Refs. [489–491]. For virtual squark exchange in the case where $M_{\tilde{q}} \gg \sqrt{s_{ep}}$, constraints can beestablished via four-fermion leptoquark-like contact interaction analysis as will be discussed in Section 7.6.1.

In the case of indirect $\not{R}_p$ decays, the squarks in a first stage decay through gauge couplings into a quark and a gaugino–higgsino ($\tilde{\chi}^0$, $\tilde{\chi}^+$) or, if $M_{\tilde{g}} \ll M_{\tilde{q}}$, into a quark and a gluino. Such squark decays involving $\not{R}_p$ couplings were discussed in detail in Section 7.3. Here again, at an *ep* collider, the dichotomy between the production of $\tilde{u}_L$ and $\tilde{d}_R$ will have important phenomenological consequences. While the $\tilde{u}_L$ might decay via $\tilde{u}_L \to u\tilde{\chi}^0_l$ or $\tilde{\chi}^+_m$, the $\tilde{d}_R$ mainly decays via $\tilde{d}_R \to d\tilde{\chi}^0_l$, the $\tilde{b}_R$ decay into a chargino being also possible via the higgsino component of the latter.
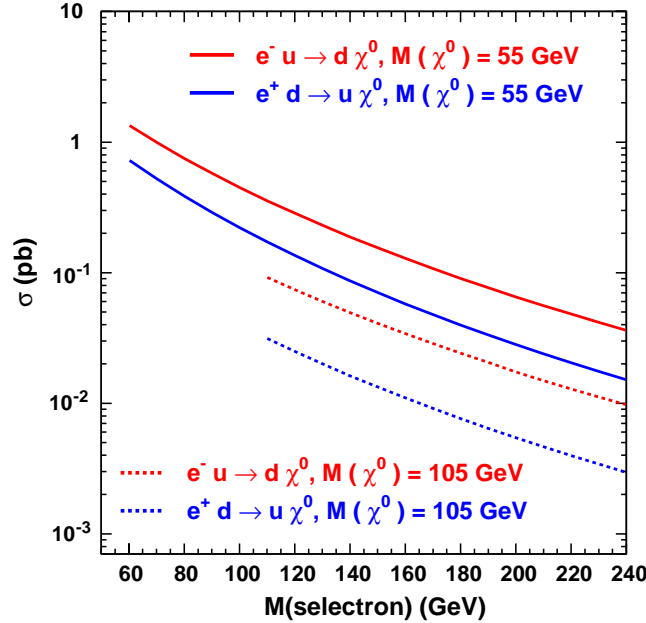
Fig. 7.24. Cross-sections for $\tilde{\chi}^0$ production in $e^{\pm}p$ collisions from t-channel selectron exchange calculated [492] for a coupling $\lambda'_{1j1} = 0.5$ and for collider center-of-mass energy of $\sqrt{s_{ep}} = 300\,\text{GeV}$.

Depending on the mixing parameters in the neutralino and chargino sectors, the dominating event topologies to be expected might depend on whether the collider is running in e^+p or in e^-p mode. Decays of $\tilde{\chi}^0$ and $\tilde{\chi}^+$ mass eigenstates were discussed in detail in Section 7.3.

Detailed discussion on the event topologies expected at an *ep* collider for single squark production in the presence of $\not{R}_p$ couplings can be found in Refs. [485–487].

Real or virtual squark exchange in the s-channel contributes to the single production of neutralinos or charginos. These can also be singly produced via $\not{R}_p$ interactions in lowest order processes involving sleptons or sneutrinos. The $\tilde{\chi}^0$ can be produced via t-channel slepton exchange or via u-channel squark exchange. The $\tilde{\chi}^+$ can be produced via t-channel sneutrino exchange.

The Fig. 7.24 shows the neutralino production cross-sections in $e^{\pm}p$ collisions expected for a coupling value $\lambda'_{11k} = 0.5$ and for an available center-of-mass energy of $\sqrt{s_{ep}}$ of 300 GeV characteristic of the HERA collider. The cross-sections are calculated [492] for selectron exchange only in the framework of the MSSM augmented by a single non-vanishing λ' coupling, for two values of $M_{\tilde{\chi}^o}$ and for $\tan\beta = 1$. Such cross-sections could be expected in case $M_{\tilde{e}} \ll M_{\tilde{q}}$. When both s-channel $\tilde{q}$ exchange and t-channel $\tilde{e}$ contribute, the interference between these cannot be neglected. For example at HERA II, constructive interference between squark and selectron exchange processes could contribute [492] up to 20% of the total $\tilde{\chi}^o$ production.

Searches for single squark production have been performed at HERA I under the hypothesis of a single dominant λ'_{1jk} coupling. The constraints obtained [493–495] by the H1 experiment are shown in Fig. 7.25. Similar results were obtained [496] by the ZEUS experiment. All possible event topologies (multijets and lepton and/or missing energy) resulting from the direct or indirect sparticle decays involving such coupling have been considered in the analysis. The HERA I results are compared to the best existing indirect bounds [259] from low-energy experiments. The λ'_{111} coupling is seen to be very severely constrained by the non-observation of neutrinoless double-beta decay. The most stringent low-energy constraints on λ'_{121} and λ'_{131} come from atomic-parity violation measurements. From these HERA I results, it can be inferred that HERA II could offer a sensitivity reach beyond the domain excluded by indirect constraints for 2nd and 3rd generation squarks.

The HERA results analyzed in the framework of $\not{R}_p$ mSUGRA are shown in Fig. 7.26 and compared to complementary $\not{R}_p$ SUSY searches made at LEP 2 and Tevatron Run I colliders. The searches were performed here also under the hypothesis of a single dominant λ'_{1jk} coupling. The results are presented as excluded domains in the parameter space of the model. The constraints from the DØ [468] experiment at the Tevatron were obtained from a search for $\tilde{q}$ pair
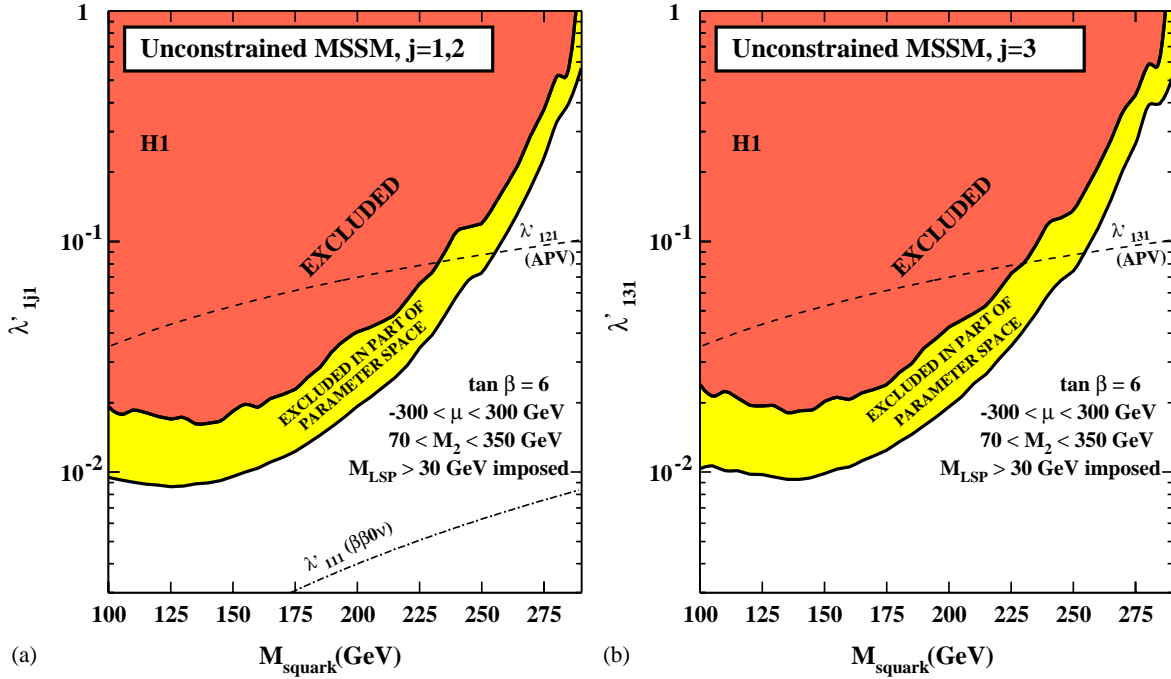
Fig. 7.25. Upper Limits (95% *CL*) on a) the coupling λ'_{1j1} with $j=1,2$ and b) λ'_{131} as a function of the squark mass for $\tan\beta=6$ in the unconstrained MSSM. The limits are obtained from a scan of the μ and M_2 parameters within $-300<\mu<300$ GeV and $70<M_2<350$ GeV and imposing that the lightest sparticle (LSP) has a mass M_{LSP} above 30 GeV. The dark shaded area is excluded for any parameter values. The light shaded area is excluded for some parameters values. The dashed–dotted curve is the indirect upper bound [259] on λ'_{111} derived from constraints on neutrinoless double-beta decays [497,498]. The dashed curves are the indirect upper bounds [259] on λ'_{1j1} derived from constraints on atomic-parity violation [499].
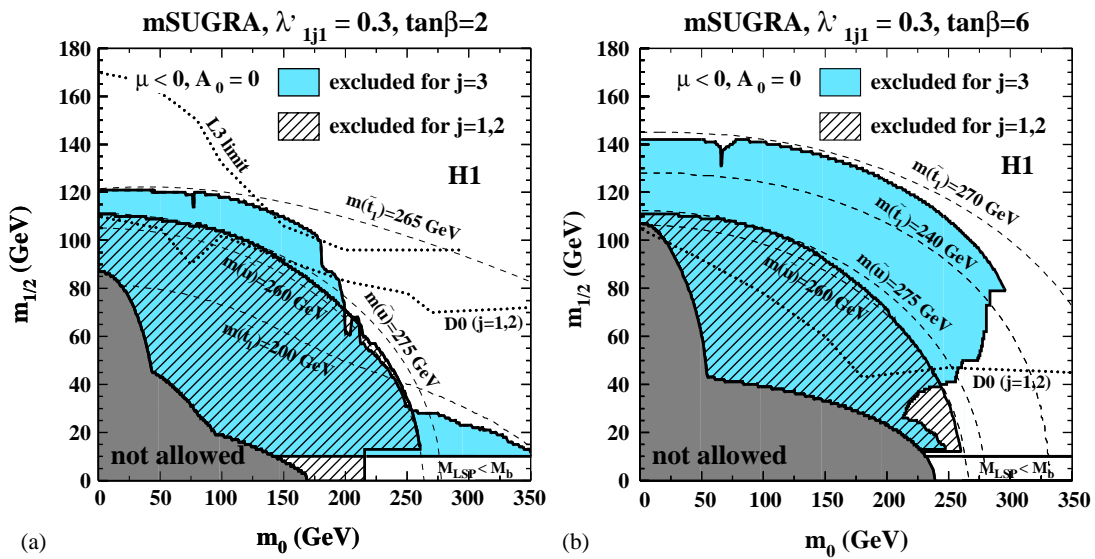
Fig. 7.26. Constraints on squark production via λ'_{1j1} in R_p-violating SUSY in the parameter space of Minimal Supergravity. Excluded domains obtained by the H1 [495] (shaded area) and DØ (dotted curves) experiments are shown for (a) $\tan\beta=2$ and (b) $\tan\beta=6$. In (a) the limit obtained by the L3 experiment at LEP 2 is also shown as the upper dotted curve. Contours of constant values for the light stop mass are drawn as dashed curves. The shaded region marked "not allowed" corresponds to points in the parameter space where the radiative electroweak symmetry breaking does not occur (or which lead to unphysical Higgs or sfermion masses). Also marked as "not allowed" in this particular analysis are cases where the LSP is the sneutrino.

production through gauge couplings. The DØ analysis profits in this framework from an approximate mass degeneracy implicitly extended to five $\tilde{q}$ flavors ($\tilde{d},\tilde{u},\tilde{s},\tilde{c},\tilde{b}$) and both (partners) chiralities ($\tilde{q}_L,\tilde{q}_R$). The $\not{R}_p$ couplings are assumed to be significantly smaller than the gauge couplings, so that direct $\not{R}_p$ decays are suppressed and each squark rather decays back into a quark and the LSP through gauge couplings. The only effect of the $\not{R}_p$ couplings is then to make the LSP unstable. The DØ analysis is further restricted to $\not{R}_p$ coupling val-ues $\gtrsim 10^{-3}$ to guarantee a negligible decay length of the LSP. In the domains considered, the LSP is almost always the lightest neutralino $\tilde{\chi}_1^0$. The $\tilde{\chi}_1^0$ decays via λ'_{1jk} into a first-generation lepton (e or ν_e) and two quarks. The analysis is restricted to $j = 1, 2$ and $k = 1, 2, 3$ and, in practice, the DØ selection of event candidates requires like-sign di-electrons accompanied by multiple jets. The constraints from the L3 experiment at LEP were obtained from a search for pair production through gauge couplings of neutralinos ($e^+e^- \rightarrow \tilde{\chi}_m^0 \tilde{\chi}_n^0$ with $m = 1, 2$ and $n = 1, \ldots, 4$), charginos ($e^+e^- \rightarrow \tilde{\chi}_1^+ \tilde{\chi}_1^-$) and scalar leptons ($e^+e^- \rightarrow \tilde{l}_R^+\tilde{l}_R^-$, $\tilde{\nu}\tilde{\nu}$).The $\not{R}_p$ couplings contribute here again in opening new decay modes for the sparticles. A negligible decay length of the sparticles through these decay modes is ensured by restricting the analysis to coupling values $\gtrsim 10^{-5}$. All possible event topologies (multijets and lepton and/or missing energy) resulting from the direct or indirect sparticle decays involving the λ'_{ijk} couplings have been considered in the L3 analysis.

For the set of mSUGRA parameters with $\tan\beta = 2$, the Tevatron experiment excludes squarks with masses $M_{\tilde{q}} <$ 243 GeV (95% CL) for any value of $M_{\tilde{g}}$ and a finite value ($\gtrsim 10^{-3}$) of λ'_{1jk} with $j = 1, 2$ and $k = 1, 2, 3$. The sensitivity decreases for the parameter set with a larger value of $\tan\beta$ due in part to a decrease of the photino component of the LSP, which implies a decrease of the branching fraction of the LSP into electrons, and in part to a softening of the final-state particles for lighter charginos and neutralinos. The best sensitivity at $\tan\beta = 2$ is offered by LEP for any of the λ'_{ijk} couplings. HERA offers a best complementary sensitivity to the coupling λ'_{131} which allows for resonant stop production via positron–quark fusion $e^+d \rightarrow \tilde{t}_1$. The HERA constraints (shown here for a coupling of electromagnetic strength, i.e. $\lambda'_{131} = 0.3$) extend beyond LEP and Tevatron constraints towards larger $\tan\beta$.

7.5.3. Single sparticle production at hadron–hadron colliders

The SUSY particles can be produced as resonances at hadron colliders through the $\not{R}_p$ interactions. This is particularly attractive as hadron colliders allow to probe for resonances over a wide mass range given the continuous energy distribution of the colliding partons. If a single $\not{R}_p$ coupling is dominant, the resonant SUSY particle may decay through the same coupling involved in its production, giving a two quark final state at the partonic level. However, it is also possible that the decay of the resonant SUSY particle is mainly due to gauge interactions, giving rise to a cascade decay. A review focusing on Tevatron Run-II can be found in [467].

7.5.3.1. Single sparticle production via λ'.

First, a resonant sneutrino can be produced in $d\bar{d}$ annihilations through the constant λ'_{ijk}. The associated formula can be written as follows [500]:

$$\sigma(d_k \bar{d}_j \rightarrow \tilde{\nu}^i \rightarrow X_1 X_2) = \frac{4}{9} \frac{\hat{s}}{m_{\tilde{\nu}^i}^2} \frac{\pi \Gamma_{d_k \bar{d}_j} \Gamma_f}{(\hat{s} - m_{\tilde{\nu}^i}^2)^2 + m_{\tilde{\nu}^i}^2 \Gamma_{\tilde{\nu}^i}^2} \ , \tag{7.13}$$

where $\Gamma_{d_k \bar{d}_j}$, and Γ_f are the partial width of the channels, $\tilde{\nu}^i \rightarrow d_k \bar{d}_j$, and, $\tilde{\nu}^i \rightarrow X_1 X_2$, respectively, $\Gamma_{\tilde{\nu}^i}$ is the total width of the sneutrino, $m_{\tilde{\nu}^i}$ is the sneutrino mass and $\hat{s}$ is the square of the parton center-of-mass energy. The factor 1/9 in front is from matching the initial colors, and $\Gamma_{d_k \bar{d}_j}$ is given by

$$\Gamma_{d_k \bar{d}_j} = \frac{3}{4} \alpha_{\lambda'_{ijk}} m_{\tilde{\nu}^i} \ , \tag{7.14}$$

where $\alpha_{\lambda'_{ijk}} = \lambda'^2_{ijk}/4\pi$. To compute the rate at a $p\bar{p}$ collider, the usual formalism of the parton model of hadrons can be used [501]:

$$\sigma(p\bar{p} \rightarrow \tilde{\nu}^i \rightarrow X_1 X_2) = \sum_{j,k} \int_{\tau_0}^1 \frac{d\tau}{\tau} \left(\frac{1}{s} \frac{dL_{jk}}{d\tau} \right) \hat{s} \sigma(d_k \bar{d}_j \rightarrow \tilde{\nu}^i \rightarrow X_1 X_2) \ , \tag{7.15}$$

where s is the center-of-mass energy squared, τ_0 is given by $\tau_0 = (M_{X_1} + M_{X_2})^2/s$ and τ is defined by $\tau = \hat{s}/s = x_1 x_2$, x_1, x_2 denoting the longitudinal momentum fractions of the initial partons j and k, respectively. The quantity $dL_{jk}/d\tau$

is the parton luminosity defined by

$$\frac{\mathrm{d}L_{jk}}{\mathrm{d}\tau} = \int_\tau^1 \frac{\mathrm{d}x_1}{x_1} [f_j^{\bar{p}}(x_1) f_k^p(\tau/x_1) + f_j^p(x_1) f_k^{\bar{p}}(\tau/x_1)] , \tag{7.16}$$

where the parton distribution $f_j^h(x_1)$ denotes the probability of finding a parton j with momentum fraction x_1 inside a hadron h, and generally depends on the Bjorken variable, Q^2, the square of the characteristic energy scale of the process under consideration. In order to see the effects of the parton distributions on the resonant sneutrino production, some values of the rates are given in the following [502]: For instance, with an initial state $d\bar{d}$ for the hard process, the cross-section value is $\sigma(p\bar{p} \to \tilde{\nu}^i) = 8.5$ nb for a sneutrino mass of 100 GeV and a coupling, $\lambda'_{i11} = 1$ at $\sqrt{s} = 2$ TeV. For identical values of the parameters and of the center-of-mass energy, the cross-section is $\sigma(p\bar{p} \to \tilde{\nu}^i) = 4$ nb with an initial state, $d\bar{s}$, and $\sigma(p\bar{p} \to \tilde{\nu}^i) = 0.8$ nb with an initial state, $d\bar{b}$. The charged slepton can also be produced as a resonance at hadron colliders from an initial state $u_j \bar{d}_k$ and via the constant λ'_{ijk}. The cross-section value is $\sigma(p\bar{p} \to \tilde{l}_L^i) = 2$ nb for $m_{\tilde{l}_L^i} = 100$ GeV, $\sqrt{s} = 2$ TeV and $\lambda'_{i11} = 1$ [502,503].

The single production of SUSY particles via λ' occurring through *two-to-two*-body processes, offers the opportunity to study the parameter space of the $\not{R}_p$ models with a quite high sensitivity at hadron colliders.

In Fig. 7.27, all the single superpartner productions which occur via λ'_{ijk} through *two-to-two*-body processes at hadron colliders and receive a contribution from a resonant SUSY particle production are presented [504]. The spin summed amplitudes of those reactions including the higgsino contributions have been calculated in [504]. In a SUGRA model, the rates of the reactions presented in Fig. 7.27 depend mainly on the m_0 and M_2 parameters.

In Fig. 7.28, the variations of the $\sigma(p\bar{p} \to \tilde{\chi}^+_{1,2} \mu^-)$ cross-sections with m_0 for fixed values of M_2, μ and $\tan\beta$ and various $\not{R}_p$ couplings of the type λ'_{2jk} at Tevatron Run II in a SUGRA model are shown [504]. The $\not{R}_p$ couplings giving the highest cross-sections have been considered. The $\sigma(p\bar{p} \to \tilde{\chi}^+_{1,2} \mu^-)$ rates decrease when m_0 increases since then the sneutrino becomes heavier and more energetic initial partons are required in order to produce the resonant sneutrino. A decrease of the cross-sections also occurs at small values of m_0, the reason being that when m_0 approaches M_2 the $\tilde{\nu}$ mass is getting closer to the $\tilde{\chi}^\pm$ masses so that the phase space factors associated to the decays $\tilde{\nu}_\mu \to \chi^\pm_{1,2} \mu^\mp$ decrease. The differences between the $\tilde{\chi}^+_1 \mu^-$ production rates occurring via the various λ'_{2jk} couplings are explained by the different partonic luminosities. Indeed, as shown in Fig. 7.27 the hard process associated to the $\tilde{\chi}^+_1 \mu^-$ production occurring through the λ'_{2jk} coupling constant has a partonic initial state $\bar{q}_j q_k$. The $\tilde{\chi}^+_1 \mu^-$ production via the λ'_{211} coupling has first generation quarks in the initial state which provide the maximum partonic luminosity.

In Fig. 7.29, the variations of the rates of the reactions $p\bar{p} \to \tilde{\chi}^-_1 \nu$, $p\bar{p} \to \tilde{\chi}^0_{1,2} \mu^-$ and $p\bar{p} \to \tilde{\chi}^0_1 \nu$ with the m_0 parameter in a SUGRA model are shown [504]. From this figure one can see that the single neutralino productions do not decrease at small m_0 values in contrast with the single chargino productions (see also Fig. 7.28). This is due to the fact that in SUGRA scenarios the $\tilde{\chi}^0_1$ and $\tilde{l}_L$ ($\tilde{l}_L = \tilde{l}_L^\pm$, $\tilde{\nu}_L$) masses are never close enough to induce a significant decrease of the phase space factor associated to the decay $\tilde{l}_L \to \tilde{\chi}^0_1 l (l = l^\pm, \nu)$. By analyzing Figs. 7.28 and 7.29, one can also see that the $\tilde{\chi}^- \nu$ ($\chi^0 \mu^-$) production rate is larger than the $\tilde{\chi}^+ \mu^-$ ($\chi^0 \nu$) production rate. The explanation is that in $p\bar{p}$ collisions the initial states of the resonant charged slepton production $u_j \bar{d}_k$, $\bar{u}_j d_k$ have higher partonic luminosities than the initial states of the resonant sneutrino production $d_j \bar{d}_k$, $\bar{d}_j d_k$.

The neutralino production in association with a charged lepton via λ' (see Fig. 7.27d) is an interesting case at Tevatron [502]. The topology of the events consists of an isolated lepton in one hemisphere balanced by a lepton plus two jets in the other hemisphere, coming from the neutralino decay via λ'. The Standard Model background arising from the production of two jets plus a Z^0, decaying into two leptons, has a cross-section of order 10^{-3} nb [501], and can be greatly reduced by excluding lepton pairs with an invariant mass equal to the Z^0 mass. The other source of Standard Model background, which is the Drell–Yan mechanism into 2 leptons accompanied by 2 jets, is suppressed by a factor, $10^{-6}/\alpha_\lambda$. Moreover, the signal can be enhanced by looking at the invariant mass of the 2 jets and the lepton in the same hemisphere, which should peak around the neutralino mass.

The single production via λ' of the neutralino together with a charged lepton can also generate clean signatures free from large Standard Model background, containing two like-sign charged leptons [255,467,504–509]. As a matter of fact, the neutralino has a decay channel into a lepton and two jets through the coupling λ'_{ijk} and due to its Majorana nature, the neutralino decays to the charge conjugate final states with equal probability: $\Gamma(\tilde{\chi}^0 \to l_i u_j \bar{d}_k) = \Gamma(\tilde{\chi}^0 \to \bar{l}_i \bar{u}_j d_k)$. Therefore, the lepton coming from the production can have the same sign than the one coming from the neutralino decay.
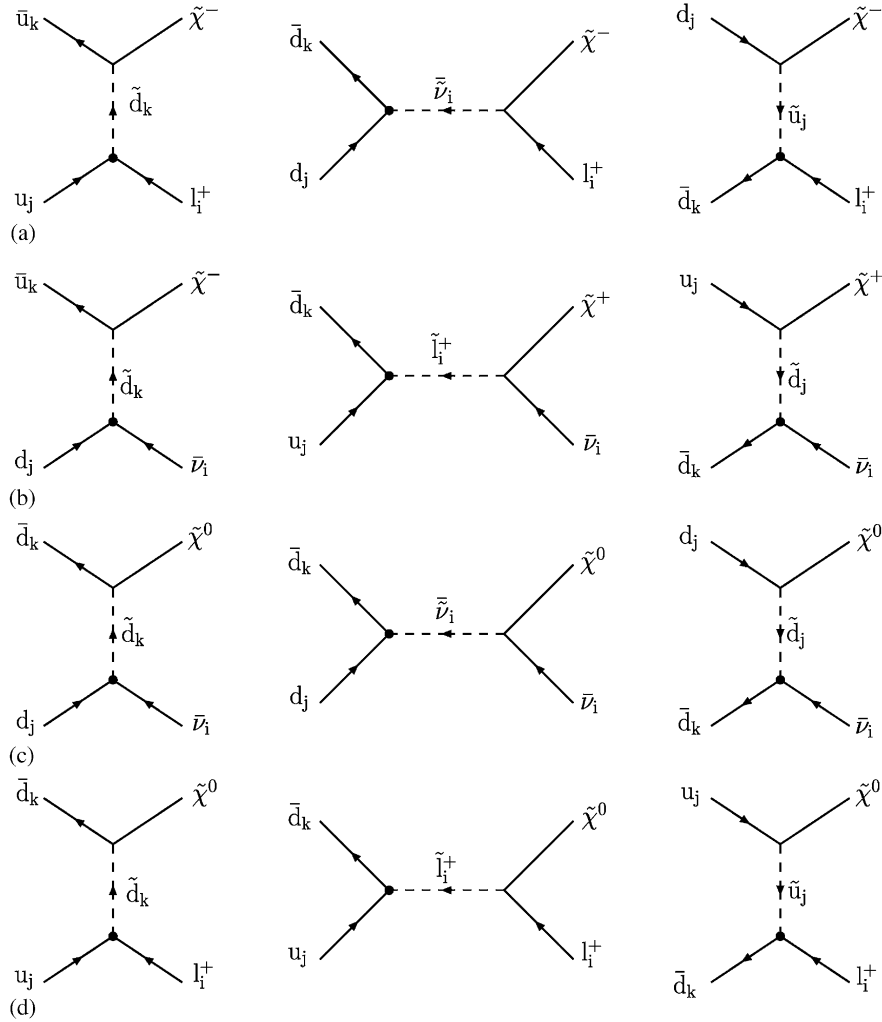
Fig. 7.27. Diagrams for the four single superpartner production reactions involving λ'_{ijk} at hadron colliders which receive a contribution from a resonant *supersymmetric* particle production. The λ'_{ijk} coupling constant is symbolised by a small circle and the arrows indicate the flow of the lepton or baryon number.

Since λ'_{111} has a strong indirect bound, it is interesting to consider the coupling constant λ'_{211}, which corresponds to the dimuons production with an initial state $u\bar{d}$ or $\bar{u}d$ (see Fig. 7.27d) composed of first generation quarks. The analysis of the like sign di-taus signature generated by the $\tilde{\chi}^0\tau^{\pm}$ production through the λ'_{311} coupling (see Fig. 7.27d) suffers from a reduction of the selection efficiency due to the tau-lepton decay. Besides, the study of the $\tilde{\chi}^0_1\mu^{\pm}$ production via λ'_{211} in a scenario where the $\tilde{\chi}^0_1$ is the LSP is particularly attractive since then the $\tilde{\chi}^0_1$ can only undergo $\not{R}_p$ decays. It was found that in a SUGRA model, such a study can probe values of the λ'_{211} coupling at the 5σ discovery level down to 2×10^{-3} (10^{-2}) for a muon–slepton mass of $m_{\tilde{\mu}_L} = 100\,\text{GeV}$ $(m_{\tilde{\mu}_L} = 300\,\text{GeV})$ with $M_2 = 100\,\text{GeV}$, $2 < \tan\beta < 10$ and $|\mu| < 10^3\,\text{GeV}$ at Tevatron Run II assuming a luminosity of $\mathscr{L} = 2\text{fb}^{-1}$ [467,505], and down to 2×10^{-3} (10^{-2}) for $m_{\tilde{\mu}_L} = 223\,\text{GeV}$ $(m_{\tilde{\mu}_L} = 540\,\text{GeV})$ with $m_{1/2} = 300\,\text{GeV}$, $A = 300\,\text{GeV}$, $\tan\beta = 2$ and $\text{sign}(\mu) > 0$ at the LHC assuming a luminosity of $\mathscr{L} = 10\text{fb}^{-1}$ [506,507]. It was also shown in [504], by using a detector response simulation, that the study of the single LSP production at Tevatron Run II $p\bar{p} \to \tilde{\chi}^0_1\mu^{\pm}$ would allow to probe $m_{1/2}$ values up to $\sim 850\,\text{GeV}$ and m_0 values up to $\sim 550\,\text{GeV}$ at the 5σ discovery level, in a SUGRA scenario where $\text{sign}(\mu) < 0$, $A = 0$, $\tan\beta = 1.5$ $\lambda'_{211} = 0.05$ and assuming a luminosity of $\mathscr{L} = 2\text{fb}^{-1}$. In the case where one considers the Standard Model background combined with the background generated by the superpartner pair production [509], the single $\tilde{\chi}^0_1$ production study based on the like sign dilepton signature analysis still allows to test large ranges of the SUGRA parameter space at Tevatron Run II or LHC, for λ'_{211} values of the same order of its present limit.
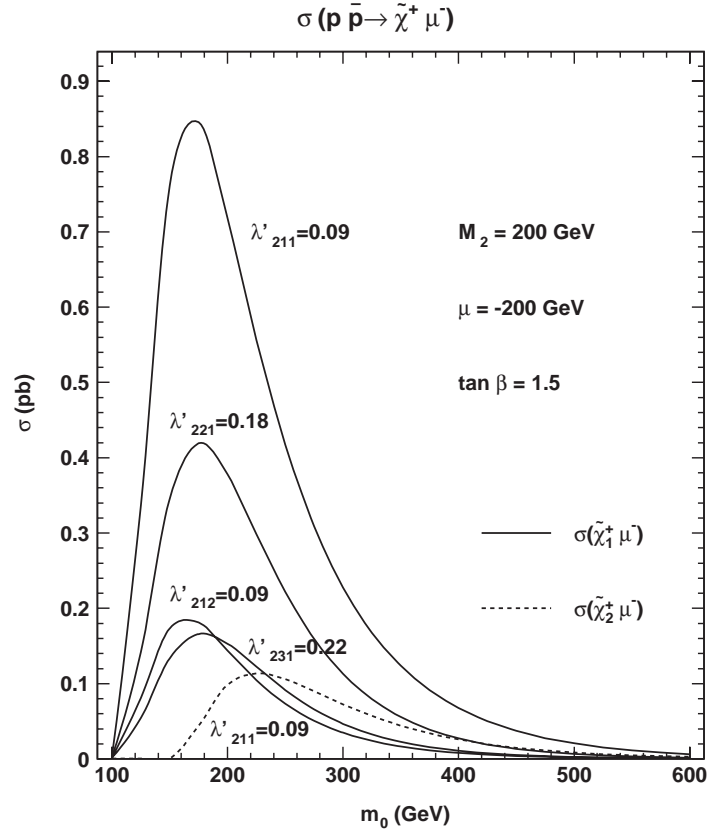
Fig. 7.28. Cross-sections (in pb) of the single chargino productions $p\bar{p} \to \tilde{\chi}^+_{1,2}\mu^-$ as a function of the m_0 parameter (in GeV). The center-of-mass energy is taken at $\sqrt{s} = 2$ TeV and the considered set of parameters is: $\lambda'_{211} = 0.09$, $M_2 = 200$ GeV, $\tan\beta = 1.5$ and $\mu = -200$ GeV. The rates for the $\tilde{\chi}^+_1$ production via the $\not{R}_p$ couplings $\lambda'_{212} = 0.09$, $\lambda'_{221} = 0.18$ and $\lambda'_{231} = 0.22$ are also given. The chosen values of the $\not{R}_p$ couplings correspond to the low-energy limits for a squark mass of 100 GeV [258].

Besides, the like sign dilepton signature analysis based on the $\tilde{\chi}^0_1\mu^\pm$ production (see Fig. 7.27d) allows the $\tilde{\chi}^0_1$ and $\tilde{\mu}^\pm_L$ mass reconstructions since the decay chain $\tilde{\mu}^\pm_L \to \tilde{\chi}^0_1\mu^\pm$, $\tilde{\chi}^0_1 \to \mu^\pm ud$ can be fully reconstructed [504,509]. Based on the like sign dilepton signature analysis, the $\tilde{\chi}^0_1$ ($\tilde{\mu}^\pm_L$) mass can be measured with a statistical error of $\sim 11(20)$ GeV at the Tevatron Run II [504].

The single $\tilde{\chi}^\pm_1$ production in association with a charged lepton (see Fig. 7.27a) is another interesting reaction at hadron colliders. In a scenario where $\tilde{\chi}^0_1$ is the LSP and $m_{\tilde{\nu}}, m_{\tilde{l}}, m_{\tilde{q}} > m_{\tilde{\chi}^\pm_1}$, this single production receives a contribution from the resonant sneutrino production and the singly produced chargino decays into quarks and leptons with branching ratios respectively of $B(\tilde{\chi}^\pm_1 \to \tilde{\chi}^0_1 d_p u_{p'}) \approx 70\%$ ($p = 1, 2, 3$; $p' = 1, 2$) and $B(\tilde{\chi}^\pm_1 \to \tilde{\chi}^0_1 l^\pm_p v_p) \approx 30\%$ due to the color factor. The neutralino decays via λ'_{ijk} either into a lepton as, $\tilde{\chi}^0_1 \to l_i u_j \bar{d}_k$, $\bar{l}_i \bar{u}_j d_k$, or into a neutrino as, $\tilde{\chi}^0_1 \to v_i d_j \bar{d}_k$, $\bar{v}_i \bar{d}_j d_k$. Hence, if both the $\tilde{\chi}^\pm_1$ and $\tilde{\chi}^0_1$ decay into charged leptons, the $\tilde{\chi}^\pm_1 l^\mp_i$ production can lead to the three charged leptons signature which has a small Standard Model background at hadron colliders [510,507,504,508,511]. The study of the three leptons signature generated by the $\tilde{\chi}^\pm_1\mu^\mp$ production via the λ'_{211} coupling constant is particularly interesting for the same reasons as above. The sensitivity to the λ'_{211} coupling obtained from this study at Tevatron Run II would reach a maximum value of ~ 0.04 for $m_0 \approx 200$ GeV in a SUGRA model with $M_2 = 200$ GeV, sign$(\mu) < 0$, $A = 0$ and $\tan\beta = 1.5$, assuming a luminosity of $\mathscr{L} = 2\text{fb}^{-1}$ [504]. The sensitivities on the λ'_{2jk} couplings that can be obtained from the trilepton analysis based on the $\tilde{\chi}^\pm_1\mu^\mp$ production at the LHC for a given set of MSSM parameters are shown in Table 7.15 [510]. For each of the λ'_{2jk} couplings the sensitivity has been obtained assuming that the considered coupling was the single dominant one. The difference between the various results presented in this table is due to the fact that each λ'_{2jk} coupling involves a specific initial state (see Fig. 7.27a) with its own parton density. Besides, all the sensitivities shown in Table 7.15 improve greatly the present low-energy constraints. The trilepton analysis based on
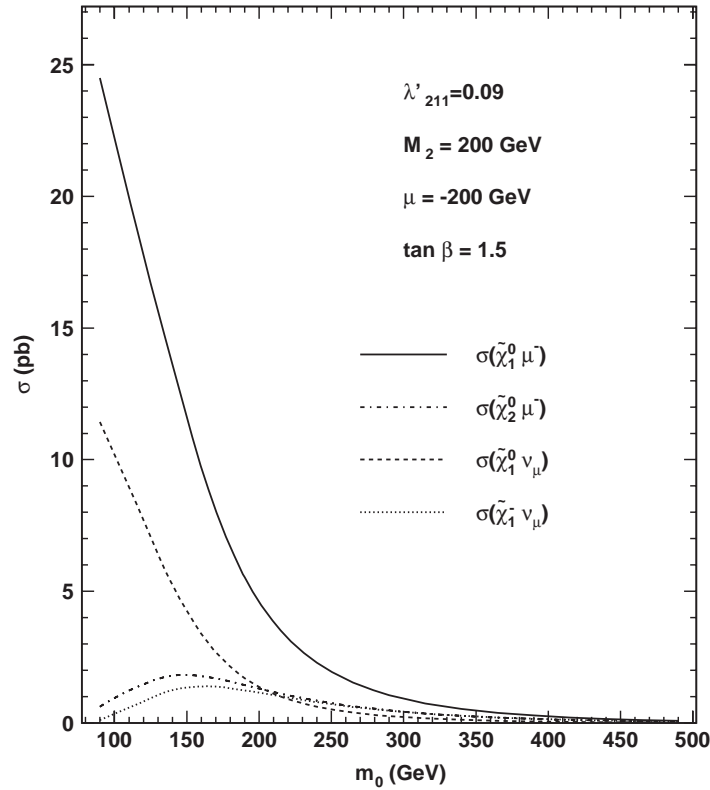
Fig. 7.29. Cross-sections (in *pb*) of the $\tilde{\chi}_1^- \nu$, $\tilde{\chi}_{1,2}^0 \mu^-$ and $\tilde{\chi}_1^0 \nu$ productions at Tevatron Run II as a function of the m_0 parameter (in GeV). The center-of-mass energy is taken at $\sqrt{s} = 2$ TeV and the considered set of parameters is: $\lambda'_{211} = 0.09$, $M_2 = 200$ GeV, $\tan \beta = 1.5$ and $\mu = -200$ GeV.

Table 7.15
Sensitivities on the λ'_{2jk} coupling constants for $\tan \beta = 1.5$, $M_1 = 100$ GeV, $M_2 = 200$ GeV, $\mu = -500$ GeV, $m_{\tilde{q}} = m_{\tilde{l}} = 300$ GeV and $m_{\tilde{\nu}} = 400$ GeV, assuming an integrated luminosity of $\mathscr{L} = 30 \text{fb}^{-1}$

λ'_{211}	λ'_{212}	λ'_{213}	λ'_{221}	λ'_{222}	λ'_{223}	λ'_{231}	λ'_{232}	λ'_{233}
0.01	0.02	0.02	0.02	0.03	0.05	0.03	0.06	0.09

the $\tilde{\chi}_1^\pm e^\mp$ ($\tilde{\chi}_1^\pm \tau^\mp$)production would allow to test the λ'_{1jk} (λ'_{3jk}) couplings constants. While the sensitivities obtained on the λ'_{1jk} couplings are expected to be of the same order of those presented in Table 7.15, the sensitivities on the λ'_{3jk} couplings should be weaker due to the tau-lepton decay. The results presented in Table 7.15 illustrate the fact that even if some studies on the single superpartner production via λ' at hadron colliders (see Fig. 7.27) only concern the λ'_{211} coupling constant, the analysis of a given single superpartner production at Tevatron or LHC allows to probe many λ'_{ijk} coupling constants down to values smaller than the corresponding limits from low-energy data.

Besides, the three leptons final state study based on the $\tilde{\chi}_1^\pm \mu^\mp$ production (see Fig. 7.27a) allows to reconstruct the $\tilde{\chi}_1^0$, $\tilde{\chi}_1^\pm$ and $\tilde{\nu}$ masses [510,507,504,508,511]. Indeed, the decay chain $\tilde{\nu}_i \to \tilde{\chi}_1^\pm l_i^\mp$, $\tilde{\chi}_1^\pm \to \tilde{\chi}_1^0 l_p^\pm \nu_p$, $\tilde{\chi}_1^0 \to l_i^\pm u_j d_k$ can be fully reconstructed since the produced charged leptons can be identified thanks to their flavors and signs. Based on the trilepton signature analysis, the $\tilde{\chi}_1^0$ mass can be measured with a statistical error of ~ 9 GeV at the Tevatron Run II [508,504] and of ~ 100 MeV at the LHC [511,507,510]. Furthermore, the width of the Gaussian shape of the invariant mass distribution associated to the $\tilde{\chi}_1^\pm$ ($\tilde{\nu}$) mass is of ~ 6 GeV (~ 10 GeV) at the LHC for the MSSM point defined by $M_1 = 75$ GeV, $M_2 = 150$ GeV, $\mu = -200$ GeV, $m_{\tilde{f}} = 300$ GeV and $A = 0$ [511,507,510].

Let us make a general remark concerning the superpartner mass reconstructions based on the single superpartner production studies at hadron colliders. The combinatorial background associated to these mass reconstructions is

smaller than in the mass reconstructions analyzes based on the supersymmetric particle pair production since in the single superpartner production studies only one cascade decay must be reconstructed.

At hadron colliders, some supersymmetric particles can also be singly produced through *two-to-two*-body processes which generally do not receive contribution from resonant superpartner production [504]. Some single productions of squark (slepton) in association with a gauge boson can occur through the exchange of a quark in the t-channel or a squark (slepton) in the s-channel via λ'' (λ'). From an initial state $g\,q$, a squark (slepton) can also be singly produced together with a quark (lepton) with a coupling constant λ'' (λ') via the exchange of a quark or a squark in the t-channel, and of a quark in the s-channel. Finally, a gluino can be produced in association with a lepton (quark) through a coupling constant λ' (λ'') via the exchange of a squark in the t-channel (and in the s-channel).

Let us enumerate the single scalar particle and gluino productions occurring via the *two-to-two*-body processes which involve the λ'_{ijk} coupling constants [504] (one must also add the charge conjugate processes):

- The gluino production $\bar{u}_j d_k \to \tilde{g} l_i$ via the exchange of a $\tilde{u}_{jL}$ ($\tilde{d}_{kR}$) squark in the t-(u-) channel.
- The squark production $\bar{d}_j g \to \tilde{d}^*_{kR} v_i$ via the exchange of a $\tilde{d}_{kR}$ squark (d_j quark) in the t-(s-) channel.
- The squark production $\bar{u}_j g \to \tilde{d}^*_{kR} l_i$ via the exchange of a $\tilde{d}_{kR}$ squark (u_j quark) in the t-(s-) channel.
- The squark production $d_k g \to \tilde{d}_{jL} v_i$ via the exchange of a $\tilde{d}_{jL}$ squark (d_k quark) in the t-(s-) channel.
- The squark production $d_k g \to \tilde{u}_{jL} l_i$ via the exchange of a $\tilde{u}_{jL}$ squark (d_k quark) in the t-(s-) channel.
- The sneutrino production $\bar{d}_j d_k \to Z \tilde{v}_{iL}$ via the exchange of a d_k or d_j quark ($\tilde{v}_{iL}$ sneutrino) in the t-(s-) channel.
- The charged slepton production $\bar{u}_j d_k \to Z \tilde{l}_{iL}$ via the exchange of a d_k or u_j quark ($\tilde{l}_{iL}$ slepton) in the t-(s-) channel.
- The sneutrino production $\bar{u}_j d_k \to W^- \tilde{v}_{iL}$ via the exchange of a d_j quark ($\tilde{l}_{iL}$ slepton) in the t-(s-) channel.
- The charged slepton production $\bar{d}_j d_k \to W^+ \tilde{l}_{iL}$ via the exchange of a u_j quark ($\tilde{v}_{iL}$ sneutrino) in the t-(s-) channel.

One must also add to this list the $g d_k \to t \tilde{l}_i$ reaction which occurs via the λ'_{i3k} coupling through the exchange of a d_k quark in the s-channel and a top quark in the t-channel [512].

Among these single productions only the $\bar{u}_j d_k \to W^- \tilde{v}_{iL}$ and $\bar{d}_j d_k \to W^+ \tilde{l}_{iL}$ reactions can receive a contribution from a resonant sparticle production. However, in most of the SUSY models, as for example the supergravity or the gauge mediated models, the mass difference between the so called left-handed charged slepton and the left-handed sneutrino is due to the D-terms so that it is fixed by the relation $m^2_{\tilde{l}^\pm_L} - m^2_{\tilde{v}_L} = \cos 2\beta M^2_W$ [513] and thus it does not exceed the W boson mass. In scenarios with large $\tan\beta$ values, a scalar particle of the third generation produced as a resonance can generally decay into the W boson due to the large mixing in the third family sfermions sector. For instance, in the SUGRA model with a large $\tan\beta$ a tau-sneutrino produced as a resonance in $d_k \bar{d}_j \to \tilde{v}_\tau$ through λ'_{3jk} can decay as $\tilde{v}_\tau \to W^\pm \tilde{\tau}^\mp_1, \tilde{\tau}^\mp_1$ being the lightest stau.

Similarly, the single scalar particle and gluino productions occurring via the *two-to-two*-body processes which involve the λ''_{ijk} coupling constants cannot receive a contribution from a resonant scalar particle production for low $\tan\beta$. Indeed, the only reactions among these *two-to-two*-body processes which can receive such a contribution are of the type $qq \to \tilde{q} \to \tilde{q} W$. In this type of reaction, the squark produced in the s-channel, is produced via λ''_{ijk} and is thus either a Right squark $\tilde{q}_R$, which does not couple to the W boson, or the squarks $\tilde{t}_{1,2}$, $\tilde{b}_{1,2}$. However, the single gluino productions occurring via the *two-to-two*-body processes which involve the λ''_{ijk} coupling constants can receive a contribution from a resonant scalar particle production.

Therefore, the single scalar particle and gluino productions occurring via the *two-to-two*-body processes are generally non-resonant single superpartner productions, as already mentioned at the beginning of this section. These non-resonant single superpartner productions have typically smaller cross-sections than the reactions receiving a contribution from a resonant superpartner production. For instance, with $m_{\tilde{q}} = 250\,\text{GeV}$, the cross-section $\sigma(p\bar{p} \to \tilde{u}_L \mu)$ is of order $\sim 10^{-3}$ pb at a center-of-mass energy of $\sqrt{s} = 2\,\text{TeV}$, assuming an R_p coupling of $\lambda'_{211} = 0.09$ [504]. However, the non-resonant single productions can lead to interesting signatures. For instance, the production, $q\bar{q} \to \tilde{f} W$ leads to the final state $2l + 2j + W$ for a non-vanishing R_p coupling constant λ' and to the signature $4j + W$ for a λ'' [255]. Furthermore, the non-resonant single productions are interesting as their cross-section involves only few SUSY parameters, namely one or two scalar superpartner(s) mass(es) and one R_p coupling constant.

The DØ collaboration searched for single slepton production through the λ'_{211} coupling in the two muons and two hadron jets channel [514]. In the absence of any evidence for an excess of events with respect to expectation from

Fig. 7.30. Diagrams for the single neutralino production reactions involving λ''_{ijk} at hadron colliders. The λ''_{ijk} coupling constant is symbolised by a small circle and the arrows indicate the flow of the baryon number.

Standard Model processes, bounds on supergravity parameters $m_{1/2}$, m_o have been set. Sneutrinos and smuons masses up to 280 GeV have been excluded.

7.5.3.2. Single sparticle production via λ''. The *B*-violating couplings λ''_{ijk} allows for resonant production of squarks at hadron colliders. Either a squark $\tilde{u}_i$ or $\tilde{d}_k$ can be produced at the resonance from an initial state, $\bar{d}_j\bar{d}_k$ or $\bar{u}_i\bar{d}_j$, respectively. For $m_{\tilde{d}^k_R} = 100$ GeV, $\sqrt{s} = 2$ TeV and $\lambda''_{11k} = 1$, the rate of the down squark production at the Tevatron is $\sigma(p\bar{p} \to \tilde{d}^k_R) = 25$ nb [502].

For $m_{\tilde{t}_1} = 600$ GeV, $\sqrt{s} = 2$ TeV and $\lambda''_{323} = 0.1$, the cross-section of the resonant stop production is $\sigma(p\bar{p} \to \tilde{t}_1) = 10^{-3}$ pb [515]. Note that this rate is higher than the stop pair production rate at the same center-of-mass energy and for the same stop mass, which is of order $\sigma(p\bar{p} \to \tilde{t}_1\tilde{t}_1) = 10^{-6}$ pb (Fig. 7.30).

The single superpartner production can also occur as a *two-to-two*-body process, through an $\not{R}_p$ coupling λ'' and an ordinary gauge interaction vertex: in baryon-number-violating models, any gaugino (including gluino) can be produced in association with a quark, in quark–quark scattering, by the exchange of a squark in the s-, t- or u-channel. Diagrams for single neutralino or gluino (respectively single chargino, resonant, non-resonant and associated production) are shown in Fig. 7.30 (respectively in Figs. 7.31–7.35).

For example, let us consider the photino and gluino production [502]: The rate values in the t- and u-channel are, $\sigma(p\bar{p} \to \tilde{\gamma}q) = 2 \times 10^{-2}$ nb, and, $\sigma(p\bar{p} \to \tilde{g}q) = 3 \times 10^{-1}$ nb, for, $m_{\tilde{q}} = m_{\tilde{g}} = m_{\tilde{\gamma}} = 100$ GeV, $\sqrt{s} = 2$ TeV and $\lambda''_{111} = 1$. The photino or gluino which is produced will then decay into three jets via the λ'' coupling, resulting in a four jets final state. The corresponding QCD background is strong: it is estimated to be about 10 nb for $\sqrt{s} = 2$ TeV [516]. Of course, the ratio signal over background can be enhanced considerably by looking at the mass distribution of the jets: the QCD 4 jets are produced relatively uncorrelated, while the trijet mass distribution of the signal should peak around the gaugino mass. However, one of the three jets may be too soft to be measured or jet coalescence may occur, especially for small values of the gaugino mass. The study of this example brings us to the conclusion that, due to high QCD background, the analysis of the single production via λ'' remains difficult.

Nevertheless, there are some specific cases where the final state can be clear and free from a large background. For instance, a $\tilde{\chi}_1^+$ chargino can be produced via λ''_{3jk} through the resonant production of a top squark as $\bar{d}_j\bar{d}_k \to \tilde{t}_1 \to b\tilde{\chi}_1^+$,
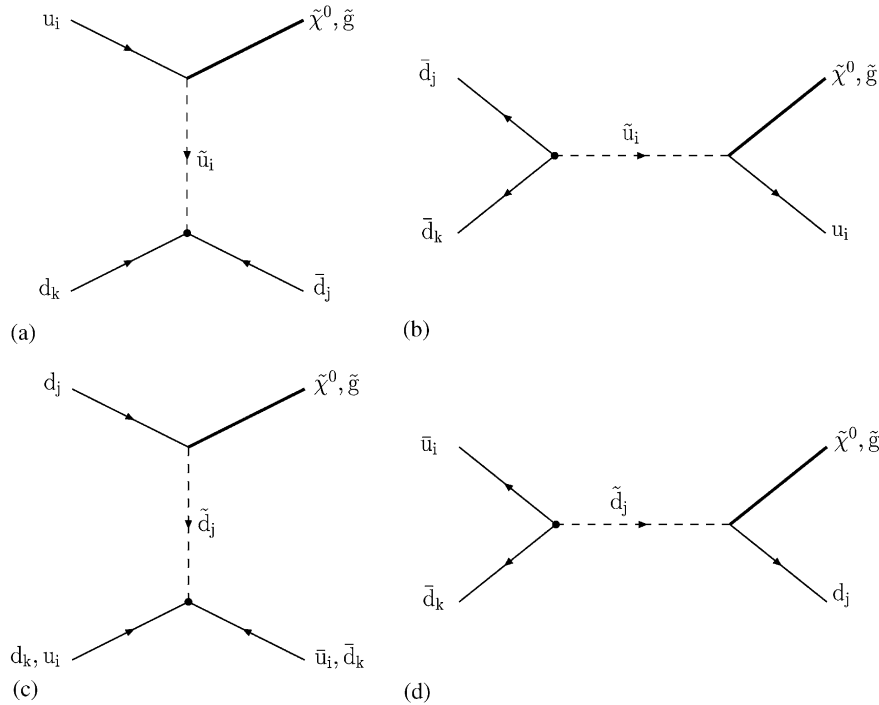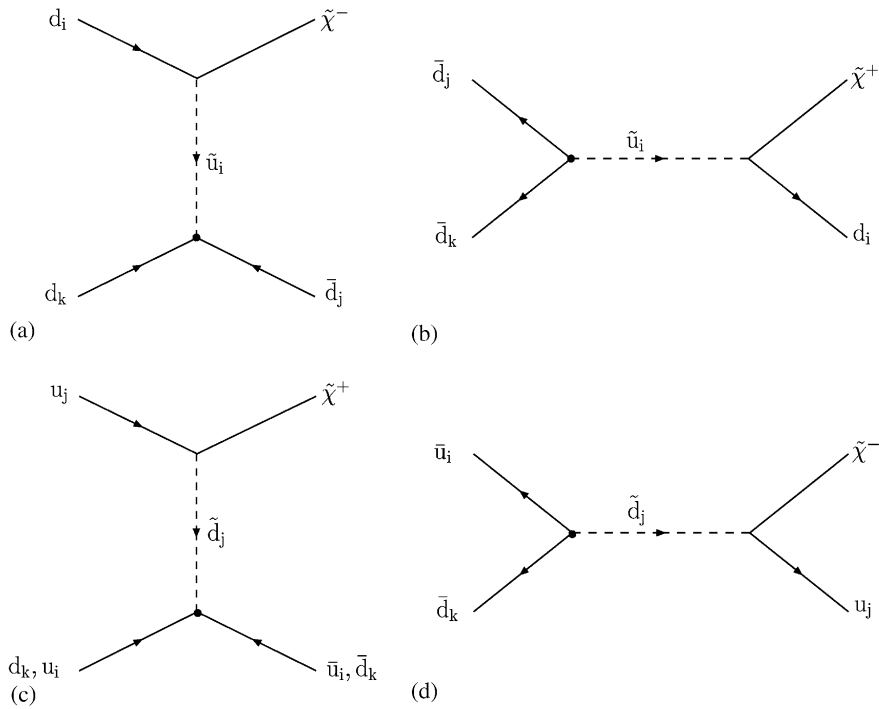
Fig. 7.31. Diagrams for the single chargino production reactions involving λ''_{ijk} at hadron colliders. The λ''_{ijk} coupling constant is symbolised by a small circle and the arrows indicate the flow of the baryon number.
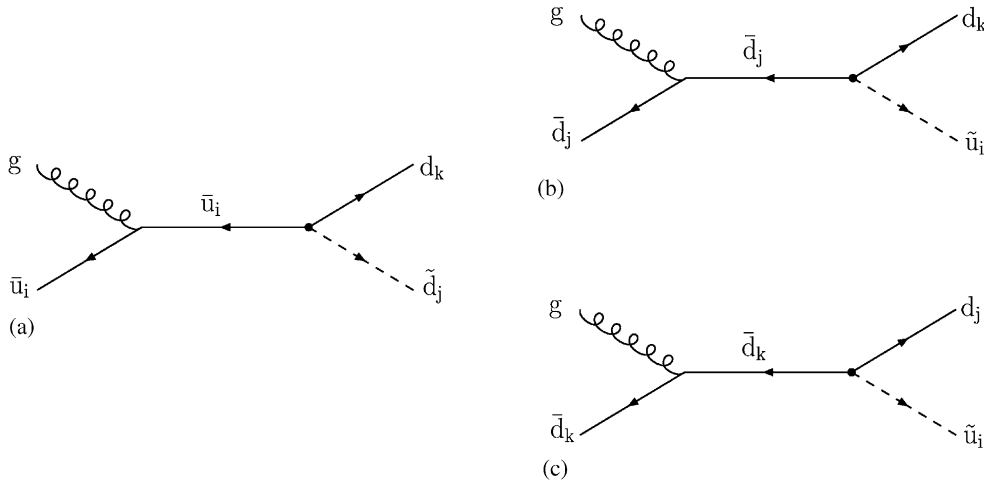
Fig. 7.32. Diagrams for the resonant production of squarks involving λ''_{ijk} at hadron colliders. The λ''_{ijk} coupling constant is symbolised by a small circle and the arrows indicate the flow of the baryon number.

$\tilde{t}_1$ being the lightest top squark, and then decay into the lightest neutralino plus leptons as $\tilde{\chi}_1^+ \rightarrow \bar{l}_i \nu_i \tilde{\chi}_1^0$ [515,467]. Due to the stop resonance, this reaction can reach high rate values. The cascade decay demands the mass hierarchy, $m_{\tilde{t}_1} > m_{\tilde{\chi}_1^+} > m_{\tilde{\chi}_1^0}$, to be respected, and by consequence is not allowed in all regions of the supergravity parameter space.Assuming λ''_{3jk} to be the single dominant $\not{R}_p$ coupling constant and the $\tilde{\chi}_1^0 = $ LSP to be lighter than the top quark, the $\tilde{\chi}_1^0$ should then be treated as a stable particle. Then, the signal for our process would be very clear since it would consist of a tagged b-quark jet, a lepton and missing transverse energy. The Standard Model background for such a signature comes from the single top quark production, via $W\,g$ fusion, and the production of a W gauge boson in association with $b\bar{b}$, $c\bar{c}$ or a jet faking a b-quark jet. Experimental studies lead to the conclusion that values of $\lambda'' > 0.03 - 0.2$ and $\lambda'' > 0.01 - 0.03$ can be excluded at the 95% confidence level for, $180\,\text{GeV} < m_{\tilde{t}_1} < 285\,\text{GeV}$,
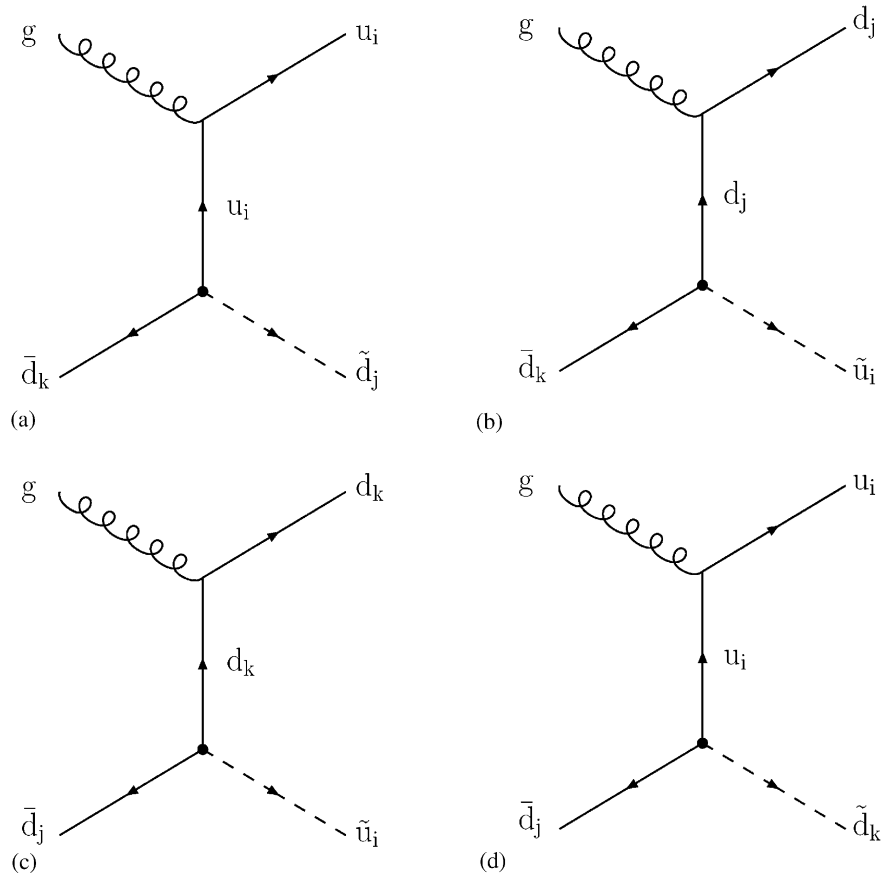
Fig. 7.33. Diagrams for the non-resonant production of squarks involving λ''_{ijk} at hadron colliders. The λ''_{ijk} coupling constant is symbolised by a small circle and the arrows indicate the flow of the baryon number.

at the Tevatron Run I ($\sqrt{s} = 1.8 \, \text{TeV}$ and $\mathscr{L} = 110 \, \text{pb}^{-1}$) and for, $180 \, \text{GeV} < m_{\tilde{t}_1} < 325 \, \text{GeV}$, at the Run II of the Tevatron ($\sqrt{s} = 2 \, \text{TeV}$ and $\int \mathscr{L} \, dt = 2 \, \text{fb}^{-1}$), respectively. This result is based on the leading-order CTEQ-4L parton distribution functions[517] and holds for the normalization, $\lambda'' = \lambda''_{312} = \lambda''_{313} = \lambda''_{323}$, and for the point of a minimal supergravity model, $m_{1/2} = 150 \, \text{GeV}$, $A_0 = -300 \, \text{GeV}$ and $\tan \beta = 4$. The constraints obtained on λ'' are stronger than the present low energy bounds.

Another particularly interesting reaction has been studied in [518]: the single gluino production $\bar{d}_j \bar{d}_k \to t \tilde{g}$ which can receive a contribution from the resonant stop production via the λ''_{3jk} coupling. In certain regions of the mSUGRA parameter space, this single gluino production can reach rates at LHC of order 10^2 fb (for $\lambda''_{3jk} = 10^{-1}$) thanks to the contribution coming from the resonant $\tilde{t}_2$ production, $\tilde{t}_2$ being the heavier top squark. The interesting point is that in these mSUGRA domains the branching ratios of the decays $\tilde{g} \to tb\tilde{\chi}_1^{\pm}$ and $\tilde{g} \to t\bar{t}\tilde{\chi}_1^0$ reach also significant values thanks to the exchange of the virtual $\tilde{t}_1$ (the lighter top squark) which is the lighter squark and has a mixing angle near $\pi/2$. By consequence, the process $pp \to t\tilde{g}(\bar{t}\tilde{g})$ can simultaneously have large cross section values at LHC and produce in a significant way a clear signature containing 3 b quarks, at least 2 charged leptons and some missing energy (due to the top quark decay $t \to blv$). Since the background associated to this final state can be greatly reduced thanks to the large b-tagging efficiency available at the LHC ($\sim 50\%$), the study of the reaction $pp \to t\tilde{g} \, (\bar{t}\tilde{g})$ should provide an effective test of the λ''_{3jk} coupling constant.

7.6. Virtual effects involving $\not{R}_p$ couplings

In a scenario where none of the supersymmetric particles can be directly produced at colliders with a significant cross-section, because of very high masses or unfavorable couplings with the Standard Model particles, the effects induced by $\not{R}_p$ could turn out to be felt only in indirect processes involving virtual sparticle exchange.
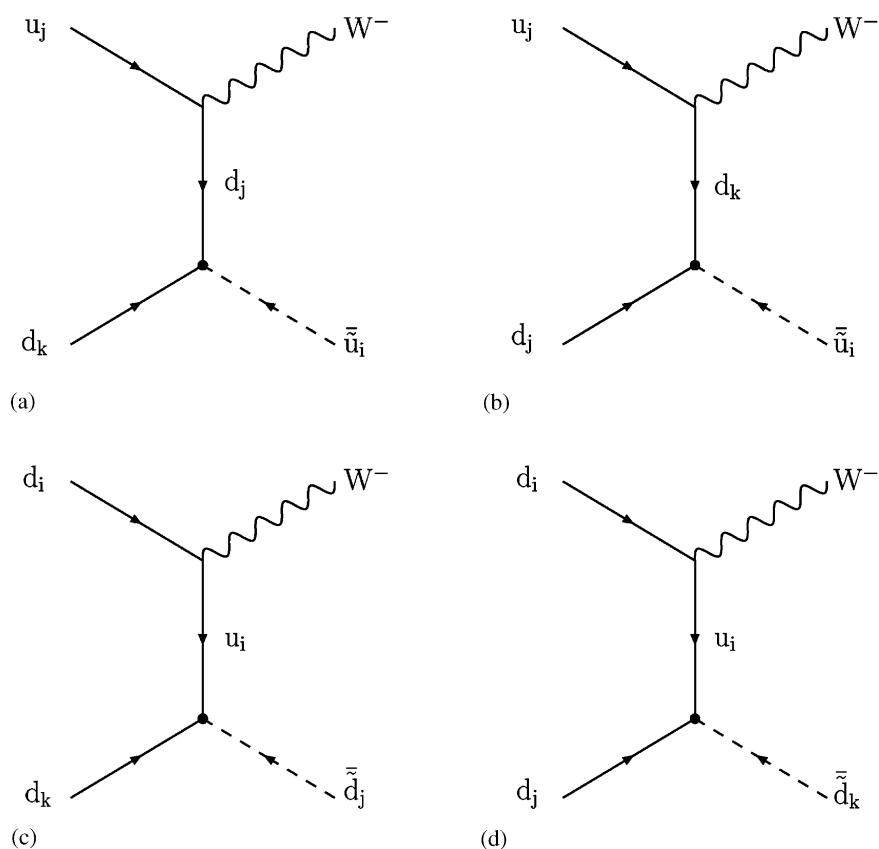
Fig. 7.34. Diagrams for the associated $\tilde{q} - W$ production involving λ''_{ijk} at hadron colliders. The λ''_{ijk} coupling constant is symbolised by a small circle and the arrows indicate the flow of the baryon number.

In contrast to single sparticle production for which a $\not{R}_p$ coupling only enter at one vertex when calculating total production rates, $\not{R}_p$ contributions (via additional sparticle exchange) to Standard Model processes are suppressed in proportion to the square of the Yukawa coupling. These processes generally imply high statistics inclusive measurements as in the case of fermion pair production and effective four-fermion contact interactions discussed in Section 7.6.1.

7.6.1. Fermion pair production

For sparticle masses far above the kinematical reach of a given collider, $\not{R}_p$ interactions could manifest themselves through effective four-fermion contact interactions interfering with Standard Model fermion pair production processes.

At leptonic colliders dilepton production can occur in the presence of a unique (or largely dominant) $\not{R}_p$ coupling. The resonant sneutrino $\tilde{\nu}_\mu$ or $\tilde{\nu}_\tau$ production via λ_{121} or λ_{131}, respectively followed by a decay through the same coupling constant (i.e. $\tilde{\nu}^i \to \bar{l}_j l_k$ via λ_{ijk}) would lead to a spectacular signature such as an excess of events Bhabha scattering events [261]. For example the cross-section of Bhabha scattering including the $\tilde{\nu}_{(\mu,\tau)}$ sneutrino s-channel exchange and the interference terms reaches 3 pb at $\sqrt{s} = m_{\tilde{\nu}_{(\mu,\tau)}} = 200\,\text{GeV}$ [519–521] for $\Gamma_{\tilde{\nu}_{(\mu,\tau)}} = 1\,\text{GeV}$ and $\lambda_{1(2,3)1} = 0.1$.

Table 7.16 shows the accessible λ couplings at e^+e^- and $\mu^+\mu^-$ colliders and fermion pair production to which a single dominant λ coupling can contribute. Except few exceptions, e^+e^- and $\mu^+\mu^-$ colliders allow to access the same λ couplings. The difference in center-of mass energies and luminosities between these two types of leptonic colliders will determine the explorable domain of these couplings.

The observation of an excess of high Q^2 events at HERA experiments [462,463] and its interpretation in terms of $\not{R}_p$ interactions has been followed by numerous discussions on dilepton production at LEP [519–524] which are beyond the scope of this review.

Di-jets production can also occur at leptonic colliders in the presence of a unique λ' coupling through the exchange of a squark in the t-channel. The $b\bar{b}$ and $c\bar{c}$ production via λ'_{1k3} and λ'_{12k}, respectively are of particular interest due to the possibility of tagging bottom, charm or light quarks (u,d,s) at the experiment level [525]. Table 7.17 shows the
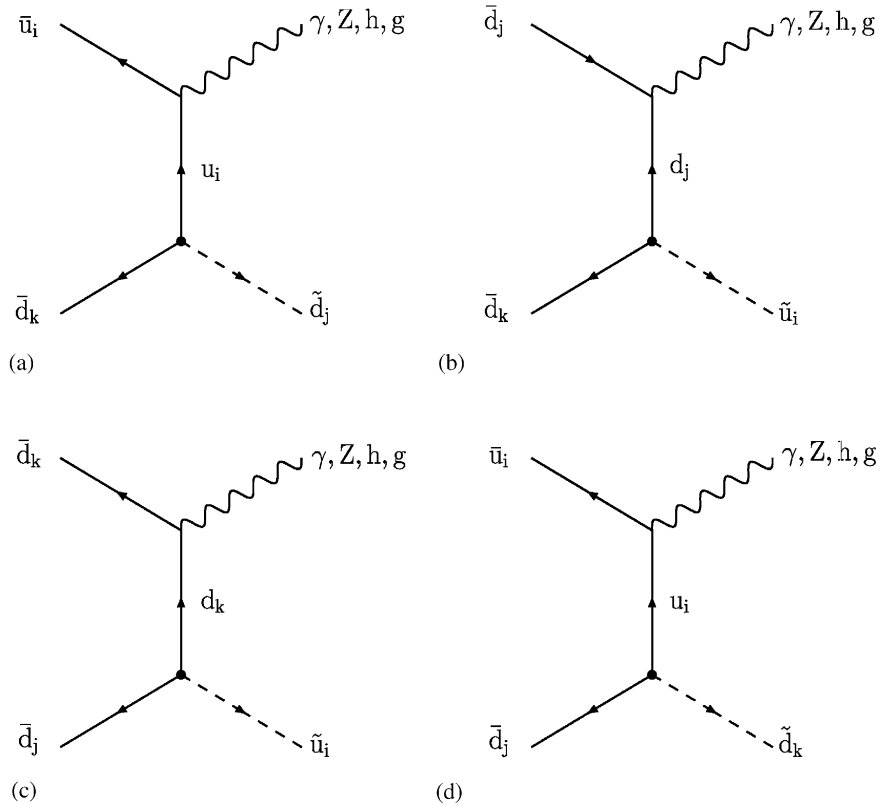
Fig. 7.35. Diagrams for the associated $\tilde{q} - \gamma$, $(-Z, -h$ and $-g)$ production involving λ''_{ijk} at hadron colliders. The λ''_{ijk} coupling constant is symbolised by a small circle and the arrows indicate the flow of the baryon number.

Table 7.16
Accessible λ couplings at e^+e^- and $\mu^+\mu^-$ colliders and fermion pair production to which a single dominant coupling can contribute

Coupling	e^+e^- colliders			$\mu^+\mu^-$ colliders		
	Final state	Exchange	Channel	Final state	Exchange	Channel
λ_{121}	e^+e^-	$\tilde{\nu}_\mu$	s	e^+e^-	$\tilde{\nu}_e$	t
	$\mu^+\mu^-$	$\tilde{\nu}_e$	t	–	–	–
λ_{122}	$\mu^+\mu^-$	$\tilde{\nu}_\mu$	t	e^+e^-	$\tilde{\nu}_\mu$	t
	–	–	–	$\mu^+\mu^-$	$\tilde{\nu}_e$	s + t
λ_{123}	$\tau^+\tau^-$	$\tilde{\nu}_\mu$	t	$\tau^+\tau^-$	$\tilde{\nu}_e$	t
λ_{131}	$\tau^+\tau^-$	$\tilde{\nu}_e$	t	–	–	–
	e^+e^-	$\tilde{\nu}_\tau$	s	–	–	–
λ_{132}	$\mu^+\mu^-$	$\tilde{\nu}_\tau$	t	e^+e^-	$\tilde{\nu}_\tau$	t
	–	–	–	$\tau^+\tau^-$	$\tilde{\nu}_e$	t
λ_{133}	$\tau^+\tau^-$	$\tilde{\nu}_\tau$	t	–	–	–
λ_{231}	$\tau^+\tau^-$	$\tilde{\nu}_\mu$	t	e^+e^-	$\tilde{\nu}_\tau$	t
	$\mu^+\mu^-$	$\tilde{\nu}_\tau$	t	–	–	–
λ_{232}	–	–	–	$\mu^+\mu^-$	$\tilde{\nu}_\tau$	s + t
	–	–	–	$\tau^+\tau^-$	$\tilde{\nu}_\mu$	t
λ_{233}	–	–	–	$\tau^+\tau^-$	$\tilde{\nu}_\tau$	t

accessible λ' couplings at e^+e^- and $\mu^+\mu^-$ colliders and fermion pair production to which a single dominant λ' coupling can contribute. In contrast to the case of λ couplings, e^+e^- and $\mu^+\mu^-$ colliders access completely different sets of λ' couplings. More specifically, in the case of λ' couplings, fermion pair production allows to explore only λ'_{1jk} at e^+e^- colliders and λ'_{2jk} at $\mu^+\mu^-$ colliders.

Table 7.17
Accessible λ' couplings at e^+e^- and $\mu^+\mu^-$ colliders and fermion pair production processes to which a single dominant coupling can contribute

Coupling	e^+e^- colliders			$\mu^+\mu^-$ colliders		
	Final state	Exchange	Channel	Final state	Exchange	Channel
λ'_{111}	$d\bar{d}$	$\tilde{u}$	t	–	–	–
λ'_{111}	$u\bar{u}$	$\tilde{d}$	t	–	–	–
λ'_{112}	$s\bar{s}$	$\tilde{u}$	t	–	–	–
λ'_{112}	$u\bar{u}$	$\tilde{s}$	t	–	–	–
λ'_{113}	$b\bar{b}$	$\tilde{u}$	t	–	–	–
λ'_{113}	$u\bar{y}$	$\tilde{b}$	t	–	–	–
λ'_{121}	$d\bar{d}$	$\tilde{c}$	t	–	–	–
λ'_{121}	$c\bar{c}$	$\tilde{d}$	t	–	–	–
λ'_{122}	$s\bar{s}$	$\tilde{c}$	t	–	–	–
λ'_{122}	$c\bar{c}$	$\tilde{s}$	t	–	–	–
λ'_{123}	$b\bar{b}$	$\tilde{c}$	t	–	–	–
λ'_{123}	$c\bar{c}$	$\tilde{b}$	t	–	–	–
λ'_{131}	$d\bar{d}$	$\tilde{t}$	t	–	–	–
λ'_{131}	$t\bar{t}$	$\tilde{d}$	t	–	–	–
λ'_{132}	$s\bar{s}$	$\tilde{t}$	t	–	–	–
λ'_{132}	$t\bar{t}$	$\tilde{s}$	t	–	–	–
λ'_{133}	$b\bar{b}$	$\tilde{t}$	t	–	–	–
λ'_{133}	$t\bar{t}$	$\tilde{b}$	t	–	–	–
λ'_{211}	–	–	–	$d\bar{d}$	$\tilde{u}$	t
λ'_{211}	–	–	–	$u\bar{u}$	$\tilde{d}$	t
λ'_{212}	–	–	–	$s\bar{s}$	$\tilde{u}$	t
λ'_{212}	–	–	–	$u\bar{u}$	$\tilde{s}$	t
λ'_{213}	–	–	–	$b\bar{b}$	$\tilde{u}$	t
λ'_{213}	–	–	–	$u\bar{y}$	$\tilde{b}$	t
λ'_{221}	–	–	–	$d\bar{d}$	$\tilde{c}$	t
λ'_{221}	–	–	–	$c\bar{c}$	$\tilde{d}$	t
λ'_{222}	–	–	–	$s\bar{s}$	$\tilde{c}$	t
λ'_{222}	–	–	–	$c\bar{c}$	$\tilde{s}$	t
λ'_{223}	–	–	–	$b\bar{b}$	$\tilde{c}$	t
λ'_{223}	–	–	–	$c\bar{c}$	$\tilde{b}$	t
λ'_{231}	–	–	–	$d\bar{d}$	$\tilde{t}$	t
λ'_{231}	–	–	–	$t\bar{t}$	$\tilde{d}$	t
λ'_{232}	–	–	–	$s\bar{s}$	$\tilde{t}$	t
λ'_{232}	–	–	–	$t\bar{t}$	$\tilde{s}$	t
λ'_{233}	–	–	–	$b\bar{b}$	$\tilde{t}$	t
λ'_{233}	–	–	–	$t\bar{t}$	$\tilde{b}$	t
λ'_{3jk}	–	–	–	–	–	–

Preliminary studies have been performed in [252] focusing on the study of $\mu^+\mu^- \to \mu^+\mu^-$ via $\tilde{v}_\tau$ involving the λ_{232} coupling and $\mu^+\mu^- \to b\bar{b}$ via $\tilde{v}_\tau$ involving the product $\lambda_{232}\lambda'_{333}$. In this case it has been found that once the mass of the $\tilde{v}_\tau$ is known from earlier stage of a e^+e^- collider or the $\mu^+\mu^-$ collider and once fixing the center-of-mass energy at $\tilde{v}_\tau$ resonance or around the resonance with the $\mu^+\mu^-$ collider, one can explore λ_{232} down to 10^{-4} with an integrated luminosity of $3\,\mathrm{fb}^{-1}$ and a beam energy resolution of 0.1%.

Further preliminary studies have been performed in [526].

At hadron colliders $\not{R}_p$ reactions can induce contributions to Standard Model di-jets or di-leptons production processes. First, the jets pair production receives contributions from reactions involving either λ' or λ'' coupling constants. As a matter of fact, a pair of quarks can be produced through the λ'' couplings with an initial state ud or $\bar{u}\bar{d}$ (dd or $\bar{d}\bar{d}$) by the exchange of a $\tilde{d}$ ($\tilde{u}$) squark in the s-channel, and also with an initial state $u\bar{u}$ or $d\bar{d}$ ($u\bar{d}$ or $\bar{u}d$) by the exchange of a $\tilde{u}$ or $\tilde{d}$ ($\tilde{d}$) squark in the t-channel. If the s-channel exchanged particle is produced on shell the resonant diagram is of course dominant with respect to the t-channel diagram. The dijet channel can also be generated via the λ' couplings from an initial state $u\bar{d}$, $\bar{u}d$ or $d\bar{d}$ through the exchange of a $\tilde{l}$ or $\tilde{v}$ slepton (respectively) in the s-channel.
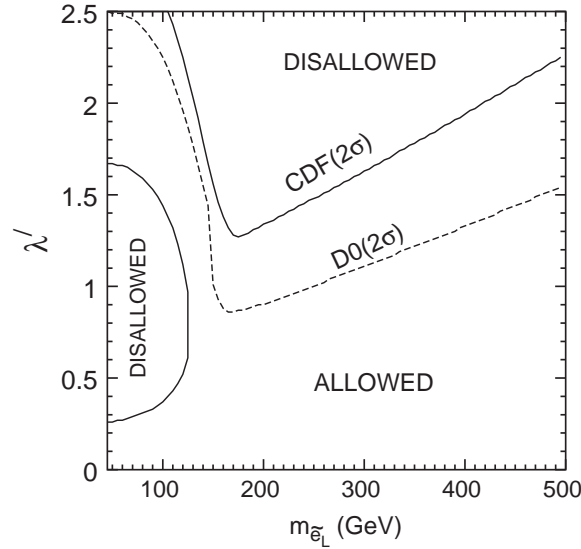
Fig. 7.36. Allowed regions in the plane of λ'_{i3k} and the mass of the left slepton in a lepton-number-violating scenario. Solid (dashed) lines correspond to the 2-σ bounds from the CDF (D0) collaborations.

If the dominant mechanism for either the slepton or the squark decay leads to two jets, the resonant production of such a scalar particle would result in a bump in the two-jet invariant mass distribution [261,502] which would be a very clean signature. However the di-jet production through $\not{R}_p$ coupling constants will be hard to study at LHC unless the narrow resonances are copiously produced given the severe expected QCD background [255,527]. This was discussed in more details above in Section 7.5.

Top quark pair production appears to be a particular case of fermion pair production at hadron colliders because if kinematically allowed new decay channels such as $t \rightarrow d\tilde{d}_R$ and $t \rightarrow d\tilde{l}_L$ can open up. The amplitudes for top quark pair production involve diagrams with an initial state $d_k\bar{d}_k$ with either a $\tilde{l}^i_L$ slepton exchange (via λ'_{i3k}) or a $\tilde{d}^i_R$ squark exchange. The supersymmetric parameter space region allowed at a 95% confidence level by the D0 and CDF data [528] on $t\bar{t}$ production cross-section have also been obtained in [529] and are shown in Fig. 7.36 in the plane $\lambda'_{i31}/m_{\tilde{l}^i_L}$ and in Fig. 7.37 in the plane $\lambda''_{31i}/m_{\tilde{d}^i_R}$. Furthermore, $\not{R}_p$ interactions being chiral, one expects the two top quarks to be polarized thus providing an additional handle to probe the details of $\not{R}_p$ couplings[530] since the polarization of the top quark pairs is very small in the Standard Model.

More complicated decay chains of the top quark such as the double cascade decays $t \rightarrow \tilde{l}^+_i d_k, \tilde{l}^+_i \rightarrow \tilde{\chi}^0 + e_i, \tilde{\chi}^0 \rightarrow v_i b\bar{d}_k + \bar{v}_i \bar{b}d_k$ where the top quark and neutralino $\not{R}_p$ decay processes are both controlled by the coupling constants λ'_{i3k} can lead to two potentially observable effects in the leptonic events namely a deviation from lepton universality and (for $k = 3$) an excess of b quark hadron events A study based on the comparison of the ratio of branching fractions for single e to single μ events $B(t\bar{t} \rightarrow (e + jets)/B(t\bar{t} \rightarrow \mu + jets)$ to the experimental ratio of events $N(e + jets)/N(\mu + jets) = 1 \left(\begin{smallmatrix} +a \\ -b \end{smallmatrix}\right)$ from the one charged lepton and two b-quark jets final state of the CDF top quark sample of Tevatron Run I gives the bound [262] $\lambda'_{13n} < 0.41$, $[n = 1, 2]$.

Another method of analysis based on an identification of this ratio with the ratio of the experimental to theoretical total production cross sections yields $\lambda'_{13n} < 0.48$. An analysis of the hadron b quarks events yields [262] $\lambda'_{133} < 0.41$.

Alternatively [104] the top quark $\not{R}_p$ decay channel $t \rightarrow b\tilde{\tau}^+$ initiated by the λ'_{333} coupling leads to signature which can not be confused with the Standard Model decay channel and can compete with it. This induces a reduction of the observed Standard Model $t\bar{t}$ event rates. The correction factor reads:

$$R_B \simeq 1.12 \; \lambda'^2_{333}\left(1 - \frac{m^2_{\tilde{\tau}_L}}{m^2_t}\right)^{-2}.$$
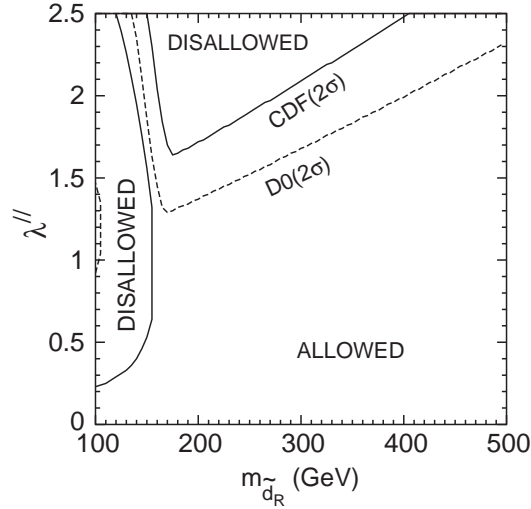(7.17)

Fig. 7.37. Allowed regions in the plane of λ''_{3ki} and the mass of the right d-squark in a baryon-number-violating scenario. Solid (dashed) lines correspond to the 2-σ bounds from the CDF (D0) collaborations.

Similarly the hadron two-body decay channels $t \rightarrow \bar{d}_j + \bar{\tilde{d}}_{kR}$ with λ'' couplings have an impact on the $t\bar{t}$ events through a modification in the fraction of hadron top quark decays. Performing a similar analysis to the one above for the $\not{R}_p$ decay modes $t \rightarrow \bar{b}\tilde{\bar{s}}$ initiated by the λ''_{323} coupling where the $t\bar{t}$ pairs cascade down to a 5 jets final state leads to an induced reduction factor on the multiple jet signal of $(1 + 0.16\lambda''^2_{323})$. Aside from ruling out the associated $\not{R}_p$ coupling constants, one can evade a conflict with the experimental observations by closing the relevant decay channels by assuming stau or squark masses larger than 150 GeV.

Before closing this subsection on fermion pair production one has to keep in mind that allowing for more than one dominant $\not{R}_p$ coupling leads to further possibilities for fermion pair production at both leptonic and hadron colliders.

At leptonic colliders, dilepton production involving two dominant λ_{ijk} couplings such as for example $e^+e^- \rightarrow \mu^+\mu^-$ involving λ_{131} and λ_{232} with s-channel $\tilde{\nu}_\tau$ exchange or $e^+e^- \rightarrow \tau^+\tau^-$ involving λ_{131} and λ_{232} with a s-channel $\tilde{\nu}_\mu$ exchange have been considered [519,523]. Di-jet production can also occur in processes involving λ_{ijk} and λ'_{ijk} couplings with s-channel $\tilde{\nu}$ exchange. For example $e^+e^- \rightarrow b\bar{b}$ involving λ_{131} and λ'_{333} or $e^+e^- \rightarrow d\bar{d}$ involving λ_{131} and λ'_{311} both with s-channel $\tilde{\nu}_\tau$ exchange have been discussed in [477,503]. Since the angular distribution of the d and $\bar{d}$ jets is nearly isotropic on the sneutrino resonance, the strong forward–backward asymmetry in the Standard Model continuum, $A_{\text{FB}}(b) \approx 0.65$ at $\sqrt{s} = 200$ GeV, is reduced to ≈ 0.03 on top of the sneutrino resonance [503].

Studies involving products of λ coupling, products of λ' and products of λ with λ' couplings at $\mu^+\mu^-$ colliders have been performed in [526].

At hadron colliders the third generation slepton resonant production i.e. $\tilde{\nu}_\tau$ tau-sneutrino (neutral current) and $\tilde{\tau}$ stau (charged current) involving weakly constrained $\lambda'_{311}\lambda_{3jk}$ coupling constants thus leading to lepton pair production, have been considered in [531] for both the Tevatron and LHC colliders. The reach in terms of the slepton mass ranges from 800 GeV at the Tevatron Run II to 4 TeV at the LHC for sizeable values of $X = \lambda'_{311}\lambda_{3jk}B_l$, B_l being the leptonic branching ratio, from $X \approx 10^{-3}$ down to $X = 10^{-(5-8)}$ the latter for small slepton masses of the order of hundred GeV. In the particular case of e^+e^- production, existing Tevatron data [532] from the CDF detector on the e^+e^- production have been exploited in [503] to derive the following bounds on the product $\lambda'_{311}\lambda_{311}$ (with some theoretical uncertainties coming from the knowledge of K factor for slepton production):

$$(\lambda'_{311}\lambda_{311})^{1/2} < 0.08\Gamma^{1/4}_{\tilde{\nu}_\tau} \tag{7.18}$$

for sneutrino masses in the range 120–250 GeV where $\Gamma_{\tilde{\nu}_\tau}$ denotes the sneutrino width in units of GeV. The particular cases of $\mu^+\mu^-$ and $\tau^+\tau^-$ productions have been considered in [315] making use of the total cross-sections above a given threshold on the dilepton invariant mass, in order to get rid of the background from the s-channel Z resonance contribution.

Furthermore, the distinction between a scalar or a new gauge boson resonance can be performed [531] by testing the lepton universality and by measuring the forward–backward asymmetry which is expected to be zero in the case of a resonant scalar production and non-zero in the case of a new gauge boson resonance as well as the leptonic charge asymmetry defined as

$$A(\eta) = \frac{\dfrac{\mathrm{d}N_+}{\mathrm{d}\eta} - \dfrac{\mathrm{d}N_-}{\mathrm{d}\eta}}{\dfrac{\mathrm{d}N_+}{\mathrm{d}\eta} + \dfrac{\mathrm{d}N_-}{\mathrm{d}\eta}} \tag{7.19}$$

where $N_\pm$ are the number of positively/negatively charged leptons of a given rapidity η. The presence of the slepton tends to drive the leptonic charge asymmetry to smaller absolute values while a new W' gauge boson substantially increases the magnitude of this asymmetry. At the Tevatron Run II, the minimum value of the product $\lambda\lambda'$ for which the asymmetry differs significantly from the Standard Model expectation is 0.1, for a $\mathscr{L} = 2\,\mathrm{fb}^{-1}$, assuming $m_{\tilde{l}} = 750\,\mathrm{GeV}$ and $\Gamma_{\tilde{l}}/m_{\tilde{l}} = 0.004$.

7.6.2. $\not{R}_p$ Contributions to FCNC

In the Standard Model flavor changing neutral current effects arise through loop diagrams. They are strongly suppressed [533–535] because of the CKM matrix unitarity and the quark mass degeneracy (except the top quark) relative to the Z boson mass. In several supersymmetric extensions of the Standard Model like the MSSM the large flavor changing neutral current effects are expected to be reduced by assuming either a degeneracy of the soft supersymmetry breaking scalars masses or an alignment of the fermion and scalar superpartners mass matrices [536]. In addition flavor changing decay rates such as $Z \to q_J \bar{q}_{J'}$ through triangle diagrams involving squarks and gluinos have been found to be small with respect the Standard Model predictions [537,538].

The $\not{R}_p$ interaction, because of its non-trivial flavor structure, opens up the possibility of observable flavor changing effects at the tree level.

The $\not{R}_p$ interactions contributions to the Z boson flavor off-diagonal decays branching ratios were discussed in Section 6.3.2.

At colliders, these flavor changing $\not{R}_p$ processes occur through the exchange of a supersymmetric scalar particle in the s- or t-channel and lead to fermion pair productions $f_J f_{J'}$ with $J \neq J'$.

Furthermore, in minimal supersymmetric extension of the Standard Model without degeneracies for sleptons masses, flavor changing effects can be induced in the supersymmetric particle pair production involving $\not{R}_p$ interactions.

At leptonic colliders, with center-of-mass energies above the Z boson pole, single top quark production such as $l_i^+ l_i^- \to t\bar{c},\ \bar{t}c$ occurring via the exchange of a $\tilde{d}_{kR}$ squark in the t-channel through the $\not{R}_p$ couplings λ'_{i2k} and λ'_{i3k} offers a clean opportunity to observe one of these tree level flavor changing neutral current effects [539–543]. Indeed single top quark production occurring at the one loop level in the Standard Model [533–535] is suppressed with respect to $b\bar{s}$ production since it does not receive large contributions from heavy fermions in the loop. Moreover the MSSM contribution has been shown to be small compared to the Standard Model one [537,538]. The cross-section of $e^+e^- \to t\bar{c} + \bar{t}c$ is shown in Fig. 7.38 from [540] for $\lambda'_{12k}\lambda'_{13k} = 0.01$ which is the order of magnitude of the low-energy constraint on this product of $\not{R}_p$ couplings for $m_{\tilde{f}} = 100\,\mathrm{GeV}$.

The reaction $e^+e^- \to t\bar{c} + \bar{t}c$ receives also contributions at one loop level from the λ'' interactions [542,540] in which a $\tilde{d}_R$ squark is involved with the λ''_{2jk} and λ''_{3jk} coupling constants. In particular the combination $\lambda''_{223}\,\lambda''_{323}$ with a low energy constraint of $\lambda''_{223}\,\lambda''_{323} < 0.625$ which is less stringent than the constraints of the other $\lambda''_{2jk}\,\lambda''_{3jk}$ combinations can lead to cross-sections as big as 1 fb for $m_{\tilde{d}_{kR}} = 100\,\mathrm{GeV}$.

The $t\bar{c}/\bar{t}c$ production can also occur at one loop level via photon–photon reactions $e^+e^- \to \gamma\gamma \to t\bar{c} + \bar{t}c$ which involve the products of $\not{R}_p$ couplings $\lambda'_{i2k}\lambda'_{i3k}$ when $\tilde{l}_{iL}$ sleptons or $\tilde{d}_{kR}$ squarks are exchanged in the loop and the products $\lambda''_{2jk}\lambda''_{3jk}$ when $\tilde{d}_R$ squarks run in the loop. Again the combinations $\lambda'_{323}\lambda'_{333}$ ($\lambda''_{223}\lambda''_{323}$) which have less stringent low-energy constraints than the other $\lambda'_{i2k}\lambda'_{i3k}$ ($\lambda''_{2jk}\lambda''_{3jk}$) combinations lead to cross-sections which are about an order of magnitude below the cross-sections of Fig. 7.38 from tree level diagrams involving $\lambda'_{12k}\,\lambda'_{13k}$. A combination of the results from the e^+e^- and $\gamma\gamma$ collisions would allow to distinguish between the λ' and λ'' effects on the $t\bar{c}/\bar{t}c$ production.

On the experimental side the $t\bar{c}$ or $\bar{t}c$ production can lead to $bcl\nu$ final state. The background from Standard Model processes such as $e^+e^- \to W^+W^- \to bcl\nu$ can then be significantly reduced by observing that the c-quark has a
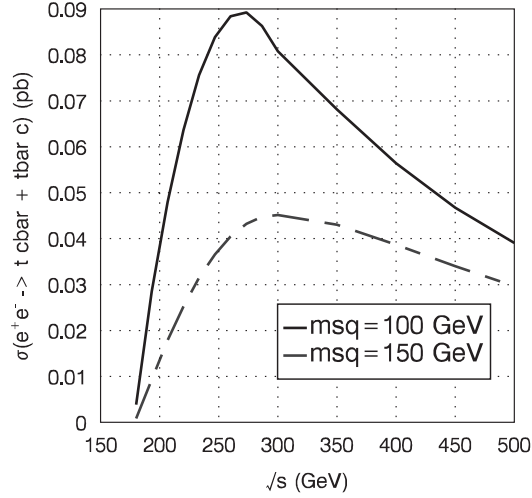
Fig. 7.38. Cross-section of the reaction $e^+e^- \to t\bar{c} + \bar{t}c$ as a function of the center-of-mass energy for $\lambda'_{12k}\lambda'_{13k} = 0.01$. The solid line corresponds to $m_{\tilde{d}_{kR}} = 100\,\text{GeV}$ and the dashed line to $m_{\tilde{d}_{kR}} = 150\,\text{GeV}$.
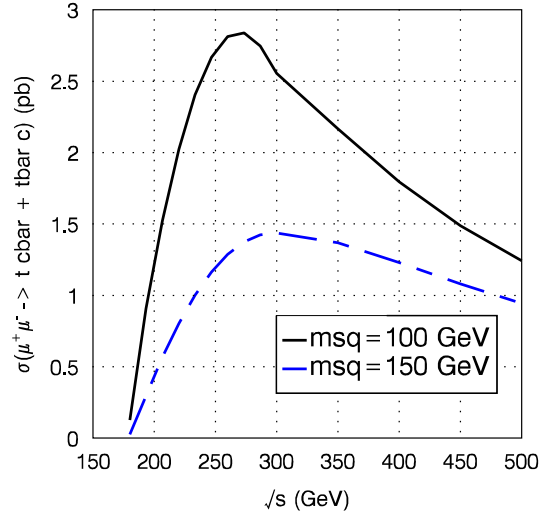
Fig. 7.39. Cross-section of the reaction $\mu^+\mu^- \to t\bar{c} + \bar{t}c$ as a function of the center-of-mass energy for $\lambda'_{223}\lambda'_{233} = 0.065$. The solid line corresponds to $m_{\tilde{d}_{kR}} = 100\,\text{GeV}$ and the dashed line to $m_{\tilde{d}_{kR}} = 150\,\text{GeV}$.

fixed energy given by [541]:

$$E(c) = (s + m_t^2 - m_c^2)/2\sqrt{s} \; . \tag{7.20}$$

Searches for $t\bar{c}$ or $\bar{t}c$ production have been performed at LEP_{II} along these lines. However they have not yet allowed to put a more stringent constraint on $\lambda'_{12k}\lambda'_{13k}$ than those coming from low energy. Searches for $t\bar{c}$ or $\bar{t}c$ production will be performed at the future linear collider. The study of the final state $bc l v$ would allow to probe values of the product $\lambda'_{12k}\lambda'_{13k}$ down to ~ 0.1 for $m_{\tilde{d}_{kR}} = 1\,\text{TeV}$ at a linear collider with a center-of-mass energy of $\sqrt{s} = 500\,\text{GeV}$ and a luminosity of $\mathscr{L} = 100\,\text{fb}^{-1}$ [541].

The $t\bar{c}$ or $\bar{t}c$ production can occur at $\mu^+\mu^-$ colliders as well. The cross-section for such a production is shown in Fig. 7.39 from [540] for $\lambda'_{223}\lambda'_{233} = 0.065$ which is equal to its low-energy limit for $m_{\tilde{f}} = 100\,\text{GeV}$. An additional motivation for this choice of $\not{R}_p$ couplings is provided by the observation that among the possible $\lambda'_{22k}\lambda'_{23k}$ combinations the $\lambda'_{223}\lambda'_{233}$ one has the less stringent low-energy constraint.

Table 7.18
Sensitivities on the product $\lambda''_{132}\lambda''_{312}$ for various $m_{\tilde{s}_R}$ at the upgraded Tevatron from the process $u_1\bar{d}_1 \to \tilde{s}_R \to t\bar{b}$ from [548]

$m_{\tilde{s}_R}$ in GeV	100	200	300	400	500	600	700	800
$\lambda''_{132}\lambda''_{312}$	0.01	0.02	0.03	0.04	0.06	0.08	0.1	0.13

Finally flavor changing effects in sfermion pair production can be investigated in high precision measurements planned to be performed for example at future leptonic linear colliders [544]. The $\not{R}_p$ interactions can generate such effects through the exchange of a neutrino in the t-channel in slepton pair production $e^+e^- \to \tilde{l}_J\tilde{l}^*_{J'}, (J \neq J')$. The flavor non-diagonal rates vary in the range $\sigma_{JJ'} \approx (\frac{\Lambda}{0.1})^4(2-20)$ fb [545] with $\Lambda = \lambda, \lambda'$ for sleptons masses $m_{\tilde{l}} < 400$ GeV as one covers center-of-mass energy regions from the Z boson pole up to the TeV *region*. Due to the strong dependence on the $\not{R}_p$ couplings, the flavor non-diagonal rates reach smaller values than the rates obtained in the flavor oscillations approach [546] which range between 250(100) and 0.1(0.01) fb for $\sqrt{s} = 190(500)$ GeV.

At hadron colliders flavor changing lepton pair productions $l_jl_{j'}$ as well as quark pair productions $q_jq_{j'}$ $(j \neq j')$ are both expected to be challenging to search for since the environment in terms of background is not as clean as the environment at leptonic colliders.

For example flavor changing lepton pair productions occur from an initial state $d_j\bar{d}_k$ $(d_k\bar{d}_k)$ through the exchange of a $\tilde{\nu}^i_L$ sneutrino ($\tilde{u}^j_L$ squark) in the s-channel (t-channel) via the couplings product $\lambda'_{ijk}\lambda_{iJJ'}$ $(\lambda'_{Jjk}\lambda'_{J'jk})$, or, from an initial state $u_j\bar{u}_j$ through the exchange of a $\tilde{d}^k_R$ squark in the t-channel via the couplings product $\lambda'_{Jjk}\lambda'_{J'jk}$. More specific studies on flavor changing lepton pair productions remain to be done.

More striking signatures of $\not{R}_p$ induced flavor changing neutral current effects could be observed in rare decays of the top quark as discussed in Section 6.4.1.

Finally the possibility of single top quark production via squark and slepton exchanges to probe several combinations of $\not{R}_p$ couplings at hadron colliders has been studied in [547–550]. Initial state partons such as $u\bar{d}$ are particularly relevant for $p\bar{p}$ colliders such as the Tevatron while the ud initial state system is more relevant for pp colliders such as the LHC.

The single top quark production $u_i\bar{d}_j \to t\bar{b}$ can occur via the exchange of a $\tilde{d}^k_R$ squark in the t-channel, through the product of couplings $\lambda''_{i3k}\lambda''_{3jk}$. The choice of the initial state of the reaction $u_i\bar{d}_j \to t\bar{b}$ fixes the flavor indices of the coupling constants product $\lambda''_{i3k}\lambda''_{3jk}$ because of the antisymmetry of the generation indices of the coupling constants λ''. Furthermore, because of the low energy constraints and the low parton luminosities, the only product of interest is $\lambda''_{132}\lambda''_{312}$. Assuming the observability criteria $\Delta\sigma/\sigma_0 > 20\%$ where $\Delta\sigma$ is the $\not{R}_p$ cross-section and σ_0 is the Standard Model cross-section, Table 7.18 from [548] shows the sensitivities on $\lambda''_{132}\lambda''_{312}$ at the upgraded Tevatron for various $m_{\tilde{s}_R}$.

The single top quark production $u_j\bar{d}_k \to t\bar{b}$ can also occur through the exchange of a $\tilde{l}^i_L$ slepton in the s-channel via the couplings product $\lambda'_{ijk}\lambda'_{i33}$. The dominant process $u\bar{d} \to \tilde{l}^i_L \to t\bar{b}$ which involves the sum of couplings $\lambda'_{111}\lambda'_{133} + \lambda'_{211}\lambda'_{233} + \lambda'_{311}\lambda'_{333}$ has been considered in [549]. According to [549] values of λ' couplings below the low energy bounds can be probed if the slepton mass lies in the range 200 GeV $< m_{\tilde{l}_L} < 340$ GeV for the upgraded Tevatron and in the range 200 GeV $< m_{\tilde{l}_L} < 400$ GeV for the LHC. Although larger parton momenta are allowed at the LHC the result is not really improved at LHC because of the relative suppression of the $\bar{d}$ quark structure function compared to the d quark one.

Turning to the case of u_id_j initial state partons, the single top quark production can also occur through the exchange of a $\tilde{d}^k_R$ squark in the s-channel via the couplings product $\lambda''_{ijk}\lambda''_{33k}$. Table 7.19 gives an example of the cross-section obtained from different initial parton states at the LHC. Sensitivities on the coupling product $\lambda''_{212}\lambda''_{332}$ at the upgraded Tevatron and at the LHC have been obtained in [549]. A more detailed simulation has been performed in [550] and the sensitivities on the coupling product $\lambda''_{212}\lambda''_{332}$ are shown in Fig. 7.40. The reaction $u_jd_k \to tb$ receives also a contribution from the exchange of a $\tilde{l}^\pm_{iL}$ slepton in the u-channel via the λ'_{ij3} and λ'_{i3k} couplings [550].

Supersymmetric particle masses reconstruction have been also performed within the framework of single top production in [550].

Table 7.19
Cross-section in *pb* of the reaction $u_i d_j \rightarrow \tilde{d}_R^k \rightarrow tb$ at LHC for a squark of mass of 600 GeV assuming and $\lambda''_{ijk} = 0.1$ and $\Gamma_{R_p}(\tilde{q}) = 0.5$ GeV where $\Gamma_{R_p}(\tilde{q})$ is the width of the exchanged squark due to *R*-parity conserving decay

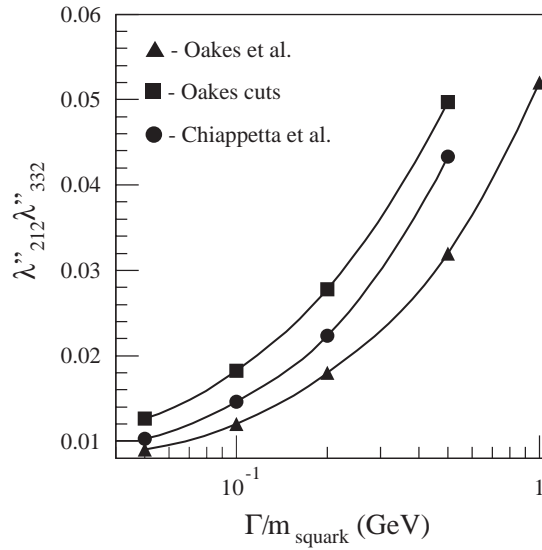| Initial partons	cd	cs	ub	cb	
Exchanged particle	$\tilde{s}$	$\tilde{d}$	$\tilde{s}$	$\tilde{d}$	$\tilde{s}$
Couplings	$\lambda''_{212}\lambda''_{332}$	$\lambda''_{212}\lambda''_{331}$	$\lambda''_{132}\lambda''_{332}$	$\lambda''_{231}\lambda''_{331}$	$\lambda''_{232}\lambda''_{332}$
Cross-section in pb	3.98	1.45	5.01	0.659	

Fig. 7.40. Sensitivity limits on the $\lambda''_{212}\lambda''_{332}$ Yukawa couplings obtained from the analysis of the reaction $cd \rightarrow \tilde{s}^* \rightarrow tb$ at the LHC after 1 year with low luminosity for $m_{\tilde{s}} = 300$ GeV, found in [550] (circles) and in [549] (triangles). The squares indicate the results obtained in [550] by applying the simplified cuts used in [549].

To summarize, the studies of single top quark production at hadron colliders [547–550] tend to indicate that the LHC is better at probing the *B*-violating couplings λ'' whereas the Tevatron and the LHC have a similar sensitivity to λ' couplings. Furthermore, this is the only framework in which the constraints on λ'' from physics at colliders are comparable or better than the low energy bounds on the λ'' coupling constants.

7.6.3. $\not{R}_p$ Contributions to CP violation

As already discussed in Section 6.3.4 the $\not{R}_p$ coupling constants can have a complex phase and hence be by themselves an independent source of *CP* violation motivating many studies on low energy $\not{R}_p$ physics. These can still lead to new tests of *CP* violation in combination with the other possible source of complex phase in supersymmetric extensions of the Standard Model such as the MSSM even if one assumes that the $\not{R}_p$ interactions are *CP* conserving. For instance the $\not{R}_p$ couplings can bring a dependence on the CKM matrix elements due to the fermion mass matrix transformation from current basis to mass basis.

A study of *CP* violation effects in association with sneutrino flavor oscillations has been carried out in Section 5.5. The *CP* violation effects from $\not{R}_p$ couplings in the $K^o \bar{K}^o$ system and in hadrons decays asymmetries has been discussed in Section 6.3.4. The *CP* asymmetries at the *Z* boson pole has been discussed in Section 6.3.4.

At colliders, *CP* violation effects from $\not{R}_p$ couplings can also be further studied from fermion pair productions either flavor changing or non flavor changing. These effects are either controlled by interference terms between tree and loop amplitudes in the case of *CP* asymmetries or directly considered from tree level processes.

Furthermore, if both non-degeneracies and mixing angles between all slepton flavors and if the *CP* odd phase do not vanish, *CP* violation asymmetries can also be observable in supersymmetric particles pair production. The *R*-parity odd interactions can provide an alternative mechanism for explaining *CP* violation asymmetries in such productions through possible ψ *CP* odd phase incorporated in the relevant dimensionless coupling constant.

At leptonic colliders the effects of $\not{R}_p$ interactions on the CP asymmetries in the processes $l^+l^- \rightarrow f_J \bar{f}_{J'}$, with $J \neq J'$, were calculated in [542]. The $\not{R}_p$ contributions to these CP asymmetries are controlled by interference terms between tree and loop level amplitudes. The discussion of loop amplitudes was restricted to the photon and Z boson vertex corrections. The off Z boson pole asymmetries is given by:

$$\mathscr{A}_{JJ'} = \frac{\sigma_{JJ'} - \sigma_{J'J}}{\sigma_{JJ'} + \sigma_{J'J}} , \tag{7.21}$$

where $\sigma_{JJ'} = \sigma(l^+l^- \rightarrow f_J \bar{f}_{J'})$. Defining ψ as the CP odd phase, these asymmetries lie at $\mathscr{A}_{JJ'} \approx (10^{-2}\text{–}10^{-3}) \sin \psi$ for leptons and quarks irrespective of whether one deals with light or heavy flavors.

The CP asymmetries $\mathscr{A}_{JJ'}$ depend on a ratio of different $\not{R}_p$ coupling constants and are therefore less sensitive to the absolute magnitude of these couplings than the flavor changing rates $\sigma_{JJ'}$ which involve higher power of the $\not{R}_p$ constants. The particular dependence of the CP asymmetries on the couplings is of the form $Im(\lambda\lambda^*\lambda\lambda^*)/\lambda^4$ and may thus lead to strong enhancement or suppression factors depending on the largely unknown flavor hierarchical structure of the involved Yukawa couplings. For example the study of single top production $l^+l^- \rightarrow t\bar{c}$ with $t \rightarrow bW \rightarrow bl\nu$ allows to learn about CP violation in the quark sector. In this reaction the CP violation can be probed through the asymmetry defined in Eq. (7.21) or via the following flavor off-diagonal CP asymmetry [541]:

$$\mathscr{A}_{+-} = \frac{\dfrac{d\sigma^+}{dE_l} - \dfrac{d\sigma^-}{dE_l}}{\dfrac{d\sigma^+}{dE_l} + \dfrac{d\sigma^-}{dE_l}} , \tag{7.22}$$

where $\sigma^+ = \sigma(l^+l^- \rightarrow t\bar{c} \rightarrow b\bar{c}l\nu)$, $\sigma^- = \sigma(l^+l^- \rightarrow \bar{t}c \rightarrow \bar{b}cl\bar{\nu})$ and E_l is the energy of the produced charged lepton. The values of this CP asymmetry $\mathscr{A}_{+-}$ range typically in $\mathscr{A}_{+-} \approx (10^{-2}\text{–}10^{-3}) \sin \psi$ for $E_l < 300\,\text{GeV}$ [541]. These $\mathscr{A}_{JJ'}$ and $\mathscr{A}_{+-}$ CP asymmetries can be enhanced up to $\sim 10^{-1} \sin \psi$ if the $\not{R}_p$ coupling constants exhibit large hierarchies with respect to the generations.

Turning now briefly to CP violation asymmetries in supersymmetric particles pair production, as in the case of flavor changing fermion pair production, the $\not{R}_p$ contributions to these CP asymmetries in scalar particles pair production are controlled by interference terms between tree and loop level amplitudes. For example the flavor non-diagonal CP asymmetries $\mathscr{A}_{JJ'}$ for the slepton pair production, $e^+e^- \rightarrow \tilde{l}_J \tilde{l}_{J'}^*$ ($J \neq J'$) are predicted to be $\mathscr{A}_{JJ'} \approx (10^{-2}\text{–}10^{-3}) \sin \psi$ [545].

Finally, the $\not{R}_p$ interactions can give rise to CP violation effects at tree level in the non flavor changing reaction $e^+e^- \rightarrow \tau^+\tau^-$ via the observation of the double spin correlations of the produced tau-leptons pair.

This possibility studied in [253] stands out as an very interesting issue by itself since previous studies of CP-violating effects in the process $e^+e^- \rightarrow \tau^+\tau^-$ which can happen for instance in models with multi-Higgs doublet or in leptoquark, Majorana $\tilde{\nu}$ or supersymmetry models, all occur at one loop level.

Here the CP asymmetries are generated from the exchange of a resonant $\tilde{\nu}_\mu$ sneutrino in the s-channel via the real coupling λ_{121} and the complex coupling λ_{323} if a $\tilde{\nu}_\mu - \bar{\tilde{\nu}}_\mu$ mixing exists. This sneutrino mixing can generate both CP-even and CP-odd spin asymmetries which are forbidden in the Standard Model and that can be measured for τ leptons at leptonic colliders. The observation of such asymmetries would provide explicit information about three different aspects of new physics: $\tilde{\nu}_\mu - \bar{\tilde{\nu}}_\mu$ mixing, CP violation and $\not{R}_p$. The sneutrino–antisneutrino mixing phenomena which have been gaining some interest recently [250,184,551] is interesting since it is closely related to the generation of neutrino masses [250,184]. The polarization asymmetries from double spin correlations of the produced tau-leptons pair provide a feasible alternative for establishing the mass splitting between the CP even $\tilde{\nu}_+^\mu$ and CP odd $\tilde{\nu}_-^\mu$ muon-sneutrino mass eigenstates[253]. These polarization asymmetries depend on the relative values of the real part, a, and the imaginary part, b, of the complex coupling constant λ_{323}. At the next linear collider with $\sqrt{s} = 500\,\text{GeV}$ [253], with the simultaneous measurement of the CP conserving and CP-violating asymmetries, the whole range $0 \leqslant b/(a+b) \leqslant 1$ can be probed to at least 3σ in the $m_{\tilde{\nu}_\mu}$ mass range of 20 GeV around resonance i.e. $\sqrt{s}-10\,\text{GeV} < m_{\tilde{\nu}_\mu} < \sqrt{s} + 10\,\text{GeV}$ even for a small mass splitting of 1 GeV.

At hadron colliders, in analogy to the case of the leptonic colliders, the resonant production of a sneutrino gives also rise to the possibility of having CP violation effects at tree level [315].

If the τ spins can be measured, *CP* violation effects in the polarization asymmetries of the hard process $d_j \bar{d}_k \rightarrow \tilde{\nu}_\mu \rightarrow \tau^+ \tau^-$ can be observed at the Tevatron. The $\not{R}_p$ coupling constant λ'_{2jk} which enters this subprocess is chosen real, while λ_{233} is taken complex in order to generate *CP* asymmetries. However, at hadron colliders, spin asymmetries deserves a careful discussion. The spin asymmetries change sign around $\sqrt{s} \approx m_{\tilde{\nu}^\mu_\pm}$ so that one has to integrate over $\sqrt{\hat{s}}$ of the initial parton system. In consequence the spin asymmetries seem too small to be measurable. Nevertheless a two-step measurement helps in overcoming this problem. In a first step one has to determine the mass of the resonant sneutrino by measuring the $\tau\tau$ invariant mass distribution and in a second step one has to integrate the absolute values of the polarization asymmetries [315].

At the Tevatron Run IIA (IIB) with $\mathscr{L} = 2\,\text{fb}^{-1}$ ($30\,\text{fb}^{-1}$), taking their low energy bounds as the values of λ'_{2jk} and $|\lambda_{233}|$ and including all j, k combinations in $d_j \bar{d}_k$ fusion, the *CP* conserving and *CP*-violating asymmetries may be detected with a sensitivity above 3σ over the mass range $155\,\text{GeV} < m_{\tilde{\nu}^\mu_\pm} < 400\,\text{GeV}$ ($155\,\text{GeV} < m_{\tilde{\nu}^\mu_\pm} < 300\,\text{GeV}$) if $\Delta m_{\tilde{\nu}_\mu} = \Gamma_{\tilde{\nu}_\mu}$ ($\Delta m_{\tilde{\nu}_\mu} = \Gamma_{\tilde{\nu}_\mu}/10$) where $\Gamma_{\tilde{\nu}_\mu}$ is the sneutrino width.

Moreover the entire range $0 \leqslant b/(a+b) \leqslant 1$ can be practically covered for $m_{\tilde{\nu}^\mu_-} = 200\,\text{GeV}$ at the Tevatron with at least 3σ standard deviations for $\Delta m_{\tilde{\nu}_\mu} = \Gamma_{\tilde{\nu}_\mu}$ ($\Delta m_{\tilde{\nu}_\mu} = \Gamma_{\tilde{\nu}_\mu}/4$).

These results show that in contrast to the case of leptonic colliders [253], the *CP* odd and *CP* even spin asymmetries can be observed over a wide $\tilde{\nu}_\mu$ sneutrino mass range of about $300\,\text{GeV}$.

8. Conclusions and prospects

After the great successes of spontaneously broken gauge theories and of the Standard Model, supersymmetric theories of particles and interactions constitute one of the best motivated frameworks for the discussion of new physics beyond the Standard Model. The reasons are profound and fundamental — although none is definitely conclusive, especially in view of the fact that the new *R*-odd superpartners have escaped, for a long time now, all experimental efforts to disclose their existence.

Among the reasons to consider supersymmetry is our desire to see bosons and fermions play similar rôles, although this is against all immediate evidence, known bosons and fermions having very different properties ! Indeed the supersymmetry algebra did not allow us to relate directly known bosons with known fermions, and we had to invent, instead, a whole new zoo of "supersymmetric particles", squarks and sleptons, gluinos, charginos and neutralinos, etc., so as to allow us to view the world as possibly supersymmetric. These objects are, precisely, the new *R*-odd particles. Not only do we have to "double everything" — which was once considered as evidence against supersymmetry — but in the usual framework of spontaneously broken gauge theories additional Higgses should also be introduced, with their associated higgsinos ! And the whole construction assumes the existence of new self-conjugate Majorana fermions, often considered as ugly beasts, only Dirac fermions being known in Nature ! Is all this too high a price to pay ? Only the future — and experiments — will tell.

But what can such supersymmetric theories do for us ? Plenty of things, many of them well-known, according to different arguments all based on the nice and attractive features of supersymmetric theories. There are also, unfortunately, less nice features, as the reader who went through detailed discussions of the many possible supersymmetry-breaking terms in *R*-parity conserving and *R*-parity-violating theories will certainly have noticed.

Among the attractive features is the fact that, in supersymmetric theories — which are closely related with gravitation — the Higgs potential is largely determined by the supersymmetry. The quartic Higgs boson self-coupling (λ in the Standard Model), or rather self-couplings (for two Higgs doublets), instead of being arbitrary, are now fixed by g^2 and $g^2 + g'^2$, a fact at the origin of many relations involving massive gauge bosons and Higgs bosons. The new particles introduced also allow for an appropriate high-energy convergence of the three $SU(3)$, $SU(2)$ and $U(1)$ gauge couplings, whose values get unified, as it would be the case in a grand-unified theory. Supersymmetric theories also have improved convergence properties at the quantum level, leading to hopes of solving or alleviating the hierarchy problems associated with the extreme smallness of the cosmological constant Λ, or the smallness of m_W and m_Z compared to the GUT or Planck scales (although these hints towards solutions would still have to survive supersymmetry-breaking). Supersymmetry usually also appears as a necessary ingredient in the construction of consistent string (and brane) theories — and, even without having to consider strings and branes at all, shows us the way towards new spacetime dimensions...

C Doctorat 93-95 : Algèbre quantique $U_{qp}(u_2)$ et ...

Ce travail porte sur l'étude des nouvelles symétries en physique. Il se compose de trois parties. La première est dédiée à l'étude de l'algèbre quantique Uqp(u2). Plus précisément, nous développons sa structure d'algèbre de Hopf et portons un intérêt particulier sur sa structure de coproduit. Les bases d'une théorie de la représentation de Uqp(u2) sont introduites, d'une part, en construisant ses représentations irréductibles de dimension finie et, d'autre part, en calculant ses coefficients de Clebsch et Gordan par la méthode de l'opérateur de projection extrémal. Nous complétons notre étude par la construction de quelques réalisations en termes de bosons déformés des algèbres quantiques $Uqp(u_2)$, $Uq(su_2)$ et $Uqp(u(1,1))$.

La deuxième partie est consacrée à la construction d'un modèle phénoménologique de rotateur non rigide se basant sur l'algèbre quantique $Uqp(u_2)$. L'énergie de rotation et les probabilités de transition réduites E2 sont obtenues en fonction des deux paramètres de déformation de l'algèbre quantique. Nous montrons comment et, dans quelle mesure, l'utilisation de la double déformation de l'algèbre $Uqp(u_2)$ permet de généraliser le modèle du rotateur en symétrie $Uq(su_2)$. Nous introduisons également un modèle de l'oscillateur anharmonique sur la base de cette algèbre quantique. Nous montrons que les systèmes physiques du rotateur non rigide et de l'oscillateur anharmonique peuvent être couplés par l'intermédiaire des paramètres de déformation de $Uqp(u_2)$. Un spectre de ro-vibration est obtenu sous la forme d'un développement à la Dunham de l'énergie.

L'objet de la troisième partie est l'application de notre modèle de rotateur à la dynamique collective de rotation dans les noyaux super-déformés des régions de masse A=130-150 et A=190 et des isomères de fission dans les actinides et les terres rares. Une analyse comparative est menée sur les énergies de transitions issues de l'ajustement et sur les valeurs des paramètres. Nous calculons à partir des expressions des énergies de rotation les moments d'inertie dynamiques. Une comparaison des résultats obtenus pour différents modèles permet de mettre en évidence le rôle des paramètres de déformation de l'algèbre quantique $Uqp(u_2)$.

Curriculum vitae

Rémi BARBIER

> Né le 28 Août 1970
>
> Deux enfants
>
> Maître de conférences à l' Université Claude Bernard Lyon 1
>
> laboratoire : IPNL UMR5822 IN2P3/CNRS
>
> mail : rbarbier@ipnl.in2p3.fr
>
> tél : 00 +33 (0)4 72 43 12 22
>
> url : www.ipnl.in2p3.fr/ebcmos

Responsabilités scientifiques :

2012 2004	*Responsable de l'équipe ebCMOS*	R&D et applis	groupe leader
2004 2002	*Responsable de l'activité imagerie*	R&D μPET	coordination
2001 1999	*Groupe de travail RPV SUSY*	Analyse DELPHI	team convenior

Note AERES 2010 de l'équipe ebCMOS : A+

Qualité scientifique et production	A+
Rayonnement et attractivité	A+
Stratégie et gouvernance	A+
Appréciation du projet	A+

Projets réalisés et coordonnés

2014 2012	*RAPID DGA MULTIMOS*	E2V	carac. et bancs
2013 2011	*LuSEApher sur ANTARES*	CPPM	proto. + appli
2010 2009	*Maturation Technologique*	Lyon Science Transfert	acqu. 10 Gbits/s
2009 2003	*Prototype ebMI5*	PHOTONIS et IPHC	proto + applis
2012 2007	*Prototype LUSIPHER*	PHOTONIS et IPHC	proto + applis
2010 2007	*FUI DZETA*	PHOTONIS	mesures et bancs
2009 2007	*Collab. de recherche*	SAGEM DS et IPHC	mesures et bancs
2004 2002	*ACI Tech. Santé INOTEP*	CERMEP et LPCML	proto. μTEP
2001	*ATIPE Jeune Chercheur*	IN2P3	capteur CMOS

Prix - Distinction
2009   *Prix de la valorisation et du transfert de technologie de l'IN2P3*

Brevet
2008   *Procédé de traitement pour un capteur sensible au photon unique et dispositif en faisant applications,*
       Barbier R. et Estre N. FR-0858504 - PCT/FR2009/052455

Encadrement de thèse
2009   *Etude de la passivation du silicium dans des conditions d'irradiation ...*
       Romain Cluzel (Bourse CIFRE)
2012   *Détection de photons uniques et super-résolution*
       Thomas Cajgfinger (Bourse école doctorale)

Expertise, revue d'articles, commissions , jury
  – Rapporteur sur projets ANR Blanc
  – Reviewer pour Nuclear Inst. and Methods in Physics Research, A
  – Membres de la commission de spécialiste section 29 UCBL (4 ans)
  – Membre du conseil de Laboratoire de l'IPNL (4 ans)
  – Membre du conseil scientifique de l'IPNL (2012)
  – membre de Jury de concours IR CNRS (Strasbourg)
  – Membre de comités de sélection MCF (Université Marseille et Paris Diderot)

Principales publications
Prototype ebCMOS : LUSIPHER	[58] [59] [60]
Prototype ebCMOS : ebMIMOSA5	[61]
Publications DELPHI en auteur principal	[62] [63] [64]
Publication sur la R-parité violée (chap. 7)	[65]
Publications sur la R&D TEP	[66] [67]
Publications du travail de doctorat	[68] [69]

Compétences scientifiques et techniques
En R&D
  – photodétecteurs : HPD, APD, MaPMT, PMT, ebCMOS, emCCD, CMOS
  – Electronique et logiciel d'acquisition de données
  – Métrologie et caractérisations aux photons uniques
  – Imagerie gamma et photons VIS et tracking CMOS
  – Méthodes de super-résolution et de tracking
  – Simulation Monte Carlo
En Physique des particules et Physique nucléaire théorique
  – Supersymétrie et violation de la R-parité, modèle Standard Masse du boson W
  – Analyse de données HEP et simulation Monte Carlo
  – Algèbre et groupe quantiques, Physique Nucléaire

Présentations -Séminaires

– Présentations aux conférences internationales : IEEE NSS, NDIP, Int. HEP (SU-SY'01 on behalf of DELPHI Collab.)
– Séminaires : IMNC (IN2P3), Journées lyonnaises de microscopie, pôle ORA ...
– Tutorial Photodetction NDIP2011 Lyon,
– Invited Talks at Int. Workshops : "lmaging and 3D electronics" Polytechnique (2007) et Ringberg All. (2008)

Enseignement de Licence, Master et réalisations pédagogiques

– Mécanique Quantique / Relativité Restreinte / Physique Nucléaire / Méthodes statistiques / Physique ondulatoire (Interférences Diffraction Réseaux) / Thermodynamique classique / Optique ondulatoire. / Mécaniqes des fluides / Electromagnétisme / Mécanique du Point / Programmation / Calcul formel - Maple / Travaux Pratiques d'optiques, d'électricité, de thermodynamique.
– Animation d'un module d'introduction à la Relativité Restreinte en L2 sous formes de TICE.
– Développement de support de Technologies de l'Information et de la communication pour l'Enseignement : co-auteur d'un module d'introduction à la relativité restreinte : cours, exercices, animations flash : Rémi Barbier et al, *Integration of information and communication technologies in special relativity teaching* **2005** *Eur. J. Phys.* **26 S13**
– Travaux Pratique sur un accélérateur Van de Graaff : expérience de Rutherford